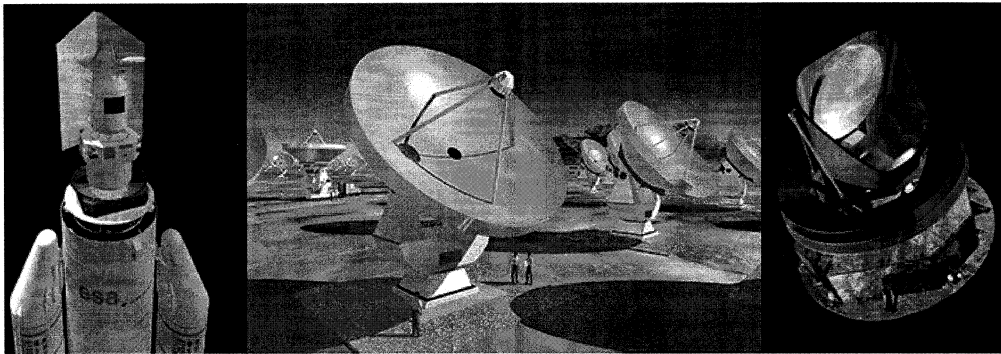


PROCEEDINGS
of the 17th INTERNATIONAL SYMPOSIUM
on SPACE TERAHERTZ TECHNOLOGY
Paris, May 10-12, 2006

Edited by Dr. Alain Maestrini & Dr. Gérard Beaudin,
Observatoire de Paris, LERMA

Observatoire de Paris, LERMA,
61, avenue de l'Observatoire,
75014 Paris, France
<http://www.space-thz.org>
Fax: +33 1 40 51 20 02

October 2007



ISSTT 2006

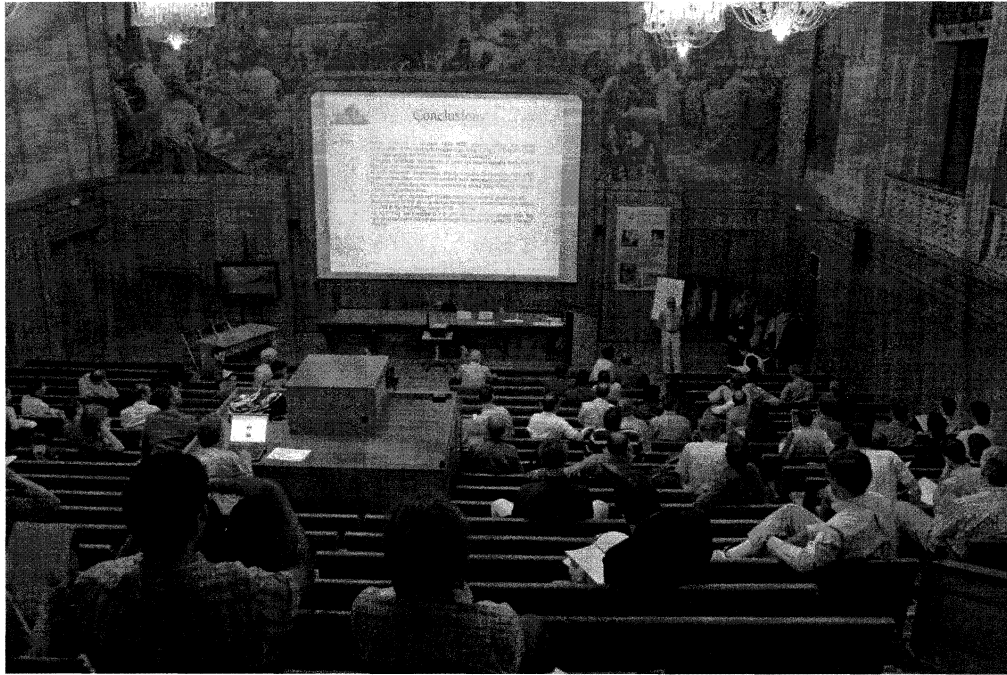
17th International
Symposium on
Space
Terahertz
Technology **Paris**
10-12 **May**

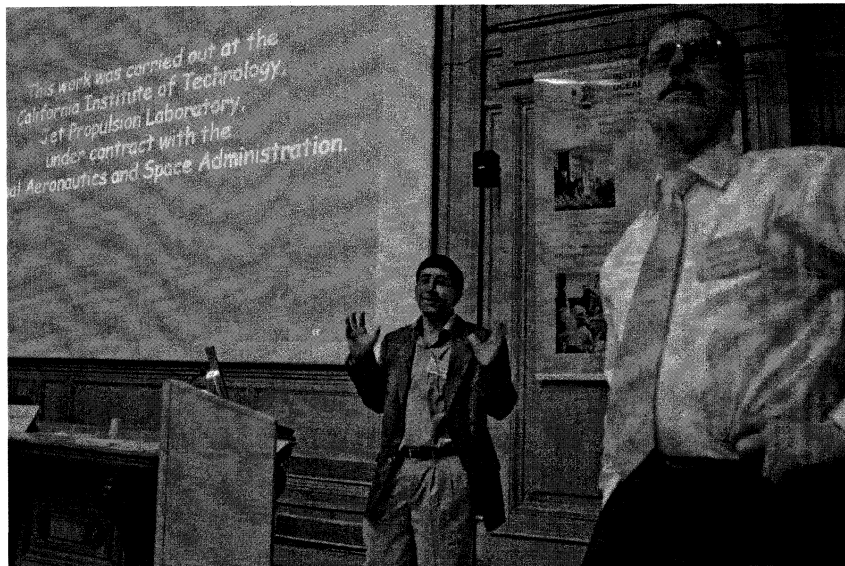
INTRODUCTION

The prime focus of the International Symposium on Space Terahertz Technology is on theory, techniques and applications in the field of space terahertz technology related areas but in reality its scope includes instrumentation for ground-based millimeter and submillimeter-wave radioastronomy. Detectors cooled or un-cooled (SIS, HEB, Schottky mixers, TES, semi-conductor bolometers, KIDs), sources (Gunn sources, frequency multipliers, FFOs, BWO, FIR lasers, photo-mixers and now QCLs), optics (lens, antennas, FSS, diplexers...) spectrometers (AOSs, auto-correlators...) and entire instruments (heterodyne cameras, bolometer arrays, HIFI, Planck,...) are the subject of this annual conference. The first 14 editions of the ISSTT conference were held in the USA. In 2005, the 16th edition was held for the first time in Europe, in Chalmers, Göteborg, Sweden. The 17th International Symposium on Space Terahertz Technology was held at the Institut Océanographique, 195 rue Saint-Jacques, 75005 Paris. The Institut Océanographique is a private institution founded in 1906 by Albert 1er, Prince of Monaco. Located in the heart of the historical center of Paris, near the Luxembourg Gardens, la Sorbonne and the Seine river, it offers an exclusive atmosphere. The entire first floor of the Institut Océanographique was dedicated to the ISSTT 2006. It included the great and the small amphitheatres, the exhibition room and the computer room (called in fact salle du conseil).

Oral presentations

Oral presentations took place in the great amphitheater only. The duration of the oral presentations was 15 minutes including questions.





Poster presentations

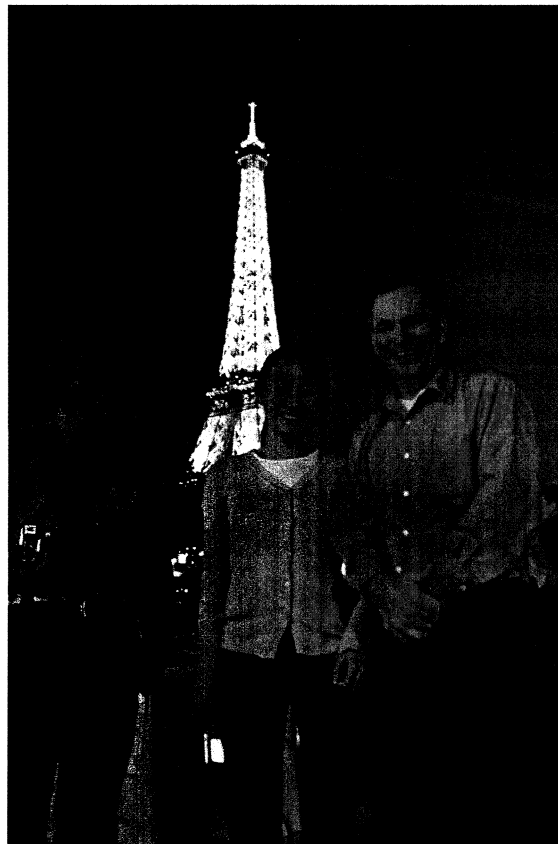
Poster sessions took place in the small amphitheater and the exhibition room located next to each other. At the entrance of each room a board indicated which posters were displayed. Posters were in vertical format up to A0 size (84x119cm). The poster session were introduced by two thirty-minute oral presentations. Dr. Jian-Ron Gao presented the first poster session while Dr. Eribert Eisele and Dr. Imran Mehdi presented the second session.

Reception at the Observatoire de Paris & Gala Diner

On Wednesday May the 10th from 18:30 to 20:00, the attendees and accompanies were invited to a reception at the Observatoire de Paris , 77 avenue Denfert Rochereau, 75014 Paris, located at only 15 minutes walk from the conference hall. Dr. Daniel Egret, director, welcomed the participants. A visit of the 17th century building was organized and an aperitif with Champagne was offered.



The gala diner was held on the river Seine, on board of the *Bel Ami*, on Thursday May 11th at 20:00 till 23:30.



ORGANIZATION

The Observatoire de Paris, the Université Pierre et Marie Curie, Supélec and the laboratoire AstroParticule et Cosmologie organized the 17th International Symposium on Space Terahertz Technology, ISSTT 2006, at the Institut Océanographique, in the historical center of Paris, on May 10-12, 2006.

The 2006 edition of the ISSTT was patronized by Prof. Pierre Encrenaz and Dr. Jean-Michel Lamarre.

For the review of the abstracts, we would like to thank the international review committee:

Prof. Thomas Crowe	Dr. Gregory Goltsman	Dr. Harald Merkel
Dr. Heribert Eisele	Dr. Karl Jacobs	Dr. Michel Piat
Prof. Neal Erickson	Dr. Anthony Kerr	Prof. Antti Räisänen
Dr. Jian-Rong Gao	Dr. Imran Mehdi	Dr. Edward Tong

The program of the conference had been arranged by the local scientific committee:

Dr Alain Maestrini (chair)		
Prof. Georges Alquié	Dr. Yan Delorme	Prof. Alain Kreisler
Dr. Gérard Beaudin	Dr. Yannick Giraud-Héraud	Dr. François Pajot
Dr. Annick Dégardin	Dr. Bruno Guillet	Dr. Michel Piat

Local organizing committee at the Observatoire de Paris:

Dr. Gérard Beaudin (chair)		
Michèle Ba-Trung	Alain Germont	Chantal Levivier
Nicole Delhayé	Dr. Bruno Guillet	Dr. Alain Maestrini
Dr. Yan Delorme	Patrice Landry	Djilali Zidani
Dr. André Deschamps	Marie-Claude Lemonnier	

with the help of Dr. Annick Dégardin and Prof. Alain Kreisler, Supélec.

The edition of proceedings of the ISSTT 2006 was arranged by Dr. Alain Maestrini at the Observatoire de Paris.

PAPERS

We accepted one hundred and two (102) abstracts. Forty-nine (49) were accepted for oral presentation while fifty-three (53) were accepted for poster presentation. For this edition of the ISSTT we had two posters sessions that were introduced by two thirty-minute oral presentations. We also had four (4) invited presentations.

SIS and HEB mixer papers represent about 40% of the total number. This underlines the importance of heterodyne detection for radio-astronomy in times where direct detection in the far-infrared makes tremendous progress toward building multi-thousand pixel cameras. New or upcoming ground-based telescopes like ALMA or APEX will use heterodyne receivers up to 950GHz and will require SIS mixers or small arrays of SIS mixers. Several authors presented their work on this type of mixer with an emphasis on side-band separation. In addition, two years before the launch of Herschel, several flight mixers for HIFI were presented. Research on HEB mixers is also a very active field, well represented at the ISSTT, due to the potential of HEB to work at THz frequencies with low noise. Several authors presented their work on THz waveguide HEB mixers or quasi-optical HEB mixers using NbN, NbTiN or MgB₂ thin films. The IF bandwidth of HEB mixers is still limited compared to other types of mixers like SIS or Schottky mixers and is the subject of several papers presented at the ISSTT.

Direct detection was well represented at the ISSTT 2006 with a dedicated oral session and a total of 11 papers including posters. Papers on single photon detectors for the far or mid-infrared and papers on instruments and technologies dedicated to CMB science were presented.

There was a relatively small number of papers on sources, 16 in total. QCLs are the subject of an increasing interest for THz local oscillators since their performances improve at a rapid pace. Photo-mixers now provide enough power for pumping SIS mixers at millimeter wavelengths. These two technologies were well represented at the ISSTT 2006. On the contrary, traditional fundamental sources like Gunn diodes or sources based on frequency multiplication were less represented at the ISSTT 2006 than in previous editions.

Several papers on novel devices and technologies like carbon-nanotubes detectors, non-linear metamaterials or MEMs were presented at the conference and a short oral session was dedicated to them. Schottky mixers, correlators, submillimeter-wave heterodyne cameras, THz heterodyne instruments, measurements of the dielectric constant of materials at submillimeter-wavelengths,... were the subject of an important number of papers, 27 in total, classified in the categories "devices, receivers, imagers and spectroscopy". Several of them could also have been presented in other categories.

The number of papers per category is the following:

- *SIS papers* : 12 oral presentations + 9 posters
- *HEB papers* : 9 oral presentations + 12 posters
- *Direct detection* : 8 oral presentations + 3 posters
- *Sources* : 6 oral presentations + 10 posters
- *Novel devices & technologies for THz* : 5 oral presentations + 1 poster
- *Devices, receivers, imagers and spectroscopy* : 9 oral presentations + 18 posters

SESSION INDEX

INVITED SESSSION	21
ORAL SESSION 1 "SIS 1"	29
POSTER SESSION 1	45
ORAL SESSION 2 "DIRECT DETECTION"	109
ORAL SESSION 3 "NOVEL DEVICES & TECHNOLOGIES for THz"	133
ORAL SESSION 4 "SIS 2"	143
INVITED PRESENTATIONS "FREQUENCY REGULATION and MANAGEMENT"	167
ORAL SESSION 5 "HEB"	175
ORAL SESSION 6 "SOURCES"	199
POSTER SESSION 2	219
ORAL SESSION 7 "DEVICES, RECEIVERS & INSTRUMENTS"	303
ORAL SESSION 8 "SUPERCONDUCTORS for IMAGERS & DETECTORS"	309
ORAL SESSION 9 "THz SPECTROSCOPY & SPECTROMETERS"	327

DETAILED SCIENTIFIC PROGRAM

(Only the presenting author is indicated)

Wednesday 10 May 2006

09:00-09:30 Conference Opening by Prof. Pierre Encrenaz.

09:30-10:15 Invited Speakers Session. Chairperson: Dr. Gérard Beaudin

Dr. JM Lamarre, Observatoire de Paris, LERMA, "The HFI instrument for Planck"

Dr. Ulf Klein, ESA, ESTEC, "Future Satellite Earth Observation Requirements and Technology in Millimetre and Sub-Millimetre Wavelength Region"

**10:45-12:00 Oral session n°1: "SIS 1".
Chairpersons: Dr. Jian-Rong Gao & Dr. Karl Jacobs**

WE1-1 Kerr: "A Superconducting 180° IF Hybrid for balanced SIS Mixers"

WE1-2 Tong: "Theory of Series-Connected Distributed SIS Mixers with Ultra-wide Instantaneous Bandwidth"

WE1-3 Justen: "RF and IF couplers for a sideband separating SIS waveguide mixer for 345 GHz focal plane array"

WE1-4 Mena: "Side-band-separating heterodyne mixer for band 9 of ALMA"

WE1-5 Karpov: "1.4 THz SIS mixer development for radio astronomy"

12:00-12:30 Poster session n°1 presentation by Dr. Jian-Rong Gao

14:00-15:30 Poster session n°1

P1-01 Banik: "VO₂ TES as Room Temperature THz Detectors"

P1-02 Camus: "Design of coplanar stripline duplexer for two-band bolometric detection integrated in large arrays of bolometers"

P1-03 Karasik: "A Phonon-Cooled Nb Direct Detector for SubMM Imaging and Spectroscopy"

P1-04 Shi: "Characterization of the Performance of a Quasi-Optical NbN Superconducting Hot-Electron Bolometer mixer"

P1-05 Gao: "Direct comparison of sensitivity between a spiral and a twin-slot HEB mixer at 1.6 THz"

P1-06 Hedden: "Characterization of Diffusion-Cooled Hot Electron Bolometers for Heterodyne Array Receiver Applications"

P1-07 Drakinskiy: "Gain bandwidth of THz NbN Hot Electron Bolometer Superconducting Mixers on thin SiO₂/SiN_x membrane"

P1-08 Drakinskiy: "16 Pixel HEB Heterodyne Receiver for 2.5 THz"

P1-09 Dauplay: "Unexpected Frequency Shift on Membrane Based Double-Slot and Double-Dipole HEB Receivers"

P1-10 Semenov: "Does the Bandwidth of a Hot Electron Bolometer depends on the Local Oscillator Frequency"

P1-11 Rodrigues-Morales: "Optimal Coupling of NbN HEB THz Mixers to Cryogenic HEMT IF Low-Noise Amplifiers"

P1-12 Baselmans: "Influence of the direct response on the heterodyne sensitivity of hot electron bolometer mixers"

P1-13 Merkel: "Quantum Noise in Hot Electron Bolometers"

- P1-14 Scherer: "Physics of ultra-thin NbN films for phonon-cooled Hot-Electron-Bolometers"
- P1-15 Kreisler: "Fabrication and characterization of ultrathin PBCO/YBCO/PBCO constrictions for further application as hot electron bolometer terahertz mixers"
- P1-16 de Lange: "The Band 3 and 4 Flight Model mixer units for HIFI"
- P1-17 Baryshev: "Design and development of a 600-720 GHz receiver for ALMA Band 9"
- P1-18 Shitov: "Development of balanced mixers for ALMA Band-10"
- P1-19 Grimes: "Analysis of subharmonic SIS mixers using SuperMix"
- P1-20 Teipen: "Analysis of the influence of Current Density J_c and DC-Quality Q on Mixer Performance around 700 GHz for more than 50 measured SIS-Mixers"
- P1-21 Navarrini: "Test of 1 mm Band Turnstile Junction Waveguide Orthomode Transducer"
- P1-22 Gulevich: "Generation of THz radiation with the use of Vortices located in Jefferson ring"
- P1-23 Febvre: "Ultrafast superconducting digital circuits and Interfaces for analysis and processing of microwave electrical signals"
- P1-24 Boussaha: "Study of Josephson Electrodynamics in Parallel Arrays of Superconductive Junctions for Submm-Wave Local Oscillator Applications"

16:00-17:55 **Oral session n°2: "Direct detection".**

Chairpersons: Dr. Gregory Goltsman & Dr. Anders Sklare

Invited talk by Dr. Philip Mauskopf, University of Wales, Cardiff, UK, "Transition Edge Superconducting detector arrays for a 40-200 μm spectrometer on the SPICA telescope"

- WE2-1 Karasik: "Ultralow NEP in the Hot-Electron Titanium Nanobolometers"
- WE2-2 Vystavkin: "To the sensitivity estimation of transition edge sensor bolometers for submillimeter waveband radiation detection operating at super low temperatures"
- WE2-3 Morozov: "Single photon counting detector for THz radioastronomy"
- WE2-4 Matsuo: "Direct detection and interferometer technologies in terahertz range"
- WE2-5 Audley: "Prototype Finline-coupled TES bolometers for CLOVER"
- WE2-6 Piat: "Precise measurement of CMB polarisation from Dome-C: the BRAIN experiment"

Thursday 11 May 2006

09:00-10:00 Oral session n°3: “Novel Devices & Technologies for THz”.
Chairpersons: Dr. Wojtek Knap & Dr. Peter Siegel

- TH1-1 Yngvesson: “Microwave Detection and Mixing in Metallic Single Wall Carbon Nanotubes and Potential for a New Terahertz Detector”
- TH1-2 Lee: “RF-to-Millimeter-wave Conductivity Spectra of Single-Walled carbon Nanotubes”
- TH1-3 Foulon: “Terahertz non linear metamaterial”
- TH1-4 Schicke: “Niobium SupraMEMS for Reconfigurable Millimeter Wave Filters”

10:30-12:00 Oral session n°4: ”SIS 2”.
Chairpersons: Dr. Anthony Kerr & Dr. Karl Schuster

- TH2-1 Vassilev: “A 211-275 GHz Sideband Separating SIS Mixer for APEX”
- TH2-2 Heyminck: “The APEX 345GHz/460GHz 7-pixel heterodyne array”
- TH2-3 Huggard: “Focal Plane Heterodyne SIS Receiver Array with Photonic LO Injection”
- TH2-4 Claude: “Performance of the Band 3 (84-116 GHz) receiver for ALMA”
- TH2-5 Serizawa: “A 385-500 GHz Balanced Mixer with a Waveguide Quadrature Hybrid Coupler”
- TH2-6 Kamikura: “A 385-500 GHz Sideband-separating (2SB) SIS Mixer Based on a Waveguide Split-Block Coupler”

12:00-12:30 Invited talk by Mrs. Nebes on Frequency Regulation and Management introduced by Dr. André Deschamps

14:00-16:00 Oral session n°5: “HEB”.
Chairpersons: Dr. Boris Karasik & Dr. Edward Tong

- TH3-1 Goltsman: “Spiral antenna coupled and directly coupled HEB mixers at frequencies from 1 to 70 THz”
- TH3-2 Skalare: “An HEB cross-bar balanced mixer at 1.5 THz”
- TH3-3 Jacobs: “1.9 THz and 1.4 THz waveguide mixers with NbTiN HEBs on Silicon Nitride Membranes”
- TH3-4 Kooi: “IF Impedance and Mixer Gain of Hot Electron Bolometers and the Perrin-Vanneste Two Temperature Model”
- TH3-5 Kuzmin: “Ultimate Cold-Electron Bolometer with SiN Tunnel Junction and Andreev Contact”
- TH3-6 Gao: “Can NbN films on 3C-SiC/Si change the IF bandwidth of hot electron bolometer mixers ?”
- TH3-7 Cherednichenko: “MgB2 thin film terahertz mixers”
- TH3-8 Merkel: “Aging of Hot Electron Bolometers”

16:30-18:00 Oral session n°6: “Sources”.
Chairpersons: Dr. Thomas Crowe & Dr. Didier Lippens

- TH4-1 Hu: “Terahertz quantum-cascade lasers as local oscillators”
- TH4-2 Hovenier: “Phase lock and free running linewidths of a two color THz quantum cascade laser”
- TH4-3 Kimberk: “A photonic Local Oscillator Module for Submillimeter Interferometry”
- TH4-4 Eisele: “Performance Improvements in Low-Noise Oscillators and Power Combiners with Harmonic-Mode InP Gunn Devices”
- TH4-5 Truscott: “Injection locked self-oscillating mixers for terahertz focal plane arrays”
- TH4-6 Hesler: “Multiplier Development for the Upper ALMA Local Oscillator Bands”

Friday 12 May 2006

09:00-09:30 **Poster session n°2 presentation by Dr. Heribert Eisele & Dr. Imran Mehdi**

09:30-10:30 **Oral session n°7: “Devices, Receivers & Instruments”.
Chairpersons: Dr. Heribert Eisele & Dr. Imran Mehdi**

- FR1-1 Schlecht: “A Novel 520 to 600 GHz Subharmonic Biasable Mixer”
- FR1-2 Chattopadhyay: “TIP : A Terahertz Interferometer for Planets - A Concept Study”
- FR1-3 Erickson: “A very Wideband Analog Autocorrelation Spectrometer”
- FR1-4 Withington: “A Modal and Quantum-Statistical Analysis of Imaging Phased Arrays and Interferometric Phased Arrays”

11:00-12:30 **Poster session n°2**

- P2-01 Thomas: “A broadband fixed-tuned 380 GHz Schottky-based subharmonic mixer”
- P2-02 Rollin: “A Low Noise Integrated Sub-Harmonic Mixer at 183GHz”
- P2-03 Siles: “Design of a 400 GHz Schottky Mixer for High Performance Operation”
- P2-04 Siles: “Design of Heterostructure Barrier Varactor Frequency Multipliers at Millimeter-wave Bands”
- P2-05 Maestrini: “A High efficiency Multiple-Anode 260-340 GHz Frequency Tripler”
- P2-06 Truscott: “A Design Methodology for Planar Triplers in Coplanar Waveguide on Thick Membranes”
- P2-07 Paveliev: “Experimental study of the harmonic generators and detectors, based on superlattices in wide frequency range 600-2200GHz”
- P2-08 El Fatimy: “Resonant terahertz detection in InGaAs/AlInAs and AlGaN/GaN - based nanometric transistors”
- P2-09 Chimot: “Terahertz emission and detection from ion-irradiated In_{0.53}Ga_{0.47}As gated at 1.55 μm”
- P2-10 Pavlov: “Spectral Characterization of a 2.5 THz Multi-Mode Quantum Cascade Laser”
- P2-11 Puetz: “Micromachined Spatial Filters for Quantum Cascade Lasers”
- P2-12 Dhillon: “Phase matched frequency mixing between telecom wavelengths and THz radiation in a quantum cascade laser”
- P2-13 Torres: “Analysis of the stable two-mode operation of a 4-sections semiconductor laser for THz generation by photomixing”
- P2-14 Tignon: “THz generation by optical rectification and competition with other nonlinear processes”
- P2-15 Saeedkia: “Theory and Design of an Edge-coupled Terahertz Photomixer Source”
- P2-16 Banik: “Catadioptric Microlenses for Submillimeter and Terahertz Applications”
- P2-17 Martin: “CFRP Mirror Technology for Submillimeter and Shorter Wavelengths”
- P2-18 Martin: “CFRP Structures for Astronomy Applications”
- P2-19 Schuster: “Micro-machined Planar THz Optics”
- P2-20 Murk: “Characterization of Micromachined Waveguide Hybrids at 345 GHz and 600 GHz”
- P2-21 Ward: “New Standards for Submillimeter Waveguides”
- P2-22 Hunter: “Quasi-Optical Faraday Rotator Design, Construction and Evaluation”
- P2-23 Candotti: “Cross-polarization characterization of GORE-TEX at ALMA band 9 frequencies”
- P2-24 North: “Rigorous Analysis of Antipodal Finline Tapers for High Performance Millimetre and Sub-millimetre Detectors”
- P2-25 Emrich: “Spectrometers for (sub)mm radiometer applications”
- P2-26 Pardo: “Atmospheric opacity above 1 THz: evaluation for the Alma site and for laboratory developments”

- P2-27 Constantin: "Terahertz frequency metrology and sensitivity issues in photomixer spectrometer"
P2-28 Nyström: "A Vector Beam Measurement System for 211-275 GHz"
P2-29 Stacey: "Detection of the 205 μm [NII] Line from the Carina Nebula"

14:00-15:00 **Oral session n°8: "Superconductors for Imagers & Detectors".**
Chairpersons: Dr. Netty Honish & Dr. Jacob Kooï

- FR2-1 Baselmans: "Development of high-Q superconducting resonators for use as kinetic inductance detectors"
FR2-2 Liu: "Development of a 585 GHz One-Dimensional Diffusion-Cooled Nb HEB Mixer Imaging Array Based on the "Reverse-Microscope" Concept"
FR2-3 Gu: "A Two Dimensional Terahertz Imaging System Using Hot Electron Bolometer Technology"
FR2-4 Groppi: "SuperCam : A 64 pixel superheterodyne camera"

15:15-16:45 **Oral session n°9: "THz Spectroscopy & spectrometers".**
Chairpersons: Dr. Neal Erickson & Dr. Wolfgang Wild

- FR3-1 Constantin: "High resolution terahertz spectroscopy of species of astrophysical interest"
FR3-2 Goy: "Quasi-Optical Characterization of Dielectric and Ferrite Materials"
FR3-3 Yagoubov: "550-650 GHz spectrometer development for TELIS"
FR3-4 Wiedner: "Condor-an Astronomical Heterodyne Receiver at 1.25 - 1.5 THz"
FR3-5 Huebers: "High resolution spectroscopy with a quantum cascade laser at 2.5 THz"
FR3-6 Hajenius: "Heterodyne receiver based on hot electron bolometer and quantum cascade laser for detection of the OH line at 3.5 THz"

16:45-17:00 **Closing of the conference by Dr. Alain Maestrini**

INVITED SESSION

Wednesday 10 May 9:30-10:15

Chaired by :

Dr. Gérard Beaudin

Dr. JM Lamarre, Observatoire de Paris, LERMA,

The HFI instrument for Planck

Dr. Ulf Klein, ESA, ESTEC,

**Future Satellite Earth Observation Requirements
and Technology in Millimetre and Sub-Millimetre
Wavelength Region**

Future Satellite Earth Observation Requirements and Technology in Millimetre and Sub-Millimetre Wavelength Region

Ulf Klein, Chung-Chi Lin, Joerg Langen, Peter de Maagt and Roland Meynart

*European Space Agency (ESTEC)
PO Box 299, NL-2200 AG Noordwijk, The Netherlands
Email: Ulf.Klein@esa.int*

Abstract

Satellite observation of Earth's atmosphere in the millimetre and sub-millimetre wavelength region is complementary to those in the visible and infrared spectral region. The emission and opacity of the atmosphere, and scattering by ice particles are all exploited for sensing various layers of the atmosphere in terms of water vapour content, temperature, molecular composition, precipitating water and ice content. Future observation requirements for limb sounding, ice cloud imaging/sounding and meteorological observations are summarized, and corresponding instrument/system concepts meeting those requirements are described.

Keywords: Atmospheric measurements, millimetre wave and sub-millimetre wave radiometry, Earth observation, meteorology, satellite remote sensing

1. INTRODUCTION

Satellite observation of the Earth's atmosphere in the millimetre and sub-millimetre (mm/sub-mm) wavelength region is complementary to those in the visible and infrared (IR) spectral region. The emission and opacity of the atmosphere, and scattering by ice particles are all exploited for sensing various layers of the atmosphere in terms of water vapour content, temperature, molecular composition, precipitating water and ice content.

Limb sounding of the atmosphere enables observation of molecular composition with high vertical resolution, which is required for understanding the global exchange and chemical processes in vertical, and the transport in horizontal direction. The exchange processes in the upper troposphere and lower stratosphere, including the formation of ice clouds, are the least well-understood area of the global atmospheric circulation and mixing. The next generation of limb sounders shall focus its observation in this atmospheric region in terms of water vapour, temperature, aerosols, ice clouds and key minor molecular components.

Observation of ice clouds in the mm/sub-mm is complementary to IR observations, and exploits their scattering property which modulates the upwelling background water vapour signature. Due to the longer wavelength as compared to the latter, the signal is more sensitive to larger ice particles and to those at lower atmospheric layers. Global distribution of ice clouds and their role on the Earth's radiative properties are two of the major uncertainties in predicting the future climate evolution. Existing general circulation models are known to fail in correctly predicting the quantity of ice in the atmosphere. Thus, global and continued observation of ice clouds represents a high priority for future satellite missions.

For meteorological applications, the definite advantage of the mm/sub-mm is its potential to provide observations under cloudy conditions. For the numerical weather prediction, the observation can be performed from low Earth orbit, whereas for nowcasting applications, high temporal resolution (e.g. 15 min.) observation from geostationary Earth orbit (36000 km) would be required. The latter applications call for a very large sensor aperture, which needs to image the Earth with a sufficient spatial resolution.

2. LIMB SOUNDING OF UPPER TROPOSPHERE AND LOWER STRATOSPHERE

The Atmospheric Composition and Upper Troposphere/Lower Stratosphere Exchange Processes mission (ACECHEM) [1], proposed as an Earth Explorer Core candidate in 2000, was studied at pre-phase A level. A further study [2] to consolidate the observation requirements confirmed the instrument complement of ACECHEM: a set of mm/sub-mm-wave and IR limb sounders with high vertical resolution, combined with the IR nadir observation by MetOp (IASI). For further consolidation of the mission objectives and demonstration of its capabilities, an airborne demonstrator MARSCHALS to be flown on the Russian Geophysica aircraft, as shown in Fig. 1, has been developed at Rutherford Appleton Laboratory [3]. The principal and most innovative objective of MARSCHALS is to simulate the capability

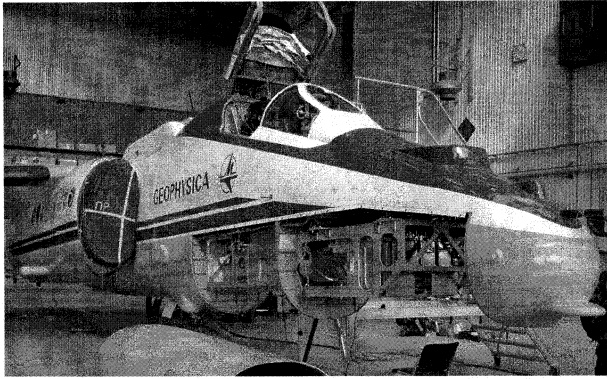


Fig. 1. MARSCHALS instrument mounted in the nose of Geophysica aircraft

of MASTER, a mm-wave limb-sounder payload of ACECHEM, for sounding O_3 , H_2O and CO at high vertical resolution in the upper troposphere/lower stratosphere (UT/LS) at bands around 300, 325 and 345 GHz. Spectra are recorded in these bands with a resolution of 200 MHz. MARSCHALS is the first limb-sounder to be explicitly designed and built for the purpose of sounding the composition of the UT/LS. A particular attribute of mm-wave measurements is their comparative insensitivity to ice clouds. However, to assess the impact on the measurements of cirrus in the UT, MARSCHALS also has a near-IR digital video camera aligned in azimuth with the 235 mm mm-wave antenna. In addition to the capability to be fitted within an aircraft, MARSCHALS can also be flown on a stratospheric balloon platform when fitted with a 400 mm antenna.

Several hardware developments have been carried out for demonstrating the antenna performance for a "MASTER"-like instrument. The five-channel (203 – 503 GHz) quasi-optical demultiplexer had been breadboarded previously [4], and an aluminium full-sized reflector breadboard was manufactured by HTS in Switzerland. The complete breadboard assembly was then tested at the EADS Astrium Ottobrunn facilities. Fig. 2 shows the ADMIRALS antenna with the Quasi-optical feedbox mounted behind the main reflector, and Fig. 3 the measured beam-pattern at 322 GHz.

3. SUB-MILLIMETRE WAVE OBSERVATION OF ICE CLOUDS

CIWSIR was proposed in 2001 as an Earth Explorer Opportunity mission [5]. It is aimed at observing distribution of ice clouds, quantifying the total ice content in the atmosphere, and understanding their impact on the Earth's climate. The proposed instrument is a 5-channel, conical scanning sub-mm-wave radiometer (see Fig. 4) on a low Earth orbit satellite including channels at 183, 325, 448, 683 and 874 GHz. Two separate antennas are used for the high and the low frequency channels, respectively, providing a footprint of 10 km at all frequencies.

At this point, activities are being finalised to improve the theoretical basis for a CIWSIR type mission such as the refinement of radiative transfer models for accurate scattering calculations by ice clouds at sub-mm-wave frequencies. The latest model features [6]:

- Polarised radiative transfer
- Spherical geometry
- Many different crystal shapes, sizes & orientations
- All particle mixtures and profiles

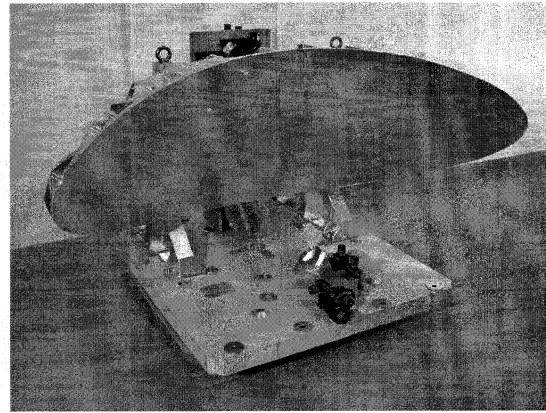


Fig. 2. ADMIRALS full-sized antenna breadboard (2200 mm \times 800 mm)

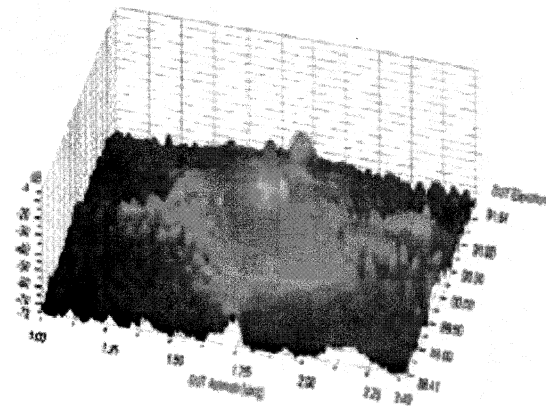


Fig. 3. Measured antenna beam-pattern at 322 GHz

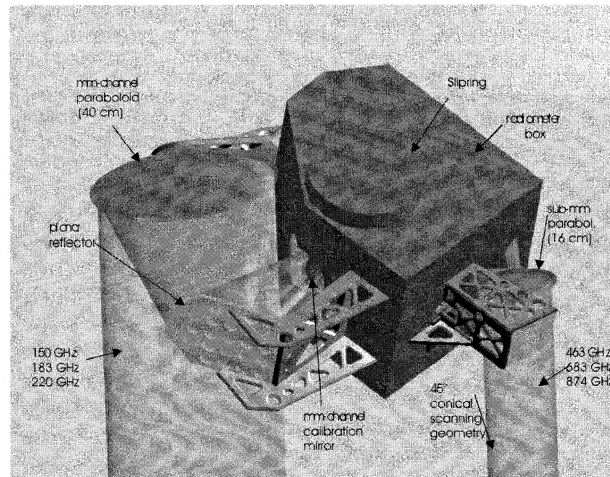


Fig. 4. CIWSIR conically scanning instrument concept consisting of separate mm- and sub-mm-wave antennas

In addition, an activity to consolidate the mission and instrument requirements for such a mission has been started. A near future activity foresees a development of an airborne demonstrator in order to gather experimental data. The technology for the 874 GHz room temperature receiver is seen as critical and would require an early development.

4. METEOROLOGICAL OBSERVATIONS FOR NUMERICAL WEATHER PREDICTION

In cooperation with EUMETSAT, the preparation for the next generation polar orbiting meteorological satellite mission (post-EPS) has been initiated in 2005, with a projected start of services in 2018. The system shall provide all-weather observation of temperature and water vapour profiles, as well as of precipitation and ocean surface wind for numerical weather prediction. The future MW sounder and imager shall provide better spatial and temporal resolution, better coverage and higher radiometric quality than the current instruments on-board the upcoming MetOp satellites. A number of candidate concepts have been developed. Among these are AMSU type cross-track scanners as shown in Fig. 5, including higher frequency channels up to 229 GHz, and conically scanning instruments reaching up to sub-mm-wave frequencies [7]. The cross-track scanner has an antenna aperture of 360 mm, resulting in a spatial resolution of 40 km at the sub-satellite point at 23 GHz. It is a compact instrument (1245 mm × 625 mm × 740 mm), which combines the capability of AMSU-A and AMSU-B with better radiometric sensitivity.

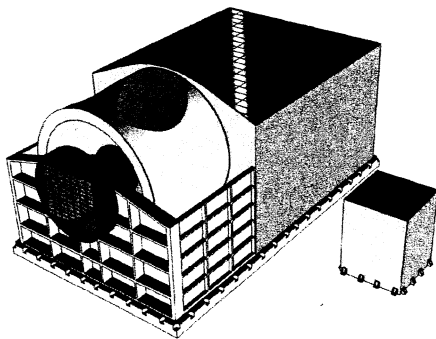


Fig. 5. AMSU type cross-track scanner

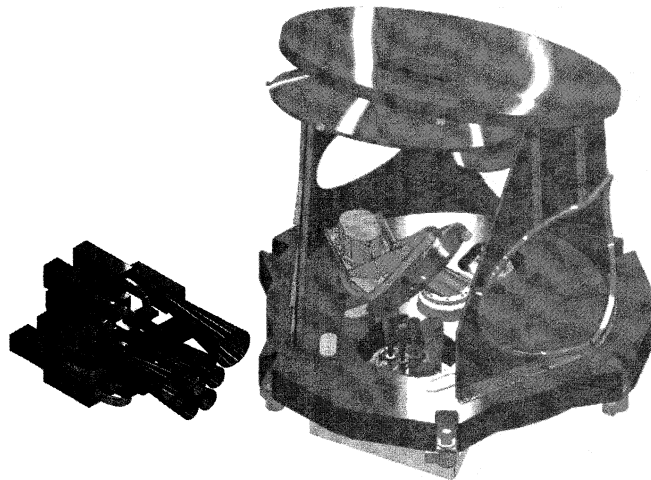


Fig. 6. Combined imaging/sounding radiometer with push-broom receivers at 54 GHz sounding band – Feed cluster shown separately on the left with 7 parallel dual-polarisation horns (the central horn is 54/118 GHz dual-frequency)

A combined imaging/sounding instrument is shown in Fig. 6, which makes use of push-broom technique with 7 parallel dual-polarisation horns in the 54 GHz sounding band, resulting in 14 parallel receivers, for achieving a very high radiometric sensitivity. For accommodating a large number of channels, two reflectors (700 and 360 mm diameter) are used to separate the low and high frequency feed clusters. The sounder/imager concepts were developed at pre-phase A level instrument studies.

As a part of early technology developments, a long-life scan mechanism, 54/118 GHz dual-frequency horn and 89 GHz direct-detection receiver are objects of breadboarding at this stage. 10 years in-orbit life is aimed for a conically scanning radiometer such as the one depicted in Fig. 6, which represents a challenging requirement. Fig. 7 shows the design of a 89 GHz direct-detection receiver frontend. A more compact, mass-efficient receiver can be built as no local oscillator is required for down-conversion. The low noise amplifier MMIC was processed at Fraunhofer Institute in Germany, and the frontend block was integrated at EADS-Astrium SAS, and is undergoing a detailed characterisation test.

5. NOWCASTING OBSERVATIONS

Millimetre and sub-mm-wave imager/sounders are considered for future meteorological and climate observation satellites. In coordination with the EUMETSAT's Meteosat Third Generation (MTG) preparatory activities, ESA is conducting studies of future microwave imager/sounder in geostationary (GEO) and medium Earth orbits (MEO) [8]. The primary advantage of a GEO orbit for remote sensing, compared with a Low-Earth (LEO) orbit, is that continuous monitoring is possible over a large area of the Earth's surface and atmosphere. This is desirable for the observation of rapidly evolving meteorological phenomena such as convective systems, precipitation and cloud patterns, enabling nowcasting.

The principal emphases in all of the concepts are the observations of precipitation, ice clouds, atmospheric motion vectors and temperature and humidity sounding with high temporal resolution (15 – 30 min.) and a horizontal resolution of better than 10 km. The proposed frequencies range from 54 to 875 GHz, out of which the bands around 54GHz, 118GHz, 183GHz, 380GHz have the highest user priority followed by the corresponding window channels 110GHz, 150GHz, 340GHz and, finally 424GHz, 683GHz, 875GHz.

The main technical challenges are the very large antenna aperture for achieving the required spatial resolution (40 folds increase in the distance to the Earth as compared to the LEO) and the necessity for imaging using two-dimensional scanning due to the absence of a relative spacecraft-Earth movement. Furthermore, other challenges are the wide frequency and the optimisation among radiometric accuracy, geographical coverage and repeat cycle. Fig. 8 shows a imager/sounder concept based on the use of a 4 m diameter reflector antenna.

A two-dimensional mechanical scanning of the reflector is limited within an area of 5000 km × 5000 km centered on Europe every 15 min. This limitation is a result of the trade-off among temporal sampling, radiometric sensitivity and coverage, and it takes into account of achievable reflector acceleration during the scan.

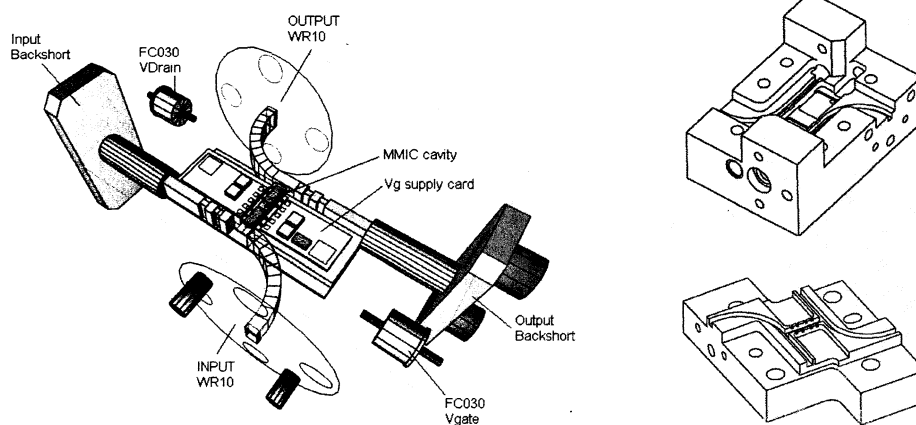


Fig. 7. 89 GHz direct-detection receiver frontend in split-block technique

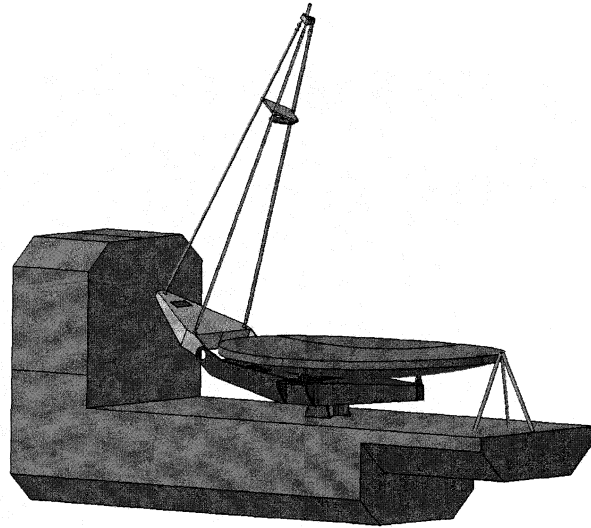


Fig. 8. GEO imager/sounder concept based on 4 m diameter mechanically scanned reflector

An alternative to the GEO concept is the use of an elliptical MEO such as 8 hours Molniya orbit with apogee at 27000 km altitude [9]. It has a repeat cycle of 24 hours and enables observation of successively Europe, North America and South-East Asia, each with 6 hours imaging period. Fig. 9 shows the satellite path over such a 24 hours period and demonstrates an optimum observation geometry (low incidence angle) for the northern hemisphere. Due to the lower altitude of the apogee with respect to the GEO, a smaller antenna can be used for a same spatial resolution, hence easing the design of the scan mechanism. From the technology point of view, radiation shielding, precise orbit analysis, scan pattern and scan mechanism are issues to be investigated in detail. For ensuring a 24-hour coverage, a total of 4 satellites would be required.

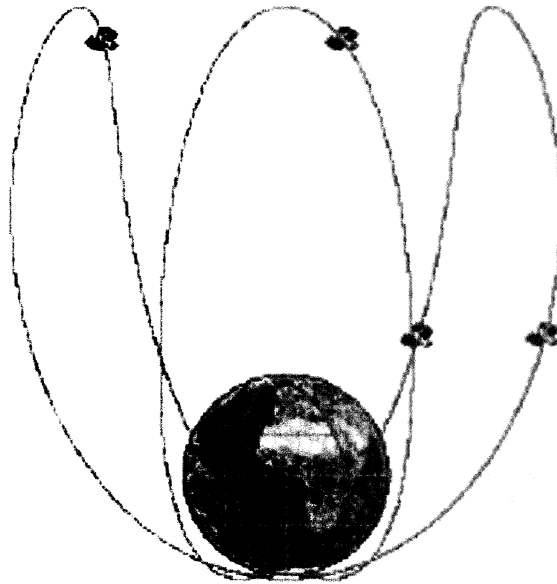


Fig. 9. MEO imager/sounder in 8-hour Molniya orbit - Satellite path over 24 hours period

The technological challenge represented by such instruments is now addressed by an ambitious demonstrator programme. Two competing concepts were investigated: a conventional, large scanning reflector antenna concept and an interferometric aperture synthesis concept. The interferometric concept showed most potential to meet the required spatial resolution from geostationary orbit, and was thus selected for a concept demonstration. In this concept, approximately 500 receivers in total are distributed to form an effective aperture of 8 m diameter. The instrument covers the highest priority frequency bands as indicated above.

6. CONCLUSION

A review of possible instrument concepts for future satellite missions in mm and sub-mm-wave spectral region was presented. For each of the application areas, the corresponding observation requirements lead to a specific radiometer design. The general trend for the future is marked by a better radiometric sensitivity and accuracy, higher spatial resolution and higher number of channels for enabling better observation quality. Very low noise receivers are required with compact volume and light weight. Receiver backends must offer high number of channels with sharp frequency cut-offs. The antenna size needs to be increased with very high mechanical stability and thermal properties, and it must be at the same time light weight. For applications requiring very large aperture, the new interferometric concept will compete against the classical reflector-based instruments. Nevertheless, such a concept still requires substantial developments in the areas of miniature frontend design, local oscillator signal generation and distribution, stable IF-signal transmission over long distances, receiver calibrations, very large number of signal-correlators, etc. A dedicated technology development has recently been started by ESA.

7. REFERENCES

- [1] ACECHEM – Atmospheric Composition Explorer for Chemistry and Climate Interaction, Report for Assessment, The Five Candidate Earth Explorer Core Missions, ESA Publication SP-1257(4), European Space Agency, Sept. 2001.
- [2] H. Kelder, “ESA CAPACITY Study – Mission Concepts for Operational Atmospheric Chemistry Monitoring,” 2005 EUMETSAT Meteorological Satellite Conference, Dubrovnik, Croatia, 19-22 Sept. 2005.
- [3] B. Moyna, E. Allouis, R. Brunt, U. Cortesi, B.N. Ellison, J. Eskill, T. Forward, T. Jones, D. Lamarre, J. Langen, P.J. de Maagt, D.N. Matheson, I. Morgan, M. Oldfield, J. Reburn and R. Siddans, “MARSCHALS: Development of an Airborne Millimeter Wave Limb Sounder,” Proceedings of SPIE Vol. 4540, International Symposium on Remote Sensing, Toulouse, France, 17-21 September 2001.
- [4] Jorgensen, R., G. Padovan, P. de Maagt, D. Lamarre, and L. Costes, “A 5-frequency millimeter wave antenna for a spaceborne limb sounding instrument”, Trans. AP, May 2001, pp.703-714
- [5] Cloud Ice Water Sub-millimetre Imaging Radiometer, University of Bremen, <http://www.sat.uni-bremen.de/projects/ciwsir/>
- [6] ARTS – The Atmospheric Radiative Transfer System, University of Bremen, <http://www.sat.uni-bremen.de/arts/>
- [7] J. Charlton, J.-M. Goutoule and U. Klein, “Instrument Concepts for a Post-EPS Microwave Mission,” EGU General Assembly, Vienna, Austria, 25-29 June 2005.
- [8] U. Klein, C.C. Lin, N. Atkinson, J. Charlton, C. Philpot, “Future Microwave Radiometers in Geostationary and Medium Earth Orbit,” IGARSS’03, Toulouse, France, 21-25 July 2003.
- [9] J. Charlton, R. Child, C. Milner, N. Atkinson and U. Klein, “Future Passive Microwave Radiometry Missions: Elliptical Orbits - a Novel Solution,” 2005 EUMETSAT Meteorological Satellite Conference, Dubrovnik, Croatia, 19-22 Sept. 2005.

ORAL SESSION n°1

« SIS 1 »

Wednesday 10 May 10:45-12:00

Chaired by :

Dr. Jia-Rong Gao & Dr. Karl Jacobs

ORAL SESSION n°1

« SIS 1 »

Wednesday 10 May 10:45-12:00

Chaired by :

Dr. Jia-Rong Gao & Dr. Karl Jacobs

A Superconducting 180° IF Hybrid for Balanced SIS Mixers

A. R. Kerr, A. W. Lichtenberger, C. M. Lyons, E. F. Lauria, L. M. Ziurys and M. R. Lambeth

Abstract—A compact 180° hybrid has been developed for use in balanced SIS mixers. The lumped-element circuit uses superconducting Nb conductors on a 1.4 mm x 0.5 mm quartz substrate and operates over 4-12 GHz.

Index Terms—Superconducting microwave devices, microwave integrated circuits, hybrid junctions, lumped-element microwave circuits, superconductor-insulator-superconductor mixers.

I. INTRODUCTION

Balanced mixers have several advantages for use in low-noise millimeter-wave receivers: (i) Sideband noise from the local oscillator is substantially reduced. (ii) The LO power required by a balanced mixer is typically 17 dB less than for a similar single-ended mixer. (iv) The dynamic range of a balanced mixer is twice that of a similar single-ended mixer. (iii) No external LO diplexer is required in the signal path. Balanced mixers are therefore appropriate when the lowest system noise is desired, particularly when LO noise is significant. For receivers in which many mixers are driven by a common LO, such as a focal plane array, the low LO power requirement of balanced mixers greatly simplifies LO generation and distribution.

The simplest balanced mixer uses a pair of single-ended mixers with the IF outputs connected in parallel. However, this requires the two mixers to be biased oppositely and presents undesirable IF impedance levels to the in-phase and out-of-phase IF components from the individual mixers. The use of an IF hybrid, as shown in Fig. 1, provides a desirable IF impedance environment for the SIS mixer elements while allowing them to be biased by a common supply. This paper describes a superconducting 180° hybrid for 4-12 GHz, small enough to be mounted inside a balanced mixer block. The hybrid can be used in cryogenic balanced mixers for any RF band.

A. R. Kerr and M. R. Lambeth are with the National Radio Astronomy Observatory, Charlottesville, VA 22903, USA.

A. W. Lichtenberger and C. M. Lyons are with the University of Virginia Microfabrication Laboratory, Charlottesville, VA 22904, USA.

E. F. Lauria and L. M. Ziurys are with the Arizona Radio Observatory, Tucson, AZ 85721, USA.

This work was supported in part by the Arizona Radio Observatory, Steward Observatory, University of Arizona, and by NSF grant #AST-0242525.

The National Radio Astronomy Observatory is a facility of the National Science Foundation operated under cooperative agreement by Associated Universities, Inc.

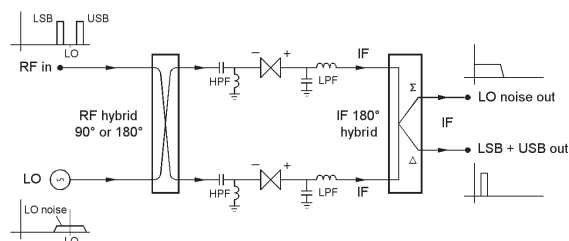


Fig. 1. Balanced SIS mixer with the same bias polarity on the two component mixers.

The requirements for the IF hybrid in a balanced SIS mixer are: (i) both even and odd mode IF signals from the SIS mixers should see a 50-ohm load, (ii) the hybrid should have a DC path which allows both mixers to be biased through the hybrid by a single bias source, (iii) the load (IF amplifier) impedance is 50 ohms; and (iv) the hybrid should be small enough to mount inside the balanced mixer block.

Hybrids can be made in several ways. Below about 1 GHz, small transformers with three windings can be used but at higher frequencies, transmission line circuits based on the rat-race design (Fig. 2(a)) are used. Because of the quarter and three-quarter wavelength lines, these are too large for convenient incorporation into a balanced mixer. The size can be reduced greatly by using a lumped-element design.

The lumped-element design of Parisi [1] is based on the rat-race hybrid and uses lumped-element transmission lines. The number of elements is greatly reduced by replacing the 270° line with a 90° *negative transmission line*. This is shown in Fig. 2(b), in which three arms of the circuit are 90° LC transmission lines and the fourth (bottom) arm is a 90° LC negative transmission line. Another lumped-element design, the lattice hybrid [2], uses lattice sections to emulate positive and negative transmission line sections, and can have very wide bandwidth, but it requires balanced sources and loads to

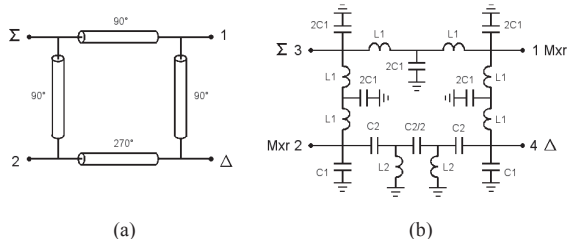


Fig. 2. (a) Rat-race hybrid. (b) The Parisi hybrid, in which the 270° transmission line is replaced by a 90° negative transmission line.

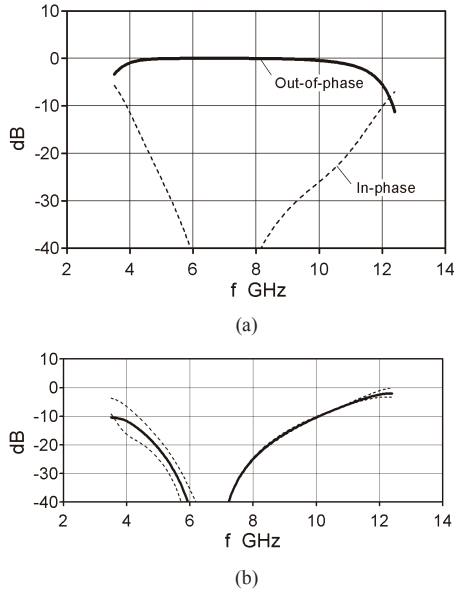


Fig. 3. Characteristics of the Parisi hybrid using the original element values. (a) Coupling to port 4 when ports 1 and 2 are excited in-phase (solid line) and out-of-phase (dashed line). (b) Reflection coefficient at port 2 when ports 1 and 2 are excited in-phase, out-of-phase (dashed lines), and with port 1 not excited (solid line).

operate correctly. In the present work, a modified version of the Parisi design is used.

II. DESIGN

Using Parisi's circuit element values, scaled to a center frequency of 8 GHz, the circuit has the response shown in Fig. 3. Figure 3(a) shows the coupling to port 4 when the mixer ports 1 and 2 are excited by equal amplitude signals out of phase (corresponding to the desired IF signal from the balanced mixer) and in phase (corresponding to the down-converted LO sideband noise). Figure 3(b) shows the return loss at port 2 as seen by a test signal when port 1 is terminated in 50 ohms or excited in or out of phase with the test signal, as occurs in an operating balanced mixer.

It was found that the circuit element values could be adjusted to give a better response over the desired 4-12 GHz band. Figure 4 shows the result of optimization with the criteria $S_{42} + S_{41} = 0$, $S_{32} - S_{31} = 0$, $S_{11} < -20$ dB, and $S_{22} < -20$ dB.

The IF output impedance of an operating SIS mixer can be much higher than 50 ohms. The characteristics of the optimized hybrid connected to 400-ohm sources at ports 1 and 2 are shown in Fig. 5. The coupling curves are normalized to the power that would be delivered to a 50-ohm load by the 400-ohm sources. For port 1 and 2 source impedances greater than 400 ohms, the characteristics change only slightly. (Note that it is not generally desirable to impedance match the IF amplifier to the (high) output impedance of an SIS mixer. While matching may improve the transducer gain of the mixer and reduce the receiver noise temperature somewhat, it is likely to degrade the RF input match of the mixer, even to

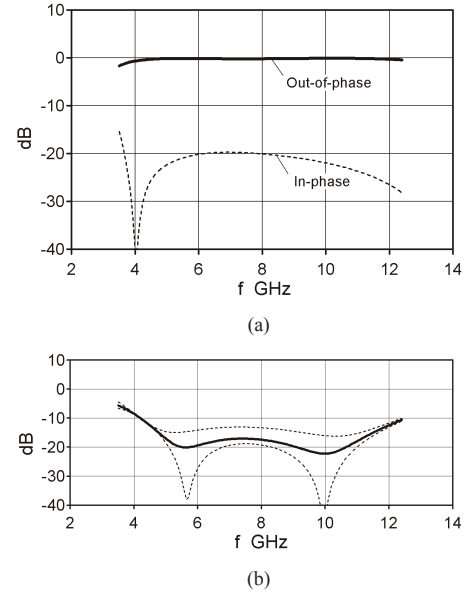


Fig. 4. Characteristics of the modified Parisi hybrid. (a) Coupling to port 4 when ports 1 and 2 are excited in-phase (solid line) and out-of-phase (dashed line). (b) Reflection coefficient at port 2 when ports 1 and 2 are excited in-phase and out-of-phase (dashed lines) and when port 1 is not excited (solid line). (Source impedances 50 ohms.)

the point of causing reflection gain, and reduces the dynamic range of the mixer.)

The hybrid was fabricated on a fused quartz substrate using niobium conductors. Inductors were planar spirals, and parallel plate capacitors had a SiO_x dielectric. The layout of the chip is shown in Fig. 6. Parasitic reactances are not negligible and are included in the equivalent circuit of Fig. 7. The parallel capacitance of the inductors and the

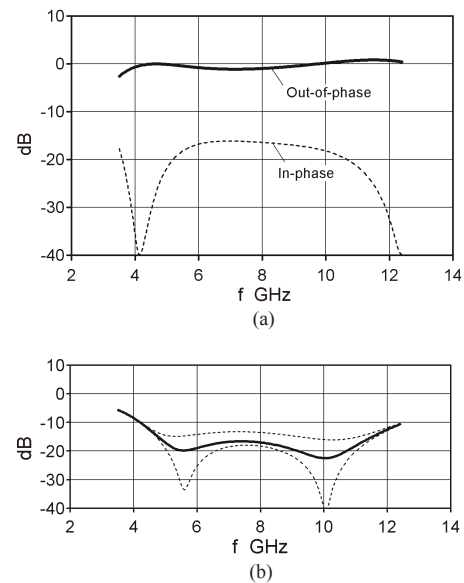


Fig. 5. Characteristics of the modified Parisi hybrid with 400- Ω sources at ports 1 and 2. (a) Coupling to port 4 when ports 1 and 2 are excited in-phase (solid line) and out-of-phase (dashed line). (b) Reflection coefficient at port 2 when ports 1 and 2 are excited in-phase and out-of-phase (dashed lines), and when port 1 is not excited (solid line).

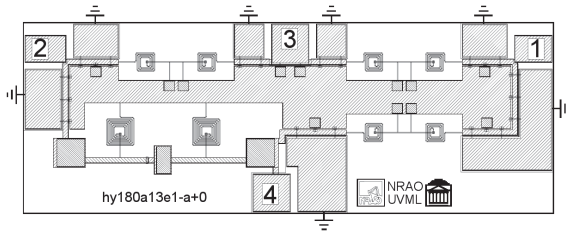


Fig. 6. Layout of the hybrid on a quartz chip. Dimensions: 1.42 mm x 0.51 mm.

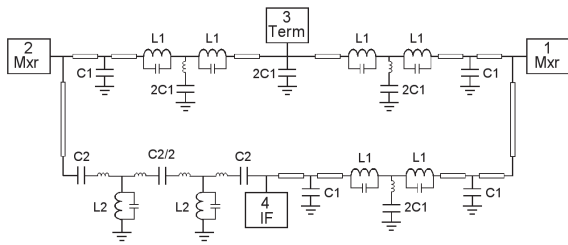


Fig. 7. Equivalent circuit of the Parisi hybrid on a chip as shown in Fig. 6, including parasitic elements.

series inductance of the capacitor leads are included, and long conductors are represented as transmission lines.

Inductors for the initial chip layout were designed to the values of the re-optimized Parisi circuit using Sonnet *em* [3], and capacitor dimensions were calculated using the simple parallel plate formula. The layout was then simulated using Sonnet, and the circuit simulator MMICAD [4] was used to find the values of the parasitic inductances and transmission line parameters by fitting the

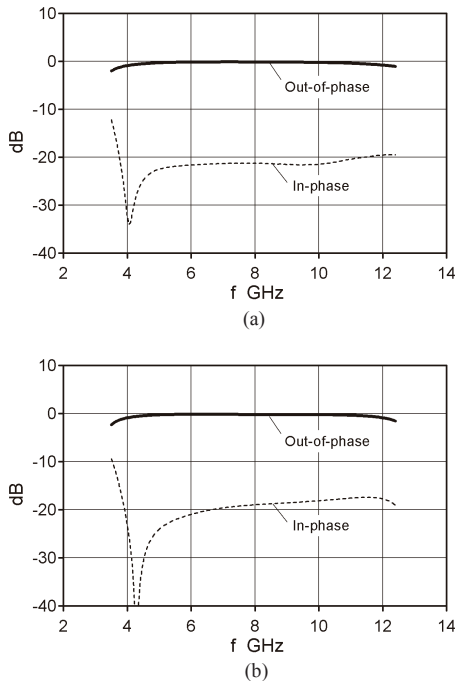


Fig. 8. (a) Sonnet simulation of the layout in Fig. 6. (b) MMICAD simulation of the circuit in Fig. 7. Showing the coupling to port 4 when ports 1 and 2 are excited in-phase and out-of-phase. All ports terminated in 50 ohms.

circuit response to the Sonnet simulation. Once the parasitic element values had been found in this way, a final optimization of the main elements, L_1 , L_2 , C_1 , C_2 , was done using MMICAD. Figure 8 shows the final Sonnet and MMICAD results.

III. FABRICATION

The hybrids are fabricated on a 250- μm fused quartz substrate in three layers: a lower conductor, an SiO_x insulating layer, and an upper Nb "wiring" layer. The lower conductor is sputter-deposited as a Nb/Ti/Nb sandwich (75/15/75 nm) with a protective overlayer of CrAu (30 nm). It is then patterned through a photoresist mask using a wet etch for the CrAu and reactive ion etching the Nb/Ti/Nb layer. Photoresist is then applied to mask the CrAu areas over which a dielectric layer is not desired, and 285 nm SiO_x is sputter deposited and patterned by liftoff. The upper Nb layer is sputter deposited over the entire wafer, followed by gold. The gold forms contacts to diagnostic capacitors elsewhere on the wafer but is removed from the area of the hybrid. The upper Nb is patterned by photolithography with RIE. In this RIE, the CrAu contact pads of the hybrid are revealed. During this etch, the thin Ti in the lower conductor prevents complete removal on the Nb around the perimeter of CrAu features neither edge-sealed by SiO_x nor fully covered by the upper Nb.

IV. MEASUREMENTS

The hybrids were tested in the four-port 50-ohm fixture shown in Fig 9. Measurements were made with two ports

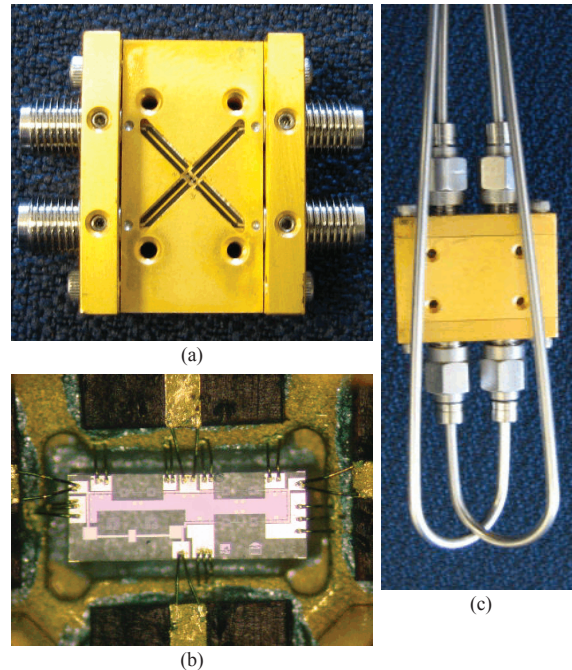


Fig. 9. (a) The four-port test fixture. (b) The hybrid chip in the test fixture showing wire bonds to the four microstrip lines and to ground. (c) The test fixture connected to four stainless-steel cables for immersion into a liquid helium storage dewar.

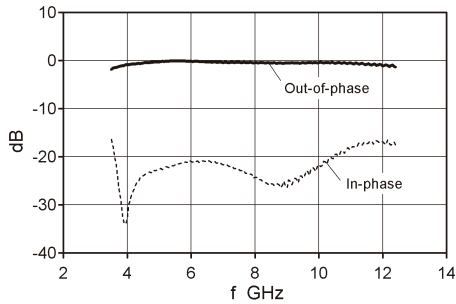


Fig. 10. Measured characteristics of the hybrid. Coupling to port 4 when ports 1 and 2 are excited in-phase and out-of-phase.

of the hybrid connected to the VNA and the other two ports terminated in 50-ohm loads. This two-port measurement was repeated six times until all combinations of ports had been measured — hence, all S-parameters of the hybrid.

As VNA calibration at the ends of cables in a liquid helium dewar is impractical, calibration was done at the room-temperature interface. The cables and test fixture were then measured, with the hybrid chip disconnected, while dipped in liquid helium, and an equivalent circuit derived for each cable connected to the test fixture. The S-parameters of the hybrid were then able to be de-embedded from measurements at the room temperature ends of the cables.

Figure 10 shows the coupling to port 4 when ports 1 and 2 are excited in-phase and out-of-phase, computed from the de-embedded S-parameter measurements (all ports terminated in 50 ohms).

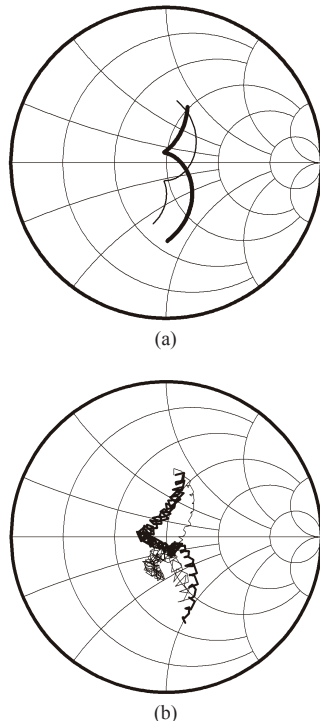


Fig. 11. Reflection coefficient at ports 1 (wide line) and 2 (narrow line) over 4-12 GHz. (a) Sonnet simulation. (b) Measured.

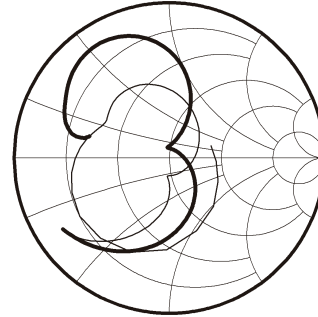


Fig. 12. Reflection coefficient at ports 1 (wide line) and 2 (narrow line) over 2-14 GHz. Sonnet simulation.

Figure 11 shows the reflection coefficient seen by each mixer connected to the hybrid.

V. DISCUSSION

The superconducting hybrid is seen to operate as designed over the 4-12 GHz band. It meets the criteria given in the introduction for use in a balanced SIS mixer. The even-mode rejection at port 4 is greater than 16 dB, which is sufficient to suppress LO sideband noise effectively in a balanced mixer. The two unit mixers can be biased in parallel from port 4 (the IF amplifier port) as long as a blocking capacitor is added in series with the 50-ohm termination on port 3. Operation of the hybrid with mixers whose IF output impedance is much larger than 50 ohms is similar to that with 50-ohm mixers. The load impedance seen by mixers connected to the hybrid is near 50 ohms within the 4-12 GHz band and is well behaved out of band as indicated in Fig. 12 (which is from the Sonnet simulation).

It is of interest to note that if the superconducting niobium is replaced with 300 nm gold conductors, for operation at room temperature, the loss of the hybrid increases by > 5 dB.

ACKNOWLEDGMENT

The authors thank Françoise Johnson for dicing and testing the hybrid chips.

REFERENCES

- [1] S. J. Parisi, "180° Lumped Element Hybrid," *IEEE Int. Microwave Symp. Digest*, pp. 1243-6, 1989.
- [2] T. Kawai, Y. Kokubo, and I. Ohta, "Broadband Lumped-Element 180-Degree Hybrids Utilizing Lattice Circuits," *IEEE Int. Microwave Symp. Digest*, pp. 47-50, 2001.
- [3] Sonnet *em*. Sonnet Software, Inc., North Syracuse, NY, <http://www.sonnetsoftware.com>.
- [4] MMICAD version2. Optotek, Ottawa, Canada, <http://www.optotek.com>.

Theory of Series-Connected Distributed SIS Mixers with Ultra-Wide Instantaneous Bandwidth

C.-Y. Edward Tong, Raymond Blundell

Abstract— Series-connected distributed lumped element SIS mixers have emerged as a new generation of sensitive heterodyne submillimeter detectors which offer very wide instantaneous bandwidth. A formalism based on the transmission (ABCD) matrix is introduced to facilitate the simulation of this type of mixer with the Quantum Theory of Mixing. The simulations confirm that the IF bandwidth is very wide, up to at least 40 GHz. This agrees with our laboratory measurements in which good Y-factors are measured up to IF in excess of 20 GHz.

Index Terms—Superconductor-insulator-superconductor mixers, distributed mixing, intermediate frequency bandwidth, submillimeter waves.

I. INTRODUCTION

SERIES-CONNECTED SIS arrays offer many advantages over single SIS device or parallel connected SIS junctions. Such mixer arrays have higher input compression level and higher input impedance in addition to lower IF capacitance. However, at higher frequencies, the current flowing in the individual junctions of a series array may be of different phase. This presents a challenge to the design of an SIS mixer using series-connected array.

Recently, a compact mixer design based on a distributed 4-junction series array has successfully been implemented in the 400 GHz frequency range [1]. This mixer has demonstrated an exceptional wide Intermediate Frequency (IF) bandwidth of up to 20 GHz. In this paper, we describe how this novel mixer design can be modeled using the Quantum Theory of Mixing [2]. In particular, a formalism using an expanded transmission (ABCD) matrix is introduced so that the circuit response at each sideband can correctly be modeled, and the phase relation between the RF voltages and currents are preserved.

This mixer may also be simulated by the Supermix software [3, 4], which use a scattering matrix approach. The advantage of using the transmission matrix is that we can tie the circuit layout directly with the conversion matrix formalism in classical [5] and quantum mixer theory.

Manuscript received May 10, 2006.

C.-Y. E. Tong and R. Blundell are with the Harvard-Smithsonian Center for Astrophysics, 60 Garden St., Cambridge, MA 02138 USA. (e-mail: etong@cfa.harvard.edu, and rblundell@cfa.harvard.edu).

II. MIXER LAYOUT

A photo of our novel mixer design is given in Fig. 1. Four SIS junctions are located on islands on the center conductor of coplanar waveguides. They are connected via short lengths of high impedance coplanar waveguides and low impedance microstrip sections. No impedance transformer is needed to feed the junction array. The distributed array is fairly well matched to a 35-ohm source impedance over a 20 – 25 % bandwidth. A nominal design calls for the use of $0.85 \mu\text{m} \times 0.85 \mu\text{m}$ junctions having a critical current density of around 13 kA/cm^2 .

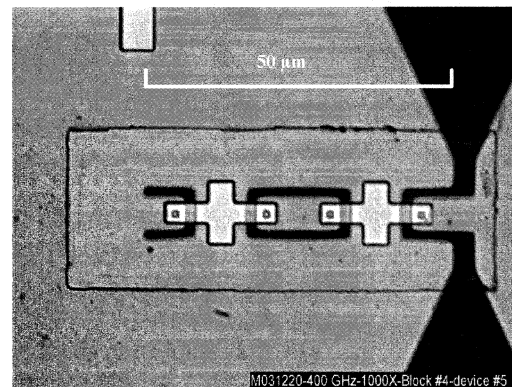


Fig. 1 Photograph of the series-connected distributed SIS mixer. The waveguide feed point is located on the right hand side of the photo. The 4 junctions are connected by sections of coplanar waveguide (CPW) and microstrip (the two white crosses).

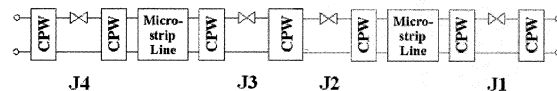


Fig. 2 Simplified schematic diagram of the SIS mixer circuit shown in Fig. 1. The junctions, J1, J2, J3 and J4 are in series positions along the artificial transmission line. The input to the circuit is to the right and the output after J4 is shorted.

A simplified schematic representation of the circuit is given in Fig. 2. It can be seen that the circuit can be broken into

cascaded blocks of circuit elements. The problem should be well described by the transmission (ABCD) matrix formalism in circuit theory.

III. LARGE SIGNAL ANALYSIS

Since the mixer under simulation works at around 400 GHz, the second harmonic frequency lies above the energy gap of Niobium. Furthermore, the individual series connected junctions are not tuned in parallel. Any harmonic current generated by the Local Oscillator (LO) drive is mostly shorted by the geometrical capacitance. This is particularly true since the $\omega_{LO}CR$ product of the junctions used is around 4. A three-frequency approximation is therefore sufficient to solve for the RF voltages impressed across the junctions by the LO.

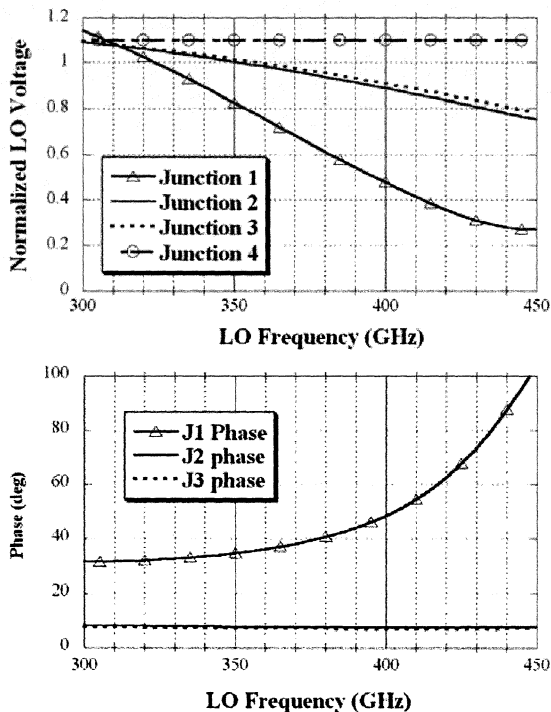


Fig. 3 Variation of the normalized LO voltage, α , as a function of the LO frequency for the 4 junctions in the array. The upper graph shows the amplitude of the voltages while the lower graph gives the phase relative to that of junction 4. In this calculation $\alpha_4 = 1.1$ is used as the starting solution.

Starting from an assumed RF voltage at the last junction in the array, we can derive the RF current flowing through the neighboring junction. In this calculation, we assume that the DC bias voltage across each junction equals 0.75 times the gap voltage. By inverting the non-linear current voltage relationship given by the Quantum Theory of Mixing, we can solve successively for the RF voltages across the other junctions in the array. The result of the large signal analysis is presented in Fig. 3. For this calculation, we have assumed that

the normalized LO voltage across the last junction of the array, $\alpha_4 = eV_4 / h\nu_{LO}$, is equal to 1.1. We note that at the low end of the band, the amplitudes of voltages have similar values but at the high end, the first junction experience the least LO drive and the LO voltage is quite different in phase compared to other junctions.

IV. EXPANDED TRANSMISSION MATRIX

Following standard mixer theory [2], we define the voltage and current vectors at any point in the mixer circuit as $\underline{v} = (v_1 \ v_0 \ v_{-1})^T$ and $\underline{i} = (i_1 \ i_0 \ i_{-1})^T$ respectively, where the subscripts 1, -1 and 0 denote the upper-side-band (USB), lower-side-band (LSB) and the IF respectively. In circuit theory, it is common to characterize a two-port network by a transmission (ABCD) matrix. We generalize it for use in our mixer simulation. The expanded transmission matrix of a mixer circuit element relates the input voltage and current vectors to the output voltage and current vectors of any two port network within the mixer circuit as:

$$\begin{pmatrix} V_{in} \\ I_{in} \end{pmatrix} = \begin{pmatrix} \mathbf{A} & \mathbf{B} \\ \mathbf{C} & \mathbf{D} \end{pmatrix} \cdot \begin{pmatrix} V_{out} \\ I_{out} \end{pmatrix} \quad (1)$$

where \mathbf{A} , \mathbf{B} , \mathbf{C} and \mathbf{D} are 3×3 matrices. For a passive section of the mixer, the elements of the expanded transmission matrix are simply diagonal matrices, the entries of which are related to the individual elements of the single-frequency transmission matrices \mathbf{T}_i for $i = 1, 0$ and -1 . Thus, in equation (1), for $X = A, B, C$ or D :

$$\mathbf{X} = \begin{pmatrix} X_1 & 0 & 0 \\ 0 & X_0 & 0 \\ 0 & 0 & X_{-1}^* \end{pmatrix} \quad (2)$$

and

$$\mathbf{T}_i = \begin{pmatrix} A_i & B_i \\ C_i & D_i \end{pmatrix} \quad (3)$$

It should be noted that all LSB entries are the conjugate of the single frequency transmission matrix representation, consistent with classical mixer theory.

Equation (1) embeds the circuit description for all the sidebands involved in the mixer simulation. In the case of the series-connected mixer element, the expanded transmission matrix that describes it would be

$$\begin{pmatrix} V_{in} \\ I_{in} \end{pmatrix} = \begin{pmatrix} \mathbf{I} & (\mathbf{Y}_c(\alpha) + \mathbf{Y}_j)^{-1} \\ \mathbf{0} & \mathbf{I} \end{pmatrix} \cdot \begin{pmatrix} V_{out} \\ I_{out} \end{pmatrix} \quad (4)$$

where \mathbf{I} is the identity matrix, $\mathbf{0}$ is the null matrix and \mathbf{Y}_j is the diagonal matrix that gives the susceptance due to the junction's geometrical capacitance at the three sideband frequencies. $\mathbf{Y}_c(\alpha)$ is the conversion admittance matrix given by the Quantum Theory of Mixing for each individual junction as a function of the normalized LO voltage, α , derived in the large signal analysis. Since the LO voltages

across the different junctions have different phases, the entries of the conversion matrix have to be multiplied by phase factors given in [5]. We have also used the low-IF assumption in formulating the conversion matrices, without considering the quantization effects at high IF. This approximation is valid for IF less than $F_{LO}/10$ [7]. Consequently, we limit the maximum IF to be 40 GHz in our simulation.

The expanded transmission matrix formalism creates a framework in which we can integrate passive transmission line elements with mixing elements. This is a very powerful tool for the simulation of the series-connected distributed mixer. The formalism can easily be generalized to simulate 5-port mixers in which harmonic effects are important. In that case, the entries to the expanded transmission matrix would be 5×5 matrices.

Once the RF voltages across individual junctions are solved in the large-signal analysis, we can formulate the expanded transmission matrix of the entire mixer circuit by matrix multiplication. The final step is to apply the boundary condition, which is $V_{out} = 0$ for our mixer layout because one side of the last junction is shorted to ground. Referring to equation (1), we can see that the final conversion admittance matrix of the mixer array is:

$$\mathbf{Y}_{final} = \mathbf{D}_{final} \cdot \mathbf{B}_{final}^{-1} \quad (5)$$

By adding the appropriate embedding admittances to \mathbf{Y}_{final} , the conversion loss of the mixer and the port impedances can be solved.

V. NOISE ANALYSIS

The shot noise generated at each junction is transformed by the entire mixer circuit before making its way to the mixer ports. Assuming that the noise generated at each device is not correlated with that generated at other devices, we can use the theorem of superposition to sum the noise power delivered to the IF port from the individual junctions, activating one junction at a time.

Referring to Fig. 4, we assume that a noise current source, $\langle I_{nj} \rangle$, is put across the junction j ($j = 1, 2, 3$ or 4). Note that the noise current is also expressed in a vector form because it has components at all three sidebands of interest. In order to solve for the noise power delivered to the embedding impedance due to $\langle I_{nj} \rangle$, we have to first calculate the expanded transmission matrix of the network lying between the source impedance and the device (marked "Front section" in the figure) and that of the network lying beyond the junction (marked "Back section"). Once the expanded transmission matrices for the front and back sections are established, we can solve for the noise impedance matrix that relates the noise voltage induced across the embedding impedance, $\langle V_{ne_j} \rangle$ to $\langle I_{nj} \rangle$:

$$\langle V_{ne_j} \rangle = \mathbf{Zn}_j \cdot \langle I_{nj} \rangle \quad (6)$$

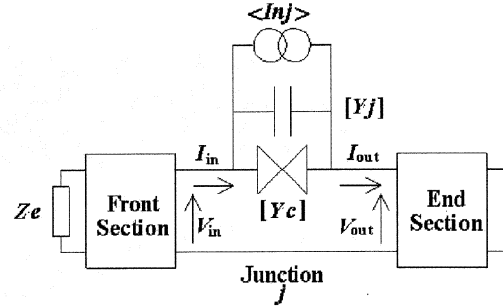


Fig. 4 A schematic representation of the mixer circuitry seen by the shot noise source associated with Junction j ($j = 1, 2, 3$ or 4). The SIS element is modeled by a capacitance matrix $[Yc]$ in parallel to its conversion matrix $[Yc]$.

The total mean-squared noise voltage delivered to the IF terminal is the sum of the contributions from all four junctions. The algebraic expression is:

$$\langle V_N^2 \rangle = \sum_{j=1}^4 \sum_{k=-1}^1 \sum_{k'=-1}^1 (\mathbf{Zn}_j)_{0,k} (\mathbf{Zn}_j)_{0,k'}^* (\mathbf{H}_j)_{k,k'} \quad (7)$$

In the above equation \mathbf{H}_j is the current correlation matrix given by the Quantum Theory of Mixing. Knowing the single-side-band conversion gain of the mixer, L_{SSB} , one can establish the single-side-band noise temperature of the mixer due to shot noise effects:

$$k_B T_{SSB} = L_{SSB} \text{Re}(Y_e(\omega_0)) \langle V_N^2 \rangle \quad (8)$$

Where k_B is the Boltzmann constant and $Y_e(\omega_0)$ is the embedding admittance at the IF. For double-side-band noise temperature, the average value of the sum of the conversion losses in both side-bands is used.

VI. SIMULATION RESULTS

We first performed a simulation of the mixer performance at a fixed IF of 5 GHz. It is found that the conversion loss of the mixer is relatively insensitive to LO drive when the normalized LO voltage across junction 4 reaches a value of 1.1. Referring to Fig. 5, the conversion losses of the mixer for both sidebands are quite flat from 320 to 420 GHz. This represents a bandwidth of about 25%, comparable to transformer-matched SIS mixer.

Then, we fix the LO frequency to the middle of the band, at 370 GHz. But we vary the IF from 2 GHz to 40 GHz. The results are plotted in Fig. 6. The calculated conversion loss of the mixer only drops by about 1 dB over this IF range. Clearly, the simulation demonstrates that our series-connected distributed mixer design offers an ultra-wide IF bandwidth.

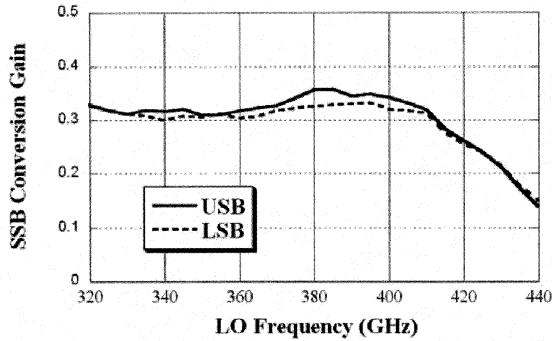


Fig. 5 Single-side-band Conversion Gain of the SIS mixer as a function of LO frequency. The IF is at 5 GHz. We also assume that $\alpha_4 = 1.1$ and the bias voltage to be 0.75 Vgap.

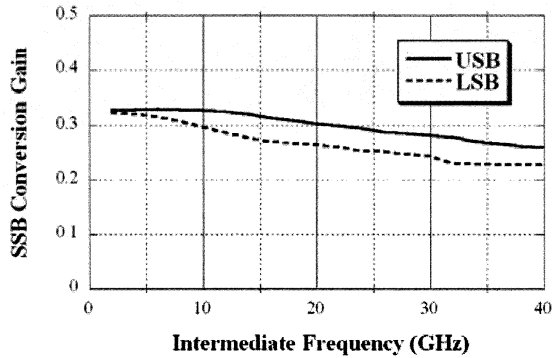


Fig. 6 Single-side-band conversion gain of the receiver as a function of the IF for an LO frequency of 370 GHz.

The double-side-band mixer noise temperature is also simulated. The result is plotted in Fig. 7. We can see that for a mixer with a low leakage current, the mixer noise temperature stays below the quantum limit ($h\nu/k \sim 18$ K at 370 GHz). The results of simulation agree with noise temperature measured in the lab. Preliminary measurements at an LO of 355 GHz have yielded double-side-band receiver noise temperatures below 80 K for IF between 15 and 20 GHz. We are currently working on the improvement of the IF circuitry to increase the bandwidth of measurement.

VII. CONCLUSION

A three-frequency expanded transmission matrix has been introduced to facilitate the modeling of the series-connected SIS junction array. This formalism offers a unified description of the frequency mixing action of the SIS and the passive transmission networks linking these series-connected devices, at all the three frequencies under consideration (signal, image and IF). Our simulation confirms that the series-connected distributed SIS mixer possesses a flat RF response over a 25% bandwidth, and at the same time offering an exceptionally wide instantaneous bandwidth of up to 40 GHz. The intrinsic

noise temperature of this class of mixer lies also below the quantum limit.

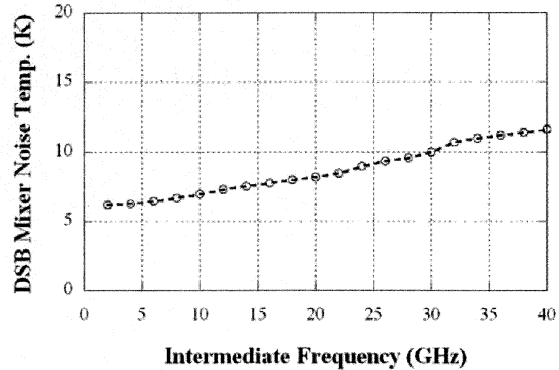


Fig. 7 Double-side-band mixer noise temperature of the SIS mixer as a function of IF for an LO frequency of 370 GHz.

REFERENCES

- [1] C.E. Tong, R. Blundell, K.G. Megerian, J.A. Stern, S.-K. Pan, and M. Popieszalski, "A distributed lumped-element SIS mixer with very wide instantaneous bandwidth," *IEEE Trans. Appl. Supercond.*, vol. 15(2), pp. 490-494, June 2005.
- [2] J.R. Tucker, and M.J. Feldman, "Quantum detection at millimeter wavelengths," *Rev. Modern Phys.*, vol. 57, pp. 1055-1113, Oct. 1995.
- [3] J. Ward, F. Rice, G. Chattopadhyay, and J. Zmuidzinas, "SuperMix: A flexible software library for high-frequency circuit simulation, including SIS mixers and superconducting elements," in *Proc. 10th Int. Symp. Space THz Tech.*, Charlottesville, VA, Ed. T. Crowe, pp. 268-280, March 1999.
- [4] F. Rice, J. Ward, *private communications*, 2006
- [5] C.-Y. E. Tong, R. Blundell, B. Bumble, J.A. Stern, and H.G. LeDuc, "Distributed mixing in a non-linear transmission line at sub-millimeter wavelengths," *IEEE Trans. Appl. Supercond.*, vol. 7, pp. 3597-3600, Jun 1997.
- [6] S.-K. Pan, and A.R. Kerr, "SIS mixer analysis with non-zero intermediate frequencies," in *Proc. 7th Int. Symp. Space THz Tech.*, Charlottesville, VA, Ed. T. Crowe, pp. 195-206, March 1996.
- [7] C.E. Tong, L. Chen, and R. Blundell, "Theory of distributed mixing and amplification in a superconducting quasi-particle nonlinear transmission line," *IEEE Trans. Microwave Theory & Tech.*, vol. 45, pp. 1086-1092, Jul. 1997.

RF and IF couplers for a sideband separating SIS waveguide mixer for a 345 GHz focal plane array

M. Justen, T. Tils, P. Pütz¹, A. Murk², C.E. Honingh, K. Jacobs

Köln Observatorium für Sub-Millimeter Astronomie, KOSMA
 1. Physikalisches Institut der Universität zu Köln,
 Zülpicher Straße 77, 50937 Köln, Germany

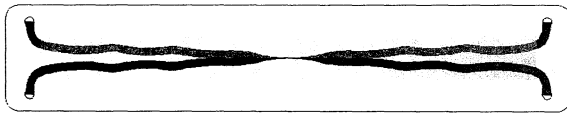
¹ Presently with Steward Observatory, University of Arizona, USA

² Institute of Applied Physics, University of Bern, Switzerland

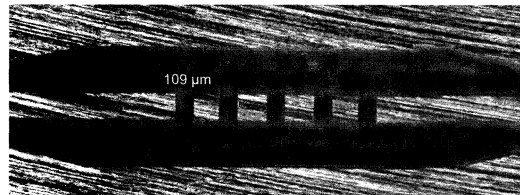
We present recent developments of a sideband separating SIS mixer at 345GHz. Special emphasis is placed on the critical design of the RF- and the IF-hybrids.

Two similar waveguide RF couplers designed for a bandwidth from 330-370 GHz are fabricated on two CNC lathes with different precision. Both couplers show adequate performance. The couplers are compared by accurate phase and amplitude measurements at the operating frequency with an ABmm vector network analyzer.

The IF signal of the two SIS junctions is recombined by a 90° -3dB hybrid. A nonuniform transmission line directional coupler has been specially designed for operation at cryogenic temperatures and integration into the mixer units. The coupling accuracy is +/-1dB over a very broad bandwidth from 1.5 to 8 GHz. Both the RF and IF hybrids are completely fabricated in house and can be easily adapted to the requirements of a focal plane array receiver.



The IF hybrid with nonuniform stripline structure. Two RT/duroid6002 substrates separated by 12µm Mylar foil. Structure size: 77.6 x 14.6 mm²



One half of a 345GHz branch line waveguide coupler in milled in brass. Coupling slit width: 109µm.

Side-band-separating heterodyne mixer for band 9 of ALMA.

F. P. Mena*, A. M. Baryshev*, J. Kooi†, G. Gerlofsma*, C. F. J. Lodewijk‡, R. Hesper*, and W. Wild*

*Space Research Organization of The Netherlands and Kapteyn Institute, University of Groningen,
Landleven 12, 9747 AD Groningen, The Netherlands

†California Institute of Technology,
MS 320-47 Pasadena, California 91125, USA

‡Kavli Institute of Nanoscience, Delft University of Technology,
Lorentzweg 1, 2628 CJ Delft, The Netherlands

Abstract— In this paper we will present the realization of a side-band-separating (2SB) heterodyne mixer for the frequency range from 602 to 720 GHz. This frequency range corresponds to band 9 band of ALMA. The mixer, in brief, consists of a quadrature hybrid, two LO injectors, two SIS junctions, and three dumping loads. All the parts were modeled and optimized prior construction. The fabricated SSB mixer exploits waveguide technology and has been constructed in the split-block technique. We used state-of-the-art CNC micromachining which permitted to obtain details as small as $\sim 70 \mu\text{m}$ with tolerances of $\sim 2 \mu\text{m}$. Finally, we will present the performance of the SIS junctions that will be used in the 2SB mixer.

I. INTRODUCTION

Of the receiver bands that are currently being constructed for the Atacama Large Millimeter Array (ALMA), only band 9, operating at the highest frequencies (602-720 GHz) uses double side-band mixers. Despite of the well known advantages of a side-band-separating (2SB) mixer, it has not been implemented in band 9 as the involved dimensions are prohibitory small. However, the current state-of-the-art micromachining technology has proved that the complicated structures necessary for this development are attainable [1], [2]. We have already reported a complete design of a 2SB mixer for band 9 together with a full simulation of the RF components [1]. The purpose of this article is to present the physical realization of such mixer including the corresponding IF circuit. We also present the testing results of the SIS junctions that will be used in the mixer. The results show a good homogeneity which are desirable for a good performance of the complete mixer.

II. 2SB MIXER BLOCK

Recently, we proposed a design for the 2SB mixer for ALMA band 9 which is reproduced in Fig. 1a.[1] The idea behind the design is to have a compact unit which will contain all the main components: defluxing magnets, DC biasing board, and the IF circuit filtering. The realization of such block is presented in Fig. 1b. It was obtained via state-of-the-art CNC micromachining. In Fig 2 we show a detailed view of the core of the mixer consisting of a quadrature hybrid, two LO injectors, two SIS junctions, and three dumping loads. The

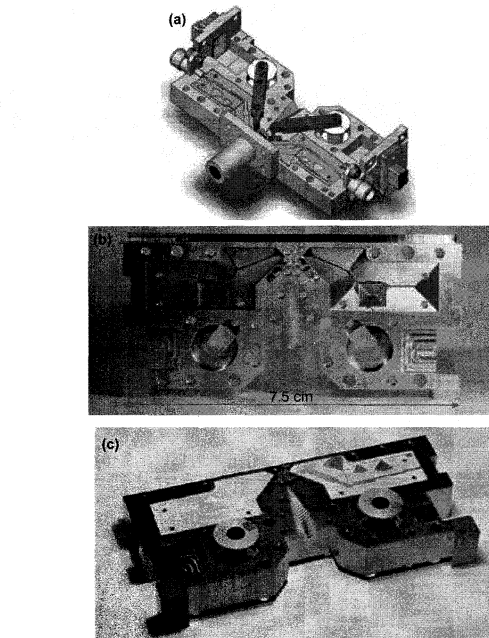


Fig. 1. (a) Proposed design of a 2SB mixer for ALMA band 9. (b) Micromachining realization of the mixer. (c) Mixer with the IF circuit board and magnets.

quality of the finishing is excellent and meets the required tolerances.[2]

III. IF CIRCUIT

For the 4 to 8 GHz IF circuit we have opted for the use of parallel coupled suspended microstrip lines. This is a compact unit containing the IF match, DC-break, bias tee, and EMI filter. The advantage of such planar structure has already been demonstrated and selected to be used in various astronomical instruments (see, for example, Ref. [3]). The already mounted circuit can be seen in Fig. 1. It has to be noted that, for this

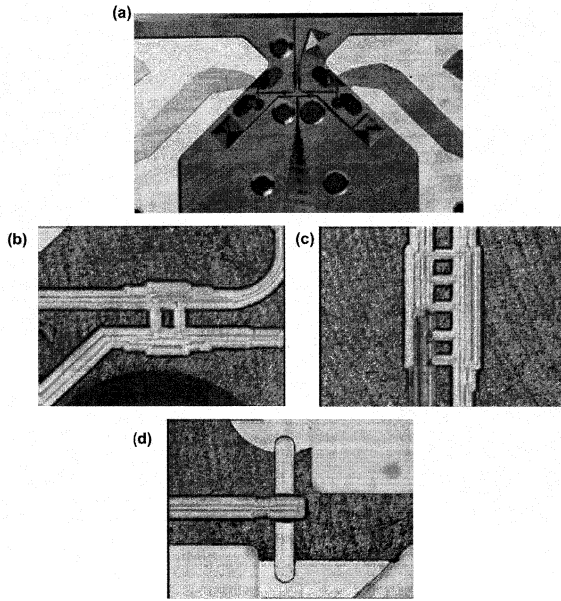


Fig. 2. (a) Detailed view of the RF components of the mixer. (b) LO injector. (c) RF quadrature hybrid. (d) Room for the mixers.

filter to work, the ground plane directly underneath the filter has to be removed. Previous to fabrication, the dimensions were optimized for a good performance in the 4 to 8 GHz frequency range. As an example of this results, in Fig. 3, we show the transmission of this IF circuit.

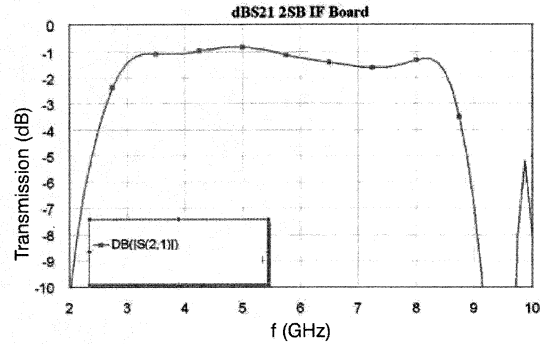


Fig. 3. Simulated transmission of the IF circuit.

IV. JUNCTIONS

For the SIS junctions we selected the design that contains both RF and IF matching. The exact layout is similar to the one presented by Risacher et al. [4] and is shown in Fig. 4. The chosen design was simulated [5] and its dimensions optimized for a maximum transmission and minimum reflection between ports 1 and 2 (see Fig. 4). We compared both a hammer type and a rectangular choke structure. The best reflection and transmission for both configurations are shown in Fig. 4. Given these results, a rectangular choke structure was fabricated.

The SIS devices were fabricated on a quartz substrate. First, a Nb monitor layer is deposited, after which an optically defined ground plane pattern of Nb/Al/AIOx/Nb is lifted off. Junctions are defined by e-beam lithography in a negative e-beam resist layer and etched out with a SF6/O2 reactive ion etch (RIE) using AlOx as a stopping layer. The junction resist pattern is subsequently used as a lift off mask for a dielectric layer of SiO2. A Nb/Au top layer is deposited and Au is etched with a wet etch in a KI/I2 solution using an optically defined mask. Finally, using an e-beam defined top wire mask pattern, the layer of Nb is etched with a SF6/O2 RIE, finishing the

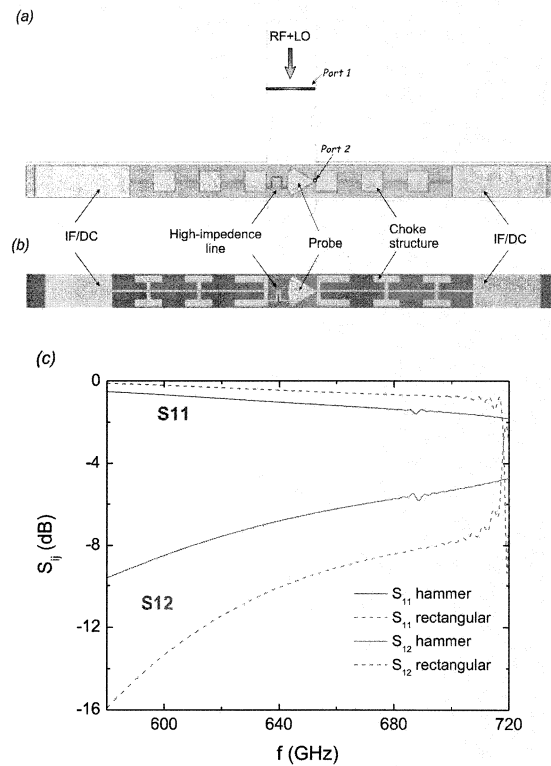


Fig. 4. (a) SIS design with a rectangular choke structure. The figure also shows the cavity where the junction will be placed. (b) SIS design with a hammer type choke. (c) Results of the simulations for the two types of choke structures.

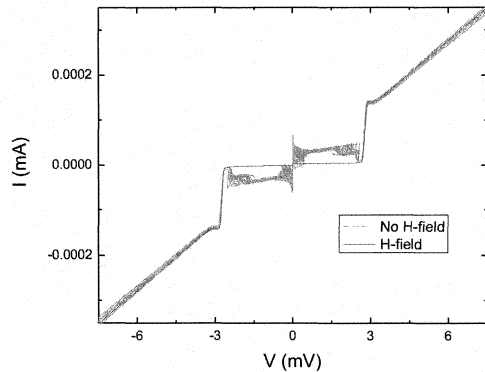


Fig. 5. IV curves of 12 different junctions intended to be used in the 2SB mixer. Notice the good repeatability necessary for a good performance of the mixer.

fabrication process. After dicing and polishing, we measured the resistance of the individual devices as indicated in Fig. 5. The results show that the chosen fabrication procedure results in a good reproducibility of the devices. This is a key element for the future performance of the mixer.

V. CONCLUSIONS

In this article we have presented the current status of the development of a side band separating mixer for ALMA band 9. Currently, all of the components have been simulated, fabricated and tested individually. The assembling is a going on task that will be completed in the next months.

ACKNOWLEDGEMENT

We gratefully acknowledge funding from NOVA, the Netherlands Research School for Astronomy, and the FP6 program of the European Union.

REFERENCES

- [1] F. P. Mena et al., *Design of a side-band-separating heterodyne mixer for band 9 of ALMA*, 16th Proc. THz Space Conference (2005).
- [2] Radiometer Physics GmbH, <http://www.radiometer-physics.de/>.
- [3] J. Kooi et al., *Heterodyne Instrumentation Upgrade at the Caltech Submillimeter Observatory*, SPIE, Millimeter and submillimeter detectors for Astronomy II, Vol 5498, pp 332-348 (2004).
- [4] C. Risacher et al., *IEEE Microwave and Wireless Components Letters*, vol. 13 (2003).
- [5] Microwave Studio, <http://www.sonnetusa.com/>.

1.4 THz SIS mixer development for radio astronomy

A. Karpov, D. Miller, F. Rice, J. A. Stern*, B. Bumble*, H. G. LeDuc*, J. Zmuidzinas

California Institute of Technology, Pasadena, CA 91125, USA

* Jet Propulsion Laboratory, Pasadena, CA 91109, USA

We report the development of a 1.4 THz SIS mixer for a heterodyne spectrometer CASIMIR aimed for the stratospheric observatory SOFIA. The goal of this work is to provide a low noise spectrometer particularly for the studies of the H_2D^+ $1_{01} - 0_{00}$ line around 1370 GHz.

In the mixer we use two Nb/AlN/NbTiN SIS junction array. The mixer has a quasi-optical design. The maximum frequency of an SIS mixer operation is close to the double gap frequency, about 1.7 THz for the hybrid Nb – NbTiN junctions having the gap voltage of 3.4-3.5 mV. This allows one to cover a significant part of the THz range with already existing SIS technology.

The LO power requirements for the designed SIS mixer are low. Based on our experience at 1.25 THz, the mixer uses about 100 – 150 nW of LO power when optimally pumped. The currently available LO sources are providing about 10 uW power, sufficient for the LO injection through a diplexer.

The SIS mixer model envisages 1.2-1.5 THz coverage with a low noise operation. In the figure below are the predictions for the on-chip SIS mixer coupling to the signal source.

The calculation gives the coupling in the 1.4 THz device only slightly less than in the 1.2 THz mixer, already proved to perform well.

The receiver test at 1.33 – 1.35 THz gives promising results for a complete receiver operation. We will discuss the limitations of the mixer performance at 1.4 THz.

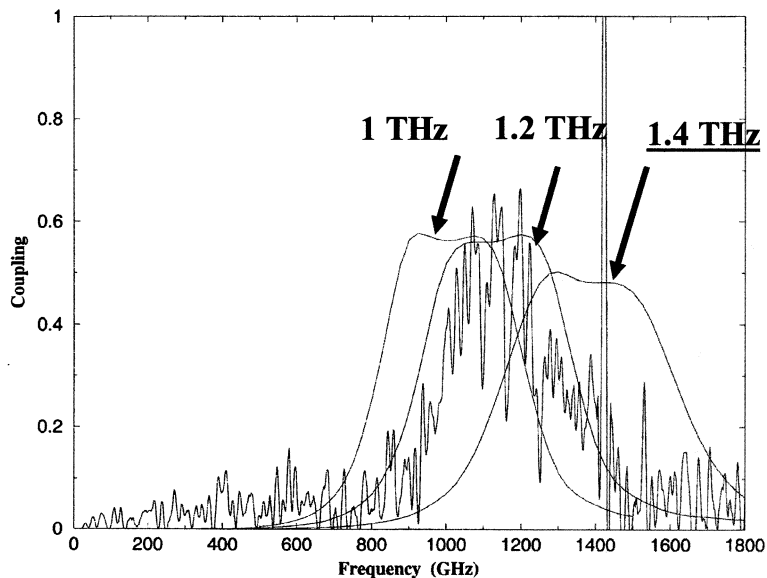


Fig. 1. Prediction of the on-chip coupling in 1 – 1.5 THz SIS mixers.

POSTER SESSION n°1

Presentation on
Wednesday 10 May 12:00-12:30

by Dr. Jian-Rong Gao

Poster session n°1 from 14:00 to 15:30

VO₂ TES as Room Temperature THz Detectors

Biddut K. Banik, Harald F. Merkel

Abstract— VO_x materials hold very high potential to be used as room temperature bolometer. A brief review on room temperature bolometers and VO_x characteristics is presented. The hysteretic metal-insulator transition behavior of a VO_x microbolometer has been investigated. An algebraic hysteresis model has been used to model the resistance-temperature characteristic of the bolometer. The magnetic limiting loop proximity (L²P) hysteresis theory is modified to represent the VO_x major and minor hysteresis loops. The responsivity of the bolometer is also calculated. Loop accommodation process is explained. Nonsymmetrical hysteretic behavior has also been discussed.

Index Terms— Bolometers, hysteresis, vanadium oxide.

I. INTRODUCTION

TODAY THz detectors are exclusively based on superconducting materials. Superconducting Tunnel Elements (SIS), Transition Edge Sensors (TES) have been used as direct detectors while Hot Electron Bolometers (HEB) has been used for heterodyne receivers without frequency limitations. These sensors have become standard solutions for radioastronomy and other remote sensing applications. In recent years, security and safety applications have emerged as potentially new applications for THz technology. Proposed systems (e.g. airport security, standoff checkpoints) for detection of explosives and concealed weapons require imaging and detection at some 20 m distance. Compared to radioastronomic applications, the requirements on spectroscopic resolution are here greatly relaxed. Interesting molecular lines are temperature and pressure-widened. Imaging is crucial, so any commercially interesting detector system must be capable to be extendable to 100s and 1000s of pixels. Commercially viable systems must operate at room temperature or even better at elevated temperature levels. The advantages of uncooled sensors include no cryogenics, and no related complicated problems including additional power requirements, thermal shielding, and limited lifetime and additional weight and bulk. The results of such a basic study are presented in this work. Room temperature THz detection using composite bolometers, nanowires and nanotechnology, antenna coupled quasi-optical systems, superconducting TES devices having high T_c (YBaCuO) have been reported. Being used in military applications in the Near Infrared and having a very good potential as direct-detection detector, the

use of vanadium oxides (VO_x) for room temperature THz detection is still virtually unexplored.

Vanadium oxide materials exhibit so-called Magnéli phase transition (i.e. between a metallic and semiconducting state) typically located at 68 °C, for the case of VO₂. Location and steepness of the transition temperature of VO_x films can be modified by varying process parameters as annealing temperature (in a sol-gel process) or doping the vanadium oxide with other cations or alternatively having a stoichiometrically inaccurate mixture of VO₂ and V₃O₄.

II. ROOM TEMPERATURE BOLOMETERS

A. A brief review

YBaCuO thin film bolometer for uncooled infrared detection has already been investigated [1] where YBaCuO on a Si substrate with and without a MgO buffer layer, and on an oxidized Si substrate with and without a MgO buffer layer were characterized. TCRs for all the films were greater than 2.5% K⁻¹. The highest TCR of 4.02% K⁻¹ was observed on the amorphous YBaCuO thin film deposited on MgO/Si without a SiO₂ layer. YBaCuO bolometers have a responsivity as high as 3.8×10⁵ V/W and a detectivity as high as 1.6×10⁹ cm Hz^{1/2}/W for 1 μA bias current and frame frequency of 30 Hz if integrated with a typical air-gap thermal isolation structure. Microbolometers have been fabricated using a thin niobium film [2] as the detector element to operate at room temperature. The reported responsivity was up to 21 V/W at a bias of 6.4 mA, and electrical noise equivalent powers (NEP) of as low as 1.1 × 10⁻¹⁰ W/√Hz at 1 kHz. Metal bolometers at room temperature made of Pt, Au, Bi, and Ni have also been investigated [3].

B. VO_x Bolometers

Vanadium oxide thin films have been adopted [4] to make a 320 × 240 pixel IR detector and the reported NETD (noise equivalent temperature difference) was smaller than 0.1K at 60 Hz frame rate. The reported TCR is -1.64%/K and thermal time constant is 12 ms. VO_x thin film bolometers have been investigated and characterized by few other research groups [5, 6]. V₂O₅/V/V₂O₅ multilayer vanadium oxide thin films have been fabricated with high temperature coefficient [7]. Another 160 × 128 uncooled infrared sensor array was reported where calculated NETD for 4.25V bolometer bias and 2.74% TCR is 72 mK with f/1.8 optics [8]. A 16 × 16 array has been reported having responsivity of 1200 V/W, a detectivity of 2.2×10 cmHz^{1/2}/W and NETD of 200 mK at 0.5 Hz frame rate [9].

Manuscript received May 11, 2006.

B. K. Banik is with the Dept. of Microtechnology and Nanoscience, Microwave Electronics Laboratory, MC2, Chalmers University of Technology, Göteborg, Sweden (e-mail: biddut.banik@mc2.chalmers.se).

H. F. Merkel is with the Dept. of Microtechnology and Nanoscience, Microwave Electronics Laboratory, MC2, Chalmers University of Technology and Food Radar AB, Göteborg, Sweden (e-mail: harald.merkel@mc2.chalmers.se).

III. VANADIUM OXIDE

A. VO_x characteristics

Several oxides of vanadium, such as VO, V_2O_3 , VO_2 , V_3O_5 , V_6O_{13} , and V_2O_5 , undergo a transition from a metal to a semiconductor or insulator phase at a critical temperature. VO_2 undergoes this transition near 68 °C as it transforms from a monoclinic to a tetragonal crystal structure, accompanied by large changes in electrical and optical behavior.

The phase transition properties make VO_x suitable for fabrication of a variety of electrical and optical devices, including electrical switching elements, thermistor thermal relays and optical switching elements. VO_x materials were used as intelligent window coatings [10]. Metal-insulator transition mechanism has been investigated [11]. The temperature and strain dependence of VO_x film resistance was also investigated [12]. Vanadium oxide films exhibit some interesting optical properties such as optical birefringence, electrochromism or optical switching [13]. The nature of the condensed phases formed upon hydrolysis and condensation.

The electrical and optical properties of VO_x largely depend on the derivation or deposition process, process temperature, ambient temperature, pressure, Stoichiometric composition, doping, grain size, type of substrate, specific orientation on its substrate [14-21]. Hysteresis width down to 1K has been reported [22]. Electrical and infrared properties of Vanadium Oxide nanocrystalline powder and thin films have been investigated [23].

Large negative temperature coefficients of resistance for high quality films have been reported [24]. Present uncooled VO_x bolometers are operated in the nonhysteretic metallic part of its resistance-temperature (R-T) curve, at temperatures below the metal-insulator (M-I) transition.

IV. VO_x CHARACTERIZATION

A. Hysteresis modeling

The magnetic limiting loop proximity (L^2P) hysteresis theory is modified to represent (1) the major hysteresis loops [25] where M_s is the saturation value, H_c is coercivity field, h_0 is a material dependent constant and δ is a sign operator.

$$M(H) = \frac{2}{\pi} M_s \arctan \frac{H - \delta H_c}{h_0} \quad (1)$$

It should be mentioned that (1) represents only the major hysteresis curve. To represent any arbitrary point (H , M) and to incorporate minor loops, (1) has been modified by [25].

$$M(H) = \frac{2}{\pi} M_s \arctan \frac{H_{pr} P(x) - \delta H_c + H}{h_0} \quad (2)$$

$$x = \frac{H - H_r}{H_{pr}} \quad (3)$$

Where, H_{pr} is the proximity field at reversal point H_r , and $P(x)$ is the proximity function. $P(x) = 1 - \sin \zeta x$ for $2\zeta x < \pi$ and $P(x) = 0$ otherwise. Here ζ and h_0 are material

dependent constants.

The temperature dependent resistivity of VO_x bolometer can be represented as (4) where R_s is the saturation value of $R(T)$ at high temperature end, χ and ψ are dependent on the saturation value of $R(T)$ at low temperature end and on R - T slope, $\nu(T)$ incorporates the hysteresis loop, w is the hysteresis width, β_g represents the slope of $\nu(T)$, T_c is the critical temperature and $\delta = \text{sign}(dT/dt)$. $\beta_g = \beta_{g^+}$ for $\delta = 1$ and $\beta_g = \beta_{g^-}$ for $\delta = -1$. Typically $\beta_{g^+} = \beta_{g^-}$ for VO_x materials but the values are different for doped VO_x , for instance, as β_g becomes dependent on δ and T [13].

$$R(T) = R_s + \chi \exp \left[\frac{\psi}{T + 273} \right] \nu(T) \quad (4)$$

$$\nu(T) = 0.5 \left[1 + \tanh \beta_g \gamma \right] \quad (5)$$

$$\gamma = \delta \frac{w}{2} + T_c - T \quad (6)$$

Fig. 1 demonstrates $\nu(T)$ and $R(T)$ for $T_c = 68$ °C, $\beta_g = \beta_{g^+} = \beta_{g^-} = 0.2$, $w = 6.5$ °C, $\chi = 20$ and $\psi = 2500$ and $R_s = 120$.

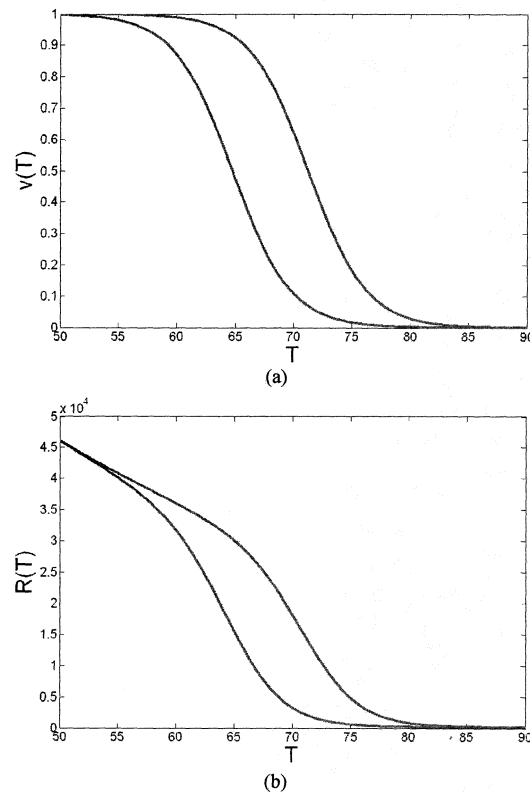


Fig. 1. (a) $\nu(T)$ and (b) $R(T)$ major loop for $T_c = 68$ °C, $w = 6.5$ °C

B. Incorporating minor loops

To incorporate minor loops, (6) can be modified with (2) to attain (7) where T_{pr} is the proximity temperature at reversal temperature point T_r . It should be noticed that for the case of major loop, $T_{pr} = w$ at any reversal point.

$$\gamma = \delta \frac{w}{2} + T_c - T + T_{pr} P(x) \quad (7)$$

$$x = \frac{T - T_r}{T_{pr}} \quad (8)$$

$$T_{pr} = \gamma_r - \frac{1}{\beta_g} \arctan(2v_r - 1) \quad (9)$$

$$P(x) = 0.5(1 - \sin \zeta x) [1 + \tanh(\pi^2 - 2\pi x)] \quad (10)$$

Here, $\gamma_r = \gamma(T_r)$ and $v_r = v(T_r)$ as in (6) and (5) consecutively. T_{pr} and γ_r are changed only at the reversal point. It should be mentioned that for calculating v_r at T_r , T_{pr} takes the value of $T_{pr}(T_r - \delta \Delta T)$, which is basically the value of T_{pr} before the reversal point. Fig.2 (a-d) demonstrates the $v(T)$ and $R(T)$ loops where the $T_{r1}=72^\circ\text{C}$ and $T_{r2}=62^\circ\text{C}$.

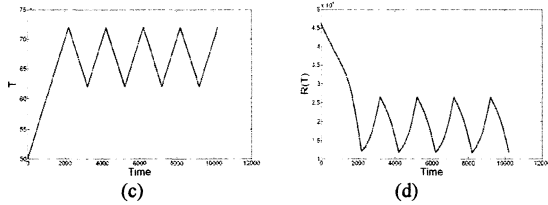
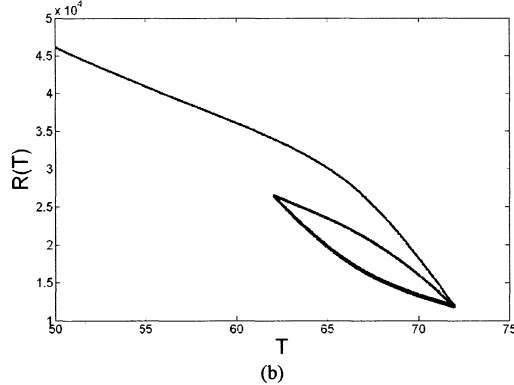
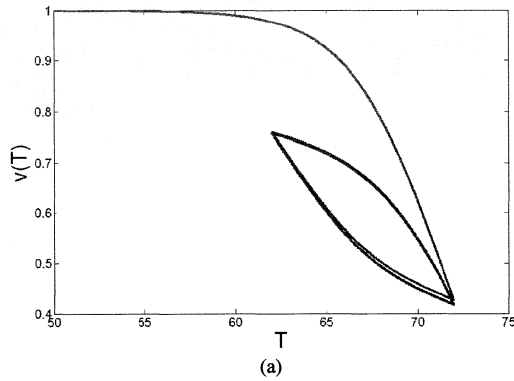


Fig. 2. (a) $v(T)$ and (b) $R(T)$ major and minor loops for $T_c = 68^\circ\text{C}$, $w = 6.5^\circ\text{C}$ and $T_{r1} = 72^\circ\text{C}$ and $T_{r2} = 62^\circ\text{C}$ (c) shows the variation of T with time and the corresponding change of $R(T)$ is presented in (d).

For smaller change in temperature, $T_{r1} = 72^\circ\text{C}$ and $T_{r2} = 67^\circ\text{C}$ and the corresponding $v(T)$ and $R(T)$ loops are presented in Fig. 3(a-d)

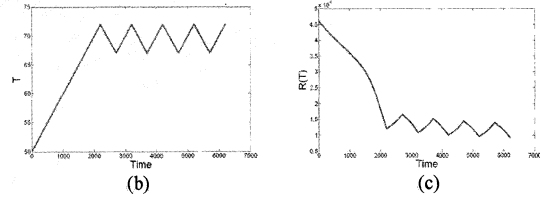
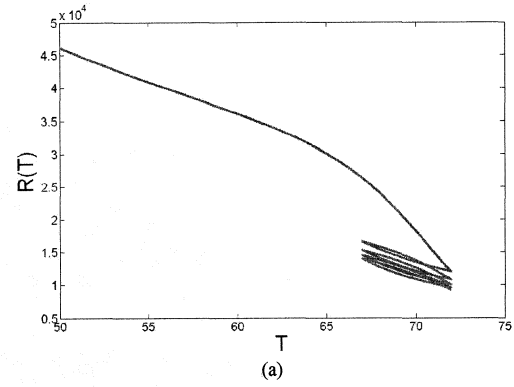


Fig. 3. (a) $v(T)$ and (b) $R(T)$ major and minor loops for $T_c = 68^\circ\text{C}$, $w = 6.5^\circ\text{C}$ and $T_{r1} = 72^\circ\text{C}$ and $T_{r2} = 67^\circ\text{C}$ (c) shows the variation of T with time and the corresponding change of $R(T)$ is presented in (d).

It can be seen from Fig. 2 that the minor loops are stabilized readily for large minor loops while Fig. 3 shows that minor loops become stabilized after few cycles. The stabilization time is inversely proportional to the area of minor loops in R-T plane. Fig. 2 and Fig. 3 explain the loop accommodation process in VO_x .

C. Nonsymmetrical hysteresis modeling

In order to realize nonsymmetrical hysteresis behavior, the hysteresis width w can be modified to express the ascending loop as (13).

$$w_- = 0.5 w_1 [1 - \tanh(\beta_{g-}(T_c - T))] + w_2 \quad (11)$$

Here w_1 and w_2 depend on the limiting values of w_- . Fig. 4 shows the $v(T)$ and $R(T)$ major loops for nonsymmetrical case.

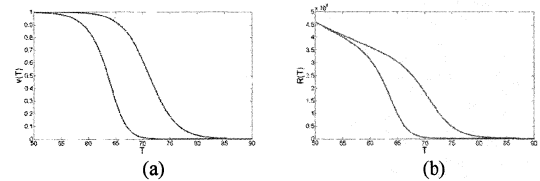


Fig. 4. (a) $v(T)$ and (b) $R(T)$ major loops for nonsymmetrical hysteresis case.

D. Responsivity

The voltage responsivity (R_v) is expressed in (12) where G_{th} is thermal conductance, V_B is bias voltage, η is absorbance and τ_{th} is thermal time constant. R_{dT} is expressed in (13). Fig. 5 shows that the responsivity is increased by a factor of 3 when the bolometer is operated in the hysteretic region.

$$R_v = \frac{\eta V_B R_{dt}}{G_{th} \sqrt{1 + (2\pi f \tau_{th})^2}} \quad (12)$$

$$R_{dT} = R_{T+\Delta T} - R_T \quad (13)$$

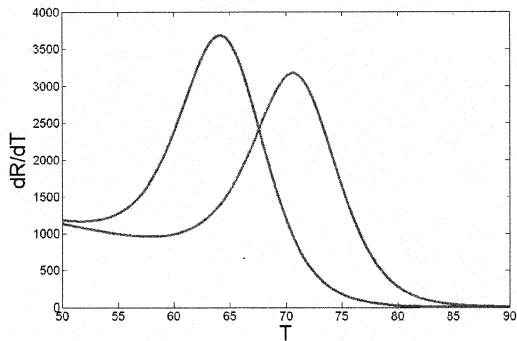


Fig. 5. R_{dT} for major ascending and descending loop; corresponds to normalized responsivity expressed in (12). For the descending loop, peak is observed at 70.66 °C.

V. CONCLUSION

VO_x materials are extremely promising for room temperature THz applications. Higher TCR can be achieved by high quality VO_x films, even with multilayer and doped films. The hysteresis width can also be minimized by fabrication process. NETD can be reduced by introducing on-chip readout circuit (ROIC). The main challenge is to operate the VO_x bolometer in the hysteretic region at suitable operating point to attain high TCR. Considering the thermal conductance (G_{th}) and thermal time constant (τ_{th}), Peltier elements can be used to cool down and heat up the bolometer to the optimum operating point.

REFERENCES

- [1] P. C. Shan, Z. Celik-Butler, D. P. Butler, A. Jahanzeb, C. M. Travers, W. Kula, and R. Sobolewski, "Investigation of semiconducting YBaCuO thin films: A new room temperature bolometer," *Journal of Applied Physics*, vol. 80, pp. 7118-23, 1996.
- [2] M. E. MacDonald and E. N. Grossman, "Niobium microbolometers for far-infrared detection," *IEEE Transactions on Microwave Theory and Techniques*, vol. 43, pp. 893-6, 1995.
- [3] V. K. Grunin, "Mathematical modeling of the temperature dependence of the parameters of uncooled metal bolometers," *Journal of Optical Technology*, vol. 68, pp. 952-5, 2001.
- [4] N. Oda, Y. Tanaka, T. Sasaki, A. Ajisawa, A. Kawahara, and S. Kurashina, "Performance of 320 x 240 bolometer-type uncooled infrared detector," *NEC Research and Development*, vol. 44, pp. 170-174, 2003.
- [5] C. Changhong, Y. Xinjian, Z. Xingrong, and X. Bifeng, "Preparation and properties of vanadium dioxide thin films for uncooled microbolometer," Beijing, China, 2000.
- [6] V. Y. Zerov, Y. V. Kulikov, V. N. Leonov, V. G. Malyarov, I. A. Khrebtov, and I. I. Shaganov, "Features of the operation of a bolometer based on a vanadium dioxide film in a temperature interval that includes a phase transition," *Journal of Optical Technology*, vol. 66, pp. 387-90, 1999.
- [7] H. Yong-Hee, C. In-Hoon, K. Ho-Kwan, P. Jong-Yeon, K. Kun-Tae, S. Hyun-Joon, and M. Sung, "Fabrication of vanadium oxide thin film with high-temperature coefficient of resistance using V_2O_5/NiO multi-layers for uncooled microbolometers," *Thin Solid Films*, vol. 425, pp. 260-4, 2003.
- [8] J. T. W. I. William J. Parrish, Glenn T. Kincaid, Jeffery L. Heath, and Jeffery D. Frank "Low-cost 160 x 128 uncooled infrared sensor

- array," *Proceedings of SPIE, Infrared Readout Electronics IV*, vol. 3360, pp. 111-119, 1998.
- [9] D. S. Tezcan, S. Eminoglu, O. S. Akar, and T. Akin, "A low cost uncooled infrared microbolometer focal plane array using the CMOS n-well layer," Interlaken, 2001.
- [10] T. D. Manning, I. P. Parkin, M. E. Pemble, D. Sheel, and D. Vernardou, "Intelligent window coatings: atmospheric pressure chemical vapor deposition of tungsten-doped vanadium dioxide," *Chemistry of Materials*, vol. 16, pp. 744-9, 2004.
- [11] A. Liebsch, H. Ishida, and G. Bihlmayer, "Coulomb correlations and orbital polarization in the metal-insulator transition of VO_2 ," *Physical Review B (Condensed Matter and Materials Physics)*, vol. 71, pp. 85109-1, 2005.
- [12] R. M. Bowman and J. M. Gregg, " VO_2 thin films: growth and the effect of applied strain on their resistance," *Journal of Materials Science: Materials in Electronics*, vol. 9, pp. 187-91, 1998.
- [13] J. Livage, G. Guzman, F. Beteille, and P. Davidson, "Optical properties of sol-gel derived vanadium oxide films," Faro, Portugal, 1997.
- [14] M. Borek, F. Qian, V. Nagabushnam, and R. K. Singh, "Pulsed laser deposition of oriented VO_2 thin films on R-cut sapphire substrates," *Applied Physics Letters*, vol. 63, pp. 3288-90, 1993.
- [15] P.-R. Zhu, S. Yamamoto, A. Miyashita, and H. Naramoto, "Pulsed laser deposition of VO_2 single crystal thin films on sapphire substrates," *Chinese Physics Letters*, vol. 15, pp. 904-6, 1998.
- [16] H. Liu, O. Vasquez, V. R. Santiago, L. Diaz, A. J. Rua, and F. E. Fernandez, "Novel pulsed-laser-deposition - VO_2 thin films for ultrafast applications," Charlotte, NC, USA, 2005.
- [17] D. Brassard, S. Fourmaux, M. Jean-Jacques, J. C. Kieffer, and M. A. El Khakani, "Grain size effect on the semiconductor-metal phase transition characteristics of magnetron-sputtered VO_2 thin films," *Applied Physics Letters*, vol. 87, pp. 51910-1, 2005.
- [18] X. Shiqing, M. Hongping, D. Shixun, and J. Zhonghong, "Study on optical and electrical switching properties and phase transition mechanism of Mo^{6+} -doped vanadium dioxide thin films," *Journal of Materials Science*, vol. 39, pp. 489-93, 2004.
- [19] M. A. Abdullaev, I. K. Kamilov, and E. I. Terukov, "Preparation and properties of stoichiometric vanadium oxides," *Inorganic Materials*, vol. 37, pp. 271-3, 2001.
- [20] G. Obermeier, D. Ciesla, S. Klimm, and S. Horn, "Pressure dependence of phase transitions in the quasi-one-dimensional metal-insulator transition system $\beta-Na_{1/3}V_2O_5$," *Physical Review B (Condensed Matter and Materials Physics)*, vol. 66, pp. 85117-1, 2002.
- [21] F. Beteille and J. Livage, "Optical switching in VO_2 thin films," Sheffield, UK, 1998.
- [22] D. H. Kim and H. S. Kwoka, "Pulsed laser deposition of VO_2 thin films," *Applied Physics Letters*, vol. 65, pp. 3188-90, 1994.
- [23] F. Guimneton, L. Sauques, J. C. Valmalette, F. Cros, and J. R. Gavarrí, "Comparative study between nanocrystalline powder and thin film of vanadium dioxide VO_2 : electrical and infrared properties," *Journal of the Physics and Chemistry of Solids*, vol. 62, pp. 1229-38, 2001.
- [24] C. D. Reintsema, E. N. Grossman, and J. A. Koch, "Improved VO_2 microbolometers for infrared imaging: operation on the semiconducting-metallic phase transition with negative electrothermal feedback," Orlando, FL, USA, 1999.
- [25] L. A. L. de Almeida, G. S. Deep, A. M. N. Lima, and H. Neff, "Limiting loop proximity hysteresis model," *IEEE Transactions on Magnetics*, vol. 39, pp. 523-8, 2003.

Design of coplanar stripline diplexer integrated in large arrays of antenna-coupled bolometers

Ph.Camus¹, D.Rauly², O.Guillaudin³, F.X.Désert⁴, A.Benoit¹, T.Durand¹

Abstract— Both in space-borne and ground instruments for cosmic microwave background (CMB) astrophysics, there is a need for large arrays of bolometers with some spectral resolution capabilities.

We propose a design for a pixel composed of a planar antenna and a stripline diplexer optimized for two photometric bands centered on 150 GHz and 220 GHz. The microwave circuit is suitable for an integration in a current antenna-coupled bolometer array.

The complexity of the circuit depends on the requested bandwidth and frequency rejection. The proposed design is based on a stripline coupler with a stub circuit to achieve the correct impedance matching between the antenna and the bolometer in the desired waveband.

The analysis of the antenna impedance and the radiation diagram is based on the HFSSTM software. The microwave circuit is then optimized by simulation with the Advanced Design System (ADSTM) from Agilent.

I. INTRODUCTION

FULLY sampled arrays of bolometers at very low temperature ($<0.3\text{K}$) are required to increase the sensitivity of modern millimeter instruments in CMB astrophysics. In order to have some spectral resolution, a classical solution is to define the needed photometric bands with a complex optical filtering scheme. A multifrequency detector array makes a better usage of the available focal plane at low temperature.

Antenna-coupled bolometers allow to separate the pixel design from the detector itself. Microstrip transmission lines can be designed to provide the desired filtering properties. Such detector architecture is proposed for several instruments [1][6]. Niobium microstrip with a silicon dioxide dielectric have very low loss up to 700 GHz [4]. We choose a solution based on a quarter wavelength coupler.

For the most demanding application in CMB polarization measurement, a phased-array of several slot-antenna is

Manuscript received May 11th, 2006. This work is partially supported by the CNES Research and Technology program.

¹ Centre de Recherche sur les Très Basses Température, 25 av. des martyrs, 38016 Grenoble Cedex 9, France

² Institut de Microélectronique, Electromagnétisme et Photonique, BP 257, 38016 Grenoble Cedex 1, France

³ Laboratoire de Physique Subatomique et de Cosmologie, Grenoble, France

⁴ Laboratoire d'Astrophysique Observatoire de Grenoble, BP 53, 38041 Grenoble Cedex 9, France

Corresponding author: philippe.camus@grenoble.cnrs.fr

foreseen [1][6]. For photometric imaging, we are proposing a planar antenna with a bow-tie geometry. The beamshape can be matched to an optic using a cold lens at $F/2$ - $F/3$ and a cold aperture below 1K to reduce the side lobe response.

II. PLANAR ANTENNA ANALYSIS

The antenna is designed to operate simultaneously in both frequency bands centered at 150 GHz and 220 GHz. These are central frequencies for the analysis of CMB anisotropies in the possible presence of foregrounds (e.g. dust, free-free and synchrotron galactic emissions). A classical wideband bow-tie planar antenna has the desired characteristics. It is also compact and suitable for an antenna array design [5] (Fig.1.). In order to obtain a high absorption efficiency, a reflective plane is placed below the antenna.

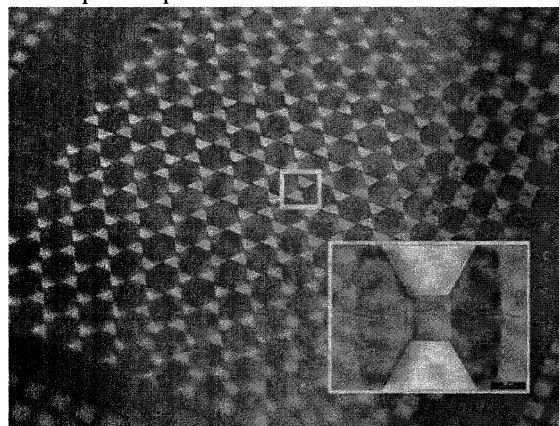


Fig. 1. Prototype array of 204 antenna-coupled bolometers [5] made at IEF/Orsay; the antennae distance is 2 mm to sample an image at $\lambda = 2$ mm with a $f/2$ optics.

The characteristics of the antenna are computed by using a commercial computer software package based on the finite element method (Ansoft HFSSTM). The impedance and the far field radiation pattern of this antenna will be presented for a single element. The properties are slightly different for a regular array of such antennae but are not presented here.

In the array fabrication process [6], the antenna is entirely deposited on a thin silicon substrate covered by a $1\mu\text{m}$ silicon nitride. In order to avoid some power loss due to surface waves in the substrates, we have to use a substrate thinner than $\lambda/\epsilon^{1/2}$ for the shortest wavelength. The high dielectric constant of the silicon substrates ($\epsilon=11.9$) requires to use a thickness less than $80\mu\text{m}$.

Micromachining fabrication techniques can be used to

remove the substrate below the antenna and, therefore, locally synthesize a low dielectric region around the antenna. In the extreme, silicon can be entirely removed, which provides a fully membrane supported antenna. The cavity around the antenna can be designed to resonate close to bow tie resonance. The antenna consists of two identical printed bows that are connected to the 2 coplanar strip lines.

The radiation pattern and the antenna impedance are computed for the optimized geometry given in Fig.2 from 100 to 300 GHz. The antenna complex impedance (Fig.3) is used to design the microstrip filter. The single antenna provides a good radiation characteristics up to 250 GHz but starts to deteriorate at 260 GHz. The antenna gain has an average value of 9 dB over the bandwidth 100-250 GHz (Fig.4).

Parameter	Dimension
W	0,58 mm
L	0,58 mm
Wf	2 μ m
Etched cavity	0,34 mm

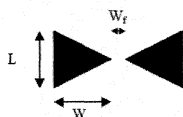


Fig.2. Optimized antenna dimensions.

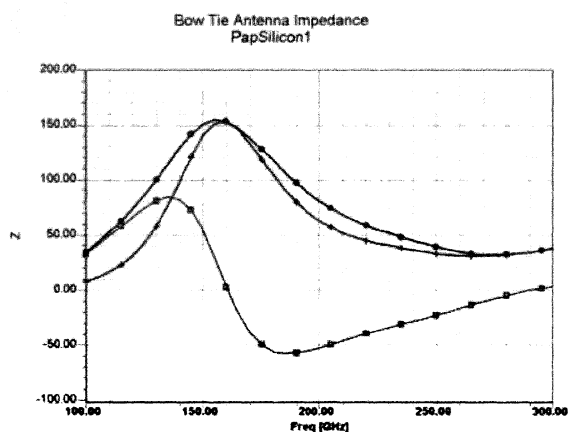


Fig. 3. Antenna complex impedance.

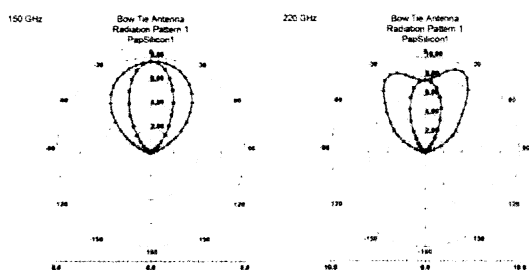


Fig. 4. Antenna radiation pattern at 150 GHz and 220 GHz; 0° is the main axis direction.

III. MICROWAVE CIRCUIT DESIGN

The theoretical circuit of the diplexer is shown on Fig.5. The signal is divided from the antenna into two filtering sub-circuits propagating it towards two resistive shunts (i.e. the bolometers), with a maximum transmission centered respectively at 150 GHz and 220 GHz. Each filter is

composed by three transmission lines, namely its is a multisection stepped-impedance structure, with a stub playing the role of a reactive obstacle. The present design includes only two sections with one obstacle. More complex structures can be proposed for a higher required slopes in the frequency response [1,2], but here is not the aim of the project. The filtering action is due to the selective matching between the shunt impedance, chosen at 200 Ω and the antenna impedance (Fig.3).

A maximum transmission across a sub-circuit is reached at a given frequency when it exhibits an input reflection coefficient S11 equal to the conjugate value S'11* of the antenna's one. As it can be seen on Fig.6, each sub-circuit reaches this matching condition, while it is close to an open circuit at the nominal frequency of the opposite sub-circuit. This last property is due to the relatively high characteristic impedance (>50 Ω) of the lines touching the antenna. These results have been optimized with the Advanced Design System software (ADSTM, Agilent).

In a first step,, we have assembled the two pre-optimized sub-circuits to the antenna port. The simulated transmission coefficients in dB from the antenna port, taking into account its complex impedance, to the bolometers is given in Fig.7-Left. At the band center frequency, the system has rejection higher than 20 dB between the required and undesirable signals. For the 150 GHz, a maximum in the transmission occurs at 245 GHz which has to be rejected by an optical filter.

In a second step, a global optimization, obtained with ADSTM, leads to the values explicated in table 1, with better rejection (Fig.7 - Right).

The lay-out of the proposed device is shown on Fig.8. The high characteristic impedance transmission lines (TL1 & TL4) are made with Coplanar Strip Lines (CPS) on a 100 μ m-thick silicon substrate, suspended on a 425 μ m deep cavity, separating it from a ground plane. Ground layer and strips made of superconducting Nb have been assumed with infinite conductivity and 0.2 μ m thickness.

The low impedance lines are Broadside Coupled Lines (BCL). They are constituted by two superposed strips, separated by 0.2 μ m thick SiO₂ layer. Practical realization could be easily done, namely for the transition CPS-BCL, with two level of metalization separated by a 0.2 μ m SiO₂ layer. It ensues a negligible offset for the theoretical coplanar parts of the device.

The final device is less than 2 mm X 2 mm and could be easily inserted in a matrix. It has two major advantages. First, the circuit connected to the antenna keeps its balanced character. This avoids undesirable additional currents which could appear within the antenna structure and affect the radiation pattern, when it is fed by an unbalanced device [3]. Second, the filter design has been made taking into account the antenna impedance, so the presented results correspond to the true insertion losses, in realistic conditions.

IV. CONCLUSION

This study gives a first estimation of the performances expected for the separation of two important frequency bands

in CMB astrophysics in an array of antenna coupled bolometers. The concept is currently under test to validate the design tool. It will be extended to a prototype array.

REFERENCES

- [1] A. Goldin, J.J. Bock, C. Hunt, A.E. Lange, H. LeDuc, A. Vayonakis, J. Zmuidzinas, "Design of Broadband filters and antennas for SAMBA", Proc. SPIE Vol. 4855 (2003)
- [2] J. Kuo, E. Shih, "Microstrip stepped-impedance resonator bandpass filter with an extended optimal rejection bandwidth", IEEE Trans MTT, vol. 51 no. 5, pp 1554-1559, may 2003
- [3] R.C. Johnson, H. Jasik, "Antenna Engineering Handbook", Third Edition, McGraw Hill (1993)
- [4] Vayonakis A. *et al*, The millimeter-wave properties of superconducting microstrip lines, LTD9 (2001)
- [5] Ukibe *et al*, Fabrication of large NbSi bolometer arrays for CMB applications, NIMA 559 (2006) 554-556
- [6] M.J.Meyers *et al*, An antenna-coupled bolometer with an integrated microstrip bandpass filter, APL 86, 114103 (2005)

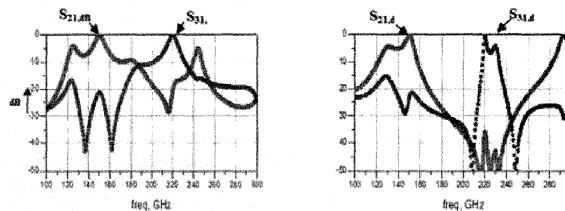


Fig. 7. (Left) Transmission S21dB and S31dB coefficients of the 3-port structure; the input port (1) is the antenna, the 200 Ω bolometers are the ports 2 and 3 (150 GHz and 220 GHz). (Right) Optimized reflection coefficients in dB.

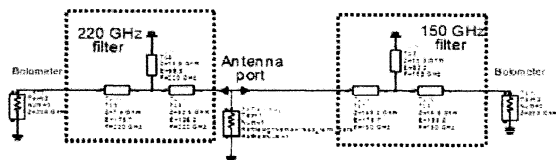


Fig. 5. Theoretical duplexer - values indicated are Z : characteristic impedance (W), E : electrical length in degrees at the design filter frequency.

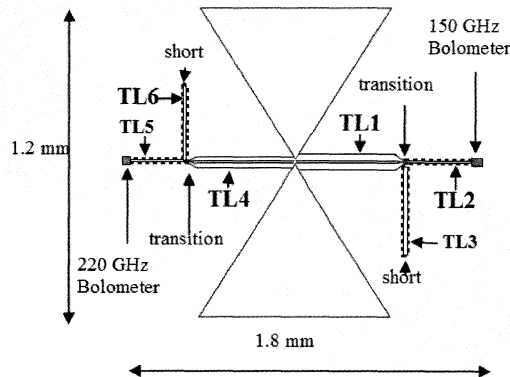


Fig. 8. Layout of the duplexer (not to scale).

Line	Electrical parameters	Physical dimensions, μm
TL1 :	Z= 57.2 Ω	W=15 μm S= 1 μm
CPS	E= 130 °	L=340 μm
TL2 :	Z= 14.1 Ω	W=1.7 μm H=0.2μm
BCL	E= 120 °	L=337 μm
TL3 :	Z= 5.1 Ω	W=6.5 μm H= 0.2 μm
BCL	E= 124.8 °	L = 349 μm
TL4 :	Z= 119.6 Ω	W=4.7 μm S=4 μm
CPS	E= 173 °	L= 304 μm
TL5 :	Z= 10.6 Ω	W=2.6 μm H=0.2μm
BCL	E= 98.8 °	L=189 μm
TL6 :	Z= 10.0 Ω	W= 2.8 μm H=0.2μm
BCL	E= 159.5 °	L = 306 μm

Table 1. Transmission lines dimensions : W is the strip width, S is the spacing and L is the physical length.

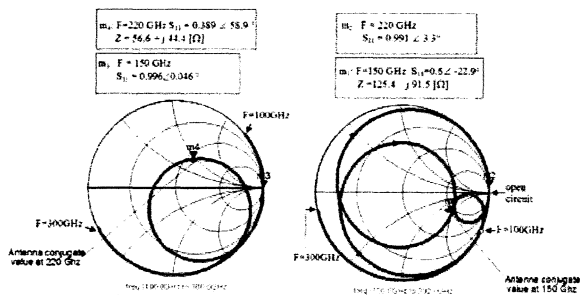


Fig.6. Input reflection coefficient of the 150 GHz filter (right) and 220 GHz (left), compared to the required conjugate value at the nominal frequency and to an open circuit (required out of band, namely at the nominal frequency of the opposite sub-circuit).

A Phonon-Cooled Nb Direct Detector for SubMM Imaging and Spectroscopy

Boris S. Karasik, Brian J. Drouin, John C. Pearson,
Timothy J. Crawford, and Henry G. Leduc

Jet Propulsion Laboratory, California Institute of Technology

We present the data on fabrication and test of an antenna-coupled Nb hot-electron direct detector. The detector device is a $1\ \mu\text{m} \times 1\ \mu\text{m} \times 12\ \text{nm}$ Nb bridge with the critical temperature $\sim 6\text{K}$ and the normal resistance of 25 Ohm. The device contacts are made from a thick ($\sim 150\ \text{nm}$) Nb film with the critical temperature $\sim 8.5\ \text{K}$. The larger energy gap in the contacts helps to confine the electron energy within the small device volume due to the Andreev reflection. The device is fabricated on a Si substrate together with the planar spiral antenna covering the 150 GHz-2 THz range. A hybridized elliptical Si lens is used for narrowing the antenna main lobe.

The detector sensitivity (NEP) and the time constant are determined by the electron-phonon interaction in the thin Nb film. The time constant is $\sim 0.4\ \text{ns}$ and does not depend on the device size. The estimated NEP due to the phonon noise is $\approx 1.5 \times 10^{-14}\ \text{W/Hz}^{1/2}$. This figure can be made by a factor of 5 smaller for a submicron size device.

The detector spectral response has been measured in the 250-990 GHz range using a set of backward-wave oscillators and was found to be essentially flat. The current work focuses on the integration of the detector with a sensitive broadband amplifier and a cold submm bandpass filter for optical NEP tests and applications in laboratory spectroscopy.

Although, neither the time constant, nor the NEP sets the record by itself, the combination of the parameters is quite unique and very desirable for a number of applications in laboratory and space spectroscopy as well as in security imaging applications.

This research was carried out in part at the Jet Propulsion Laboratory, California Institute of Technology, under a contract with the National Aeronautics and Space Administration.

Characterization of Quasi-Optical NbN Phonon-cooled Superconducting HEB Mixers

Ling Jiang, Wei Miao, Wen Zhang, Ning Li, Zhen Hui Lin, Qi Jun Yao, Sheng-Cai Shi, Sergey I. Svechnikov, Yury B. Vakhtomin, Sergey V. Antipov, Boris M. Voronov, Natalia S. Kaurova, and Gregory N. Gol'tsman

Abstract—In this paper, we thoroughly investigate the performance of quasi-optical NbN phonon-cooled superconducting hot-electron bolometer (HEB) mixers, cryogenically cooled by a close-cycled 4-K refrigerator at 500 GHz and 850 GHz. The uncorrected lowest receiver noise temperatures measured are 800 K at 500 GHz without anti-reflection coating, and 1000 K @ 850 GHz with a 50 μm thick Mylar anti-reflection coating. The dependence of receiver noise temperature on the critical current and bath temperature of HEB mixer is also investigated here. Lifetime of quasi-optical superconducting NbN HEB mixers of different volumes, room temperature resistances, and critical temperatures are thoroughly studied. Increased room temperature resistance with time over the initial resistance changes between 1 and 1.2, and the reduced critical current with time over the initial value fluctuates slightly around 0.7 for most HEB mixers even of different volumes, room temperature resistances, and critical temperatures. The critical current degrades sharply while room temperature resistance varies over 1.25.

Index Terms—Superconducting HEB mixer, noise temperature, anti-reflection coating, bath temperature, critical current, lifetime, room temperature resistance.

I. INTRODUCTION

In recent decades, phonon-cooled superconducting hot electron bolometer (HEB) mixers have developed as the most sensitive heterodyne detector in the THz region. The double sideband (DSB) receiver noise temperature of phonon-cooled NbN superconducting HEB mixers has approached eight times the quantum limit ($8h\nu/k$) [1] and the required LO power is only tens of nanowatts.

To develop this heterodyne receiver technology for real astronomical and atmospheric observations, which usually

require long-period operation, we have concentrated on the performance characterization of phonon-cooled NbN superconducting HEB mixers with a close-cycled 4 K refrigerator. It has been indeed demonstrated that although being with an ultra-thin NbN film (~ 3.5 nm), phonon-cooled NbN superconducting HEB mixers can survive the mechanical vibration and temperature fluctuation of 4-K close-cycled cryocoolers (GM two-stage type) [2]. In this paper, we measure the receiver noise performance of quasi-optical NbN superconducting HEB mixers at 500 GHz and 850 GHz with an anti-reflection coating. The dependence of receiver noise temperature on the critical current and bath temperature is also investigated. To obtain reliable operation of superconducting NbN HEB mixer with 4-K close-cycled refrigerator, it is also crucial to investigate the lifetime of NbN HEB mixers. The reduction of critical current with time as a function of the increase of room temperature resistance is demonstrated for different HEB mixers.

II. MEASUREMENT SETUP

The measured quasi-optical NbN superconducting HEB mixer chip was fabricated in Moscow State Pedagogical University (MSPU), as shown in Fig. 1. The ultra-thin (3.5 nm) NbN superconducting film bridge is contacted to the spiral antenna by the two sides contact pads. The RF and LO signals are coupled to the ultra-thin NbN superconducting film bridge through the log - spiral antenna, where mixing happens.

An IR filter made of two layers of Zitex A155 [3] on the 40-K shield of the 4-K cryostat is used to block the IR thermal radiation into HEB mixer. The quasi-optical NbN superconducting HEB mixer chip was glued onto the flat surface of a hyper-hemispherical silicon lens of a diameter of 12 mm, which was adopted to focus the RF and LO signals to the log-spiral antenna. The hyper-hemispherical silicon lens with the superconducting HEB mixer chip was then put into a copper mixer block, which includes a 50- Ω coplanar waveguide transmission line with one port connected to the HEB mixer chip (via silver paste) and the other to the IF and DC output port. To further reduce IR thermal radiation into the superconducting HEB mixer, we used a copper shield to cover the whole mixer block. The shield indeed had a window of 25 mm diameter covered with a layer of Zitex G104 for RF and LO signal coupling. The whole mixer block and the 4-K shield

Manuscript received May 30, 2006. This work was supported by the NSFC under Contracts No. 10390163 and No. 10211120645, the CAS under Contract No. KJCX2-SW-T2, and the RFBR under Contract No. 04-02-39016.

L. Jiang, W. Miao, W. Zhang, N. Li, Z. H. Lin, Q. J. Yao, are with Purple Mountain Observatory, NAOC, Graduate University of Chinese Academy of Sciences, Nanjing, China. S. C. Shi is with Purple Mountain Observatory, NAOC, CAS, Nanjing, China. Phone: 86-25-83332203; fax: 86-25-83332206; e-mail: ljiang@mwlab.pmo.ac.cn.

S. I. Svechnikov, Y. B. Vakhtomin, S.V. Antipov, B. M. Voronov, N.S. Kaurova, and G. N. Goltsman are with Department of Physics, Moscow State Pedagogical University, Moscow, Russia

were both mounted on the 4-K cold plate of the close-cycled cryostat.

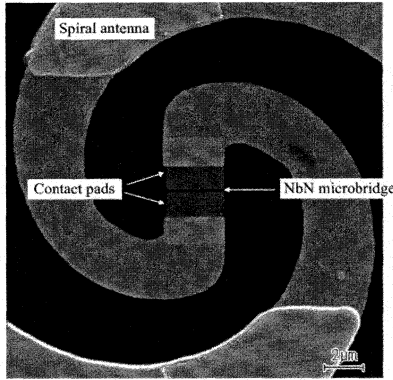


Fig. 1 Photograph of the measured quasi-optical NbN superconducting HEB mixer chip. The HEB device consists of the NbN microbridge and two contact pads in either side. Au spiral antenna is deposited in the outer layer.

We used the conventional Y-factor method to measure the noise performance of the quasi-optical NbN superconducting HEB mixer. The schematic of measurement setup is displayed in Fig. 2. A beam splitter made of a 15- μm thick Mylar film [4] was employed to couple the RF and LO signals into the vacuum window (15- μm thick Mylar film) of the 4-K cryostat. The RF signal was from a chopper, indeed a 295-K and 77-K blackbody. The 500- and 850-GHz LO source was provided by a BWO (backward wave oscillator). The IF output signal of the quasi-optical superconducting HEB mixer went through a bias-tee, a 0.8-2 GHz cooled HEMT low noise amplifier (of 36-dB gain) and a room-temperature amplifier (of 45-dB gain), a bandpass filter (1.5 \pm 0.055 GHz), and was finally measured by a square-law detector of a sensitivity of 1 mV/ μW .

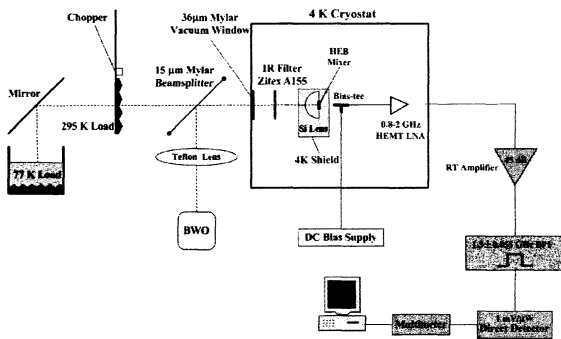


Fig. 2 Schematic of the receiver noise temperature measurement setup.

III. MEASUREMENT RESULTS

A. Receiver noise temperature measurement at 500 and 850 GHz

We measured the receiver DSB noise temperature at 500 and 850 GHz. The uncorrected lowest receiver noise temperature measured at 500 GHz is 800 K without an anti-reflection coating, as shown in Fig. 3. The optimum operating point is located in $V_{\text{bias}}=1\text{mV}$, $I_{\text{bias}}=34\mu\text{A}$.

In order to further reduce the receiver noise temperature, we cover a Mylar anti-reflection coating on the surface of hemispherical Si lens to decrease the impedance mismatching between Si lens and free space. The optimum thickness of Mylar film ($\epsilon_{\text{Mylar}} \approx \sqrt{\epsilon_{\text{Si}}}$) was chosen as 50 μm at 850 GHz.

Fig. 4 shows the receiver noise temperature for different LO pumping levels and dc biases at 850 GHz. The lowest receiver noise temperature was measured 1000 K @ 850 GHz. The receiver noise temperature is reduced by 30% compared that without anti-reflection coating.

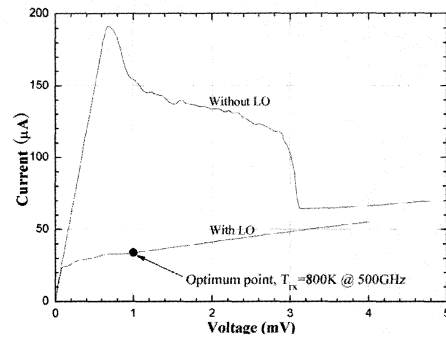


Fig. 3 Receiver noise temperature measured is 800 K at 500 GHz without an anti-reflection coating.

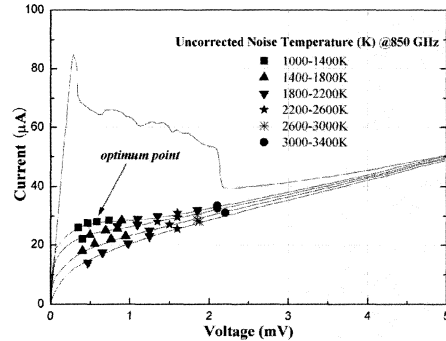


Fig. 4 Receiver noise temperature was measured for different LO pumping levels and dc biases at 850 GHz with a 50- μm thick Mylar film as anti-reflection coating. The lowest receiver noise temperature measured was 1000 K at 850 GHz.

B. Receiver noise temperature vs. critical current and bath temperature

Dependence of the receiver noise temperature on critical current and bath temperature was also investigated at 500 GHz. The HEB mixer has a width of 2.4 μm , length of 0.2 μm , and critical temperature of 9.4 K. Fig. 5 shows the IV curves and measured receiver noise temperatures for different critical currents. Note that the Si hemispherical lens wasn't covered by an anti-reflection coating. It is clearly that the receiver noise temperature deteriorates with the reduction of critical current. The HEB mixer temperature at different critical currents can be estimated from the following equation [5]

$$I_c(T) = I_c(0) * \left[1 - \left(\frac{T}{T_c} \right)^2 \right] * \left[1 - \left(\frac{T}{T_c} \right)^4 \right]^{0.5} \quad (1)$$

Its validity has been successfully checked. Fig. 6 exhibits the receiver noise temperature and mixer critical current change with HEB mixer bath temperature. Below bath temperature of 5.6 K, the receiver noise temperature change very slowly. However, while the bath temperature increases

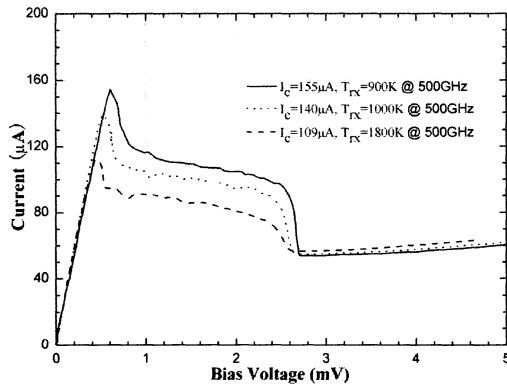


Fig. 5 IV curves and measured receiver noise temperature for different critical currents at 500 GHz without an anti-reflection coating.

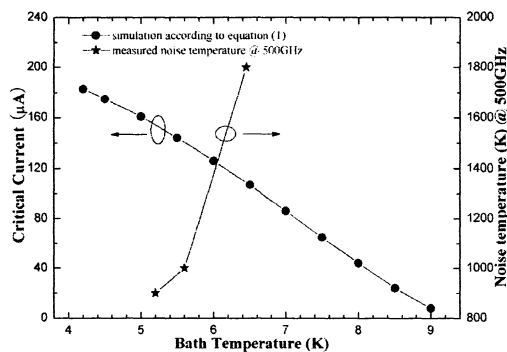


Fig. 6 Mixer critical current and receiver noise temperature measured at 500 GHz as a function of mixer bath temperature. The HEB device has width=2.4 μm , length=0.2 μm , $T_c=9.4$ K. circle symbol is obtained from equation (1).

beyond 5.6 K, the receiver noise temperature deteriorates sharply. We also measured another HEB device, which shows similar variation rule. The lowest HEB mixer temperature (i.e., 5.2 K) is 1 K larger than liquid helium temperature 4.2 K due to the bad thermal conductance between the mixer block and cold plate of the 4-K cryostat.

C. Lifetime of superconducting HEB mixer

Lifetime of NbN HEB mixers have been investigated by M. Hajenius etc. [6], which indicates the standard HEB devices without passivation layer have a 15% increase in room temperature resistance and a 30% reduction in critical current about half a year after fabrication. We measured the variation of mixer room temperature resistance vs. that of critical current at an interval for these standard NbN HEB devices deposited in Si substrate of different volumes, room temperature resistance, and critical temperatures, as shown in Fig. 7. The room temperature resistance and critical current were measured, respectively in 10 days and 500 days after fabrication. The variation of room temperature resistance (characterized by $R_{300\text{K}, 500 \text{ days}} / R_{300\text{K}, 10 \text{ days}}$) changes mainly from 1 to 1.2, and critical current fluctuates slightly around 0.7 (defined by $I_{c, 500 \text{ days}} / I_{c, 10 \text{ days}}$) for most HEB devices even of different volumes, room temperature resistances, and critical temperatures. Furthermore, the critical current deteriorates strongly with the room temperature resistance changes beyond 1.25.

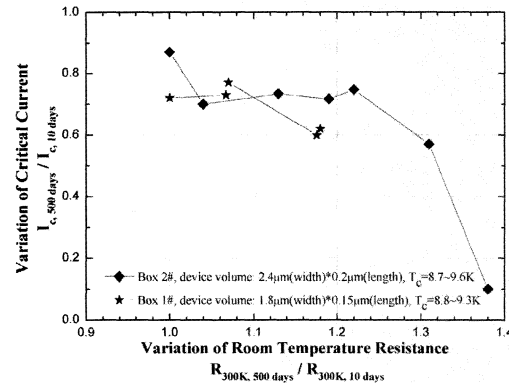


Fig. 7 Variation of critical current vs. room temperature resistance for different HEB devices at an interval, indicated in 10 and 500 days after fabrication. For most HEB devices of different volumes, room temperature resistance, and critical temperatures, the increased room temperature resistance over initial resistance varies from 1 to 1.2 and the reduced critical current over initial one fluctuates slightly around 0.7. The critical current deteriorates sharply with the further increment of normal resistance beyond 1.25.

IV. CONCLUSION

We have thoroughly investigated the receiver DSB noise temperature of quasi-optical phonon-cooled NbN superconducting HEB mixer, which is cooled by a 4-K close-cycled refrigerator. The measured lowest receiver DSB noise temperatures are 800 K at 500 GHz without

anti-reflection coating and 1000 K at 850 GHz with a 50- μm thick Mylar anti-reflection coating. The receiver noise temperature changes inversely with the critical current, and the receiver DSB noise temperature is found to deteriorate strongly beyond bath temperature of 5.6 K. Increased room temperature resistance over initial resistance varies from 1 to 1.2 for most HEB devices of different volumes, room temperature resistances, and critical temperatures, and the reduced critical current over initial one fluctuates slightly around 0.7. While the room temperature resistance varies beyond 1.25, critical current deteriorates strongly.

V. ACKNOWLEDGMENT

We are very grateful to X. F. Shen, D.R. Yang, Q. G. huang, and S. H. Chen of PMO for technical support.

REFERENCES

- [1] J. J. A. Baselmans, M. Hajenius, J. R. Gao, T. M. Klapwijk, P. A. J. de Korte, B. Voronov, and G. Gol'tsman, "Doubling of sensitivity and bandwidth in phonon cooled hot electron bolometer mixers," *Applied Physics Letts.*, vol. 84, no. 11, pp. 1958-1960, 2004.
- [2] L. Jiang, J. Li, W. Zhang, Q. J. Yao, Z. L. Lin, S. C. Shi, Y. B. Vachtomin, S.V. Antipov, S. I. Svechnikov, B. M. Voronov, and G. N. Goltsman, "Characterization of NbN HEB mixers cooled by a close-cycled 4 Kelvin refrigerator," *IEEE Trans. Applied Supercond.*, vol. 15, no. 2, pp. 511-513, June 2005.
- [3] ZITEX 100% PTFE Membranes, Saint-Gobain Performance Plastics Corp., France.
- [4] Mylar Polyester Films, Dupont Corp., USA.
- [5] S. Cherednichenko, M. Kroug, H. Merkel, E. Kollberg, D. Loudkov, K. Smirnov, B. Voronov, G. Gol'tsman, , E. Gershenson, "Local oscillator power requirement and saturation effects in NbN HEB mixers," *Proc. of 12th International Symposium on Space Terahertz Technology*, pp. 273-285, 2001.
- [6] M. Hajenius, Z. Q. Yang, J. J. A. Baselmans and J. R. Gao, "Lifetime of NbN Hot Electron Bolometer Mixers," *Proc. of 16th International Symposium on Space Terahertz Technology*, pp. 217-221.

Direct comparison of the sensitivity of a spiral and a twin-slot antenna coupled HEB mixer at 1.6 THz

J.R. Gao, M. Hajenius, Z.Q. Yang, T.M. Klapwijk, W. Miao, S. C. Shi, B. Voronov, and G. Gol'tsman

Abstract— To make a direct comparison of the sensitivity between a spiral and a twin-slot antenna coupled HEB mixer, we designed both types of mixers and fabricated them in a single processing-run and on the same wafer. Both mixers have similar dimensions of NbN bridges (1.5-2 $\mu\text{m} \times 0.2 \mu\text{m}$). At 1.6 THz we obtained a nearly identical receiver noise temperature from both mixers (only 5% difference), which is in a good agreement with the simulation based on semi-analytical models for both antennas. In addition, by using a bandpass filter to reduce the direct detection effect and lowering the bath temperature to 2.4 K, we measured the lowest receiver noise temperature of 700 K at 1.63 THz using the twin-slot antenna mixer.

Index Terms—Hot electron bolometer mixer, twin-slot antenna, spiral antenna, and THz.

I. INTRODUCTION

Spiral antennas are extremely useful for laboratory tests to evaluate HEB mixers at different frequencies because of the broad RF bandwidth as a result of a non-resonating frequency response. However, such antennas have a circular polarization, so they are less favorable for actual applications in a telescope. In contrast, twin-slot antennas are resonant ones with a linear polarization and an acceptable beam pattern. Therefore they are more desirable for real applications. Because of the resonant type of antenna, to reach the maximum RF coupling at a designed frequency the impedance matching between antenna and HEB is more important. This is partly due to the fact that the theoretical design model has not been fully developed for THz frequencies and partly due to the fact that the bridge impedance should be under good control during the fabrication.

Manuscript received June 30, 2006. The work is financially supported by the EU through RadioNet, by KNAW through the China-Netherlands Exchange program, and by the INTAS program.

J.R. Gao, M. Hajenius, and Z.Q. Yang are with SRON Netherlands Institute for Space Research, Utrecht/Groningen, the Netherlands. The first two authors are also with Kavli Institute of NanoScience, Faculty of Applied Sciences, Delft University of Technology, Lorentzweg 1, 2628 CJ, Delft, the Netherlands.(corresponding author: J.R. Gao with e-mail: J.R.Gao@tnw.tudelft.nl).

T.M. Klapwijk is with Kavli Institute of NanoScience, Faculty of Applied Sciences, Delft University of Technology, Lorentzweg 1, 2628 CJ, Delft, the Netherlands.

W. Miao and S. C. Shi are with Purple Mountain Observatory (PMO), National Astronomical Observatories of China (NAOC), Chinese Academy of Sciences, Nanjing, China.

B. Voronov and G. Gol'tsman are with Moscow State Pedagogical University (MSPU), Moscow 119435, Russia.

Spiral antenna coupled NbN HEB mixers tend to show lower receiver noise temperatures than reported for twin-slot antenna mixers. However, there has so far been very few work dedicated to a direct comparison between these two types of antenna coupled mixers [1]. Such a comparison turns out to be difficult. One of the reasons is that, due to different antenna geometries and corresponding fabrication recipes, it is very challenging to fabricate both types of mixers in a single wafer and a single processing-run in order to make a sensible comparison. Here we report a direct comparison of the heterodyne sensitivity at 1.6 THz using two types of mixers fabricated on the same wafer with the same process.

II. THEORETICAL CONSIDERATIONS OF THE HETERODYNE SENSITIVITY

The DSB receiver noise temperature T_{rec} of a HEB mixer reflects the effective noise temperature and gain of the cascade of the RF optical components, mixer, and IF (amplifier) chain, and is given by

$$T_{\text{rec}} = \left(T_{\text{RF}} + \frac{T_{\text{Mix,SSB}}}{2G_{\text{RF}}} + \frac{T_{\text{IF}}}{2G_{\text{RF}}G_{\text{Mix,SSB}}} \right) \quad (1)$$

where T_{RF} and G_{RF} are the equivalent noise temperature and gain of the RF optics, respectively. $T_{\text{Mix,SSB}}$ and $G_{\text{Mix,SSB}}$ the SSB mixer noise temperature and gain, and T_{IF} the noise temperature of the IF chain. In practice, the RF power coupling between antenna and HEB detector is not 100%, thus there will be an additional loss term added into the G_{Mix} or G_{RF} . Furthermore, if the DC resistance of the HEB at the operating point is different from the input impedance (50 Ω) of IF amplifier, there will be impedance mismatching between the HEB and IF amplifier. Consequently, this will reduce the mixer gain and thus increase the receiver noise temperature [2,3]. It becomes obvious that, to compare the sensitivity of two types mixers due to different antennas, ideally one needs the exact same HEB devices, which can guarantee the same mixer noise temperature, gain, and IF impedance. As discussed in the next section, the input impedances of two antennas are not the same. Hence, it is unrealistic to use the exact same device size, which determines the impedance. In this work, we choose HEBs that are essentially identical, but slightly different in widths in order to satisfy the RF impedance matching.

III. HEB MIXERS

Mixers used are phonon-cooled HEBs based on a standard NbN film of about 5.5 nm on a Si substrate [4] which is sputtered grown at MSPU, Moscow. It has a superconducting critical temperature of 10 K. For the fabrication, we use a similar process as described in ref.[5] for both types of mixers except for a new fabrication step for both antenna structures. All devices are made on the same wafer. The DC resistance versus temperature data of HEBs from this batch, together with the earlier RF measurements of similar batches, suggests that the reproducibility in the performance among different HEBs is excellent (~10 %).

A. Spiral antenna mixer

We start with a mixer that is coupled to a self-complementary spiral antenna. It is similar to what used in our previous work [6]. The detailed antenna structure is illustrated by the SEM micrograph in Figure 1, in which the bolometer locates in the center of the antenna and has a width of 2 μm and a length of 0.2 μm . The ratio of length and width, together with the sheet resistance of the film, defines the normal state DC resistance, which is 96 Ω (at low temperatures) and is in our case assumed to be same as the RF impedance.

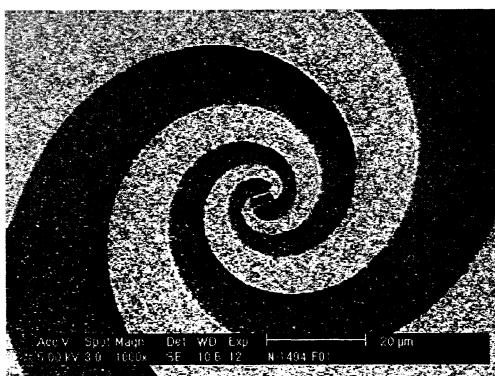


FIG. 1 SEM micrograph of a self-complementary spiral antenna coupled HEB mixer on Si substrate. The NbN HEB has a width of 2 μm and a length of 0.2 μm , giving a low temperature normal state resistance of 96 Ω . The dark part in the center is a remaining e-beam resist, which is used to define the width of the HEB.

The feed impedance of this spiral antenna has been simulated using HFSS. We made an attempt to simulate the feed impedance by taking the Si substrate with an actual thickness (340 μm) using HFSS. We failed to complete the simulation because of the existence of surface waves in the substrate due to the fact that the substrate is electrically larger in comparison with the spiral antenna. To eliminate the surface waves, we apply the Perfectly Matched Layer (PML) method [7]. This provides a reflectionless interface between the PML layer and the substrate at all incident angles, where the surface waves are suppressed. Figure 2 shows the calculated feed impedance of the spiral antenna

on a Si substrate of 10 μm at frequencies around 1.6 THz. Although in this calculation we used a thickness of 10 μm , this result should be valid for the actual device. We find 88.6 Ω for the real part of the impedance and only -3.3 Ω for the reactance, which is consistent with what calculated using the textbook analytical expression for the impedance. Having known the impedances of the antenna and the HEB, we calculate the power coupling efficiency from the antenna to the HEB and find it to be nearly 100% around 1.6 THz. In the impedance simulation, we assume a zero thickness of the metal layer and neglect any resistive loss. Furthermore, we also neglect the effect of the main beam efficiency [8] in estimating the coupling efficiency.

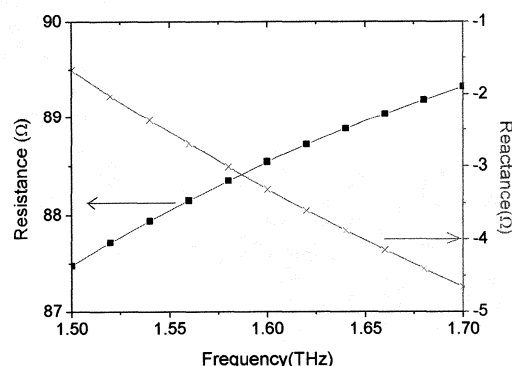


FIG. 2. Simulated feed-impedance of a self-complementary spiral antenna on a Si substrate using HFSS. To suppress the surface waves, we have to apply the Perfectly Matched Layer (PML) method. The device simulated is identical to the one shown in figure 1.

B. Twin-slot antenna mixer

The twin-slot mixer used is illustrated by the SEM micrograph in figure 3. The bridge has a width of 1.5 μm and a length of 0.2 μm , which results in a normal state DC resistance of 130 Ω at low temperatures. The antenna is designed for the center frequency of 1.6 THz and has the following dimensions: the slot length L is $0.30\lambda_0$ with λ_0 ($=187.5 \mu\text{m}$) the free space wavelength. The slot separation S is $0.17\lambda_0$, the slot width W is $0.07L$. The CPW transmission line used to connect the two slots to the HEB has a central line width of 2.8 μm and a gap of 1.4 μm , yielding a characteristic impedance of 51 Ω [9]. The RF filter structure consists of three sections each consisting of one high-(70 Ω) and one low-impedance (26 Ω) segment, all of which are quarter wavelength long. Applying the same approach in ref. [8], we calculate a real impedance of 44 Ω for the twin-slot antenna, while a reactance of only -0.6 Ω . The CPW transmission line transforms the antenna impedance to the feed impedance of 116 Ω as the real part and 9 Ω as the imaginary. We find a power coupling efficiency of 90 % for this mixer if we take the main beam efficiency into account, but nearly 100 % if we ignore the effect of main beam efficiency. Note that in this calculation we also neglect resistive loss. In essence, despite of the different antennas, the power coupling efficiencies for both

mixers are identical.

IV. HETERODYNE MEASUREMENT RESULTS

Both mixers were characterized in the same RF test setup as shown in figure 4. As local oscillator, we apply a gas laser operating at a frequency of 1.63 THz. We first characterize both HEB mixers using a non-optimal RF setup, in which a Si lens without anti-reflection coating is used and two Zytex heat filters are mounted at 4 K and 77 K behind the HEB cryostat window. In this case, RF loss in the optical path for the hot/cold load is -4.5 dB

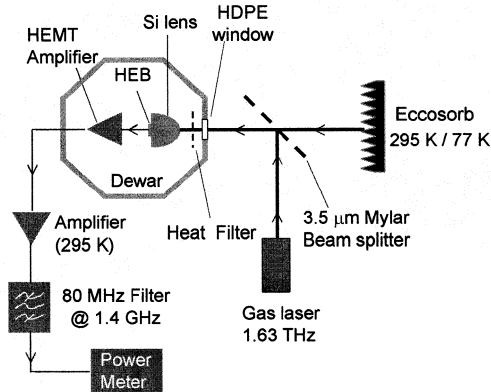


FIG 4. Heterodyne test setup used for the measurements in figure 5.

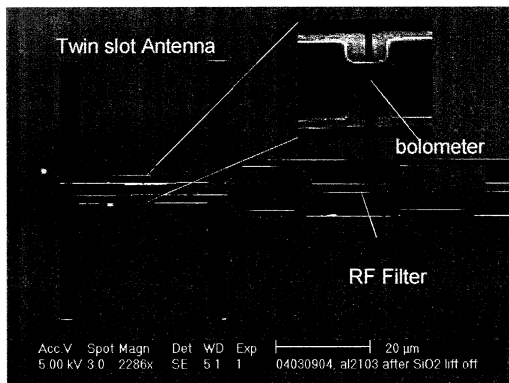


FIG. 3. SEM micrograph of a twin slot antenna coupled NbN HEB mixer (the upper figure). The bright area is covered with metal Au layer, while the dark area is the Si substrate. Between the two slots, there is a CPW transmission line that connects the slots to the superconducting bridge. In the middle of the CPW line, the HEB is located. The RF filter structure is shown in the right side of the micrograph. The NbN bridge is 1.5 μm in width and 0.2 μm in length, resulting in a normal state DC resistance of 130 Ω at low temperatures. The inset shows the zoom of the bridge area.

Figure 5 shows DSB receiver noise temperatures together with pumped IV curves measured for both HEB mixers. For the spiral mixer, the minimum T_{rec} is 1090 K found at a bias voltage of ~ 0.6 mV and the optimal LO power of 350 nW. The latter is determined using the isothermal technique. For the twin-slot mixer, the minimum T_{rec} is 1020 K at a bias voltage of 0.8 mV and the optimal LO power of 305 nW. The twin-slot device gives a 5 % lower noise

temperature. However, this difference is comparable to the uncertainty of the measurement and thus we conclude that there is no real difference in the sensitivity at 1.6 THz between two different mixers. This result is actually a bit surprising because there are two additional factors, which might cause a difference in the sensitivity. The first one is the direct detection effect due to broadband hot/cold load blackbody radiation occurred at the Y-factor measurement [10]. One would expect a more direct detection effect in the spiral mixer because of its wider RF bandwidth. This effect, based on the measurement of a comparable spiral device, would give an increase of $<10\%$ in the noise temperature using the standard Y-factor method. The second is the difference in the resistance of the HEBs at operating point, which will influence the mixer gain [3]. The twin-slot device due to a high resistance should have better impedance matching to the amplifier. Apparently these two effects do not contribute a substantial difference in the sensitivity.

To determine the ultimate receiver noise temperature of such mixers, we replaced the lens with an anti-reflection coated one and removed also the Zytex filters to reduce RF loss. In addition, we added a bandpass filter (200 GHz bandwidth centered at 1.6 THz [11]) at 4.2 K cold plate to reduce the direct detection effect. In this case the RF loss is reduced to -2.8 dB. We measured a T_{rec} of 700 K in the twin-slot mixer (without any corrections of the optical loss) and a SSB mixer gain of -6.4 dB at a DC bias voltage of 0.7 mV and the optimal LO power of 330 nW. The value of 700 K was obtained at a reduced bath temperature of 2.4 K and is 10 % lower than what found at 4.3 K. Note this sensitivity is same as our earlier result using a twin-slot mixer, but after annealing the device in vacuum [12]. Besides, we find that a reduction of the output noise of the mixer causes the decrease of T_{rec} at 2.4 K after comparing the mixer gains and output noises at two different temperatures. In this case,

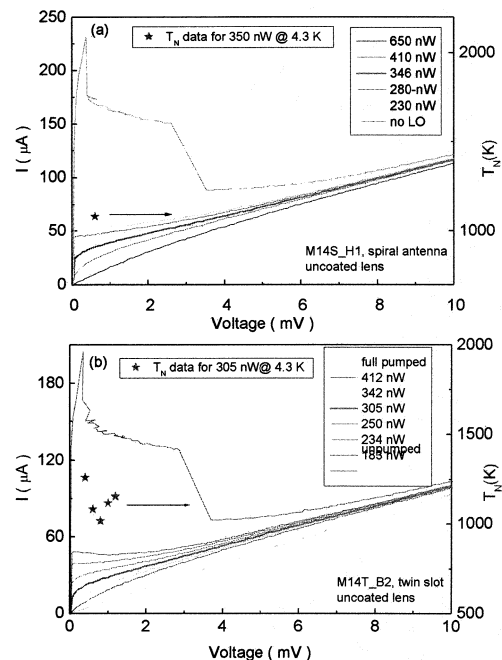


FIG.5. Current-voltage characteristics (full lines, left axis) of a NbN HEB mixer without and with radiation from the QCL at 1.6 THz. The measured receiver noise temperature T_{rec} (symbols, right axis) versus the bias voltage for the optimal LO power at the HEB. (a) for the spiral antenna mixer, while (b) for the twin-slot mixer.

the mixer gain and the output noise are -6.1 dB and 209 K, respectively, at 4.3 K, and -6.4 dB and 158 K at 2.4 K.

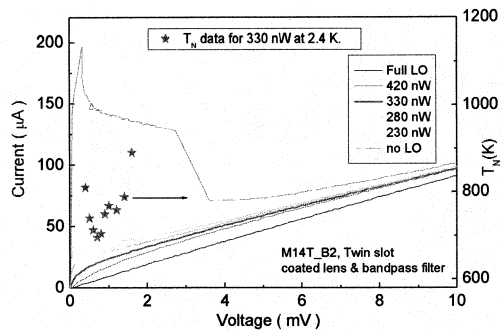


FIG 6. Current-voltage characteristics (full lines, left axis) of the twin slot antenna coupled NbN HEB mixer without and with radiation from the QCL at 1.6 THz. The receiver noise temperature T_{rec} (symbols, right axis) versus the bias voltage for the optimal LO power at the HEB, which was measured at a reduced bath temperature of 2.4 K and with an additional bandpass filter centred at 1.6 THz.

V. CONCLUSIONS

By comparing the receiver noise temperatures of two similar HEB mixers either using a spiral or a twin-slot antenna, we find that they have a very comparable sensitivity, suggesting that there is no real difference in the RF power coupling efficiency of the antenna at 1.6 THz. The result is in a good agreement with the calculated one based on semi-analytical models for both antennas. Furthermore, by reducing the direct detection effect and by reducing the bath temperature, we measured a receiver noise temperature of 700 K using the twin-slot mixer, which is the lowest at this frequency.

ACKNOWLEDGMENT

We acknowledge P. Khosropanah and J.J.A. Baselmans for useful discussions.

REFERENCES

- [1] S. Cherednichenko, P. Khosropanah, E. Kollberg, M. Kroug, and H. Merkel, "Terahertz superconducting hot-electron bolometer mixers", *Physica C* 372-376, 407 (2002).
- [2] R. S. Nebosis, A. D. Semenov, Yu. P. Gousev, and K. F. Renk, "Rigorous Analyses of a Superconducting Hot- Electron Bolometer Mixer, Theory and Comparison with Experiment", 7th International Symposium on Space Terahertz Technology, Charlottesville, March 1996.
- [3] J. W. Kooi, J. J. A. Baselmans, J. R. Gao, P. Dieleman, Z. Q. Yang, A. Baryshev, M. Hajenius, G. de Lange, and T. M. Klapwijk, "IF impedance and mixer gain of phonon cooled hot-electron bolometers and the Perrin- Vanneste two temperature model", The 16th Int. Symp. on Space terahertz Technology, 2-4 May 2005, Gothenburg, Sweden. P465.
- [4] J.R. Gao, F.D. Tichelaar, B. Voronov, M. Hajenius, E. Grishina, T.M. Klapwijk, G. Gol'tsman, and C.A. Zorman, "Can NbN films on 3C-SiC/Si change the IF bandwidth of hot electron bolometer mixers?", *These proceedings*.
- [5] M. Hajenius, J. J. A. Baselmans, J. R. Gao, T.M. Klapwijk, P. A. J. de Korte, B. Voronov and G. Gol'tsman, Low noise NbN superconducting hot electron bolometer mixers at 1.9 and 2.5 THz, *Supercond. Sci. Technol.* 17, S224-S228 (2004).
- [6] J. J. A. Baselmans, M. Hajenius, J. R. Gao, T. M. Klapwijk, P. A. J. de Korte, B. Voronov and G. Gol'tsman, "Doubling of sensitivity and

bandwidth in phonon cooled hot electron bolometer mixers", *Appl. Phys. Lett.*, 84, 1958(2004).

- [7] J. P. Berenger, "A perfectly matched layer for the absorption of electromagnetic waves", *J. Comp. Phys.* vol. 114, pp. 185-200, 1994.
- [8] W.F.M. Ganzhevles, L.R. Swart, J.R. Gao, T.M. Klapwijk, and P.A.J. de Korte, "Direct response of twin slot antenna coupled hot-electron bolometer mixers designed for 2.5 THz radiation detection", *Applied Physics Letters*, vol. 76, no. 22, 2000, p. 3304-3306.
- [9] P. Focardi, A. Neto, and W.R. McGrath, "Coplanar-waveguide-based terahertz hot-electron-bolometer mixers with improved embedding circuit description" *IEEE Transactions on Microwave Theory and Techniques*, 50, 2374 (2002).
- [10] J. J. A. Baselmans, A. Baryshev, S. F. Reker, M. Hajenius, J. R. Gao, T. M. Klapwijk, Yu. Vachtomin, S. Maslennikov, S. Antipov, B. Voronov, and G. Gol'tsman, "Direct detection effect in small volume hot electron bolometer mixers", *Appl. Phys. Lett.* 86, 163503 (2005).
- [11] A metal mesh RF bandpass filter, which is supplied by QMC Instruments Ltd., Cardiff University, Cardiff, U.K. It has a center frequency of 1.6 THz, at which the loss is only -0.97 dB at 300 K, and has an effective bandwidth of 200 GHz.
- [12] Z. Q. Yang, M. Hajenius, J. J. A. Baselmans, J. R. Gao, B. Voronov, and G. N. Gol'tsman, "Reduced noise in NbN hot electron bolometer mixers by annealing", *Supercond. Sci. Technol.* 19, L9-L12 (2006) (Rapid Com.).

Characterization of Diffusion-Cooled Hot-Electron Bolometers for Heterodyne Array Receiver Applications

Abigail Hedden¹, Matthew Reese², Daniel Santavicca², Luigi Frunzio², and Daniel Prober²,
Patrick Pütz^{1,3}, Christopher Groppi¹, and Christopher Walker¹

¹*Steward Observatory, University of Arizona, 933 N Cherry Ave, Tucson, AZ 85721, USA*

²*Department of Applied Physics, Yale University, 15 Prospect Street, New Haven, CT 06520, USA*

³*KOSMA, I. Physikalisches Institut der Universität zu Köln, Zùlpicher Str. 77, 50937 Köln, Germany*

We are characterizing the performance of diffusion-cooled hot-electron bolometers (HEBs) as mixing elements for superheterodyne receivers. The objective of this work is developing mixer technology for submillimeter and THz astronomical applications and assessing usability for heterodyne array cameras. HEBs currently are the most sensitive mixing devices in the THz region and in contrary to SIS mixers do not exhibit a material dependent upper mixing frequency limit. In particular the diffusion-cooled HEBs can offer a larger IF bandwidth than the phonon-cooled HEBs, which gains importance with increasing operation frequency of the astronomical application. The HEB devices were fabricated at Yale University with an in-situ two-step deposition process on fused quartz substrates. The waveguide HEB devices consist of a several hundred nanometer long, 10 nm thin Nb micro bridge between two normal metal pads made of proximitized Nb/Al bilayers that also define the RF choke structure. DC and RF device performance at microwave frequencies (10s of GHz) is measured at Yale University and then extended to submillimeter frequencies (345 and 810 GHz) at the University of Arizona. The submillimeter heterodyne measurements use waveguide mixer blocks of proven design, with the 345 GHz block being a modification of a DesertSTAR mixer, manufactured on Arizona's Kern MMP micromilling machine, and the 810 GHz block originating from KOSMA. We will present the fabrication process, discuss DC I-V and R-T as well as RF and IF results and set the goals for array camera development based on waveguide mixer technology at THz frequencies.

Gain bandwidth of NbN Heterodyne Hot Electron Bolometer Superconducting Mixers made on thin SiO_2/Si_3N_4 membrane

Vladimir Drakinskiy

Dept of Microtechnology and Nanoscience,
Microwave Electronics Laboratory,
Chalmers University of Technology,
SE-412 96 Gothenburg, Sweden

Email: vladimir.drakinskiy@mc2.chalmers.se

Jean Baubert

LERMA - Paris Observatory,
77, Avenue Denfert-Rochereau,
75014, Paris, France

Sergey Cherednichenko

Dept of Microtechnology and Nanoscience,
Microwave Electronics Laboratory,
Chalmers University of Technology,
SE-412 96 Gothenburg, Sweden

Abstract— We present results of the gain bandwidth investigation of NbN HEB mixers made on 1.4 μm thick SiO_2/Si_3N_4 stress-less membrane, and bulk- $Si/SiO_2/Si_3N_4$. We have found that the gain bandwidth of the devices made on these substrates is 0.6-0.9 GHz while on bare- Si it is 3.5 GHz. The final objective of this work is to process membrane based NbN HEB mixers for a 4x4 pixel heterodyne camera for 2.5 and 4.7 THz. SHAHRA (Submm Heterodyne Array for High speed Radio Astronomy) is a project supported by ESA.

I. INTRODUCTION

Superconducting hot-electron bolometric (HEB) mixers have been demonstrated to be suitable devices for low noise and wide band heterodyne receivers at THz frequencies. Several international projects such as the Stratospheric Observatory for Infrared Astronomy (SOFIA) [1] and the Far Infrared and Submillimeter Space Telescope (Herschel) [2] will use HEB technology for atmospheric research and radio astronomy. Detection of submillimeter lines of OH (2.5 THz), HD (2.7 THz) and OI (4.7 THz) presents a high interest for radioastronomers [3]. It provides a strong motivation for the development of low-noise receivers for operation at THz frequencies. Depending on the RF coupling technique mixers are divided into two categories: waveguide mixers and quasi-optical mixers. As the RF frequency increases, machining of the waveguide mixers becomes more difficult. Therefore, quasi-optical mixers are more often used above 1 THz. In a quasi-optical heterodyne receiver the mixer (usually of a few m in size) is coupled to a planar antenna on a dielectric substrate. In order to minimize the back lobes, the substrates with high dielectric constants are selected (*silicon*, *MgO*). Moreover, for avoiding substrate modes and for beam collimation the substrate is clamped on the back of a spherical or an elliptical lens. In order to make an array out of lens antenna detectors two concepts have been proposed: a single lens for the whole antenna array, and an array of lenses with a single antenna on each lens (fly-eye technique). It has been discussed [4], [5] that scaling of both approaches to frequencies higher than 2 THz will be difficult. A few approaches suitable for scaling

both in frequency and in number of pixels of the array have been discussed [6], [5], [7], where the HEB mixer is placed on an electrically thin substrate (membrane). Moreover, size of an antenna depends on dielectric constant, ϵ_r . For example, for a slot antenna the slot length is about $0.5 \lambda_e$ (effective wavelength), where $\lambda_e = \frac{\lambda_0}{\sqrt{\epsilon_{eff}}}$. The effective dielectric constant, ϵ_{eff} , on the dielectric/vacuum interface for the static case is $\sqrt{\frac{\epsilon_r+1}{2}}$. ϵ_r of the freestanding SiO_2/Si_3N_4 stress-less membrane is considered to be 1, since the wavelength at 2.5 THz, 2.7 THz and 4.7 THz is much larger than the membrane thickness when ϵ_r for bulk- Si equal 11.9. However, it remains unclear what will happen to the gain bandwidth when the HEB mixer is placed on such a membrane.

The first mixing experiments at millimeter-wave frequencies, employing superconducting thin films, were performed in 1990th [8]. Recently, technological development has mainly concentrated on NbN HEBs. The so called phonon-cooled NbN HEBs show very low noise (10-15 times the quantum limit) at 0.5-2.5 THz frequencies. The -3dB gain bandwidth achieved at the optimal operation point is about 3.7 GHz for the devices on crystalline quartz with MgO buffer layer [9], 4.5 GHz for MgO [10], 4 GHz on Si [11], 3.7 GHz on sapphire [12], 5.2 GHz on Si with MgO buffer layer and 2 nm thick NbN film [13].

In this paper we investigate the gain bandwidth of NbN mixer on freestanding SiO_2/Si_3N_4 stress-less membrane. SiO_2/Si_3N_4 is either a 1.4 μm membrane or a buffer layer between NbN film and bulk- Si substrate.

II. DEVICE FABRICATION ON MEMBRANE AND MEASUREMENT SETUP

The device fabrication are made of a 35 Å NbN film [14] on bulk- $Si/SiO_2/Si_3N_4$ substrate. The superconducting transition temperature and the room temperature sheet resistance of the film are 8.3 K and 660-700 Ω/square , respectively. The contact pads (80 nm Au) and the antenna (200 nm Au) are fabricated, using consecutive steps of electron beam

lithography and lift-off process. The bolometer bridge is then covered by a SiO_2 , which protects the NbN during ion milling. In the next step, Ar ion milling is used, to etch away the NbN film from the whole wafer, except from the bolometer bridge and under the antenna pads. The bolometers are $3.5 \mu\text{m}$ wide and $0.4 \mu\text{m}$ long. To make membrane we have removed Si_3N_4 , SiO_2 layers and Si from the back side until reaching the SiO_2 membrane on the top face. The first step is done by Reactive Ion Etching. The second one is achieved by using of the Deep Reactive Ion Etch, DRIE, technique. The DRIE method is a time multiplexed system where isotropic etching is altered with a polymer depositing step, passivation. The passivation is performed with C_4F_8 plasma which deposits a Teflon like film on the wafer surface and trench wall. The following etching with SF_6 plasma etches areas parallel to the surface at a higher rate than trench walls thereby breaking through the bottom protective layer prior to the wall passivation etching the bottom silicon [15]. The superconducting critical temperature of the final device is 1 K lower than the initial. The measurement setup is shown

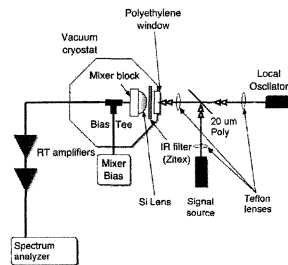


Fig. 1. Gain bandwidth measurement setup

in Figure 1. The HEB bandwidth was measured by detecting a mixing signal from two monochromatic sources (backward wave oscillators (BWO) for 600-700 GHz), one is used as a Local Oscillator (LO) and the other as a signal source. BWO RF power was combined by a $20 \mu\text{m}$ Polyethylene beam-splitter and arrived into a liquid-helium cooled vacuum cryostat through a window and an IR filter. The mixer block consisted of a silicon lens with a HEB clamped on the flat side of the lens. The mixer bath temperature was about 4.5 K. The signal source frequency was kept constant while the LO frequency was tuned in order to measure the IF signal at different IF. A bias-T was used to feed the bias to the mixer and to transmit the intermediate frequency signal to room temperature wideband amplifiers (0.1-20 GHz). The signal was amplitude and the frequency measured by a spectrum analyzer. The HEB bias point was controlled by the LO power and a DC voltage source. The DC parameters of the measured devices are shown in the Table I.

III. MEASUREMENTS RESULTS

For a single time constant bolometric mixer the mixer conversion gain $G(f_{IF})$ follows the intermediate frequency

f_{IF} as:

$$G(f_{IF}) = \frac{G(0)}{1 + \left(\frac{f_{IF}}{f_{gain}}\right)^2} \quad (1)$$

where f_{gain} is the 3dB cut-off frequency:

$$f_{gain} = \frac{1}{2\pi\tau_{mix}} \quad (2)$$

τ_{mix} is the mixer time constant, which differ from the electron cooling time τ_θ due to presence of the bias current:

$$\tau_{mix} = \frac{\tau_\theta}{1 - A} \quad (3)$$

where A is electro-thermal feedback and equals:

$$A = C_{dc} I_0^2 \frac{R_L - R_0}{R_L + R_0} \quad (4)$$

where I_0 is the bias current, R_0 is the bolometer resistance at the operating point, R_L is the IF load resistance. τ_{mix} can be longer or shorter of the τ_θ depending on the impedance of the mixers in that point.

C_{dc} is the dc responsivity of the HEB and is defined as:

$$C_{dc} = \frac{\partial R}{\partial P} = \frac{\partial R}{\partial \theta} \frac{\partial \theta}{\partial P} = \frac{\partial R}{\partial \theta} \frac{1}{G_{th}} = \frac{\partial R}{\partial \theta} \frac{\tau_{e-ph}}{c_e V} \quad (5)$$

where G_{th} is the thermal conductance between electrons and phonons, V is the volume of the bolometer.

We investigated devices made on SiO_2/Si_3N_4 stress-less membrane, bulk- $Si/SiO_2/Si_3N_4$ and bare- Si .

Gain bandwidth of 3.5 nm thin NbN hot-electron mixers made on bare- Si was reported by many authors and averages 3.5-4 GHz. We used such device as a standard to calibrate the set-up. At the bias point where the lowest noise temperature can be expected, the IV-curves had negative differential resistance. It is can be when the signal and LO frequencies are not high enough so that f_{LO} , $f_s < 2\Delta/h$, (2Δ is the energy gap, h is the Plank constant). We used a heater to suppress the NbN superconducting energy gap and to get smooth IV-curve during this measurements. In fact, we increased the bath temperature of the device. As an indicator we used the HEB's critical current, which was suppressed by a factor of 2 after the heater was switched on. The results of the gain bandwidth measurements for the all measured devices are shown in Table II and Figures 2- 4.

The superconducting transition temperature of the devices on SiO_2/Si_3N_4 and bulk- $Si/SiO_2/Si_3N_4$ was lower than on bare- Si and the critical current in the cryostat was nearly half of the value in LHe. The mixer effective volume and $\frac{\partial R}{\partial \theta}$ are not known exactly. Therefore, all mixers were measured at several bias points and $\frac{\partial R}{\partial \theta}$ and the mixer volume were adjusted so the electron temperature relaxation time τ_θ is the same for a particular sample (indeed for a phonon cooled HEB the electron relaxation time shall be bias independent). The operation points correspond to the optimum noise performance of the devices which were chosen by analogy with devices are

TABLE I

THE PARAMETERS OF THE MEASURED DEVICES. FOR ALL DEVICES THE WIDTH WAS $A=3.5 \mu\text{m}$, LENGTH $B=0.4 \mu\text{m}$, FILM THICKNESS $D=3.5 \text{nm}$.

Device Id.		S001-16	S001-17	S001-4	S08-n
Resistance	$R (\Omega)$	210	217	212	111
Critical current at 4.2K/and in the cryostat	$I_C (\mu\text{A})$	105/55	115/49	100/52	380/320
Critical temperature	$T_c (K)$	7.2	7.5	7.2	8.3
Substrate		$\text{SiO}_2/\text{Si}_3\text{N}_4$		$\text{bulk-Si}/\text{SiO}_2/\text{Si}_3\text{N}_4$	bare-Si
Thickness of the substrate	$D (\mu\text{m})$	1.4		400+1.4	350

TABLE II

SUMMARY OF THE MEASUREMENTS RESULTS FOR ALL DEVICES. DC RESISTANCE IN THE OPERATION POINT $R_0 = \frac{U_0}{I_0}$, TEMPERATURE DERIVATIVE OF THE RESISTANCE $\frac{\partial R}{\partial \theta}$ ARE USED TO CALCULATE THE ELECTRO THERMAL FEEDBACK COEFFICIENT A . $\tau_{mix} = \frac{1}{2\pi f_{gain}}$ IS THE MIXER TIME CONSTANT OBTAINED FROM THE 3dB GAIN BANDWIDTH f_{gain} . τ_θ IS THE ELECTRON RELAXATION TIME OBTAINED AFTER CALIBRATION OF τ_{mix} FOR THE ELECTRO THERMAL FEEDBACK. THE MIXER EFFECTIVE VOLUME IS $2.3 * 10^{-3} \mu\text{m}^3$.

Device Id.	Bias point	f_{gain}, GHz	R_0, Ohm	$\frac{\partial R}{\partial \theta}, \text{Ohm/K}$	A^1	τ_{mix}, ps	τ_θ, ps
S001-16	1) 0.5mV, 24uA	0.92	20.8	200	0.31	173	119
	2) 0.5mV, 27uA	0.73	18.5	200	0.44	218	123
S001-17	3) 0.8mV, 28uA	0.95	28.6	200	0.25	168	126
S001-4	1) 0.5mV, 15uA	0.85	33	200	0.06	187	176
	2) 0.5mV, 19uA	0.73	26.3	200	0.15	218	186
	3) 0.5mV, 22uA	0.66	22.7	200	0.24	241	184
	4) 0.5mV, 25uA	0.57	20	200	0.35	279	182
S08-n	1) 1.1mV, 26uA	4.9	42.3	200	0.05	32	31
	2) 1.1mV, 41uA	3.7	27	200	0.312	43	23
	3) 1.45mV, 30uA	5.27	48	200	0.014	30	30

$$^1 A = C_{dc} I_0^2 \frac{R_L - R_0}{R_L + R_0}$$

to be used for band 6 of HIFI instrument on the Herschel Space Observatory.

The measured $G(f_{IF})$ curve was approximated with a single polynomial curve (1) and f_{gain} was obtained minimizing the standard deviation of the experimental curve from the approximation. Then using the formulae (2) and (3) the electron relaxation time τ_θ was calculated. Comparing τ_θ of HEB on different substrates we analyze the effect of the membrane on the electron cooling rate.

The $\tau_\theta \propto (\tau_{e-ph}, \frac{C_e}{C_p}, \tau_{esc})$, where τ_{e-ph} (the electron-phonon interaction time), C_e and C_p (electron and phonon specific heat, respectively) are temperature dependent. Hot electrons, characterized by an electron temperature θ , close to T_c , are cooled by scattering with phonons and subsequent phonon transfer into the substrate. In thin NbN films the electron-phonon interaction time τ_{e-ph} has been investigated in [16], [8]:

$$\tau_{e-ph} \approx \frac{500}{\theta^{1.6}} [\text{ps}] \quad (6)$$

The τ_{e-ph} is about 21 ps at 7.2 K and 17 ps at 8.3 K. It shows that $\frac{C_e}{C_p}$ and τ_{esc} make the capital contribution into τ_θ . Phonon escape time (τ_{esc}) is a characteristic time, which determines the heat transfer rate from phonons of the film to the substrate (the film thickness is much less than the phonon diffusion length) and depends on the film thickness, d , and the film/substrate acoustic match, α , [8], [17]:

$$\tau_{esc} \approx \frac{4d}{\alpha u} \quad (7)$$

where u is the sound velocity in the film.

For NbN films on *silicon* and *sapphire* substrates $\tau_{esc} = 7d$ (ps) [12], where d is in nm, on bulk *MgO* substrates $\tau_{esc} = 5d$ (ps) [18], and on *crystal quartz* (SiO_2) $\tau_{esc} = 10d$ (ps) [19]. For the NbN on $\text{SiO}_2/\text{Si}_3\text{N}_4$ membrane and on bulk- $\text{Si}/\text{SiO}_2/\text{Si}_3\text{N}_4$ has been obtained the phonon escape time 17d (ps) and 26d (ps), respectively. When it is considered that thickness of NbN film is the same for all devices, we can see from (7) the film/substrate acoustic match, α , can make the difference of τ_{esc} for different substrates, but after some calculations we can conclude that the acoustic mismatch can not explain the large difference of the phonon transmission for *Si*, *sapphire*, *MgO* on one side and specially Si_3N_4 on the other side. The acoustic mismatch approach is valid under conditions of specular phonon reflection. However, when the phonon wavelength becomes comparable with the defects on the substrate surface a fraction of diffusive scattered phonons increases. As a result, the phonon transmission through the film/substrate interface decreases. Typical specification for the substrates surface roughness is 0.1-1nm and as is well known, *silicon*, *sapphire* and *MgO* have better surface quality comparing to SiO_2 and Si_3N_4 that also confirmed by superconductor transition temperature for the ultrathin NbN films, which is lower for SiO_2 and Si_3N_4 than on other substrates.

IV. CONCLUSION

We have measured different devices made on bare-*Si*, 1.4 μm thick $\text{SiO}_2/\text{Si}_3\text{N}_4$ stress-less membrane and bulk- $\text{Si}/\text{SiO}_2/\text{Si}_3\text{N}_4$. We have found that gain bandwidth of the devices made on two last substrates are narrower than on bare-*Si* and it is not wider than 1 GHz. One reason is: T_c of NbN

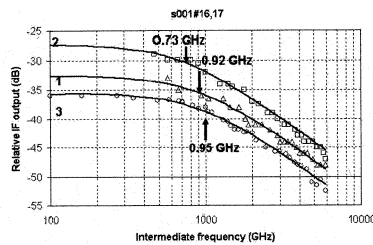


Fig. 2. IF bandwidth measurements of HEBs based on $\text{SiO}_2/\text{Si}_3\text{N}_4$ stressless membrane.

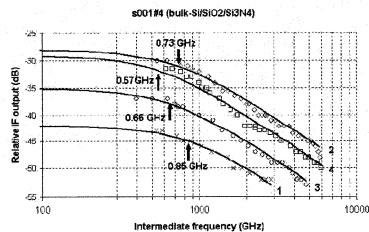


Fig. 3. The IF bandwidth measurements of bulk- $\text{Si}/\text{SiO}_2/\text{Si}_3\text{N}_4$ based HEB mixer (S001-4).

film on $\text{SiO}_2/\text{Si}_3\text{N}_4$ and bulk- $\text{Si}/\text{SiO}_2/\text{Si}_3\text{N}_4$ is lower. Other reason is: roughness of NbN film on $\text{SiO}_2/\text{Si}_3\text{N}_4$ is higher as compared with NbN on bare-Si [20] that increases the phonon escape time. Moreover, the gain bandwidth does not depend on whether Si is etched from under $\text{SiO}_2/\text{Si}_3\text{N}_4$ membrane or not, i.e. it is determined by the processes on the $\text{Si}_3\text{N}_4/\text{NbN}$ interface.

One way of increasing of the gain bandwidth is the increase the critical temperature of the film, which can be done by deposition of a buffer layer. Hopefully, it also can improve an acoustical match on film/substrate interface. Our latest experiments have shown that application of MgO buffer layer on top of Si_3N_4 increases T_c from 7.5 K to 11.2 K for 3.5 nm NbN films. Measurements of these devices in progress. Other solutions can be fabrication of the devices on SOI substrates.

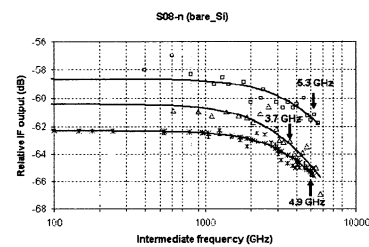


Fig. 4. IF bandwidth measurements of bare-Si based HEB mixer (S08-n).

REFERENCES

- [1] H.W. Huebers, J. Schubert, A.D. Semenov, B. Voronov, G. Gershenzon, Gol'tsman, G., and G. Shwaab. A heterodyne receiver for terahertz frequencies for SOFIA. In *Proceeding of SPIE Conference on Airborne Astronomy Systems*, March 2000.
- [2] G.L. Pilbratt, J. Cernicharo, A.M. Heras, T. Prusti, and R. Harris. The Herschel mission, scientific objectives. In *Proceeding of Symposium "The Promise of the Herschel Space Observatory"*, Toledo, Spain, pages 13–20, December 2000.
- [3] www.sofia.usra.edu.
- [4] J. Baubert, M. Salez, H. Merkel, P. Pons, S. Cherednichenko, B. Lecomte, V. Drakinskiy, G. Gol'tsman, and B. Leone. IF gain bandwidth of membrane-based NbN Hot Electron Bolometers for SHAHIRA. *Applied Superconductivity, IEEE Transactions on*, 15(2):505–510.
- [5] J. Baubert, M. Salez, H. Merkel, P. Pons, Y. Delomre, and B. Lecomte. IF gain bandwidth of membrane-based NbN Hot Electron Bolometers for SHAHIRA. In *MM and subMM detectors for radioastronomy II, J.Zmuidzinas, W.S.Holland, S. Withington eds., 5498, p.667, Proc. SPIE Int. Soc. Opt. Eng., 2004*.
- [6] D.F. Filipovic, W.Y. Ali-Ahmad, and G.M. Rebeiz. Millimeter-wave double-dipole antennas for high-gain integrated reflector illumination. *IEEE Transactions on Microwave Theory and Techniques*, 40(5):962–967, May 1992.
- [7] C.K. Walker, C.E. Groppiu, C.D. d'Aubigny, C. Kulesa, A. Hedden, D. Prober, I. Siddiqi, J. Kooi, G. Chen, and A.W. Lichtenberger. Millimeter-wave and terahertz integrated circuit antenna. In *Proc. SPIE, vol. 4855*, pages 349–354, 2003.
- [8] E.M. Gershenzon, G.N. Gol'tsman, I.G. Gogidze, Y.P. Gusev, A.I. Elant'ev, B.S. Karasik, and A.D. Semenov. Millimeter and submillimeter range mixer based on electronic heating of superconducting films in the resistive state. *Sov. Phys. Superconductivity*, 3(10):1582, 1990.
- [9] D. Meledin, P.-Y.E. Tong, R. Blundell, N. Kurova, K. Smirnov, B. Voronov, and G. Gol'tsman. Study of the IF Bandwidth of the NbN HEB mixers based on crystalline quartz substrate with an MgO buffer layer. *Applied Superconductivity, IEEE Transactions on*, 13(2):164–167.
- [10] M. Kroug, S. Cherednichenko, M. Choumas, H. Merkel, E. Kollberg, H.-W. Huebers, H. Richter, D. Loudkov, B. Voronov, and G. Gol'tsman. HEB quasi-optical heterodyne receiver for THz frequencies. In *Proceeding of 12th International Symposium on Space Terahertz Technology*, pages 244–252, 2001.
- [11] H. Ekstrom, E. Kollberg, P. Yagoubov, G. Gol'tsman, E. Gershenzon, and K.S. Yngvevsson. Gain and noise bandwidth of nbn hot-electron bolometric mixers. *J. Appl. Phys. Lett.*, 70(24):3296–3298, June, 1997.
- [12] S. Cherednichenko, P. Yagoubov, K. Il'in, G. Goltsman, and E. Gershenzon. Large bandwidth of NbN phonon-cooled hot-electron bolometer mixers on sapphire substrate. In *Proceeding of 8th International Symposium on Space Terahertz Technology*, pages 245–257, 1997.
- [13] Yu.B. Vachtomin, M.I. Finkel, S.V. Antipov, B.M. Voronov, K.V. Smirnov, N.S. Kurova, V.N. Drakinskiy, and G. Goltsman. Gain Bandwidth of phonon-cooled HEB mixer made of NbN thin film with MgO buffer layer on Si. In *Proceeding of 13th International Symposium on Space Terahertz Technology*, pages 259–270, 2002.
- [14] NbN films are provided by Moscow State Pedagogical Univ. (Russia).
- [15] Robert Bosch Gmbh, US.Pat.4855017, and 4784720, German Pat. 4241045c1.
- [16] Yu. Gousev, G. Gol'tsman, A. Semenov, and E. Gershenzon. Broadband ultrafast superconducting NbN detector for electromagnetic radiation. *J. Appl. Phys.*, 75(7):3695–3697, Apr. 1994.
- [17] A.V. Sergeev and M.YU. Reizer. Photoresponce mechanisms of thin superconducting films and superconducting detectors. *International Journal of Modern Physics B*, 10(6):635–667, 1996.
- [18] P. Yagoubov, M. Kroug, H. Merkel, E. Kollberg, J. Schubert, H.-W. Huebers, S. Svechnikov, B. Voronov, G. Goltsman, and Z. Wang. Hot electron bolometric mixers based on NbN films deposited on MgO substrates. In *Proc. Europ. Conf. on Appl. Superconductivity (EUCAS'99)*, 1999.
- [19] J. Kawamura, R. Blundell, C.E. Tong, G. Goltsman, E. Gershenzon, B. Voronov, and S. Cherednichenko. Low noise NbN lattice-cooled superconducting hot-electron bolometric mixers at submillimeter wavelengths. *J. Appl. Phys. Lett.*, 70(12):1619–1621, March, 1997.
- [20] J. Baubert. Submillimeter heterodyne array for high-speed ratio astronomy. *Thesis for the degree of licentiate of engineering*, 2005. Chalmers University of Technology.

16 Pixel HEB Heterodyne Receiver for 2.5 THz

S.Cherednichenko^{*a}, V.Drakinskiy^a, J.Baubert^b, B.Lecomte^b, F.Dauplay^b, J.-M.Krieg^b, Y.Delorme^b,
A.Feret^b, H.-W.Hübers^c, A.D.Semenov^c, P.Pons^d.

Abstract— A 16 pixel heterodyne receiver for 2.5 THz has been developed based on NbN superconducting hot-electron bolometer (HEB) mixers. The receiver uses a quasioptical RF coupling approach where HEB mixers are integrated into double dipole antennas on 1.5 μ m thick Si₃N₄/ SiO₂ membranes. Spherical mirrors (one per pixel) and backshort distance from the antenna have been used to design the output mixer beam profile. We present here the results of the antenna simulations using HFSS and ADS, as well as the beam calculations after the collimating mirror.

Index Terms— HEB mixer, THz camera, NbN films, membrane.

I. INTRODUCTION

All major ground based subMM/THz telescopes (AST/RO, CSO, JCMT, HHT, KOSMA) are now equipped with array heterodyne receivers. Two observatories which allow for observations above 1 THz will become operational in the next two years: SOFIA in 2006 and ESA's Herschel Space Observatory in 2007. SOFIA's first generation heterodyne receivers (GREAT [1] and CASIMIR [2]) are single pixel or dual pixel receivers. However two proposals for array receivers on board of SOFIA have been published. These are STAR (Universität Köln) and FAR (University of Arizona). While STAR focuses on the 1.7-1.9 THz band, FAR is going to cover a wide band from 1.5 THz to 3 THz.

NbN hot-electron bolometer (HEB) mixers [3] are currently the devices of choice for heterodyne THz receivers. Among the radioastronomical instruments where NbN HEB mixers are used are: HIFI 1.4-1.9 THz band (Herschel Space observatory); TELIS, SOFIA, Receiver Lab Telescope in Chile (SAO), APEX. A DSB noise temperature of about 450 K has been achieved for 500-700 GHz, 700 K at 1.6THz and 1100 K at 2.5 THz [4, 5, 6], 6400 K at 5.2 THz [7]. Above 1 THz there is no other device which can match this performance. The local oscillator (LO) power, required to drive an HEB mixer is 200+300 nW (determined by the mixer size and superconducting critical temperature). Such low LO

power requirements allow for use multiplier chains which produce >10 μ W power up to 1.9 THz [8]. The electron energy relaxation time sets a limit for the highest intermediate frequency (IF) for the HEB mixers. For NbN HEB mixers the 3dB gain roll-off frequency is 3.5 GHz [9, 10], while the noise bandwidth is about 6 GHz. The HEB mixers can employ either waveguide (WG) or quasioptical (QO) RF coupling scheme. The development of the former has resulted in laser silicon micromachining [11], and electroplating technique [12]. Traditional machining has also been used up to 1.5 THz [13]. QO technique has been used up to 5THz [7]. Comparing both WG and QO techniques the challenge of fabrication of THz receivers consisting of tens or hundreds of pixels has to be considered. In this paper we discuss development of a QO HEB heterodyne camera for 2.5 THz with a possibility to upgrade it to higher frequencies. The philosophy of our design is to have as more integrated components as possible. Such integration could be organized on a pixel bases (completely integrated pixels, separate pixels compose the array) or on an array bases (separate parts common for the whole array). We have chosen the second option, i.e. the camera consists of a detector array, optic array, etc.

Lens antennas have been the most popular solution in QO receivers. A large variety of antenna types has been studied: double slot, double dipole, spiral, log-periodical, ring slot, etc. The choice of the antenna is determined mainly by the input bandwidth and the embedding impedance. The beam properties are almost the same for all these antennas and are defined by the lenses. The antennas are fabricated on a dielectric (semiconductor) wafer and are placed on the back side of a spherical or elliptical lens. The lens eliminates substrate mode loss, which is otherwise unavoidable since the wafer thickness is larger than the THz wavelength. Beams with up to 90% Gaussicity can be achieved with the lens/antenna approach. This has been experimentally verified at subMM wavelengths. The antennas (integrated with mixers) are fabricated lithographically and can be numbered hundreds and thousands on a single wafer.

Two concepts for the QO arrays exist. The first one is the so called fly-eye approach [14]. In this case a lens is integrated with a single detector (mixer). Then, the lenses (one per pixel) are integrated in a 1D or 2D arrays. The array's filling factor is limited by the lens diameter, i.e. the detectors can not be positioned closer to each other than the lens diameter. The lens diameter can be reduced at the expense of the angular dimension of the beam (the diffraction limited beam has a divergence angle of $F/(D\lambda)$, where F is the focal distance, D is the lens diameter, and λ is the wavelength). The fly-eye approach requires also a large amount of lenses and assembly

Manuscript received May 30, 2006. This work was financed by ESA contract 16940, and by funding from the European Community's sixth Framework Programme under RadioNet R113CT 2003 5058187.

Authors are with: ^a) the Microwave Electronic Laboratory, MC2, Chalmers University of Technology, SE-412 96, Gothenburg, Sweden, ^b) Observatoire de Paris, LERMA, 77, Avenue Denfert-Rochereau, 75014, Paris, France, ^c) German Aerospace Center (DLR), Institute of Planetary Research, 12489 Berlin, Germany, ^d) LAAS, Toulouse, France.

(corresponding author S.Cherednichenko, e-mail: sergei.cherednichenko@mc2.chalmers.se).

procedures. However, it is quite a straightforward approach and it is suitable for small size THz arrays.

In the second array concept a single lens is used for the whole array [15]. In this case the detector array is made on a separate wafer and it is attached to a single lens. The lens has to be big in order to minimize the risk of the beam distortion. The beam distortion comes from the fact that all detectors but one will be placed off-axis of the lens. The distortion increases with the ratio of D/d , where d is the distance from the antenna to the lens's main optical axis. However, much larger array filling factors can be achieved. In this case the minimal interpixel distance is limited by the antenna dimensions (typically of the order of the wavelength) and by the on-chip read-out electronics.

A QO RF coupling scheme can be also realized without lenses when the antenna is placed on a substrate which is much thinner than the wavelength. It has been shown, that in order to avoid substrate modes the substrate has to be not thicker than $0.02\lambda_e$, where λ_e is the wavelength in the dielectric, i.e. of the order of $1\ \mu\text{m}$ thick. Such thin substrates are possible to obtain by utilizing $\text{SiO}_2/\text{Si}_3\text{N}_4$ membranes [16]. For 2.5 THz $\lambda_e=47\ \mu\text{m}$ (in $\text{SiO}_2/\text{Si}_3\text{N}_4$), therefore $0.02\lambda_e=1\ \mu\text{m}$. An interesting approach has been proposed in [17] where a Double Dipole Antenna (DDA) on a membrane backed with a back short was in the focus of a small parabolic reflector. 37 dB reflector gain was achieved at 2.5 THz with about 10% bandwidth. We adopted this approach for the HEB mixer camera which we present below.

II. CAMERA DESIGN

A. Camera architecture

A single pixel optical scheme is shown in Fig. 1. The DDA antenna is placed on a stress less $\text{Si}_3\text{N}_4/\text{SiO}_2$ membrane which is $1.5\ \mu\text{m}$ thick. A backshort (above the DDA) reduces the back lobe and increases the beam directivity. A spherical (or parabolic) mirror collimates the beam. Our design is 4×4 pixel. All 16 DDA/HEBs are fabricated on a single silicon wafer (see in this proceedings [18]). The backshort array is fabricated by a similar technique on the same type of membrane, and it is fixed on top of the HEB array. The mirror array is made on a single plate which minimizes the assembly of the camera. The HEB array is bonding to a single IF board which includes bias-Ts, and IF connectors for all 16 channels (see Fig. 2). The distance between pixels was chosen from the Airy disk diameter ($A=2.44\lambda F/D$, F being the F -number of the telescope and D is the telescope diameter). We used SOFIA telescope specifications as a mark. At 2.5 THz, we have $A_{2.5}=5738\ \mu\text{m}$. We fixed the distance between pixels at 6mm. Since the radiation has to go through the HEB wafer once again after reflection from the collimating mirror, we minimized the IF read out line width and lead them in a way not to obscure the beam propagation.

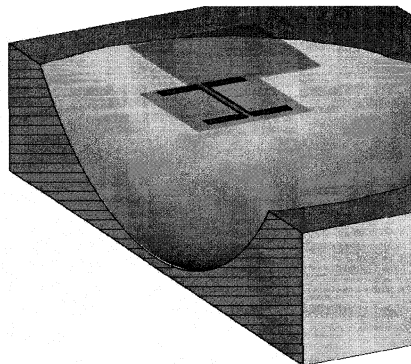


Fig. 1. A single pixel layout. The HEB mixer is integrated in a planar antenna with a backshort to minimize the back lobe loss. Both antenna and the backshort are placed on thin membranes above the collimating mirror.

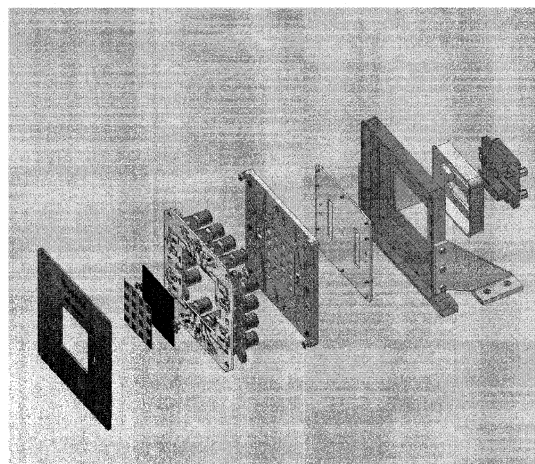


Fig. 2. Camera design: exploded view. From left to right: protection cap, backshort wafer, HEB wafer, IF board, mirror plate, dc board, housing, dc connector holder, dc connectors.

B. Antenna simulations

We used commercial software such as HFSS, ADS and CST Microwave Studio in order to simulate the response of an DDA with a backshort. Dipole antenna theory was used for an initial approximation [19]. The real and imaginary part of the antenna impedance (as seen in the HEB terminals) was obtained as function of frequency (Fig. 4) and the antenna geometry and the impedance matching network (Fig. 3) was optimized that the real impedance at the resonance frequency (2.5THz in our case) was acceptable for an HEB mixer (about 100 Ohm). The antenna response was estimated from antenna S11 parameters (Fig. 5). The results of the simulation were verified by comparing the published double slot antenna designs (DSA) on silicon against experimental results (e.g. [20]).

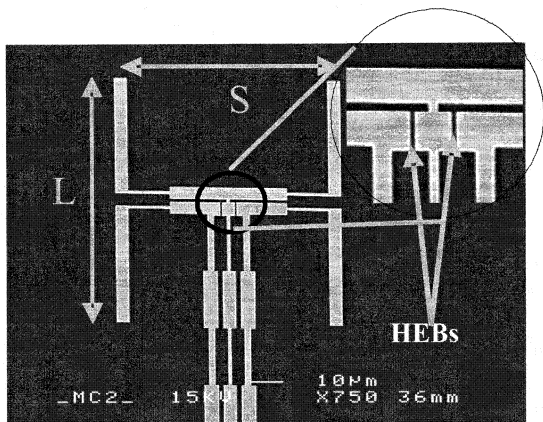


Fig. 3. A scanning Electron Microscope image of the Double Dipole Antenna with the choke filter. Two section impedance transformer is used to match the HEBs to the dipole antenna. $L=82\mu\text{m}$, $S=66\mu\text{m}$, $w=4\mu\text{m}$.

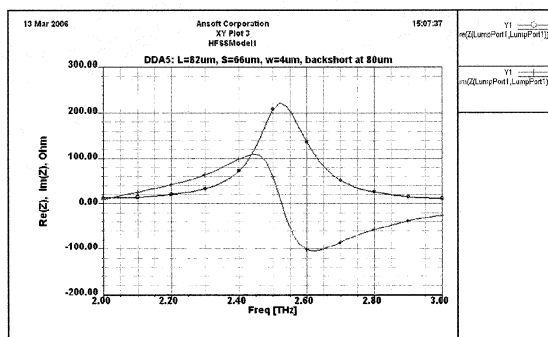


Fig. 4. Simulation of the impedance (real and imaginary part) of the DDA at the HEB terminals.

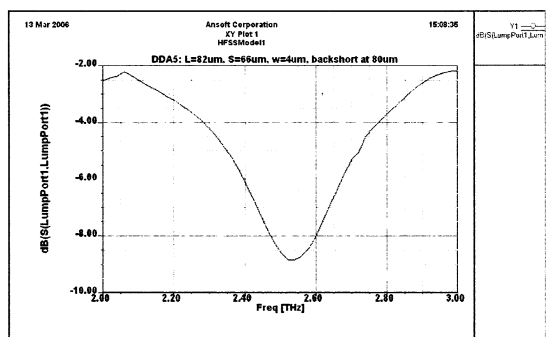


Fig. 5. Simulation of the S11 parameter of the DDA loaded on two parallel HEBs with 200 Ohm each.

C. Beam simulations

The far field of the DDA was simulated with the same software. We have found that ADS simulations are fast and differ from HFSS and CST only at the angles more than $\pm 60^\circ$ (the far field always tends to zero at 90° in ADS). 3D simulators (HFSS and CST) require much more time and computer resources. However they provide more precise

results (Fig. 6). We verified the validity of our calculations by comparing DSA and DDA beam simulations to those published by other authors (both theoretical and experimental). We have found that withdrawing the backshort from the DDA (on the membrane) the beam directivity increases, however the side lobe level increases. In order to keep the collimating mirror small enough (about 3mm in diameter) with the DDA at the mirror's focal plane, the beam FWHM has to be within 40° . In this case the edge taper on the 3mm mirror will be below -20dB. With the backshot at $80\mu\text{m}$ from the antenna we obtain the DDA beam FWHM to be about 32° (Fig. 6) with the side lobes below -10dB. The main beam can be approximated by a Gaussian beam with the waist of $w_{01}=75\mu\text{m}$. For a spherical mirror ($R=5.56\text{mm}$) the output beam pattern was calculated for several DDA positions using GRASP (Fig. 8). For the mirror- to- DDA distance of 2.2 mm the output beam waist is $w_{02}=0.6\text{mm}$. We shall note that by using parabolic mirrors with f-numbers smaller than for spherical mirrors the DDA can be positioned closer to the mirror. Therefore the backshort can be put closer to the DDA. It will result in lower side lobes with still low beam truncation at the mirror edges.

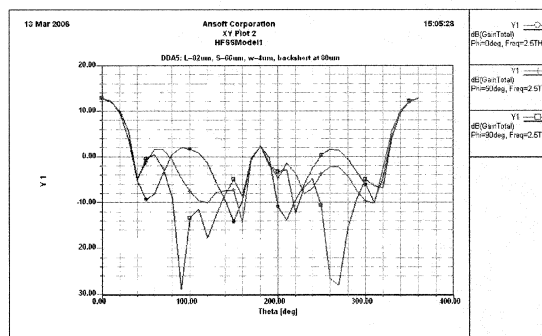


Fig. 6. Simulation of the DDA (on membrane) far field beam pattern (with a $200\mu\text{m} \times 200\mu\text{m}$ backshort at $80\mu\text{m}$ above the antenna plane).

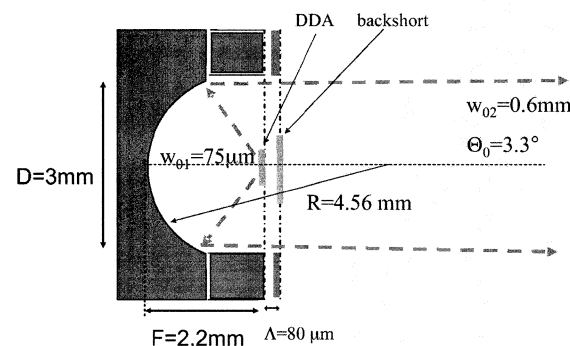


Fig. 7. The beam tracing from the DDA through the collimating mirror. The DDA beam was approximated (using Fig. 6) as a Gaussian beam with a waist of $75\mu\text{m}$. The output beam has a waist of 0.6mm which corresponds to the divergence angle (by $1/e^2$) of 3.3° . The calculations are done for 2.5 THz.

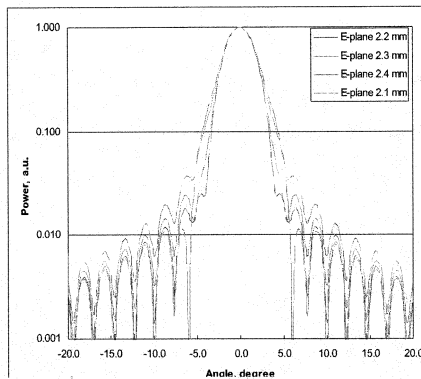


Fig. 8. Beam pater of the DDA/spherical mirror system. The mirror is 3mm in diameter sphere with the radius of curvature of 4.56 mm. The beam waist is 0.6mm when the DDA is 2.2mm away from the mirror apex.

III. CONCLUSION.

In the conclusions we can summarize that: the HEB technology allows design and fabrication of heterodyne cameras from both LO power requirements (not more than 200 nW per pixel), and noise performance ($T_n \approx 10h\nu/k$), quasioptical mixers on membranes enable quite straightforward fabrication of arrays of 16 pixels and more; the approach can be scaled up in frequency without any substantial redesign; such software as ADS, HFSS, CST Microwave Studio can be used for simulations of both S-parameters and beam properties of THz planar antennas.

Acknowledgements.

For the HEB mixers we used NbN films deposited at Moscow State Pedagogical University (Russia). This work was financed by ESA contract 16940, and by funding from the European Community's sixth Framework Programme under RadioNet R113CT 2003 5058187.

REFERENCES:

- 1 R. Güsten, I. Camara, P. Hartogh, H.-W. Hübers, U. U. Graf, K. Jacobs, C. Kasemann, H.-P. Röser, R. T. Schieder, G. Schneider, O. Siebertz, J. Stutzki, G. Villanueva, A. Wagner, P. Van der Wal, and A. Wunsch, in *Airborne Telescope Systems II*, R. K. Melugin and H. P. Röser, eds., Proc. SPIE **4857**, pp. 56-61, 2002.
- 2 M. L. Edgar and J. Zmuidzinas, in *Airborne Telescope Systems*, R. K. Melugin and H. P. Röser, eds., Proc. SPIE **4014**, pp. 31-42, 2000.
- 3 E. M. Gershenson, G. N. Gol'tsman, I. G. Gogidze, A. I. Elant'ev, B. S. Karasik and A. D. Semenov, *Sov. Phys. Superconductivity*, **3**, 1582, 1990
- 4 S. Cherednichenko, M. Kroug, P. Khosropanah, A. Adam, H. Merkel, E. Kollberg, D. Loudkov, B. Voronov, G. Gol'tsman, H.-W. Huebers, H. Richter, *Physica C*, vol.372, pp.427-431, Aug. 2002.
- 5 J.Kawamura, R.Blundell, C.E.Tong, G.Gol'tsman, E.Gershenson, B.Voronov and S.Cherednichenko *Applied Physics Letters*, **70**(12), pp.1619-1621, 24 March,1997.
- 6 M.Kroug, S.Cherednichenko, H.Merkel, E.Kollberg, B.Voronov, G.Gol'tsman H.-W.Huebers, H.Richter, *IEEE Trans. on Appl. Supercond.* Vol.11, n.11, pp. 962-965, 2001
- 7 H.-W. Hübers, A. Semenov, H. Richter, M. Schwarz, B. Günther, K. Smirnov, G. Gol'tsman, and B. Voronov, in: *Millimeter and Submillimeter Detectors for Astronomy II*, J. Zmuidzinas, W. S. Holland, and S. Withington, eds., Proc. SPIE **5498**, pp. 579-586, 2004.
- 8 A.Maestrini et al, *IEEE Microwave and Wireless Comp.Lett.*, vol. 14, NO. 6, June 2004, pp.253-255.
- 9 H.Ekström, E.Kollberg, P.Yagoubov, G. Gol'tsman, E. Gershenson, and K.S. Yngvesson, *Appl. Phys. Lett.* **70**, 3296 (1997).
- 10 S. Cherednichenko, P. Yagoubov, K. Il'in, G. Gol'tsman and E. Gershenson. Proc. 8th Intl. Symp. Space Terahertz Technol., 245, (1997), Cambridge, MA, USA.
- 11 C.K.Walker, C.E.Groppiu, C.D.d'Aubigny, C.Kulesa, A.Hedden, D.Prober, I.Siddiqi, J.Kooi, G.Chen, and A.W.Lichtenberger, Proc. SPIE **4855**,349 (2003).
- 12 D.Meledin et al, Proc. International Symposium on Space Terahertz Technology, May2-4, 2005, Gothenburg.
- 13 C.-Y. E. Tong, D. Meledin, D. Loudkov, R. Blundell, N. Erickson, J. Kawamura, I. Mehdi, and G. Gol'tsman, 2003 IEEE MTT Intl. Microwave Symp. Digest, **2**, 751 (2003).
- 14 T.H.Büttgenbach, *IEEE MTT*, vol.40, no.10, October 1993, pp.1750-1761.
- 15 D.F.Filipovic, G.P.Gauthier, S.Raman, and G.M.Rebeiz, *IEEE Trans. Ant.Prop.* vol.45, no.5, May 1997, pp.760-766.
- 16 C.C.Ling, J.C.Landry, H.Dave, G.Chin, and G.M.Rebeiz, *IEEE Trans. MTT*, vol.42, no.4, April 1994, pp.758-760.
- 17 D.F.Filipovic, W.YAli-Ahmad, and G.M.Rebeiz, *IEEE Trans. MTT*, vol.40, no.5, May 1992, pp.962-967.
- 18 V.Drakinskiy, J.Baubert, S.Cherednichenko, "Gain bandwidth of THz NbN HEB superconducting mixers on thin SiO₂/Si₃N₄ membrane", in this proceedings of 17th Symposium on Space THz Technology, 2006.
- 19 M. Kominami, D. M. Pozar, and D. H. Schaubert, *IEEE Trans. Antennas Propag.* vol. 33, pp. 600-607, June 1985.
- 20 D. Loudkov, P. Khosropanah, S. Cherednichenko, A. Adam, H. Merkel, E. Kollberg, G. Gol'tsman, Proc. 13th International Symposium on Space Terahertz Technology, Cambridge, MA, March 2002

Unexpected Frequency Shift on Membrane Based Double-Slot and Double-Dipole HEB Receivers

F. Dauplay, J. Baubert, Y. Delorme, Bruno Guillet (*)
S. Cherednichenko, V. Drakinskiy, P. Khosropanah (**)

(*) : LERMA, Observatory of Paris, 77 avenue Denfert-Rochereau, 75014, Paris, France

(**) : MC2 Dept. Microtechnology and Nanoscience, Microwave Electronics Laboratory,
Chalmers University of Technology, SE-412 96 Gothenburg, Sweden

Email : frederic.dauplay@obspm.fr

Double-slot and double-dipole antennas are one of the main choices in quasi-optical sub-millimetre heterodyne receivers design. Being easily adapted to planar technology, they are widely used for their frequency and polarisation selectivity, symmetrical gaussian beam shape.

This type of antenna will resonate, in theory, at the frequency determined by antenna's length. But frequency shift may take place and depend on the electrical characteristics of the antenna's substrate or the device connected to the antenna.

In this paper, we'll report on the analysis results of the frequency shifts observed on the membrane based double-slot HEB receivers working around 2 THz. Intensive simulations have been performed with CST Microwave Studio and have shown that several technical parameters (such as HEB's impedance, dielectric constant of the substrate, ...) can strongly influence the resonance frequency given by the antenna's length.

These analysis and the comparative study between simulation and FTS measurement will lead to the understanding of the observed frequency shift as well as to control or guide some technical parameters' choice during the receiver's design and fabrication.

Intermediate Frequency Bandwidth of a Hot-Electron Mixer: Comparison with Bolometric Models

Alexei Semenov, Konstantin Il'in, Michael Siegel, Andrey Smirnov, Sergey Pavlov, Heiko Richter, Heinz-Wilhelm Hübers

Abstract—The gain bandwidth of a superconducting NbN hot-electron mixer quasioptically coupled to radiation was evaluated in different operation conditions and compared to presently known bolometric mixer models. Heterodyne regime was obtained with a 2.5 THz quantum cascade laser as a local oscillator and alternating thermal loads and also by mixing radiation of the quantum cascade laser and a gas laser. The results rather agree with the hot-spot mixer model than with any of the homogeneous bolometric models.

Index Terms — bolometers, gain measurements, superconducting devices, thin film devices.

I. INTRODUCTION

SHORTLY after the introduction of superconducting thin-film hot-electron bolometric mixers [1,2] their usable intermediate frequency (IF) band has been recognized as one of the most important parameters. In terahertz heterodyne applications, this is the lack of tunable radiation sources that enhances the importance of the gain bandwidth of hot-electron bolometric mixers. Since the factors limiting the bandwidth are the thermal coupling of the film to a substrate and diffusion of electrons and phonons in the film (for details see e.g. the reviews [3]), great efforts were made in order to decrease the thickness and the lateral size of the mixers as well as to find an optimal substrate material for a particular superconducting film. During the last decades suitability of many materials for heterodyne detection were evaluated but only NbN and NbTiN superconducting films met the requirements of practical applications [4]. For bolometers made from NbN films, phonons leaving the film through the film-substrate interface dominate the cooling process. Substrates from crystalline MgO [5] have demonstrated the best thermal coupling to NbN films whereas substrates from Si, although providing a slightly weaker coupling, have been shown

[6,7] to better compromise with all practical constraints. There is no common opinion on whether the thermal coupling to a substrate [8] or the intrinsic interaction times [9] limit the IF bandwidth of mixers from NbTiN films. However, independently on the substrate used, these mixers exhibit a bandwidth noticeably smaller than mixers from NbN films.

Besides the practical importance of realizing a possibly large IF bandwidth, studying the bandwidth variations with the change of the mixer operation regime allows one to better understand the mixing mechanism. The bolometric models introduced so far are the homogeneous hot-electron models [10, 11, 12] and the hot-spot model [13,14] with the zero phonon escape time. In this paper we compare the IF bandwidth measured at 2.5 THz for the NbN hot-electron mixer with the predictions of these two models and with earlier published data.

II. DEVICE FABRICATION AND MEASUREMENTS

The films were deposited on optically polished R-plane sapphire substrates by DC magnetron sputtering of pure Nb target in Ar+N₂ gas mixture. The substrates were laid on the surface of a heater without any thermo-conducting glue. The temperature of the heater during deposition was kept at 750 °C. The base pressure in the sputtering chamber was approximately 2·10⁻⁷ mbar at room temperature and reached an order of magnitude higher value when the temperature of the heater increased to 750 °C. During deposition the partial pressure of Ar and N₂ was 5·10⁻³ mbar and 7·10⁻⁴ mbar, respectively. The nominal deposition time was 14 sec. Using ellipsometry we found for our films a thickness of 5 ± 1 nm that corresponded to a deposition rate of ≈ 0.65 nm sec⁻¹. The superconducting transition temperature T_C taken as the temperature corresponding to the offset of the film resistance was measured for freshly deposited films by means of the standard four-probe method. Depending on the stoichiometric composition, T_C varied between 9.5 K and 11 K whereas the width of the transition was ≈ 0.9 K and remained almost unchanged for all compositions. The surface resistance of our films at the maximum of the temperature dependence of the resistance amounted at ≈ 1000 Ω per square that was approximately 1.3 times larger than the square resistance measured at room temperature.

Manuscript received May 11, 2006. This work was supported in part by the parliament of Berlin under the scholarship for A. Smirnov.

A. D. Semenov, H. Richter, S. Pavlov and H.-W. Hübers are with the German Aerospace Center, 12489 Berlin, Germany (phone: +49 30 670 55 505; e-mail: alexei.semenov@dlr.de).

K. Il'in and M. Siegel are with The Institute of Micro- and Nanosystems, University of Karlsruhe, 76187 Karlsruhe, Germany (e-mail: k.ilin@ims.uni-karlsruhe.de).

A. Smirnov is on leave from the State Pedagogical University, 119435 Moscow, Russia.

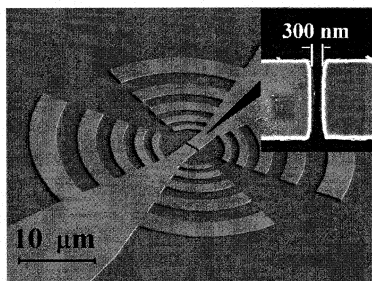


Fig. 1. Picture of the log-periodic antenna and the slit in the center (inset) taken with a scanning electron microscope.

The hot-electron bolometers were manufactured by means of electron-beam lithography in the following three-step sequence. First we wrote a set of global and local alignment marks in an electron-beam resist layer from polymethylmethacrylate (PMMA) spun to a thickness of 200 nm on a bare NbN film. Then we deposited a Ti/Au (10/50 nm) bi-layer for the lift-off process. Due to a high material contrast between NbN and Au, such bi-layer formed high quality (sharp and strait) alignment marks which were easy to recognize even under relatively thick resist layers used in the next fabrication steps. Second we opened the window for the antenna in the newly spun 400 nm PMMA and deposited in the opening a 250-nm thick Au layer sandwiched between two 10-nm Ti layers. The length of the bolometer was defined at this stage as the width of the slit between the antenna arms. The third lithography was made in the negative electron-beam resist. In the center of the antenna we formed a rectangle from the resist that defined the width of the bolometer. Finally, using the rectangle and the top titanium layer of the antenna structure as masks, we removed the unprotected part of the NbN film by ion milling. Typically bolometers with a size of $2 \times 0.25 \mu\text{m}^2$ (width \times length) had $T_c \approx 7.8 \text{ K}$ and a resistance of 160Ω at the room temperature. Fig. 1 shows the antenna and the central slit where the bolometer is located.

Radiation was coupled to the bolometer by an extended hemispherical Si lens. The bolometer with the lens was cooled to 4.5 K in a cryostat with optical access through a polymethylpentene (TPX) window kept at the room temperature and a quartz filter mounted on the 77 K screen. The noise temperature and the conversion efficiency were measured with a conventional radiometric method in that radiation of a local oscillator (LO) at a frequency of 2.5 THz was applied to the bolometer and its response at the intermediate frequency to alternating hot and cold loads was recorded with the lock-in technique. The loads were at an air distance of 50 cm from the cryostat window. We have verified that attenuation of water vapors in the upper and lower sub-bands of our IF band varied in the range smaller than 0.2 dB. Radiation of the load and the local oscillator was combined by a Mylar beam-splitter with a thickness of 6 μm . A chain of broadband cooled low-noise and room temperature amplifiers raised the level of the response signal. In order to maximize the response we eliminated truncation of the bolometer field of view and fully covered it with the loads. The transmission coefficient S_{21} of the IF

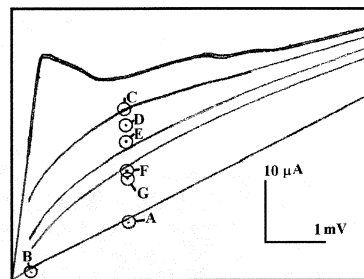


Fig. 2. Set of dc voltage-bias characteristics for few (increasing from top to bottom) levels of the LO power. The upper curve was taken without LO power. IF bandwidth and the noise temperature were measured in the operation conditions shown by encircled points.

amplifiers was directly determined as the portion of the “white” noise passing through the chain. The Johnson noise in excess to the intrinsic noise of the first amplifier was produced by the same bolometer driven in the normal state by a sufficiently high LO power. The IF response of the bolometer was then normalized with the S_{21} parameter that gave us the relative conversion efficiency. The use of a very stable quantum cascade laser (QCL) [15] as a local oscillator made it possible to sample the IF band with a resolution of 2 MHz. The mixer was dc voltage-biased to a value corresponding to the smallest measurable noise temperature. The IF dependence of both the mixer noise temperature and the response was then measured at different levels of the LO power, which in turn resulted in different bias currents. Fig. 2 shows dc bias characteristics taken at different LO levels. The point labeled “B” (normal state, no bias) was used to measure the transmission of the IF chain.

We complemented this technique by mixing radiation of the QCL and a gas laser with our bolometer. In this case the IF signal of the bolometer mixer was normalized with the IF signal of a Schottky diode backed by the same amplifier chain (only room temperature amplifiers were used in this experiment). The gas laser was operated at a constant power acting as local oscillator. We scanned the IF band by tuning QCL-frequency with the dc current-bias. A non-stabilized line-width of the QCL less than 1 MHz was sufficient to provide desired accuracy of the gain measurements.

III. DATA AND ANALYSIS

The noise temperature and the normalized conversion efficiency related to the position of the load are shown in Figs. 3 and 4, respectively. Data shown in the pictures were acquired in the conditions labeled with “D” in Fig. 2. Since the mixer noise due to thermal fluctuations decreases along with the mixing product, the noise temperature slowly varies at low intermediate frequencies and exhibits an upturn when the thermal noise drops below the frequency independent Johnson noise. Standing waves in the mixer bias board and also between the board and the first amplifier resulted in the resonance peaks seen in the IF dependence of the noise temperature in Fig 3. As a result of the normalization procedure, which we used to obtain the relative gain, the peaks almost disappeared in the IF dependence of the

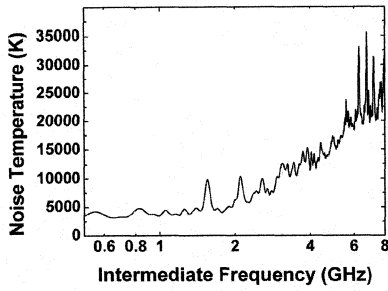


Fig. 3. Noise temperature referred to the position of the load as function of the intermediate frequency.

conversion efficiency (Fig. 4). The normalization enormously enhanced the accuracy with which the roll-off frequency of the conversion efficiency was determined. Two methods of gain measurements provide complementary results that coincide fairly well in the frequency range from 0.5 GHz to 2 GHz where the methods overlap. We obtained a 3-dB roll-off frequency F_0 by fitting our experimental IF dependence of the gain with the following relaxation dependence

$$G(F) = \frac{1}{1 + (F/F_0)^2}, \quad (1)$$

where F denotes the intermediate frequency. Thus defined roll-off frequencies are plotted in Fig. 5 as function of the bias current. With the decrease of the LO power (increase of the current) the experimental IF bandwidth decreases from 3.5 GHz to 2.2 GHz. The median value reasonably corresponds to the gain bandwidth of 3.7 GHz measured [16] for somewhat thinner mixer devices on sapphire substrates. Along with the decrease of the bandwidth the noise temperature passes the minimum at the LO power corresponding to $F_0 \approx 2.5$ GHz. We shall emphasize that the minimum value of the noise temperature presented in the Fig. 5 is related to the hot-cold loads. The noise temperature related to the tip of the lens amounts at 1050 K that is close to the best values reported at 2.5 THz.

We compare measured IF dependence of the relative gain with the predictions of the PV [10], KE [11] and NS [12] models (abbreviation is made in all three cases after the names of first two authors). Formally, it is possible to fit experimental data with either model. However each fit would require different fitting parameters. The criterion for applicability of the particular model should be coincidence of the parameters extracted from the fitting procedure with the known material parameters. In the framework of the PV model the IF dependence of the relative gain is

$$G_{PV}(\omega) = |\eta(\omega)|^2 = \left| \frac{1}{1 + j\omega\tau_1} \frac{1 + j\omega\tau_3}{1 + j\omega\tau_2} \right|^2, \quad (2)$$

where $\omega = 2\pi F$ and the characteristic times τ_1 , τ_2 and τ_3 are connected with the electron-phonon interaction time τ_{eph} , phonon escape time τ_{es} and the ratio $R_{eph} = c_e/c_{ph}$ of the electron c_e and phonon c_{ph} specific heat as follows

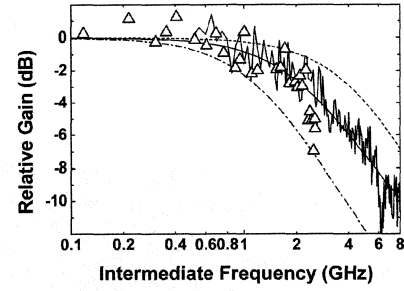


Fig. 4. Relative conversion efficiency of the mixer measured with the hot-cold technique (solid noisy line) and by means of the mixing product of the QCL and the gas laser (open triangles). Smooth lines show the model gain that was computed in the framework of the KE (dotted) NS (solid) and PV (dash-dotted) models with the same set of mixer parameters.

$$\begin{aligned} \frac{1}{\tau_1} &= \frac{1}{2} \left(\frac{\tau_{es} + \tau_{\theta}}{\tau_{eph}\tau_{es}} \right) \left[1 + \sqrt{1 - \frac{4\tau_{eph}\tau_{es}}{(\tau_{es} + \tau_{\theta})^2}} \right] \\ \frac{1}{\tau_2} &= \frac{1}{2} \left(\frac{\tau_{es} + \tau_{\theta}}{\tau_{eph}\tau_{es}} \right) \left[1 - \sqrt{1 - \frac{4\tau_{eph}\tau_{es}}{(\tau_{es} + \tau_{\theta})^2}} \right] \\ \frac{1}{\tau_3} &= \frac{\tau_{\theta}}{\tau_{eph}\tau_{es}}; \quad \tau_{\theta} = \tau_{eph} + R_{eph}\tau_{es}. \end{aligned} \quad (3)$$

The KE and NS models include the heating of the mixer by the bias current and the electro-thermal feedback through the IF load. These are essentially the same phenomena that are responsible for the decrease of the response time of a voltage-biased transition edge sensor [17]. Formally the effect of the feedback is described with the self-heating factor C . It can be extracted from the dc bias characteristics as $C = (R_d R) / (R_d + R)$ where R_d and R are the differential and dc resistance of the bolometer in the operation conditions. In both models the relative gain of the mixer connected to an IF load with the real resistance R_0 can be presented as

$$G(\omega) = \frac{|C(R - R_0) + (R + R_0)|^2}{|C(R - R_0) + (R + R_0)\varphi(\omega)|^2} \quad (4)$$

with either $\varphi(\omega) = \eta(\omega)^{-1}$ in the NS or $\varphi(\omega) = 1 + j\omega\tau_{\theta}$ in the KE model. The KE model relies on an approximation of the PV model at $\tau_{eph} \gg R_{eph}\tau_{es}$ that fairly good describes e.g. Nb bolometers. In the NS model the effective temperature of phonons T_{ph} is supposed to differ from the effective electron temperature T_e and has to be calculated via steady-state energy balance equations. The difference between T_{ph} and T_e influences the interaction times and the specific heat ratio. Fig. 4 shows the relative gain that we have computed in the framework of each model with the same set of parameters. Experimental data ($C = 0.55$) are best fit by the NS model with $\tau_{es} = 38$ ps assuming the following temperature dependences of the parameters: τ_{eph} [ps] = $474 T^{-1.6}$, $c_{ph} = 9.8 T^3$ and $c_e = 280 T$ (c_{ph} and c_e are in $J cm^{-3} K^{-1}$; temperature in Kelvins). We computed $T_{ph} = 6.9$ K using $T_e = 7.5$ K that was the value found from the superconducting resistive transition $R(T)$ for the actual dc resistance of the bolometer. The best-fit parameters coincide with the parameters concluded from the pulse measurements [18] if one assumes τ_{es} [ps] = $8 d$ [nm] where

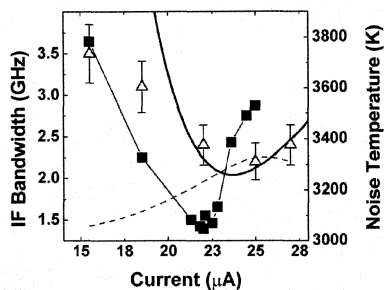


Fig. 5. IF bandwidth (open symbols) and the noise temperature (closed symbols) measured at different levels of the LO power are shown as function of the corresponding bias current. The broken solid line is to guide the eyes. Smooth lines show the IF bandwidth computed with the hot-spot model (solid line) and with the NS model (dashed line).

d is the bolometer thickness. Fitting the experimental gain with the KE model would require a noticeably larger $\tau_{es} \approx 130$ ps.

Defining the model bandwidth as the 3-dB roll-off frequency of the model gain and using the experimental values of C and T_e , we computed the bandwidth for each LO power. The bandwidth obtained with the NS model (dashed line in Fig. 5) is obviously inconsistent with the experimental data. Similar disagreement was found for other two uniform bolometric models.

The hot-spot (HS) approach, which was used [14] to analytically evaluate the IF bandwidth, invoked the velocity of the boundary between the normal spot and superconducting portion of an infinitely long bolometer. The velocity was found by solving time dependent diffusion equations for hot-electrons. Phonons with their actual temperature can also be included at the expense of analytical transparency [19]. For the limited range of bias currents the HS-model gain is

$$G_{HS}(\omega) \propto \left| 1 + \omega^2 \tau_\theta^2 \left(\sqrt{\frac{J^2 \rho_n \tau_\theta}{c_e (T_C - T)}} - 1 \right)^2 + j\omega \tau_\theta \right|^{-2}, \quad (5)$$

where J is the density of the bias current and ρ_n the normal-state resistivity. The current dependence of the IF bandwidth computed with Eq. 5 is shown in Fig. 5 with the solid line. The HS model follows the trend in the experimental data. However, the approximation of a free normal domain is still too schematic. It does not take into account the effect of the contacts that restricts the movement of the domain walls and thus decreases the bandwidth. This is most likely the reason for the disagreement between the model and the experiment at small currents when the size of the normal domain approaches the length of the bolometer.

In conclusion, we have shown that, contrary to homogeneous bolometric models, the hot-spot model of the hot-electron mixer describes both the intermediate frequency dependence of the mixer gain and the variation of the bandwidth with the applied local oscillator power.

REFERENCES

[1] E. M. Gershenzon, G. N. Gol'tsman, I. G. Goghidze, A. I. Elant'ev, B. S. Karasik and A. D. Semenov, "Millimeter and submillimeter

range mixer based on electronic heating of superconducting films in the resistive state," *Sov. Phys. Superconductivity*, vol. 3 (10), pp. 1582-1597, 1990.

[2] D. E. Prober, "Superconducting terahertz mixer using a transition-edge microbolometer," *Appl. Phys. Lett.*, vol. 62, No. 17, pp. 2119-2121, February 1993.

[3] A. D. Semenov, G. N. Gol'tsman and R. Sobolewski, "Hot-electron effect in superconductors and its application for radiation sensors," *Superconductor Science and Technology*, vol. 15(4), pp. R1-R16, April 2002.

[4] J. Zmuidzinas and P. L. Richards, "Superconducting detectors and mixers for millimeter and submillimeter astrophysics," *Proceedings of the IEEE*, vol. 92, No.10, pp. 1597-1616, October 2004.

[5] P. Yagoubov, M. Kroug, H. Merkel, E. Kollberg, J. Schubert, H.-W. Hübers, S. Svechnikov, B. Voronov, G. Gol'tsman, and Z. Wang, "Hot Electron Bolometric Mixers Based on NbN Films Deposited on MgO substrates", in *Proc. Europ. Conf. on Appl. Superconductivity*, Barcelona, 1999, pp. 687-690.

[6] S. Cherednichenko, M. Kroug, P. Khosropanah, A. Adam, H. Merkel, E. Kollberg, D. Loudkov, B. Voronov, G. Gol'tsman, H.-W. Hübers, H. Richter, "1.6 THz HEB mixer for far infrared space telescope (Herschel)," *Physica C*, vol.372-376, pp.427-431, August 2002.

[7] A. Semenov, H.-W. Hübers, H. Richter, M. Birk, M. Krocka, U. Mair, K. Smirnov, G. Gol'tsman, B. Voronov, "2.5 THz heterodyne receiver with NbN hot-electron bolometric mixer," *Physica C*, vol. 372-376, pp. 448-453, August 2002.

[8] G. Gol'tsman, M. Finkel, Y. Vachtomin, S. Antipov, V. Drakinski, N. Kaurova, B. Voronov, "Gain bandwidth and noise temperature of NbTiN HEB mixer," in *Proc. of the 14th Int. Symp. on Space Terahertz Technology*, Tucson AZ, 2003, pp. 276-285.

[9] S. Bedorf, P. Muñoz, T. Tils, C. E. Honing, and K. Jacobs, "Development of phonon-cooled NbTiN HEB heterodyne mixer for GREAT," in *Proc. of the 16th Int. Symp. on Space Terahertz Technology*, Gothenburg, 2005, pp. 276-285.

[10] N. Perrin and C. Vanneste, "Response of superconducting films to a periodic optical irradiation", *Phys. Rev. B*, vol. 28 (9), pp. 5150-5172, November 1983.

[11] B. S. Karasik and A. I. Elant'ev, "Analysis of the noise performance of a hot-electron superconducting bolometer mixer," *Appl. Phys. Lett.*, vol. 68, pp.853-855, February 1996.

[12] R. S. Nebosis, A. D. Semenov, Yu. P. Gousev and K. F. Renk, "Rigorous analysis of superconducting hot-electron bolometer mixer: theory and comparison with experiment," in *Proc. of the 7th Int. Symp. on Space Terahertz Technology*, Charlottesville, VA, 1996, pp. 601-613.

[13] D. Wilms Floet, E. Miedema, T. M. Klapwijk, J. R. Gao, "Hot-spot mixing: a framework for heterodyne mixing in superconducting hot-electron bolometers," *Applied Physics Letters*, vol. 74, No. 3, pp. 433-435, January 1999.

[14] A. Semenov and H.-W. Hübers, "Bandwidth of a hot-electron bolometer mixer according to the hot-spot model," *IEEE Transaction on Applied Superconductivity*, vol. 11, pp. 196-199, March 2001.

[15] H.-W. Hübers, S. G. Pavlov, A. D. Semenov, R. Köhler, L. Mahler, A. Tredicucci, H. E. Beere, D. A. Ritchie, E. H. Linfield, "Terahertz quantum cascade laser as local oscillator in a heterodyne receiver", *Optics Express*, vol. 13, No. 15, pp. 5890-5896, July 2005.

[16] S. Cherednichenko, P. Yagoubov, K. Il'in, G. Gol'tsman, and E. Gershenzon, "Large bandwidth of NbN phonon-cooled hot-electron bolometer mixers on sapphire substrates," in *Proc. of the 8th Int. Symp. on Space Terahertz Technology*, Cambridge, MA, 1997, pp. 245-257.

[17] K. D. Irwin, "An application of electrothermal feedback for high resolution cryogenic particle detectors," *Appl. Phys. Lett.*, vol. 66, pp. 1998-2000, April 1995.

[18] A. D. Semenov, R. S. Nebosis, Yu. P. Gousev, M. A. Heusinger, and K. F. Renk, "Analysis of the nonequilibrium photoresponse of superconducting films to pulsed radiation by use of a two-temperature model", *Phys. Rev. B* vol. 52(1), pp.581-590, July 1995.

[19] H. Merkel, P. Khosropanah, D. Wilms Floet, P. Yagoubov, and E. Kollberg, "Conversion gain and fluctuation noise of phonon cooled hot electron bolometer in hot spot regime," *IEEE Transactions MTT*, vol. 48, pp. 690-699, April 2000.

Optimal Coupling of NbN HEB THz Mixers to Cryogenic HEMT IF Low-Noise Amplifiers

Fernando Rodriguez-Morales, Sigfrid Yngvesson, Dazhen Gu, Eyal Gerecht,
Niklas Wadefalk, Ric Zannoni, and John Nicholson

Abstract— We are proposing a general approach to find the optimal coupling conditions between a NbN HEB mixer and its corresponding HEMT IF amplifier. We present our progress towards the development of suitable models for the analysis of the mixer/LNA sub-system in HEB terahertz down-converters. Our modeling approach takes into account parasitic reactances from the antenna and coplanar waveguide (CPW) structures, wire-bonds, the effect of the biasing networks, etc. We discuss the implementation of a lumped-element matching network designed based on the optimal matching considerations, which can in principle be integrated into an MMIC LNA. Finally, we suggest packaging schemes to further reduce the size of the integrated receivers in order to accommodate a larger number of pixels in a focal plane array.

Index Terms— HEB mixers, integrated terahertz receivers, MMIC low-noise amplifiers, HEB IF impedance.

I. INTRODUCTION

HOT ELECTRON BOLOMETRIC (HEB) mixer technology is gradually reaching maturity, and a wide range of new applications is presently emerging. The technical interest in HEB receiver systems is being shifted towards the development of imaging arrays for surveillance and biomedical applications [1], in addition to the more traditional radio-astronomy receivers. In such systems, it is essential that the HEB mixers are placed in close proximity with the intermediate frequency (IF) amplifiers, in order to realize a small size array while achieving the minimum inter-element spacing required for enhanced spatial resolution. The integration of HEB mixers with MMIC IF amplifiers has been addressed in previous papers by the authors [2], [3]. These receivers have demonstrated near-quantum limited noise performance (in the range of $10-20 \times hf/k$) and very wide effective IF bandwidths (up to 5 GHz).

In these detectors, the effective bandwidth is predominantly constrained by a non-trivial relationship between the mixer and the LNA. Modeling this interaction both accurately and rigorously has been a major challenge, particularly because presently available models for HEBs lack completeness [4], [5]. Furthermore, the noise parameters of the amplifier change as the IF output impedance of the phonon-cooled mixer varies for different operating conditions [6].

In order to better understand this mutual coupling and thereby optimize the performance of the integrated down-converters, it becomes necessary to develop suitable models

F. Rodriguez-Morales, K.S. Yngvesson, D. Gu, E. Gerecht, R. Zannoni, and J. Nicholson are with the University of Massachusetts at Amherst, Amherst, MA 01002 USA (e-mail: frodrigu@ecs.umass.edu); N. Wadefalk is with Chalmers University of Technology, SE-412 96, Göteborg, Sweden.

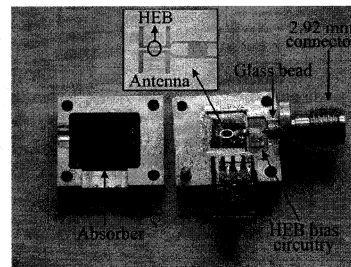


Fig. 1. Inside view of the fixture employed for HEB impedance characterization. The antenna shown in this picture corresponds to a twin-slot design (used for 750 GHz and 1.2 THz, respectively). A log-periodic antenna structure was used for 1.6 THz.

that will be useful in deriving optimum design guidelines for an HEB-HEMT system, as was done by Weinreb for the SIS-HEMT case [7]. This paper presents our progress towards the development of such models. We start by discussing methodologies to accurately determine the HEB IF output impedance for different dynamic conditions, using Automatic Network Analyzer (ANA) measurements. Next, we discuss different alternatives to accomplish the optimal coupling of the HEB mixer with the IF amplifier. Finally, we propose different packaging schemes in order to use the optimized receivers as the basis for compact arrays with denser element population.

II. IF SMALL SIGNAL IMPEDANCE MEASUREMENTS

We have obtained the small signal IF impedance Z of various receiver devices operating under different dynamic conditions. The magnitude and phase of the scattering parameter S_{11} have been measured under the presence of LO laser illumination and dc-bias, using an Agilent E5071B ANA. The measurements have been completed on three separate devices for three different LO frequencies: 750 GHz, 1.2 THz, and 1.6 THz. For the 750 GHz and 1.2 THz experiments we used twin-slot antennas integrated with $4 \mu\text{m} \times 5 \mu\text{m}$ HEB devices. The device under test (DUT) for 1.6 THz had dimensions $4 \mu\text{m} \times 6 \mu\text{m}$ and was integrated with a self-complementary log-periodic antenna. The IF range used was 300 kHz to 5 GHz, which covers the typical IF bandwidth for most phonon-cooled NbN HEB mixers. The measurements required an initial one-port short-open-load (SOL) calibration inside the cryostat, in contrast to the TRL calibration employed in [8]. The calibration was done by putting each of the standards into the dewar in three consecutive thermal cycles

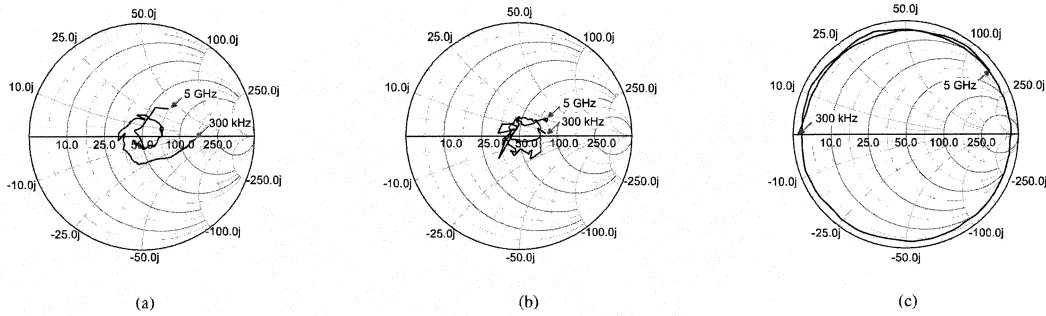


Fig. 2. Examples of Smith chart plots of the parameter S_{11} obtained for two different devices under different biasing (optimum) conditions: (a) 750 GHz LO for 0.5 mV, 39 μ A; (b) 1.6 THz LO for 0.5 mV, 46 μ A; and (c) superconducting short used as reflect standard for de-embedding.

and measuring the corresponding S_{11} using the ANA. The power level from the network analyzer was -48 dBm. The specimens were mounted on a special fixture (shown in Fig 1), which includes a broadband biasing circuit constructed from quartz wire-bondable resistors.

The stability properties of HEB devices change with different biasing networks [9] and the source impedance presented to the LNA is slightly affected by the parasitics introduced by this circuit. Therefore it is important to complete these measurements with the same biasing scheme as will be used in the actual receivers. The use of resistors with a high self-resonant frequency (SRF) facilitates removing the effect of the dc-network from the measurement via de-embedding, which is convenient for device modeling.

A. Raw Reflection Coefficient

Fig. 2 shows examples of Smith chart plots of the reflection coefficient for two of the measured devices, as obtained with the network analyzer. These are the actual source impedances seen by the low-noise amplifier at the given operating points, including parasitic reactances in the circuit derived from the antenna structure, wire-bonds, transmission line transitions, etc. Though the HEB impedance determines the main contribution to the total input reflection coefficient of the LNA, parasitic reactances in the circuit should not be neglected when designing the appropriate input matching network for minimum noise.

B. HEB Impedance De-Embedding

The HEB IF small signal was carefully de-embedded from the measured reflection coefficient (S_{11}). The preceding SOL cryogenic calibration was used in combination with the S-parameters of two measured known loads (superconducting and normal state of the bolometer, respectively) to obtain a circuit model for the fixture parasitics. Computer simulations were then used to predict the response of an open circuit in place of the HEB device. A one-port error model was then obtained by means of the above new "standards". The error model accounts for the directivity error e_{00} , the source match error e_{11} , as well as the reflection tracking error (e_{10} e_{01}). Using these error terms, the HEB IF small signal impedance

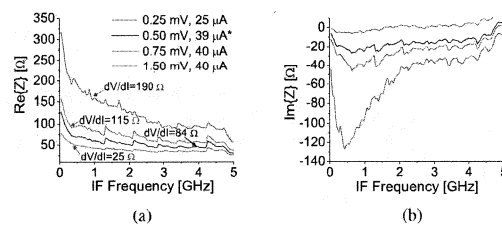


Fig. 3. De-embedded impedance for an HEB receiver device operating at 750 GHz: (a) Real part, and (b) Imaginary part.

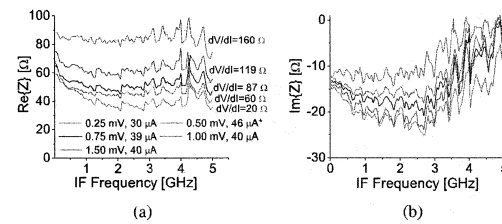


Fig. 4. De-embedded impedance for an HEB receiver device operating at 1.6 THz: (a) Real part, and (b) Imaginary part.

can be accurately extracted from the microwave reflection measurements. Fig. 3 and Fig. 4 show the de-embedded results for two of the measured devices. The * symbol indicates the optimum conditions for minimum receiver noise, which were found after subsequent noise measurements were performed on these devices.

C. Discussion

There is a strong correlation between the numerical value of the dynamic differential resistance obtained from the dc IV curves, dV/dI , and the real part of the impedance, $\text{Re}\{Z\}$. This holds true specially for IF frequencies between 1 to 5 GHz, where the impedance is also dominated by its real part. As expected, the reactive part of Z is purely capacitive over the entire frequency range.

The corresponding dV/dI for different operating points appears in Tables I and II. These tables also include a summary

TABLE I
SUMMARIZED RESULTS FOR Z AND dV/dI AT 750 GHz.

Operating Point	$\text{Re}\{Z\}$ [Ohms] 1GHz/4GHz	$\text{Im}\{Z\}$ [Ohms] 1GHz/4GHz	dV/dI [Ohms]
0.25 mV, 25 μA	42/35	-4/0	24
0.50 mV, 39 μA^*	60/42	-23/-11	84
0.75 mV, 40 μA	85/58	-39/-18	114
1.50 mV, 40 μA	158/95	-93/-31	190

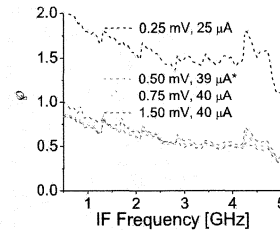
TABLE II
SUMMARIZED RESULTS FOR Z AND dV/dI AT 1.6 THz.

Operating Point	$\text{Re}\{Z\}$ [Ohms] 1GHz/4GHz	$\text{Im}\{Z\}$ [Ohms] 1GHz/4GHz	dV/dI [Ohms]
0.25 mV, 30 μA	42/42	-22/-11.0	16
0.50 mV, 46 μA^*	46/52	-19/-10.4	60
0.75 mV, 39 μA	50/58	-17/-4.5	88
1.00 mV, 40 μA	61/76	-15/-2.8	119
1.50 mV, 45 μA	82/95	-12/-1.5	160

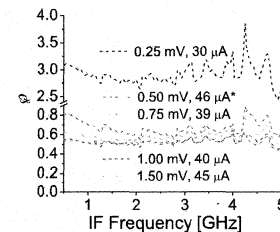
of the results presented previously in Figs. 3 and 4. Fig. 5 displays the ratio between $\text{Re}\{Z\}$ and dV/dI (φ) throughout the important IF range, which has been calculated to emphasize the above correlation. This ratio remains in the order of 0.5–0.8 for biasing points near the optimum. For the 750 GHz device the measurements are in fair qualitative agreement with the so-called *standard model* (uniform bolometer heating) [8], [10], while being substantially different for 1.2 THz (not shown) and 1.6 THz. It is noteworthy that 750 GHz is below the bandgap frequency of the superconductor, which may partly explain this discrepancy. More measurements need to be performed at 1.0 THz and above in order to resolve the deviation of these results from the standard model and to better understand the dependency of Z with respect to frequency, biasing conditions, and device parameters. To date, we have developed the capability for accurately determining the reflection coefficient seen by the IF amplifier as well as the contribution of the HEB IF output impedance alone.

III. HEB-LNA COUPLING

In order to realize the best trade-off between low-noise figure and wide bandwidth, the coupling between the HEB mixer output and the HEMT LNA input needs to be studied. This analysis evidently requires the knowledge of the impedance presented by the HEB and surrounding circuitry, which was the center of our discussion in the previous Section. Once this source impedance is known through either modeling or measurements, an appropriate input matching network (IMN) can be designed to transform the HEB IF output impedance into the intended optimum source impedance Z_{opt} required by the LNA (Fig. 6). Since the input impedance of a HEMT-based amplifier is mainly dominated by the gate-to-source capacitive reactance of the first transistor stage, the IMN should behave as a series inductor. Such IMN has already been successfully implemented by our group in the form of a multi-section microstrip transformer but other alternatives are being



(a)



(b)

Fig. 5. Ratio between the real part of Z and the differential dynamic resistance for different operating points for: (a) 750 GHz LO; (b) 1.6 THz LO. For the 750 GHz LO and low IF frequencies φ is nearly unity, in agreement with the standard model.

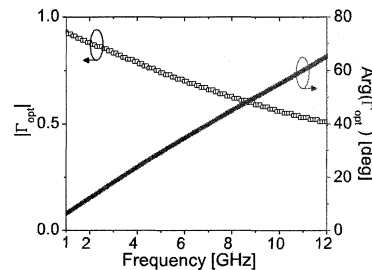


Fig. 6. Simulated optimum input reflection coefficient Γ_{opt} for our previously developed MMIC LNA (without any matching network).

investigated. The use of a lumped-element matching network or wire-bonds as inductive elements as proposed in [11] (Fig. 7), will help further reduce the size of the HEB down-converter while maintaining the low-noise characteristics.

IV. NEW ARRAY PACKAGING SCHEMES

Our group has previously demonstrated the first heterodyne focal plane array receiver unit designed for operation at terahertz frequencies. This FPA module uses integrated receiver elements arranged in a fly's eye configuration [2]. The number of elements in such array can be augmented straightforwardly up to $2 \times n$. Nevertheless, for a larger FPA this approach would lack adequate space for complete IF and DC-bias circuits and will present potential difficulties in thermal power dissipation. To overcome these problems, future extensions to our work include investigating alternative packaging schemes

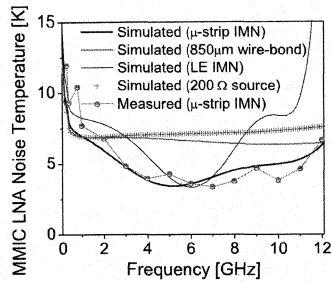


Fig. 7. Noise performance variation of our previously developed MMIC LNA IF amplifier for different input matching circuits. The + symbol corresponds to an hypothetical case in which the HEB IF impedance is purely real and equal to 200 Ω .

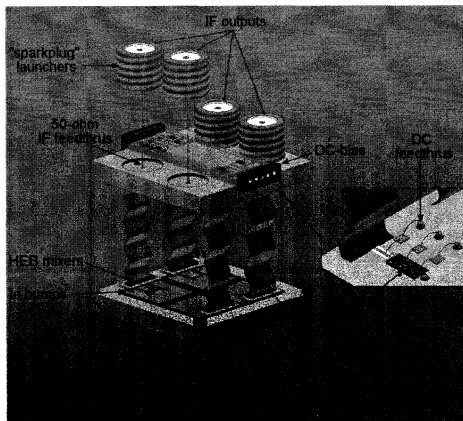


Fig. 8. The proposed configuration for the prototype 2 x 2 element terahertz heterodyne focal plane array; (inset) Placement of IF MMIC LNAs.

to integrate all the receiver elements more compactly, using a three-dimensional configuration. An illustration of one such prototype FPA is presented in Fig. 8.

An important feature of this layout is the incorporation of polyimide (Kapton) ribbons with CPW transmission lines designed to carry the IF and dc-biasing signals. These Kapton lines minimize the thermal conduction from the HEB board (which is at 4 K) to the IF board in Fig. 8. The IF board containing the MMIC LNAs can be cooled to a higher temperature (15 K to 20 K) without affecting the noise performance of the chips. We have started investigating the properties of the flexible CPWs in order to achieve highly integrated FPAs. As a first step we have performed full electromagnetic analysis of the response of a CPW transformer fabricated on flexible substrate ($\epsilon_r=3.5$). The circuit has been designed as the IMN for our previously developed MMIC LNA. The simulations include the effect of the wire bonds used to contact the HEB and LNA chips at either end of the transformer. The performance of this transformer is comparable with that of the microstrip implementation over the entire band of interest.

V. CONCLUSION

Highly integrated receiver modules with high functionality can be very attractive for imaging and other terahertz applications. We are addressing the modeling of the optimal coupling between HEB mixers integrated with HEMT IF amplifiers.

As a first step, we have developed de-embedding routines to obtain the HEB small signal impedance as a function of IF frequency and under various operating conditions. We have discussed the correlation between the real part of the impedance and the dynamic resistance of the mixer. We have also been able to accurately determine the source impedance presented to the LNA by the HEB chip and surrounding circuitry. We have proposed various alternatives for an optimal input matching circuit for the LNA, which can be integrated into the amplifier itself. Lastly, we have started the investigation of new packaging schemes for array receivers. These new schemes include the development of highly integrated modules connected in a three-dimensional configuration using Kapton CPW lines. These HEB down-converters will be the basis of large FPAs for the next-generation terahertz imagers.

ACKNOWLEDGMENT

We would like to thank Dr. S. Weinreb for kindly supplying the MMIC chips used in our integrated receivers.

REFERENCES

- [1] D. Gu, E. Gerecht, F. Rodriguez-Morales, and S. Yngvesson, "A Two Dimensional Terahertz Imaging System Using Hot Electron Bolometer Technology," this symposium.
- [2] F. Rodriguez-Morales, K. S. Yngvesson, E. Gerecht, N. Wadefalk, J. Nicholson, D. Gu, X. Zhao, T. Goyette, and J. Waldman, "A Terahertz Focal Plane Array Using HEB Superconducting Mixers and MMIC IF Amplifiers," *IEEE Microw. Wireless Comp. Lett.*, vol. 15, no. 4, pp. 199–201, Apr. 2005.
- [3] F. Rodriguez-Morales, S. Yngvesson, R. Zannoni, E. Gerecht, D. Gu, N. Wadefalk, and J. Nicholson, "Development of Integrated HEB/MMIC Receivers for Near-Range Terahertz Imaging," *IEEE Trans. Microw. Theory Tech.*, vol. 54, no. 6, Jun. 2006.
- [4] H. Ekstroem, B. Karasik, E. Kollberg, and S. Yngvesson, "Conversion Gain and Noise of Niobium Superconducting Hot-Electron Mixers," *IEEE Trans. Microw. Theory Tech.*, vol. 43, no. 4, pp. 938–947, Apr. 1995.
- [5] H. Merkel, P. Khosropanah, P. Yagoubov, and E. Kollberg, "A Hot-Spot Mixer Model for Phonon-Cooled NbN Hot Electron Bolometric Mixers," *IEEE Trans. on Appl. Superconduct.*, vol. 9, no. 2, pp. 4201–4204, Jun. 1999.
- [6] R. Hu and S. Weinreb, "A Novel Wide-Band Noise Parameter Measurement Method and its Cryogenic Application," *IEEE Trans. Microw. Theory Tech.*, vol. 52, no. 5, pp. 1498–1507, May 2004.
- [7] S. Weinreb, "SIS Mixer to HEMT Amplifier Optimum Coupling Network," *IEEE Trans. Microw. Theory Tech.*, vol. 35, no. 11, pp. 1067–1069, Nov. 1987.
- [8] F. Rodriguez-Morales and K. S. Yngvesson, "Impedance and Bandwidth Characterization of NbN Hot Electron Bolometric Mixers," in *Proc. 14th Int. Symp. Space Terahertz Tech.*, Tucson, Az, Apr. 2003, pp. 431–438.
- [9] Y. Zhuang, "Linear and Nonlinear Characteristics of NbN Hot Electron Bolometer Devices," Ph.D. dissertation, University of Massachusetts Amherst, USA, 2002.
- [10] J. Kooi, J. J. A. Baselmans, J. R. Gao, T. M. Klapwijk, M. Hajenius, P. Dieleman, A. Baryshev, and G. de Lange, "IF Impedance and Mixer Gain of Hot Electron Bolometers and the Perrin-Vanneste Two Temperature Model," this symposium.
- [11] F. Rodriguez-Morales, E. Gerecht, D. Gu, R. Zannoni, S. Yngvesson, N. Wadefalk, and J. Nicholson, "Performance Improvement of Integrated HEB-MMIC Receivers for Multi-Pixel Terahertz Focal Plane Arrays," in *Proc. 16th Int. Symp. Space Terahertz Tech.*, Goteborg, Sweden, May 2005, pp. 246–250.

Influence of the direct response on the heterodyne sensitivity of hot electron bolometer mixers

J.J.A. Baselmans, A. Baryshev, M. Hajenius, J.R. Gao, T.M. Klapwijk, B. Voronov, and G. Gol'tsman

We present a detailed experimental study of the direct detection effect in a small volume ($0.15\mu\text{m} \times 1\mu\text{m}$) NbN hot electron bolometer mixer. It is a quasioptical mixer with a twin slot antenna designed for 700 GHz and the measurement was done at a LO frequency of 670 GHz. The direct detection effect is characterized by a change in the mixer bias current when switching broadband radiation from a 300 K hot load to a 77 K cold load in a standard Y factor measurement. The result is, depending on the receiver under study, an increase or decrease in the receiver noise temperature. We find that the small signal noise temperature, which is the noise temperature that would be observed without the presence of the direct detection effect, and thus the one that is relevant for an astronomical observation, is 20% lower than the noise temperature obtained using 300 K and 77 K calibration loads. Thus, in our case the direct detection effect reduces the mixer sensitivity. These results are in good agreement with previous measurement at THz frequencies [1]. Other experiments report an increase in mixer sensitivity [2]. To analyze this discrepancy we have designed a separate set of experiments to find out the physical origin of the direct detection effect. Possible candidates are the bias current dependence of the mixer gain and the bias current dependence of the IF match. We measured directly the change in mixer IF match and receiver gain due to the direct detection effect. From these measurements we conclude that the direct detection effect is caused by a combination of bias current reduction when switching from the 77 K to the 300 K load in combination with the bias current dependence of the receiver gain. The bias current dependence of the receiver gain is shown to be mainly caused by the current dependence of the mixer gain. We also find that an increase in receiver sensitivity due to the direct detection effect is only possible if the noise temperature change due to the direct detection is dominated by the mixer-amplifier IF match.

[1] J.J.A. Baselmans, A. Baryshev, S.F. Reker, M. Hajenius, J.R. Gao, T.M. Klapwijk, Yu.Vachtomin, S. Maslennikov, S. Antipov, B. Voronov, and G. Gol'tsman., *Appl. Phys. Lett.* **86**, 163503 (2005).

[2] S. Svechnokov, A. Verevkin, B. Voronov, E. Menschikov. E. Gershenson, G. Gol'tsman, 9th Int. Symp. On Space THz. Techn., 45, (1999).

Quantum Noise in Resistive Mixers

Harald F. Merkel, Biddut K. Banik ^a

^aChalmers University of Technology

ABSTRACT

Release E : Derivation of the quantum noise of a mixer using second order quantization methods

Keywords: quantum noise

1. QUANTUM THEORY OF DIRECT DETECTION

In order to establish some necessary relations, let us consider first a quantum physical approach to direct detection. There the receiver (i.e. a diode) generates a certain amount of photoelectrons per incident detected photon. The quantum efficiency η is assumed unity in the following sections. The detection of the incident radiation is equivalent to the counting operator of the incident photons. The charge operator \hat{Q} governing the photon absorption and ideal photoelectron generation in a diode is given by the scalar product of a field operator \hat{A} with its hermitian applied to any initial and final quantum state α . This scalar product yields the number of photoelectrons when multiplying the scalar product with the carrier charge q .

$$\hat{Q} = q\hat{A}^\dagger \hat{A} \quad (1)$$

Then the net charge $\langle \hat{Q} \rangle$ absorbed in the diode during a coherent state α becomes:

$$\langle \hat{Q} \rangle := \langle \alpha | \hat{Q} | \alpha \rangle = q \langle \alpha | \hat{A}^\dagger \hat{A} | \alpha \rangle = q |\alpha|^2 = q \langle n \rangle \quad (2)$$

Applying the commutator on the numbering operator, we can calculate the second order moment after sorting the operators in creators and destructors as follows:

$$\langle \hat{Q}^2 \rangle := \langle \alpha | \hat{Q}^2 | \alpha \rangle = q^2 \langle \alpha | \hat{A}^\dagger \hat{A} \hat{A}^\dagger \hat{A} | \alpha \rangle = q^2 |\alpha|^4 + q^2 |\alpha|^2 = q^2 \langle n \rangle^2 + q^2 \langle n \rangle \quad (3)$$

$$\langle \hat{Q}^2 \rangle - \langle \hat{Q} \rangle^2 = q^2 \langle n \rangle \quad (4)$$

It is important to note that the squared variance of the charge absorbed in the diode is equal to the number density indicating that the photon and the subsequent electron flow is completely uncorrelated. As a consequence there is a one-to-one correspondence between the photon flux and the flux of the generated photoelectrons. As we will see later, this is the major difference between a diode and a bolometric receiver where the photons "integrate up" and create a hot spot. This causes the variance to be only half a RF quantum in the limit of an infinitely slow bolometer whereas the mean value is obtained in the same way as for the diode.

Chalmers University of Technology, MC2, Kemigården 9, SE 412 96 Göteborg, Sweden

2. COHERENT QUANTUM LIMITED HETERODYNE DETECTION

Superimposing a Local Oscillator and a Radio Frequency Signal one arrives at a field in front of the mixer as:

$$\hat{B} = \hat{A}_{LO} + \hat{A}_{RF}; \hat{A}_{LO(RF)} = \alpha_{LO(RF)} e^{i\omega_{LO(RF)} \cdot t} \quad (5)$$

For an non-balanced heterodyne detection, the charge generated in a detector is similar to 1 for a small RF signal compared to the LO:

$$\hat{Q} = q \cdot \hat{B}^\dagger \hat{B} = q \cdot (\hat{A}_{LO} + \hat{A}_{RF})^\dagger \cdot (\hat{A}_{LO} + \hat{A}_{RF}) \approx q \cdot (\hat{A}_{LO}^\dagger \hat{A}_{LO} + \hat{A}_{RF}^\dagger \hat{A}_{LO} + \hat{A}_{LO}^\dagger \hat{A}_{RF}) \quad (6)$$

The mean value of the photons observed by the detector is thus:

$$\langle Q \rangle = 2|\alpha_{LO}\alpha_{RF}| \cos((\omega_{RF} - \omega_{LO})t) + |\alpha_{LO}|^2 + |\alpha_{RF}|^2 \quad (7)$$

On our way to calculate the quantum noise of the detector, we have to evaluate the second moment of the distribution too. It is given by the following relation in much of same way as in 3:

$$\langle Q^2 \rangle = \langle \alpha_{LO} | \langle \alpha_{RF} | Q Q | \alpha_{RF} \rangle | \alpha_{LO} \rangle \quad (8)$$

In addition we need:

$$\langle Q \rangle^2 = \begin{aligned} & 4|\alpha_{LO}\alpha_{RF}|^2 \cos^2((\omega_{RF} - \omega_{LO})t)^2 + \dots \\ & \dots + 4|\alpha_{LO}|^3 |\alpha_{RF}| \cos((\omega_{RF} - \omega_{LO})t) + \dots \\ & \dots + 4|\alpha_{LO}| |\alpha_{RF}|^3 \cos((\omega_{RF} - \omega_{LO})t) + 2|\alpha_{LO}\alpha_{RF}|^2 + \dots \\ & \dots + |\alpha_{LO}|^4 + |\alpha_{RF}|^4 \end{aligned} \quad (9)$$

In time average, the squared mean value becomes:

$$\int_{t=0}^T \langle Q \rangle^2 dt = 4|\alpha_{LO}\alpha_{RF}|^2 + |\alpha_{LO}|^4 + |\alpha_{RF}|^4 \quad (10)$$

Taking only the signal part into account one arrives at:

$$\int_{t=0}^T \langle S \rangle^2 dt = 4|\alpha_{LO}\alpha_{RF}|^2 + |\alpha_{RF}|^4 \quad (11)$$

Now we are able to calculate the variance of the distribution as:

$$\langle Q \rangle = 2|\alpha_{LO}\alpha_{RF}| \cos((\omega_{RF} - \omega_{LO})t) + |\alpha_{LO}|^2 + |\alpha_{RF}|^2 \quad (12)$$

$$+2(|\alpha_{LO}|^2 + |\alpha_{RF}|^2) < \langle Q^2 \rangle - \langle Q \rangle^2 < +2(|\alpha_{LO}| + |\alpha_{RF}|)^2 \quad (13)$$

From this the signal-to-noise ratio is at first glance obtained as:

$$\frac{\langle Q \rangle^2}{\langle Q^2 \rangle - \langle Q \rangle^2} = \frac{4|\alpha_{LO}\alpha_{RF}|^2 + |\alpha_{LO}|^4 + |\alpha_{RF}|^4}{+2|\alpha_{LO}|^2 + 4|\alpha_{LO}\alpha_{RF}| + 2|\alpha_{RF}|^2} \approx \frac{1}{2} |\alpha_{LO}|^2 \quad (14)$$

Nevertheless, one has to exclude the LO fluctuations from the signal term. A more correct relation is then obtained as:

$$\frac{\langle S \rangle^2}{\langle Q^2 \rangle - \langle Q \rangle^2} = \frac{4|\alpha_{LO}\alpha_{RF}|^2 + |\alpha_{RF}|^4}{+2|\alpha_{LO}|^2 + 4|\alpha_{LO}\alpha_{RF}| + 2|\alpha_{RF}|^2} \approx |\alpha_{RF}|^2 \quad (15)$$

This is a result identical to the derivation in Haus given for a balanced diode mixer.

3. SOLVING THE QUANTUM NOISE FOR ARBITRARY DISTRIBUTED PHOTON PROBABILITY DENSITIES

In the general case it is not acceptable to approximate the photon number density probability function by a simple Poisson distribution. There general relations must be derived based on only a single assumption - the expectation value of the photon counting process yields μ photons. As in the Poisson case, this value is broken down in an integer part n and a fractional part less than unity q . Then the probability density to measure exactly m photons becomes:

$$p_m^S = (1-q) \int_{n \rightarrow -\infty}^{+\infty} p(m-n) dm + q \int_{n \rightarrow -\infty}^{+\infty} p(m-(n+1)) dm \quad (16)$$

using the Kronecker delta δ_x . Calculating the expectation value of this distribution yields μ as shown by inspection, for the variance one obtains:

$$D_\phi^2 = \sum_{m=0}^{\infty} (m - \mu)^2 \cdot p_m = \sqrt{q(1-q)} \quad (17)$$

Obviously $\sqrt{q(1-q)}$ indicates the "average measurement error" associated with a measurement on the quantum mechanical system. This error is not dependent on the number of photons measured. It is as a quantization noise in Analog Digital Converters simply related to the value of the least significant bit of the conversion.

From a noise point of view, one has to calculate the maximum value of this variance. The maximum error is thus obtained when the time averaged photon number is exactly a half away from the next integer. Therefore the maximum variance is:

$$\frac{dD_\phi^2}{d\mu} = 1 - 2q = 0 \rightarrow D_{\phi,max}^2 = \frac{1}{2} \left(1 - \frac{1}{2}\right) = \frac{1}{4} \quad (18)$$

This corresponds to the well-known half quantum noise from Literature. Now we have to invoke ergodicity stating that all statistical moments obtained on a set of measurements on a set of identical quantum system performed at a time point are identical to the time average of measurements performed on a single quantum system within a time interval. Then we are allowed to state the following

A field problem involving a certain photon flow per time unit $\frac{\mu}{\Delta t}$ will show a power flow and its maximum variance given by :

$$P_{RF} = \frac{\mu}{\Delta t} h\nu_{RF}; D_{\phi,max} = \frac{1}{\Delta t} \frac{1}{2} h\nu_{RF} \quad (19)$$

Assuming that the radiation is time correlated with a time being larger than the inverse RF bandwidth of the system $\tau_{corr} > \frac{1}{B}$. Then, the band limited power density involves a correlated photon flow and its variance as given by :

$$P_{RF,B} = \mu h\nu_{RF} B = \langle P \rangle; D_{\phi,max,B} = \frac{1}{2} h\nu_{RF} B = p \quad (20)$$

4. A HEB HEATED BY RF BAND LIMITED ELECTROMAGNETIC RADIATION

Applying the above radiation $\langle P \rangle$ to a resistor results in photon absorption in the resistor therefore diminishing the power flow to subsequent parts in the circuit. Nevertheless the variance p is not affected by this absorption since the variance does not depend on the number of photons involved with the flow. This situation becomes inherently different as soon as this resistor becomes nonlinear (by e.g. heating). Applying two sources of radiation, a strong LO given by $\langle P_{LO} \rangle$ and a weak signal source $\langle P_{RF} \rangle$ to a bolometer results in photon absorption. Using a simple heating model for a bolometer one obtains after suppressing the small second order terms:

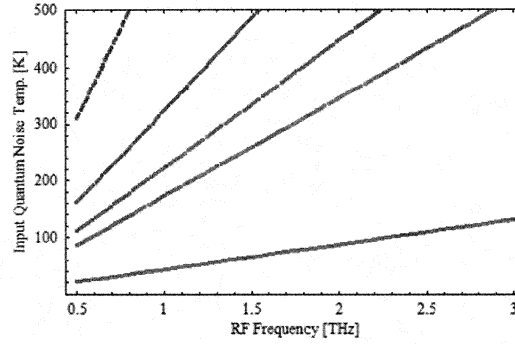


Figure 1. DSB Input Quantum Noise as a function of the RF frequency in the operating point.

$$R(P) = R(\langle P_{LO} + P_{RF} \rangle) + C_{RF} \cdot (\langle P_{LO} \rangle \cdot p_{RF} + \langle P_{RF} \rangle \cdot p_{LO}) + C_{DC} P_{DC} = R_0 + C_{RF} \cdot (\langle P_{LO} \rangle \cdot \frac{1}{2} h \nu_{RF} B) + C_{DC} P_{DC} \quad (21)$$

This is the way how quantum noise is downconverted in a bolometer. Thus quantum noise follows the thermal fluctuation noise mechanism and becomes later on band-limited within the IF bandwidth of the system. It does therefore not deteriorate the noise bandwidth of the system.

Blackbody radiation is caused by a superposition of quantized hollow modes created in a body at a given physical temperature. The time average of the radiation e.g. emitted by the warm optics in front of the receiver (determined by optics losses L_{optics} and the optics temperature T_{optics}) is given by Planck's radiation law found in literature [e.g. Laloć- Tannoudji La mécanique quantique p.280]:

$$\langle P_{Planck, optics} \rangle = L_{optics} \frac{h \nu_{RF} B}{e^{\frac{h \nu_{RF}}{k_B T_{optics}}} - 1} \quad (22)$$

In the next step we search for an equivalent thermal noise source at the input to generate the same resistance fluctuation as in 21. This equivalent source is attenuated by optical losses and acts on the whole HEB. In first order, only the fraction heating the hot spot region is able to cause a resistance fluctuation.

$$L_{optics} \cdot \frac{R_0}{R_N} \cdot \frac{h \nu_{RF} B}{e^{\frac{h \nu_{RF}}{k_B T_{QN}}} - 1} \approx \frac{1}{2} h \nu_{RF} B \quad (23)$$

Therefore the equivalent noise temperature due to quantum noise becomes:

$$T_{QN} \approx \frac{h \nu}{k \log(1 + 2 \cdot (1 - L_{optics}) \cdot \frac{R_0}{R_n})} \quad (24)$$

Please observe that the quantum noise has the same IF bandwidth limitation as the conversion gain. It does therefore not decrease the noise bandwidth of the HEB receiver. The quantum noise occurs at the point where the frequency conversion takes place. Quantum noise is therefore not subject to any optical losses. The "graininess" of the incoming signal is preserved by any losses in front of the bolometer. Referring to output noise powers this is directly obvious. Nevertheless following engineering traditions, noise contributions are usually considered as equivalent input noise temperatures. Consequently the quantum noise at the input increases with increasing optical losses. At frequencies above 2THz, quantum noise dominates the receiver noise.

Physics of ultra-thin NbN films for phonon-cooled Hot-Electron-Bolometers

T. Scherer, M. Schicke and K.-F. Schuster

IRAM, Institut de Radioastronomie Millimetrique, 38406 St Martin d'Herès, France

We present an in depth study of the influence of growth conditions and substrate materials for ultra-thin NbN films as used for phonon-cooled hot electron bolometer (HEB) mixers. The electrical characteristics of the films are compared in with results from synchrotron X-ray and Raman scattering as well as from Spectro-Ellipsometrie. Measurements on device performance like IF-BW and mixer noise are correlated with the various film characteristics and conclusions are drawn on the importance of various mechanisms involved in the phonon-cooling path of the HEB device.

**FABRICATION AND CHARACTERIZATION OF ULTRATHIN
PBCO/YBCO/PBCO CONSTRICTIONS FOR FURTHER APPLICATION AS
HOT ELECTRON BOLOMETER TERAHERTZ MIXERS**

*A. J. Kreisler¹, A. F. Dégardin¹
Ch. Peroz^{1,2}, J-C. Villégier²
M. Chaubet³*

¹ Laboratoire de génie électrique des universités Paris 6 et Paris 11 (LGEP), UMR 8507 CNRS-Supelec, GIF SUR YVETTE, France

² Laboratoire de cryophysique, CEA-Grenoble, France

³ Centre national d'études spatiales (CNES), Toulouse, France

Superconducting Hot Electron Bolometer (HEB) mixers are a competitive alternative to Schottky diode mixers or other conventional superconducting receiver technologies in the terahertz frequency range because of their ultra wide bandwidth (from millimeter waves to the visible), high conversion gain, and low intrinsic noise level, even at 77 K.

A technological process has been successfully developed for fabricating stacked $\text{YBa}_2\text{Cu}_3\text{O}_{7-x}$ (YBCO) and $\text{PrBa}_2\text{Cu}_3\text{O}_{7-y}$ (PBCO) ultra-thin films (in the 15 to 40 nm thickness range) on a configuration of constrictions (in the 0.8 to 0.45 μm^2 range), elaborated on MgO (100) substrates by hollow cathode magnetron sputtering. A combination of electronic and UV lithography steps followed by selective etching techniques were used to realize HEB mixers based on these constrictions covered by a planar gold antenna of the log-periodic type, aiming at covering the 1 millimeter to 30 micrometer wavelength range.

High values of critical temperature in the 85 to 91 K range, as well as critical current densities reaching $2 \cdot 10^7 \text{ A/cm}^2$ at 77 K were measured (electrical transport); the temperature coefficient value of the resistance was 0.4-0.5 per kelvin. These characteristics were stable upon ageing, thermal cycling and after the gold antenna fabrication step.

Further characterization steps concern the device bolometric response in the direct detection mode at 850 nm wavelength up to 1 GHz modulation frequency. They also concern the device response in the heterodyne detection mode at 2.5 THz, using two gas laser sources.

Study undertaken with CNES support, under contract # 2002/0440/00

Corresponding author : Alain.Kreisler@supelec.fr

The Band 3 and 4 Flight Model mixer units for HIFI

**G. de Lange, B.D. Jackson, M. Eggen, H. Golstein, W.M. Laauwen, L. de Jong,
S. Kikken, C. Pieters, H. Smit, and D. Van Nguyen**
SRON National Institute for Space Research
Postbus 800, 9700 AV Groningen, The Netherlands

T. Zijlstra, M. Kroug, and T.M. Klapwijk
Department of Applied Physics (DIMES), Delft University of Technology
Lorentzweg 1, 2628 CJ Delft, The Netherlands

The Heterodyne Instrument for the Far-Infrared (HIFI) is in its final stage of assembly. It will cover the 0.48-1.9 THz frequency range. This frequency range is divided into 7 bands. SRON is developing the band 3 and 4 SIS waveguide mixer units. Band 3 and 4 cover the 800-960 GHz and 960-1120 GHz frequency range, respectively. Each of these bands contains two mixers for dual polarization measurements. The mixers have a corrugated horn antenna and operate with a 4-8 GHz IF bandwidth. Nb/AlO_x/Nb SIS tunnel junctions with NbTiN/Al wiring layers are used as mixing element. Besides the heterodyne functionality, the units also incorporate a superconducting magnet, an internal ESD/EMC protection circuit, a 4-8 GHz bias T, and a de-flux heater.

The mechanical and optical design is to a large extent driven by the specific environmental requirements for a space mission, the mass and thermal budget, and the electrical and optical interfaces with the rest of the instrument.

In the paper we discuss the design and performance of the Flight Model mixer units. The DSB receiver noise temperature as measured in the laboratory (with warm optics) vary from 220-315 K in the band 3 frequency range and 330-600 K in band 4. With the cold HIFI optics and the absence of atmospheric losses, the noise temperature will drop to 150-250 K and 250-350 K for band 3 and 4, respectively.

Design and development of a 600-720 GHz receiver for ALMA Band 9

A.M. Baryshev, R. Hesper, F.P. Mena, B.D. Jackson, J. Adema, H. Schaeffer,
J. Barkhof and W. Wild

SRON National Institute for Space Research and the Kapteyn Institute, University of
Groningen, Landleven 12, 9747 AD Groningen, The Netherlands

M. Candotti

National University of Ireland, Maynooth, Co. Kildare, (Ireland)

C. Lodewijk, D. Loudkov, T. Zijlstra, O. Noroozian, and T.M. Klapwijk
Kavli Institute for Nanoscience, Faculty of Applied Science, Delft University of
Technology, Lorentzweg 1, 2628 CJ Delft, The Netherlands

Abstract

This paper describes the design and development of the ALMA Band 9 receiver cartridges. The ALMA project is a collaboration between Europe, North America, and Japan to build an aperture synthesis telescope consisting of at least 64 12-m antennas located at 5000 m altitude in Chile. In its full configuration, ALMA will observe in 10 frequency bands between 30 and 950 GHz, and will provide astronomers with unprecedented sensitivity and spatial resolution at millimetre and sub-millimetre wavelengths. Band 9, covering 600-720 GHz, is the highest frequency band in the baseline ALMA project, and will thus offer the telescope's highest spatial resolutions.

The ALMA Band 9 cartridge is a compact unit containing the core of a 600-720 GHz heterodyne receiver front-end that can be easily inserted into and removed from the ALMA cryostat. In particular, its core technologies include low-noise, broadband SIS mixers; an electronically-tunable solid-state local oscillator; and low-noise cryogenic IF amplifiers. These components are built into a rigid opto-mechanical structure that includes a compact optical assembly mounted on the cartridge's 4 K stage that combines the astronomical and local oscillator signals and focuses them into two SIS mixers.

In this report we present the noise measurement with an emphasis on the extreme large IF bandwidth (4-12 GHz). IF- gain slope, receiver linearity/saturation, receiver beam pattern and cross polarization level measurements will be presented and compared with expectations. The receiver phase and amplitude stability measurements will be presented and the system aspects related to interferometer will be discussed. Finally, a detailed measurement of LO noise contribution will be presented. This measurement was done by comparing receiver noise measured with internal ALMA LO (multipliers power amplifiers combination) to receiver noise measured by means of Gunn diode, followed by a x2x3 multiplier.

Development of Balanced SIS Mixers for ALMA Band-10

Sergey V. Shitov, Oleg V. Koryukin, Yoshinori Uzawa, Takashi Noguchi,
Andrey V. Uvarov, Ilya A. Cohn

Abstract—A few concepts of a wide-band balanced SIS mixer employing submicron-sized SIS junctions are under development for 787-950 GHz frequency range. A quasioptical DSB balanced mixer with integrated cross-slot antenna is considered as the less laborious and cheaper option. The silicon lens-antenna beam efficiency is expected above 80 % across the whole band with first-order sidelobe below -16 dB.

To use the conservative horn antenna solution, a single-chamber waveguide DSB balanced mixer is developed. Two equal probe-type SIS chips are inserted into a full-height waveguide through its opposite broad walls; these two mixers are driven by the signal waveguide in series. The LO current is transferred to the mixers in parallel via a capacitive probe inserted through the narrow wall of the signal waveguide from the neighboring LO waveguide. The HFSS model demonstrated the LO power coupling efficiency above -3 dB, almost perfect signal transfer and the LO cross talk below -30 dB that take into account misalignment (misbalance) of the chips.

It is demonstrated numerically using Tucker's 3-port model that unequal pump of junctions of a twin-SIS mixer can lead, in spite of the perfect signal coupling, to degradation of the gain performance up to -3 dB, especially at the top of the ALMA Band-10.

Index Terms—SIS mixer, balanced mixer, lens antenna.

I. INTRODUCTION

The LO power required for a THz-band SIS mixer can be below 1 μ W. However, the simple LO coupling circuit, which uses a thin-film beam splitter, wastes usually more than 90% of the available LO power into a termination load. The commercially available wide-band tunerless LO sources [1] can presently provide only few microwatts in the THz range. To reduce the LO power requirements, a balanced mixer is that possible solution. One may estimate the figure

Manuscript received May 11, 2006. This work was supported in part by the ALMA-J Office, National Astronomical Observatory of Japan and by the Russian State Programs "Support of Leading Scientific Schools in Russia" (grant 1548.2003.2) and Program for Basic Research "Problems of Radio Physics" (Department of Physical Sciences, Russian Academy of Science) in direction "Applications in Terahertz Range".

Sergey V. Shitov is with the National Astronomical Observatory of Japan, Mitaka, Tokyo 181-8588, Japan and with the Institute of Radio Engineering and Electronics, Russian Academy of Sciences, Moscow 125009, Russia (phone: +81-422-34-3879; fax: +81-422-34-3864; e-mail: s.shitov@nao.ac.jp).

Yoshinori Uzawa and Takashi Noguchi are with the National Astronomical Observatory of Japan, Mitaka, Tokyo 181-8588, Japan (e-mails: y.uzawa@nao.ac.jp, t.noguchi@nao.ac.jp).

Oleg V. Koryukin, Andrey V. Uvarov and Ilya A. Cohn are with the Institute of Radio Engineering and Electronics, Russian Academy of Sciences, Moscow 125009, Russia (e-mails: koryukin@hitech.cplire.ru, uvarov@hitech.cplire.ru, cohn@hitech.cplire.ru).

down to only 2-3 μ W for a two-polarized SIS receiver, if submicron SIS junctions are used in the balanced mixer configuration.

There are a few options for waveguide balanced and side-band separating mixers employing the straightforward connection of the DSB mixers using hybrid couplers [2]. However, the low-loss operation of the waveguide-based connections and the required balancing of the mixers both are of a great concern in the THz frequency range. This is a good reason to look for the more compact design of the RF circuit for waveguide or/and consider an integrated quasioptical SIS mixer design.

It is known that the conversion gain of a SIS junction is reducing essentially above the gap frequency, and it turns negligibly low above twice the gap frequency. The ALMA Band-10 DSB receiver specification for T_{RX} is 230 K within 80% of the band 787-950 GHz and 345 K at any frequency of the band. The IF range of 4-12 GHz is required for the DSB receiver with ripples below 4 dB within each 2 GHz segment. All these make the accurate design of the mixer's RF and IF circuits very important.

Since the Q-factor of a SIS junction at submillimeter wavelength is high ($Q \gg 1$), the twin-SIS junction [3]-[5] is a good solution providing about twice RF bandwidth of a single junction. However, it is known that two junctions in the twin-SIS are unequally coupled at RF across the band, thus providing less gain than one can expect from the equivalent junction of the same R_p . This effect is difficult to estimate experimentally, since two junctions are connected in parallel at DC. The growing importance of such accurate analysis in THz range can be motivated with concern of the essential drop of conversion gain of a Nb-based SIS mixer closer to 1 THz. To analyze the effect of unequal pump and dynamic resistance for a two-junction SIS mixer, the Tucker's 3-port model can be used yet being expanded to multi-junction mixing arrays.

II. BALANCED MIXER DESIGN

A. Quasioptical SIS mixer

A few concepts of a wide-band balanced SIS mixer employing submicron-sized SIS junctions ($A = 0.5 \text{ sq.}\mu\text{m}$) are under development at NAOJ for ALMA Band-10. Considering a general THz-range SIS mixer, the quasioptical (QO) lens-antenna approach seems less laborious, that is confirmed experimentally [6]. Quasioptical chips are easier to process, and they can be handled with much less caution. It is worth to add here that high-quality epitaxial films of NbN [7], which is a promising option for a

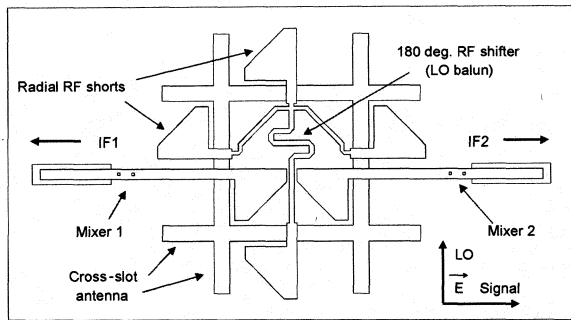


Fig. 1. Layout of quasi-optical balanced SIS mixer chip for use with silicon immersion lens. The outer rectangle presents ground plane (metallization) of slot-antenna circuit.

low-loss tuning circuit, can be grown presumably on MgO high-dielectric ($\epsilon = 9.6$) substrate, that is difficult to use with waveguides. The simplified layout of the QO balanced mixer is presented in Fig. 1. The mixer employs two double-slot antennas, which are crossing each other in the areas of minimum RF current [8], thus minimizing both cross-talk and beam distortion. These two antennas are able to receive separately two orthogonal polarizations, one for LO and another for signal. The signal is coupled from vertical slots into the two twin-SIS mixers, Mixer 1 and Mixer 2. The LO power is first combined from two horizontal slots using a stripline 180-degree RF shifter (LO balun); then it is spitted in half and injected to the signal slots exciting them in *anti-phase* in respect to the phase of the signal. This prevents emissions of LO power in the direction of the signal beam, and the low signal-to-LO coupling can be achieved. Since the wide IF band (4-12 GHz), it is difficult to combine the anti-phased IF signals, IF 1 and IF 2 using a distributed 180-degree balun circuit (hybrid coupler). A series IF connection or an opposite polarity of the dc bias of the mixers [2] are that practicable solutions. Note that present design uses only two twin-SIS mixers, but not four as in [6]. Simulation predicts a wide-band RF performance of such mixer employing a parallel-feed tuning circuit; the IF range of 4-12 GHz is expected. However, such wide-band IF performance of the full receiver may need an IF amplifier integrated with the mixer block similar to [9].

The beam quality is the main concern of the quasi-optical lens-antenna mixers. A few groups [10], [11] have carefully simulated the silicon lens-antenna. In spite its beam efficiency at the secondary reflector is not as good as for corrugated horns, we may expect the figure above 80 % across the whole ALMA Band-10 (for -10 dB taper at the subreflector). The lens-antenna sidelobes are the result of truncation of the printed antenna beam inside the lens due to the effect of full internal reflection. This makes the first-order sidelobes typically at -16 dB. The beam-width of a diffraction-limited lens-antenna is known to be defined by the diameter of the lens. This advantageous feature allows removing the intervening optics (ellipsoidal mirrors). The Gaussian impurity of the beam does not play now important role making resulting (system) beam nearly the same as for high-quality corrugated horn. The optical system of the cartridge with QO balanced mixers is presented in Fig. 2.

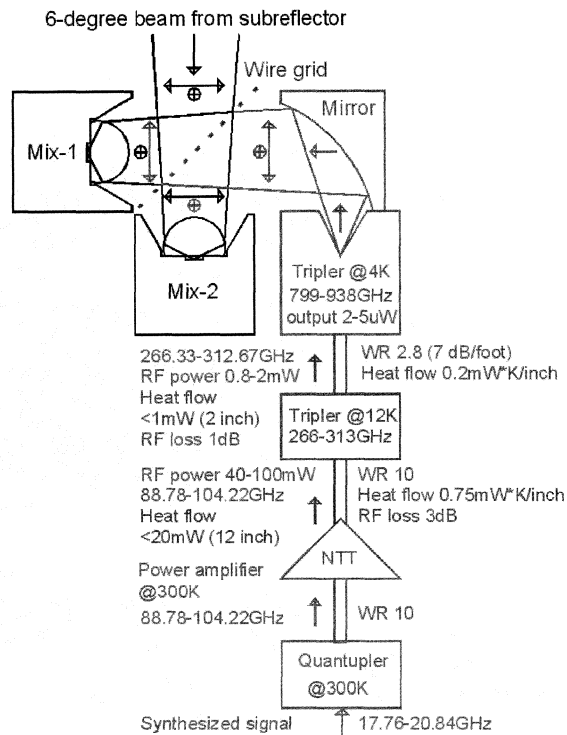


Fig. 2. Optical scheme of double-polarized receiver including quasi-optical balanced SIS mixer and tunerless LO chain.

B. Single-chamber waveguide SIS mixer

The new single-chamber waveguide DSB balanced SIS mixer presented in Fig. 3 can be used with a corrugated horn antenna launcher. Two equal probe-type SIS chips are inserted into a full-height waveguide through its broad walls, so the two mixers are driven from the signal waveguide port in series. The LO current is transferred to the mixers in parallel via a capacitive probe inserted through the narrow wall. This LO probe is an extension of a microstrip line which is penetrating into a neighbouring LO waveguide as shown in Fig. 3. The mechanical approach assumes a flat backpiece (backshort) for the signal waveguide, which is designed using the split-block technique (E-plane symmetry). The LO waveguide is to be split along the wide (common) wall, since the small RF loss or/and some non-flatness are not so important for the LO

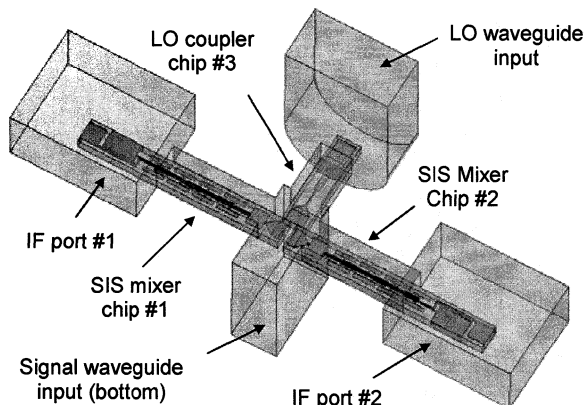


Fig. 3. HFSS 3-D model of THz-range waveguide balanced SIS mixer.

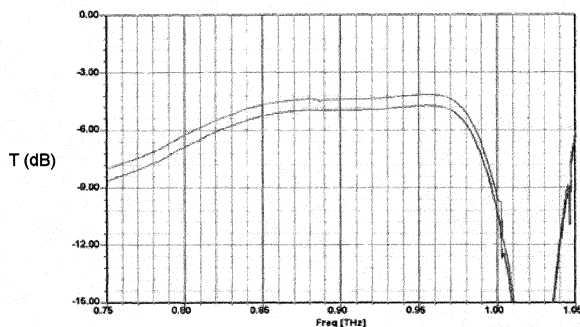


Fig. 4. Transmission of LO power to Mixer 1 and Mixer 2 of the waveguide balanced SIS mixer from Fig. 3 in presence of 10-micron misalignment of the LO-probe chip. Note difference of about 0.5 dB.

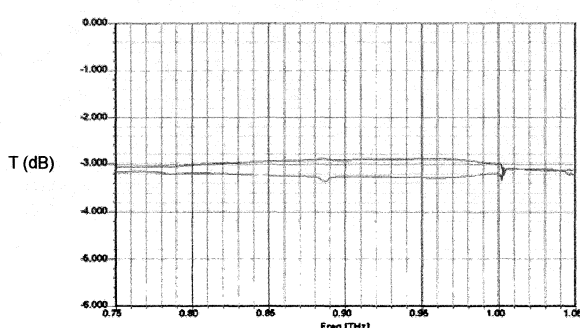


Fig. 5. Transmission of signal to Mixer 1 and Mixer 2 of the waveguide balanced SIS mixer from Fig. 3 in presence of 10-micron misalignment of the LO-probe chip. Note difference of less than 0.5 dB.

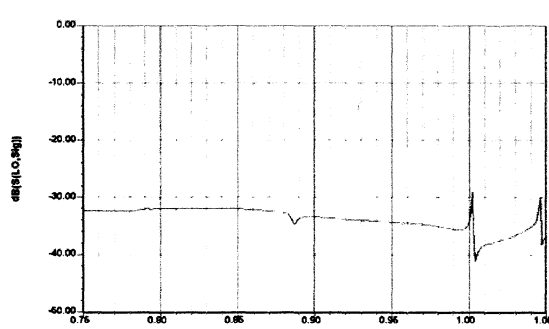


Fig. 6. Signal-to-LO port isolation for the waveguide balanced SIS mixer from Fig. 3 in presence of 10-micron misalignment of the LO-probe chip.

path.

Both signal and LO chips are simulated with HFSS. The simulation demonstrated the LO power coupling efficiency above -3 dB, the signal reflection loss below -20 dB across whole band and the LO cross-talk below -30 dB that take into account the possible 10-um misalignment of the chips. These numerical results are presented in Fig. 4, Fig. 5 and Fig. 6.

III. TWIN-JUNCTION MIXER ANALYSIS

We have developed a numerical method based on the Tucker's theory (3-port) and solved the I-V curves of the twin-SIS junction separately. The simulated circuit is tuned

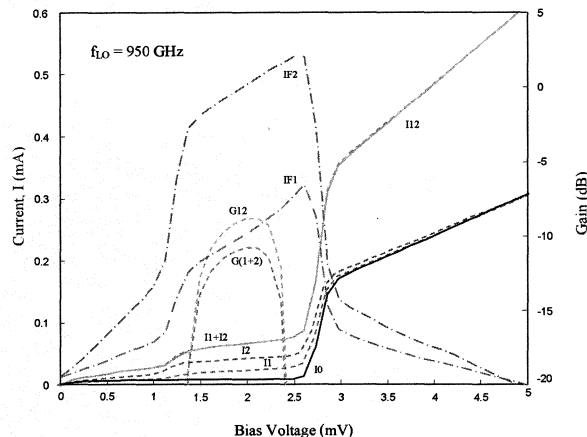


Fig. 7. Simulated I-V curves of the individual junctions of a twin-SIS mixer at 950 GHz. Curves are denoted as following: I0 – un-pumped IV-curve of one SIS junction, I1 and I2 – pumped junction 1 (SIS1) and junction 2 (SIS2), I12 – IV-curve of the equally pumped single junction mixer, IF1 and IF2 – IF current amplitudes generated by SIS1 and SIS2 (i. e. output currents), G12 – mixer gain calculated for equivalent SIS junction I12, G(1+2) – gain calculated with currents IF1 and IF2 for unequally pumped pair SIS1+SIS2.

covering whole ALMA Band-10 with roll-off less than 1 dB at 950 GHz. This case represents a mixer from Fig. 1 (Mixer 1 or Mixer 2). The effect of unequal pump is clearly demonstrated in Fig. 7. The junction with lower pump is shunting the common IF load (LNA) being essentially less efficient at IF. For this reason the mixer gain drops about 3 dB, if compare to the gain predicted with equivalent SIS junction. This seems a general property (problem) of a twin- or multi-junction SIS mixer with the parallel RF connection. Note that twin-SIS mixer with series RF feed [5], [6] has always equal condition for both junctions and thus providing a better performance.

ACKNOWLEDGMENT

Authors thank M. Isiguro, T. Hasegawa, T. de Graauw, Y. Sekimoto and I. Asayama for many fruitful discussions.

REFERENCES

- [1] *Virginia Diodes Inc.* [Online]. Available: <http://www.virginiadiodes.com>.
- [2] S. M. X. Claude, C. T. Cunningham, A. R. Kerr, S.-K. Pan, "Design of a Sideband-Separating Balanced SIS Mixer Based on Waveguide Hybrids" ALMA Memo 316, 20 September 2000 [Online]. Available: <http://www.alma.nrao.edu/memos/html-memos/alma316/memo316.pdf>
- [3] T. Noguchi, K. Sunada, J. Inatani, "An SIS mixer with integrated tuning circuit (II) - A proposal of SQUID-type mixer," *Proc. 39th Spring Meeting of the Japanese Society of Appl. Physics*, Tokyo, Japan, p. 76, March 1992.
- [4] J. Zmuidzinas, H. G. LeDuc, J. A. Stern, and S. R. Cypher, "Two junction tuning circuits for submillimeter SIS mixers," *IEEE Trans. Microwave Theory Tech.*, vol. 42, pp. 698–706, Apr. 1994.
- [5] M. Bin, M. C. Gaidis, J. Zmuidzinas, T. G. Phillips, H. G. LeDuc, "Low-noise 1 THz niobium superconducting tunnel junction mixer with normal metal tuning circuit," *Appl. Phys. Lett.*, vol. 68, pp. 1714–1716, 1996.
- [6] S. Shitov, B. Jackson, A. Baryshev, A. Markov, N. Iosad, J. Gao, T. Klapwijk, "A low-noise double-dipole antenna SIS mixer at 1 THz," *Physica C*, vol. 372, no. 1, pp. 374–377, 2002.
- [7] Y. Uzawa, Z. Wang, A. Kawakami, "Terahertz NbN/AlN/NbN mixers with Al/SiO/NbN microstrip tuning circuits," *Appl. Phys. Lett.*, vol. 73, no. 5, pp. 680–682, 1998.

- [8] G. Chattopadhyay, F. Rice, D. Miller, H. LeDuc, J. Zmuidzinis, "A 530-GHz balanced mixer," *IEEE Microwave Guided Wave Lett.*, vol. 9, no. 11, pp. 467-469, Nov. 1999.
- [9] S. Padin, D. P. Woody, J. A. Stern, H. G. LeDuc, R. Blundell, C. E. Tong, M. W. Pospieszalski, "An integrated SIS mixer and HEMT IF amplifier," *IEEE Trans. Microwave Theory Tech.*, vol. 44, pp. 987-987-990, June 1996.
- [10] D. Filipovic, S. Gearhart, and G. Rebeiz, "Double-slot antennas on extended hemispherical and elliptic silicon dielectric lenses," *IEEE Trans. Microwave Theory Tech.*, vol. 41, pp. 1738-1749, Oct. 1993.
- [11] M. J. M. van der Vorst. *Integrated lens antennas for submillimetre-wave applications*. PhD thesis, ISBN 90-386-1590-6. Technical Univ. of Eindhoven, Netherlands, Apr. 1999.

Analysis of subharmonic SIS mixers using SuperMix

Paul Grimes*, Ghassan Yassin*, Phichet Kittara[†] and Stafford Withington[‡]

*Astrophysics, Oxford University, Denys Wilkinson Building, Keble Road,
Oxford, OX1 3RH, United Kingdom. Email:pxg@astro.ox.ac.uk

[†]Mathematical Physics Research Group, Dept. of Physics, Mahidol University,
Rama 6 Rd, Rachathawi, Bangkok 10400, Thailand

[‡]Cavendish Laboratory, Cambridge University,
Madingley Road, Cambridge, CB3 0HE, United Kingdom.

Abstract—Sub-harmonically pumped SIS mixers operating at very high LO harmonics have been used to measure beam patterns of SIS mixers in the laboratory, and to measure the line-widths and phase-locking performance of flux-flow oscillators. Using the sub-harmonically pumped mode of operation for beam pattern measurements allows the measurement to be carried with a single phase-locked sub-mm source, without a beamsplitter in front of the mixer feed. This allows the near field amplitude and phase to be measured, and allows the far field pattern to be measured at very high angles which would be blocked by the presence of a beamsplitter.

Kittara, Withington and Yassin[1] have recently described a procedure for modelling the non-linear behaviour of very high harmonic SIS mixers. They use a fully non-linear multitone mixer theory[2] to analyse the behaviour of a SIS mixer pumped by the 20th harmonic of a 13.5 GHz LO signal, with the mixer down-converting both sidebands around 270 GHz to a 1.4 GHz IF. This analysis shows that sub-harmonic mixers can achieve reasonable dynamic range. The pattern of behaviour seen in the simulations are in remarkable agreement with published experimental results[3].

In this work we describe the small-signal behaviour of sub-harmonic SIS mixers using the CalTech's SuperMix software[4]. This method has the advantage of faster convergence than the non-linear analysis and hence allows the exploration of the complex behaviour of subharmonic SIS mixers. Our analysis is compared Kittara *et al*'s results. We show that SuperMix can accurately calculate the small-signal behaviour of high harmonic SIS mixers, as well as providing predictions of mixer noise performance.

I. INTRODUCTION

Fundamental mode SIS junction mixers are the most sensitive heterodyne receivers throughout the high mm-wave and sub-mm bands. This sensitivity is due to the very high nonlinearity of the SIS junction IV curve. This same nonlinearity can be used to generate many harmonics of the LO signal, allowing the SIS junction to be used as a subharmonically pumped mixer. Subharmonically pumped mixers using low harmonic number have been reported[5], and higher harmonic numbers have been used to study the line-width and phase-locking of flux flow oscillators[6].

A particularly effective use of a high harmonic number subharmonic SIS mixer was reported by Baryshev *et al*[3]. They reported the use of a subharmonic pumping of an SIS mixer in measuring the amplitude and phase of the beam pattern of a (fundamental mode) mixer at 640 GHz. The 15 GHz LO signal was injected via directional coupler at the IF output of the mixer (fig. 1), with the mixer being operated at the 42nd harmonic. The RF test signal was provided by a phase-locked Gunn oscillator feeding a Schottky diode doubler and tripler multiplier chain in the

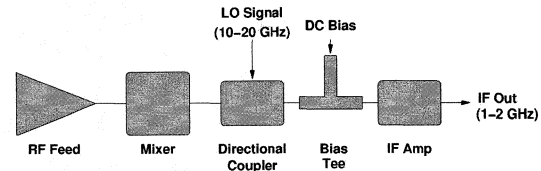


Fig. 1. Schematic of the subharmonic SIS receiver reported by Baryshev *et al*[3].

far field of the mixer feed. This measurement system has two distinct advantages. Firstly, only one phase-locked mm-wave source is required, and secondly, as the microwave LO signal is injected through the IF output of the mixer, no LO injection optics are required in the optical system and the measured beam pattern is that of the mixer feed alone.

The behaviour of the pumped IV curves and IF output power (and hence mixer conversion loss) reported by Baryshev *et al* is particularly striking. Unlike a fundamental mode mm-wave SIS mixer, no photon steps are visible in the pumped IV curves, as the photon voltages are less than the width of the junction nonlinearity. When the mixer is pumped by a low frequency LO and a mm-wave RF signal, the IF output power against bias curve has several peaks both above and below the junction gap voltage. The widths of these peaks do not seem to be related to either the RF or LO photon voltages, and the widths of the peaks varies strongly with LO pump level.

In order to optimise the effectiveness of subharmonic mixers used in these applications, it is vital that the behaviour of the mixer can be predicted. In this work we compare two numerical models of subharmonic SIS mixers. The first of these is CalTech's SuperMix software library, which has been widely used to simulate and design fundamental mode mixers. The second is the MultiTone software package, based on a recently published fully nonlinear model of quantum mixing[2]. This second package is of particular interest to non-astronomical uses of subharmonically pumped SIS mixers, as it allows the dynamic range of the mixer to be predicted. However, the SuperMix library has other advantages, as it can incorporate complex superconducting circuits, and several SIS junctions.

II. SUPERMIX AND MULTITONE SIMULATIONS OF SUBHARMONIC MIXERS

SuperMix[4] is a software library developed at the California Institute of Technology to allow the simulation of

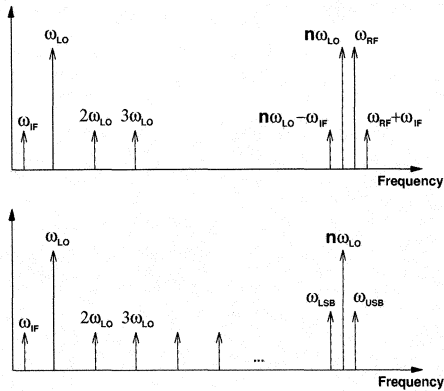


Fig. 2. Harmonics included in (top) MultiTone and (bottom) SuperMix simulations of the subharmonic mixer.

fundamental mode SIS mixers and their associated superconducting circuits and IF systems. The portion of the library that simulates the behaviour of SIS mixers is based on a generalisation of Tucker's theory of quantum mixing in SIS junctions[7]. SuperMix allows any number of harmonics of the LO frequency and any number of SIS junctions to be simultaneously solved for large signals, while the conversion between the RF and IF sidebands is calculated by perturbing the harmonic balance over the LO harmonics, in the limit of small sideband signals.

A further generalisation of Tucker theory has recently been presented by Withington, Kittara and Yassin[2]. Although currently limited to a single tunnel junction, this completely quantum model of SIS mixing allows the tunnel junction to be excited by any number non-harmonically related frequencies of arbitrary amplitude. This model allows signals at all sidebands and LO harmonics to be arbitrarily large, therefore allowing the behaviour of saturating SIS mixers to be rigorously calculated. We have previously shown that the MultiTone software, based on this model gives identical results to SuperMix, in the limit of small sideband signals[8].

Kittara *et al*[1] have recently carried out simulations of subharmonic SIS mixers using the MultiTone software. The MultiTone model of subharmonic mixers is somewhat complicated by a limitation of the software (but not the overall model), due to which only the first three harmonics of a signal can be included. The MultiTone model of a subharmonic mixer therefore uses separate signals at the LO frequency ω_{LO} , the n th harmonic of the LO $n\omega_{LO}$, the upper sideband of the n th harmonic $\omega_{RF} = n\omega_{LO} + \omega_{IF}$ and the IF signal ω_{IF} . In order to get accurate results, undriven signals must also be included at the lower sideband of the n th harmonic $\omega_{LO} - \omega_{IF}$, and $\omega_{RF} + \omega_{IF}$. This scheme is outlined in fig. 2. The effect of the mixer circuits is included by setting an embedding impedance for each harmonic included in the harmonic balance.

In the SuperMix model of the subharmonic mixer, the first n harmonics of the LO frequency are included in the harmonic balance, while the mixer conversion between the upper and lower sidebands and the IF are calculated in the small-signal limit. SuperMix divides the embedding circuits of the mixer into three distinct circuits; the DC bias circuit, the IF output circuit and the RF circuit, to which the LO must be connected. In order to simulate a subharmonic mixer with

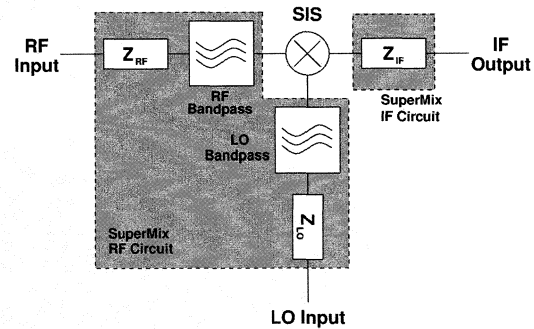


Fig. 3. Schematic of the circuits used within the SuperMix simulations of the subharmonic mixer.

different LO and RF embedding impedances, the RF circuit of the subharmonic mixer consists of two branches, with the signals in each branch selected by idealised bandpass filters between the embedding impedance and the junction (fig. 3). The RF bandpass filter has perfect transmission between $n\omega_{LO} - \omega_{IF}$ and $n\omega_{LO} + \omega_{IF}$, while the LO bandpass filter has perfect transmission in a narrow band about ω_{LO} . Outside of these bands, both filters are perfectly reflecting.

We have found that SuperMix's harmonic balance routine will often fail to converge when simulating a subharmonic mixer, particularly when the LO pump level is close to the optimum. This problem occurs because the accuracy of the calculation of the RF currents through the junction is hard coded in the SuperMix SIS junction model. Although the preset tolerances are adequate for most fundamental mode mixers, these tolerances cause the balancing of very high harmonics to fail. We have worked around this problem by including many higher LO harmonics in the calculation, e.g. 90 harmonics are required to simulate the 20th harmonic mixer presented here at all pump levels. This comes at a cost of greatly increased execution time, as the harmonic balance must now be carried out over many more harmonics than strictly necessary. A better alternative would be to alter the SuperMix library, so that the user can set the tolerances in the RF current calculation.

III. SIMULATION RESULTS

In this section we compare the results of SuperMix based simulations with those obtained from the MultiTone software for a specific idealised mixer. The mixer is pumped by an LO at a normalised frequency of 0.02, corresponding to 13.5 GHz for a niobium junction. The mixer is operated at the 20th harmonic of the LO (normalised frequency 0.40 ~ 270 GHz) with an IF of 0.002 ~ 1.35 GHz. The embedding impedances of the IF, LO, the 20th harmonic of the LO, and the RF sidebands are set to unity, while all other intermediate (and higher) LO harmonics have an embedding impedance equal to zero. The response function of the junction is given by the polynomial quotient approximation

$$I(V) = \frac{V^n}{1 + V^{n-1}}, \quad (1)$$

with $n = 50$. The sharpness of this IV curve roughly corresponds to that of a high quality niobium/aluminium oxide junction.

Fig. 4 compares the pumped IV curves from SuperMix and MultiTone at various LO drive level $\alpha = \omega_g V_{LO} / \omega_{LO}$.

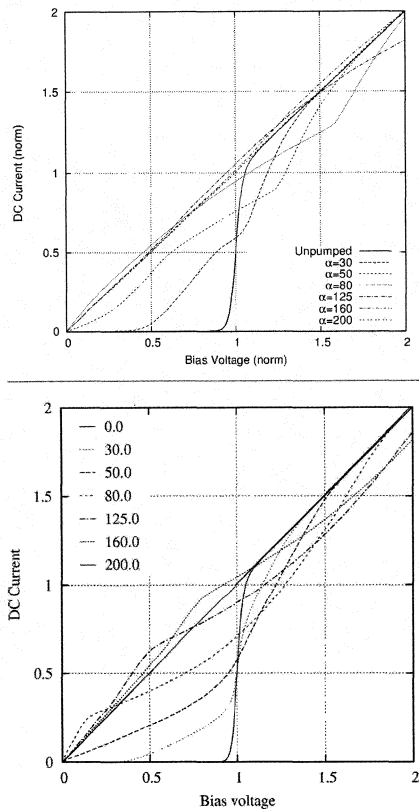


Fig. 4. (top) SuperMix and (bottom) MultiTone simulated pumped IV curves for a 20th harmonic mixer pumped at $\omega_{LO} = 0.02 \sim 13.4$ GHz for a Nb junction. In all of the following results, the MultiTone results have a gap voltage of 2.8 mV, while the SuperMix bias voltages are normalised to a gap voltage of 1.0.

Although the SuperMix and MultiTone pumped curves are different, both are reasonably consistent with the measured IV curves reported by Baryshev *et al.* The differences between the two simulation methods are probably due to both the different harmonics used in each calculation, and differences between the embedding circuits used. More work, including alterations to both software packages, will be required to get good agreement between these results.

Figures 5 and 6 compare the mixer conversion losses predicted by the two software packages at two different LO drive levels. Due to differences between the operation of the two software packages, the actual values of the conversion loss cannot be directly compared. Instead the IF output power predicted by MultiTone for a small fixed RF input power is compared with the small-signal conversion loss from SuperMix. Both sets of results produce the same number of peaks in the IF output, although heights and widths of these peaks differ, with the MultiTone results looking closer to the experimental results of Baryshev *et al.* The uneven nature of the peaks in both the experimental and MultiTone results is due to the high RF signal level used in both cases. This situation cannot be simulated by SuperMix.

In both the experimental data and the MultiTone simulations, the RF signal can be larger than the signal generated at the *n*th harmonic of the LO, for reasonably small RF signals. In this case the RF and LO *n*th harmonic swap roles, with the mixer being partially pumped by the RF signal. Despite

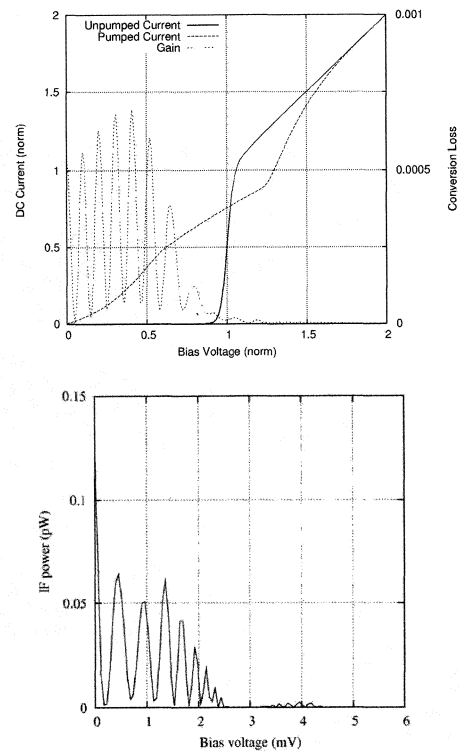


Fig. 5. (top) SuperMix calculated conversion gain and (bottom) MultiTone simulated IF output power for the 20th harmonic mixer. The LO drive level is $\alpha = 50$, and the RF signal power in the MultiTone simulation is 472 pW.

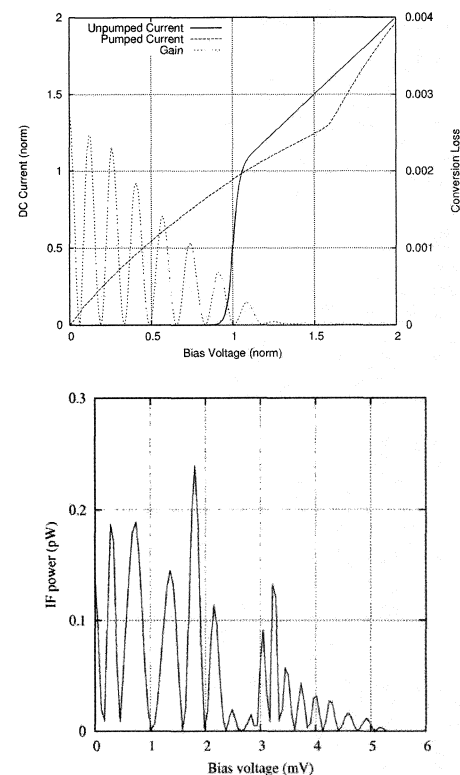


Fig. 6. (top) SuperMix calculated conversion gain and (bottom) MultiTone simulated IF output power for the 20th harmonic mixer. The LO drive level is $\alpha = 80$, and the RF signal power in the MultiTone simulation is 472 pW.

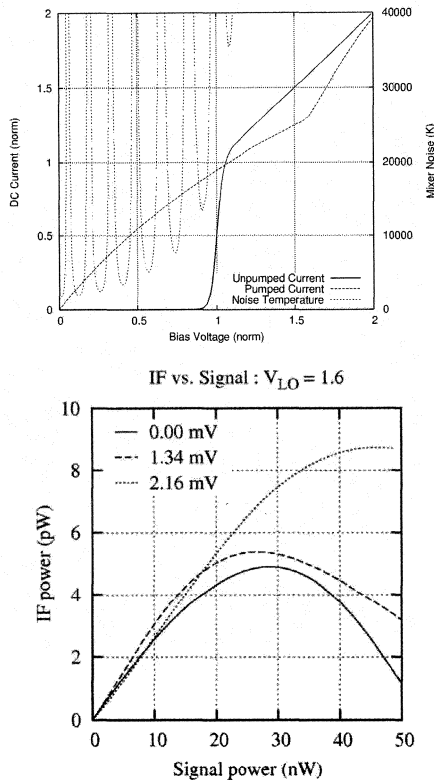


Fig. 7. (top) SuperMix calculated noise temperatures of the 20th harmonic mixer at a LO drive level of $\alpha = 80$. (bottom) MultiTone results for the saturation of the IF signal at increasing RF signal levels at three bias voltages.

this, the IF output of the mixer is still linear in the RF power up to a few nanowatts. The relatively large RF signal is the cause of the differences between the SuperMix small-signal conversion gain and the IF output power in the MultiTone and experimental results, which use a moderate RF signal level.

Figure 7 illustrates one of the main differences between SuperMix simulations and the MultiTone software package. MultiTone cannot produce simulated noise temperature data, while SuperMix can only analyse mixers in the limit of small signals at frequencies other than the LO and its harmonics. The mixer noise temperature is dominated by the high conversion loss (more than 25 dB at all bias points) rather than high noise in the IF band, and this could be considerably improved with better choice of the various embedding impedances.

Finally, in figure 8 we plot the mixer conversion loss from SuperMix against the LO drive voltage at three bias points. At non-zero bias voltages the conversion loss against LO voltage curve is strongly peaked. The best conversion loss occurs at zero bias, and at this point the mixer is least sensitive to variations in the LO power.

IV. CONCLUSIONS

Both SuperMix and MultiTone based simulations can analyse subharmonically pumped SIS mixers, although some contortions are required to carry out these calculations. SuperMix simulations are particularly useful when designing, and finding the basic operating state of subharmonically

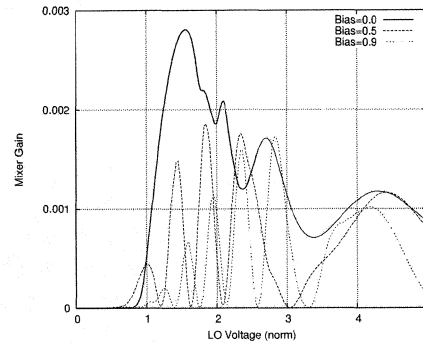


Fig. 8. SuperMix calculated conversion gain of the 20th harmonic mixer as a function of LO power at three bias voltages.

pumped mixers. However in many applications, the subharmonic mixer will be operated with a moderate RF signal power. MultiTone simulations of the mixer will be essential in ensuring the linearity of the mixer over the dynamic range of the measurement in these applications, and when comparing simulations with the performance of mixers fed by a moderate RF signal.

Both software packages require further work to carry out these simulations in a simple and transparent way. In particular, the accuracy of SuperMix's RF current calculation routine should be adjusted to allow the accurate calculation of high LO harmonic currents, and the MultiTone software should be altered to include all the harmonics of the LO signal up to the harmonic number of the mixer. It should then be simple to simulate more realistic subharmonically pumped SIS mixers, and to compare measured performance with both SuperMix and MultiTone simulations.

REFERENCES

- [1] P. Kittara, S. Withington, and G. Yassin, "Theoretical and numerical analysis of very high harmonic superconducting (SIS) mixers," (*in prep*), 2006.
- [2] S. Withington, P. Kittara, and G. Yassin, "Multitone quantum simulations of saturating tunnel junction mixers," *J. Appl. Phys.*, vol. 93, pp. 9812–9822, 2003.
- [3] A. Baryshev, M. Carter, R. Hesper, S. Wijnholds, W. Jellema, and T. Zijlstra, "Use of subharmonically pumped sis mixer with high harmonics number phase and amplitude antenna measurements," in *Proc. 13th Int. Symp. Space THz Tech.*, pp. 551–558, 2002.
- [4] J. Ward, F. Rice, G. Chattopadhyay, and J. Zmuidzinas, "SuperMix: A flexible software library for high-frequency circuit simulation, including SIS mixers and superconducting elements," in *Proceedings of the 10th Int. Symp. on Space THz Tech.*, p. 269, 1999.
- [5] V. Y. Belitsky, I. L. Serpuchenko, M. A. Tarasov, and A. N. Vystavkin *Int. Conf. on mm waves and far infrared tech.*, vol. Beijing, China, pp. 268–271, 1989.
- [6] V. P. Koshelets, S. V. Shitov, L. V. Filippenko, V. L. Vaks, J. Mygind, A. B. Baryshev, W. Luinge, and N. Whyborn *Rev. of Sci. Instr.*, vol. 71, pp. 289–293, 2000.
- [7] J. R. Tucker, "Quantum limited detection in tunnel junction mixers," *IEEE J. of Quantum Electronics*, vol. 15, p. 1234, 1979.
- [8] P. K. Grimes, S. Withington, G. Yassin, and P. Kittara, "Quantum multitone simulations of saturation in SIS mixers," *Proceedings of the SPIE*, vol. 5498, 2004.

Analysis of the Influence of Current Density j_c and DC-Quality Q on Mixer Performance around 700 GHz for more than 50 measured SIS-Mixers

R. Teipen¹, M. Justen, T. Tils, M. Schultz, S. Glenz, P. Pütz, C.E. Honingh, K. Jacobs

KOSMA, I. Physikalisches Institut, Universität zu Köln
Zülpicher Straße 77, 50937 Köln, Germany

For the development of the band 2 mixers (636-802 GHz) for the HIFI instrument on the Herschel Space Observatory² the RF-performance of more than 50 mixers with Nb/Al₂O₃/Nb-junctions fabricated at KOSMA have been characterized. Based on the DC-characteristics and RF-performance the choice of the best devices for the flight mixers has been made. According to the results the design approach of the mixers is revisited.

During the SIS-device development process the device parameters (gap-voltage V_{Gap} , current density j_c , dc-quality $Q = R(2 \text{ mV})/R_N$, strip-line conductivity σ and accuracy of junction-area) have been optimized. Because of the Nb-gap at 700 GHz the power losses of the NbTiN/SiO₂/Nb micro strip matching circuit are much lower in the lower frequency region (5%) than in the upper frequency band (33%). In addition to these micro strip losses the parameters j_c and Q show the strongest impact on the mixer performance. These two parameters can not be optimized independently since a higher j_c implies a thinner barrier and lower Q .

To evaluate the trade-off for an optimum combination of j_c and Q the noise performance for more than 50 experimental I-V-curves with the FM-design embedding impedance is calculated from Tucker's theory for different values of j_c . The reduction in receiver noise caused by an improved Q becomes small for values of $Q > 8-10$. The reduction in receiver noise caused by a higher j_c is much larger in the upper frequency band with high micro strip losses. The calculations together with a fabrication-dependent relation of realizable j_c and Q can be used as a guideline for optimum design parameter for j_c .

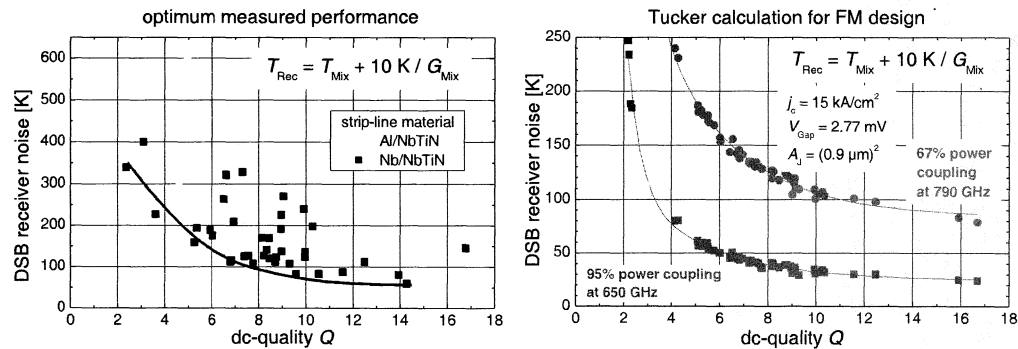


Figure 1: Receiver performance dependence on junction DC-quality Q . Left: measured optimum performance of mixers in HIFI band 2. Right: calculated receiver noise (Tucker) for measured I-V-curves as function of DC-quality Q . The data show the results for two frequency points of the FM-design embedding impedance.

¹Email rteipen@ph1.uni-koeln.de

²<http://sci.esa.int/herschel>

Test of 1 mm Band Turnstile Junction Waveguide Orthomode Transducer

Alessandro Navarrini, Alberto Bolatto, and Richard L. Plambeck

Abstract—We tested five prototype waveguide orthomode transducers (OMTs) designed for the 200-270 GHz frequency band. These OMTs, based on a turnstile junction, have identical designs [1], but were fabricated by different manufacturers using different techniques and materials. The OMTs were tested at NRAO, Charlottesville, using a Vector Network Analyzer (VNA) in the frequency range 210-310 GHz. Three of the OMTs have average room temperature insertion loss of ~ 1 dB or better, average input and output reflection of approx -18 dB, and cross-polarization and isolation of order -30 dB over 210-270 GHz.

The integrity of the tuning stub in the turnstile junction is the key for good performance: a gap between the quadrants there causes additional losses up to several tenths of a dB. Filling up the gap with indium gave, for the OMT with best performance, a transmission loss better than -0.8 dB over the entire 210-290 GHz band. Input and output reflections are better than -12 dB, with cross-polarization and isolation better than -25 dB across the same band.

Index Terms— Radio astronomy, Turnstile junction, Power combiner, Polarimetry, Waveguide transitions

I. INTRODUCTION

We are constructing OMTs for dual polarization 200-270 GHz receivers on the CARMA array. The design of the

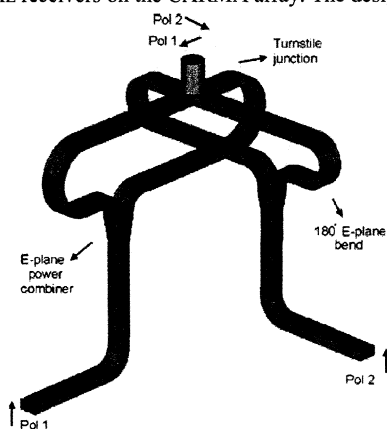


Fig. 1. Internal view of the full OMT. Opposite ports of the turnstile junction are brought together with E-plane bends and power combiners.

The authors are with the Radio Astronomy Laboratory (RAL), University of California, Berkeley, CA 94720 (e-mail: navarrin@astro.berkeley.edu).

This work was supported in part by the National Science Foundation under Grant AST-0228963.

OMT is discussed in [1] and [2]. The device has a circular waveguide input (diameter 1.12 mm) and two WR3.7 rectangular waveguide outputs (0.94 mm x 0.47 mm). The OMT, illustrated in Fig. 1, utilizes a turnstile junction and two E-plane power combiners [3]. A tuning stub located at the base of the circular waveguide matches the input over a full frequency band.

II. MECHANICAL BLOCKS

The OMT is constructed by dividing the structure of Fig. 1 into four blocks that intersect along the circular waveguide axis. The tuning stub at the base of the turnstile junction is split into four identical sections that are machined at the same time as the rectangular waveguides. The OMT, shown in Fig. 2, accepts a standard UG387 flange at its input so it can mate with our existing feed-horns. Custom mini-flanges are used for the WR3.7 output waveguides of the OMT for compactness of the device. The mini-flanges are identical to those of the ALMA Band 6 OMTs and SIS mixers, where the

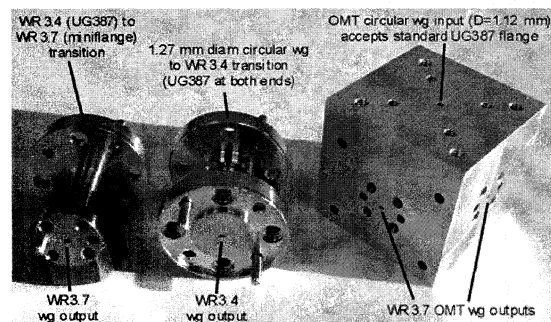


Fig. 2. View of assembled OMT (on the right) with the circular waveguide input on top and the two WR3.7 waveguide outputs with custom mini-flanges. Two of the 19.05 mm long transitions used for testing are shown to the left of the OMT.

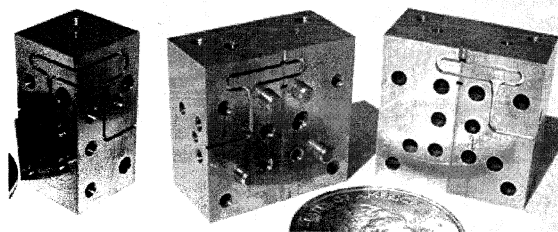


Fig. 3. OMT n. 2 machined at RAL. Left) View of one of the four quarters. Right) View of assembled mating pairs of blocks showing the waveguide circuitry for Pol 2.

alignment pins and screw holes are on a 7.11 mm diameter bolt circle. Our OMT is a cube 23 mm on a side. The electrical path length from the circular waveguide at the input of the OMT to the WR3.7 waveguide outputs is ~ 28 mm for Pol 1 and ~ 30 mm for Pol 2.

Fig. 3 shows photos of one of the four blocks and of the mated block pairs. Details of the internal waveguide circuitry of the OMT are shown in the photos of Fig. 4. Five OMTs of identical design were fabricated by different manufacturers using different materials and machining techniques. Their main features are summarized in Table 1. Measurement results allowed to compare OMTs performance in relation to mechanical tolerances.

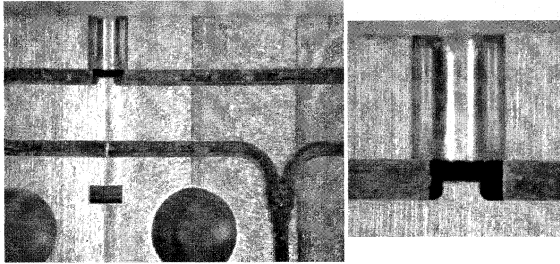


Fig. 4. OMT n. 5 machined at Univ. of Arizona. View of an assembled mating pair of blocks showing the internal waveguide circuitry of turnstile junction, and power combiner (on the left), and the details of the tuning stub at the turnstile junction circular waveguide base (on the right).

TABLE I

OMT n.	Machined by	Material	Notes
1	RAL, Berkeley, CA	Aluminum	Four blocks machined from a single bar
2	RAL, Berkeley, CA	TeCu	Four blocks machined from a single bar
3	Protofab, Petaluma, CA	TeCu	Blocks machined individually
4	Custom Microwave Inc., Longmont, CO	Gold plated brass	Blocks machined individually
5	Univ. of Arizona, Tucson, AZ	Gold plated brass	Blocks machined individually.

The four blocks of OMTs n. 1 and n. 2 were machined in our own shop (RAL) at one time as part of a single $12.7 \times 12.7 \times 165$ mm³ metal bar using a numerically controlled milling machine (CNC Tree Journeyman 350 equipped with high speed Astro-E500 spindle 50000 rpm.) Inspection of the blocks with the optical microscope showed that the maximum offset between rectangular waveguide cuts in block halves is approximately 0.040 mm. The four blocks of the other three OMTs were fabricated individually using machines capable of achieving better accuracy. The maximum offset between waveguide cuts in block halves of OMT n. 5, fabricated at University of Arizona using a Kern Micro milling machine, was less than 0.015 mm. Unfortunately, the tuning stub and one of the power combiners of such OMT were slightly damaged after we sent it out for gold plating.

III. MEASUREMENT SETUP

We tested the five OMTs during the week 24-28 October 2005, at NRAO, Charlottesville, using an Agilent 85106C Vector Network Analyzer (VNA) equipped with Oleson WR3.4 millimeter-wave test set extensions. A schematic of the cross-polarization test setup is shown in Fig. 5.

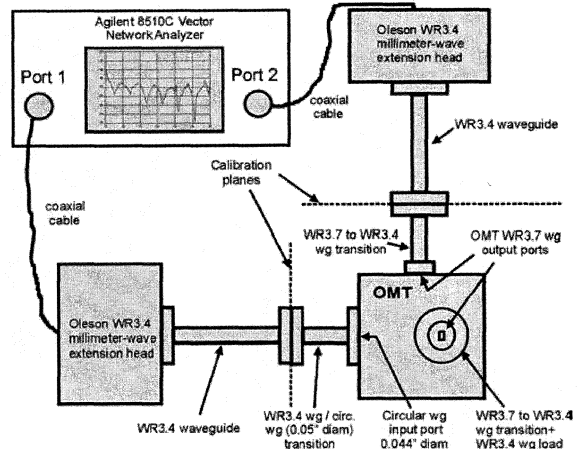


Fig. 5. S-parameter measurement of the OMT with the VNA. The particular configuration refers to the cross-polarization measurement.

The VNA was calibrated at the WR3.4 waveguide at the outputs of the extension heads using a two-port TRL calibration with Oleson WR3.4 calibration kit. A Custom Microwave transition from WR3.4 rectangular waveguide to 1.27 mm diameter circular waveguide (Fig. 2) was attached to the 1.12 mm circular waveguide input of the OMT. Although the locating pins of the OMT input flange are on the normal 14.27 mm diameter bolt circle, it was not possible to locate the waveguide screws in their normal positions, so a special aluminum clamp was made to bolt the OMT to the flange of the transition (Fig. 6.)

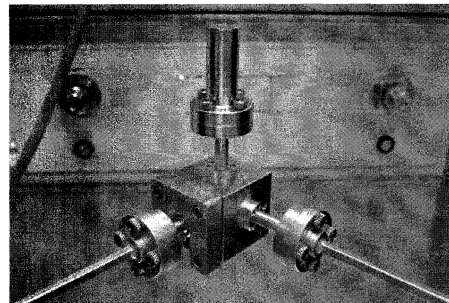


Fig. 6. Pol 1 transmission measurement of the OMT with the VNA. An aluminum clamp is used to attach the WR3.4 to 1.27 mm diameter circular waveguide transition at the input of the OMT (on the left.) One of the OMT WR3.7 output is attached to the WR3.4 waveguide connected to the mm-wave extension head of the VNA through a WR3.7 to WR3.4 transition (on the right.) The second OMT WR3.7 output (on top) is terminated into a WR3.4 waveguide load through a WR3.7 to WR3.4 transition. A single two-port measurement in this configuration provides the direct and reverse transmission as well as the input and output reflection of the OMT with transitions.

IV. EXPERIMENTAL RESULTS

We tested the OMTs between the minimum operating frequency of the VNA, 210 GHz, up to 310 GHz. This range overlaps with most of our OMT design band, 200-270 GHz. Between 210-215 GHz the measurements have a higher noise level because of the lower power level of the VNA in that frequency range.

A. Tuning stub fix

Tests of the OMTs showed that their good performance depends on the integrity of the tuning stub located at the base of the circular waveguide. Three of the OMTs had small imperfections and gaps between quadrants at the tuning stub. After filling the gap with indium, the insertion loss improved by several tenths of a dB in most cases. Fig. 7 shows photos of the tuning stub of OMT n. 3 before and after fix. Fig. 8 shows that the transmission of both polarization channels of that OMT improved from an average value across the band of ~ 1 dB to a value of ~ 0.6 dB, which is similar in overall level to the value predicted by the electromagnetic simulation. The measured room temperature transmission is above -0.8 dB across 210-290 GHz. After tuning stub fix, the average insertion loss of three of the OMTs was ~ 1 dB or better across the same band.

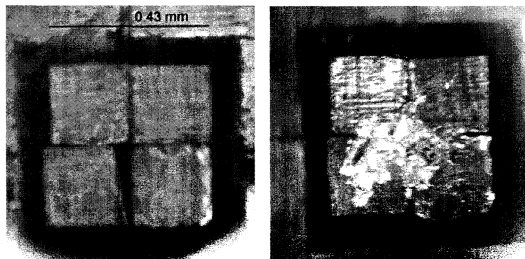


Fig. 7. Magnified top view of the tuning stub before (left) and after (right) filling up the gap with indium of OMT n. 3. After tuning stub fix, the value of insertion loss of this OMT improved by approximately 0.4 dB across the band.

The input reflection and cross-polarization measurements of OMT n. 3 after tuning stub fix are given in Fig. 9. The input reflections, unchanged after the fix, are below -12 dB across 210-290 GHz. The small differences between the measured reflection coefficients for the two polarization channels indicate that they are electrically very similar. The output reflections are similar, in overall level and shape, to those at the input. The cross-polarization and isolation levels are both below -25 dB; one of the two polarization channels improved by ~ 5 dB after fix, bringing the average levels across the band from -30 dB down to -35 dB.

B. Transmission resonances

Two of the OMTs had problems, showing narrow and deep transmission resonances in the band of interest. Fig. 10 shows the measured transmission of OMT n. 2 with deep resonances below the -4 dB level. Experiments with a K-band scale model of the OMT indicate that these resonances are probably related to fabrication errors that cause a misalignment of one (or more) of the four quarters of the OMT.

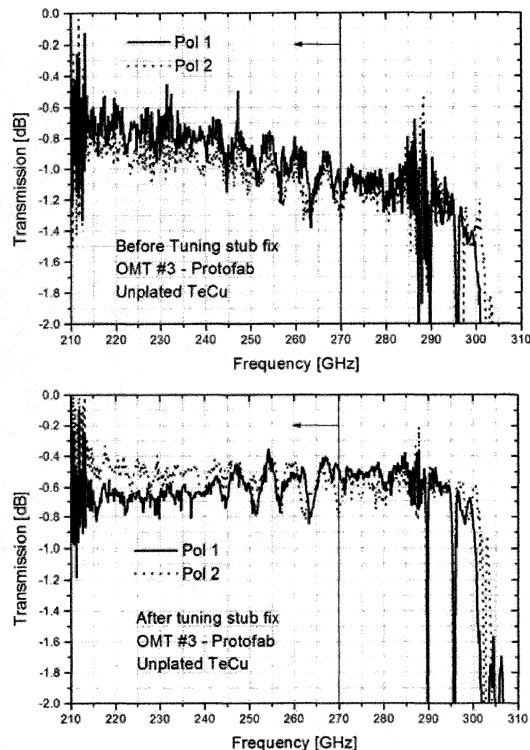


Fig. 8. Pol 1 and Pol 2 transmission measurement of OMT n. 3 before (top) and after (bottom) tuning stub fix. The vertical line in the graphs delimits the nominal highest frequency of the band at 270 GHz.

A difference in the electrical length of opposite waveguide arms between the turnstile junction and the power combiner causes the appearance of a series of resonances in the transmission of the OMT. Energy coming from the turnstile junction reflects back from the power combiner when the two signals reaching it are not exactly 180° out of phase. Electromagnetic simulations of the three-port model of Fig. 1 with imbalanced waveguide sidearm lengths, performed with CST Microwave Studio [4], confirm the appearance of deep transmission resonances across the band. The depth of the resonances increases with sidearm length difference; an increase in the waveguide losses makes the resonances shallower and broader. Resonances in the transmission of the OMT are also expected when the physical lengths of the two waveguide sidearms are identical, but one of the sidearms has a different electrical length from the other: an offset along the midplane of the rectangular waveguides caused by a lateral misalignment of block halves changes the propagation constant (and hence the phase velocity) with respect to a waveguide with no offset. Thus, if one of the four blocks of the OMT is offset along the circular waveguide axis, the two waveguide sidearms of each polarization channel will have different electrical lengths. Because of the different physical length of WR3.7 waveguide sections in different blocks, the

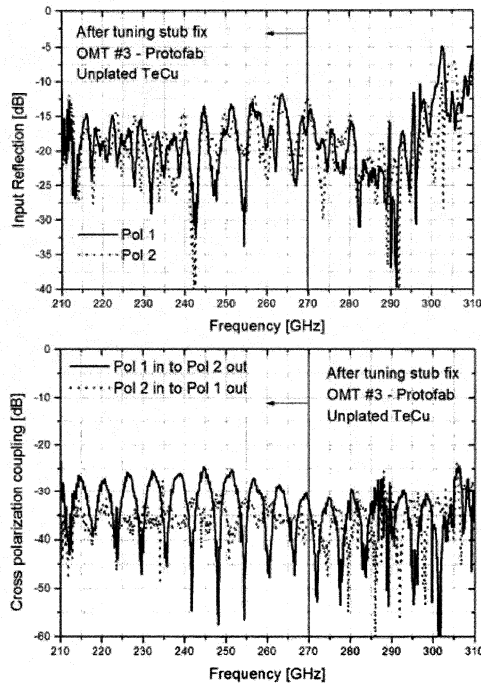


Fig. 9. Pol 1 and Pol 2 input reflection (top), and cross polarization coupling (bottom) of OMT n. 3 after tuning stub fix.

electrical length difference depends on which one of the four blocks is offset with respect to the others. For example, an offset of the block having the shortest waveguide cut sections (the one without power combiners), causes an offset along the midplane of an ~ 10 mm long section of WR3.7 waveguide associated with the polarization channel n. 1 on one of the lateral sidearms, but not on the other (the physical length of the sidearms between the turnstile junction and the power combiner is ~ 14 mm and ~ 13 mm for polarization channels 1 and 2, respectively.) To give an estimate of the electrical length difference between two sidearms caused by an offset of one of the blocks along the axis of our OMT, we performed electromagnetic simulations of: *a*) a straight 10 mm long section of WR3.7 waveguide; *b*) a same length waveguide laterally misaligned along the midplane (see Fig. 11.) The difference between the phase of the two transmissions is ~ 12 deg at 230GHz for an offset of 0.025 mm. At the same frequency, the phase difference between two WR3.7 waveguides (with no offset) with length difference 0.025 mm is ~ 5 deg, less than half that value. Therefore, a given amount of misalignment of one of the blocks along the circular waveguide axis (caused, for example, by loose locating pins) is expected to be more harmful to the OMT performance than fabrication errors causing the same amount of length difference between turnstile junction waveguide sidearms. A design of the OMT that minimizes the physical length difference between WR3.7 waveguide sections in different blocks should help reduce this problem.

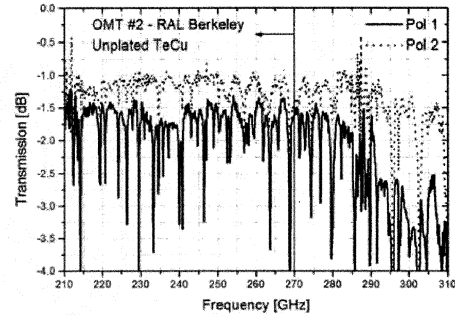


Fig. 10. Pol 1 and Pol 2 transmission of OMT n. 2.

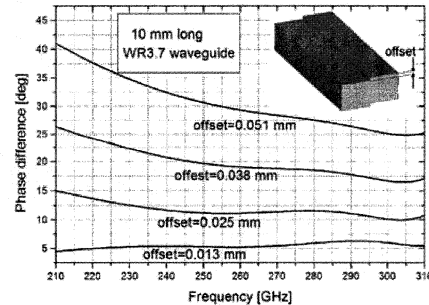


Fig. 11. Transmission phase differences between a straight 10 mm long WR3.7 waveguide and a same length waveguide section where block halves are offset by 0.013 mm, 0.025 mm, 0.038 mm, 0.051 mm.

V. CONCLUSIONS

We tested five prototype turnstile junction waveguide orthomode transducers for the 1 mm band. Three of the OMTs have average room temperature insertion loss of ~ 1 dB or better, average input and output reflection of about -18 dB, and cross-polarization and isolation of order -30 dB over 210-270 GHz. The performance of the OMTs improved after filling small gaps between quadrants at the turnstile junction tuning stub with indium: the insertion loss decreased by several tenths of a dB across the band. The OMT that gave best performance has insertion loss better than 0.8 dB across 210-290 GHz.

VI. ACKNOWLEDGEMENTS

We thank C. Groppi at University of Arizona and D. Chow at RAL Berkeley for manufacturing some of the OMTs. We thank D. Koller and T. Kerr at NRAO for their help during the tests.

REFERENCES

- [1] A. Navarrini and R. L. Plambeck, "A Turnstile Junction Waveguide Orthomode Transducer," *IEEE Trans. Microwave Theory Tech.*, vol. 54, no 1, pp. 272-277, Jan 2006.
- [2] A. Navarrini and R. L. Plambeck, "A Turnstile Junction Waveguide Orthomode Transducer for the 1 mm Band," 16th International Symposium on Space Terahertz Technology, Gothenburg, Sweden, May 2-4, 2005.
- [3] A. R. Kerr, "Elements for E-plane Split-Blocks Waveguide Circuits," NRAO, ALMA Memo No. 381, Jul. 2001.
- [4] CST Microwave Studio. Bűdinger Str. 2 a, D-64289 Darmstadt, Germany.

**Generation of THz radiation with the use of Vortices
Located in Josephson ring.**

D.R. Gulevich, F. V. Kusmartsev,
Department of Physics, Loughborough University, Loughborough, LE11 3TU, UK

Today, novel technologies are emerging from electronic devices that become smaller and smaller. We have studied tiny metal superconducting rings separated by an insulator and forming annular Josephson junction. At low temperature, in superconducting state the current generates Josephson vortices. We have created such fluxons experimentally and have theoretically estimated the probability of their formation. The experiment and theory are in perfect agreement. These vortices may generate electromagnetic radiation with terahertz frequencies. We describe simple structures which can work as generators of such radiation. With the use of the proposed generators many modern day problems may be tackled, from detecting of cancer to security imaging with continuous scanning.

Ultrafast Superconducting Digital Circuits for Analysis and Processing of Microwave Signals

Pascal Febvre, Torsten Reich, Thomas Ortlepp and F. Hermann Uhlmann

Abstract— Rapid-Single-Flux-Quantum (RSFQ) digital circuits based on shunted Josephson junctions have been shown to be able to digitally process signals up to several hundreds GHz. The principle of operation is based on the generation, transport and processing of picosecond voltage pulses of 2.07 mV.ps quantized area, which corresponds to one quantum flux $h/2e$. Operation of RSFQ circuits can be performed with clock frequencies of the order of 20 to 50 GHz with present technology. We will present current developments and experimental results obtained so far, based on circuits developed in the JeSEF RSFQ process of IPHT Jena[1], using a 1 kA/cm² shunted Nb/Al-AIOx/Nb junctions. Some particular potential applications for space will be emphasized.

Index Terms—superconductor, RSFQ, Single-Flux-Quantum, superconducting electronics

I. INTRODUCTION

WITH their high intrinsic speed of several tens of GHz and very low dissipation, superconductive circuits open the way to high-speed digital electronics. In Rapid Single Flux Quantum (RSFQ) digital circuits based on shunted Josephson junctions [2], digital data are transmitted through picosecond voltage pulses with quantized area of 2.07 mV-ps, corresponding to one magnetic flux quantum Φ_0 . Hence, the pulse voltage is weak, of the order of 1 mV or less: it corresponds to pulses of about 2 ps duration, depending on the technological process under concern. It is possible to use such a technology to develop different ultrafast processing circuits like Analog-to-Digital Converters (ADCs), autocorrelators, processors or routers. Such circuits can work with clock frequencies above 20 GHz and can reach hundreds of GHz if they are based on the most aggressive technologies. These circuits rely on basic RSFQ cells that can process quanta of magnetic flux under the form of picosecond voltage pulses. The pulses are usually transmitted through RSFQ transmission lines. Flip-flop cells are used to transform the SFQ pulses in Non-Return-to-Zero (NRZ) signals, compatible with classical semiconductor electronics.

Manuscript received May 31, 2006.

Pascal Febvre is with the Microwave and Characterization Laboratory (LAHC), University of Savoie, 73376 Le Bourget du Lac, France. (e-mail: pascal.febvre@univ-savoie.fr).

Torsten Reich, Thomas Ortlepp and F. Hermann Uhlmann are with the Department of Electrical Engineering and Electromagnetic Fields, University of Technology Ilmenau, PO Box 10 05 65, D-98684 Ilmenau, Germany.

II. RSFQ BASICS

The basic element for RSFQ logic is the Resistively-Shunted Josephson junction. For the common RSFQ processes, the resistive shunt is deposited externally. Nevertheless, self-shunted Josephson junctions (naturally occurring for high- T_c materials) present some advantages in terms of integration and ultimate frequencies, though this kind of technology is not yet mastered to make complex circuits. Figure 1 shows the equivalent electrical circuit of a shunted Josephson junction. To keep the following analysis general, we will call R_{shunt} the total shunt resistor of the junction, composed of the junction normal resistance R_N in parallel with an eventual external shunt resistor.

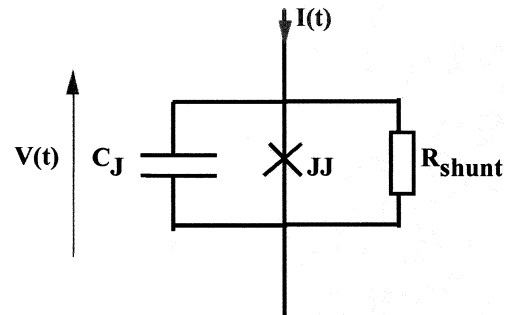


Figure 1: RSJ electrical model of a Josephson junction shunted by an external shunt resistor R_{shunt} . C_J is the Josephson junction capacitance.

The two Josephson equations, controlling the dynamics of the Josephson current are:

$$I_J = I_c \sin \varphi(t) \text{ and } V(t) = \frac{\Phi_0}{2\pi} \frac{\partial \varphi(t)}{\partial t} \quad (1)$$

where $\Phi_0 = \frac{h}{2e}$ is the magnetic flux quantum, φ the difference between the phases of the two macroscopic wavefunctions associated to the two superconductors forming the Josephson junction and I_c its critical current. The total current flowing through the device can be written:

$$I = C_J \frac{dV(t)}{dt} + \frac{1}{R_{shunt}} V(t) + I_c \sin \varphi(t) \quad (2)$$

If one writes L_{J0} , the zero-current Josephson inductance, usually defined by[3]:

$$L_{J0} = \frac{\Phi_0}{2\pi I_c} \quad (3)$$

and $i = \frac{I}{I_c}$ the reduced current flowing through the device, equation (2) can be rewritten under the usual form, using equations (1):

$$i = L_{J0} C_J \frac{\partial^2 \varphi(t)}{\partial t^2} + \frac{L_{J0}}{R_{shunt}} \frac{\partial \varphi(t)}{\partial t} + \sin \varphi(t) \quad (4)$$

For low values of the phases, the sinus is about linear and equation (4) is simply the one of a parallel RLC circuit, whose dynamics is well known. Three natural frequencies appear:

1- the plasma angular frequency of the parallel LC circuit

$$\omega_{pl} = \frac{1}{\sqrt{L_{J0} C_J}} \quad \text{associated to the period:}$$

$$\tau_{pl} = 2\pi \sqrt{L_{J0} C_J};$$

2- the cutoff angular frequency of the parallel LR circuit

$$\omega_{LR} = \frac{R_{shunt}}{L_{J0}} \quad \text{associated to the relaxation time}$$

$$\tau_{LR} = \frac{L_{J0}}{R_{shunt}};$$

3- the cutoff frequency of the parallel RC circuit associated to the relaxation time $\tau_{RC} = R_{shunt} C_J$.

Equation (4) can be rewritten:

$$i = \frac{\partial^2 \varphi(t)}{\partial \tau^2} + \frac{1}{\sqrt{\beta_c}} \frac{\partial \varphi(t)}{\partial \tau} + \sin \varphi(t) \quad (5)$$

where $\tau = \omega_{pl} t$ is the time normalized to the Josephson junction plasma period and β_c is the McCumber parameter defined by:

$$\beta_c = \left(\frac{\omega_{LR}}{\omega_{pl}} \right)^2 = \frac{\tau_{RC}}{\tau_{LR}} = \frac{R_{shunt}^2 C_J}{L_{J0}} = \frac{2\pi R_{shunt}^2 C_J I_c}{\Phi_0} \quad (6)$$

Normalized equation (5) is identical for all Josephson junctions and can be considered as a law of corresponding states for Josephson devices. The time constants defined above can be rewritten as follows:

$$\tau_{RC} = \frac{\sqrt{\beta_c}}{2\pi} \tau_{pl}; \tau_{LR} = \frac{1}{2\pi \sqrt{\beta_c}} \tau_{pl}; \tau_{pl} = \sqrt{\frac{2\pi \Phi_0 C_S}{j_c}}$$

where C_s is the specific capacitance of the Josephson junction and j_c the Josephson junction critical current density.

It is well known that, for a linear parallel RLC circuit ($\sin \varphi \approx \varphi$) the damping coefficient is:

$$\xi = \frac{1}{2\sqrt{\beta_c}} \quad (7)$$

while the envelope of the signal decreases as $\exp(-\xi \omega_{pl} t)$ in the damped oscillatory and critical regimes. This means, from the above expressions of ξ and ω_{pl} , that the relaxation time constant of a shunted Josephson junction excited by a short electrical signal, is $2 \tau_{RC}$. For junctions without external shunts, the parallel resistor of figure 1 is simply the

normal state resistance R_N . For such hysteretic junctions, the McCumber parameter is usually high, above 10, which corresponds to quite high values of the relaxation time constant $2 \tau_{RC}$. For instance, for a typical $4 \mu\text{m}^2$ junction with a current density of about 10 kA/cm^2 , $2 \tau_{RC} = 4.6 \text{ ps}$. If one defines the ultimate frequency by $1/(12\tau_{RC})$, corresponding to the time needed by the junction to switch to a resistive mode (3 times $2\tau_{RC}$) and switch back to initial state (3 times $2\tau_{RC}$ again), one finds an ultimate frequency of operation of about 40 GHz with an aggressive high-current density technology. This partly explains why the initial Josephson latching logic developed in the early eighties never met the expectations and has been given up.

In order to increase the speed of the circuits, the RC constant has to be lowered, by either reducing R or C_J . Since the capacitance is proportional to the size of the junction, a reduction of the junction size will not lower the RC constant since the normal resistance R_N will increase proportionally. Even for the case of a resistor R made out of an external shunt resistor, independent of the junction size, a reduction of the junction size will decrease the critical current, increase the Josephson inductance, hence the LR constant. Moreover, some noise considerations have to be taken into account if one uses very small Josephson junctions. A better solution is to externally shunt the Josephson junction to reduce the RC constant while keeping it high enough not to increase too much the LR constant.

The optimum trade-off is clearly obtained when the RC constant is lowered to reach the LR constant. From equation (6), this case is reached when the McCumber parameter β_c is equal to unity. Consequently, the LR and RC time constants become directly connected to the Josephson plasma time constant. The new characteristic time constant is

$$\tau_0 = \sqrt{\frac{\Phi_0 C_S}{2\pi j_c}} = \frac{1}{2\pi} \tau_{pl}. \quad \text{The associated maximum clock}$$

frequency of operation can be defined by

$$f_{0,max} = \frac{1}{2\pi \tau_0} = \frac{1}{\tau_{pl}} = \sqrt{\frac{j_c}{2\pi \Phi_0 C_S}}. \quad \text{It is shown in}$$

figure 2.

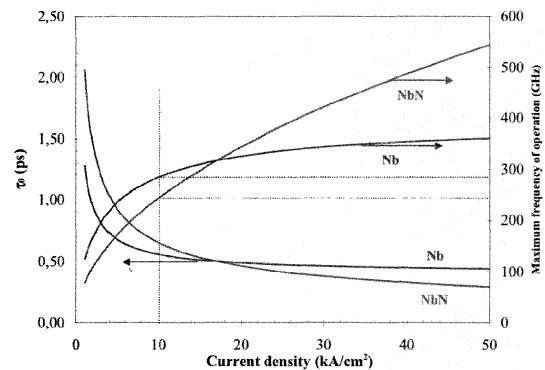


Figure 2: Expected maximum frequency of operation of RSFQ circuits for Nb-based and NbN-based Josephson junctions.

By appropriately shunting the Josephson junctions so that the McCumber parameter is one, one can then perform dynamic switching at high speed [4]. Depending on how the junctions are arranged within superconducting loops,

quantized picosecond pulses, associated to the dynamic switching of the Josephson junctions, can be generated, propagated and stored in some cells under the form of quanta of magnetic flux. To account for such behaviour, the non-linear response of Josephson junctions need to be put back in equation (2). Though the solution of this general equation is much less trivial than its linear counterpart, the global behaviour, in terms of relaxation times, remains unchanged.

III. APPLICATION TO DIGITAL SQUIDS

A. Introduction

It is possible to use the RSFQ technology to develop digital Superconducting Quantum Interferometer Devices (SQUIDs). These devices can count quanta of magnetic flux under the form of picosecond voltage pulses. The pulses are processed by RSFQ transmission lines and flip-flop cells which transform the SFQ pulses in Non-Return-to-Zero (NRZ) signals, compatible with classical semiconductor electronics. The main advantage of digital SQUIDs, compared to their analog counterparts, is their theoretically infinite dynamics, which should permit to measure absolute magnetic fields with a very high accuracy. The other advantage is connected to their intrinsic very high slew-rate, of the order of $10^9 \Phi_0/\text{sec}$, corresponding to the digital clock rate of the SFQ circuits.

B. Principle of operation and results

The principle of operation of the digital SQUID is presented in [5-6]. Figure 3 shows the circuit diagram of the SQUID.

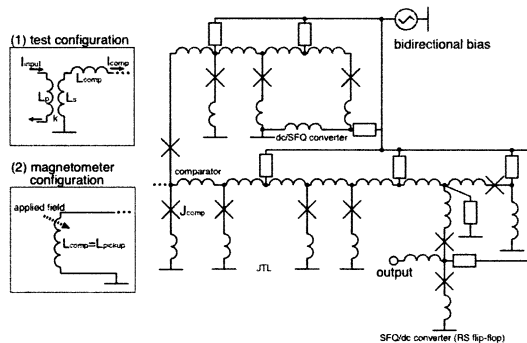


Figure 3: Lumped circuit diagram of the digital SQUID device. Test configuration (1) is used to test the SFQ part of the SQUID device, while the magnetometer configuration (2) is the configuration to be used for regular operation.

A new interesting feature about such SQUIDs deals with its bidirectional bias which consists of a train of alternate negative and positive SFQ pulses, generated by the clocked dc/SFQ converter. It allows to "follow" the signal to measure with only one digital output. Indeed, the output signal consists of negative or positive SFQ pulses, depending respectively whether the signal to measure increases or decreases. The key part of this device is the ac SQUID defined by the comparator junction J_{comp} in parallel with inductance L_{comp} (see figure 3). This junction switches, generating an SFQ pulse which is processed by the JTL and the SFQ/dc converter, in two cases: a) when the additional

current produced by an increase of the magnetic field to detect adds up in the comparator junction with the current associated to a positive SFQ pulse: a positive SFQ pulse is getting out of the ac SQUID loop; b) when the current negative variation produced by a decrease of the magnetic field to detect adds up with the current associated to a negative SFQ pulse: a negative SFQ pulse is getting out of the ac SQUID loop. In other cases, for each negative of positive clock pulse coming on J_{comp} junction, there is no generated output pulse. A picture of such a digital SQUID is shown in Figure 4. It has been fabricated in a certified ISO9001 foundry at IPHT Jena [1]. The shunted Josephson junctions, based on a Nb/Al-Al₂O₃/Nb trilayer, have a current density of 1 kA/cm² and an $R_N I_C$ product of 256 μV .

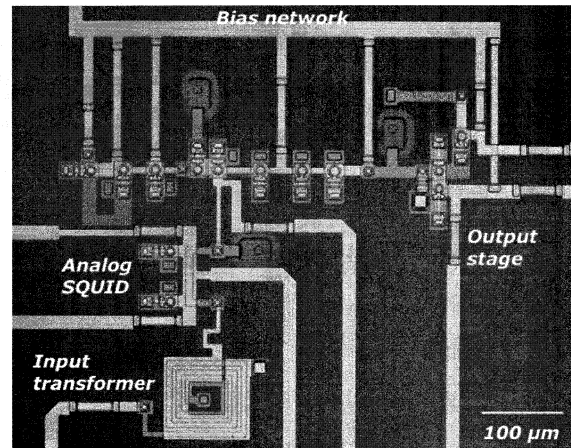


Figure 4: Picture of the digital SQUID made of 11 shunted Nb/Al-Al₂O₃/Nb Josephson junctions. Junctions have a current density of 1 kA/cm². Fabrication has been performed at IPHT Jena in Germany. The analog SQUID on the left is not part of the overall circuit described in figure 1. It has been added there for additional functionalities, not described in this article.

Figure 5 shows the output signal measured with a low-frequency 1 kHz digital clock. The signal to be measured is a 5 Hz sinusoidal pattern.

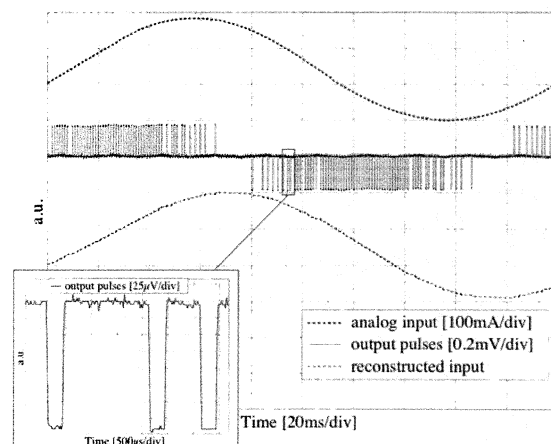


Figure 5: Measurement of a sinusoidal input signal corresponding to a magnetic field variation (top curve). The central curve shows the measured signal at the digital SQUID output. The bottom curve shows the input signal reconstructed from the digital measurements.

IV. CONCLUSION

The first successful measurements of RSFQ circuits for digital SQUIDs have been performed. This technology presents some interest for very high-speed processing of ultrafast signals, that can be fed from and transmitted to the "room-temperature world", and sensitive detection of magnetic and electro-magnetic signals. To that regards, space scientific applications have always been a powerful engine to pull such technologies. Connected to that particular point, we foresee different fields for which such technologies are of high interest, like low-consumption, high-speed and high resolution broadband autocorrelators, or on-chip multiplexing for future submillimeter heterodyne imaging systems.

ACKNOWLEDGMENT

We want to strongly acknowledge the contribution of Juergen Kunert and Hans-Georg Meyer from IPHT Jena for the device fabrication and helpful advice. One of us (T Reich) would like to thank SCENET—European Network for Superconductivity for financial support during his scientific exchange stay that allowed him to perform the experimental measurements presented in this paper.

REFERENCES

- [1] http://www.ipht-jena.de/BEREICH_1/abt13_cryo_electronics/index.html
- [2] K. K. Likharev and V. K. Semenov, "RSFQ logic/memory family: A new Josephson-junction digital technology for sub-terahertz-clock-frequency digital systems," *IEEE Trans. Appl. Supercond.*, vol. 1, pp. 3-28, 1991.
- [3] A. Barone and G. Paterno, *Physics and Applications of the Josephson Effect*, John Wiley & Sons Inc., 1982.
- [4] W. Chen, A. V. Rylyakov, Vijay Patel, J. E. Lukens, and K. K. Likharev, " Rapid Single Flux Quantum T-Flip Flop Operating up to 770 GHz," *IEEE Trans. on Appl. Supercond.* vol. 9, pp. 3212-3215, June 1999.
- [5] T. Reich, T. Ortlepp and H.F. Uhlmann, Digital SQUID sensor based on SFQ technique, *IEEE Trans. Appl. Supercond.*, vol. 15, no. 2, pp. 304-307, 2005.
- [6] T. Reich, T. Ortlepp, H.F. Uhlmann and P. Febvre, Experimental analysis of a digital SQUID device at 4.2 K, *Superconductor, Science and Technology*, vol. 18, no. 8, pp. 1077-1081, August 2005.

STUDY OF JOSEPHSON ELECTRODYNAMICS IN PARALLEL ARRAYS OF SUPERCONDUCTIVE JUNCTIONS FOR SUBMM-WAVE LOCAL OSCILLATOR APPLICATIONS

Morvan Salez, Faouzi Boussaha

LERMA, Observatoire de Paris, 77 avenue Denfert-Rochereau, 75014 PARIS - France

Jean-Guy Caputo, Lionel Loukitch

Laboratoire de Mathématique, INSA de Rouen, B.P.8, 76131 Mont-Saint-Aignan cedex - France

Abstract - Submillimeter-wave fully integrated superconducting receivers (SIR) including on a single chip an SIS mixer, a planar antenna and a Long Josephson Junction (LJJ) operated as local oscillator (LO) have been successfully developed by Koshelets et al [1,2] at IREE-Moscow (Institute of Radio Engineering and Electronics) and SRON (Space Research Organization of the Netherlands). These SIRs are potentially ideal for post-Herschel submm-wave spaceborne instruments, remote ground-based observatories like Dome C-Antarctica, and for heterodyne applications other than astronomy like sensing the upper Earth atmosphere, imaging heterodyne receivers in medicine, contraband... We propose that multijunction non-uniform arrays ($N \times$ SIS junctions ($N > 2$)) connected in parallel by a Nb stripline, initially developed at LERMA for mixing operation [3] could also be operated as a submm-wave LO, by using the demonstrated existence and propagation of fluxons in these arrays. So far only cavity resonant modes have been observed, yet flux-flow oscillator (FFO) modes are in theory achievable by proper design. Multijunction-based FFOs may be an interesting alternative to LJJ-based FFOs in SIRs, allowing wide LO tunability, wide impedance matching bandwidths, and increased design flexibility and control of technological parameters. In this paper, we present a numerical study of the Josephson electrostatics in this kind of device. In addition, a tentative measurements of output power from 5 junction array with current density of ~ 10 kA/cm² at submm-wave frequencies will be presented.

[1] V.P. Koshelets, S.V. Shitov, A.B. Ermakov, O.V. Koryukin, L.V. Filippenko, A. V. Khudchenko, M. Yu. Torgashin, P. Yagoubov, R. Hoogeveen, O.M. Pylypenko, "Superconducting Integrated Receiver for TELIS", Report 2ET06 at the Applied Superconductivity Conference ASC'2004, USA, October 2004.

[2] V. Koshelets and J. Mygind, "Flux Flow Oscillators for Superconducting Integrated Submm Wave Receivers," Studies of High Temperature Superconductors 39 (2001), 213–244,. Ed. A.V. Narlikar, NOVA Science Publishers, New York.

[3] Boussaha F.; Salez M.; Delorme Y.; Féret A.; Lecomte B.; Westerberg K.; Chaubet M. Submillimeter mixers based on superconductive parallel junction arrays SPIE; 1st Int.Symp; "Microtechnologies for the New Millennium 2003 "; Maspalomas; Canary Islands; Spain ; 19-20 mai 2003.

ORAL SESSION n°2

« Direct detection »

Wednesday 10 May 16:00-17:55

Chaired by:

Dr. Gregory Goltsman & Dr. Anders Skalare

**Transition Edge Superconducting detector arrays for a 40-200 μm
spectrometer on the SPICA telescope**

Philip Mauskopf,
University of Wales, Cardiff, UK

Invited paper

We present the detector requirements for a spectrometer instrument designed to cover the 40-200 μm wavelength range from a cooled space-borne telescope such as the proposed Japanese SPICA mission.

We discuss possible solutions using transition edge superconducting (TES) bolometers for achieving the required detector sensitivity, speed, dynamic range and number of pixels within the constraints of a space-borne platform.

Ultralow NEP in Hot-Electron Titanium Nanobolometers

Jian Wei[‡], David Olaya[‡], Sergei Pereverzev, Boris S. Karasik[§], Jonathan H. Kawamura, William R. McGrath, Andrei V. Sergeev, and Michael E. Gershenson

Abstract—We have developed a hot-electron superconducting transition-edge sensor (TES) that is capable of counting THz photons and operates at $T = 0.3\text{K}$. We fabricated superconducting Ti nanosensors with Nb contacts with a volume of $\sim 3 \times 10^{-3} \mu\text{m}^3$ on planar Si substrate and have measured the thermal conductance due to the weak electron-phonon coupling in the material $G = 4 \times 10^{-14} \text{W/K}$ at 0.3 K. The corresponding $NEP = 3 \times 10^{-19} \text{W/Hz}^{1/2}$. This Hot-Electron Direct Detector (HEDD) is expected to have a sufficient energy resolution for detecting individual photons with $\nu > 1 \text{THz}$ where $NEP \sim 3 \times 10^{-20} \text{W/Hz}^{1/2}$ is needed for space spectroscopy.

Index Terms—radiation detectors, submillimeter wave detectors, bolometers, superconducting devices

I. INTRODUCTION

SEVERAL advanced space submillimeter astronomy missions (SAFIR [1,2], SPECS [3], SPICA [4]) have been recently proposed. These missions will make a dramatic impact on the achievable sensitivity in the spectrometer with moderate resolution ($R = \nu/\Delta\nu \sim 1000$) due to active cooling of telescope mirrors down to $\sim 4 \text{K}$. This deep cooling would significantly reduce the telescope emissivity and enable realization of the background-limited noise equivalent power (NEP) $\sim 10^{-19}$ - $10^{-20} \text{W/Hz}^{1/2}$ at submillimeter wavelengths (see Fig. 1). However, the NEP of state-of-the-art direct detectors [2,5] needs to be lowered by almost two orders of magnitude to meet this goal. The membrane supported bolometers have come close to meeting the sensitivity goals [6]: a low phonon conductance has been achieved in long ($\sim 8 \text{mm}$) Si_3N_4 beams suggesting an $NEP \sim 10^{-19} \text{W/Hz}^{1/2}$ in the 50-100 mK temperature range. The further decrease of the thermal conductance is hindered by the weakening of the temperature dependence of the thermal conductance due to transition to ballistic phonon transport.

Besides the more traditional photon-integrating mode of operation, a photon counting mode may be required to achieve the lowest NEP . Background-limited operation

Manuscript received May 11, 2006. The work at Rutgers was supported in part by the NASA grant NNG04GD55G and the Rutgers Academic Excellence Fund. The research of BSK, JHK and WRM was carried out at the Jet Propulsion Laboratory, California Institute of Technology, under a contact with the National Aeronautics and Space Administration.

J. Wei, D. Olaya, S. Pereverzev and M. Gershenson are with Rutgers University, Piscataway, NJ 08854, USA.

B. Karasik, J. Kawamura, and W. McGrath are with the Jet Propulsion Laboratory, California Institute of Technology, Pasadena, CA 91109, USA.

A. Sergeev is with SUNY at Buffalo, Buffalo, NY 14260.

[‡] These authors contributed equally to this work.

[§] Corresponding author. Phone: 818-393-4438, email: boris.s.karasik@jpl.nasa.gov

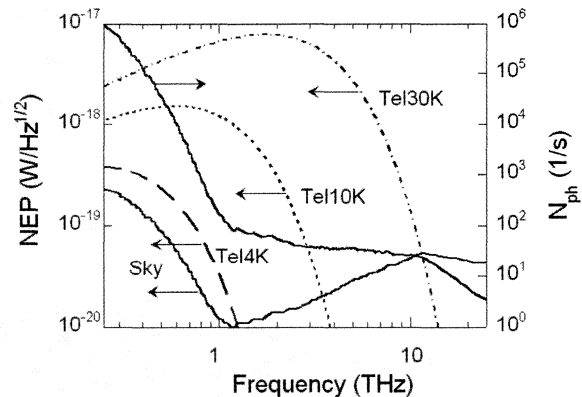


Fig. 1. The NEP limited by the background and by the telescope emission (5% emissivity, mirror temperature 4K, 10K, and 30K) for a moderate resolution spectrometer ($R = 1000$, single mode) and the arrival rate for background photons. The latter is less than 100s^{-1} above 1 THz. Below 1 THz, the major contribution is due to the Cosmic Microwave Background radiation; at higher frequencies, radiation from the galactic core and dust clouds dominates.

above 1 THz would correspond to a very low photon arrival rate [7]:

$$N_{ph} = \frac{1}{2} \left(\eta \frac{NEP}{h\nu} \right)^2 < 100 \text{s}^{-1}, \quad (1)$$

(η is the optical coupling efficiency). A detector with a time constant τ will integrate a photon flux if $N_{ph}\tau \gg 1$. Therefore, a background limited integrating detector must have a time constant of 0.1 s or greater. Such a long time constant is problematic for many detector concepts: typically, τ does not exceed a few milliseconds for hot-electron detectors and kinetic inductance detectors, so they both would have to operate in the photon counting mode for the detection of weak signals. Although the photon counting mode in the THz range has been considered in several papers (see, e.g., [7,8,9]), the detection of individual THz photons has been demonstrated only using the quantum-dot devices [10]. The latter approach has been recently advanced towards practical application in terahertz microscopy [11]. The drawback of the quantum-dot detector for space applications is a necessity to use strong magnetic field for the most sensitive operation and the lack, at present, of a multiplexed readout for a large array of such detectors.

II. HOT-ELECTRON DIRECT DETECTOR

We are pursuing a Hot-Electron Direct Detector (= hot-electron TES), which can operate in both photon-integrating

and photon-counting modes at 0.3 K [12]. The idea of improving the sensitivity of bolometers by employing the hot-electron effects at ultra-low temperatures has been developed by several groups over a number of years [7,13,14,15,16]. The fundamental limit of the NEP is set in this case by the thermal energy fluctuations:

$$NEP = \sqrt{2k_B T_e^2 C_e(T_e, V) / \tau_{e-ph}(T_e)}. \quad (2)$$

Here $C_e = \gamma V T_e$ is the electron heat capacity, V is the sensor volume, γ is the Sommerfeld constant, and τ_{e-ph} is the electron-phonon energy relaxation time. The sensitivity increases with decreasing the sensor volume and lowering the electron temperature T_e . Especially strong is the effect of lowering T_e : $NEP_{c-ph} \sim T_e^{7/2}$ because of a very rapid increase of the electron-phonon relaxation time $\tau_{e-ph} \propto T_e^{-4}$ in disordered conductors at ultra-low temperatures (see, e.g., [17,18]). Since the electron temperature is always $\sim T_C$ in hot-electron TES, then lowering T_e requires reducing T_C to the desired level. This can be achieved by magnetic ion implantation, e.g. ^{55}Mn ions work well on Ti [19]. Using conventional nanolithographic methods, the volume of metallic nanostructures can be reduced down to $\sim 10^{-21} \text{ m}^3$,

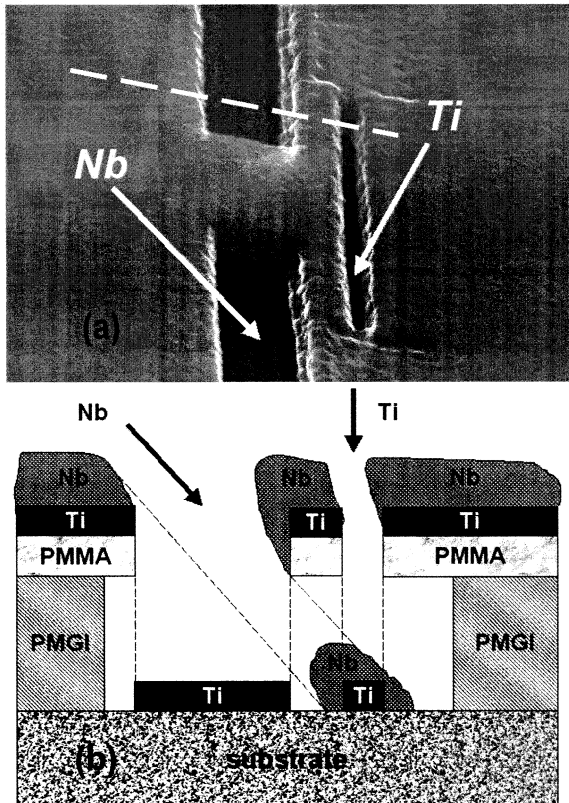


Fig. 2. (a) Shadow mask used for the fabrication of Ti HEDDs (the SEM picture has been taken after the deposition of Ti and Nb films). The arrows show the directions in which Nb and Ti were deposited. (b) Cross section along the dashed line on panel (a). A two-layer lift-off mask consists of the top 0.1- μm -thick PMMA layer, used as a high-resolution electron resist, and the bottom 0.3- μm -thick layer of polymer PMGI. A deep undercut in the bottom layer allows for the overlap of the films deposited at different incident angles: Ti is deposited along the direction normal to the plane of a substrate; Nb is deposited at 45° incidence angle and perpendicular to the long dimension of the 1- μm -long slit.

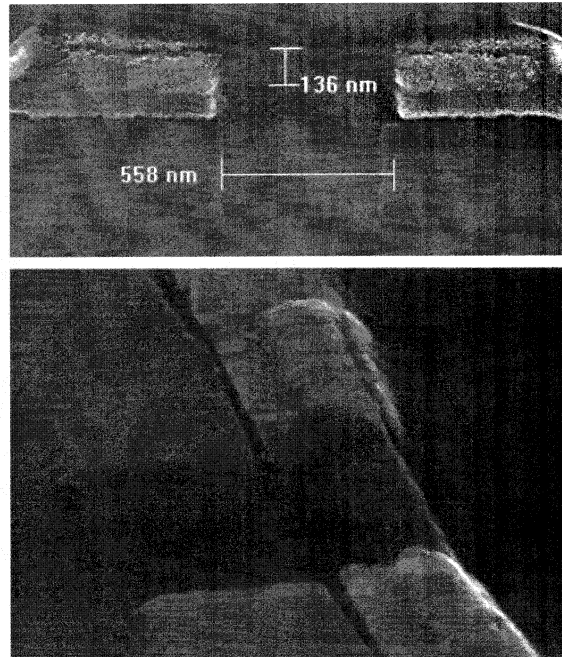


Fig. 3. SEM image of a Ti nanosensor. Top view: the Ti nanosensor with dimensions $0.04\mu\text{m} \times 0.14\mu\text{m} \times 0.56\mu\text{m}$ is flanked by Nb current leads (Ti is dark gray and Nb is light gray). The rest of Ti film is separated from the Ti nanosensor and Nb leads by trenches, which are clearly seen on the bottom microphotograph taken at an angle.

which translates into $C_e(0.3 \text{ K}) \sim 10^{-19} \text{ J/K}$. For such a nanosensor, the predicted NEP can be $10^{-19} \text{ W/Hz}^{1/2}$ at $T \approx 0.3 \text{ K}$ and $10^{-20} \text{ W/Hz}^{1/2}$ at $T \approx 0.1 \text{ K}$ [12]. However, even a record long $\tau_{e-ph} \sim 20 \text{ ms}$ measured in thin Hf and Ti films at 40 mK [18] is insufficiently long for integrating photons with $N_{ph} \sim 100 \text{ s}^{-1}$.

Equation (2) assumes that the electron-phonon relaxation is the only mechanism of energy dissipation. To prevent the energy flow from the antenna-coupled nanosensor, the electrical leads to the nanostructure should be made of a superconductor with a sufficiently large superconducting gap: in this case, while electrical current can freely flow across the normal metal-superconductor interface, the outdiffusion of “hot” electrons is blocked by Andreev reflection. The detector design should also ensure the suppression of photon emission by electrons in the frequency range corresponding to the operating temperature 0.3K ($\sim 10 \text{ GHz}$) [20]; this, however, can be achieved simultaneously with a good impedance match between the sensor and the embedded circuit.

We have been systematically working on the realization of ultra-sensitive HEDDs for a number of years [12,18,21,22] and recently achieved the expected thermal characteristics in nanoscale Ti HEDDs with Nb Andreev contacts.

A. Fabrication procedure

The HEDD element is a transition edge nanosensor made from thin Ti film with superconducting transition temperature $T_C \sim 0.2\text{-}0.4 \text{ K}$. The current leads to the nanosensor are fabricated from Nb films with $T_C \sim 8.5 \text{ K}$; a large superconducting gap in Nb blocks outdiffusion of “hot” electrons to the current leads. The nanostructure is fabricated on a silicon substrate using electron-beam

lithography and e-gun deposition of Ti and Nb. For the fabrication of an oxide-free Ti/Nb interface, we have used the so-called "shadow mask" technique: Ti and Nb films were sequentially deposited at different angles through a "shadow" mask without breaking vacuum. An SEM image of a "shadow" mask is shown in Fig. 2. After developing the resist, the substrates were mounted in an oil-free deposition system with a base pressure $\sim 1 \times 10^{-9}$ mbar equipped with a cryo-pump and sorption pumps. To reduce substrate/resist heating in the process of deposition of Nb (melting $T = 2468^\circ\text{C}$), the substrate holder was positioned at a large distance from the e-gun source (~ 40 cm). The substrate holder can tilt the substrate at an angle with respect to the direction to the e-gun source. Thin Ti film was deposited at a deposition rate $\sim 1.5\text{-}3$ nm/s along the direction normal to the plane of the substrate, Nb was deposited at a rate 0.5 nm/s along the direction which was at a 45° angle to the substrate and perpendicular to the long dimension of the nanosensor. Because the resist thickness exceeds the width of the narrow channel, Nb film covers only the ends of the Ti nanosensor.

A Ti device with typical dimensions is shown in Fig. 3. Among different tested devices the normal-state resistance ranges between 50-100 Ohm and the critical temperature is between 0.2-0.4 K. The minimum device width is set by the e-beam lithography. Further reduction of the device length is problematic: for nanosensors with length comparable to the thermal length $L_C = \sqrt{\hbar D/k_B T}$, where D is the diffusion constant, the superconducting transition temperature will be significantly increased due to the proximity effect between Ti nanosensor and Nb current leads. For the studied Ti films with diffusion constant $D \sim 4$ cm²/s, L_C is of the order of 0.1 μm at $T = 0.3\text{K}$. Also, if the length of the Ti nanosensor is smaller than the electron thermalization length, the frequency-dependent response and drop in sensitivity might be expected at $\hbar\nu > \Delta\text{Nb}$ ($\nu > 0.3$ THz). For this reason we do not make HEDD devices shorter than ~ 0.5 μm .

B. Measurement of the thermal conductance

Measurements of the thermal conductance G have been performed in the dilution refrigerator equipped with several stages of low-pass electrical filters thermally anchored to the 1K pot and mixing chamber; the filters were designed to suppress both the low-frequency interferences and rf noise over the frequency range from kHz to several GHz. Because of high sensitivity, the devices can be overheated above their superconducting transition temperature by electromagnetic noise with the power $\delta T_C C_e / \tau_{e-ph} \leq 1$ fW.

Figure 4 illustrates the measurement of the thermal conductance $G = C_e / \tau_{e-ph}$ between the electrons in a nanosensor and the thermal bath. The resistance of devices was measured by an AC (13 Hz) resistance bridge using a small (typically, 0.1-1 nA) measuring current. The Ti nanosensor was slightly heated by a DC current, and the difference between the electron temperature T_e and the equilibrium bath temperature T_{ph} was determined by observing the temperature shift of the superconducting transition. This method assumes that the non-equilibrium electron distribution function can be characterized with an effective electron temperature. This assumption is valid at

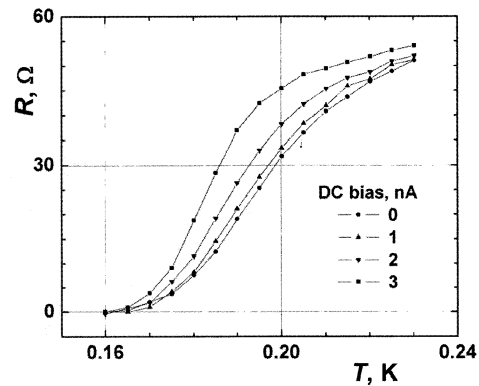


Fig. 4. Measurements of the thermal conductivity between the electrons in a Ti HEDD device with dimensions $0.04\mu\text{m} \times 0.14\mu\text{m} \times 0.56\mu\text{m}$ and the thermal bath. The shift of the superconducting transition is caused by the Joule heat generated in the sample by the DC bias current.

sub-Kelvin temperatures, where the electron-electron scattering rate in thin films exceeds by many orders of magnitude the electron-phonon scattering rate [13]. To measure G at $T < T_C$ the superconducting transition is suppressed to lower temperatures by applying a magnetic field perpendicular to the plane of the nanosensor. The thermal conductivity was found from the balance equation:

$$RI_{DC}^2 = G(T_e)(T_e - T_{ph}), \quad (3)$$

which holds if $T_e - T_{ph} \ll T_{ph}$. For the device with dimensions $0.04\mu\text{m} \times 0.14\mu\text{m} \times 0.56\mu\text{m}$ (Fig. 3), we obtained $G(0.3\text{K}) = 4 \times 10^{-14}$ W/K. The value of G normalized to volume $G(0.3\text{K})/V = 1.2 \times 10^7$ W/(K·m³) agrees very well with the corresponding value of G/V measured for much larger meander-patterned Ti films with dimensions $0.04\mu\text{m} \times 5\mu\text{m} \times 100,000\mu\text{m}$ (note that the length of 10 cm for the latter structures is much greater than the diffusion length over the electron-phonon relaxation time, $L_{e-ph} = (D\tau_{e-ph})^{1/2}$). The scaling of G with the sensor volume (over 6 orders of magnitude) provides an experimental proof that in both types of structures, the nanostructures with superconducting contacts and much larger Ti meanders, the dominant mechanism of energy dissipation at $T = 0.3\text{K}$ is electron-phonon scattering, and that the energy relaxation due to outdiffusion of hot electrons can be neglected. The measured values of G are in good agreement with the estimate of G on the basis of the theory of electron-phonon energy relaxation in disordered conductors [17] and our previous measurements of the electron-phonon relaxation rate in disordered Ti films [18].

C. Modeling of the device performance

The Ti HEDD will operate in the voltage-biased TES mode; that is, its operating temperature will be somewhat lower than T_C , and the resistance at the operating point, R , will be much smaller than the normal resistance R_N . This biasing mode enables the device to simultaneously match to the antenna impedance and couple well to the SQUID. Indeed, if the DC resistance at the operating point is ~ 1 Ω , the device Johnson noise would exceed the noise of a typical DC SQUID; at the same time, a much higher impedance of

the device in the THz range (~ 50 - 100Ω) facilitates coupling of the device to a planar antenna. The signal photon will be absorbed and increase the electron temperature in the nanosensor. The increase in electron temperature will cause the current to decrease, and will be registered by the SQUID-based readout. The response time of these devices is controlled by the electron-phonon energy relaxation time τ_{e-ph} (~ 5 - $20 \mu\text{s}$ at 0.3K , depending on disorder in Ti films and substrate material). If necessary, the response time can be further reduced by using the negative electrothermal feedback (ETF) [23]: $\tau = \tau_{e-ph}/(1+L)$, where L is the ETF loop gain.

In the photon integrating mode, the thermal-fluctuations-limited NEP for the developed HEDD with dimensions $0.04\mu\text{m} \times 0.1\mu\text{m} \times 0.5\mu\text{m}$ will be less than $3 \times 10^{-19} \text{ W/Hz}^{1/2}$ at 0.3 K (see Eq. 2).

Since the time constant of the detector is not sufficiently long to integrate the background photons arriving at a rate $< 100 \text{ s}^{-1}$, the photon-counting mode should be used to achieve the highest sensitivity at $\nu > 1 \text{ THz}$. This case has been considered some of us earlier [7]. The analysis show that for the device with dimensions $0.04\mu\text{m} \times 0.1\mu\text{m} \times 0.5\mu\text{m}$, the energy resolution at 0.3K , δE , corresponds to the "red boundary" $\nu_R = \delta E/h = 0.24 \text{ THz}$. The dynamic range $(\tau N_{ph}^{1/2})^{-1} \sim 50 \text{ dB}$ ($N_{ph}^{1/2}$ is the minimum signal which can be distinguished from the background) and the detector NEP at 1 THz is less than $10^{-20} \text{ W/Hz}^{1/2}$ if the discrimination threshold $E_T \approx 3.5 \delta E$.

III. CONCLUSION

We have demonstrated a superconducting Hot-Electron Direct Detector with a record-low NEP = $3 \times 10^{-19} \text{ W/Hz}^{1/2}$ at 0.3 K . This operating temperature can be achieved by He3 sorption cooling; for comparison, similar sensitivity in the conventional bolometers can be realized only at 0.1K or below, which requires dilution refrigeration or adiabatic demagnetization cooling techniques. In its most sensitive photon counting mode, this detector would be suitable for a background limited spectrometer with moderate resolution ($R \sim 1000$) for SAFIR and other space-born far-IR telescopes with cryogenically cooled mirrors. For higher background applications (e.g., CMBPol), HEDD offers the background limited sensitivity at $T = 0.3\text{K}$. The hot-electron detectors have two other important advantages: (a) they are fabricated on bulk substrates, and (b) they have a very short time constant allowing for a high data rate. The HEDDs can be readily matched to a planar antenna since the device RF impedance is in the range 50 - 100Ω and the device size is much smaller than the wavelength. As with other transition-edge sensors, the HEDD is compatible with SQUID-based multiplexing read-out circuits

REFERENCES

[1] <http://safir.jpl.nasa.gov/technologies.shtml>.
 [2]. D.J. Benford and S.H. Moseley, "Cryogenic detectors for infrared astronomy: the Single Aperture Far-InfraRed (SAFIR) Observatory," *Nucl. Instr. Meth. Phys. Res. A* 520(1-3), 379-383 (2004).
 [3]. D. Leisawitz, "NASA's far-IR/submillimeter roadmap missions: SAFIR and SPECS," *Adv. Space Res.* 34(3), 631-636 (2004).

[4]. T. Nakagawa, "SPICA: space infrared telescope for cosmology and astrophysics," *Adv. Space Res.* 34(3), 645-650 (2004).
 [5]. J.J. Bock, P. Day, A. Goldin, H.G. LeDuc, C. Hunt, A. Lange et al., "Antenna-coupled bolometer array for astrophysics," *Proc. Far-IR, SubMM & MM Detector Technology Workshop, April 1-3, 2002, Monterey, CA*, 224-229.
 [6]. M. Kenyon, P.K. Day, C.M. Bradford, J.J. Bock, and H.G. LeDuc, "Background-limited membrane-isolated TES bolometers for far-IR/submillimeter direct-detection spectroscopy," *Nucl. Instr. & Meth. Phys. Res. A* 559, 456-458 (2006).
 [7]. B.S. Karasik and A.V. Sergeev, "THz Hot-Electron Photon Counter," *IEEE Trans. Appl. Supercond.* 15(2), 618-621 (2005).
 [8]. R.J. Schoelkopf, S.H. Moseley, C.M. Stahle, P. Wahlgren, and P. Delsing, "A concept for a submillimeter-wave single-photon counter," *IEEE Trans. Appl. Supercond.* 9(2), Pt.3, 2935-2939 (1999).
 [9]. A. Semenov, A. Engel, K. Il'in, G. Gol'tsman, M. Siegel and H.W. Hubers, "Ultimate performance of a superconducting quantum detector," *Eur. Phys. J. Appl. Phys.* 21(3), 171-178 (2003).
 [10]. S. Komiyama, O. Astafiev, V. Antonov, T. Kutsuwa, and H. Hirai, "A single-photon detector in the far-infrared range," *Nature* 403, 405-407 (2000); O. Astafiev, S. Komiyama, T. Kutsuwa, V. Antonov, Y. Kawaguchi, and K. Hirakawa, "Single-photon detector in the microwave range," *Appl. Phys. Lett.* 80(22), 4250-4252 (2002); H. Hashiba, V. Antonov, L. Kulik, S. Komiyama, and C. Stanley, "Highly sensitive detector for submillimeter wavelength range," *Appl. Phys. Lett.* 85(24), 6036-6038 (2004).
 [11]. K. Ikushima, Y. Yoshimura, T. Hasegawa, S. Komiyama, T. Ueda, and K. Hirakawa, "Photon-counting microscopy of terahertz radiation," *Appl. Phys. Lett.* 88, 152110 (2006).
 [12]. B.S. Karasik, W.R. McGrath, M.E. Gershenson, and A.V. Sergeev, "Photon-noise-limited direct detector based on disorder-controlled electron heating," *J. Appl. Phys.* 87(10), 7586-7588 (2000).
 [13]. E. M. Gershenson, M. E. Gershenson, G. N. Gol'tsman, A. D. Semenov, and A. V. Sergeev, "Heating of electrons in a superconductor in the resistive state by electromagnetic radiation," *Sov. Phys.-JETP* 59, 442-450 (1984).
 [14]. M. Nahum and J.M. Martinis, "Ultrasensitive hot-electron microbolometer," *Appl. Phys. Lett.* 63, 3075-3077 (1993).
 [15]. B. Cabrera, R.M. Clarke, P. Colling, A.J. Miller, S. Nam, R.W. Romani, "Detection of single infrared, optical, and ultraviolet photons using superconducting transition edge sensors," *Appl. Phys. Lett.* 73(6), 735-737 (1998).
 [16]. T.A. Lee, P.L. Richards, S.W. Nam, B. Cabrera, and K.D. Irwin, "A superconducting bolometer with strong electrothermal feedback," *Appl. Phys. Lett.* 69, 1801-1803 (1996).
 [17]. A. Sergeev and V. Mitin, "Electron-phonon interaction in disordered conductors: Static and vibrating scattering potentials," *Phys. Rev. B* 61(9), 6041-6047 (2000).
 [18]. M.E. Gershenson, D. Gong, T. Sato, B.S. Karasik, A.V. Sergeev, "Millisecond electron-phonon relaxation in ultrathin disordered metal films at millikelvin temperatures," *Appl. Phys. Lett.* 79, 2049-2051 (2001).
 [19]. B.A. Young, J.R. Williams, S.W. Deiker, S.T. Ruggiero, and B. Cabrera, "Using ion implantation to adjust the transition temperature of superconducting films," *Nucl. Instr. Meth. Phys. Res. A* 520, 307-310 (2004).
 [20]. D.R. Schmidt, R.J. Schoelkopf, and A.N. Cleland, "Photon-Mediated Thermal Relaxation of Electrons in Nanostructures," *Phys. Rev. Lett.* 93, 045901 (2004).
 [21]. B.S. Karasik, B. Delact, W.R. McGrath, J. Wei, M.E. Gershenson, and A.V. Sergeev, "Experimental Study of Superconducting Hot-Electron Sensors for Submm Astronomy," *IEEE Trans. Appl. Supercond.* 13(2), 188-191 (2003).
 [22]. B.S. Karasik, A.V. Sergeev, D. Olaya, J. Wei, M.E. Gershenson, J.H. Kawamura, and W.R. McGrath, "A Photon Counting Hot-Electron Bolometer for Space THz Spectroscopy," *Proc. 16th Int. Symp. Space Terahertz Technol., May 2-4, 2005, Gothenburg, Sweden*, 543-548.
 [23]. K.D. Irwin, "An application of electrothermal feedback for high resolution cryogenic particle detection," *Appl. Phys. Lett.* 66, 1998-2000 (1995).

To the Sensitivity Estimation of TES Bolometers for SubMM Radiation Detection Operating at Super Low Temperatures

Alexander N. Vystavkin, Alla G. Kovalenko, Ilya A. Cohn

Abstract – The electron energy balance equation was modified to take into account the effect of transfer of hot electron power from TES bolometer absorber combined with the sensor to the biasing circuit with the electron current. Estimation calculations have shown that the power flow connected with said transfer is negligibly small in comparison with the hot electron power transfer to the thin metal film structure and substrate through electron-phonon interactions for studied earlier molybdenum-copper bi-layer thin film structures in 0.08 – 0.4 K temperature range [1]. The obtained equation was used to estimate a ratio of current decrement to incident radiation power (current sensitivity) of the TES bolometers as well. There were no significant reducing changes in the TES bolometers current sensitivity found at fixed bias voltage across the absorber for the studied structures except the case at temperatures 0.3 K and less and, especially, at absorber lengths 1 μ and less when the current sensitivity gain of order of several tens have been calculated.

Keywords—Astronomy, millimeter- and submillimeter-wave detectors, superconducting devices, transition edge sensor (TES) bolometers.

I. INTRODUCTION

BI-LAYER Mo/Cu structures showing the superconducting transition with critical temperature tailored by layer thicknesses can be used as the basis for the constructing supersensitive transition edge sensor (TES) hot-electron bolometers with combined absorber-sensor [1]. The results of measurements of resistance temperature dependences of such structures were reported at previous Symposium ISSTT-16 [1]. Using said dependences and the electron energy balance equation [2, 1]

$$P_J = U \cdot I = \Sigma \nu (T_e^5 - T_{ph}^5), \quad (1)$$

IV- and power-voltage curves of possible bolometers on the basis of measured Mo/Cu structure samples and then parameters of possible bolometers were calculated. In (1) U is the fixed bias voltage, I is the bias current, T_e is the hot-electron temperature, T_{ph} is the temperature of phonons, i.e. of the thin metal film and substrate, $\Sigma \cong 3 \text{ nW} \cdot \text{K}^{-5} \cdot \mu\text{m}^{-3}$ is the material parameter taken from [3] where the electron energy balance equation for thin normal metal film bolometer on Si

Manuscript received May 10, 2006. This work was supported in part by the Program No 29 "Electromagnetic waves of the Terahertz band" of Russian Academy of Sciences.

Authors A. N. Vystavkin (corresponding author: phone: 7-095-203-25-05; fax: 7-095-203-84-14; e-mail: vyst@hitech.cplire.ru), A. G. Kovalenko and I. A. Cohn are with the Institute of Radioengineering and Electronics of Russian Academy of Sciences, 11 Mokhovaya Street, 125009 Moscow, Russian Federation.

substrate at the same temperatures has been studied, $\nu \mu\text{m}^3$ is volume of the bolometer absorber. Definitions for (1) and details of calculations are given in [1] and summary of measured parameters of samples and calculated characteristics of possible bolometers are given in Table I.

II. ESTIMATION OF EFFECT OF HOT ELECTRON POWER FLOW-OUT FROM ABSORBER-SENSOR TO THE BIASING CIRCUIT

Mentioned above calculations are made under set of assumptions [1] one of which is that absorber-electrode contacts provide Andreev reflection [4] blocking hot electron power flow-out from the absorber-sensor to the bias circuit. What will happen when contacts will be not Andreev ones but ordinary? To answer this question one may take as a basis the expression for thermal capacity of electrons in metals [5]

$$C_v = \frac{\pi^2}{2} \cdot \frac{Nk^2T_e}{E_F(0)} \text{ J/K}, \quad (2)$$

where N is amount of electrons for which the thermal capacity is to be determined, $k \approx 1,38 \cdot 10^{-23}$ J/K is Boltzman constant, T_e K is electron temperature, $E_F(0)$ is Fermi energy equal for metals at low temperatures $E_F(0) = 1 \dots 10$ eV [5]. We consider N as an amount of electrons entering absorber-sensor and leaving it simultaneously per second as a current. If so, we may express N through the current I A:

$$N = I / e \text{ s}^{-1}, \quad (3)$$

where I C/s is electrical current, $e \cong 1.6 \cdot 10^{-19}$ C is electron charge. Taking into account that the temperature of entering electrons is T_{ph} K i.e. the temperature of the thin metal film and substrate (phonons) and the temperature of leaving (hot) electrons is T_e we may obtain from (2) and (3) expressions for powers leaving the absorber-sensor together with hot electrons and entering it together with bias current:

$$P_e = \frac{\pi^2}{2} \cdot \frac{Ik^2T_e^2}{eE_F(0)} = \beta IT_e^2, \quad P_{ph} = \frac{\pi^2}{2} \cdot \frac{Ik^2T_{ph}^2}{eE_F(0)} = \beta IT_{ph}^2 \text{ W}, \quad (4)$$

$$\text{where } \beta = \frac{\pi^2}{2} \cdot \frac{k^2}{eE_F(0)}. \quad (5)$$

Adding the difference $(P_e - P_{ph})$ to the right side of (1) we obtain the electron energy balance equation for the case when the effect of hot electron power flow-out from the absorber-sensor to the bias circuit is present:

Table I

Sample	Sample thicknesses, nm		T_c , K	R_n , Ohm	$\alpha = \frac{T}{R} \cdot \frac{dR}{dT}$	U , μ V	S_I , A/W	NEP , $W/Hz^{1/2}$
	Mo	Cu						
1	2	3	4	5	6	7	8	9
a	12	0	0,93	67	1070	-	-	-
b	15	35	0,4	2,9	150	10^{-7}	10^7	$4 \cdot 10^{-19}$
c	12	35	0,27	2,6	320	10^{-8}	10^8	$4 \cdot 10^{-20}$
d	12	100	0,08	0,6	510	10^{-9}	10^9	$4 \cdot 10^{-21}$

(1 - 6) - for $15 \times 1.5 \text{ mm}^2$ samples, (7 - 9) - for $8 \times 0.8 \text{ }\mu\text{m}^2$ possible bolometers. $S_I = |\Delta I| / P_{rad} = 1/U$, $NEP = \sqrt{i_{noise}^2} / S_I$, $\sqrt{i_{noise}^2}$ is the rms noise current of SQUID readout-amplifier next to the bolometer. In our case $\cong 4 \cdot 10^{-12} \text{ A/Hz}^{1/2}$

$$P_J = U \cdot I = \Sigma \nu (T_e^5 - T_{ph}^5) + \beta I (T_e^2 - T_{ph}^2). \quad (6)$$

Calculations have shown that the value of second member in right side of equation (6) is not higher than 1% of the first member for all values of $R(T_e)$, U , T_e , T_{ph} (two latter $\sim T_c$) in operating points given in Table I and for minimal of above-mentioned value of Fermi energy $E_F(0) = 1 \text{ eV} = 1,6 \cdot 10^{-19} \text{ J}$. This correlation remains at the reducing of transverse dimensions of possible bolometers down to $0.8 \times 0.08 \text{ }\mu\text{m}^2$. Described situation means that the hot electron power flow-out with the electrical current in our considered Mo/Cu structures case is more than two orders less intensive of the hot electron power flow-out owing to the electron-phonon interactions. It is easy to explain: second power flow-out takes place through relatively small contact areas when first one takes place through whole absorber-sensor volume. By this reason IV- and power-voltage curves calculated in [1] for bolometers with Andreev contacts will not differ noticeably from similar curves when contacts are not of Andreev type but ordinary.

Now with the purpose to estimate the current sensitivity and NEP of considering bolometers for the case when two mechanisms of hot electron power flow-out are acting we add to (1) in a similar way with [1] a radiation power P_{rad} to Joule power $U \cdot I$ and small additions ΔI and ΔT for current and temperature:

$$U(I + \Delta I) + P_{rad} = \Sigma \nu [(T_e + \Delta T)^5 - T_{ph}^5] + \beta(I + \Delta I) [(T_e + \Delta T)^2 - T_{ph}^2]. \quad (7)$$

We assume that like in [1] the fixed bias voltage U is applied to absorber-sensor what provides the negative electrothermal feedback action in electron system [2]. The equation for small values can be extracted from (7):

$$U \Delta I + P_{rad} \cong 5 \Sigma M T_e^4 \Delta T + \beta (T_e^2 - T_{ph}^2) \Delta I + 2 \beta I T_e \Delta T. \quad (8)$$

After simple transformation $\frac{U}{R + \Delta R} \cong \frac{U}{R} - \frac{U \Delta R}{R^2} = I - I \cdot \frac{\Delta R}{R} = I + \Delta I$ we have $\Delta I = -I \cdot \frac{\Delta R}{R}$ and $\frac{\Delta R}{R} = -\frac{\Delta I}{I}$. Then taking into account the relation $\alpha \cong (T_e / R) \cdot (\Delta R / \Delta T_e)$ (see Table I) one obtains $\Delta T \cong \frac{1}{\alpha} T \frac{\Delta R}{R} \cong -\frac{1}{\alpha} T \frac{\Delta I}{I}$. Substituting obtained expression for ΔT to (8) and taking into account values of α given in Table I one may see that members containing ΔT are negligibly small in comparison with other ones and we can write:

$$U \Delta I + P_{rad} \cong \beta (T_e^2 - T_{ph}^2) \Delta I. \quad (9)$$

We consider at first the case when contacts to the absorber-sensor are made of a superconductor with high critical temperature providing the Andreev reflection of electrons in the absorber-sensor from these contacts. In this case the member in right side of (9) is absent and we have:

$$U \Delta I + P_{rad} \cong 0. \quad (9')$$

One can obtain from (9') the expression for S_I (see Table I).

In this given point we consider in more details the action of said above negative electrothermal feedback in electron system of absorber-sensor [2]. The fixed bias voltage and very sharp dependence of the absorber-sensor resistance on electron temperature (see [1]) leads to the arising of an electron thermostat. When a deviation of electron temperature takes place in this thermostat by any reason this deviation leads to the variation of the absorber-sensor resistance and consequently of the current through it. This current variation has such direction that the change of dissipated Joule power $U \Delta I$ compensates the variation of electron temperature. For instance when the reason of electron temperature variation is the incident radiation power P_{rad} absorbed by the absorber the Joule power change $U \Delta I$ is equal to P_{rad} with opposite sign. The described mechanism of negative electrothermal feedback was discovered by Irvin [2]. Described consideration will be useful in subsequent discussion.

We return to the equation (9). One factor is more now in the electron thermostat operation [see (6)]. This is the hot electron power flow-out with the electrical current, i. e. $\beta I (T_e^2 - T_{ph}^2)$. The corresponding member $\beta (T_e^2 - T_{ph}^2) \Delta I$ has appeared in (9). One may obtain the expression for bolometer current sensitivity from (9) when the hot electron power flow-out with the electrical current takes place:

$$S_I = \frac{-\Delta I}{U \Delta I - \beta (T_e^2 - T_{ph}^2) \Delta I} = \frac{1}{U(1 - \eta)}, \quad (10)$$

$$\text{where } \eta = \frac{\beta (T_e^2 - T_{ph}^2)}{U}. \quad (11)$$

One may see from (10) that in considered case the bolometer current sensitivity is gained in comparison with the case when the hot electron power flow-out to the bias circuit is absent owing to the blocking it by Andreev reflection. This gain is explained by the action of negative electrothermal feedback. The member $\beta (T_e^2 - T_{ph}^2) \Delta I$ in (9)

reduces the hot electron power flow-out with the electrical current owing to the reducing of this current for value ΔI . This means that hot electron temperature is increasing. As a result of this increasing the negative electrothermal feedback increases the value of current reducing more. Something similar to iterative process is arising and stops when the power equilibrium will be restored, i. e. the equation (9) will be satisfied. To estimate η determined by (11) and then current sensitivity gain determined by (10) one has to know the Fermi energy $E_F(0)$ and to calculate β . We estimate η for lower value $E_F(0)$ of given above ones, i.e. $E_F(0) = 1 \text{ eV} = 1,6 \cdot 10^{-19} \text{ J}$. Results of estimation using temperatures and bias voltages given in Table I are summarized in Table II. The bolometers with dimensions $l \times w \sim 0.1 \times 0.2$ and $0.8 \times 0.08 \mu\text{m}^2$ based on the structures **c** and **d** respectively have $\eta \approx 0,98$ and gain ≈ 50 . In other cases η is small in comparison with unit and, consequently, current sensitivities and NEP's are practically the same as in the absence of the hot electron power flow-out to biasing circuit with electrical current (Table I).

Table II

Samples	Transverse dimensions of absorber-sensor $l \times w, \mu\text{m}^2$	η
b - d	$\sim 80 \times 8$	$\sim 0.01 \dots 0.02$
b - d	$\sim 8 \times 0.8$	$\sim 0.1 \dots 0.2$
c	$\sim 0.1 \times 0.2$	$\rightarrow 1$
d	$\sim 0.8 \times 0.08$	$\rightarrow 1$

III. CONCLUSION

- Modified electron energy balance equation containing the member taking into account the transfer of hot electron

power from TES bolometer absorber-sensor to the biasing circuit with the electron current is derived.

- Analysis made on the basis of this equation has shown that the hot electron power flow-out from the TES bolometer absorber-sensor to the bias circuit in case of bi-layer Mo/Cu thin film structures is negligibly small in comparison with the hot electron power flow-out from electron system to the metal film and substrate through electron-phonon interactions. This hot electron power flow-out to the bias circuit has not noticeable influence on IV- and power-voltage characteristics of TES bolometers.

- The hot electron power flow-out from the absorber-sensor to the bias circuit does not deteriorate the bolometer current sensitivity. On the contrary, at rather small transverse dimensions and low temperatures of bolometers it leads to the regenerative gain of the current sensitivity.

- To achieve a practical realization of the regenerative gain phenomenon the thorough investigation of material characteristics as well as fabrication technology and design development are needed.

REFERENCES

- [1] A. N. Vystavkin, A. G. Kovalenko, S. A. Kovtonyuk, Study of superconducting transition in a Mo/Cu thin film structure and estimation of sensitivity of SUBMM waveband region TES bolometers on the basis of such a structure, Proc. of 16-th Intern. Symp. on Space Terahertz Technology, Gothenburg, Sweden, 31 April - 4 May, 2005,
- [2] K. D. Irwin, An application of electrothermal feedback for high resolution cryogenic particle detection, Appl. Phys. Lett., 1995, 10 April, 66 (15), pp. 1998-2000.
- [3] D. V. Chouvaev, L. S. Kuzmin, M. A. Tarasov, P. Sundqvist, M. Willander, T. Claeson, Hot-electron microbolometer with Andreev mirrors for THz space applications, Proc. of 9th Intern. Symp. on Space Terahertz Technology, March 1998, Pasadena, CA, USA.
- [4] A. F. Andreev, Thermal conductivity of superconductors intermediate state, *Soviet Phys. ZhETP*, 1964, v. 46, # 5, pp. 1823-1828.
- [5] F. Pobell, Matter and Methods at Low Temperatures, Springer-Verlag, 1992.

Single Photon counting detector for THz radioastronomy.

M. Tarkhov¹, D. Morozov^{1,2}, P. Mauskopf², V. Seleznev¹, A. Korneev¹, N. Kaurova¹
I. Rubtsova¹, O. Minaeva¹, B. Voronov¹, and G. Goltsman¹.

¹Moscow State Pedagogical University, Moscow 119992, Russia

²Cardiff University, Cardiff, CF24 3YB, Wales, UK

Abstract — In this paper we present the results of the research on the superconducting NbN-ultrathin-film single-photon detectors (SSPD) which are capable to detect single quanta in middle IR range. The detection mechanism is based on the hotspot formation in quasi-two-dimensional superconducting structures upon photon absorption. Spectral measurements showed that up to $5.7 \mu\text{m}$ wavelength (52 THz) the SSPD exhibits single-photon sensitivity. Reduction of operation temperature to 1.6 K allowed us to measure quantum efficiency of $\sim 1\%$ at 60 THz. Although further decrease of the operation temperature far below 1 K does not lead to any significant increase of quantum efficiency. We expect that the improvement of the SSPD's performance at reduced operation temperature will make SSPD a practical detector with high characteristics for much lower THz frequencies as well.

Index Terms— Superconducting single photon detector, Hot spot, Infrared range, ultrathin films.

I. INTRODUCTION

The development of the terahertz instrumentation is closely connected with the improvement of terahertz radiation detectors. Although single-photon detection in terahertz range is very attractive for radioastronomy, realization of even middle infrared single-photon detection is still a challenging task. An increasing interest in the range of $3 \mu\text{m}$ - $5 \mu\text{m}$ (100THz - 60THz) is connected with the usage of the atmosphere window suitable for ground-based observation. Meanwhile such observation is significantly hampered by the Earth thermal background.

In our early papers we have already reported on the superconducting single-photon detector (SSPD) based on ultrathin NbN film that outperforms avalanche photodiodes and photomultiplier tubes by such parameters as counting rate, quantum efficiency and level of dark counts [1,2,3]. In this paper we report the result of our recent research on the quantum efficiency in the middle infrared range $3 \mu\text{m}$ - $5 \mu\text{m}$ (100THz - 60THz).

II. TOPOLOGY AND SSPD FABRICATION PROCESS.

The design of SSPD chip and the SEM image of the SSPD active area are presented in the figure 1. The SSPD consists of the sensitive element placed in the center of the chip between two golden contact pads designed for 50-Ohm coplanar transmission line.

The sensitive element of the SSPD is a narrow (80 - 120 nm) stripe patterned from 4-nm-thick NbN film as a meander-shaped structure covering a square area of $10 \times 10 \mu\text{m}^2$ with the filling factor up to 0.6 (the ratio of the area covered by NbN film to the whole area of the SSPD sensitive element). The total length of the meander reaches $\sim 500 \mu\text{m}$.

The superconducting NbN film used for SSPD fabrication is deposited on the sapphire substrate by reactive magnetron sputtering in the argon and nitrogen mixture. During the deposition process the substrate is heated up to 850°C temperature thus leading to the epitaxial growth of the film. The high quality of the film is proved by such parameters as surface resistance 400-500 Ohm/square, critical temperature $T_c = 10-11 \text{ K}$, and superconducting transition width $\Delta T_c \sim 0.3 \text{ K}$. The sensitive element of the SSPD is patterned by the direct electron beam lithography and reactive ion etching. [5].

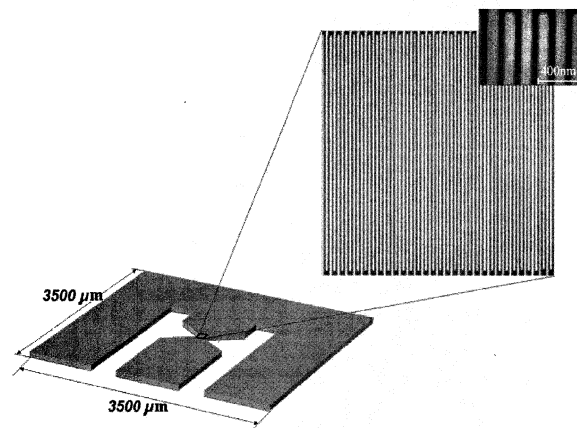


Fig. 1. Detector chip and photograph of SSPD sensitive element.

This work was partly supported by the INTAS project 03-51-4145. Funding from the European Commission is acknowledged under project "SINPHONIA", contract number NMP4-CT-2005-16433.

For optimal operation of the detector, it is important that the width of the superconducting stripe is uniform within the accuracy of several nanometers. Thus the reduction of the stripe edge nonuniformity allowed us to produce narrow enough stripe (80-120 nm), which lead to significant increase of the quantum efficiency.

III. SSPDS PHOTON-DETECTION MECHANISM

The single-photon detection mechanism by the superconducting stripe maintained at a temperature essentially below critical temperature and carrying current close to the critical is based on the local hotspot (normal region) formation in the place where a photon was absorbed [4].

Upon the absorption of a photon with the energy $\hbar\omega \gg 2\Delta$ by a Cooper pair a high energy (nonequilibrium) quasiparticle appears. Due to electron-electron interaction, secondary excited quasiparticles are created in the avalanche multiplication process with the characteristic electron-electron interaction time.

As the average energy of the quasiparticles reduces, the number of quasiparticles increases to the amount of $\hbar\omega/2\Delta$ by the order of magnitude, it leads to the local suppression of superconductivity and hotspot formation. The initial size of the hotspot, $2\lambda_T$ (λ_T is the thermalization length, i.e. the length at which the average energy of the excited quasiparticles reduces to the value of Δ), is determined by the ratio $\hbar\omega/2\Delta$, by the thermalization time of nonequilibrium quasiparticles τ_T (i.e. the time during which the average energy of excited quasiparticles decreases to Δ) and by the diffusivity of normal metal D . During the time by the order of magnitude equal to the thermalization time, the hotspot grows due to diffusion of hot electrons (quasiparticles) from the center of the hotspot. The growth of the hotspot leads to the extrusion of the supercurrent from the normal part of the film to the sides of the stripe. If the transport current density around the hotspot exceeds the critical current density the entire cross-section of the film becomes resistive leading to the appearance of a voltage pulse with amplitude proportional to the magnitude of the transport current. Subsequent recombination of the quasiparticles leads to the decrease of the hotspot and superconductivity restores.

IV. EXPERIMENTAL SETUP AND MEASURED RESULTS

A. Experimental setup.

To research how quantum efficiency of the SSPD depends on temperature in the 1.6 K - 4.2 K range we used a double-wall cryogenic insert for transport dewar (see fig. 2). The temperature below 4.2 K was achieved by pumping of the helium vapour from the insert. Controlling the helium vapour pressure we reached desired temperature which was measured by the previously calibrated pressure sensor.

SSPD was mounted to a 50-Ohm coplanar line which was, in turn, connected to a rigid coaxial cable. The SSPD was illuminated by LEDs (light emitting diodes) operated at

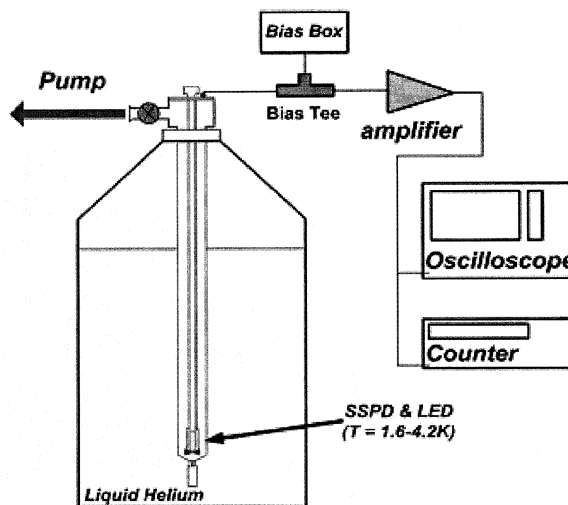


Fig. 2. Experimental setup for SSPD count measurements at 1.6K-4.2K temperature range for $3\mu\text{m}$ and $5\mu\text{m}$ wavelength.

cryogenic temperature which were mounted on the same holder with the SSPD.

DC biasing of the SSPD was performed with a home-built bias-T which consisted of a capacitor transmitting high frequency signal and a resistor of 20-100 Ohm in the DC arm of the bias-T. The response signal of the SSPD was amplified by room temperature amplifiers.

The voltage transients of the SSPD photoresponse were observed with the single-shot oscilloscope and were counted by the electronic counter. The SSPD was biased in the voltage source mode. The experimental setup is presented in the figure 2.

Broadband spectral characteristic of SSPD in the wavelength range of $0.6\text{-}5.7\mu\text{m}$ were also studied in an optical cryostat. Pumping of helium vapour from the cryostat allowed us to perform experiments in temperature range 3 K-5 K. As the monochromatic light source we used the infrared spectrometer. The radiation was delivered to the detector installed in the optical cryostat as a free-space propagating beam and was focused by a set of mirrors. We used sapphire (in the wavelength range $0.6\text{-}1\mu\text{m}$) or silicon (in the range $1\text{-}5.7\mu\text{m}$) input windows of the cryostat. Electronic read-out was the same as described above.

Quantum efficiency (QE) was determined as the ratio of electrical photoresponse pulses of the SSPD to the number of photons incident on the SSPD active area of $10 \times 10\mu\text{m}^2$. The power of LEDs was controlled by their bias current thus ensuring that it remains constant during the experiment. The power of the spectrometer was calibrated separately with a Golay cell.

For better accuracy of QE measurements, as a reference point we used the value of QE measured at $1.3\text{-}\mu\text{m}$ wavelength in a calibrated setup similar to one described in our previous publications [3].

B. Experimental Results.

Figure 3 presents QE vs. wavelength measured at 3 K and

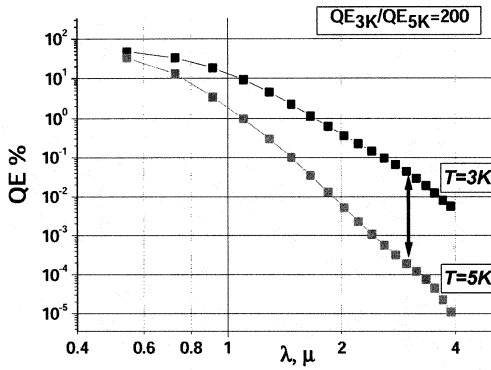


Fig. 3. Spectrum dependence of QE for SSPD at 3K and 5K both spectrum characteristics were researched at 0.94 I_c bias current.

5 K temperatures with infrared spectrometer as the light source. The SSPD transport current was equal to 0.94 I_c . We have shown that the decrease of the operation temperature significantly improves quantum efficiency in the middle infrared range, i.e. the ratio of quantum efficiencies at 3 μm wavelength (marked by an arrow in fig. 3) is more than two orders of magnitude.

The spectral sensitivity is strongly dependent on the SSPD transport current I_b , as well. The maximum QE was observed at currents very close to the critical current I_c (see fig. 4).

To determine how QE at 5- μm -wavelength depends on the temperature we used the experimental setup with cryogenic insert described above.

Figure 5 shows the temperature dependence of QE at different transport currents. One can see a significant increase of QE with the reduction of temperature from 5 K to 1.6 K. At transport current of 0.95 I_c it is of about two orders of magnitude whereas at $I_b=0.86I_c$ the increase of QE is almost four orders of magnitude. At temperature below 2 K one can see that the dependence of QE on temperature becomes less steep compared to higher temperatures. This trend is much clear for 3 μm wavelength and 0.4-2.5 K temperature range: figure 6 presents SSPD

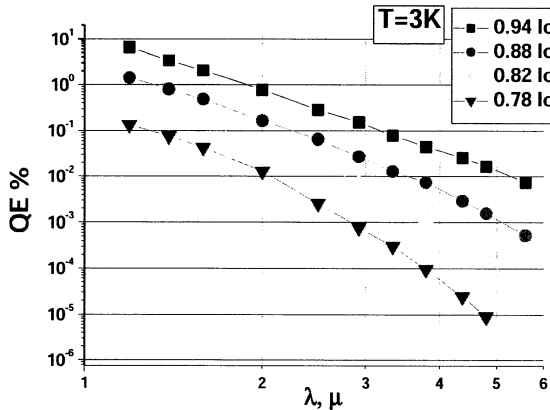


Fig. 4. Spectrum dependence SSPD at 3K temperature and different transport currents in range 0.78 to 0.94 of I_c .

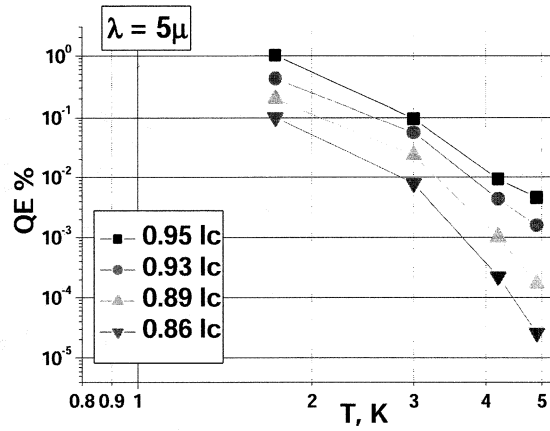


Fig. 5. QE versus temperature at the different bias current for 5 μm wavelength.

count rate measured at constant LED power and constant ratio of I_b/I_c .

To compare the SSPD with traditional integrating detectors at 5 μm wavelength we estimated the noise equivalent power (NEP) of the SSPD. For single-photon

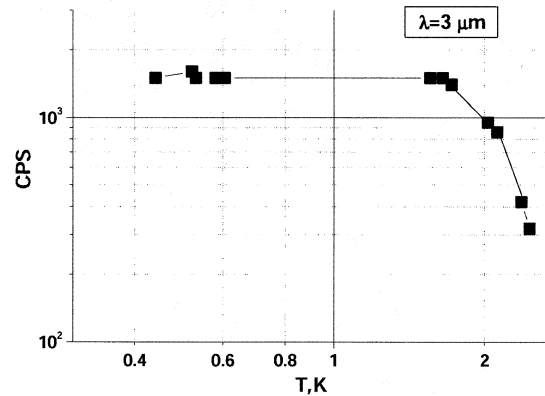


Fig. 6. Count per second versus temperature 3 μm wavelength.

detectors NEP is given by

$$NEP = \frac{h \cdot \nu}{QE} \cdot \sqrt{2R},$$

where $h\nu$ is the quantum energy, QE is quantum efficiency at a given wavelength and R is dark count rate. In [6] we reported that R exponentially drops with SSPD transport current decrease and at 2 K temperature the best measured value of R was $2 \times 10^{-4} \text{ s}^{-1}$ for $I_b/I_c=0.89$. Taking QE values from figure 5 we have the best NEP value of $8 \times 10^{-21} \text{ W/Hz}^{1/2}$ at 5 μm and bias current 0.89 I_c .

V. CONCLUSION

We have demonstrated that the reduction of operation temperature leads to significant improvement of the SSPD quantum efficiency in the middle infrared range. At operation temperature of 1.6 K, the SSPD exhibits quantum efficiency of 1% at 5 μm wavelength.. Taking into account

extremely low level of dark counts of $2 \times 10^{-4} \text{s}^{-1}$ we obtained noise equivalent power of $8 \times 10^{-21} \text{ W/Hz}^{1/2}$ at $5 \mu\text{m}$ wavelength (60THz). This makes SSPD a practical detector high frequency for THz astronomy.

REFERENCES

- [1] G. Gol'tsman, O. Okunev, G. Chulkova, A. Lipatov, A. Semenov, K. Smirnov, B. Voronov, A. Dzardanov, C. Williams, R. Sobolewski, "Picosecond superconducting single-photon optical detector" *Applied Physics Letters* 79 (2001): 705-707
- [2] A. Verevkin, J. Zhang, R. Sobolewski, A. Lipatov, O. Okunev, G. Chulkova, A. Korneev, K. Smirnov, G. Gol'tsman, A. Semenov, "Detection efficiency of large-active-area NbN single-photon superconducting detectors in ultraviolet to near-infrared range.", *Applied Physics Letters*, v. 80, №25, pp.4687-4689, 2002.
- [3] A. Korneev, P. Kouminov, V. Matvienko, G. Chulkova, K. Smirnov, B. Voronov, and G. N. Gol'tsman, M. Currie, W. Lo and K. Wilsher, J. Zhang, W. Slysz, A. Pearlman, A. Verevkin, and Roman Sobolewski, "Sensitivity and gigahertz counting performance of NbN superconducting single-photon detectors", *Applied Physics Letters* volume 84, number 26, 28 June 2004, pp 5338-5340
- [4] A. Semenov, G. Gol'tsman, A. Korneev, "Quantum detection by current carrying superconducting film", *Physica C*, 352 (2001) pp. 349-356
- [5] G. N. Gol'tsman, K. Smirnov, P. Kouminov, B. Voronov, N. Kaurova, V. Drakinsky J. Zhang, A. Verevkin, and R. Sobolewski, "Fabrication of Nanostructured Superconducting Single-Photon Detectors," *IEEE Transactions On Applied Superconductivity*, Vol. 13, No. 2, June 2003, pp. 192-195
- [6] A. Korneev, V. Matvienko, O. Minaeva, I. Milostnaya, I. Rubtsova, G. Chulkova, K. Smirnov, B. Voronov, G. Gol'tsman, W. Slysz, A. Pearlman, A. Verevkin, R. Sobolewski, "Quantum efficiency and noise equivalent power of nanostructured, NbN, single-photon detectors in the wavelength range from visible to infrared", *IEEE Trans. on Appl. Supercond.*, (2005) 15(2), 571-574

Direct Detection and Interferometer Technologies in Terahertz Region

Hiroshi Matsuo

Abstract—Two innovative direct detection technologies in terahertz region are reviewed. One is superconducting direct detector and another is bolometric interferometer. Combination of the two technologies would be useful for high dynamic range imaging in terahertz frequencies. We have developed SIS photon detectors, which have band-pass response in the atmospheric window at 675 GHz. With 300 K background radiation, detectors operate under shot noise limit with NEP of about 10^{-15} W/Hz^{0.5} at 0.3 K. The same detector give NEP of 10^{-14} W/Hz^{0.5} at 4.2 K with thermal shot noise limit, which is better than 4.2 K bolometers. Integrated cryogenic readout is designed using GaAs-JFETs. We are also working on Multi-Fourier Transform interferometer (MuFT), which is a kind of bolometric interferometer. Martin-Puplett type interferometer with double input aperture is used to make aperture synthesis images in wide band with spectral and polarization information. Dynamic range of the obtained images are superior to heterodyne interferometers because of good u-v coverage owing to the wide frequency band. Combined with heliostat installed in Nobeyama Radio Observatory we made imaging experiments with astronomical sources. Installation of focal plane array of bolometric detectors or SIS photon detectors is planned to increase observing field of view appreciably.

Index Terms—superconducting direct detector, SIS photon detectors, focal plane array, bolometric interferometer, Martin-Puplett type interferometer, high dynamic range imaging

I. INTRODUCTION

DEVELOPMENT of direct detector technology is important because of their high sensitivity and broad frequency coverage as well as large number of detector pixels to make wide field observations. What is more important for terahertz imaging system is high dynamic range imaging not only for intensity scale but also for frequency coverage and field of view.

Direct detection systems have great advantage over heterodyne system for its simplicity and their sensitivity which is not limited by the heterodyne quantum limit. For this reason two dimensional array of TES bolometers and superconducting direct detectors have been developed. I will discuss on the importance of high dynamic range imaging system using superconducting direct detectors and bolometric interferometers. Both of these technologies have recently been applied for astronomical observations [1], [2].

This work was supported by grant-in-aid of the Japan Society of Promotion of Science No.13304015, 16204010 and 18206042.

H. Matsuo is with Advanced Technology Center, National Astronomical Observatory of Japan, Mitaka, Tokyo 181-8588 Japan (e-mail: h.matsuo@nao.ac.jp).

II. HIGH DYNAMIC RANGE IMAGING IN THZ REGION

A. Intensity Scale

For submillimeter-wave ground-based observation, atmospheric background is around 100 pW and background limited NEP is about 10^{-16} W/Hz^{0.5}. Hence, dynamic range of 10^6 is required. Observation from space requires NEP of 10^{-18} to 10^{-19} W/Hz^{0.5} to achieve background limited performance. For calibration purpose we would observe planet or asteroid which have 10-100 pW of input radiation power and high dynamic range of about 10^8 is required. These numbers are not easy to realize with bolometric detectors. Superconducting direct detectors have advantage over TES bolometer because of their quantum response with high dynamic range [3].

B. Frequency Coverage

Instantaneous frequency coverage of direct detectors is much larger than heterodyne receivers in terahertz frequencies. For spectroscopic observation with direct detectors, either Fourier transform spectrometer, grating spectrometer or Fabry-Perot spectrometer is used in front of focal plane detectors. The size of the spectrometer typically limit spectral resolution to about 100 MHz or $\nu/\Delta\nu < 10^4$ for 1 THz in case of Fourier transform spectrometers. Because spectrometers with direct detectors do not suffer from the quantum limit of heterodyne receivers, they can achieve higher performance at higher frequencies.

C. Field of View and Angular Resolution

Focal plane array of bolometric detectors are being built. However, for single dish observations, angular resolution is limited by the diffraction of the telescope aperture. Aperture synthesis interferometers give much higher angular resolution, but have limited field of view. It is not easy to install focal plane array of heterodyne interferometer with wide frequency coverage. On the other hand, bolometric interferometers combined with focal plane array is an attractive solution, which can be accommodated with focal plane array of direct detectors with wide frequency coverage.

D. High Fidelity Image

Combination of all the features discussed above result in high fidelity imaging in terahertz frequencies. This is the goal of our imaging instrument with superconducting direct detectors and bolometric interferometers, which could be applied to variety field of terahertz technologies [4].

III. SIS PHOTON DETECTORS

We have developed SIS photon detectors in submillimeter-wave, which are antenna-coupled superconducting direct detectors based on photon assisted tunneling of quasi-particle [5], [6]. Their input coupling is designed using distributed junction array to match atmospheric window at 675 GHz. Fig. 1 shows a schematic I-V curve of superconducting tunnel junction with and without photon illumination. When incident photon is coupled to antenna connected to each electrode of a tunnel junction, quasi-particle tunneling step is observed.

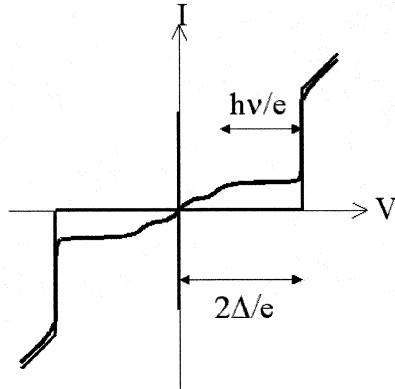


Fig. 1. Idealized current vs. voltage characteristics of SIS junctions, with no radiation input (thin line) and with input photon energy ($h\nu$) of about 2/3 of the gap energy (2Δ), where photon assisted tunneling step (thick line) is shown [3].

The current increase is observed so that one photon creates one quasi-particle tunnel through the junction. Responsivity of the SIS photon detector and their noise performance can be expressed as:

$$S = \eta \cdot \frac{e}{h\nu} \left[\text{A/W} \right] \quad (1)$$

$$N = \sqrt{2eI} \left[\text{A}/\sqrt{\text{Hz}} \right] \quad (2)$$

$$\text{NEP} = N/S = \frac{h\nu}{\eta} \cdot \sqrt{\frac{2I}{e}} \left[\text{W}/\sqrt{\text{Hz}} \right] \quad (3)$$

where η is a quantum efficiency and I is a leakage current. For leakage current of 100 pA and quantum efficiency of 0.5, we could get NEP of $3 \times 10^{-17} \text{ W/Hz}^{0.5}$. Actual performance we have measured for 650 GHz SIS photon detectors is quantum efficiency of 0.2 and optical NEP of $1.6 \times 10^{-16} \text{ W/Hz}^{0.5}$ [5].

One of the features of these detectors is that they work under shot noise limit under various operating conditions. Under background loading of effective temperature of 300 K, they show close to a shot noise limited performance with NEP of about $10^{-15} \text{ W/Hz}^{0.5}$ [1]. For operating temperature of 4.2 K, they also show shot noise limited performance of thermal leakage current of the tunnel junction and their NEP is about $10^{-14} \text{ W/Hz}^{0.5}$ [3].

Another feature is that SIS photon detectors have high saturation current of the order of 100 μA , and their dynamic range is expected to be larger than 10^9 [3], whereas measurement have shown that dynamic range is larger than 10^7 and can be used for variety of terahertz application fields

[4].

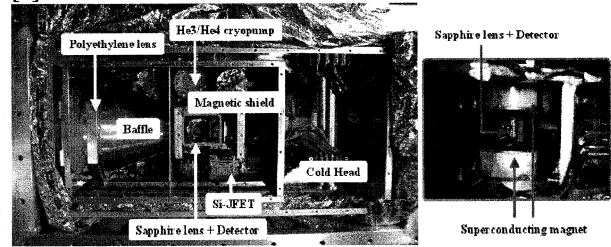


Fig. 2. Setup inside ASTE cryostat and close up view of detector part. Cryostat is cooled by GM cooler and He3-He4 sorption fridge. SIS photon detectors are installed at backside of hyper-hemispherical sapphire lens [1].

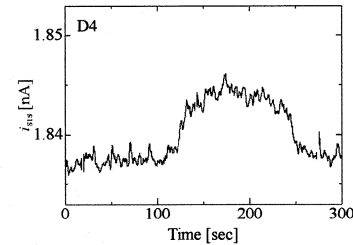


Fig. 3. Drift scan observation of the moon with SISCAM-9 in ASTE under estimated atmospheric transmittance of 1% [1].

We have fabricated 9-element array of 650 GHz SIS photon detectors and installed in a cryostat for submillimeter-wave astronomical observations. Fig. 2 shows the setup inside the cryostat. We call the observing system as SISCAM-9 or superconductive submillimeter-wave camera with nine detector element. SISCAM-9 is installed in a 10-m diameter submillimeter-wave telescope in Atacama, ASTE, Atacama Submillimeter Telescope Experiment [7].

The performance of SIS photon detectors in the ASTE cryostat is that their noise is about ten larger than the shot noise of input photo current through the junction that is 3 nA on average.

After we have made evaluation of I-V characteristics and noise measurement in ASTE, we have performed observation of moon, which is the first run to observe an astronomical source with superconducting direct detectors. Fig. 3 shows the drift scan measurement of the moon for one of the detector channel.

To realize large format array of SIS photon detectors, integrating amplifier with multiplexed readout is being developed using GaAs-JFET technology [8]. GaAs-JFETs operate as low noise device at 0.3 K with power dissipation of less than 1 μW . Using capacitive trans-impedance amplifier (CTIA) photo current of SIS photon detector can be integrated on feedback capacitor and the signal can be multiplexed.

IV. MUFT INTERFEROMETER

The multi Fourier transform interferometer, or MuFT, is an aperture synthesis bolometric interferometer with spectroscopic and polarization information [9]. Focal plane array could be used to increase observing field of view. Schematic presentation of MuFT is given in Fig. 4. Light collecting part, LiC, defines the baseline of the interferometer. Fourier interferometer part, FI, have two input polarizer and a beam combiner, each made of wiregrid for the Martin Puplett

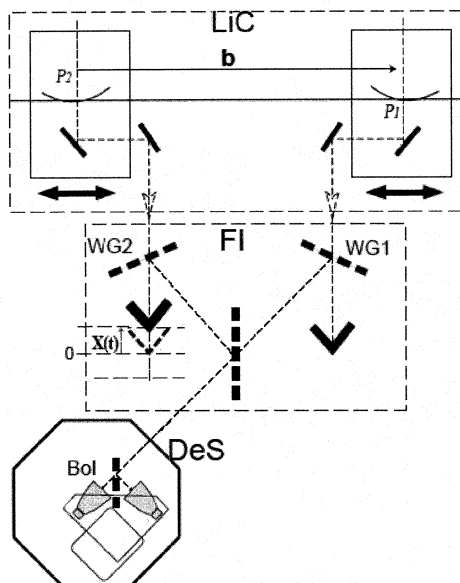


Fig. 4. Schematic optical arrangement of the MuFT. This is based on Martin-Puplett interferometer using wire grids as input polarizers and a beam combiner [9].

type interferometer. Dual polarization bolometric detectors can be used as detector and sampling part, DeS. Because the interferometer is Martin Puplett type with wiregrid polarizers, combination of wire direction gives independent measure of four stokes parameters, I, Q, U and V.

Actual optical setup of MuFT is shown in Fig. 5. The beam diameter is 50 mm and input beams coming from above are reflected by wiregrids aside to rooftop mirrors. The reflected beams then go through the wiregrid to the combiner to the left. One of the rooftop mirrors is continuously driven by a voice coil at right bottom in the figure.

We have made laboratory experiment to image a blackbody source to confirm the basic principle of MuFT interferometers with 1.5 K bolometers that operate from 100 GHz to 900 GHz. Because of the large frequency coverage of bolometric detectors, u-v sampling is good enough to get low sidelobe images even with limited number of baselines [10].



Fig. 5. Picture of the MuFT interferometer. Two input beams come from the top into the wire grid polarizers, then reflected aside to corner reflectors.

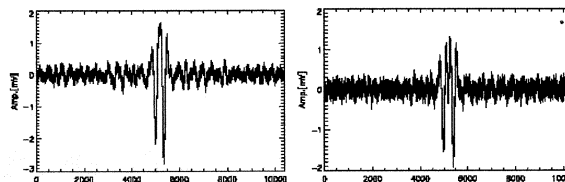


Fig. 6. Mutual coherence interferograms of the sun obtained by the MuFT with baseline lengths of 12 cm (left) and 16 cm (right) [2].

We have installed the MuFT with a heliostat in Nobeyama Radio Observatory. The heliostat has 700 mm diameter primary mirror and maximum baseline is about 400 mm, which is limited by optical configurations. Fig. 6 shows an example of mutual correlation interferogram obtained during observation of the sun. We used single element bolometer operating at 1.5 K. for the measurement. Frequency range of the detector is from 100 GHz to 900 GHz. But because of the limitation of atmospheric transmittance, observation is essentially made in millimeter-wave frequencies. Fourier transformation of these interferograms show the interference fringe is consistent with the size of the sun with different baseline spacing [2].

V. COMBINATION OF TWO TECHNOLOGIES

Although the developments of SIS photon detectors and MuFT interferometers are being done separately, combination of these technologies would enhance observing capability appreciably. Because MuFT interferometer is a direct detection interferometer, amount of data rate is small. Hence, focal plane imaging array can be easily accommodated with MuFT interferometer, that is identical to Fourier transform spectrometers with focal plan imaging array.

As an example, using two 1-m diameter telescopes with maximum baseline of 100 m in space and 1000-element focal plane array detectors at 1 THz with NEP of 10^{-18} W/Hz^{0.5}, we could achieve sensitivity of 100 μ Jy/Hz^{0.5} with observing field of view of more than 1000 arcmin² and angular resolution of less than 1 arcsecond. With MuFT interferometer, spectral and polarization information is also acquired. High dynamic range imaging in intensity scale, frequency range and observing field of view, could be achieved simultaneously.

VI. CONCLUSION

We have presented development of two direct detection technologies, which could be used to make high dynamic range imaging in terahertz frequencies. These technologies have already shown their performance as astronomical instrumentation. It is of great interest to combine these technologies for future high dynamic range imaging in terahertz frequency region.

ACKNOWLEDGMENT

The author acknowledge Terahertz development groups in NAOJ and RIKEN, and Hirohiko M. Shimizu of KEK for supporting developments of superconducting direct detectors. MuFT interferometer is being developed under collaboration between Tohoku University and NAOJ.

REFERENCES

- [1] Y. Mori et al., "Development of Superconductive Imaging Submillimeter-wave CAMera with nine detector elements (SISCAM-9)", 2006, Proc. SPIE 6275, in press.
- [2] I.S. Ohta et al., "Astronomical mm and sub-mm observations with Multi-Fourier Transform interferometer in 2005 and 2006", 2006, Proc. SPIE 6275, in press.
- [3] H. Matsuo et al., "Performance of SIS photon detectors for superconductive imaging submillimeter-wave camera (SISCAM)", 2006, Proc. SPIE 6275, in press.
- [4] S. Ariyoshi et al., "Terahertz imaging with a direct detector based on superconducting tunnel junctions", 2006, Appl. Phys. Lett. 88, 203503.
- [5] S. Ariyoshi et al., "Characterization of an STJ-based direct detector of submillimeter waves", 2005, IEEE Trans. Appl. Supercond. 15, 920-923.
- [6] H. Matsuo et al., "Design of wide-field submillimeter-wave camera using SIS photon detectors", 2004, Proc. SPIE 5498, 371-380.
- [7] H. Ezawa, R. Kawabe, K. Kohno, S. Yamamoto, "The Atacama Submillimeter Telescope Experiment (ASTE)", 2004, Proc. SPIE 5489, 763-772.
- [8] H. Nagata, J. Kobayashi, H. Matsuo, M. Fujiwara, "Progress on GaAs cryogenic readout circuits for SISCAM", 2006, Proc. SPIE 6275, in press.
- [9] I. S. Ohta, M. Hattori and H. Matsuo, "Development of Multi-Fourier Transform interferometer: Fundamental", 2006, Applied. Opt. 45, 2576-2585.
- [10] I. S. Ohta, M. Hattori, H. Matsuo, "Development of super broadband interferometer in FIR", 2004, Proc. SPIE 5487, 1563-1570.

Prototype finline-coupled TES bolometers for C_ℓOVER

Michael D. Audley, Robert W. Barker, Michael Crane, Roger Dace, Dorota Glowacka, David J. Goldie, Anthony N. Lasenby, Howard M. Stevenson, Vassilka Tsaneva, Stafford Withington, Paul Grimes, Bradley Johnson, Ghassan Yassin, Lucio Piccirillo, Giampaolo Pisano, William D. Duncan, Gene C. Hilton, Kent D. Irwin, Carl D. Reintsema, and Mark Halpern

Abstract— C_ℓOVER is an experiment which aims to detect the signature of gravitational waves from inflation by measuring the B-mode polarization of the cosmic microwave background. C_ℓOVER consists of three telescopes operating at 97, 150, and 220 GHz. The 97-GHz telescope has 160 feedhorns in its focal plane while the 150 and 220-GHz telescopes have 256 horns each. The horns are arranged in a hexagonal array and feed a polarimeter which uses finline-coupled TES bolometers as detectors. To detect the two polarizations the 97-GHz telescope has 320 detectors while the 150 and 220-GHz telescopes have 512 detectors each. To achieve the target NEPs (1.5, 2.5, and 4.5×10^{-17} W/√Hz) the detectors are cooled to 100 mK for the 97 and 150-GHz polarimeters and 230 mK for the 220-GHz polarimeter. Each detector is fabricated as a single chip to ensure a 100% operational focal plane. The detectors are contained in linear modules made of copper which form split-block waveguides. The detector modules contain 16 or 20 detectors each for compatibility with the hexagonal arrays of horns in the telescopes' focal planes. Each detector module contains a time-division SQUID multiplexer to read out the detectors. Further amplification of the multiplexed signals is provided by SQUID series arrays. The first prototype detectors for C_ℓOVER operate with a bath temperature of 230 mK and are used to validate the detector design as well as the polarimeter technology. We describe the design of the C_ℓOVER detectors, detector blocks, and readout, and present preliminary measurements of the prototype detectors' performance.

Index Terms— Submillimeter wave detectors, Finline transitions, Superconducting radiation detectors.

I. INTRODUCTION

A. Scientific motivation

THOMSON scattering of primaevial radiation in the early Universe can lead to linear polarization[1] in the cosmic microwave background (CMB). The polarization depends on

Manuscript received May 31, 2006. CLOVER is funded by the Particle Physics and Astronomy Research Council.

M. D. Audley (corresponding author: phone: +44(0)1223-337-309; fax: +44(0)1223-354-599; e-mail: audley@mrao.cam.ac.uk), R. W. Barker, M. Crane, R. J. Dace, D. Glowacka, D. J. Goldie, A. N. Lasenby, H. M. Stevenson, V. N. Tsaneva, and S. Withington are with the Cavendish Laboratory, University of Cambridge, JJ Thomson Ave, Cambridge, CB3 0HE, UK.

P. K. Grimes, B. Johnson, and G. Yassin are with the Department of Physics, University of Oxford, Denys Wilkinson Building, Keble Road, Oxford, OX1 3RH, UK.

L. Piccirillo and G. Pisano are with the School of Physics and Astronomy, Cardiff University, 5, The Parade, Cardiff, CF24 3YB, Wales, UK.

W. D. Duncan and K. D. Irwin are with the National Institute of Standards and Technology, Boulder, CO 80305 USA.

M. Halpern is with the University of British Columbia, Department of Physics and Astronomy, 6224 Agricultural Rd., Vancouver, B.C., V6T 1Z1, Canada.

density fluctuations, and thus carries cosmological information which is complimentary to the well-studied temperature anisotropies of the CMB. The linear polarization may be decomposed into a curl-free part and a divergence-free part, denoted E- and B-mode respectively, by analogy with the electric field strength E and magnetic induction B . Linear density perturbations do not produce B-mode polarization, while tensor perturbations, as might be produced by gravitational waves, produce E- and B-mode polarization with similar amplitude[2], [3]. Thus, by measuring the B-mode polarization of the CMB with C_ℓOVER we hope to make an indirect detection of a background of primordial gravitational waves.

B. Overview of C_ℓOVER

The C_ℓOVER experiment is described in detail elsewhere[4]. C_ℓOVER consists of three telescopes observing at frequencies of 97, 150, and 220 GHz. The focal plane of each telescope will be populated by feed horns, each connected to a polarimeter. The polarimeter technology is yet to be determined. As part of the technology development program for C_ℓOVER we are constructing a Single Pixel Demonstrator. This instrument will contain six TES detectors, allowing us to evaluate different polarization technologies, as well as validating the detector design.

II. C_ℓOVER DETECTORS

A. Detector Requirements

For maximum sensitivity, we require that the detectors be background-limited, i.e. the contributions to the noise equivalent power (NEP) from the detectors and readout must be less than half of the photon noise from the sky:

$$NEP_{det}^2 + NEP_{ro}^2 \leq \frac{1}{4} NEP_{photon}^2 \quad (1)$$

Once the detectors are background-limited the only way to improve the sensitivity is to increase the number of detectors. C_ℓOVER's sensitivity requirements mean that we need 160 horns at 97 GHz and 256 each at 150 and 220 GHz. Because the polarimeter splits the power from each horn into two modes which must be measured independently, the number of detectors is twice this. We require a detector time constant of less than 1 ms. Also, the detectors must be able to absorb the power incident from the sky without saturation. This power is variable and depends on the weather. The power-handling

TABLE I
C_ℓOVER DETECTOR REQUIREMENTS AT THE THREE OPERATING
FREQUENCIES.

Centre Frequency (GHz)	Band (GHz)	Number of detectors	NEP Requirement (10^{-17} W/ $\sqrt{\text{Hz}}$)	Power Handling (pW)
97	82–112	320	1.5	6.7
150	127.5–172.5	512	2.5	11.5
220	195–255	512	4.5	18.8

requirement is for the detectors to be able to operate for 75% of the time at the site. The detector requirements are summarized in Table I.

B. Detector Architecture

The current configuration has a single TES on each chip, fed by a single finline. There are two main reasons for going against the current trend towards large monolithic arrays. First, because the focal plane is populated by feedhorns, the waveguides coming from the polarimeter are on a pitch which is much larger than the size of the detectors. The horn diameters are 18.4, 12.77, and 8.4 mm at 97, 150, and 220 GHz, respectively. A monolithic array would have large inactive areas between active elements, increasing the number of wafers that would have to be processed, and hence the cost and manufacturing time. Second, because high sensitivity is essential for achieving C_ℓOVER's science goals, we decided to fabricate each detector on a single chip so that good devices could be selected to guarantee that all the detectors in each focal plane are working. The chips are micromachined and diced by deep reactive ion etching (DRIE) at the Scottish Microelectronics Centre.

C. R.F. Design

To reach background-limited sensitivity C_ℓOVER's bolometers must have a high absorption efficiency. Power is coupled from the waveguide to the TES planar circuit using an antipodal finline taper consisting of two superconducting fins of Nb separated by 400 nm of SiO₂ [5], [6] (see Fig. 1). The lower Nb layer is 250 nm thick. The upper layer is 500 nm thick to ensure reliable lift-off patterning with the step over the oxide layer. The whole structure is deposited on one side of a 225- μm silicon substrate. Before the fins overlap, the thickness of the SiO₂ is much less than that of the silicon and the structure behaves as a unilateral finline. As the fins overlap, the structure starts to behave like a parallel-plate waveguide with an effective width equal to the overlap region. When the width of the overlap region becomes large enough for fringing effects to be negligible, a transition to a microstrip mode has been performed. The microstrip is then tapered to the required width. C_ℓOVER uses a 3- μm Nb microstrip with a characteristic impedance of 20 Ω to deliver power to the TES.

The detector chip's 225- μm silicon substrate loads the waveguide in which it sits, changing the waveguide impedance. To prevent reflections the chip has a tapered end

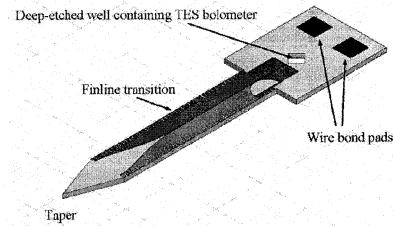


Fig. 1. Layout of prototype C_ℓOVER detector chip.

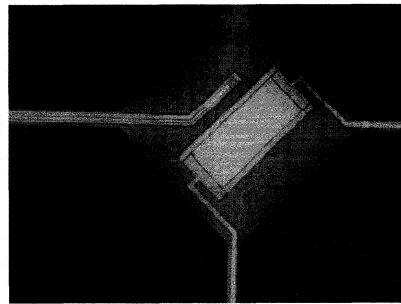


Fig. 2. C_ℓOVER prototype bolometer silicon nitride island showing TES and microstrip leading to termination resistor.

which provides a gradual impedance transition. The prototype detectors for the Single Pixel Demonstrator sit in a WR-10 waveguide and have a taper angle of 40°. This angle was chosen based on finite-element electromagnetic modelling.

D. Bolometer Design

C_ℓOVER's bolometers are low-stress silicon nitride islands suspended on four legs (see Fig. 2). The nitride is 0.5 μm thick. The thermal conductance to the thermal bath is controlled by the four nitride legs. The microstrip carrying power from the finline to the bolometer is terminated by a 20- Ω Au/Cu resistor which dissipates the incoming power as heat that the superconducting transition edge sensor (TES) can detect. A shunt resistor in parallel with the TES ensures that it is voltage biased so that it operates in the regime of strong negative electrothermal feedback [7]. For example, if the temperature drops, so does the resistance of the TES. Since it is biased at constant voltage, this means that the current, and hence the Joule power, will increase, heating up the TES. Conversely, if the temperature increases the resistance will increase, reducing the current, and thus the Joule heating. This means that the TES operates at a bias point that is in a stable equilibrium. Thus, the TES is self-biasing. There is no need for a temperature controller to ensure that it remains at the correct bias point. Also, the electrothermal feedback cancels out temperature fluctuations which has the effect of suppressing the Johnson noise.

The TES films in C_ℓOVER are Mo/Cu proximity-effect bilayers. The transitions of the bilayers can be made as sharp as 1–2 mK for high sensitivity. The sensitivity of the TES

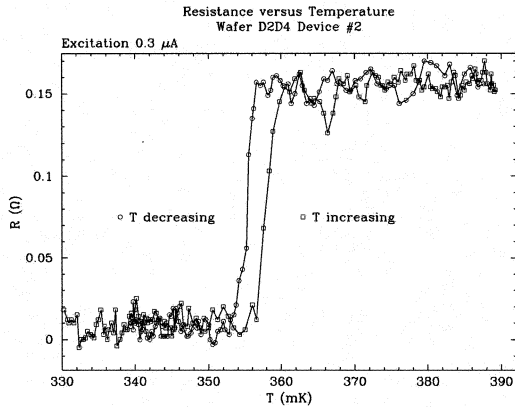


Fig. 3. Resistance versus temperature plot for one of the prototype C_eOVER detectors. The transition is about 3 mK wide from top to bottom.

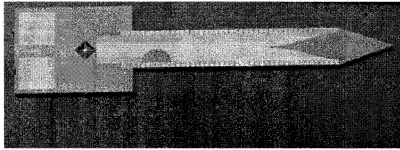


Fig. 4. Prototype C_eOVER detector chip. The chip is about 16 mm long.

shown in Fig. 3 is $\alpha = \frac{T}{R} \frac{dR}{dT} = \frac{d \log R}{d \log T} > 100$. We can also tune the transition temperature (T_c) of the films to the desired value by choosing the film thicknesses.

The operating temperature of C_eOVER 's detectors is chosen to meet the NEP requirements and is dominated by the phonon noise. Cooling is provided by a Cryomech PT-410 pulse-tube cooler, a high-capacity Simon Chase He-7 cooler, and a miniature dilution refrigerator[8]. Because a TES is a low-impedance device it is not very susceptible to microphonics, making it feasible to use a pulse-tube cooler. The 97 and 150-GHz detectors will operate with a base temperature of 100 mK and $T_c = 190$ mK, while the 220-GHz detectors require a base temperature of 230 mK and $T_c = 430$ mK.

All of the detectors for the Single Pixel Demonstrator have been fabricated and are undergoing testing. Figure 4 shows a prototype C_eOVER detector chip. We plan to carry out RF measurements of the C_eOVER detectors in the near future using a cryogenic black body source.

III. DETECTOR READOUT AND PACKAGING

A. Readout

Given the large number of detectors in this instrument (320 at 97 GHz and 512 each at 150 and 220 GHz) some form of multiplexing is needed to have a manageable number of wires from room temperature. We use 1×32 time-domain SQUID multiplexers[9], [10] fabricated by the National Institute of Standards and Technology. All the multiplexer chips in each of C_eOVER 's three telescopes share address lines, significantly reducing the number of wires needed to room temperature. The SQUID series arrays[11] that provide the third stage of amplification are mounted in eight-chip modules which provide

the necessary magnetic shielding. These modules are heat-sunk to the 4-K stage of the cryostat and they are connected to the multiplexer PCB with superconducting NbTi twisted pairs. Room-temperature multi-channel electronics (MCE), developed by the University of British Columbia, provide SQUID control and readout as well as TES bias. C_eOVER 's MCE is similar to that used by SCUBA-2[12].

B. Populating the Focal Plane

The feedhorns are arranged in a hexagonal array. However, the 1×32 multiplexer chips we are using lend themselves more naturally to a planar configuration where we have up to 16 horns in a row. We therefore had to come up with a compromise arrangement which would allow us to tile the focal plane efficiently. As shown in Fig. 5 we split the 97-GHz focal plane into three regions. Clockwise from upper right these are a 7×7 -horn parallelogram, an 8×7 -horn parallelogram, and an 8×8 -horn parallelogram. The two waveguides corresponding to each horn are arranged so that they are all parallel within one of these regions. This allows us to cover each region with linear detector blocks stacked on top of each other with an offset to match the hexagonal horn pitch. The orientation of one of these detector blocks is shown by a dark rectangle in each of the three regions. The main advantage of this arrangement is that it allows us to use identical detector blocks to cover a focal plane, reducing cost and complexity. The 97-GHz focal plane needs 22 detector blocks to cover it. The scheme for covering the 150- and 220-GHz focal planes is similar, except that the horns are arranged in a hexagon with a side of ten horns. This means that there are 28 detector blocks, each containing 20 detectors and one 1×32 multiplexer chip.

This scheme has the apparent disadvantage that we are under-using the 1×32 multiplexer chips by a factor of up to two, increasing the number needed. However, because we are not using all of the first-stage SQUIDs on a multiplexer chip, we can connect the detectors to those SQUIDs that have the most similar critical currents. This optimizes the first-stage SQUID biasing, reducing the noise contribution from this stage of the readout. Reducing the number of detectors multiplexed by each multiplexer chip also reduces the aliased readout noise, improving the NEP. Another advantage of under-using the multiplexer chips is that we can use chips where not all the first-stage SQUIDs are functioning, reducing the cost per chip.

C. Detector Block

The detector block comes in two halves, upper and lower. When these are put together they form split-block waveguides, into which the finlines protrude. The edges of the finlines stick into shallow slots in the sides of the waveguides for grounding. The serrations on the edges of the finlines (see Fig. 1) are there to prevent unwanted modes from propagating. A simplified view of a detector block holding four detectors is shown in Fig. 6.

Aluminium wire bonds provide electrical connections from the detector chip to a PCB carrying the multiplexer, inductors,

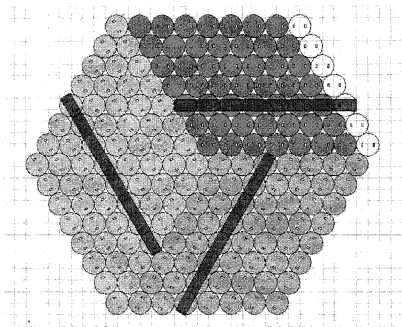


Fig. 5. Layout of 90-GHz focal plane. The dark rectangles show the orientation of linear detector blocks.

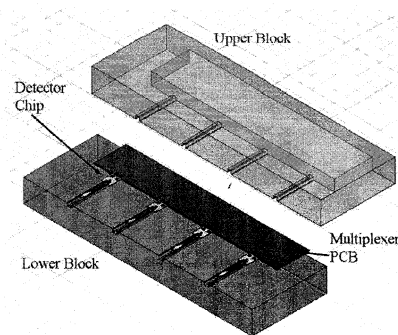


Fig. 6. Detector block concept showing how four detectors would be mounted in a block. The upper and lower blocks form waveguides in which the fin lines sit.

and shunt resistors. This PCB has gold-plated copper tracks and as much of the copper as possible is left on the board to help with heatsinking. The gold is deposited by electroplating in order to avoid the use of a nickel undercoat. The traces are tinned with solder to make them superconducting. The PCB is enclosed in a copper can which is wrapped in niobium foil under which there is a layer of Metglas[®] 2705M, a high-permeability amorphous metal foil (Hitachi Metals Inc.). The Nb foil excludes magnetic fields while the Metglas diverts any trapped flux away from the SQUIDs. Further magnetic shielding is provided by high-permeability shields built into the cryostat.

D. Detector Mounting Scheme

In the final instrument each detector block will carry either 16 or 20 detectors. We would like to be able to remove and replace one of these detectors without disturbing the others. Thus, we mount each detector chip on an individual copper chip holder, which is then mounted in the detector block.

We must make good thermal contact to the back of each detector chip, while at the same time relieving stresses caused by differential contraction that could demount or break the chip. We fix the chip to a chip holder using Stycast 1266 epoxy. The chip holder has a well in the centre to divert excess epoxy away from the suspended nitride island.

IV. CONCLUSION

We have developed a process that allows us to mass-produce finline-coupled TES bolometers. This is the first time TES detectors have been mass-produced in the United Kingdom. We have produced prototype detectors for C₀OVER and found that the TES films are of high quality, making for sensitive detectors. More development of the thermal design is needed to achieve the required power handling. We expect to measure the R.F. response of these detectors in the near future, demonstrating the operation of a finline transition on a silicon substrate for the first time.

ACKNOWLEDGMENT

The authors would like to thank Andrew Bunting at the Scottish Microelectronics Centre of the University of Edinburgh for carrying out the DRIE and for his helpful advice.

REFERENCES

- [1] M. J. Rees, "Polarization and Spectrum of the Primeval Radiation in an Anisotropic Universe," *ApJ*, vol. 153, pp. L1+, July 1968.
- [2] U. Seljak and M. Zaldarriaga, "Signature of Gravity Waves in the Polarization of the Microwave Background," *Physical Review Letters*, vol. 78, pp. 2054–2057, Mar. 1997.
- [3] M. Kamionkowski, A. Kosowsky, and A. Stebbins, "A Probe of Primordial Gravity Waves and Vorticity," *Physical Review Letters*, vol. 78, pp. 2058–2061, Mar. 1997.
- [4] P. G. Calisse, P. A. R. Ade, M. D. Audley, P. Cabella, A. D. Challinor, P. Ferreira, W. K. Gear, D. J. Goldie, P. K. Grimes, K. Isaac, M. E. Jones, B. Kiernan, M. Crane, R. W. Barker, K. Grainge, P. F. Horner, B. J. Johnson, A. N. Lasenby, B. Maffei, P. D. Mauskopf, S. J. Melhuish, C. E. North, A. Orlando, S. M. Parsley, L. Piccirillo, L. Pietranera, O. E. Mallie, G. Pisano, G. Savini, H. M. Stevenson, A. C. Taylor, G. Teleberg, I. Thomas, V. N. Tsaneva, C. E. Tucker, R. Tucker, I. Walker, S. Wilcox, S. Withington, G. Yassin, L. Dunlop, D. Glowacka, D. T. O'Dea, G. Rocha, and A. C. Readhead, "Clover: a high-sensitivity polarization instrument for CMB B-mode observations," 2006, *Proceedings of the SPIE*, vol. 6275, in press.
- [5] G. Yassin and S. Withington, "Electromagnetic models for superconducting millimetre-wave and sub-millimetre-wave microstrip transmission lines," *Journal of Physics D Applied Physics*, vol. 28, pp. 1983–1991, Sept. 1995.
- [6] G. Yassin, S. Withington, M. Buffey, K. Jacobs, and S. Wulff, "A 350-GHz SIS antipodal finline mixer," *IEEE Trans. on Microwave Theory and Techniques*, vol. 48, no. 4, pp. 662–669, 2000.
- [7] K. D. Irwin, "Phonon-Mediated Particle Detection Using Superconducting Tungsten Transition-Edge Sensors," Ph.D. dissertation, Stanford University, Stanford, California, 1995.
- [8] G. Teleberg and L. Piccirillo, "A miniature dilution refrigerator for sub-Kelvin detector arrays," 2006, *Proceedings of the SPIE*, vol. 6275, in press.
- [9] J. A. Chervenak, K. D. Irwin, E. N. Grossman, J. M. Martinis, C. D. Reintsema, and M. E. Huber, "Superconducting multiplexer for arrays of transition edge sensors," *Applied Physics Letters*, vol. 74, pp. 4043–4045, June 1999.
- [10] P. A. J. de Korte, J. Beyer, S. Deiker, G. C. Hilton, K. D. Irwin, M. Macintosh, S. W. Nam, C. D. Reintsema, L. R. Vale, and M. E. Huber, "Time-division superconducting quantum interference device multiplexer for transition-edge sensors," *Review of Scientific Instruments*, vol. 74, pp. 3807–3815, Aug. 2003.
- [11] R. P. Welty and J. M. Martinis, "Two-stage integrated SQUID amplifier with series array output," *IEEE Transactions on Applied Superconductivity*, vol. 3, pp. 2605–2608, Mar. 1993.
- [12] M. D. Audley, W. S. Holland, T. Hodson, M. Macintosh, I. Robson, K. D. Irwin, G. Hilton, W. D. Duncan, C. Reintsema, A. J. Walton, W. Parkes, P. A. R. Ade, I. Walker, M. Fich, J. Kycia, M. Halpern, D. A. Naylor, G. Mitchell, and P. Bastien, "An update on the SCUBA-2 project," in *Millimeter and Submillimeter Detectors for Astronomy II. Proceedings of the SPIE, Volume 5498*, J. Zmuidzinas, W. S. Holland, and S. Withington, Eds., Oct. 2004, pp. 63–77.

Precise measurement of CMB polarisation from Dome-C: the BRAIN experiment.

M. Piat¹, E. Bréelle¹, C. Dufour¹, Y. Giraud-Héraud¹, S. Masi², G. Polenta²,
BRAIN collaboration

¹*APC, Paris, France*

²*University La Sapienza, Roma, Italy*

³*University of Wales Cardiff, UK.*

The characterisation of CMB polarisation is one of the next challenges in observational cosmology. This is especially true for the so-called B-modes that are at least 3 orders of magnitude lower than CMB temperature fluctuations. A precise measurement of the angular power spectrum of these B-modes will give important constraints on inflation parameters.

In this talk, I will describe the BRAIN experiments based on bolometric interferometry and dedicated to CMB polarisation measurement. A high rejection of systematic effects is obtained thanks to interferometry technique while the use of low temperature bolometers allows for high sensitivity. This experiment is proposed to be installed in Dome-C, Antarctica, to take advantage of the extreme dryness of the atmosphere and to allow long integration time. A first campaign has been carried out this year at Dome-C to install and test a cryogenic system able to operate automatically during the Antarctic winter. With this system we have also carried out a measurements of the Stokes parameters of atmospheric emission at 145GHz.

ORAL SESSION n°3

« Novel Devices & Technologies for THz »

Thursday 11 May 09:00-10:00

Chaired by :

Dr. Wojtek Knap & Dr. Peter Siegel

Microwave Detection and Mixing in Metallic Single Wall Carbon Nanotubes and Potential for a New Terahertz Detector

K.S. Yngvesson, F. Rodriguez-Morales, R. Zannoni, J. Nicholson, M. Fischetti and J. Appenzeller

Abstract— This paper reports measurements of microwave (up to 4.5 GHz) detection in metallic single-walled carbon nanotubes. The measured voltage responsivity was found to be 114 V/W at 77K and 9,000 V/W at 4.2K. We also demonstrated heterodyne detection at 1 GHz. Above 1.3 GHz the detector response falls off by 12 dB/octave. The detection mechanism can be explained based on standard microwave detector theory and the nonlinearity of the DC IV-curve, the so-called “zero-bias anomaly”. We discuss the possible causes of this nonlinearity. While the frequency response is limited by circuit parasitics in this measurement, we discuss evidence that indicates that the intrinsic effect is much faster and that applications of carbon nanotubes as terahertz detectors are feasible.

Index Terms—terahertz detectors, single wall carbon nanotubes, microwave detectors, contact resistance.

I. INTRODUCTION

The availability of Single Wall Carbon Nanotubes (SWNTs) has stimulated considerable recent exploration of different ideas for use of SWNTs in new electronic devices [1]. SWNTs have different electronic band structures depending on their chirality, and can be either metallic or semiconducting [2]. Much of the research so far has been concentrated on the semiconducting version of SWNTs (s-SWNTs), in particular with the prospect of developing a high-performance Carbon Nanotube Field Effect Transistor (CN-FET) [3], [4]. Other applications that have been proposed are to detectors for microwave or terahertz frequencies. Schottky barriers exist at the contacts of semiconducting SWNTs [5], [6], and were fabricated and analyzed for use as terahertz detectors by Manohara *et al.* [7]. Experimental results were recently published by Rosenblatt *et al.* [8] demonstrating detection of microwaves up to 50 GHz, as well as by Pesetski *et al.* [9] who measured heterodyne detection with flat frequency-dependence up to 23 GHz. These references [7]-[9] all used the s-SWNT-FET configuration. Metallic SWNTs (m-SWNTs) also have considerable potential for detector applications, and one of us (KSY) recently proposed a very fast terahertz detector based on the hot electron bolometric

(HEB) effect [10],[11]. In the present paper we report experimental results for a device using an m-SWNT that detects microwaves in the low GHz range, based on a traditional IV-curve nonlinearity at 77 K, and that shows much enhanced direct detection responsivity at 4 K. The device described here operates both as a direct (DC output) detector and as a heterodyne detector (difference frequency output up to at least 200 MHz). In this paper we will discuss the experimental results and interpret these in terms of the detection mechanisms involved. We also discuss the potential of this type of detector for application at terahertz frequencies.

II. EXPERIMENTAL RESULTS

A. Experimental Procedures

SWNTs used in our study were grown using laser ablation [12]. CNTs with diameters between 0.6 nm and 1.5 nm were spun from solution onto a p+-doped silicon substrate covered with 100 nm of silicon oxide. Contact strips of width 350nm were made with 20 nm of Ti followed by 100 nm of Au, and were connected to 80 μ m x 80 μ m contact pads. The length of the tubes between contacts is known to be in the range of 300nm to 500nm. The silicon chip was placed in a small copper enclosure (with a metallic cover) to isolate it from external radiation, see Figure 1. The contact pads were connected by wire bonds to (1) a microstrip transmission line that was in turn connected to a standard coaxial connector installed in the side of the enclosure; and (2) the ground plane of the enclosure. The silicon substrate was left electrically insulated in order to minimize parasitic reactances. The assembly was placed in a liquid helium vacuum dewar and pumped to a good vacuum for at least one day in order to remove most of the surface contaminations on the CNT. A well shielded stainless steel coaxial cable makes the sample accessible from the outside of the dewar. We used a programmable DC power supply (Keithley) to provide a voltage source bias to the device through the coaxial cable. The DC supply also measured the DC voltage and current, and these were read by a computer for further processing. Microwave sources (Agilent) were also fed to the coaxial cable, and different sources (DC and microwave) were separated through the use of commercial bias tees.

B. I-V-Curves

It is well-known that Ti/Au contacts yield a contact resistance that is usually quite high and strongly dependent on the nanotube diameter [13]-[15]. The devices used in our study had contact resistances that were in the range of a few hundred k Ω to a few M Ω . It is also known that the

K.S. Yngvesson, F. Rodriguez-Morales, R. Zannoni, J. Nicholson and M. Fischetti are with the Department of Electrical and Computer Engineering, University of Massachusetts, Amherst, MA 10003, USA. e-mail: yngvesson@ecs.umass.edu

J. Appenzeller is with IBM T.J. Watson Research Center, PO Box 2128, Yorktown Heights, NY 10598, USA.

This work was supported by a grant for Nanoscale Exploratory Research from the National Science Foundation (ECS-0508436).

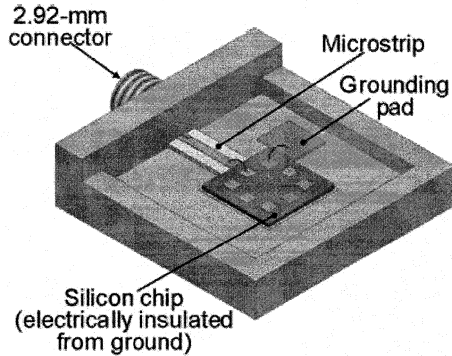


Figure 1. The experimental fixture used in this work.

conductance of such CNTs shows a “zero-bias anomaly” [16], i.e. the differential conductance (dI/dV) plotted as a function of bias voltage (V) shows a dip at low values of V with a width of about ± 400 mV [17]. This presents a nonlinearity in the IV-curve (Figure 2) that we exploited for microwave detection. Similar IV-curves were obtained for devices fabricated at IBM and at UMass/Amherst, but the results presented here are for devices fabricated at IBM.

The zero-bias anomaly “dip” is also evident from the additional plot of dI/dV in Figure 2. This dip deepens as the temperature is decreased (the curves shown in Figure 2 were taken at 77K). At larger voltages the IV-curve shows a linear dependence between current and bias with a slight decrease in dI/dV for the highest voltage range. Except for the zero-bias anomaly, the IV-curve can thus be assumed to be due to a (roughly) constant contact resistance, that is almost independent of the temperature. Evidence from other metallic CNTs [18] indicates that the electrons have mean free paths of about $1\mu\text{m}$; thus in our tubes they travel ballistically from contact to contact. The zero-bias anomaly is usually ascribed to the very strong electron-electron Coulomb interactions in one-dimensional conductors that necessitates treating the electrons as a collective, plasmon-like, medium known as a “Luttinger liquid” (“LL”). Tunneling from the contacts into the LL is suppressed at low temperatures, which explains why the conductance approaches zero. It has been suggested that the behavior of the conductance in the entire temperature range from 4 K to 300 K can be better explained as being due to a combination of effects, the LL effect, and that of interfacial barriers at the contacts [15]. The LL effect is expected to be important only in the lowest temperature range. As made clear in the paper mentioned above [15], a complete understanding of the contacts between the one-dimensional m-SWNTs and a 3-D metal is not yet available.

As microwaves were applied to the SWNT at 77K, we recorded a change in the device DC current (ΔI), and plotted this versus DC bias voltage (Figure 3 (a)). This recording was done by measuring the voltage across a series resistance with a lock-in amplifier, while square wave modulating the microwave source. The DC power supply was still configured as a voltage source. The microwave reflection coefficient (S_{11}) was also measured with an automatic network analyzer, see Figure 4. This particular recording was obtained for a CNT with resistance of a few $M\Omega$, but similar results were

obtained for in total three samples. A resonance is seen at about 1.28

C. Microwave Measurements

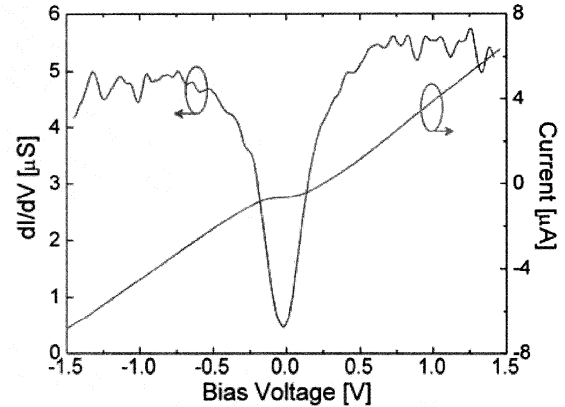


Figure 2. Measured IV-curve for a SWNT at 77 K (right scale); dI/dV based on the IV-curve (left scale).

GHz, which we interpret as being due to the combined effect of the bond wires, the contact pads and the connecting strips, situated on top of the oxide and the doped silicon chip. The equivalent circuit shown in the inset of Figure 4 was used to produce a good fit to the magnitude of S_{11} , as shown in Figure 4. For this fit we used the full S_{11} data, including the real and imaginary parts (not shown explicitly). We also used the model to predict the measured detected change in current versus frequency, plotted in Figure 4 for two different microwave power levels. The detected signal is essentially independent of frequency below the resonance, indicating that the effect of any parasitic reactance is negligible at frequencies below about 900 MHz. Above the resonance frequency, the response falls off by 12 dB per octave, in good agreement with the model. The highest frequency at which we detected the signal was 4.5 GHz, limited by the sensitivity of our measurement system. Given that s-SWNTs detected microwaves up to 23GHz and 50GHz, respectively [7]-[9] it is reasonable to assume that the detection effect we report here for m-SWNTs will extend to similarly high frequencies, once parasitic effects have been minimized.

At 77 K, the detected DC current change (ΔI) depends linearly on the microwave power (a “square law detector”) up to a power of about 0.02 mW; the detected current change then decreases smoothly after passing a maximum at about 1 mW, see Figure 5. The linear current responsivity at low MW powers was found to be $S_I = \Delta I/P_{MW} = 455 \mu\text{A/W}$, based on the measured output power at the microwave source (P_{MW}). The bias voltage dependence at 4K also follows that of d^2I/dV^2 as shown in Figure 3(b). As the microwave power was increased from that used in Figure 3(b), the detector response increased in a series of discontinuous steps, that occurred at a reproducible set of MW power levels. Further investigation of the device behavior at 4K is required to clarify these phenomena, and will be covered in a future paper.

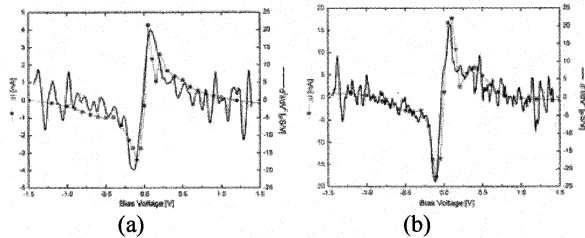


Figure 3. Detected DC current change (ΔI ; points connected with line segments) due to microwave signal at 900 MHz, compared with d^2I/dV^2 (full drawn), at (a) input power -20dBm, $T=77K$; (b) input power -30dBm, $T=4K$.

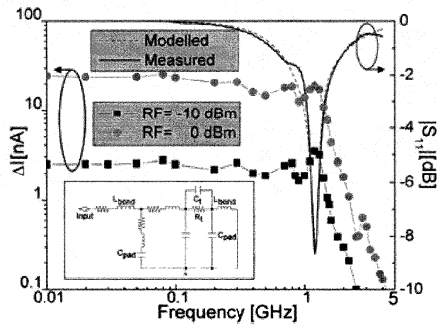


Figure 4. Microwave frequency dependence of the detected DC current change (at two power levels; left scale) and the magnitude of the reflection coefficient S_{11} (right scale; dB units), compared with the data predicted from the circuit model. Inset: Circuit model.

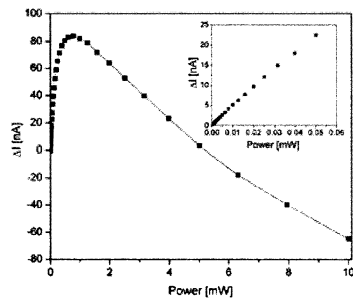


Figure 5. The DC current change (ΔI) at negative peak of Figure 3(a), as a function of microwave power. Temperature: 77K. Inset: expanded view of the part of this figure corresponding to the lowest power range.

The current responsivity can be converted to a voltage responsivity (S_V) by multiplying with the device resistance, 250 k Ω , yielding $S_V = 114$ V/W at 77K. At 4K the measured voltage responsivity was 9,000 V/W at low MW power levels. Higher resistance CNTs have lower values for S_I , roughly in inverse proportion to the resistance, and therefore have about the same S_V . Using standard small-signal microwave detector theory [20] we can calculate the current responsivity from the following expression:

$$\Delta I = (1/4) * (d^2I/dV^2) * V_{MW}^2 \quad (1)$$

Here, V_{MW} is the peak microwave voltage. The factor d^2I/dV^2 was calculated from the measured IV-curve, and is compared with ΔI in Figure 3 (a) and (b). The small

oscillations in the plot of d^2I/dV^2 are an artifact of the measurement method caused by the finite steps produced by the voltage source. The linear dependence of ΔI on MW power in the small-signal regime, as shown in the inset of Figure 4, indicates that Eq. (1) applies. Further, the bias voltage dependence of ΔI at 77K agrees well with that of d^2I/dV^2 (Figure 3). For a microwave power of 10 μ W we use Eq. (1) to estimate ΔI in the range 5nA to 20nA, depending on the detailed assumptions made about the values of the equivalent circuit elements in Figure 4. The measured value is 5nA, and this quantitative agreement within expected error bars gives further strong support to the interpretation that the detector operates as a standard microwave detector with a response that can be predicted from its IV-curve. For higher microwave powers, the small signal approximation becomes invalid, and the response becomes nonlinear, as is clear from Figure 5. We note that since the transport in the m-SWNT is ballistic, the entire nonlinearity of the detector is due to the contact resistance.

We next demonstrated *heterodyne* detection in the same SWNT by connecting it to two microwave sources with different microwave frequencies f_1 (designated as the ‘‘Local oscillator, LO’’) and f_2 (‘‘RF or signal frequency’’), while measuring the output power (or voltage) at the difference frequency (IF), ($|f_1 - f_2|$). The IF power seen on a spectrum analyzer (inset in Figure 6) was essentially independent of the IF frequency up to 200 MHz. Detecting a higher IF was not possible due to the properties of the bias tees used. The detected IF voltage response versus DC bias voltage at 77K and 4K, respectively, is shown in Figure 6.

For the data plotted in Figure 6 we used a more sensitive method of detecting the IF on a lock-in amplifier. The reference voltage for the lock-in amplifier was created by employing a separate commercial microwave mixer to mix f_1 and f_2 , see e.g. Sazonova et al. [20]. Typical frequency combinations used were f_1 and f_2 near 1 GHz, with an IF of 50 kHz. Again, parasitic circuit elements on the chip decreased the mixer efficiency for f_1 and f_2 above 1 GHz. As for the direct detection case, the response follows d^2I/dV^2 when the bias voltage is varied. This indicates that the heterodyne detection mechanism is attributable to the IV-curve using standard mixer theory.

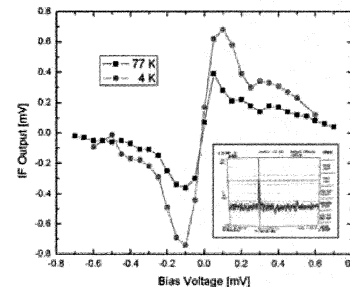


Figure 6. IF output voltage of the detector at 77K (black) and 4K (red) in the heterodyne mode.

We estimate a total mixer conversion loss at 77K to a 50 Ω IF amplifier of 95dB, much of which is due to the high

mismatch loss (60 dB total) to a device with 250 k Ω resistance. Lower resistance SWNTs [16],[18] would show lower mismatch loss as mixers. Note, however, that the higher resistance SWNTs show very good performance as *direct* detectors.

III. DISCUSSION

We now want to further discuss some of the implications of our experimental data. We have shown that sensitive detection of microwaves is possible in an m-SWNT. The detector response follows standard microwave detector theory, based on the zero-bias anomaly (ZBA) nonlinearity in the IV-curve. The origin of the ZBA has been much discussed, and this discussion is still ongoing. Especially interesting is to understand how the character of the electron transport changes as the temperature and the bias voltage are changed. The Luttinger liquid (LL) theory has been invoked to explain the ZBA, with the main experimental evidence for this theory being provided by the power-law dependence of the conductance on eV/kT [19]. Further microwave detector studies would be useful for exploring this problem. The fact that the microwave detection response is well predicted by the DC IV-curve indicates that whatever effect that causes the ZBA, it operates at speeds up to at least 4.5 GHz. This frequency limit is presently set only by the parasitics of the circuit, not the SWNT. It would be of great interest to extend the studies of coupling high frequency fields to SWNTs from the gigahertz range to the terahertz range in order to explore the intrinsic speed of the SWNT. Resonances in the LL are predicted to occur at frequencies in the terahertz range for the length of SWNTs studied here [23], but the losses under these conditions are not well known. Another paper at this conference [24] reports measurements up to 50 GHz of a frequency-dependent loss in non-contacted SWNTs, so this issue needs further exploration. The contact resistance is also predicted to be shunted by the contact capacitance at these high frequencies. We propose that terahertz detection may occur based on three different potential mechanisms:

1) Electrons tunnel into the LL plasmon medium ($Z_0 \sim 10$ k Ω [23]) which is heated and changes its resistance creating an HEB type effect. This mechanism requires operation in the lower temperature range (up to 10-20 K). The nonlinearity would now be located in the SWNT itself, not in the contacts as in the experiments described above. Tuning the frequency should provide a means of directly probing the LL medium, which has so far been mainly studied by more indirect methods.

2) Tunneling is fast enough that the electron current follows the THz frequency voltage similar to what happens in the 1 GHz device we have demonstrated; detection would then occur due to the nonlinear contact resistance. The maximum frequency for operation in this mode would be determined by the RC time-constant. The relevant capacitance values are very low, so operation up to THz frequencies should be feasible for SWNTs in the lower resistance range (e.g. parallel CNTs; see the discussion of the parallel case of Schottky diodes [7]).

3) Lower resistance SWNTs show nonlinear IV-curves at higher voltages (above 0.2 V) due to the onset of optical phonon emission [16],[18]. These should allow operation in the HEB mode, as proposed earlier [10],[11].

In conclusion, it appears very promising to extend the present study toward exploration of potential terahertz detectors based on m-SWNTs. Both direct and heterodyne detectors may be considered. The impedance matching may be easier at terahertz frequencies where the contact resistance is partly shunted by the contact capacitance.

ACKNOWLEDGMENT

The authors thank Eric Polizzi and Eyal Gerecht for stimulating discussions. We also thank undergraduate students Justin Burkhart, Stephan Adams and Alex de Geofroy for help with the measurements.

REFERENCES

- [1] P.L. McEuen, M. S. Fuhrer, and H. Park, *IEEE Trans. Nanotechnol.*, **1**, 78 (2002).
- [2] R. Saito, G. Dresselhaus, and M.S. Dresselhaus, *Physical Properties of Carbon Nanotubes* (Imperial College Press, London, 1998).
- [3] Y.-M. Lin, J. Appenzeller, J. Knoch, and Ph. Avouris, *IEEE Trans. Nanotechnol.* **4**, 481 (2005).
- [4] A. Javey, J. Guo, D.B. Farmer, Q. Wang, D. Wang, R.G. Gordon, M. Lundstrom, and H. Dai, *Nano Lett.* **4**, 447 (2004).
- [5] S. Heinze, J. Tersoff, R. Martel, V. Derycke, J. Appenzeller, and Ph. Avouris, *PRL* **89**, 106801 (2002).
- [6] J. Appenzeller, J. Knoch, V. Derycke, R. Martel, S. Wind, and Ph. Avouris, *PRL* **89**, 126801 (2002).
- [7] H.M. Manohara, E.W. Wong, E. Schlecht, B.D. Hunt, and P.H. Siegel, *Nano Lett.* **5**, 1469 (2005).
- [8] S. Rosenblatt, H. Lin, V. Sazonova, S. Tiwari, and P.L. McEuen, *Appl. Phys. Lett.* **87**, 153111 (2005).
- [9] A. A. Pesetski, J.E. Baumgardner, E. Folk, J. Przybysz, J. D. Adam, and H. Zhang, *Appl. Phys. Lett.*, **88**, 113103 (2006).
- [10] K.S. Yngvesson, *Appl. Phys. Lett.* **87**, 043503 (2005).
- [11] K.S. Yngvesson, 16th Intern. Symp. Space Terahertz Technol., Gothenburg, Sweden, May 2005.
- [12] A. Thess, R. Lee, P. Nikolaev, H. Dai, P. Petit, J. Robert, C. Xu, Y.H. Lee, S.G. Kim, A.G. Rinzler, D.T. Colbert, G.E. Scuseria, D. Tomanek, J.E. Fischer, and R.E. Smalley, *Science* **273**, 483 (1996).
- [13] Z. Chen, J. Appenzeller, J. Knoch, Y.-M. Lin, and Ph. Avouris, *Nano Lett.* **5**, 1497 (2005).
- [14] W. Kim, A. Javey, R. Tu, J. Cao, Q. Wang, and H. Dai, *Appl. Phys. Lett.* **87**, 173101 (2005).
- [15] Th. Hunger, B. Lengeler, and J. Appenzeller, *Phys. Rev. B*, **69**, 195406 (2004).
- [16] Z. Yao, C.L. Kane, and C. Dekker, *Phys. Rev. Lett.* **84**, 2941 (2000).
- [17] CNTs with higher resistance values had a wider dip in conductance.
- [18] A. Javey, J. Guo, M. Paulsson, Q. Wang, D. Mann, M. Lundstrom, and H. Dai, *Phys. Rev. Lett.* **92**, 106804-1 (2004).
- [19] M. Bockrath, D.H. Cobden, J. Lu, A.G. Rinzler, R. E. Smalley, L. Balents and P. L. McEuen, *Nature* **397**, 598 (1999).
- [20] K.S. Yngvesson, *Microwave Semiconductor Devices* (Kluwer Academic Publishers, Norwell, MA, 1991).
- [21] V. Sazonova, Y. Yaish, H. Ustunel, D. Roundy, T.A. Arias and P. L. McEuen, *Nature* **431**, 284 (2004).
- [22] S. Li, Z. Yu, S-F. Yen, W.C. Tang, and P.J. Burke, *Nano Lett.* **4**, 753 (2004).
- [23] P.J. Burke, *IEEE Trans. Nano Technol.* **1**, 129 (2002).
- [24] M. Lee et al., this conference proceedings.

RF-to-Millimeter-wave Conductivity Spectra of Single-Walled Carbon Nanotubes

Mark Lee, C. Highstrete, E. A. Shaner, F. E. Jones, A. A. Talin, D. B. Robinson, and
P. M. Dentinger
Sandia National Laboratories, Albuquerque, New Mexico, and Livermore, CA, USA

There have been several theoretical proposals that single-walled carbon nanotubes (SWCNTs) may have very unique and highly desirable electrodynamic properties for microwave-thru-terahertz applications.^{1,2} These properties arise from the combination of very high purity achievable and quasi-one-dimensional nature of the electronic conduction in SWCNTs, as evidenced by reports of quantized DC conductance in short (few μm length) SWCNTs.³ If electrical conductance in SWCNTs is quantum ballistic in nature, then the AC response can conceivably have ultra-low intrinsic loss and be able to follow frequencies far higher than conventional metals and semiconductors. It has been proposed that such ballistic conduction can be used to make SWCNTs a very wide bandwidth submillimeter-wave mixer.⁴ Some recent experimental reports on the RF and microwave properties of SWCNTs report either a frequency-independent loss or a loss that falls below measurement uncertainties.^{5,6,7} However, most of these measurements suffer from poor signal-to-noise arising from large systematic uncertainties and/or large instrumental loss.

We report on a detailed investigation of the AC response of small arrays of SWCNTs from 0.01 to 50 GHz using a coplanar waveguide (CPW) platform compatible with both broadband S -parameter measurements and directed assembly of SWCNTs. Utilizing AC dielectrophoresis and lithographic masking techniques, small numbers of SWCNTs, prepared with and without surfactants, were assembled in regular, localized arrays across the gaps between CPW signal and ground electrodes. This aligns the SWCNTs with the propagating electric field polarization and so maximizes coupling of the SWCNTs to the electromagnetic field. The complex conductivity of the SWCNT array is deduced from vector network analyzer measurements of the change in S -parameters, ΔS , of a CPW before and after SWCNT assembly. Using careful calibration, the ratios of ΔS_{11} and ΔS_{21} to random errors are of order 20 dB and the ratios of ΔS_{11} and ΔS_{21} to systematic errors is at least 10 dB.

At room temperature, we have found direct evidence that 1 to 3 μm long SWCNTs have clear, frequency-dependent loss that scales roughly as $f^{1/2}$, qualitatively similar to skin-depth loss. The SWCNTs also have a non-trivial frequency-dependent reactance. A detailed analysis of this data will be presented.

Sandia is a multiprogram laboratory operated by Sandia Corporation, a Lockheed Martin Company, for the United States Department of Energy's National Nuclear Security Administration under contract DE-AC04-94AL85000.

¹F. Léonard, J. Tersoff, *Appl. Phys. Lett.* **81**, 4835 (2002)

²P. J. Burke, *IEEE Trans. Nanotech.*, **1**, 129 (2002)

³D. Mann, *et al.*, *Nano Lett.* **3**, 1541 (2003)

⁴K. S. Yngvesson, *Appl. Phys. Lett.* **87**, 048503 (2005)

⁵J. Appenzeller, D. J. Frank, *Appl. Phys. Lett.* **84**, 1771 (2004)

⁶Z. Yu, P. J. Burke, *Nano Lett.* **5**, 1403 (2005)

⁷S. Rosenblatt, *et al.*, *Appl. Phys. Lett.* **87**, 153111 (2005)

TERAHERTZ NON LINEAR METAMATERIALS

M.F. Foulon¹, D. Yarekha¹, T. Crépin and D. Lippens¹

¹Institut d'Electronique, de Microélectronique et de Nanotechnologie(IEMN)
 Université des Sciences et Technologies de Lille
 Avenue Poincaré, BP 69, 69652 Villeneuve d'Ascq Cedex, France
Michel.foulon@IEMN.univ-lille1.fr

Metamaterial Tehnology is now attracted an increasing interest with the prospect to achieve new functionalities afforded by the synthesis of an effective negative refractive index . So far however the main effort has been paid to the study of linear electromagnetic properties while a number of novel effects can be foreseen if non linear discrete devices are integrated in such left handed media. Basically a double approach can be used for the synthesis of negative refractive Index materials (NRIM) either by using particles as the so-called split ring resonator [1] or the phase advance scheme which is obtained by periodically loaded a transmission by series capacitance and self inductance. For the latter, a first paper on numerical modelling and expected effects was published in the literature. Recently, the first experimental demonstration of wave propagation phenomena in non linear left handed media was reported also using a one dimensional system. The originality of this communication stems mainly for the use of a transmission lines periodically loaded by an Heterostructure Barrier Varactor [3]. This kind of device show symmetric C-V characteristics. Main emphasis was also focused on harmonic multiplication whereas also parametric effects are expected in such systems.

When a transmission line is periodically loaded by a varactor in shunt (see fig. 1(a) where the devices interconnects here the two strips of a Co-Planar Strip line) the line becomes frequency selective with a low-pass filter type [4]. The propagation is forward up to a corner frequency called the Bragg frequency[2]. By integrating now the devices in series namely to the place where fixed parallel plate capacitance are apparent in the layout, the propagation becomes backward with a high-pass filter frequency behaviour. Therefore depending on the balance between parallel and series element a composite electromagnetic behaviour can be achieved [3]. At the present stage, we are modelling the non-linear behaviour either in the time domain or the frequency one by means of the commercial code ADS by Agilent. Enhancement in the up-conversion efficiency over a broad band can be pointed out in the left handed propagation regime. Further advantage can also be foreseen with the use of MIRM's from the frequency filtering effect and from the radiation guided regimes [4].

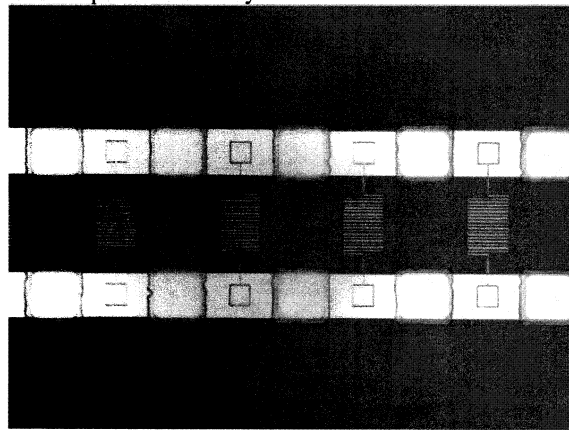


Fig. 1 (a) Left handed transmission lines in a CPS technology

- [1] T. Crépin, J. F. Lampin, T. Decoopman, X. Mélique, L. Desplanques and D. Lippens, *Appl. Phys. Lett.* **87**, 104105 (2005)
 [2] J. M. Duchamp, P. Ferrari, M. Fernandez, A. Jrad, X. Mélique, J. Tao S. Arscott, D. Lippens and R. G Harrison, *IEEE Trans Microwave Theory and Technique*, **51**, 1105 (2003)
 [3] C. Caloz, I. H. Lin and T. Itoh, *Microwave Opt. Technol. Lett.*, **40**, 471 (2004)
 [4] A. B. Kozyrev, H. Kim, A. J. Karbassi, and D. W. van der Weide, *Appl. Phys. Lett.* **87**, 121109 (2005)

Niobium SupraMEMS for Reconfigurable Millimeter Wave Filters

M. Schicke¹, A. Navarrini², P. Ferrari³, T. Zöpfl⁴, F. Wittmann⁴, W. Bedyk⁴,
G. Schrag⁴, and K. F. Schuster¹

¹ Institut de RadioAstronomie Millimétrique (IRAM), 300 rue de la piscine, 38406 St.
Martin d'Hères, France

² Radio Astronomy Lab, University of California, 601 Campbell Hall, Berkeley, CA,
USA

³ Institute for Microelectronics Electromagnetism and Photonics, 23 rue de Martyrs,
38016 Grenoble, FRANCE

⁴ Institute for Physics of Electrotechnology, Munich University of Technology,
Arcisstraße 21, 80290 Munich, GERMANY

Reconfigurable passive superconducting devices for the mm-wave regime offer a wide range of novel applications in scientific and industrial remote sensing. We developed a surface mounted Niobium MEMS technology that can be integrated with a wide range of cryogenic semiconductor and superconducting circuits. A first generation of circuits using our Niobium SupraMEMS has been optimized for radio astronomical applications. In this paper we present the micro-mechanical and electrical characterization of the devices. Extended mechanical modeling results in an improved understanding of the specific behavior of metallic cryogenic MEMS devices. The influence of the fabrication procedure on the mechanical properties of the devices and the resulting limitations are discussed. A particular design for improved tuning range has been investigated.

ORAL SESSION n°4

« SIS 2 »

Thursday 11 May 10:30-12:00

Chaired by :

Dr. Anthony Kerr & Dr. Karl Schuster

A 211-275 GHz Sideband Separating SIS Mixer for APEX

V. Vassilev, R. Monje, A. Pavolotsky, D. Dochev, D. Henke and V. Belitsky, *Member, IEEE*

Abstract— We present the results of the development and characterization of the sideband separating (2SB) SIS mixer for the APEX band 1, 211-275 GHz.

All mixer components, except the IF hybrid, are integrated into a single mixer block. The sideband separation is achieved by using a quadrature scheme where a local oscillator (LO) pumps two identical SIS mixers. The RF power is divided using a waveguide branch line coupler and directed with 90° phase difference to the ends of the substrate, where each path is coupled to the mixer chip through a waveguide to microstrip transition.

Preliminary tests of this 2SB mixer show a sideband suppression ratio of about 12 dB and a typical SSB noise temperature of 80K.

Index Terms—SIS mixer, sideband separating mixers, quadrature hybrid

I. INTRODUCTION

APEX, the Atacama Pathfinder Experiment [1], is a collaboration between the Max Planck Institute for Radio astronomy, Onsala Space Observatory, and the European Southern Observatory. APEX is a 12 m single dish telescope with a surface accuracy of 17 μm (rms) allowing observations in the sub-mm region.

The Onsala Space Observatory is committed to providing single pixel heterodyne receivers covering the following bands:

Band	RF range, GHz	Mixer type
APEX 1	211-275	sideband separating
APEX 2	275-370	sideband separating
APEX 3	375-500	sideband separating
APEX T2	1250-1390	balanced

This paper concentrates on the development of the band 1 sideband separating (2SB) mixer. The motivation for using 2SB mixers for radio astronomical applications at mm-wavelengths is that the noise performance of a double-sideband (DSB) heterodyne receiver is often limited by the atmospheric noise fed into the system via the image band. Thus, to increase the system sensitivity, 2SB or single sideband (SSB) operation is preferred.

Sideband separation is achieved by using a quadrature scheme where the RF power is divided and applied with 90°

phase difference to two identical mixer junctions. The mixer junctions are pumped by a local oscillator (LO) with either 0° or 180° phase difference.

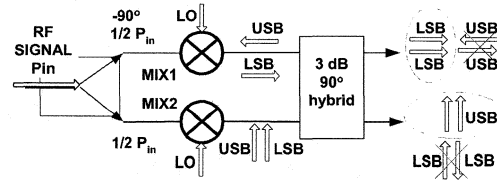


Figure 1 Block diagram of the sideband separating mixer. To illustrate the sideband cancellation, the relative phases of the sideband signals are shown at different points of the mixer. USB and LSB stand for Upper and Lower Side Band respectively.

Sideband separation, using the quadrature scheme illustrated above, does not use any tunable RF filter components and has been demonstrated at mm-wavelengths [2]-[6]. The degree of sideband suppression is directly related to the magnitude and phase balance of the RF and LO power applied to the mixers and the symmetry of the circuitry.

II. MIXER DESIGN

A. Mixer Configuration

The mixer block layout is shown in Figure 2 where the corrugated horn is followed by a RF quadrature hybrid. The divided RF power is coupled to the mixer substrate by two RF radial probes at the ends of the chip.

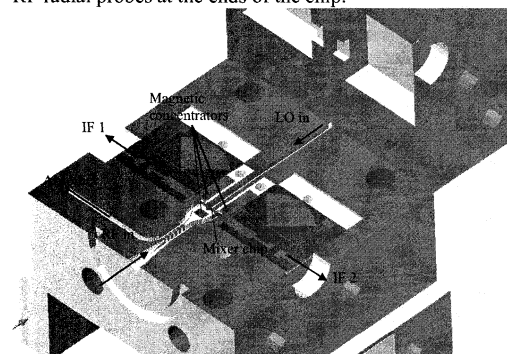


Figure 2 The bottom part of the mixer block accommodates the mixer chip, two bias-Ts and an absorber to terminate the idle port of the RF waveguide hybrid.

The LO power is applied to the middle of the substrate

Manuscript received Mai 31, 2006.

Authors are with the Group for Advanced Receiver Development, Onsala Space Observatory, Chalmers University of Technology (e-mail: vevas@oso.chalmers.se).

and is divided by double probes which extend into the LO waveguide.

Individual magnetic fields are applied to the SIS junctions using two external coils. Magnetic concentrators bring the magnetic field in close vicinity to the junctions, thus a very little current (about 1 mA per coil) is needed to suppress the super current.

A closer look at the mixer chip is shown in Figure 3. The RF is coupled from a full-height waveguide to a microstrip line by a pair of radial probes. A high impedance line is attached to the radial end of the probe. This line together with a RF choke provides RF/DC isolation and is used to inject DC for mixer biasing and to extract the IF [7].

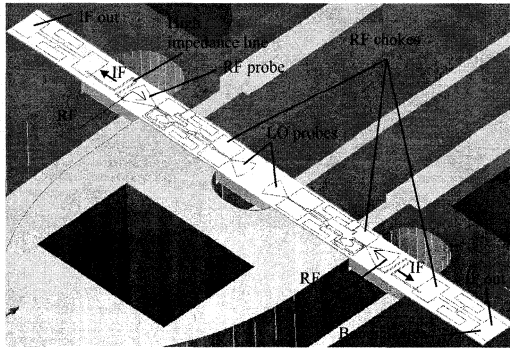


Figure 3 The 2SB mixer chip coupled to the RF/LO waveguides. The two central RF chokes provide ground for the SIS and their tuning circuitry while the chokes at the ends of the substrate provide RF/IF isolation. The relatively large area of the last choke section facilitates bonding to the Bias-T.

A second pair of radial probes divides the LO power and provides the transition from waveguide to microstrip line [8]. The two central RF chokes provide a ground for the SIS and its tuning circuitry.

The IF is extracted through the RF probe, a high impedance line, and a second choke. The high impedance line and the choke prevent RF leakage to the IF port, while at IF they represent a small inductance.

B. Tuning Circuitry

The mixer tuning circuitry, illustrated in Figure 4, uses a $\lambda/4$ transformer section to match the RF probe to the SIS junction. The same transformer section is used as a part of a directional coupler providing -17 dB LO coupling to RF. To provide the required coupling ratio and to avoid small gap between the lines of the coupler, two perforations in the ground plane are introduced. In order to terminate the idle port of the LO coupler, we use an elliptical planar termination [9], [10], which is made of a resistive normal-metal film. The termination is designed such that it occupies a minimum area on the substrate and provides return loss $S_{11} < -10$ dB over the whole LO band. The required sheet resistance of the film forming the dot is obtained by sputtering Ti in N_2 atmosphere, resulting in a Ti/N_2 mixture with the desired resistivity.

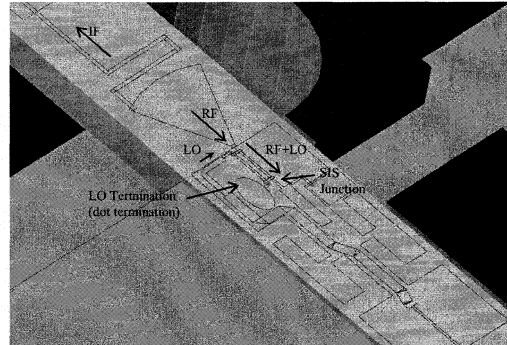


Figure 4 The mixer tuning circuitry uses a directional coupler to couple LO to RF. To provide the required coupling ratio of -17 dB and to keep the RF and LO lines well separated, two perforations in the ground plane are introduced. The RF line of the coupler is also used to match the real part of the SIS RF impedance to the signal source (the RF probe).

C. Nb Superconducting IF hybrid

To achieve as compact as possible 2SB mixer assembly, and to minimize losses, we use a superconducting IF hybrid. The hybrid is a traditional Lange coupler made of Nb thin film lines on a 300um quartz substrate using the same process as for the mixer fabrication. To simplify the circuitry we use an additional SiO_2 layer as an insulator and a second layer of Nb film to connect bridges instead of bond wires. The covered bandwidth exceeds the 4-8 GHz band.

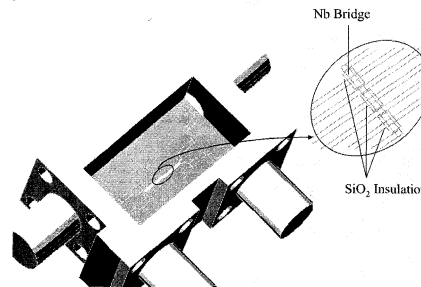


Figure 5 A picture of the superconducting IF hybrid. To achieve as compact design as possible, the width of the hybrid matches the width of the mixer block and thus can be connected without using only SMA adapters.

III. MIXER MEASUREMENTS

A. Measurements in DSB mode

To evaluate the symmetry of the branches of the 2SB mixer and to calculate the gain and the noise of each mixer, initial tests were performed in a DSB configuration as shown below.

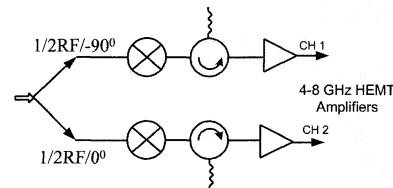


Figure 6 A DSB mixer configuration for the initial tests.

The DSB measurements were performed at different LO frequencies and for different LO powers. These measurements were used to choose optimum LO pumping power and pairs of bias points where both mixers have similar gains and minimum noise for each LO frequency.

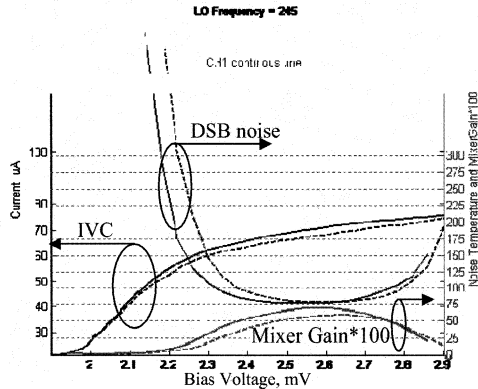


Figure 7 An example of mixer measurements in DSB mode. SIS mixer gains can be extracted by measurements of the linear region of the unpumped IVC's, thus the IF gains can be subtracted from the total gain.

Since the RF hybrid is present in the DSB tests, the measured DSB noise closely predicts the SSB noise when the IF hybrid is connected and the mixer is operated in sideband separating mode.

B. Sideband separating measurements

When operated in 2SB mode the IF hybrid is connected to the mixer as shown in the figure below.

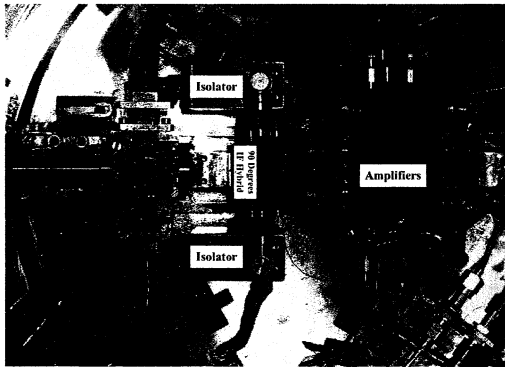


Figure 8 A picture of the setup used in the mixer measurement in 2SB mode. The mixer IF outputs are connected to isolators followed by the IF quadrature hybrid and amplifiers. The IF band is 4-8 GHz.

The sideband rejection is measured by injecting a pilot signal generated by a harmonic mixer pumped with frequency around 12 GHz. The frequency of the pilot signal is changed a few times at RF for each of the sidebands, the IF spectrum is taken each time at both IF outputs of the mixer. This results in couple of values for the LSB/USB and USB/LSB rejection ratios per single LO frequency. The

sideband rejection is the difference between the peak values at IF for both sidebands (the system IF gain is nearly the same for both channels). This measurement is illustrated in Figure 9.

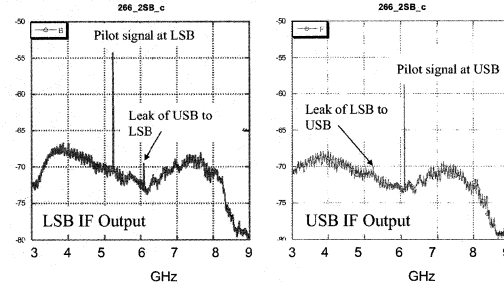


Figure 9 Illustration of the sideband rejection ratio measurement for LO frequency 266 GHz. Two pilot signals are generated (one in the LSB, one in the USB), the rejection ratios are calculated by taking the difference in the peak value at LSB/USB IF outputs of the mixer.

The measured rejection ratios and SSB noise temperatures are shown in Figure 10.

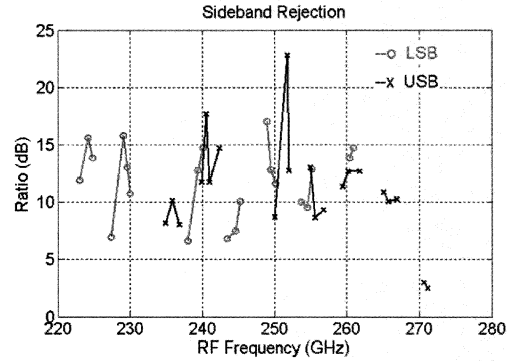


Figure 10 The measured sideband rejection ratios.

For each LO frequency the Y-factor is measured with a spectrum analyzer at both sidebands. The measured noise temperature is shown in Figure 11.

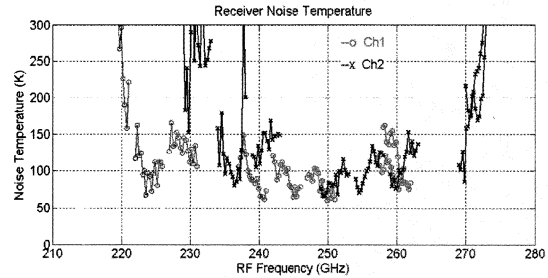


Figure 11 The measured receiver noise temperature. This noise is uncorrected for the image band contribution, if it is assumed that typical rejection ratio is 12 dB, the SSB noise temperature would be 6% higher than the temperature shown in the plot.

IV. CONCLUSION

We present the design and initial results of a 2SB mixer for Band 1 of the APEX telescope. The results presented here are preliminary and further mixer characterization is required to verify the limit of the mixer performance. The mixer setup is still not optimized e.g. the phase difference between the isolators was recently measured to be 20° limiting the obtainable rejection ratios. Different configurations will be also tested, e.g. rearranging the order of the IF components.

ACKNOWLEDGMENT

Thanks to Sven-Erik Ferm for his effort on fabricating the mixer block. This work is a part of the APEX Project, supported by the Swedish Research Council and the Wallenberg Foundation by their respective grants.

REFERENCES

- [1] <http://www.apex-telescope.org/>.
- [2] A. R. Kerr, S.-K. Pan and H. G. LeDuc, "An integrated sideband separating SIS mixer for 200-280 GHz", Proc. of the Ninth Space Terahertz Technology Symposium, pp.215-222, Pasadena, USA, March, 1998.
- [3] R. L. Akeson, J. E. Carlstrom, D. P. Woody, J. Kawamura, A. R. Kerr, S.-K. Pan and K. Wan, "Development of a Sideband Separation Receiver at 100GHz", Proc of Fourth International Symposium on Space Terahertz Technology, pp.12-17, Los Angeles, USA, March, 1993.
- [4] S. M. X. Claude, C. T. Cunningham, A. R. Kerr, and S.-K. Pan, "Design of a Sideband-Separating Balanced SIS Mixer Based on Waveguide Hybrids", *ALMA Memo 316*, <http://www.alma.nrao.edu/memos/>
- [5] S. Asayama, et al., "An Integrated Sideband-Separating SIS mixer Based on Waveguide Split Block for 100 GHz Band", ALMA Memo 453, <http://www.alma.nrao.edu/memo/>, April 2003. C. J. Kaufman, Rocky Mountain Research Lab., Boulder, CO, private communication, May 1995.
- [6] W. Shan, S. Asayama, M. Kamikura, T. Noguchi, S. Shi and Y. Sekimoto, "Development of a 385-500 GHz SIS Mixer for ALMA Band 8", Proc. of the 16th Symposium on Space Terahertz Technology, pp.175-180, Gothenburg, Sweden, Mai, 2005.
- [7] C. Risacher, V. Vassilev, A. Pavolotsky and V. Belitsky, "Waveguide - to Microstrip Transition with Integrated Bias-T", *IEEE Microwave and Wireless Components Letters*, Vol. 13, pp. 262-246, July 2003.
- [8] V. Vassilev, V. Belitsky, D. Urbain, S. Kovtonyuk, "A New 3 dB Power Divider for MM-Wavelengths", *IEEE Microwave and Wireless Components Letters*, page 30-32, vol.11, January 2001.
- [9] B. Oldfield, "Connector and termination construction above 50 GHz," *Applied Microwave & Wireless*, pp. 56-66, April 2001.
- [10] R. R. Monje, Vessan V. Vassilev, A. Pavolotsky and V. Belitsky, "High Quality Microstrip Termination for MMIC and Millimeter-Wave Applications", *IEEE MTT-S International Microwave Symposium*, ISSN: 01490-645X, pages 1827-1830, Long Beach, California, June 12-17, 2005.

The APEX 345GHz/460GHz 7-pixel heterodyne array

S. Heyminck, R. Güsten, C. Kasemann, J. Stutzki, K. Jacobs, C.E. Honingh and U.U. Graf

Abstract—Since August 2005 the Atacama Pathfinder Experiment (APEX), a novel 12m submillimeter telescope is in science operation. As a powerful mapping tool for the 345 GHz and the 460 GHz atmospheric windows we launched the development of a dual-color 7-pixel heterodyne array receiver. The beam pattern is planned to be hexagonal while both colors will be observed simultaneously in orthogonal polarizations. We present the opto-mechanical layout including numerical optics simulations.

Index heterodyne arrays, submillimeter wave receivers, submillimeter wave spectroscopy

I. INTRODUCTION

APEX¹ [1] offers outstanding observing conditions (see also Fig. 1) in the submillimeter wavelength regime (from 1mm to 200 μ m). Currently, as first-generation instruments, a single-pixel 345 GHz facility receiver [2] and FLASH [3], a dual-channel 460 GHz/810 GHz MPIfR PI-instrument, are available for heterodyne observations.

To make best use of the telescope time for spectroscopic mapping projects heterodyne arrays are widely used (e.g., SMART [4], HERA [5] or CHAMP [6]). With the new CHAMP⁺-array [7] a powerful heterodyne-mapper for the 660 GHz and the 810 GHz atmospheric windows will go into commissioning at APEX in August 2006, but still a comparable array for the 345 and the 460 GHz atmospheric windows is missing. In collaboration with the Universität zu Köln, providing the SIS-mixer units for both frequency bands we launched the development for such a “low-frequency” array in February this year. This paper briefly describes the design and the receiver layout including first simulations of the optical layout.

II. THE RECEIVER

The new array will be located in the Nasmyth B-cabin (right cabin) of the telescope where also the CHAMP⁺ array is mounted. This implies strong design boundaries due to the

S. Heyminck, R. Güsten and C. Kasemann are with the Max-Planck-Institut für Radioastronomie, Auf dem Hügel 69, 53121 Bonn / Germany (correspond to heyminck@mpef-bonn.mpg.de, phone: +49-(0)228-525-176).

J. Stutzki, K. Jacobs, C.E. Honingh and U.U. Graf are with the I. Physikalisches Institut der Universität zu Köln, Zùlpicher Straße 77, 50937 Köln / Germany.

¹ APEX is a collaboration between the Max-Planck-Institut für Radioastronomie, the European Southern Observatory, and the Onsala Space Observatory

limited space available and also because parts of the existing

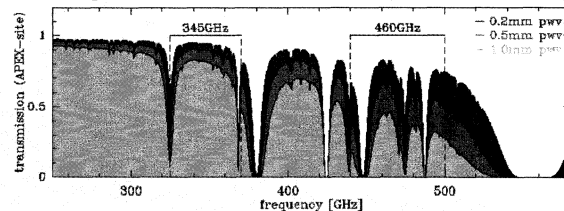


Fig. 1. The zenith transmission of the atmosphere above the APEX site for 1 mm, 0.5 mm and 0.2 mm precipitable water vapor (pwv) is shown. The baseline tuning ranges for both colors are also given in the plot.

CHAMP⁺ optics have to be shared.

The performance goal for each channel of an array receiver always should be to be as good as a single pixel receiver. This is primarily an optics concern since all other parts follow more or less the same design as for a single pixel receiver.

To improve sensitivities single-sideband (SSB) filters are foreseen for both sub-arrays. To avoid losses due to a coupling foil a Martin-Puplett interferometer as diplexer is chosen.

For the beam spacing we decided for 2 FWHM for both sub-arrays (see Fig. 2), which is a good compromise between the losses at the individual beam apertures, when separated before the mixer horn-antennas, and the filling factor of the field-of-view). A K-mirror design with a resulting image rotation-angle of more than 360° acts as image de-rotator for the array.

The high machining accuracy of modern CNC-milling machines allows designing the filter-unit including the SSB-

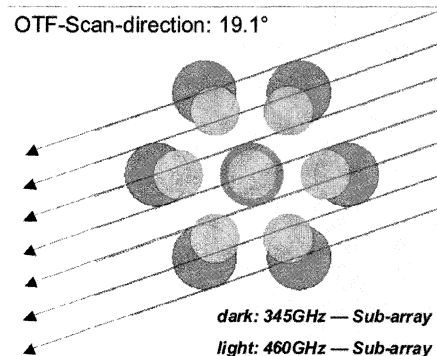


Fig. 2. Footprint of the array planned. Due to the closest spacing for both sub-arrays only the center pixels match in position. An on-the-fly scan-direction of 19.1° will lead to a (projected) beam spacing of 0.5 FWHM.

filters, the duplexers, and the calibration unit as one monolithic block (without the need of adjustment possibilities).

III. OPTICS

For a dual-frequency receiver one of the prime optical requirements beside optimum performance, is to match both frequencies simultaneously to the telescope. Also the LO power must be supplied efficiently to the individual mixer. In the following the optics setup developed so far is explained. The overall layout is fixed, but optimizations are still ongoing.

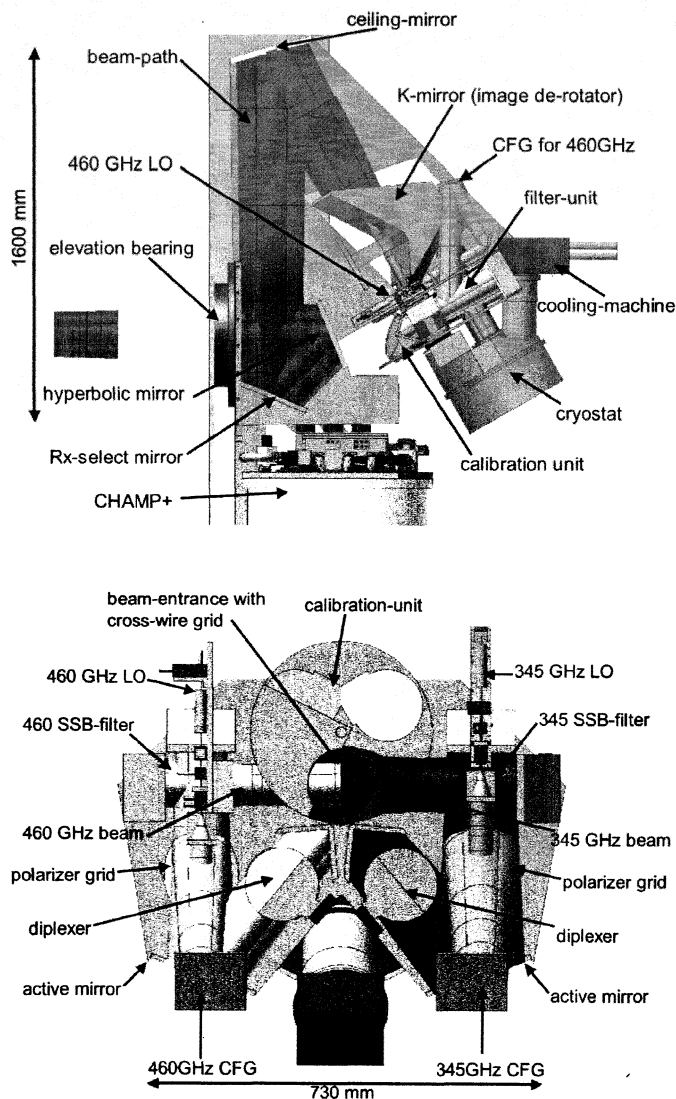


Fig. 3. Schematics of the array-receiver as planned so far. The upper figure shows the optics layout within the APEX Nasmyth-B cabin. The figure below visualizes the optics of the filter-unit.

A. Signal path

For frequency independent re-imaging of the telescope signal we use two Gaussian telescope setups [8]. The first of the two re-images the telescope signal through the narrow elevation bearing of the telescope (this setup is also used by the CHAMP+-array and therefore a given design-constrain). The second one gains additional optical path-length to implement the image de-rotator, the SSB-filter and the diplexer. In addition, it collimates the signals and therefore decreases the size of the cryostat-window down to ≈ 100 mm.

The optics layout is explained in Fig. 3: seen from the telescope, the signal is re-directed towards the Nasmyth B-cabin by the first mirror of the first Gaussian telescope (not shown in the figure). This mirror is mounted on a movable arm inside the Cassegrain cabin, selecting between the two Nasmyth ports. The second mirror of the Gaussian telescope, a concave hyperbolic mirror is located inside the Nasmyth-B cabin and reflects the signal towards a flat mirror that selects between the two arrays in the cabin.

For the new array the signal is reflected upwards to the first mirror of the second Gaussian telescope, which is mounted directly under the cabin ceiling. The image de-rotator follows before the signal enters the filter-unit. Here it first passes the calibration unit, is then split by a cross-wire grid into two orthogonal polarizations. Beneath this grid the cryostat-window for the SSB-filter image side-band termination is located. The image side-band is terminated on an absorber-cone attached to the 4 K-stage.

Calibration will be performed with an internal calibration setup. For a cold load measurement the cross-wire grid is replaced by a flat mirror reflecting the image and the signal-band of one of the two sub-arrays into the cryostat onto the image side-band absorber. To calibrate both sub-arrays a second measurement reflecting this one onto the cold absorber must be taken. For measuring a hot-load an ambient temperature absorber will be placed into the beam-path.

After separating both colors the SSB-filters follow. The second mirror of the Gaussian-telescope is placed between the SSB-filter and the diplexer.

Now the signal enters the cryostat where all individual signals are re-imaged to match the mixer beam to the telescope.

Several numerical simulations of the optics have been done to predict the behavior especially of the off-center pixels. We inserted a Gaussian fundamental mode with the width expected by the horn antenna of the given

frequency and then calculated the overlap-integral with the nominal Gaussian fundamental mode at the telescope focal plane. As a brief summary, for all calculations performed so far, the Gaussicity at the telescope focal plane is above 96% for all pixels under all conditions. As an example the resulting field-distribution (phase and amplitude) of the center-pixel of the 345GHz sub-array and the less efficiently coupling off-axis pixel for 90° elevation and no image-rotation are displayed in Fig. 4. The simulations show no strong elevation dependency of the optics setup (change in Gaussicity is in the order of 0.6%, see also Fig. 6).

B. LO-path

The LO-signal required for the heterodyne mixing process is provided by two commercial LO-chains. Collimating Fourier gratings (CFGs)[9][10] provide the signal splitting into the seven beams required. A CFG is a combination of a diffraction grating designed to match the required beam-

pattern and a parabolic mirror to collimate the resulting diffraction orders. The CFG allows to match the LO directly to the signal path without additional optics. Fig. 5 shows the grating structure and the resulting diffraction pattern as a simulation. The usable bandwidth of the grating is about 15% ($\pm 7.5\%$).

IV. MIXERS

The Universität zu Köln develops the overall mixer design (junction, tuning structures and mixer block) and also fabricates the devices. The mixers will follow the standard DSB fixed backshort waveguide design of the KOSMA-group, like for example used for HIFI Band 2, scaled back to 345 GHz and 460 GHz. Integrated are also internal tuning structures and superconductive magnets to suppress the AC-Josephson effect. In Fig. 7 the CAD-model of such a standard mixer-block is shown.

The IF-band is specified to be 4-8 GHz while the goal for

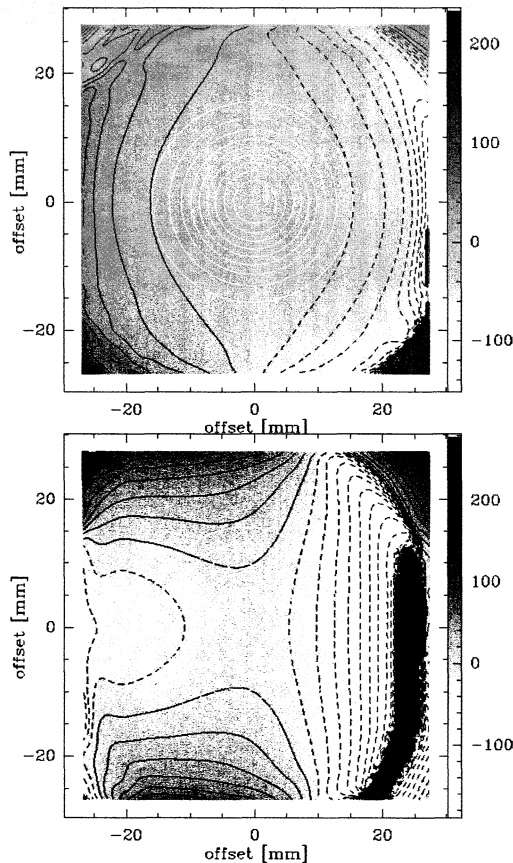


Fig. 4. Results of the optics simulations: the figures (upper figure for the center pixel at 345 GHz; lower figure for the less performing off-axis pixel of the same frequency) show the phase-distribution in grayscale, with black contours in steps of 15°. The white contours display the field-amplitude in steps of 10% of the maximum amplitude. The overlap-integral gives 99.8% Gaussicity for the center and 96.8% for the off-axis pixel.

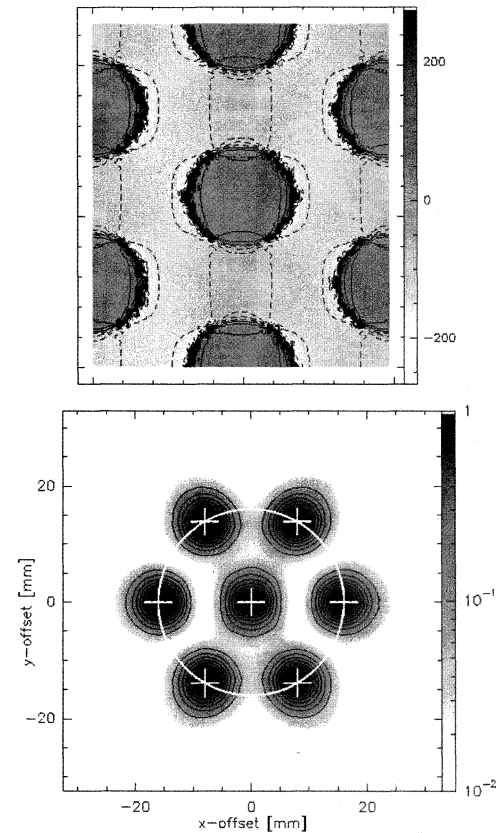


Fig. 5. Phase sensitive structure (left hand side) of the CFG for the LO-splitting. The contour-levels are in steps of 18°-phaseshift. The structure is stretched to have a side-ratio of $\sqrt{3}$ to achieve a round diffraction pattern. Below the simulated diffraction pattern is shown. White crosses mark the nominal positions of the individual mixers. The contour-levels are in steps of 10% of the maximum intensity. Approx. 11% of the incident power is redirected into each of the 7 diffraction orders.

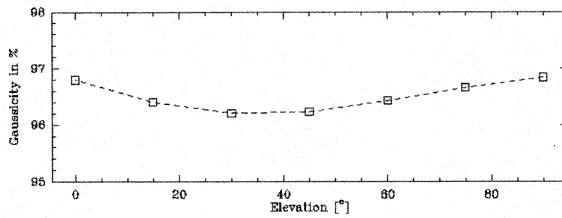


Fig. 6. Numerical simulation of the elevation dependency of one of the off-center beams at 345 GHz.

the mixer DSB noise-temperature (measured after the horn antenna) is ~ 40 K for the 345 GHz band and ~ 60 K for the 460 GHz band.

V. ELECTRONICS

The electronics can be split into two major parts: the mixer-electronics (bias, magnet current and heater) and the IF-processing.

For the bias-electronics we plan for a modular system. Each module contains the electronics for a single mixer and is controlled via computer. Stacking of several modules will easily be possible. All mixers can be set or read out nearly in parallel which makes effective auto-tuning of all mixers within the array possible for the future.

The IF-electronics can be split into two parts: First the HEMT amplifiers (developed in-house at MPIfR) sitting on the 4 K-stage followed by additional amplifiers directly after the vacuum feed through, and second the IF-processor with internal total power detectors and adjustable attenuators matching the signal to the backends. The IF-processor as well as the 32-channel MACS autocorrelator system as backend is part of the CHAMP⁺ array, which has the capability to switch between two array receivers. The usable bandwidth is up to 2 GHz per pixel (using two 1 GHz correlator bands for each of the pixels) with a spectral resolution of 1 MHz. A high-

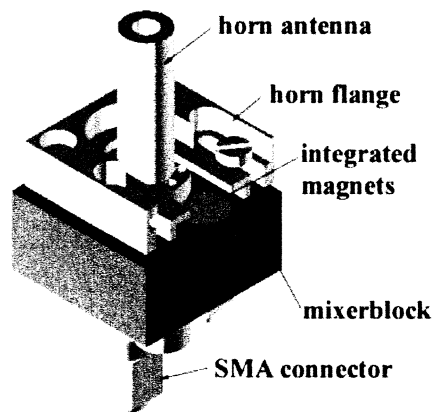


Fig. 7. CAD-drawing of the Cologne standard waveguide mixer block.

resolution mode with a bandwidth of 2×500 MHz and spectral resolution of 256 kHz is also available.

TABLE I
TECHNICAL DATA OF BOTH SUB-ARRAYS.

Sub-array	$\nu = 345$ GHz	$\nu = 460$ GHz
Tuning range (baseline)	<325 – 370 GHz	440 – 500 GHz
IF-bandwidth	4 – 8 GHz	4 – 8 GHz
Half power beam width	17.3"	13.3"
Autocorrelator Backend		
normal resolution mode		
bandwidth	2×1 GHz	2×1 GHz
channel spacing	2×870 km/s	2×650 km/s
channel spacing	1 MHz	1 MHz
channel spacing	0.87 km/s	0.65 km/s
high resolution mode		
bandwidth	2×500 MHz	2×500 MHz
channel spacing	2×435 km/s	2×325 km/s
channel spacing	256 kHz	256 kHz
channel spacing	0.22 km/s	0.16 km/s

VI. REFERENCES

- [1] Güsten, R., Nyman, L.A., Schilke, P., Menten, K., Cesarsky, C. and Booth, R. "The Atacama Pathfinder Experiment (APEX) – a new sub-millimeter facility for southern skies –", A&A special issue 2006, to be published.
- [2] Risacher, C., Vassiliev, V., Monje, R., Lapkin, I., Belitsky, V., Pavolotsky, A., et al., "A 0.8mm heterodyne facility receiver for the APEX telescope", A&A special issue 2006, to be published.
- [3] Heyminck, S., Kasemann, C., Güsten, R., de Lange, G. and Graf, U.U., "The First-Light APEX Submillimeter Heterodyne instrument FLASH", A&A special issue 2006, to be published.
- [4] Graf, U.U., Heyminck, S., Michael, E.A., Stanko, S., Honingh, C.E., Jacobs, K., et al., "SMART, the KOSMA Sub-Millimeter Array Receiver for Two Frequencies", in Millimeter and Submillimeter Detectors for Astronomy, 2003, (Proc. SPIE Vol. 4855, 322-329)
- [5] Schuster, K.-F., et al., "The IRAM 230GHz multibeam SIS receiver", in Imaging at Radio through Submillimeter Wavelength, vol. 217, Astron. Society of the Pacific, 1999.
- [6] Güsten, R. et al. 1998, in Advanced Technologie MMW, Radio, and Terahertz Telescopes, ed. T. G. Phillips (Proc. SPIE Vol. 3357, 167-177)
- [7] Güsten, R., et al., "CHAMP: A powerful array receiver for the APEX telescope", in Proc of SPIE 2006 (to be published).
- [8] Goldsmith, P., "Quasioptical Systems", IEEE Press, 1998.
- [9] Heyminck, S. and Graf, U.U., "Array-Receiver LO Unit using collimating Fourier-Gratings", Proc. of the 12th ISSIT, 563-570
- [10] Graf, U.U. and Heyminck, S. 2001, "Fourier Gratings as Submillimeter Beam Splitters", IEEE Trans AP, Vol. 49(4), 542-546

Focal Plane Heterodyne SIS Receiver Array with Photonic LO Injection

P.G. Huggard & B.N. Ellison
Rutherford Appleton Laboratory
Chilton, Didcot, OX11 0QX, UK

A-L. Fontana, B. Lazareff & A. Navarrini,
Institut de Radio Astronomie Millimétrique
300, rue de la Piscine-38406 St. Martin d'Herès Cedex - France

Abstract

We present the design and first results from a 130 GHz -170 GHz SIS receiver array driven by a photonic local oscillator. This development has been jointly carried out by the Institut de Radio Astronomie Millimétrique (IRAM) and the Rutherford Appleton Laboratory. The work is partially funded by the EU AMSTAR/Radionet programme. The project goal is to build a four-pixel focal plane array demonstrator, composed of double sideband SIS mixers pumped by a photomixer integrated into the receiver cryostat, and to test the array on IRAM's Pico Veleta Telescope in Granada, Spain.

The photomixer and the SIS mixer designed were first characterised separately. The output power available from the p-i-n photodiode based photomixer at room temperature is greater than 10 μ W in the 125 GHz – 175 GHz frequency range. This was achieved for around 10 mW of optical input power, $\lambda \approx 1550$ nm, and a corresponding photocurrent of 4 mA. Little change in output power is observed when the optical fibre coupled photomixer is cooled to below 30 K. The average double sideband noise temperature of the SIS mixer – when measured using a conventional local oscillator (LO) source comprising a Gunn diode oscillator followed by a frequency doubler - was found to be 40 K over the frequency range 130 GHz to 170 GHz. Tests performed on the same SIS receiver pumped by a room temperature photomixer LO have shown a) that the output power delivered by the photonic LO is more than sufficient to pump the SIS mixer over the same frequency range and b) that the measured noise temperature is virtually identical to that obtained with the doubled Gunn LO.

The four-pixel linear array and associated receiver optics design are presented. This array configuration was chosen to be simple, compact, and to allow straightforward extension into a two-dimensional 16-pixel array. The receiver array optics have been designed to meet general requirements for sensitivity, compactness for cold optics integration, and minimisation of thermal loading on the cold stages of the cryostat.

The performance of this type of receiver, measured in terms of bandwidth coverage, noise temperature, LO integration, compactness, elimination of spurious harmonics and thermal budget, represents a clear demonstration of the excellent potential offered by the photonic LO approach with regard to the construction of future large format focal plane array receivers.

Performance of the Band 3 (84-116 GHz) receiver for ALMA

S. Claude, F. Jiang, P. Niranjana, P. Dindo, D. Erickson, K. Yeung, D. Derald, D. Duncan, D. Garcia, D. Henke, B. Leckie, M. Pflieger, G. Rodrigues, K. Szeto, P. Welle, I. Wood and K. Caputa, A. Lichtenberger and S-K. Pan

Abstract— Band 3 covering 84 to 116 GHz is one of the ten bands that will form the Front End Receiver for the Atacama Large Millimetre Array. A Band 3 receiver prototype and one unit have been assembled and tested at the Herzberg Institute of Astrophysics. This paper will give an overview of the Band 3 design and also present the performance of the first deliverable unit. The single sideband (SSB) system noise exceeds the specifications ($TSSB < 37$ K) over the full RF band with a minimum TSSB of 26 K and a maximum of 34 K. In addition to details of the system noise performance other characteristics such as image rejection and cross-polarization are also presented.

I. INTRODUCTION

THE Atacama Large Millimetre Array (ALMA), that will be built in the Atacama desert in Chile at 5000 m altitude, consists of an array of 50, 12 m antennas operating in the millimetre and sub-millimetre range. An additional 16 antennae array will form the Atacama Compact Array. The Band 3 receivers, covering the frequency range 84-116 GHz, will operate in spectroscopic and continuum modes on both arrays.

II. RECEIVER DESIGN

The receiver consists of a cartridge (Fig. 1) that can be inserted in the main ALMA front-end cryostat. The signal collected by the telescope is focussed to the Band 3 cartridge using a set of warm mirrors (one flat and one ellipsoidal) that are fixed to the top surface of the front-end cryostat [1]. Note that the data presented in this paper were taken without the warm mirrors. After the vacuum window (consisting of a moulded high-density polyethylene disk with anti-reflection grooves on both sides), IR filtering is done at 80 K will be a PFA moulded disk and at 15 K with a Mupore membrane [1].

On the 4 K stage the input signal is collected by a corrugated aluminium feedhorn and its PTFE plano-convex lens [1]. The two orthogonal polarizations (0 and 1) are

split using an Orthomode Transducer (OMT) [2]. From that point, the two polarization channels are identical in design and therefore only one of the two will be described.

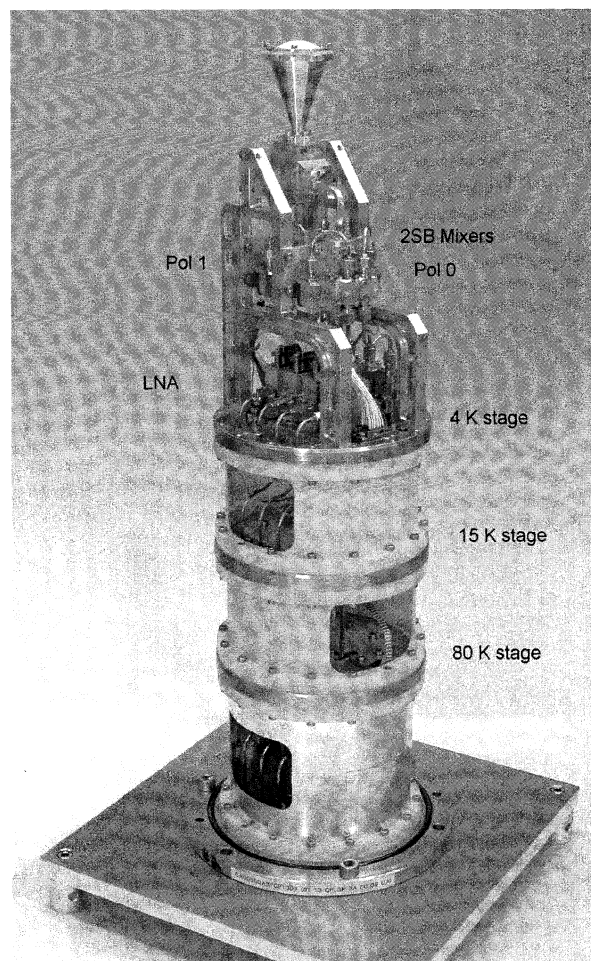


Fig. 1: Photograph of the Band 3 cartridge (height is 508.5 mm)

The RF signal (84-116 GHz) is down converted to 4-8 GHz using a side-band separating (2SB) mixer unit which is described in detail in [3]. The outputs of the 2SB unit are the upper sideband (USB) and the lower sideband (LSB) centred at 6 GHz. The signals are then amplified with cryogenic low noise amplifiers [4] fixed to the 4K stage. Since these amplifiers are optimized for low noise, bandwidth, and gain (rather than the input RF impedance match) the use of 4-8 GHz isolators (from Pamtech)

S. Claude, F. Jiang, P. Niranjana, P. Dindo, D. Erickson, K. Yeung, D. Derald, D. Duncan, D. Garcia, D. Henke, B. Leckie, M. Pflieger, G. Rodrigues, K. Szeto, P. Welle, I. Wood and K. Caputa are with the Herzberg Institute of Astrophysics of the National Research Council, Victoria, BC, Canada (phone: (250) 363-0030; fax: (250) 363-0045; e-mail: stephane.clauder@nrc.ca).

A. Lichtenberger is with the University of Virginia, Charlottesville, USA

S-K. Pan is with the National Radio Astronomy Observatory, Charlottesville, USA

prevents signal reflections between the mixer unit and the amplifier.

The IF signals are then brought out to the cartridge vacuum flange using UT85 BeCu-SS coaxial cables. In order to satisfy the ALMA IF power level requirements, 30 dB room temperature IF amplifiers (one per IF channel) are added at the output of the cartridge.

To facilitate troubleshooting during operation, temperature sensors are placed at each stage of the cartridge and on each mixer assembly. Bias voltages for the mixers and the amplifiers are fed through two MDM-51 connectors on the vacuum flange. Inside the vacuum and room temperature, a mixer and LNA bias protection circuit card, consisting of clamp diodes, is connected to the MDM-51 feedthrough. The card also generates an electronic serial number for the cartridge and polarisation number. A standard twisted pair wiring harness (36 AWG phosphor-bronze, 450mm long), with MDM-25 connectors on each end, feeds the bias from the 300 K to the 4 K plate. Each amplifier has an integrated bias circuit for the SIS mixers.

The local oscillator (LO), of which a full description can be found in [5], is generated by a YIG oscillator (15-18 GHz). The LO signal is amplified and frequency multiplied by 6 before it is fed through the WR-10 vacuum feedthrough. A Mylar membrane is used to provide the vacuum seal for all feedthrough waveguides. The LO is brought to the mixer unit using an SS WR-10 waveguide (one per polarization) with bends to allow for thermal contractions between the different cryogenic stages. To attenuate the LO thermal noise, a 10 dB absorber is inserted at the 4 K end of the waveguide.

III. RECEIVER PERFORMANCE

A. Receiver noise temperature

The Band 3 receiver is tested at HIA using a three stage cryostat, provided by the National Astronomy Observatory of Japan (NAOJ). The Band 3 cartridge noise temperature is measured using a liquid nitrogen load (bucket with absorber liner) and a room temperature load. A chopper wheel switches the input signal from the hot to the cold load. The output IF of the receiver is filtered using a fixed bandpass 4 GHz filter for the wideband measurement or a 100 MHz YIG filter for narrow band measurements. The signal is then amplified before it is detected by an Agilent 4418B power meter and an Agilent 4412A CW power sensor. The receiver noise temperature of the Band 3 receiver is using the standard equation:

$$T_{rec} = \frac{Th - Tc \times Y}{Y - 1} \text{ where}$$

$$Y = \frac{PHin}{PCin}$$

Th and Tc are the calibrated hot and cold load temperatures. Since the liquid nitrogen bucket is seen by the feedhorn after a couple of mirror reflections, the true temperature of the cold load is not the same as the temperature of the boiling point of liquid nitrogen which is 77.35 K. The cold load is calibrated by placing a cone made of the AN72 Eccosorb

absorbing material directly over the cryostat window. Tc is calculated to be 83.3K

$PHin$ and $PCin$ are power meter readings when the hot and the cold loads are presented to the input of the band 3 receiver. Therefore, $Trec$ is the measured single side band noise temperature, un-corrected for imperfect image rejection. The corrected single side band noise temperature is calculated as follows;

$$T_{SSB} = Trec \left(1 + \frac{1}{R} \right)$$

where

R is the image rejection.

If the measured receiver noise is 37 K, the added noise can be 3.7 K for a 10 dB image rejection or 0.37 K for a 20 dB image rejection. Typically, for the band 3 receiver, a 15 dB image rejection (see section B below) is obtained so the added noise is 1.1 K. Noise temperatures presented in this paper are corrected for the imperfect image rejection of the 2SB mixers.

In the ALMA cryostat, the Band 3 mixers will be operated at a temperature of 4 K +/-0.25 K. Furthermore, a separate tuning table will be used for each of the mixers. Therefore, it is important to generate the tuning table (mixer bias and LO power as function of LO frequency) for optimum noise performance at the prescribed operating temperature. Table 1 was generated by tuning the mixer of a prototype cartridge at 3.75 K and then the receiver noise was measured when the mixer was operated at 4.00 K and then 4.25 K. The same procedure was then followed at 4 K and then at 4.25 K. Tuning the mixer at 4.00 K provides the optimum noise performance for a mixer that will be operated between 3.75 and 4.25 K. When the mixers are cooled the I-V curves are changed so that the energy gap is increasing. As a result, the optimum bias is varying with operating temperature. It should be noted that for consistency with the ALMA cryostat, all mixer noise data presented in this paper were taken at 4.00 K. An improvement of 1.7 K can be obtained if the cryostat is cooling the mixers at 3.75 K.

Mixer tuning temperature (K)	Measured Treceiver		
	@ 3.75K	@ 4.00K	@ 4.25K
3.75	37.1	39.8	44.5
4.00	36.9	38.6	42.1
4.25	38.1	39.3	41.1

Table 1: Polarization 0 USB mixer temperature – Band 3 prototype

The Band 3 receiver single sideband noise performance is plotted for each of the four IF channels as a function of the RF frequency in Fig 2. Each point corresponds to an average of the noise taken in 4 GHz band centered at 6 GHz. Therefore, the receiver can detect signals within the full RF bandwidth 84-116 GHz simultaneously with two polarizations. The noise temperature specification is such that the noise must be less than 37 K for 80 % of the RF band and less than 62 K for any point within the RF band. This noise includes the input cryostat window at the input end and the warm IF amplifiers at the output end.

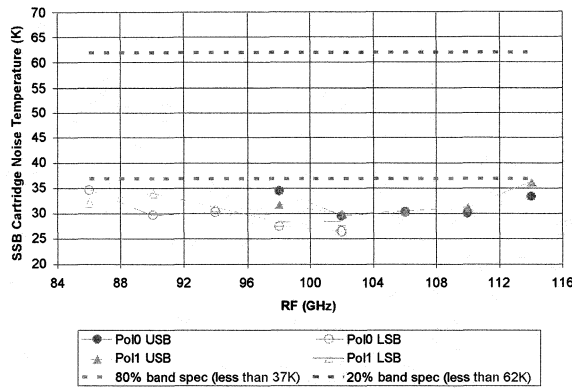


Fig 2. Band 3 Receiver broadband noise temperature

Using a 100 GHz YIG filter, the narrow band noise is also measured for each channel between 4 and 8 GHz. The noise must be less than +/-25% of the average noise. An example is shown in Fig 3.

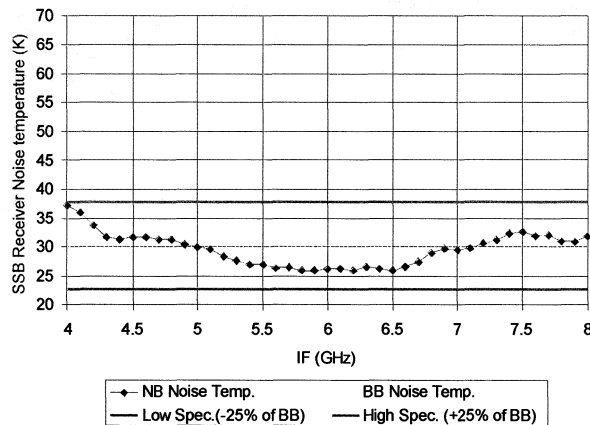


Fig 3: Narrow band noise temperature at LO=100 GHz, Mixer at 4.00K, Pol 0-USB

The noise temperature of the Band 3 cartridge, using a 2SB mixer, can be expressed by the following equation.

$$T_{receiverSSB} = 2(T_{receiverDSB}) + L_{optics}T_{load} - T_{optics}$$

where

T_{load} is 4.2 K, as the image side in the 2SB mixer is terminated by an absorber.

The optics, consist of all the components between the RF vacuum window to the input of the mixer units, $T_{optics}=2.5$ K, and $L_{optic}=0.4$ dB

This analysis assumes a perfect image rejection since the noise results in Fig. 2 have already been corrected.

And finally, $T_{receiverDSB}$ is the double side band noise of the mixer including the LO sideband noise which is less than 1 K. Also, the use of a cryogenic attenuator (10 dB) between the LO and the 16 dB coupler reduces the thermal LO noise to a value of 2 K which is included in the $T_{receiverDSB}$.

$T_{receiverDSB}$ excludes the input optics as it is taken at the input of the mixer. The DSB noise consists of the mixer noise and gain in cascade with the cryogenic IF amplifier.

The noise contribution of the isolator is 1 to 2 K. As for the mixer [6], its noise is estimated to be 5 to 10 K and conversion loss to be 0.8 to 3 dB. The IF chain noise is dominated by the noise of the cryogenic amplifier since its gain, 35 dB, makes the noise contribution of the subsequent component negligible, i.e. of the order of 0.1 K. The noise of the cryogenic amplifiers is 3.5 K, averaged across the full IF band width. As a result, $T_{receiverDSB}$ is equal 13K for best mixer gain and noise, and can be up to 22 K in the worst case.

Taking all the above mentioned noise contributions, the total estimated SSB noise varies from 25 K to 42 K. In practice, the noise varies from 26 K to 36K across the RF band for the four IF channels. It must be noted that the quantum noise at 100 GHz is $h\nu/k=4.8$ K. Therefore, the best measured noise, 26 K at 102 GHz, is obtained with a mixer operating close to the quantum limit.

B. Image Rejection

In order to measure the image band suppression, a CW signal is injected through the hot load, using a WR-10 waveguide probe and detected in both upper and lower sidebands by the Band 3 receiver. The CW signal is generated by using an Agilent E8257D synthesizer and a X6 Millitech Multiplier. The image rejection of the cartridge is found by using the techniques of Kerr et. al described in [7]. The technique requires the measurement of heat power levels as listed in Table 2.

Input	OutputPort Detection
Hot Load	USB
Cold Load	USB
Cold Load	LSB
Hot Load	LSB
Signal source in LSB	LSB
Signal source in LSB	USB
Signal source in USB	USB
Signal source in USB	LSB

Table 2. Configuration of the input and output ports for the measurement of the image rejection.

The image rejection is measured in narrow band mode with a 100 MHz YIG filter across the IF band, for each LO frequency. An example is shown in Fig 4.

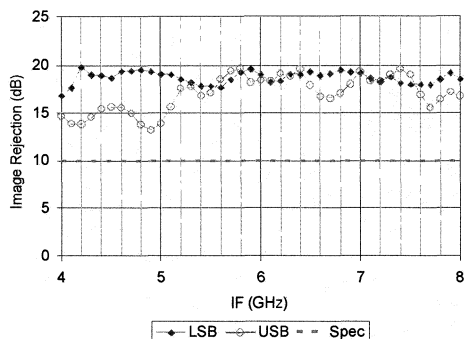


Fig 4: Image Rejection of the Pol 0, LSB and USB, in narrow band mode, at LO=100 GHz.

For each LO frequency, an average was calculated and plotted against the receiver RF bandwidth, in Fig. 5, for the four channels.

The only element in the cartridge that contributes to the image rejection quantity is the 2SB mixer described in [3]. The variation across the IF can be controlled by phase matching the IF cables connecting the DSB mixers and the IF quadrature coupler. The phase and amplitude imbalance of this later component is important as well.

On the RF side, the Phase and amplitude imbalance must be controlled by maintaining a high machining tolerance (5 microns) on the RF waveguide coupler. Also, the gain match of the DSB mixer must be controlled by RF pre-screening prior to the forming the 2SB assembly.

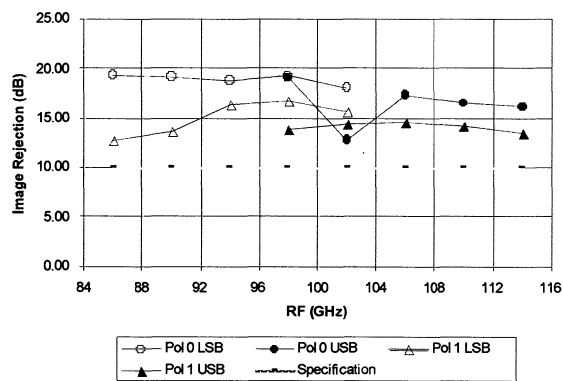


Fig. 5: Image rejection of the four channels

C. Cross-Polarization

Radiating a CW signal using a WR-10 waveguide in front of the receiver window allows to measure the cross polarisation of the Band 3 receiver. The optics of the receiver including the vacuum window, IR filters and corrugated horn plus lens, are not the dominant contributor to the cross polarisation, as opposed to the OMT, described in [2], which is the principal component generating the small amount of cross-polarisation shown in Fig. 6.

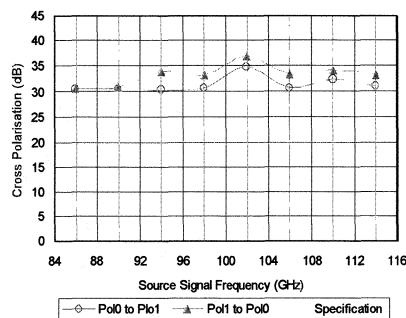


Fig 6. On-axis cross-polarisation

REFERENCES

- [1] M. Carter et al. "ALMA Front-end Optics", SPIE Conference, Glasgow, U.K. June 21-25, 2004 pp 1074-1084 Vol. 5489
- [2] Edward J. et al. "The Boifot Orthomode Junction", ALMA MEMO #425, 2002/05/22
- [3] P. Dindo et al. "Design and Characterization of Two Sideband SIS Mixer RF Hybrids for the Band 3 Receiver (84-116 GHz)", 30th Int. Conf. Infrared and Millimeter Waves, Williamsburg, USA, September 19-23, 2005.
- [4] N. Jiang et al. "Low-noise InP HEMT amplifier", Proceedings of the SPIE, Volume 5489, pp. 848-857 (2004).
- [5] E. Bryerton et al. "Development of Electronically Tuned Local Oscillators for ALMA", 30th Int. Conf. Infrared and Millimeter Waves, Williamsburg, USA, September 19-23, 2005
- [6] S.-K. Pan et al "A Fixed-Tuned SIS Mixer with Ultra-Wide-Band IF and Quantum-Limited Sensitivity for ALMA Band3 (84-116 GHz) Receivers", 15th International Symposium on Space Terahertz Technology, April 2004.
- [7] A.Kerr et al. "Sideband Calibration of Millimeter-Wave Receivers", ALMA Memo #357, March 27, 2001.

A 385-500GHz Balanced Mixer with a Waveguide Quadrature Hybrid Coupler

Yasutaka SERIZAWA^{1,2}, Yutaro SEKIMOTO^{1,2}, Tetsuya ITO², Wenlei SHAN^{2,3},
Toshiaki KAMBA², Naohisa SATOU², Mamoru KAMIKURA^{1,2}

Abstract—We developed a 385-500GHz balanced mixer with a waveguide quadrature hybrid coupler. The balanced mixer consists of an RF quadrature hybrid coupler, two double sideband (DSB) SIS mixers with noise temperature of $\sim 60\text{K}$, and an IF 180 degree hybrid coupler covering 4 - 8 GHz IF band. An RF quadrature hybrid coupler was designed and fabricated whose fabrication error was within $5\mu\text{m}$. The noise temperatures of the balanced mixer was similar to those of two DSB mixers in spite of adding an RF quadrature hybrid and an IF coupler. The required LO power for pumping the balanced mixer was reduced by $\sim 12\text{dB}$ on average compared with those for the DSB mixers and -15dB coupler. The sideband noise of the local oscillator (a quintupler + a Gunn oscillator) was measured to be 20K at offset frequency of 4 - 8 GHz, which corresponds to $70\text{K}/\mu\text{W}$. To authors' knowledge, this is the first direct measurement of LO sideband noise at submillimeter range. If a varistor quintupler degrades the signal-to-noise by 10dB (K. Saini 2003 [1]), the sideband noise of a Gunn oscillator is $7\text{K}/\mu\text{W}$ at the offset frequency of 0.8-1.6 GHz.

Index Terms—balanced mixer, LO sideband noise, noise temperature

I. INTRODUCTION

BALANCED mixers are useful components of receivers for radio astronomy at submillimeter and terahertz frequency range, where enough LO power is not available. Balanced mixers have some advantages over single-ended mixers. 1: The required LO power is substantially less than that of a single-ended mixer. 2: The LO sideband noise can be reduced. So far, several balanced mixers have been developed at submillimeter-wave bands, such as a 180-420GHz waveguide type [2], a 200-300GHz coplanar waveguide type [3], and a 530GHz quasioptical type [4], and a 1.32THz waveguide type (HEB) [5]. However, noise temperature of a balanced mixer and a single-ended mixer has not been compared. In present work, we not only compare noise temperature of a balanced mixer and a single-ended mixer, but also derive sideband noise of a local oscillator.

Manuscript received May 31, 2006. This work was partially supported by Grant-in-Aid of JSPS No. 17340058.

¹Department of Astronomy, School of Science, the University of Tokyo
²Advanced Technology Center, National Astronomical Observatory of Japan, National Institutes of Natural Sciences, 2-21-1 Osawa, Mitaka-shi, 181-8588 Tokyo, Japan(phone:+81-422-34-3981;fax:+81-422-34-3864)

³Purple Mountain Observatory, Chinese Academy of Sciences
Yasutaka SERIZAWA E-mail: serizawa.yasutaka@nao.ac.jp

There are two types of balanced mixers. One is quadrature-hybrid type, and the other is 180-degree-hybrid type. In present work, we used the former type of the balanced mixer, because the quadrature hybrid at this frequency has been established by M. Kamikura et al. [6].

LO signal is usually coupled into a single-ended mixer with a LO coupler. The coupling of LO signal is ~ -15 to -20 dB, so that most of LO power is wasted in LO coupler. Taking account of use of 3-dB coupler in balanced mixers, the required LO power for a balanced mixer can be reduced by 12-17dB compared with that for single-ended mixers.

II. BALANCED MIXER AND SETUP

A. RF quadrature hybrid

We designed and fabricated a waveguide type quadrature hybrid coupler optimized to 385-500 GHz frequency band [7]. The waveguide size is $508\mu\text{m} \times 254\mu\text{m}$ (WR2.0). The design values and measurement values of the branch lines are shown in Fig.1. The fabrication error is within $\sim 5\mu\text{m}$.

We designed it with a commercial 3D electromagnetic field simulator, HFSS (High Frequency Structure Simulator). The quadrature hybrid is split at the edge of the E-plane to reduce the loss resulting from the misalignment of the two split blocks [6]. The transmission of this coupler was measured and was similar to that of [6].

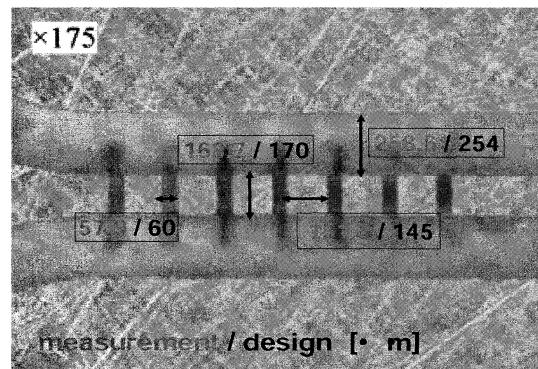


Fig. 1. The macrograph of branch lines of a 90 degree hybrid coupler. Dimensions are in μm . The fabrication error is within $\sim 5\mu\text{m}$. The depth of the waveguide is $508\mu\text{m}$.

B. Single-ended mixer

Single ended mixer for this balanced mixer is an SIS mixer developed by W. L. Shan et al. [8] [9]. It is Nb-based parallel connected twin junction. The Josephson current was suppressed with a super-conducting magnet. The input waveguide size is WR2.0 (508 × 254 μm).

C. Local oscillator

Local oscillator is composed of a Gunn oscillator (~ 90 GHz) from RPG [10] and a cryogenic frequency multiplier or a varistor quintupler from VDI [11]. The LO power was measured at the input of the balanced mixer at room temperature. If the quintupler is cooled from 300K to 12K, its efficiency would increase by 20%.

D. The balanced mixer

Fig.2 shows the block diagram of the balanced mixer and its system. The balanced mixer consists of an RF quadrature hybrid coupler, two single-ended (DSB) mixers, and an IF 180 degree hybrid coupler. In the IF system, isolators and IF amplifiers are used in and out of the cryostat.

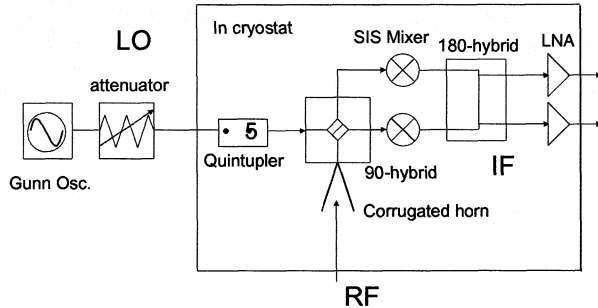


Fig. 2. Block diagram of the balanced mixer. We used an RF quadrature-type balanced mixer. The balanced mixer consists of an RF quadrature hybrid, two SIS mixers, and an IF 180 degree hybrid.

III. MEASUREMENTS

A. Noise temperature

We first measured the noise temperatures of two single-ended mixers by Y-factor method using hot (300K) and cold (77K) load. The mixers were in a vacuum dewar cooled to about 4 K. The RF signal was fed into the LO coupler via a corrugated horn [12]. Noise temperatures of the single-ended SIS mixers were measured with a -15 dB waveguide LO coupler [6]. Then the noise temperature of the balanced mixer was measured.

Fig.3 and Fig.4 show the I-V curves and noise temperatures of the single-ended mixers and the balanced mixer respectively. At LO frequency of 450GHz, the balanced mixer has almost the same noise temperature as the single-ended mixers.

Frequency dependence of noise temperatures of single-ended mixers and the balanced mixer is shown in Fig.5. The noise temperatures of two single-ended mixers are similar (especially at higher frequencies), so that the conversion gain of single-ended mixers may be similar at higher frequencies. As expected, there is no significant increase in noise temperature of the balanced mixer in spite of adding the quadrature hybrid and the IF 180 degree hybrid.

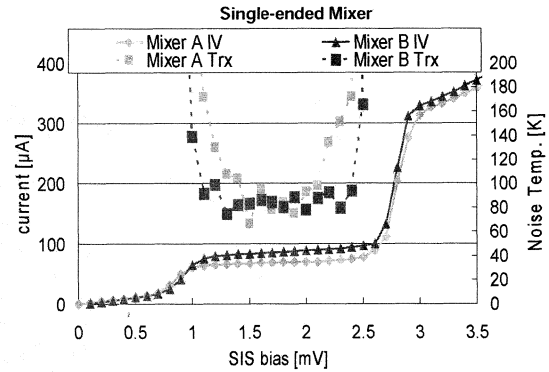


Fig.3. The IV curves and noise temperatures of the single-ended mixers in the IF band of 4-8GHz. The LO frequency is 450GHz.

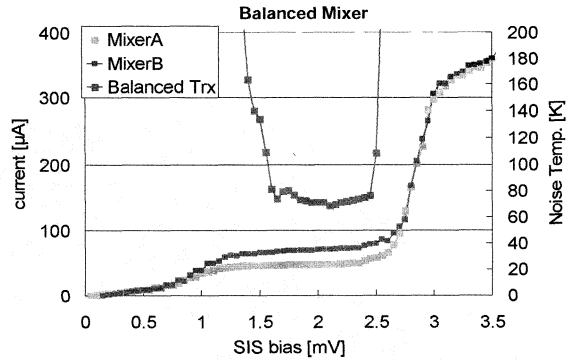


Fig. 4. The IV curves and noise temperatures of the balanced mixer in the IF band of 4-8GHz. The LO frequency is 450GHz (band center).

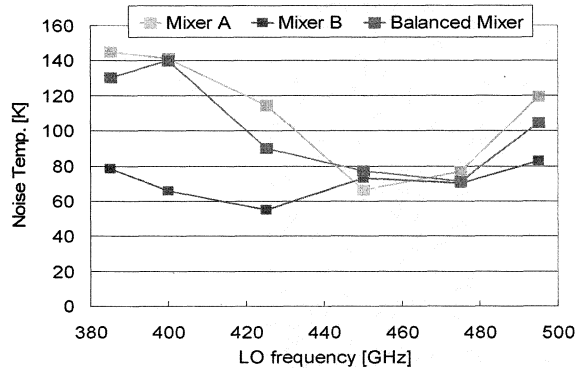


Fig. 5. The noise temperature of two single-ended mixers and the balanced mixer. There is no significant increase of noise temperature due to adding the RF quadrature hybrid and IF 180 degree hybrid.

B. LO power

Fig.6 shows the required LO powers for two single-ended mixers and the balanced mixer. In case of measuring noise temperature of the single-ended mixers and the balanced mixer at 4K, the parameters of the Gunn oscillator and the attenuator were recorded. The LO powers required for the single-ended mixers and the balanced mixer were measured at room temperature with the same parameters as in case of 4K. Then we compared the measured LO power of the balanced mixer with that of each single-ended mixer. The result is shown in Fig.6. The cooling effect of 20 % increase in efficiency of a quintupler is common to both the single-ended mixers and the balanced mixer. The effect is not

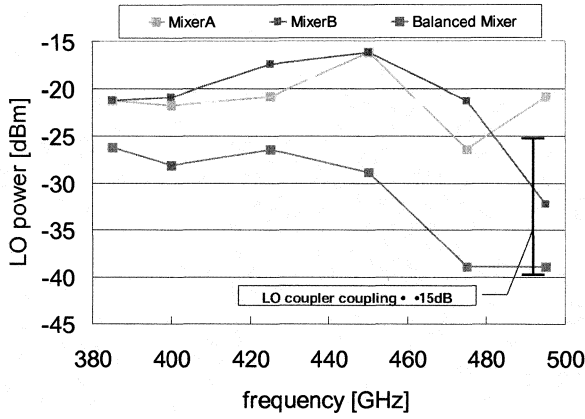


Fig. 6. Required LO power required for pumping SIS mixers was measured at the input of the balanced mixer at room temperature. The required LO power is reduced by ~12dB on average. The LO coupling of -15 dB for single-ended mixers is indicated for reference.

corrected in this Figure.

It can be found that the required LO power for the balanced mixer is reduced by ~ 12dB on average. Furthermore, at higher frequencies the LO power reduction is better than at lower frequencies. This is consistent with a fact that the two DSB mixers have the same noise temperature (see Fig.5). According to Fig.5, at lower frequencies two SIS mixers may have relatively different conversion losses, but at higher frequencies they may have similar conversion losses.

C. LO sideband noise

We measured LO sideband noise of a quintupler + a Gunn oscillator. Fig.7 explains a derivation of LO sideband noise. The leakage δ which expresses the ratio of the LO sideband noise outputted from the signal port is defined (see Fig.7).

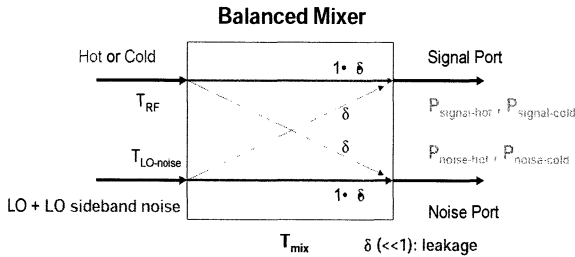


Fig. 7. Simplified derivation of LO sideband noise from a balanced mixer. The balanced mixer consisting of a quadrature hybrid, two single-ended SIS mixers, and an 180 degree hybrid can be regarded as one component whose noise temperature is T_{mix} . The leakage δ is 0 if the balanced mixer works ideally.

If the balanced mixer works ideal, the δ should be 0. In fact, the leakage of the LO sideband noise and that of the signal are not the same, but we considered those are the same in the first order approximation. P_{signal} and P_{noise} are the powers outputted from the signal and noise ports, respectively. Then, the following equations are derived. (Δf : band width)

$$P_{signal} = G_{IFsignal} k_B [(1 - \delta)T_{RF} + \{T_{mix} + \delta T_{LO-noise}\}] \Delta f \quad (1)$$

$$P_{noise} = G_{IFnoise} k_B [\delta T_{RF} + \{T_{mix} + (1 - \delta)T_{LO-noise}\}] \Delta f \quad (2)$$

Fig.8-10 shows the results derived from measurements with integrated IF frequency of 4 – 8 GHz. The signal and noise ports interchange with changing SIS bias polarity. The four

data points from bias polarities of two SIS mixers were obtained.

The values of δ are lower at higher frequencies, which is consistent with the similar conversion gains of two SIS mixers at higher frequencies. The value of 0.03 corresponds to noise reduction ratio of - 17 dB. Fig.9 shows the values of T_{mix} . The result is consistent with the measured noise temperatures of the balanced mixer (Fig.5). Fig.10 shows the LO sideband noise ($T_{LO-noise}$) integrated in the IF frequency of 4 – 8 GHz.

Fig.11 shows IF-frequency dependence of δ , T_{mix} , and $T_{LO-noise}$. The mixer noise temperature T_{mix} and the leakage δ are flat over IF frequency from 4 – 8 GHz, but the LO sideband noise $T_{LO-noise}$ has large ripples. It is due to standing

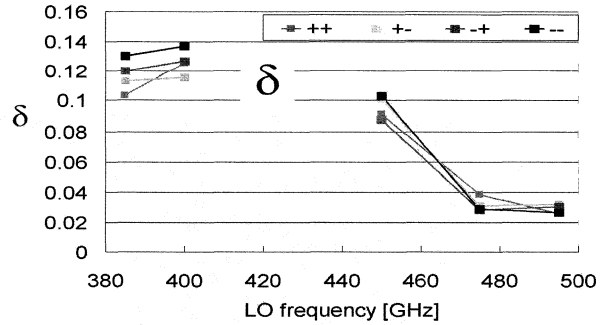


Fig. 8. The measurement result of the leakage δ . The difference of the colors expresses the polarity of two mixer biases.

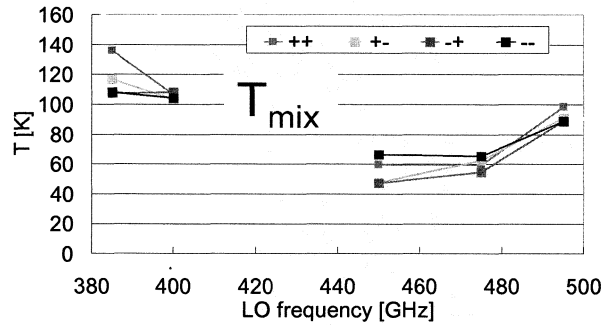


Fig. 9. Derived noise temperature of the balanced mixer in the IF frequency of 4 – 8 GHz. The difference of color expresses the polarity of two mixer

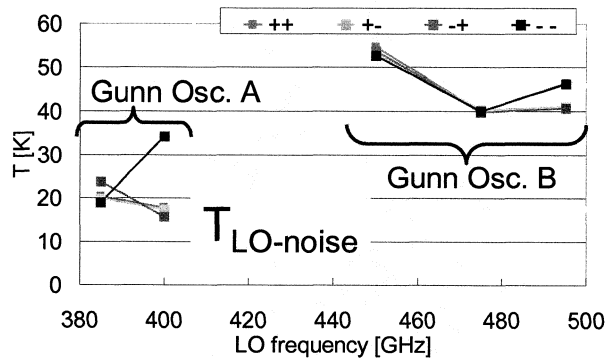


Fig. 10. Derived LO sideband noise ($T_{LO-noise}$) in the IF frequency of 4-8 GHz. Note that a Gunn oscillator used for 380-400GHz is different from that for 450-500 GHz. The difference of color expresses the polarity of two mixer biases.

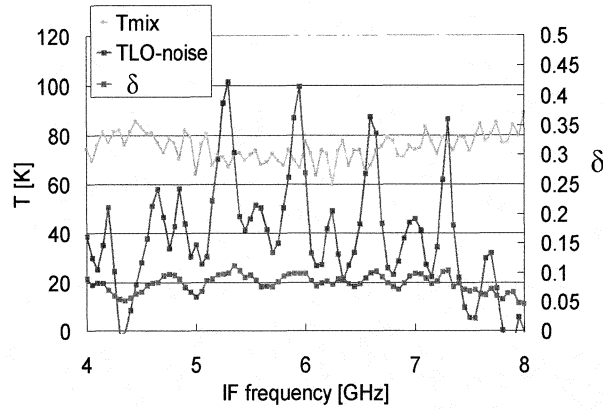


Fig. 11. IF-frequency dependence of leakage δ , mixer noise temperature T_{mix} , and LO sideband noise $T_{\text{LO-noise}}$.

waves in the LO path. The LO sideband noise without the ripple was $\sim 20\text{K}$. $T_{\text{LO-noise}}$ at lower frequencies where there wouldn't be such large ripples was also $\sim 20\text{K}$. This means that noise temperature of a DSB mixer at this frequency includes LO sideband noise of 10K . This fact is consistent with the difference of noise temperatures of Fig.5 and Fig.9.

Based on the calculated LO power for a SIS junction of $0.13\mu\text{W}$ [13], the input power for the balanced mixer is $\sim 0.3\mu\text{W}$ (3dB quadrature hybrid). So, the LO sideband noise whose offset is 4-8GHz is $70\text{K}/\mu\text{W}$ (quintupler + Gunn oscillator). K. Saini (2003) [1] calculated that a varistor quintupler degrades the signal-to-noise by 10dB. According to it, the sideband noise of a Gunn oscillator corresponds to $\sim 7\text{K}/\mu\text{W}$ whose offset is 0.8-1.6GHz.

The shot noise is given as the following equation [14].

$$T_{\text{shot}} = \frac{P_{\text{shot}}}{k_B \Delta f} = \frac{2e}{k_B} I_{\text{bias}} R \quad (3)$$

Substituting $I_{\text{bias}}=0.2\text{A}$ and $R=10\text{V}/0.2\text{A}=50\Omega$ (operating values of the Gunn oscillator) into the above equation yields $T_{\text{shot}}=2.3 \times 10^5 \text{K}$. The output power of the carrier signal of a Gunn oscillator is $\sim 3 \times 10^4 \mu\text{W}$. Therefore, the sideband noise of Gunn oscillator is estimated to $\sim 8\text{K}/\mu\text{W}$ or -160dBc/Hz from shot noise.

Following the above results, LO sideband noise for an typical SIS mixer covering any frequencies can be estimated. The LO power for a single-ended mixer at 100GHz is ([13])

$$P_{\text{LO}} = \left(\alpha_n \frac{N_j h f}{e} \right)^2 / 2R_N = 0.017 [\mu\text{W}] \quad (4)$$

, where $\alpha_n \sim 1$, N_j (the number of the junction)=2, h : Planck constant, $f=100\text{GHz}$, e : electron charge magnitude, and R_N (normal resistance)= 20Ω . Thus, a single-ended SIS mixer pumped with a Gunn oscillator at 100GHz should have an LO sideband noise of $\sim 7 [\text{K}/\mu\text{W}] \times 0.017 [\mu\text{W}] = 0.12 [\text{K}]$, which is not easy to measure. The LO power required for pumping an SIS mixer is proportional to the square of frequency [13]. In general, a multiplier degrades sideband noise by $20\log(n)$ or the square of multiplication (n : multiplication) [14]. That is, the LO sideband noise of multiplier chain for SIS mixers is roughly proportional to the 4th power of frequency. For example, a single-ended SIS

mixer operating at 1THz with 10 times multiplication would have a sideband noise of $10 [\text{K}] \times (1\text{THz} / 500\text{GHz})^4 = 160 [\text{K}] \sim 3.3hf/k$, which can be major of the low noise THz receiver.

IV. CONCLUSION

We developed and measured a 385-500GHz waveguide and modular type balanced mixer with a waveguide quadrature hybrid coupler. The measured noise temperature is almost the same as that of each single-ended mixer. There is no significant increase of noise temperature due to adding the quadrature hybrid and the IF 180 degree hybrid. The required LO power is less than the single ended mixers by $\sim 12 \text{dB}$ on average. Furthermore, based on the result of measurement of the output power we estimated the LO sideband noise using the balanced mixer. LO sideband noise (a quintupler + a Gunn oscillator) for two mixers was measured to be $\sim 20\text{K}$ or $70\text{K}/\mu\text{W}$. Sideband noise of a Gunn oscillator was derived to be $\sim 7\text{K}/\mu\text{W}$, which is consistent with shot noise.

ACKNOWLEDGMENT

We are grateful to Junji Inatani of NAOJ for many helpful advices to this work. The authors would also like to thank Yu Tomimura, Yoshizo Iizuka, Shin'ichiro Asayama, Takashi Noguchi and Yoshinori Uzawa of NAOJ.

REFERENCES

- [1] K.S. Saini, "Development of Frequency Multiplier Technology for ALMA", a dissertation at the University of Virginia, 2003. <http://www.alma.nrao.edu/memos/html-memos/alma337/memo337.pdf>
- [2] J. W. Kooi, A. Kovács, B. Bumble, G. Chattopadhyay, M. L. Edgar, S. Kaye, R. LeDuc, J. Zmuidzinas, and T. G. Phillips, "Heterodyne Instrumentation Upgrade at the Caltech Submillimeter Observatory", *SPIE, Astronomical Telescopes and Instrumentation*, 2004. http://www.submm.caltech.edu/cso/receivers/papers/spie_2004.pdf
- [3] A. R. Kerr, S.-K. Pan, A. W. Lichtenberger, N. Horner, J. E. Effland, and K. Crady, "A Single-chip Balanced SIS Mixer For 200-300 GHz", *proceedings of 11th International Symposium on Space Terahertz Technology (ISSTT)*, 2000. <http://www.alma.nrao.edu/memos/html-memos/alma308/memo308.pdf>
- [4] G. Chattopadhyay, F. Rice, D. Miller, H.G. LeDuc, and J. Zmuidzinas, "A 530-GHz Balanced Mixer", *IEEE Microwave and Guided Wave Letters*, Vol. 9, No. 11, 1999.
- [5] M. Pantaleev, D. Meledin, A. Pavolotsky, C. Risacher, and V. Belitsky, "Design of a Balanced Waveguide HEB Mixer for APEX 1.32THz Receiver", *proceedings of 15th ISSTT*, 2004.
- [6] M. Kamikura, Y. Tomimura, Y. Sekimoto, S. Asayama, W.L. Shan, N. Satou, Y. Iizuka, T. Ito, T. Kamba, Y. Serizawa, and T. Noguchi, "A 385 - 500 GHz Sideband-Separating (2SB) SIS Mixer Based on a Waveguide Split-Block Coupler", *International Journal of Infrared and Millimeter Waves*, in press.
- [7] Oshima Prototype Engineering, <http://www.ijinet.or.jp/oshima/>.
- [8] W.L. Shan, T. Noguchi, S. C. Shi, and Y. Sekimoto, "Design and Development of SIS Mixers for ALMA Band 8", *IEEE Trans. Appl. Superconductivity*, Volume 15, Issue 2, pp. 503 - 506, 2005.
- [9] W.L. Shan, S. Asayama, M. Kamikura, T. Noguchi, S. C. Shi and Y. Sekimoto, "Development of a 385 - 500 GHz SIS mixer for ALMA band 8", *proceedings of the 16th ISSTT*, 2005.
- [10] RPG Radiometer Physics GmbH, Meckenheim, Germany.
- [11] Virginia Diode Inc., <http://www.virginiadiodes.com/index.htm>.
- [12] M. Matsunaga, T. Matsunaga, and Y. Sekimoto, "Analysis of submillimeter-wave horn antennas for submillimeter-wave telescopes", *SPIE*, vol. 5445, pp. 446-449, 2004.
- [13] J.R. Tucker and M.J. Feldman, "Quantum detection at millimeter wavelengths", *Reviews of Modern Physics*, Vol. 57, No. 4, pp. 1055-1113, 1985.
- [14] S.A. Maas, "Noise in Linear and Nonlinear Circuits", Artech House Inc, 2005.

A 385-500 GHz 2SB SIS Mixer Based on a Waveguide Split-Block Coupler

Mamoru Kamikura^{1,2}, Wenlei Shan^{2,3}, Yu Tomimura^{1,2}, Yutaro Sekimoto^{1,2}, Shin'ichiro Asayama², Naohisa Satou², Yoshizo Iizuka², Tetsuya Ito², Toshiaki Kamba², Yasutaka Serizawa^{1,2}, and Takashi Noguchi²

Abstract—We have developed a 385-500 GHz sideband-separating (2SB) mixer, which is based on a waveguide split-block coupler at the edge of the E-plane of the waveguide, for the Atacama Large Millimeter/submillimeter Array (ALMA). An RF/LO coupler, which contains an RF quadrature hybrid, two LO couplers, and an in-phase power divider, was designed with the issue of mechanical tolerance taken into account. The single-sideband (SSB) noise temperature of a receiver using the RF/LO coupler is 104 K at the band center, which corresponds to 5 times the quantum noise limit (hf/k) in SSB, and 280 K at the band edges. The image rejection ratio of the receiver was found to be larger than 9.5 dB and typically 15 dB in the 385-500 GHz band.

Index Terms—sideband-separating (2SB) superconductor-insulator-superconductor (SIS) mixer, waveguide split-block coupler, RF quadrature hybrid, ALMA

I. INTRODUCTION

The Atacama Large Millimeter/submillimeter Array (ALMA) [1] covers atmospheric windows from 30 GHz to 950 GHz in 10 frequency bands with relative bandwidth of 20-30%. To improve the performance of the receiver, sideband separation is effective because it reduces the atmospheric noise [2].

Although there are several ways to achieve a 2SB mixer, we have selected a waveguide based 2SB mixer because it is compact, has no moving part, and good performance up to 370 GHz was reported by Claude (275-370 GHz) [3]. So far other waveguide based 2SB mixers were developed by Claude *et al.* (211-275 GHz) [4], Asayama *et al.* (90-115 GHz) [5], Chin *et al.* (86-116 GHz) [6], Vassilev *et al.* (85-115 GHz) [7], Kerr *et al.* (211-275 GHz) [8], Kamikura *et al.* (385-500 GHz) [9]. In this paper we present the recent results of the 2SB mixer for the 385-500 GHz band; compared to that described in [9], designs of an RF quadrature hybrid, an LO coupler, and the waveguide loads are revised.

A block diagram of a sideband-separating (2SB) mixer with two double-sideband (DSB) mixers is shown in Fig. 1, which is similar to that described in [3-9]. It consists of two DSB mixers, an IF quadrature hybrid, and an RF/LO coupler, which contains an RF quadrature hybrid, two LO couplers, an in-phase power divider, and three waveguide loads.

Manuscript received May 31, 2006.

This work was partially supported by Grant-in-Aid of JSPS No. 17340058.

¹Department of Astronomy, School of Science, the University of Tokyo.

²Advanced Technology Center, National Astronomical Observatory of Japan, National Institutes of Natural Sciences, 2-21-1 Osawa, Mitaka-shi, 181-8588 Tokyo, Japan.

³Purple Mountain Observatory, Chinese Academy of Sciences, 2 West Beijing Road, Nanjing 210008, China.

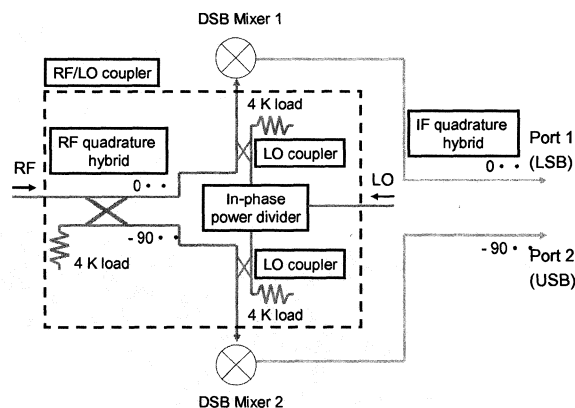


Fig. 1. Block diagram of a 2SB mixer [3-9]. RF/LO coupler contains an RF quadrature hybrid, two LO couplers, an in-phase power divider, and three waveguide loads.

II. RF/LO COUPLER DESIGN

The design of an RF/LO coupler is shown in Fig. 2. To reduce the loss resulting from the misalignment of the two split blocks, the RF/LO coupler is split at the edge of the E-plane. At submillimeter wavelengths (~ 0.6 mm), the size of the waveguide and branch lines become smaller. The branch lines can be fabricated with electrical discharge machining. On the other hand, the waveguide itself can be made with direct machining. The alignment between the machining and electrical discharge machining is not easy. Since the alignment error degrades the performance of the 2SB mixer, split-block coupler at the edge of the E-plane was used. Compared with the split block in the middle of the E-plane as described in [3-8], the alignment of the two blocks becomes easier. We took care to ensure contact between the two blocks at the edge of the E-plane by arranging 4 screws effectively. The design is a scaled model described in [5] referring to [4]. The waveguide size of the RF/LO coupler is $559 \mu\text{m} \times 280 \mu\text{m}$ (WR 2.2).

The unit of the RF/LO coupler were designed with a commercial 3D electromagnetic field simulator, HFSS (High Frequency Structure Simulator) [10]. We took into account conductor loss for the TE₁₀ mode because the higher modes are evanescent modes in the waveguide. The conductivity of gold at 4 K is assumed to be 1.1×10^9 S/m, which includes the effect of the surface roughness ($\sim 2 \mu\text{m}$) of the waveguide as described in [11]. The conductor loss of the waveguide of the RF/LO coupler other than the RF quadrature hybrid and the LO coupler at 4 K was around 0.2 dB for the waveguide length of 20 mm.

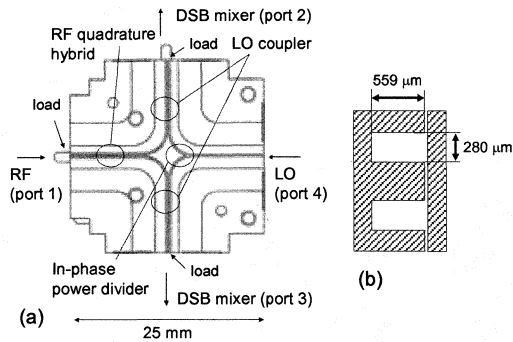


Fig. 2. (a) Design of the RF/LO coupler. (b) Close-up of the side view of the RF/LO coupler.

A. RF quadrature hybrid

An RF quadrature hybrid is a four-port coupler as shown in Fig. 3. The fourth port is terminated by a waveguide load. The two waveguides are separated by broad walls and are coupled through shunt guides approximately $\lambda_g/4$ long. It is a 3 dB power divider with a 90 degree phase difference between the two outputs.

The RF quadrature hybrid was designed to have amplitude and phase imbalances of < 2.5 dB and < 10 degrees, respectively. These are required to achieve a 10 dB or larger image rejection ratio (IRR) of the 2SB mixer as described in [12].

The 58 μm width of the branch-line coupler was optimized from the electrical discharge machining. The number of branch lines and the dimensions were optimized as shown in Fig. 3. We have selected an 8 branch-line coupler.

At submillimeter wavelengths mechanical tolerance becomes very severe. The mechanical tolerance of the branch-line widths of the RF quadrature hybrid was studied in Fig. 4. We found that typical machining errors of ~ 5 μm do not affect the RF performance.

B. Waveguide load

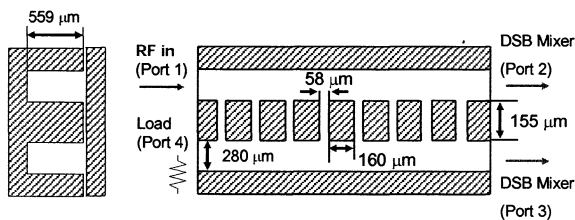


Fig. 3. Dimensions of the RF quadrature hybrid.

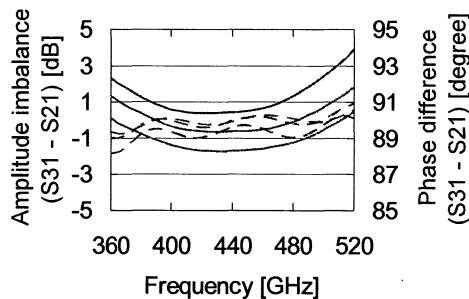


Fig. 4. Mechanical tolerance of the branch-line widths of the RF quadrature hybrid. The graph shows the amplitude imbalance and phase difference when no mechanical error exists (red lines) and the branch-line widths are smaller (blue lines) or larger (green lines) by 5 μm than the design values. Port definitions are as shown in Fig. 3.

For the material of the waveguide load of the RF/LO coupler, we have used MF116 [13], which is described in [14]. MF116 is made of iron powder and epoxy resin. The shape of the load is shown in Fig. 5 (a). Simulated input return loss of the load was as low as -40 dB at 440 GHz as shown in Fig. 5 (b).

C. In-phase power divider

The in-phase power divider of the RF/LO coupler is an E-plane Y-junction. We have chosen to use an in-phase power divider of 3.0 mm radii. The input return loss of the in-phase power divider is < -24 dB from simulation.

D. LO coupler

From the point of view of an SIS mixer, lower coupling is desirable to minimize the loss of RF signals. However, the LO power is generally limited at the submillimeter wavelengths. In the case of this receiver, it was around 80 μW at the output of the cryogenic multiplier. Thus we have designed a -15 dB LO coupler with 3 slots as shown in Fig. 6, which is consistent with LO power calculation.

The 35 μm width of the slot was optimized from the electrical discharge machining. The number of slots and the dimensions of the LO coupler were optimized as shown in Fig. 6. The mechanical tolerance of the slot widths of the LO coupler was studied as shown in Fig. 7. We found that typical machining error of ~ 5 μm do not affect the LO performance.

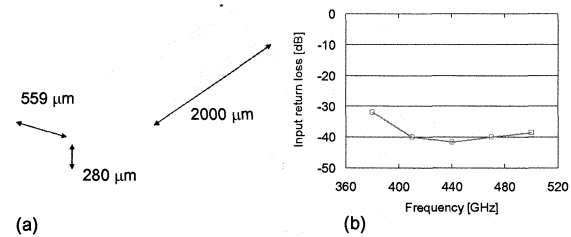


Fig. 5. (a) Shape of the waveguide load. (b) The simulated input return loss.

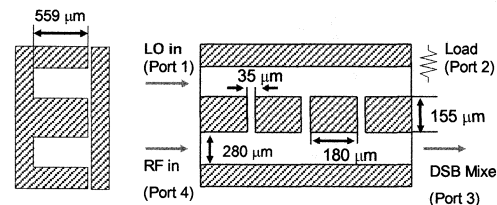


Fig. 6. Dimensions of the LO coupler.

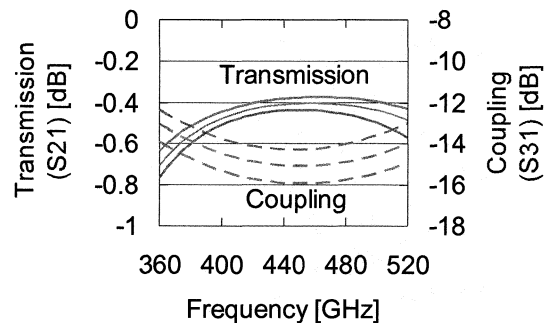


Fig. 7. Mechanical tolerance of the slot widths of the LO coupler. The graph shows transmission, and coupling when no mechanical error exists (red lines) and the branch-line widths are smaller (blue lines) or larger (green lines) by 5 μm than the design values. Port definitions are as shown in Fig. 6.

III. MEASUREMENT RESULTS

The RF/LO coupler was fabricated by Oshima Prototype Engineering [15]. The waveguide was made with direct machining and the branch lines were made with electrical discharge machining. The material is gold-plated TeCu. Three waveguide loads for the RF/LO coupler were made of MF116 [13].

Mechanical measurements with a microscope and measurements with a vector network analyzer (VNA) were done. The mechanically measured values were calibrated with a high precision scale, HL-250 [16]. The accuracy of the measurements was around $2\ \mu\text{m}$, which was derived from the reproducibility of the measurements.

We have assembled a VNA for the 385-500 GHz band, using commercial components. Some S-parameters of the RF/LO coupler were measured with the VNA. The dynamic range is around 50 dB, and the amplitude and phase stability is around 0.1 dB and 1 degree in 1 hour, respectively.

To compare the measurements and the simulations at room temperature, we assumed that the conductivity of gold at room temperature is $1.1 \times 10^7\ \text{S/m}$, which includes the surface roughness ($\sim 2\ \mu\text{m}$) of the waveguide as described in [11].

A. RF quadrature hybrid

A 6 branch-line coupler, which is based on the design described in [9], was evaluated. From the mechanical measurement, a typical mechanical error was around $5\ \mu\text{m}$. The measurements with the VNA at room temperature and simulation are compared as shown in Fig. 8. The maximum amplitude and phase imbalances were 1.7 dB and 12 degrees, respectively.

From simulation, the loss of the RF quadrature hybrid was -0.5 dB, the loss of the waveguide at room temperature was -1.4 dB, and the transmission of the LO coupler was -0.4 dB. For the simulation, we used the dimensions from the mechanical measurements. These results are consistent with the measured results with the VNA. The error bars were derived from the reproducibility of the measurements.

B. In-phase power divider and LO coupler

A 2 slot coupler, which is based on the design described in [9], was evaluated. We measured the insertion loss the LO coupler as shown in Fig. 9. The loss was found to be -20 dB at room temperature.

From simulation, the coupling of the LO coupler was -15.5 dB, the loss of the waveguide at room temperature was -1.4 dB, and the loss of the in-phase power divider was -3.1 dB. These results are consistent with the results from the measurements with the VNA.

IV. RECEIVER PERFORMANCE

A. Cartridge-type receiver

A cartridge-type receiver [17] including the 2SB mixer was evaluated in a cartridge test cryostat [18]. The receiver consists of three cold stages with operating temperatures of 4 K, 15 K, and 110 K. A corrugated horn was designed by Matsunaga *et al.* [19]. CLNAs with 3-stage GaAs transistors and cryogenic isolators for the 4-8 GHz IF band have noise temperatures around 12 K. The coaxial cable was bent to connect between the DSB mixers and the IF quadrature hybrid, whose locations are not optimized.

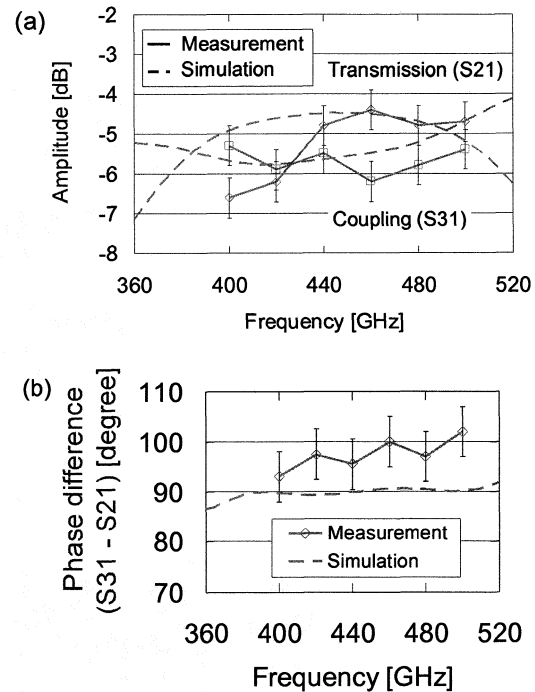


Fig. 8. Measured (solid line with points) and simulated (dashed line) results of (a) transmission and coupling of the RF quadrature hybrid, (b) phase difference of the RF quadrature hybrid. The error bars were derived from the reproducibility of the measurements. Port definitions are as shown in Fig. 2.

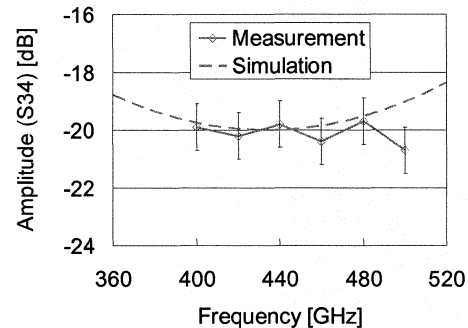


Fig. 9. Measured (solid line with points) and simulated (dashed line) results of the insertion loss of the LO coupler. The error bars were derived from the reproducibility of the measurements. Port definitions are as shown in Fig. 2.

The DSB mixer for the 385-500 GHz band has been developed by Shan *et al.* [20-21]. Two Nb-AlO_x-Nb SIS (Superconductor-Insulator-Superconductor) tunneling junctions are parallel connected (PCTJ: parallel-connected twin junction [22]) as a tuning circuit in the DSB mixer.

The DSB mixer has a noise temperature as low as 3 times the quantum noise limit (hf/k) with relative bandwidth of 20%. Fig. 10 shows typical IV power curves of the DSB mixers. The superconducting magnet current was 10 mA to suppress the Josephson current of the SIS mixer. Josephson current is suppressed successfully.

The LO was a combination of a Gunn oscillator, a power amplifier, and a quintupler. The quintupler was mounted on the 15 K stage of the cartridge. On the other hand, the Gunn oscillator and the power amplifier were outside the vacuum vessel. The 78-100 GHz signal generated by the Gunn oscillator is amplified to $\sim 100\ \text{mW}$ by the power amplifier.

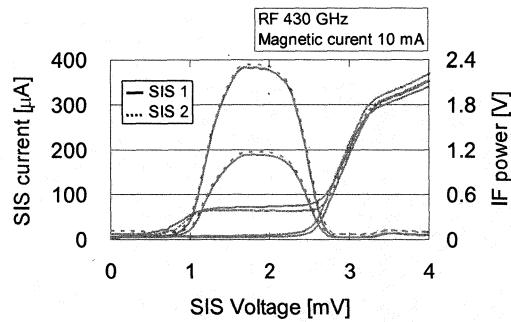


Fig. 10. Typical IV power curves of the DSB mixers

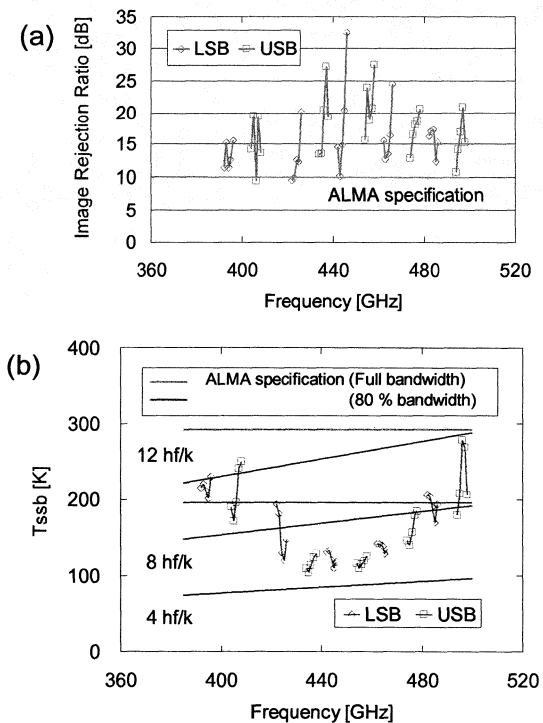


Fig. 11. (a) Image rejection ratio and (b) SSB noise temperature of the 2SB mixer measured with a cartridge-type receiver.

B. Image rejection ratio and noise temperature

Image rejection ratio (IRR) was measured as shown in Fig. 11 (a) with the method from Kerr *et al.* [23]. The IRR was larger than 9.5 dB and typically 15 dB in the 385-500 GHz band.

The single-sideband (SSB) noise temperature of the cartridge for the 385-500 GHz band was measured with the Y-factor technique using a hot (300 K) and cold load (77 K) placed in front of the input window, as shown in Fig. 11 (b). The SSB noise temperature was 104 K around 435 GHz, which corresponds to 5 hf/k , and less than 280 K in the 385-500 GHz band.

ACKNOWLEDGMENT

We are grateful to Sheng-Cai Shi of Purple Mountain Observatory for collaborative developments of submillimeter receivers. The authors would also like to thank Junji Inatani, and members of ALMA-J.

REFERENCES

- [1] R. L. Brown, W. Wild, C. Cunningham, "ALMA - the Atacama large millimeter array," *Advances in Space Research*, vol. 34, issue 3, pp. 555-559, 2004.
- [2] S. Guilloteau, "DSB versus SSB and Bandwidth/Sensitivity tradeoff," *ALMA Memo 393*, 2002.
- [3] S. Claude, "Sideband-Separating SIS Mixer for ALMA Band 7, 275-370 GHz," *Proc. 14th Int. Symp. on Space Terahertz Tech.*, 2003.
- [4] S. M. X. Claude and C. T. Cunningham, A. R. Kerr and S.-K. Pan, "Design of a Sideband-Separating Balanced SIS Mixer Based on Waveguide Hybrids," *ALMA Memo 316*, 2000.
- [5] S. Asayama, H. Ogawa, T. Noguchi, K. Suzuki, H. Andoh, and A. Mizuno, "An Integrated Sideband-Separating SIS mixer Based on Waveguide Split Block for 100 GHz Band," *ALMA Memo 453*, 2003.
- [6] C. C. Chin, D. Derald, J. Sebesta, F. Jiang, P. Dindo, G. Rodrigues, *et al.*, "A Low Noise 100 GHz Sideband-Separating Receiver," *Int. J. Infrared and Millimeter Waves*, vol. 25, no. 4, pp. 569-600, 2004.
- [7] V. Vassilev, V. Belitsky, C. Risacher, I. Lapkin, A. Pavolotsky and E. Sundin, "A Sideband Separating Mixer for 85-115 GHz," *IEEE Microwave and Wireless Components Letters*, vol. 14, no. 6, pp. 256-258, 2004.
- [8] A. R. Kerr, S.-K. Pan, E. F. Lauria, A. W. Lichtenberger, J. Zhang, M. W. Pospiealski, *et al.*, "The ALMA Band 6 (211-275 GHz) Sideband-Separating SIS Mixer-Preamplifier," *Proc. 15th Int. Symp. on Space Terahertz Tech.*, 2004.
- [9] M. Kamikura, Y. Tomimura, Y. Sekimoto, S. Asayama, W. L. Shan, N. Satou, *et al.*, "A 385-500 GHz sideband-separating (2SB) SIS mixer based on a waveguide split-block coupler," *Int. J. Infrared and Millimeter Waves*, in press.
- [10] Ansoft Corporation, <http://www.ansoft.com/>.
- [11] Ansoft HFSS, Maxwell Online Help System, pp. 298, 1996-2002 Ansoft corporation.
- [12] A. R. Kerr and S.-K. Pan, "Design of Planar Image Separating and Balanced Mixers," *Proc. 7th Int. Symp. on Space Terahertz Tech.*, pp. 207-219, Available as *ALMA Memo 151*, 1996.
- [13] Emerson & Cuming Microwave Products, <http://www.eccosorb.co.jp/>.
- [14] A. R. Keer, H. Moseley, E. Wollack, W. Grammer, G. Reiland, R. Henry, *et al.*, "MF-112 and MF-116: compact waveguide loads and FTS measurements at room temperature and 5 K," *ALMA Memo 494*, 2004.
- [15] Oshima Prototype Engineering, <http://www.ijnet.or.jp/oshima/>.
- [16] Mitsutoyo Co., <http://www.mitsutoyo.co.jp/eng/index.html>.
- [17] N. Satou *et al.*, "A submillimeter cartridge-type receiver for ALMA Band 8 (385 - 500 GHz)," in preparation.
- [18] Y. Sekimoto, T. Kamba, S. Yokogawa, M. Sugimoto, T. Okuda, R. Kandori, *et al.*, "Cartridge Test Cryostats for ALMA Front End," *ALMA Memo 455*, 2003.
- [19] M. Matsunaga, T. Matsunaga, Y. Sekimoto, "Analysis of submillimeter-wave horn antennas for submillimeter-wave telescopes," *SPIE*, vol. 5445, pp. 446-449, 2004.
- [20] W. L. Shan, T. Noguchi, S. C. Shi, Y. Sekimoto, "Design and Development of SIS Mixers for ALMA Band 8," *IEEE Trans. Appl. Superconductivity*, vol. 15, issue 2, pp. 503 - 506, 2005.
- [21] W. L. Shan, S. Asayama, M. Kamikura, T. Noguchi, S. C. Shi and Y. Sekimoto, "Development of a 385 - 500 GHz SIS mixer for ALMA band 8," *Proc. 16th Int. Symp. on Space Terahertz Tech.*, 2005.
- [22] S. C. Shi, T. Noguchi, and J. Inatani, "Development of a 500-GHz Band SIS Mixer," *IEEE Trans. Appl. Superconductivity*, vol. 7, issue 2, pp.2587-2590, 1997.
- [23] A. R. Kerr, S.-K. Pan and J. E. Effland, "Sideband Calibration of Millimeter-Wave Receivers," *ALMA Memo 357*, 2001.

INVITED PRESENTATION

Thursday 11 May 12:00-12:30

**Mss Nebes,
Frequency Regulation and Management**

Introduced by Dr. André Deschamps

Frequency Regulation and Management

Anne-Marie NEBES - ANFR

Agence Nationale des Fréquences – Maison Alfort - 94704

Abstract— *Radio frequencies spectrum is a scarce resource with special properties:*

- *Part of public propriety, but its use on a national basis must take into account the uses of neighbour countries that must be protected against interferences.*

- *Scarce, but inexhaustible, unlike oil, for instance.*

Explosion of technologies using electromagnetic waves, especially those relating to mobile applications leads to strong pressure on this resource, economic value of which is increasing.

For these reasons, certain economists call in question again both the lawfulness of public actors in charge of the frequencies management and the methods of this management.

Because of its specificity, frequencies spectrum is a resource that must be regulated, on order to be used in a rational and optimised way.

Because of propagation properties, this regulation is carried out at two levels:

-International level, for radio frequencies does not consider boundaries.

-National level, because frequencies are used on national basis, by each sovereign state.

The present talk is centred on three main axes:

1: Specific constraints relating to frequencies spectrum use: Rights and duties of frequencies users such as those result from international and national rules.

2 International bodies involved in frequencies management: global level (ITU) and regional level (for ex: CEPT and E.U)

3- An example of national organisation: the ANFR in France.

I. RIGHTS AND DUTIES OF FREQUENCY'S USERS:

Frequencies spectrum is the public property of each sovereign state. For that, it is impossible to sell it: it is placed at users disposal, at national level, during period of time depending on technologies evolution and economic global development, type of players-operators and manufacturers- and type of equipments put on the market. This resource must be used, depending on national allocations, based on international sharing, under specified conditions and for limited periods

A. International regulatory provisions:

At global level, those provisions are defined in ITU frame. ITU is a specialized UN s' organisation, gathering 188 countries, and in charge of promoting efficient telecommunications development, by defining regulation, standardization of equipments and technical cooperation with less advanced countries.

Rights and duties of state Members, relating to frequencies

uses, result from Union Constitution, and especially, from Radio Regulations, that is annexed to the Constitution. International treaty, ratified by national parliament, the R.R is invested with a stronger power than the national law. It contains provisions relating to:

- a) The conditions of utilisation of the frequencies bands included between 9KHz and 1000 GHz;
- b) The conditions of protection of frequencies utilisation

1) Conditions of radio frequencies bands utilisation

The regulatory rigidity of the RR

R.R .Article 5 now allocates the frequencies bands, until 275 GHz, between the different radio services; such as they are defined at its article 1, according to propagation characteristics and technologies evolutions.

Radio services include:

Fixed and mobile Services

Terrestrial and space Services

Active and passive Services.

The RR establish to categories of services: " Primary "service , witch benefits of priority, and "secondary " service.

Stations of "secondary" services shall not cause interference to stations of "primary" service to witch frequencies are already assigned or to witch frequencies may be assigned at a later date, and cannot claim protection against harmful interference from station of a " primary" service to witch frequencies are already assigned or to witch frequencies may be assigned at a later date.

Because it is scarce, the spectrum is very often shared between two, or more than two primary (or primary and secondary) services.

This sharing can be on "equal rights ", between primary services if they are expected to be compatibles a priory (ex: Fixed and fixed satellite service in frequencies bands above 1GHz.)

Otherwise, the RR shares the world into three Regions, corresponding to the main continents

R1: Europe and Africa

R2: North and South America

R3: Asia, Australia, and Oceania.

So, frequency bands, according to propagation conditions, type of radio services, but also economical stake, market size, are allocated on a worldwide basis (R1-R2-R3) or on Regional basis.

Mechanisms introducing flexibility:

The notion of radio service:

The idea of radio service is wider as the idea of radio system.

It allows consequently equipments evolution without question of uses rights, which is essential in order to guarantee the profitability of economic investments resulting of the network expansion.

The footnotes

Definition of additional (services allocated plus others) and alternative (services of footnote instead of) allocations.

During a radio conference, some countries can derogate to allocation provisions of the frequencies Table under the

condition that they register their name (and the name of the additional or alternative service in a footnote. Such as the notion of service, the footnote is a way to introduce flexibility in the international allocation Table

2) Protection conditions of frequency:

The purpose of frequencies management is to operate at the same time the maximum of transmitters, without interference, taking into account that:

- Frequencies bands are shared between services;
- Frequencies channels are re-used at a specified distance from the previous utilisations.

To be protected against interference, frequencies assignments shall benefit of "international recognition". To get this recognition, frequencies assignments shall be, either:

- Registered in the Master International Frequency Register, up-dated by the ITU. The date of receipt of the frequencies assignments, under the condition that they are in accordance with RR provisions, provides to their "anteriority rights":

That means that other administrations shall take these previous assignments under consideration when making their own assignments in order to avoid harmful interferences.

- Or in accordance with assignments included in a Plan, if the Plan has been concluded in the ITU.

It is necessary to record frequencies assignments, for passive services too, in the Master file, in order to get protection against interference and to keep uses of rights, if the band is re-allocated.

Provision RR 11.12 stipulates that: "Any frequency to be used for reception by particular radio astronomy station may be notified if it is desired that such data be included in the Master Register."

B. National regulatory provisions:

At national level, the international sharing is completed and précised by the national regulation.

In France, the "Tableau national de repartition des bands de frequences" annexed to a decree taken by the Prime Minister completes the international sharing.

This document, based on the international allocation Table to radio services, adds the national ministers and "Independent Authorities" which, either use frequencies for their own needs – government utilisations- or give licences for commercial and private needs.

For these national users, called by the French law as "affectataires", frequencies can be used based on "exclusivity" if they are designated as single user, or based on sharing either with priority, or with not same rights.

It is possible to use frequencies not in accordance with the RR Article 5, but assignments in such cases cannot get international recognition, and shall not cause interference to assignments of other administrations used in accordance with the RR.

It is mandatory to register assignments in the national data file, called the "Fichier national des fréquences", in order to get national protection against national interference and to be registered in the international Master register.

II. - INTERNATIONAL FREQUENCY MANAGEMENT ORGANISATIONS:

A. ITU: The worldwide organisation dealing with frequency management:

Issued from the European Conference dealing with the regulation of telegraph system in 1865, ITU is the oldest of the international inter-governmental organisations. For this reason, all other international organisations took ITU as model, United Nations too.

ITU is composed by two kinds of bodies: Regulatory and permanent bodies

1) Regulatory bodies:

Plenipotentiary conference, mainly in charge of:

- Electing the General Secretary, the Vice General Secretary, the Directors of the 3 Boards, the Members of the Committee, and the members of Administrative Council
- Determining the budget of the Union

- Modifying, as such as necessary, provisions contained in the ITU Constitution and Convention.

Administrative Council, in charge of:

- Representing the Plenipotentiary conference, it holds each year, to look at budget, and for execution of the Constitution, Convention, Regulations (R.R)and Conferences provisions .

RR Committee:

Composed by representatives of countries Members, it meets about two weeks per year and examines the Radio Bureau activities.

Radio Conferences, in charge of

Modifying the RR and ITU Plans provisions, in accordance with their agendas

Radio Assembly, in charge of:

Establish, through specialized Committees, Recommendations and Reports relating to technical and operating conditions of radio equipments.

2) Permanent Bodies

General Secretariat

Organized in Departments, ITU General Secretariat is under the general Secretary's authority.

It deals with:

- Preparation and execution of the budget
- Secretariat works organisation and employees nomination
- Organisation of ITU conferences and publication of their Finals Acts
- Bring in legal advices for the Union of which the general secretary is the legal representative

Radio Bureau

It deals with frequencies assignments registration for Terrestrial and space Services. It up-date the Master Register, in accordance with provisions contained in the RR and Finals Acts of ITU Regional Conferences.

This data base contains all assignments for all radio services which benefit of international recognition.

The Radio, Development, and Telecommunication standardization Sectors:

Under the Director's authority, each Sector allows the participation of the I.T.U Members to the works of the Union.

Relating to radio Sector, the Sector organizes the meetings of radio Assembly, and its working parties.

B. An example of regional organization: CEPT and UE:

In order to reach the harmonization of frequencies bands utilization, relative extended market, European western countries have been working together since the sixties, building up an organization called the "Conference Européenne des Postes et Telecommunications" (CEPT). All groups of countries, in each continent, are also gathered in regional organizations (ex: CITEL, for America continent). CEPT gathers more than 40 countries from western and eastern Europe, also includes Turkey and Russia. Through the "Comité des communications électroniques" (ECC), a working Party (CPG) has been set up in order to reach compromises and write European common proposal (ECP) for the ITU conferences.

The European Union (EU) has regulatory power to harmonize frequencies bands and operating conditions inside the Union.

The "Directives" when adopted need the Members States to modify their national laws.

III. AN EXEMPLE OF NATIONAL FREQUENCY MANAGEMENT: FRENCH ANFR

The French present organization results from the Telecommunication Regulation Law from 1996. This law gave to a state agency the "Agence nationale des fréquences" (ANFR) the planning managing and the monitoring of radio frequencies, taking nevertheless under consideration the competences of the 11 ministries and Authorities users of frequencies- for their own needs, or to licence private users-
The ANFR has Administrative Council, composed by representative members of frequencies users, and radio experts.

A general director directs it.

The ANFR is composed of:

A. Four technical Directions:

La direction de la planification du spectre et des affaires internationales (DPSAI):

It deals with :

- The making up of national position for international meetings
- Proposals of the national frequencies repartition, the TNRBF, which the prime minister shall approve.
- Manage the spectrum in a prospective way
- Manage a relocation found in order to facilitate the frequencies utilisation evolution.

La Direction du contrôle technique du spectre (DTCS)

Including seven technical services, spread on the territory, this Direction is equipped with 50 fixed monitoring stations and with 26 mobile monitoring stations.

It deals with:

- The interferences resolution
- The de detection of illegal uses
- The organization and coordination of monitoring of radio spectrum, for the benefit of all ministries and authorities users of frequency.

-The checking of radio equipments, in order to ensure that they are in accordance with technical standards.

La Direction des conventions avec les affectataires (DCA)

It deals with:

The conclusion of conventions in order to perform works relating to frequencies management for national users of frequencies.

La Direction de la gestion nationale des fréquences (DGNF)

It deals with:

The up-date of the frequency files required for frequencies coordination and registration

The up-date of the radio stations file.

B. Consultative Committees:

ANFR performs its tasks by working together with the « Affectataires », inside "consultative committees", set up by the Administrative Council

These committees are organized around three main kinds of competences:

a) Frequency planning:

« Commission de planification des fréquences » (CPF), dealing with the national allocation Table .

Around this main Committee, are gathered:

-"Commission d'assignation des fréquences" (CAF), dealing with frequency registration.

-"Commission des coordinations aux frontières"(CCF), dealing with international coordination.

-"Commission de contrôle du spectre," dealing with national monitoring policy.

b) International aspects:

"Commission des conférences radioélectriques", (CCR) to which are gathered:

-"Commission des conférences des radiocommunications" (CCR), dealing with preparation of ITU conferences.

- « Commission de l'Assemblée des radiocommunications », dealing with preparation of ITU radio standardisation and operational conditions meetings.

-"Commission des affaires Européennes", dealing with questions relating to European policy concerning radio sector.

c) Synthesis and prospective aspects:

« Commission de synthèse et prospective »(CSPR), to which are gathered:

"Commission de compatibilité électromagnétique" (CCE)

« Commission des revues du spectre (CDRS)

« Commission du fonds de réaménagement du spectre » (CFRS)

« Commission de valorisation du spectre » (CVS).

Such a mechanism is very interesting, because it associates all frequency users – for governmental and commercial uses -to the decision process.

All users know the constraints relating to frequency uses, and can defend their position in order to reach the necessary compromises between opposite and, sometimes very political, interests.

THE SPECIFICITY OF SCIENTIFIC USE OF SPECTRUM.

André Deschamps – Observatoire de Paris – Paris 75014

Abstract— *The progress of technologies induces a need of bandwidth in the frequency spectrum, which is full in most countries. In consequence administrations have to balance two opposite concepts : public and private, market and progress of basic knowledge*

I. RIGHTS AND PROTECTION:

Article 5 of the RR (Radio Regulations) specifies all allocation bands from 9 kHz to 1000 GHz in the whole world, as well as the rights of protection against harmful interferences.

To day, only frequency bands up to 275 GHz are allocated.

A. Below 275 GHz

1) In primary exclusive frequency bands

The footnote 5.340 of RR indicates a list of bands where emissions are strictly prohibited in all the countries members of ITU. These frequency bands are called “exclusive bands”. Obviously, those bands are dedicated to passive services.

Twenty-one frequency bands defined from 1400 MHz to 252 GHz are allocated for passive use to:

- Earth Exploration Satellite Service (EESS)
- Space Research Service (SRS)
- Radio Astronomy (RAS)

2) In primary shared frequency bands.

The footnote 5.149 of the RR asks to Administrations to take “all practicable steps to protect passive services against harmful interference”. Thirty-nine frequency bands are defined all over the world, from 13360 kHz to 114.25 GHz. These frequency bands are shared principally with space borne and airborne stations.

Regulation agencies of each country are responsible of application of these footnotes, so the difference in interpretation of the RR by different governments could moderate the protection of scientific bands in some countries.

3) In secondary shared frequency bands.

A secondary allocation does not give any right to any protection in this frequency band. So, passive services may only be “victim” inside of these frequency bands.

4) Outside of attributed frequency bands.

Users of non-attributed frequency bands have strictly no right to practice emission. On another hand, if the EMC field is sufficiently low, the interferences produced are not detectable by so called “victims”.

Reversely, scientific use outside of attributed bands is very difficult, considering the increasing number of operators. Use of Radio Quiet Zone could be envisaged. Also device development in a Faraday Cage is generally used when observation of distant phenomena is not required.

B. Between 275GHz and 1000 GHz

Article 5.565 of the RR gives recommendations on this part of the spectrum, for experimental applications : “The frequency band 275 – 1000 GHz may be used by administrations for experimentation with, and development of, various and passive services. In this band a need has been identified for the following spectral line measurement for passive service”

Are listed eight bands for Radio astronomy and seventeen bands for passive EES and SRS.

As these bands are not allocated, so this article could conclude : “Administrations are urged to take all practicable steps to protect these passive services from harmful interference until the date when the allocation is established”

C. Above 1 THz

The spectrum actually covered by ITU-R rules has an upper limit at 1 GHz. Part of the agenda of the next World Radio Conference in 2007 (WRC-07) is to discuss on the part of spectrum above 1 THz up to 3 THz.

Radio astronomers have identified twenty-three frequency bands of interest to the community, taking in account a Doppler shift of ± 300 km/s. Some scientists believe that a red shift of $+300 / -1000$ km/s is more appropriate. Other people believe that it could be more efficient to keep five very wide bands free of interferences.

It is to be noticed that agenda of WRC-07 (In 2007) was approved in WRC-03, so the WRC-07 will decide of the agenda of WRC-11 (in 2011).

II. SCIENTIFIC FREQUENCY BANDS IN JEOPARDY.

The progress of technologies induces a need of bandwidth in the frequency spectrum, which is full in most countries. In consequence administrations have to balance two opposite concepts : public and private, market and progress of basic knowledge. If traders are able to compute the price of one megahertz, the scientists couldn't.

A. The impact of new technologies.

The introduction of new technologies and new applications requires new access to the spectrum. But in most industrial countries, there is no part of spectrum unallocated. For some years, making part of spectrum available to satisfy the European harmonization has required the relocation of many users. Some users have the possibility to move from one frequency band to another, with appropriate funding from administration.

This flexibility is not possible for the scientific frequency bands whose numerical values are derived from universal physical laws.

So the administrations have to balance with the economical (short term) value and the scientific (long term) value of each part of the spectrum attributed for the scientific use.

Everybody can imagine the weight of scientists compared to operators.

Frequency management politics is very different depending on different countries; fortunately, in France, ANFR plays an important role to prevent the degradation of the quality of the spectrum.

Some new technologies such as Ultra Wide Bandwidth (UWB) will be very soon used by a large amount of users. This technology is dedicated to the global market (not subject to licensing). This justifies technical studies at international (European) level to protect the quality of spectrum. Scientific users (and particularly passive users) of spectrum are highly concerned with these studies, due to the high sensitivity of the receivers (radio telescopes). This action, by CEPT ECC TG3 / 63 and IUT-R TG 1/8, is now under development.

The European «Radio Spectrum Policy Group» engages an action called «Scientific Use of Spectrum». The main objective of this request is to develop a policy approach, which ensures that the specific constraints on spectrum used by scientific services, and in particular by passive services, are taken into account within the overall European policy goals. A list of frequency bands used for scientific purpose, will be bring for discussion. The public consultation is to be finalized in August 2006. The opinion will be presented for approval in October 2006. This action does not concern frequencies above 270 GHz.

The result of this request for opinion is not obvious. In some countries, the goal is to preserve the frequency bands used for science, but in others countries it is to balance costs and benefits of scientific use versus costs and benefits economical use.

III. THE NEED OF BANDWIDTH FOR OPERATORS

A. In primary exclusive bands

Primary exclusive bands are protected by footnote 5.340 of the RR. This footnote was created to protect passive services from active services noting the vulnerability of passive measurements. The text is very clear and explicit: "All emissions are prohibited in following bands", and the bands are listed. Nevertheless, an exception has occurred: the Automotive Short Range Radar between 23,6 and 24 GHz. The band 23.6-24 GHz is of primary interest by itself to measure water vapour and liquid water.

1) The SRR24 short story.

A group of car manufacturers and suppliers organise themselves in a consortium called "SARA" who plans to implement SRR's in cars. This device operates around 24 GHz.

European Commission for licensing was approached for a standard development

A work group, including scientific community was constituted by ECC to study SRR compatibility with allocated services (EESS passive, RAS)

Following a very hard discussion, an interim implementation of SRRs in band 23.6 - 24 GHz was applied, despite of scientific community protest.

On the other hand, it was admitted that SRR (assuming use of power levels defined by US) cannot share the band 23.6 - 24 GHz without limitations including:

- Permanent band attributed for SRRs will be around 79 GHz
- Implementation of SRRs in band 23.6 - 24 GHz is temporary
- Maximum of 7 % of cars with SRR will be allowed
- Sale of cars with SRR24 will end in 2013, and be replaced by cars with SRR79.
- Automatic switch off facilities is mandatory inside specified areas (radio telescopes).

As an example the radio telescope of IRAM in Plateau de Bure and Observatoire de Bordeaux have received a protection in a 35 km radius area. The CE report says : "The temporary introduction of automotive short-range radar in the 24 GHz range radio spectrum band has an exceptional character and must not be considered as a precedent for the possible introduction of other applications in the bands where ITU Radio Regulations footnote 5.340 applies, be it for temporary or permanent use."

For the first time there will be an active use in a band protected by footnote 5.340, people could believe this is a unique exception.

B. In shared bands

Up now, the sharing of frequency bands protected by the footnote 5.149 was not so difficult to be managed, due to the large availability of frequency modification from the concerned operator.

Due to the extension of the bandwidth occupancy (asked by the operators) the part of the spectrum not used inside of a given geographical area has become scarce.

Other techniques of management, like time sharing inside of a given frequency bands, are now taken in account. For example, if a radio observatory did not use a specific frequency band during a defined time interval (some weeks, some month) some operator wishes to use this frequency band during this time.

The same technique is used in non-attributed bands: in this case observations are done during low radio traffic hours.

C. Quiet zones for science.

1) The frequency "quiet" parts of the spectrum

It could seem obvious that the upper part of the spectrum (approximately above 50 GHz) is free of interferences, including the lines not legally attributed to science. This may be true to day, because the technology for current applications (telecom, UWB, broadcasting, etc) is not yet ready to use this part of spectrum. Tomorrow, the quick improvement of technology will allow the occupancy by the operators of the upper part of the frequency spectrum. The scientific community must be aware to attach importance to the protection of this part of spectrum. This could be done by the way of each national administration, accordingly with the RR.

2) The geographical radio quiet zones (RQZ)

The increase of radio telescopes sensitivity has enabled the detection and the study of objects at very long distance, presenting a very important red shift. Most of the time, this phenomenon shifts the observed lines out of the allocated bands. This is particularly restrictive for the Square Kilometre Array (SKA) telescopes at 21 cm, but all the future ground based radio telescopes are concerned (ALMA, etc)

It is obvious that the increase of scientific frequency bands is very unlikely, so the installation of future radio telescopes (SKA, ALMA, etc.) in a Radio Quiet Zone is the best compromise.

A good example is the National Radio Quiet Zone, which is a 13000 square miles region in West Virginia and Virginia around the Green Bank Observatory site.

IV. CONCLUSION

The introduction of new technologies requires new access to the spectrum. But in most industrial countries, there is no part of spectrum unallocated. Flexibility is not possible for the scientific frequency bands whose numerical values are derived from universal physical laws.

Everybody must be aware that operators and traders are now looking at the part of the spectrum used for science.

ORAL SESSION n°5

« HEB »

Thursday 11 May 14:00-16:00

Chaired by :

Dr. Boris Karasik & Dr. Edward Tong

Spiral antenna coupled and directly coupled NbN HEB mixers in the frequency range from 1 to 70 THz

S.N. Maslennikov, M.I. Finkel, S.V. Antipov, S.L. Polyakov, W. Zhang, R. Ozhegov, Yu.B. Vachtomin, S.I. Svechnikov, K.V. Smirnov, Yu.P. Korotetskaya, N.S. Kaurova, B.M. Voronov, and G.N. Gol'tsman
Moscow State Pedagogical University, Moscow, 119992, Russia, Email: onduty@rplab.ru

Abstract—We investigate both antenna coupled and directly coupled HEB mixers at several LO frequencies within the range of 2.5 THz to 70 THz. H₂O (2.5÷10.7 THz), and CO₂ (30 THz) gas discharge lasers are used as the local oscillators. The noise temperature of antenna coupled mixers is measured at LO frequencies of 2.5 THz, 3.8 THz, and 30 THz. The results for both antenna coupled and directly coupled mixer types are compared. The devices with in-plane dimensions of $5 \times 5 \mu\text{m}^2$ are pumped by LO radiation at 10.7 THz. The directly coupled HEB demonstrates nearly flat dependence of responsivity on frequency in the range of 25÷64 THz.

Index Terms—Superconducting radiation detectors, Hot carriers, Bolometers, Mixers.

I. INTRODUCTION

The performance of antenna coupled NbN HEB mixers is mostly investigated at the frequencies below 5 THz [1], [2]. There are only two other types of the mixers, except for HEB mixer, which are being developed for terahertz range – Schottky and SIS mixers, but at frequencies above 1.25 THz SIS mixer is not applicable yet [3] and Schottky one demonstrates much worse sensitivity, not sufficient for most applications [4]. Although antenna coupled NbN HEB mixer significantly outperforms Schottky or SIS one in the sensitivity at frequencies over 1.2 THz, its own noise performance becomes essentially worse when LO frequency exceeds 4 THz. It is believed that this is caused by smaller size of planar antenna at higher frequencies and accordingly smaller area of the contacts between the sensitive NbN bridge and Au antenna. As a result the contact resistance increases as well as RF losses [5].

It has been suggested to use the structures coupled to the radiation directly i.e. without any additional Au planar antenna patterned on the mixer chip [6]. In this case the sensitive bridge itself is appeared to be an absorber, and the contacts, being in the IF circuit, are appeared to be excluded from RF circuit at all.

This article is devoted to the work aimed at the realization of the idea of directly coupled mixer which can improve NbN HEB mixers performance at higher terahertz LO frequencies and also make them applicable in the middle IR.

II. ANTENNA COUPLED MIXER AT 2.5 AND 3.8 THZ

Let us consider our results achieved for antenna coupled NbN HEB mixers at LO frequencies below 4 THz. The DSB

noise temperature of our NbN HEB mixers at 2.5 THz is reported to be about 1300 K, while at 3.8 THz the noise temperature value is increased up to 3100 K [7]. Both the values are still more than one order of magnitude higher than the quantum limit at corresponding frequencies and amount to $11 \frac{hf_{LO}}{k}$ and to $17 \frac{hf_{LO}}{k}$, respectively. In these expressions f_{LO} is the LO frequency. Such an increase of antenna coupled mixer noise temperature can not be explained by taking into account the quantum noise only. The most probable explanation is the raise of RF losses partly due to contact resistance which increases with the LO frequency. This contacts resistance mostly affect RF current because at the LO frequency the sheet resistance of NbN layer ($\sim 500 \frac{\Omega}{\square}$) is 3 orders of magnitude higher than that of covering Au layer ($\sim 0.8 \frac{\Omega}{\square}$). Due to this fact the RF current flows into active NbN film only in the small area near the edges of the antenna (fig. 1). The characteristic antenna size may depend on RF frequency in a manner that if frequency is increased a smaller antenna should be chosen for integration with the sensitive bridge. As a result, at higher frequencies the areas where RF current flows become smaller and smaller, the effective contact resistance is increased, and consequently, noise temperature becomes worse.

III. DIRECTLY COUPLED MIXER AT 30 THZ

The NbN HEB mixer designed for the frequency of 30 THz do not have an additional planar antenna integrated with its sensitive bridge. It utilizes an ability of electron subsystem of disordered NbN film to absorb incident radiation directly. For preliminary experiments we have chosen the most simple configuration of the sensitive bridge. Active area of NbN film between Au IF contacts was patterned in a form of a rectangle with dimensions close to $30 \times 20 \mu\text{m}^2$ (fig. 2). If the wave front of LO beam is flat the LO radiation is focused on the film in a spot with the diameter limited by diffraction. At the

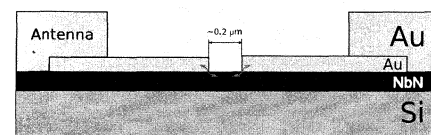


Fig. 1. RF current in the contacts between sensitive NbN bridge and Au antenna. The small area where RF current flows is denoted by the arrows.

LO frequency of 30 THz the diameter of the diffraction limited LO spot is about $5 \mu\text{m}$ that is less than the dimension of the sensitive area side (fig. 3), so it can be stated that all the absorption of incident radiation only occurs inside the NbN bridge contour.

The form of the LO wave front affects the pumping of directly coupled HEB mixer. If LO spot is smaller than the superconducting bridge (fig. 3, left graph) superconducting DC current may flow around it. Corresponding IV – curve is marked as “diffraction limited LO spot” in fig. 4. In the case of defocused LO the whole NbN bridge is pumped to the resistive state (fig. 3, right graph) and corresponded IV–curve is marked as “slightly defocused LO spot”. It should be noted that both the curves highlighted in fig. 4 correspond to the same LO power.

Another reason to defocus the LO spot follows from the fact

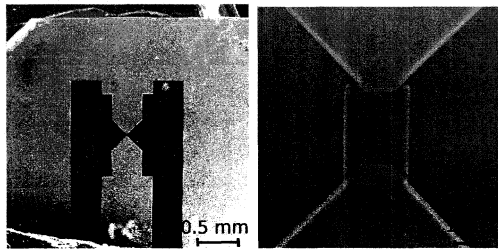


Fig. 2. SEM photos of directly lens coupled NbN HEB mixer.

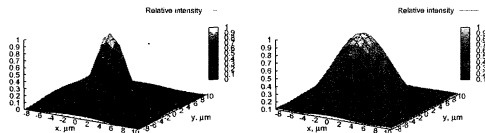


Fig. 3. Simulated intensity of LO spot on the NbN sensitive bridge at 30 THz. The left graph corresponds to the flat wave front, while the right graph corresponds to the situation when the LO spot is slightly defocused. The dimensions of x - y planes shown in the images are close to the in-plane dimensions of NbN sensitive bridge. The simulation are given for hemispherical Ge lens with the diameter of 12 mm and extension length of 1.96 mm.

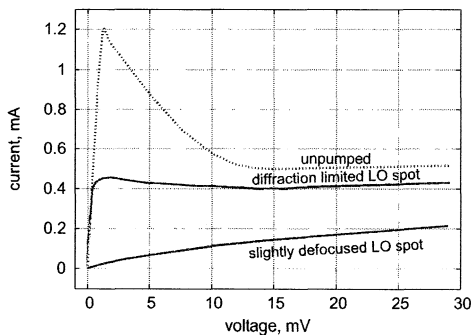


Fig. 4. IV – curves versus LO spot for directly coupled NbN HEB.

that down conversion of RF signal happens only in the area pumped by LO. In particular, in the noise temperature measurement the image of the hot/cold black body load overlap all the mixer’s sensitive area. As LO spot may be smaller than the device area overlapped by the load image, not all parts of this area may be involved in the down conversion. In order to involve all the sensitive area into the down conversion it is sufficient to make the diameter of the LO spot to be close to the active area size. This can be achieved by a slight defocussing of the LO spot.

The optimal absorbed LO power for directly coupled NbN HEB was estimated by isothermal technique. Its value amounts to $20 \mu\text{W}$ [6]. It should be noted that this value is at least 20 times higher than that for antenna coupled mixers. At the same time, there is no lack of powerful radiation sources in the infrared region containing, in particular, the frequency of 30 THz at which the experiments on the noise temperature measurement were carried out. At lower frequencies (5–10 THz) sufficient LO power can be obtained by use of recently introduced quantum cascade lasers.

The noise temperature at 30 THz for directly coupled NbN HEB mixers was measured by Y-factor technique using a CO_2 gas discharge laser as LO. Only two measurements were done – with 600 K and 1200 K hot black body loads. In both measurements a room temperature black body was used as a cold load. The *Callen & Welton noise temperature* was close to 2300 K, that was amounted to 3 times of the quantum limit [6].

The responsivity of the receiver was investigated in the detection mode using a chopped filament and a room temperature black body as the signal loads. In order to obtain a rough dependence of the receiver’s responsivity versus frequency a set of bandpass dispersion filters was used (fig. 5). For certain filter the responsivity is expressed as:

$$s \approx \frac{U_r}{\int_0^\infty T(\nu) (D_\nu(\nu, T_{bb}) - D_\nu(\nu, T_r)) d\nu} \quad (1)$$

where D_ν is the incident power per unit bandwidth, $T(\nu)$ is the dependence of the filter transmission versus frequency, $T_r \approx 296 \text{ K}$ and $T_{bb} \approx 1200 \text{ K}$ are the room and filament temperatures, respectively, and U_r is the response voltage.

In the experiments, U_r was measured by a lock-in amplifier for each filter of the set, and then the responsivity was calculated using (1) (fig. 5).

It can be concluded that at the frequencies $\lesssim 25 \text{ THz}$ the device responsivity is cut by Ge input window of the cryostat and the lens, while at the frequencies $\gtrsim 25 \text{ THz}$ the responsivity is almost flat and close to $70 \frac{\text{V}}{\text{W}}$.

The radiation pattern of the heterodyne receiver based on directly coupled NbN HEB mixer is narrower than that of log-spiral antenna coupled HEB and amounts to 0.6° [6]. This experimental result is in good agreement with simulation of Gaussian radiation pattern for the sensitive area with in-plane dimensions of $20 \times 20 \mu\text{m}^2$ (fig. 6).

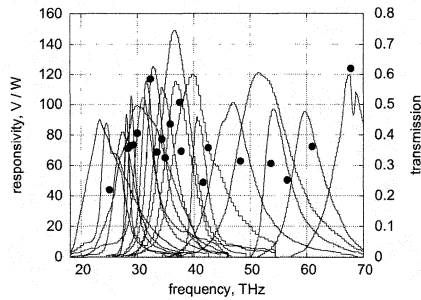


Fig. 5. The dependence of the receiver's responsivity versus frequency (filled circles) and the transmissions of the bandpass filters used in the experiment (lines).

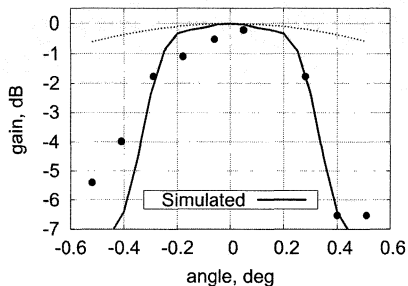


Fig. 6. Radiation pattern of directly coupled NbN HEB mixer based receiver at 30 THz (solid circles). Dotted line corresponds to the radiation pattern of the system consisting of Si lens, spiral antenna and a mixer at 2.5 THz [8]. Solid line corresponds to the simulation given for hemispherical Ge lens with the diameter of 12 mm and extension length of 1.96 mm. More detailed description of the receiver is given in [6].

IV. HEB MIXER FOR 10.7 THZ LO FREQUENCY

The H₂O gas discharge laser used for investigation of the noise temperature at 2.5 THz and 3.8 THz has also an emission line at 10.7 THz. However the intensity of this line is not enough to pump the directly coupled HEB mixers with the active area dimensions of $30 \times 20 \mu\text{m}^2 \times 4 \text{ nm}$. Investigations at 10.7 THz were performed using HEB mixers with smaller, $5 \times 5 \mu\text{m}^2$, active area. The coupling of smaller mixer with LO radiation at 10.7 THz is strongly dependent on the orientation of the mixer relatively to the polarization of LO. More power is absorbed by the mixer if \vec{E} is directed across the slot between the Au contacts (fig. 7). This can be explained if we consider this contacts as an antenna.

V. CONCLUSIONS

Planar antenna coupled NbN HEB mixers exhibit low noise temperature at the terahertz frequencies: from 0.7 to 2.5 THz it is close to $10 \frac{hf_{LO}}{k}$ and at 3.8 THz it is about $17 \frac{hf_{LO}}{k}$ (3100 K). At higher terahertz frequencies it goes up much steeper because of antenna and contacts losses. Preliminary investigations of directly coupled to radiation NbN HEB mixer demonstrate high sensitivity that can be obtained with this type of coupling: at 30 THz Callen & Welton noise temperature is about 2300 K that is close to $3 \frac{hf_{LO}}{k}$.

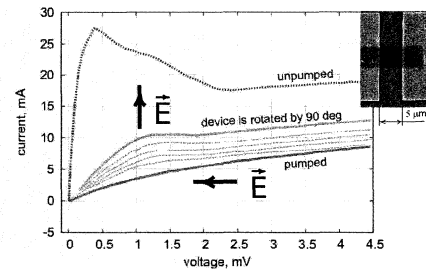


Fig. 7. LO pumped IV-curves for $5 \times 5 \mu\text{m}^2$ device at 10.7 THz.

For $30 \times 20 \mu\text{m}^2$ device the optimal absorbed LO power is about $20 \mu\text{W}$. Responsivity of the device versus frequency is almost flat and amounts to $70 \frac{\text{V}}{\text{W}}$ in the frequency range of 20÷70 THz. At 10.7 THz we pumped $5 \times 5 \mu\text{m}^2$ device that is smaller than the radiation spot and did not have enough LO power to pump $30 \times 20 \mu\text{m}^2$ device.

ACKNOWLEDGMENTS

Research supported by:
INTAS, under contract 03-51-4145;
Russian Foundation for Basic Research under contracts RFBR N 05-02-08207 and RFBR N 04-02-39016.

REFERENCES

- [1] J. Schubert, A. Semenov, G. Gol'tsman, H.-W. Hübers, G. Schwaab, B. Voronov, and E. Gershenzon, *Supercond. Sci. Technol.*, no. 12, p. 748, 1999.
- [2] M. Kroug, S. Cherednichenko, H. Merkel, E. Kollberg, B. Voronov, G. Gol'tsman, H.-W. Hübers, and H. Richter, "NbN hot electron bolometric mixers for terahertz receivers," *IEEE Transactions on Applied Superconductivity*, vol. 11, no. 1, pp. 962–965, Mar. 2001.
- [3] A. Karpov, D. Müller, F. R. Rice, J. A. Stern, B. Bumble, H. G. LeDuc, and J. Zmuidzinas, "Low-noise SIS mixer for far-infrared radio astronomy," in *Proc. SPIE*, vol. 5498, Glasgow, Scotland, UK, June 2004, pp. 616–621.
- [4] A. Betz and R. Borejko, "A practical Schottky mixer for 5 THz," in *Proc. 7th international symposium on space terahertz technology*, 1996, p. 503.
- [5] J. Baselmans, M. Hajenius, J. Gao, T. Klapwijk, P. de Korte, B. Voronov, and G. Gol'tsman, "Doubling of sensitivity and bandwidth in phonon cooled hot electron bolometer mixers," *Appl. Phys. Lett.*, vol. 84, no. 11, p. 1958, Mar. 2004.
- [6] M. Finkel, S. Maslennikov, Y. Vachtomin, S. Svechnikov, K. Smirnov, V. Seleznev, Y. Korotetskaya, N. Kaurova, B. Voronov, and G. Gol'tsman, "Hot electron bolometer mixer for 20 - 40 THz frequency range," in *Proc. 16th international symposium on space terahertz technology*, Göteborg, Sweden, May 2005.
- [7] Y. Vachtomin, S. Antipov, S. Maslennikov, K. Smirnov, S. Polyakov, N. Kaurova, E. Grishina, B. Voronov, and G. Gol'tsman, "Noise temperature measurements of NbN phonon-cooled hot electron bolometer mixer at 2.5 and 3.8 THz," in *Proc. 15th international symposium on space terahertz technology*, Northampton, Massachusetts, USA, Apr. 2004, pp. 236–241.
- [8] A. Semenov, Heinz.-Wilhelm Hübers, H. Richter, M. Birk, M. Krocka, U. Mair, K. Smirnov, G. Gol'tsman, and B. Voronov, "Performance of terahertz heterodyne receiver with a superconducting hot-electron mixer," in *Proc. 13th international symposium on space terahertz technology*. Cambridge, MA, USA: Harvard University, Mar. 2002, pp. 229–234.

An HEB cross-bar balanced mixer at 1.5 THz

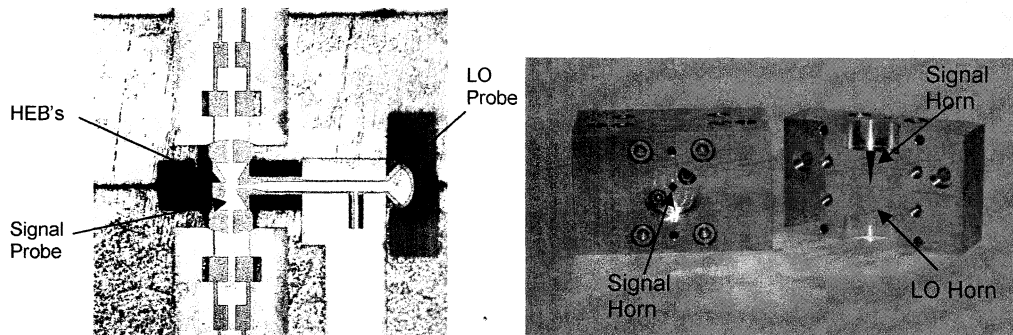
A. Skalare, J. Stern

Jet Propulsion Laboratory, California Institute of Technology

In this presentation we will describe the development of a hot-electron bolometer (HEB) cross-bar balanced mixer circuit that could simplify the injection of local oscillator power in future focal plane mixer arrays. The effort is targeted towards potential use in instruments for SAFIR, but also towards smaller instrumentation that could fit into a future mission under NASA's SMEX or MIDEX definitions. The goal is to demonstrate a low-noise laboratory receiver that can be frequency tuned, that uses a solid-state local oscillator and that has no moving parts.

Our approach is to fabricate HEB's on shaped thin silicon substrates and to install these into a waveguide mixer, taking advantage of the low losses and the high beam-quality of waveguide horn antennas as well as giving scalability to higher frequencies. Silicon-On-Insulator (SOI) technology provides thin (6 microns) membrane substrates for the mixer circuits. These substrates can be given arbitrary shape by deep-trench etching, and gold tabs (beam-leads) are formed along the edges of the substrates to contact the circuits and to clamp the chips tightly into a split-block waveguide fixture. This mixer concept should work at frequencies up to several terahertz without the power leakages and resonance modes that would result from thicker substrates or large extended membranes. A cross-bar circuit is used so that the local oscillator (LO) power can be coupled to the mixer via a separate waveguide, thereby achieving high coupling efficiencies for both the detection signal and local oscillator without using an external interferometer. The mixing elements are superconducting NbTiN and NbN HEB's. The entire mixer has been machined and assembled at the time of this writing, but has not yet been tested - further results are pending and will be presented at the symposium.

This work was performed at the Jet Propulsion Laboratory, California Institute of Technology, under a contract with the National Aeronautics and Space Administration.



1.9 THz and 1.4 THz waveguide mixers with NbTiN HEBs on Silicon Nitride Membranes

P. P. Muñoz, S. Bedorf, C.E. Honingh, K. Jacobs¹

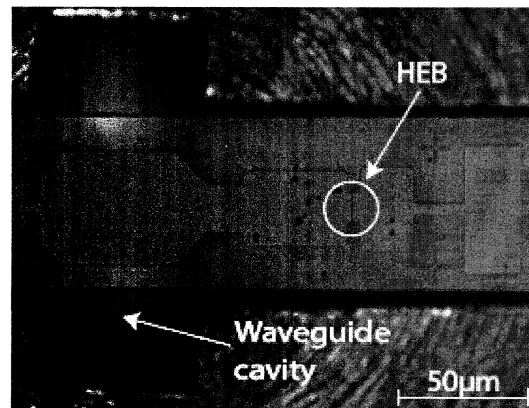
KOSMA, I. Physikalisches Institut, Universität zu Köln
Zùlpicher Straße 77, D-50937 Köln, Germany

We developed waveguide HEB mixers for the GREAT instrument on SOFIA at 1.9 THz and for the ground-based receiver CONDOR at 1.4 THz. The latter has been taking astronomical data recently at the APEX telescope on the Atacama site.

The HEBs with a dimension of $0.4 \times 4 \mu\text{m}$ consist of 3-5nm thick NbTiN films deposited at 800°C on Silicon wafers covered with a $2 \mu\text{m}$ thick layer of low-stress Silicon Nitride. The waveguide probe and the RF blocking filter are 200nm thick gold films. The contacts to the bolometer are made of a NbTiN/Au bilayer after performing an Oxygen/Argon plasma cleaning step. After backside Silicon etching, an individual membrane device is flip-chip bonded to a separately fabricated Silicon support frame. The frame is glued into a fixed-backshort waveguide block that has the necessary recess for the Silicon frame and a substrate channel for the device substrate. The 1.9 THz waveguide with a height and width of $59 \mu\text{m} \times 133 \mu\text{m}$ is stamped $59 \mu\text{m}$ deep into the copper block.

At 1.9 THz, the full receiver setup in the SOFIA flight configuration achieved an average uncorrected noise temperature of ~ 2000 K over the IF band, limited from 1.25 to 1.75 GHz by the cryogenic isolator. The 1.4 THz receiver achieved ~ 1500 K in the same IF band. The IF bandwidth and sensitivity of the bolometers seems not to be strongly affected by the cooling through the thin membrane only.

The mixers were LO-pumped by a Backward Wave Oscillator followed by a frequency tripler (Radiometer Physics GmbH, Meckenheim) at 1.9 THz and with a solid state amplifier/multiplier chain (Virginia Diodes, Inc., Charlottesville, VA), driven by a synthesizer at around 19 GHz, at 1.4 THz. The duplexers are Martin-Puplett interferometers. Details of the CONDOR receiver are given in a contribution by Martina Wiedner et al. submitted to this conference.



Photograph of the 1.9 THz waveguide mixer with the NbTiN HEB and RF filter circuit visible through the semi-transparent Silicon Nitride membrane.

¹ E-mail jacobs@ph1.uni-koeln.de

IF Impedance and Mixer Gain of Hot-Electron Bolometers and the Perrin-Vanneste Two Temperature Model

J. W. Kooi¹, J. J. A. Baselmans², J. R. Gao³, T. M. Klapwijk³, M. Hajenius³,
P. Dieleman⁴, A. Baryshev⁴, and G. de Lange⁴.

We have measured the frequency dependent IF impedance and mixer conversion gain of a small area NbN hot-electron bolometer (HEB). The device used is a twin slot antenna coupled NbN HEB mixer with a bridge area of 1×0.15 mm, and a critical temperature of 8.3K. In the experiment the local oscillator (LO) frequency was 1.300 THz, and the intermediate frequency (IF) 0.05-10 GHz. We find that the measured data can be described in a self consistent manner with a thin film model presented by Nebosis, Semenov, Gousev, and Renk, that is based on the two temperature electron-phonon heat balance equations of Perrin-Vanneste. From these results the thermal time constant, governing the gain bandwidth of HEB mixers, is observed to not only be a function of the electron-phonon scattering time and phonon escape time, but also a function of electron temperature. The latter is due to the temperature dependence of the electron and phonon specific heat. Because hot electron bolometers nominally operate at, or slightly above, the critical temperature (T_c) of the superconducting film, where local resistivity as a function of electron temperature is largest, it follows that the critical temperature of the film plays an important role in determining the HEB mixer gain bandwidth. For an NbN based hot electron bolometer, the maximum predicted gain bandwidth is approximately 5.5 GHz, given a film thickness of 3.5 nm and a $T_c=12$ K.

Both the measured impedance and calibrated mixer gain data are used to determine (fit) values for t_{eph} , t_{esc} , and c_e/c_{ph} in the NSGR model. We demonstrate that in this way the model provides a self consistent set of parameter values. Results agree well with literature, and provide an excellent agreement between model and measurement, inclusive of electro-thermal feedback modulations.

¹California Institute of Technology, MS 320-47, Pasadena, California 91125, USA.
E-mail: kooi@caltech.edu, <http://www.submm.caltech.edu/cso/reveivers.html>

²SRON Netherlands Institute for Space Research, Sorbonnelaan 2, 3584 CA Utrecht, The Netherlands.

³Kavli Institute of Nanoscience, Faculty of Applied Sciences, Delft University of Technology, Lorentzweg 1, 2628 CJ Delft, The Netherlands.

⁴SRON Netherlands Institute for Space Research, Landleven 12, 9747 AD Groningen, The Netherlands.

Optimal Cold-Electron Bolometer with a Superconductor-Insulator-Normal Tunnel Junction and an Andreev Contact

Leonid Kuzmin

Abstract— A novel concept of the optimal Cold-Electron Bolometer (CEB) with a Superconductor-Insulator-Normal (SIN) Tunnel Junction and Andreev SN contact has been proposed. This concept has been developed to improve noise properties of the CEB by increasing current responsivity for SQUID readout (in voltage-biased mode) in comparison with classical CEB concept comprising two SIN tunnel junctions. In this configuration the power of incoming signal is not split between two series junctions and the current response of a single junction is twice larger in comparison with double junction structure.

The signal is concentrated from antenna to an absorber through capacitance of the tunnel junction from one side and Andreev contact from another side. HF matching is realized by resistance of a normal metal absorber that is independent on tunnel junction parameters. The volume of a normal metal is partly squeezed due to proximity effect of a superconducting electrode from the Andreev contact that also increases efficiency of the electron cooling.

The concept is based on direct electron cooling of the absorber by SIN tunnel junction that serves as negative electrothermal feedback for the signal. Noise properties are considerably improved by decreasing the electron temperature. Ultimate performance of the CEB is determined by optical load converted to shot noise of the signal readout. The goal is to achieve noise-equivalent power (NEP) of the CEB with standard SQUID readout less than photon noise. Ultimate NEP better than photon noise can be achieved practically in wide range of power loads from 0.1 fW (SPICA) to 30 pW (OLIMPO, CLOVER, PILOT). Applicability of the CEB to post-Herschel space missions looks very promising.

Index Terms— Cold-Electron Bolometer, SIN tunnel junction, Andreev contact, SQUID readout

I. INTRODUCTION

Cosmology experiments in the last few years (WMAP, BOOMERanG, SDSS) have discovered that the Universe consists of 73% **Dark Energy**, 23% **Dark Matter**, and only 4% ordinary matter. The most shocking news is acceleration of the Universe by unknown forces due to the increasing dominance of a mysterious dark energy. The prove of existence of the Dark Energy and Dark Matter has been recognized by magazine Science as the Breakthrough of the Year [1]. Experiments to resolve the nature of the mysterious dark Universe require a new generation of telescopes with increased accuracy of resolution including

polarization CMB measurements. There are several cosmology instruments (CLOVER, EBEX, BICEP, QUIET) that are being designed to measure the polarization in the Cosmic Microwave Background (CMB). The *B*-mode polarization is generated entirely by primordial gravitational waves.

The project OLIMPO is a 2.6 m balloon-borne telescope, aimed at measuring the Sunyaev-Zeldovich effect in clusters of Galaxies. We will use typical requirements on detector system from OLIMPO project for development of optimal concept of bolometer. The OLIMPO detector system consists of four bolometer arrays at 140, 220, 410 and 540 GHz. The bolometer arrays should operate in 300 mK cryostat. The estimated optical loading on the OLIMPO detectors in flight, P_o , determines the required detector parameters and the ultimate sensitivity of the instrument. The optical loading is dominated by emission from the warm telescope plus the emission from the 2.73 K CMB. The power on each detector at 140, 220, 410 and 540 GHz is 4, 6, 14 and 28 pW respectively [2],[3]. From these values we can calculate the fundamental limit to sensitivity from photon noise and express this in terms of an NEP.

A new generation of detectors is needed for these advanced telescopes. One of these technologies is the Capacitively Coupled Cold-Electron Bolometer (CEB) with SQUID readout [4]-[6]. The SQUID readout has been already developed for TES bolometers with typical sensitivity of 1 pA/Hz^{1/2}. The goal is to achieve noise-equivalent power (NEP) of the CEB with standard SQUID readout less than photon noise. The CEB is a planar antenna-coupled superconducting detector with high sensitivity and high dynamic range due to use of SIN tunnel junctions for electron cooling and strong electrothermal feedback [4]. To achieve noise matching with SQUID for the estimated in-flight optical power load, a CEB with smaller junction resistance (larger area) has to be used. However, a standard shadow evaporation technique does not give opportunity to do junctions with area more than 1 μm^2 . Some optimization of properties should be done to realize noise matching for available area of the junctions or a new technology of SIN junctions should be developed.

In this paper, we will analyze an optimal configuration of CEB with one SIN junction and Andreev SN contact instead of a traditional CEB with two SIN junctions in series.

Manuscript received May 31, 2006 This work was supported in part by the Swedish Research Council Grant. L. Kuzmin is with the Chalmers University of Technology, 412 96 Gothenburg, Sweden (phone: +46 31 7723608; fax: +46 31 7723471; e-mail: Leonid.kuzmin@mc2.chalmers.se).

II. CONCEPT OF AN OPTIMAL BOLOMETER WITH ONE SIN TUNNEL JUNCTION AND SN ANDREEV CONTACT

To increase efficiency of CEB for current readout, an optimal configuration of CEB with capacitively coupled SIN junction and Andreev SN contact has been considered (Fig. 1). This concept has been proposed to improve noise properties by increasing responsivity of the CEB for SQUID current readout (in voltage-biased mode). In this configuration the power of incoming signal is not split between two series junctions and the current response is realized by a single junction increasing twice responsivity in comparison to double junction structure. It should lead to decrease of amplifier noise and the junction shot noise. The volume of a normal metal is partly squeezed due to proximity effect of a superconducting electrode from the Andreev contact that further increases efficiency of the electron cooling without degradation of HF coupling.

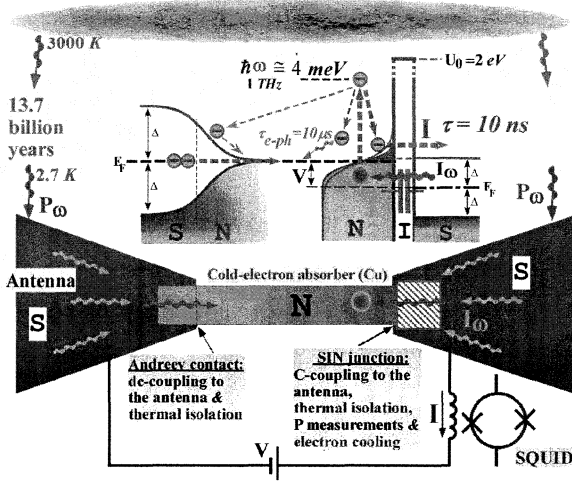


Fig 1. Schematic of the optimal Cold-Electron Bolometer (CEB) with capacitive coupling to the antenna and a SQUID readout. The CEB comprises a planar superconducting antenna and an absorber coupled through capacitance of SIN tunnel junction and SN Andreev contact. The SIN tunnel junction is used also for electron cooling and power measurements by SQUID readout system.

The signal is concentrated from an antenna to the absorber through capacitance of the tunnel junction and Andreev contact. HF matching is realized by resistance of a normal absorber that is independent on tunnel junction parameters.

The concept is based on *direct electron cooling* of the absorber that serves as strong *negative electrothermal feedback* for the signal. This feedback is analogous to the TES (transition-edge sensor) [6] but artificial dc heating is replaced by *direct electron cooling* to minimum temperature. It could lead to a principle breakthrough in realization of supersensitive detectors. Noise properties are considerably improved by decreasing the electron temperature. The loop gain of electrothermal feedback could exceed 1000. The response time is reduced by electrothermal feedback to 10 ns in comparison with the intrinsic e-ph time constant of 10 μs.

The CEB in voltage-biased mode gives opportunity to increase dynamic range by removing all incoming power from supersensitive absorber to the next stage of readout system (SQUID) with higher dynamic range. The CEB with one SIN junction and one Andreev contact has almost twice

higher responsivity than the traditional CEB with two SIN junctions in series. It gives opportunity to realize ultimate noise properties. However, the strength of electron cooling is higher in double junction structure due to two junctions working for cooling. Due to this reason improvement of responsivity and other related properties is less than two times.

III. MODEL

For analysis we use a concept of CEB with strong electrothermal feedback due to electron cooling analyzed in detail in Ref. [4]. The operation of CEB can be analyzed using heat balance equation [4],[9]:

$$P_{cool}(V, T_e, T_{ph}) + \Sigma \Lambda (T_e^5 - T_{ph}^5) + \frac{V^2}{R_j} + I^2 R_{abs} + C_\Lambda \frac{dT}{dt} = P_0 + \delta P(t) \quad (1)$$

Here, $\Sigma \Lambda (T_e^5 - T_{ph}^5)$ is the heat flow from electron to the phonon subsystems in the absorber, Σ is a material constant, Λ - a volume of the absorber, T_e and T_{ph} are, respectively, the electron and phonon temperatures of the absorber;

$P_{cool}(V, T_e, T_{ph})$ - cooling power of the SIN tunnel junction; $C_\Lambda = \Lambda \gamma T_e$ is the specific heat capacity of the absorber; R_j - resistance of tunnel junction; R_{abs} - resistance of the absorber; $P(t)$ - the incoming rf power. We can separate Eq. (1) into the time independent term,

$$\Sigma \Lambda (T_{e0}^5 - T_{ph0}^5) + P_{cool0}(V, T_{e0}, T_{ph0}) = P_0, \text{ and the time independent term,}$$

$$\left(\frac{\partial P_{cool}}{\partial T} + 5 \Sigma \Lambda T_e^4 + i \omega C_\Lambda \right) \delta T = \delta P. \quad (2)$$

The first term, $G_{cool} = \partial P_{cool} / \partial T$, is the cooling thermal conductance of the SIN junction that gives the negative electrothermal feedback (ETF); when it is large, it reduces the temperature response δT because cooling power, P_{cool} , compensates the change of signal power in the bolometer.

The second, $G_{e-ph} = 5 \Sigma \Lambda T_e^4$, is electron-phonon thermal conductance of the absorber. From Eq. (2) we define an effective complex thermal conductance which controls the temperature response of CEB to the incident signal power

$$G_{eff} = G_{cool} + G_{e-ph} + i \omega C_\Lambda \quad (3)$$

In analogy with TES [7], the effective thermal conductance of the CEB is increased by the effect of electron cooling (negative ETF).

Here we assume that the SIN tunnel junction is voltage-biased, and the current is measured by SQUID [4],[6]. The sensitivity of the device is then characterized by the current responsivity S_I , which is the ratio of the current change and the change in the power load of the bolometer,

$$S_I = \frac{\partial I}{\partial P_\omega} = \frac{\partial I / \partial T}{G_{cool} + G_{e-ph} + i \omega C_\Lambda} = \frac{\partial I / \partial T}{G_{cool}} \frac{L}{(L+1)[1+i\omega\tau]} \quad (4)$$

where $L = G_{cool} / G_{e-ph} \gg 1$ is ETF gain and

$$\tau = C_\Lambda / G_{e-ph} = \tau_0 / (L+1) \quad (5)$$

is an effective time constant, $\tau_0 = C_\Lambda / G_{e-ph}$ ($\approx 10 \mu s$ at 100 mK).

Strength of electrothermal feedback is estimated as:

$$L(\omega) = \frac{G_{cool}}{G_{e-ph}(1+i\omega\tau)} = \frac{\partial I / \partial T}{G_{cool} + G_{e-ph} + i\omega C_{\Lambda}} \quad (6)$$

Noise properties are characterized by the NEP, which is the sum of three different contributions:

$$NEP_{total}^2 = NEP_{e-ph}^2 + NEP_{SIN}^2 + \frac{\delta I^2}{S_I^2} \quad (7)$$

$$NEP_{e-ph}^2 = 10k_B \Sigma \Lambda (T_e^6 + T_{ph}^6) \quad (8)$$

is the noise associated with electron-phonon interaction; NEP_{SIN}^2 is the noise of the SIN tunnel junctions, and the last term $\delta I^2/S_I^2$ is the noise of an amplifier (SQUID), δI , which is expressed in pA/Hz^{1/2}.

The noise of the NIS tunnel junctions, NEP_{SIN}^2 , has three components: shot noise $2eI/S_I^2$, the fluctuations of the heat flow through the tunnel junctions and the correlation term between these two processes

$$NEP_{SIN}^2 = \delta P_{\omega}^2 - 2 \frac{\delta P_{\omega} \delta I_{\omega}}{S_I} + \frac{\delta I_{\omega}^2}{S_I^2} \quad (9)$$

It is necessary to take into account the effect of the electron cooling of the metallic strip by the SIN tunnel junction. For every chosen voltage we first solve the heat balance equation, find the electron temperature in the metallic strip, and then we determine current responsivity and NEP.

IV. COMPARISON OF THE CEB WITH ONE TUNNEL JUNCTION AND SN CONTACT AND CEB WITH TWO TUNNEL JUNCTIONS

The analysis of the Cold-Electron Bolometer (CEB) shows that the optimal configuration of the is a CEB with a voltage-biased SIN Tunnel Junction and an Andreev SN contact. The optimal readout is a SQUID amperemeter.

We have analyzed the concept of an optimal hot-electron bolometer in the presence of the typical background power load ($P_0 = 4$ pW) [3] for fixed sensitivity of the SQUID-amplifier (0.5 pA/Hz^{1/2}) [8].

Photon noise:
$$NEP_{phot} = \sqrt{2P_0 * hf} \quad (10)$$

For channel 140 GHz: $NEP_{phot} = 2,7 * 10^{-17}$ W/Hz^{1/2}.

The total NEP of CEB should be less than photon noise.

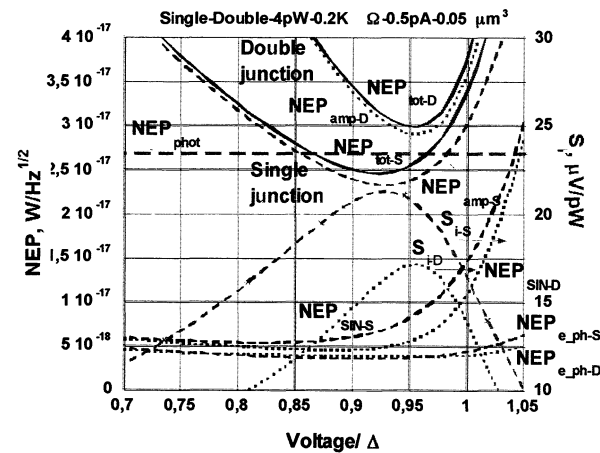


Fig. 2. Total NEP and NEP components for the single junction CEB (solid lines) and for the double junction CEB (dashed lines). The $NEP_{phot} = 2,7 * 10^{-17}$ W/Hz^{1/2}. Current responsivity S_I is shown for both cases referred to the right axis. Parameters: $i_{amp} = 0.5$ pA/Hz^{1/2} (SQUID), $R = 0.2$ kOhm (one junction), $Vol = 0.03 \mu m^3$ (single junction) and $0.05 \mu m^3$ (double junction), power load $P_0 = 4$ pW.

The Fig. 2 shows results of simulation for Single Junction CEB (SJ-CEB) and Double Junction CEB (DJ-CEB) for maximum area of tunnel junction, $0,5 \mu m^2$, available by shadow evaporation technique. Volume of absorber is larger for DJ-CEB due to the additional tunnel junction. The Fig. 2 shows decrease of the total NEP for SJ-CEB in comparison to DJ-CEB. The level of NEP_{phot} has been achieved for SJ-CEB. This improvement is achieved mainly due to decrease of a NEP_{amp} (SQUID) related directly to the responsivity S_I (7). The responsivity is determined mainly by cooling conductance G_{cool} (4). The G_{cool} is increased twice for two junction CEB (2). For series connection of two junctions it leads to twice decrease of current responsivity (4).

V. DEPENDENCE OF THE NOISE PERFORMANCE ON BATH TEMPERATURE

Responsivity of the CEB is very sensitive to the electron temperature of the absorber. The next step would be to check influence of the bath temperature on an NEP.

The Fig. 2 shows comparison of the NEP of a Single Junction CEB at two bath temperatures: 300 and 100 mK.

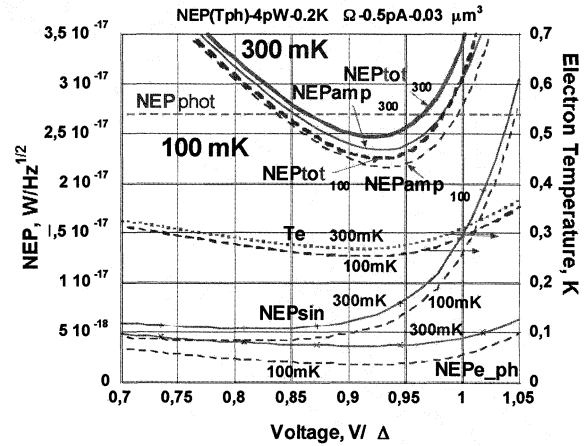


Fig. 3. The NEP of the single junction CEB in dependence on voltage for two bath temperatures: 300 mK (solid lines) and 100 mK (dashed lines). Electron temperature of absorber T_e referred to the right axis is shown for the same bath temperatures. Parameters of the CEB are the same as for Fig. 2: $i_{amp} = 0.5$ pA/Hz^{1/2} (SQUID), $R = 0.2$ kOhm, $\Lambda = 0.03 \mu m^3$, $P_0 = 4$ pW, $NEP_{phot} = 2,7 * 10^{-17}$ W/Hz^{1/2}.

Simulations show that dependence of NEP_{tot} on bath temperature is surprisingly very weak (Fig. 3). The reason can be clear seen from the electron temperature T_e dependence. For bath temperatures 300 and 100 mK the T_e is approximately the same at the level of 250 mK. This level is determined mainly by high power load of 4 pW and is not sensitive to bath temperature (through e-ph conductance).

VI. DEPENDENCE OF THE NOISE PERFORMANCE ON JUNCTION RESISTANCE

Taking into account high power load it is reasonable to test the junction with lower resistance (higher cooling ability). The Fig. 4 shows comparison of NEP for two values of junction resistance: 0.2 kΩ and 0.1 kΩ. Other parameters are the same as for SJ-CEB in Fig. 2 and 3.

Simulations show that dependence of NEP_{tot} on junction resistance is very strong (Fig. 4). The reason can be clear

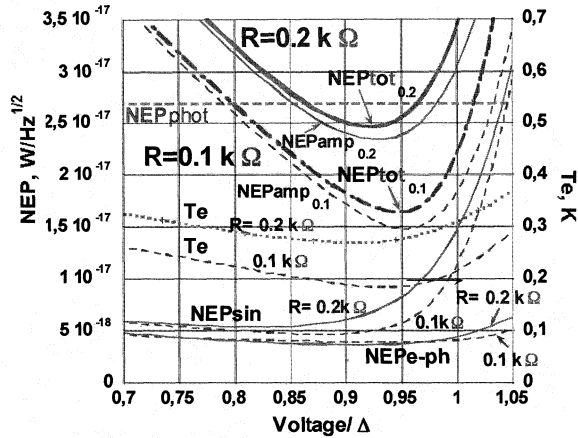


Fig. 4. Dependence of the NEP of a single junction CEB on voltage for two SIN junction resistances: 0.2 kΩ (solid lines) and 0.1 kΩ (dashed lines). Electron temperature of absorber T_e (right axis) is shown for the same junction resistances. Other parameters are as for Fig. 2 and 3.

seen from electron temperature T_e dependence. For higher ohmic junction, the T_e is at the level of 270 mK when for lower ohmic one, the T_e is around 180 mK due to stronger cooling conductance. This leads to lower level of energy quantization of hot electrons in the absorber [4] with proper increase of current response on incoming power. Proportionally, the NEPamp is decreased leading to decrease of NEPtot. It is interesting to stress that other NEP components are not changed too much due to this decrease of T_e due to other dominating reasons of their origin.

Due to this strong influence on noise performance, it is reasonable to check influence of R in wider range of values. The Fig. 5 shows dependence of the NEP on junction resistance R from 25 Ω to 400 Ω. The area of junction has been changed proportionally from 8 μm² to 0.5 μm².

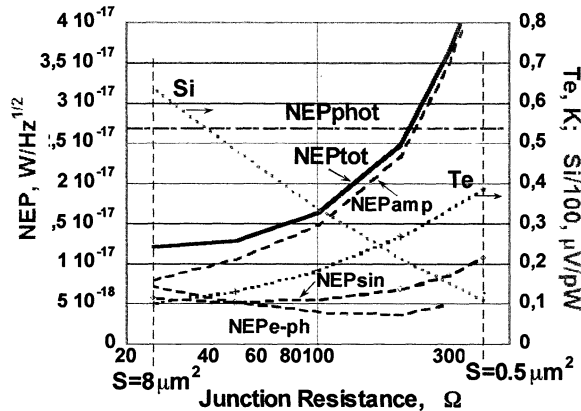


Fig. 5. Dependence of the NEP on resistance of SIN tunnel junction (and area) for the single junction CEB. The electron temperature of the absorber, T_e , and responsivity, S_i , are shown referred to the right axis. Other parameters are the same as for Fig. 2-4: $i_{imp}=0.5$ pA/Hz^{1/2}, $T=300$ mK, $A=0.03$ μm², $P_0=4$ pW, $NEP_{phot}=2.7 \cdot 10^{-17}$ W/Hz^{1/2}, $T=300$ mK.

Simulations show that dependence of NEPtot on junction resistance is very strong in some region of resistance (Fig. 5). Starting from higher ohmic junctions, one can see strong decrease of total NEP from 400 Ω to 100 Ω related to decrease of NEPamp (dependent on S_i). The CEB is moving to background limited operation determined by shot noise due to power load. Then, the total NEP shows some saturation in the region from 100 Ω to 25 Ω related with

increase of NEPe_ph. The NEPe_ph is related with volume of absorber (8) and is naturally increased when volume is increased proportionally to the area of the junction.

Final value of NEPtot is much less than NEPphot in the region of R lower than 100 Ohm.

CEB array. This range of resistances could be achieved also by an array of parallel CEBs. The analysis shows that the array will act as a single CEB with a sum of junction areas and parallel connection of resistances of absorbers.

Absorber overheating. Simulations show that dc power dissipated in absorber could lead to additional overheating of the absorber. The effective decision could be to use a superconducting absorber with normal metal traps [10]. Superconducting absorber would act effectively as a normal metal for frequencies higher than superconducting energy gap (35 GHz for Al) and as a superconductor for dc bias without any dissipation of energy. Another decision is bilayer of normal metal (Cr) and superconductor (Al) for absorber. In this case we spread the normal metal trap to the whole absorber.

VII. CONCLUSION

A novel concept of the optimal Cold-Electron Bolometer (CEB) with a Superconductor-Insulator-Normal (SIN) Tunnel Junction and Andreev SN contact has been developed. This concept with standard SQUID readout gives unique opportunity to achieve the NEP less than photon noise for any optical power load.

The key moment is increasing twice the current responsivity of the CEB in comparison with classical CEB with two SIN tunnel junctions. The most important parameter to achieve ultimate NEP is resistance of the junction determining cooling efficiency of the bolometer.

Applicability of the CEB to post-Herschel missions looks very promising for all range of telescopes from ground based to space telescopes.

Useful discussion with Dmitry Golubev is acknowledged.

REFERENCES

- [1] C. Seife, BREAKTHROUGH OF THE YEAR 2003: "Illuminating the Dark Universe", *Science*, vol. 302, pp. 2038-2039, Dec. 2003.
- [2] S. Masi et al., OLIMPO: a balloon-borne, arcminute-resolution survey of the sky, in *16th ESA Symposium on Rocket and Balloon Programmes*, June 2003, St.Gallen (2003), ESA-SP-530, 557-560
- [3] L. Kuzmin, and P. Mauskopf, "Superconducting Cold-Electron Bolometer with JFET Readout for OLIMPO Balloon Telescope", *Proceedings of the ISSTT-05*, Gothenburg, pp 549-554, May 2005
- [4] L. Kuzmin "Ultimate Cold-Electron Bolometer with Strong Electrothermal Feedback", *Proc. of SPIE conference "Millimeters and Submillimeter Detectors"*, 5498, p 349, Glasgow, June 2004.
- [5] L. Kuzmin, "Optimal Cold-Electron Bolometer with Superconductor-Insulator-Normal Tunnel Junction and Andreev Contact", *Proc. of ISSTT conference*, Paris, May 10-12, 2006
- [6] L. Kuzmin and D. Golubev "On the concept of an optimal hot-electron bolometer with NIS tunnel junctions". *Physica C* 372-376, pp 378-382 (2002).
- [7] A. Lee, P. Richards, S. Nam, B. Cabrera, K. Irwin, *Applied Physics Letters*, 69, (1996) 1801.
- [8] www.supracon.com.
- [9] D. Golubev and L. Kuzmin. Nonequilibrium theory of the hot-electron bolometer with NIS tunnel junction. *Journal of Applied Physics*. 89, 6464-6472 (2001).
- [10] Leonid Kuzmin, "Superconducting Cold-Electron Bolometer with Proximity Traps", *Microelectronic Engineering*, 69, p. 309, 2003.

Can NbN films on 3C-SiC/Si change the IF bandwidth of hot electron bolometer mixers?

J.R. Gao, M. Hajenius, F.D. Tichelaar, B. Voronov, E. Grishina, T. M. Klapwijk, G. Gol'tsman, and C.A. Zorman

Abstract— We realized ultra thin NbN films sputtered grown on a 3C-SiC/Si substrate. The film with a thickness of 3.5-4.5 nm shows a T_c of 11.8 K, which is the highest T_c observed among ultra thin NbN films on different substrates. The high-resolution transmission electron microscopy (HRTEM) studies show that the film has a monocrystalline structure, confirming the epitaxial growth on the 3C-SiC. Based on a two-temperature model and input parameters from standard NbN films on Si, simulations predict that the new film can increase the IF bandwidth of a HEB mixer by about a factor of 2 in comparison to the standard films. In addition, we find standard NbN films on Si with a T_c of 9.4 K have a thickness of around 5.5 nm, being thicker than expected (3.5 nm).

Index Terms—Hot electron bolometer mixer, thin superconducting films, NbN film, and 3C-SiC

NbN hot electron bolometer (HEB) mixers in combination with THz quantum cascade lasers¹ are a promising heterodyne detection technology for future astronomic and Earth's science space missions for the frequency range from 2 to 6 THz. However, the limited IF gain bandwidth of HEB mixers based on standard NbN thin film on a Si substrate tends to restrict their application^{2,3}. It is highly desirable to develop new ways to enlarge the bandwidth. Although replacing standard Si by MgO as "substrate", the NbN films grown epitaxially have an increased critical temperature (T_c)⁴. They have demonstrated an improved IF bandwidth from 3 GHz to 4.5 GHz. But MgO is hygroscopic and is therefore incompatible with space applications.

We realized, for the first time, ultra thin NbN films on a 3C-SiC buffer layer⁵ on a Si substrate, which are sputtered grown at a substrate temperature of 800 °C. The 3C-SiC buffer layer was produced at Case Western Reserve University (USA), which is heteroepitaxially grown on a Si substrate and is 1 μm thick, while the NbN films were

realized at Moscow State Pedagogical University (Russia). Due to the perfect lattice matching, a 3.5-4.5 nm thick film shows a T_c of 11.8 K, which is the highest T_c observed among ultra thin NbN films. The measured resistance versus temperature is given in figure 1. The monocrystalline structure and the thickness of the NbN film are evaluated through high-resolution transmission electron microscopy (HRTEM). Figure 2 shows a HRTEM micrograph of the NbN film on a 3C-SiC buffer layer, together with a zoom view. We also find a lattice constant of 4.36Å for the 3C-SiC layer and 4.39Å for the NbN thin film on the SiC layer. Note that the first realization of NbN films on 3C-SiC buffer layer was reported by Shoji *et al.*⁶. However, those are thick films with a thickness of 100 nm.

Our HRTEM studies, as an offshoot, also show that standard NbN films on Si with a T_c of 9.4 K have a thickness of around 5.5 nm, being thicker than 3.5 nm, which is expected from the sputtering rate calibrated from thick NbN films⁴. Figure 3 shows two HRTEM micrographs of NbN on Si, one being for the film with a T_c of 9.4 K and the other being for the film with a slightly higher T_c (9.8 K). The latter turns out to be around 6 nm thick. As indicated in the inset, such films have a polycrystalline structure.

Based on a two-temperature model^{7,8} and input parameters from standard NbN films on Si, simulations predict that the new film can increase the IF bandwidth by at

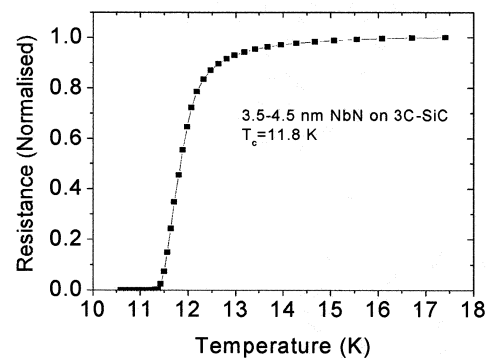


FIG. 1. Measured resistance as a function of temperature for an ultra thin NbN film epitaxially grown on a 3C-SiC buffer layer on a Si substrate.

least a factor of 2 in comparison to NbN films on Si. The result is shown in figure 3. The physical reason is that the higher T_c favors a shorter thermal time constant because of

Manuscript received June 30, 2006. The work is financially supported by the EU through RadioNet and by INTAS program.

J.R. Gao and M. Hajenius, are with SRON Netherlands Institute for Space Research, Utrecht, the Netherlands, and they are also with Kavli Institute of NanoScience, Faculty of Applied Sciences, Delft University of Technology, Lorentzweg 1, 2628 CJ, Delft, the Netherlands. (corresponding author: J.R. Gao with e-mail: J.R.Gao@tnw.tudelft.nl).

F.D. Tichelaar and T.M. Klapwijk are with Kavli Institute of NanoScience, Faculty of Applied Sciences, Delft University of Technology, Lorentzweg 1, 2628 CJ, Delft, the Netherlands.

B. Voronov, E. Grishina, and G. Gol'tsman are with Moscow State Pedagogical University (MSPU), Moscow 119435, Russia.

C.A. Zorman is with Case Western Reserve University, Ohio, USA

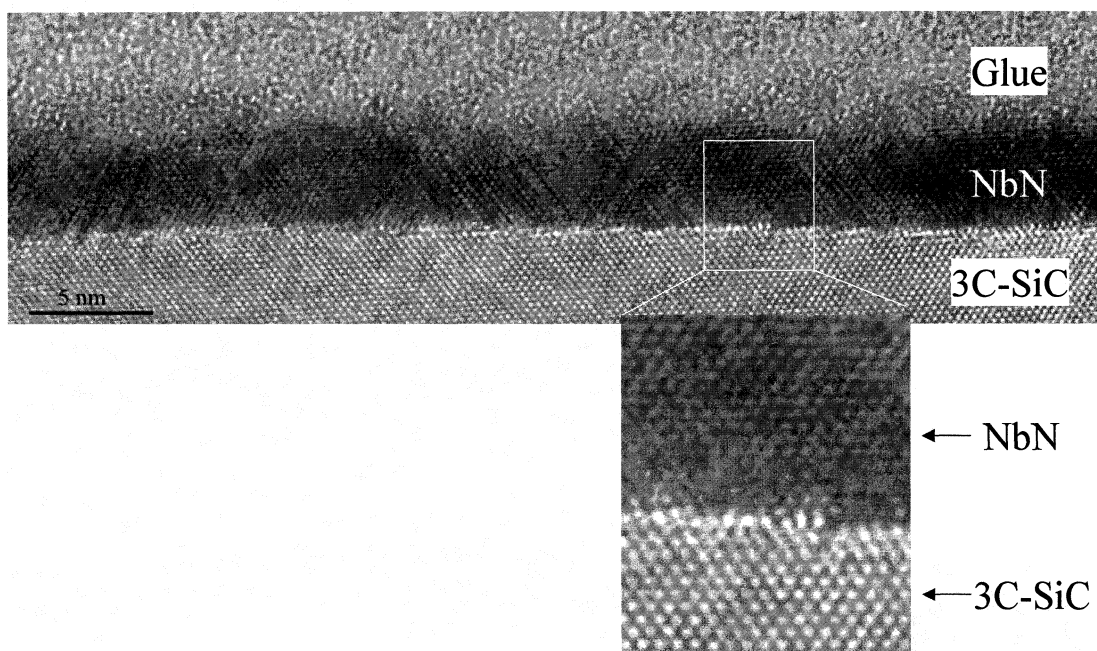


FIG.2. HRTEM micrograph of a thin NbN film grown on a 3C-SiC buffer layer. From the top, the glue, NbN film, and SiC layer are seen. The glue is used to prepare the specimen for HRTEM inspection. A zoom view of the NbN film on 3C-SiC, which illustrates a monocrystalline structure of the NbN layer.

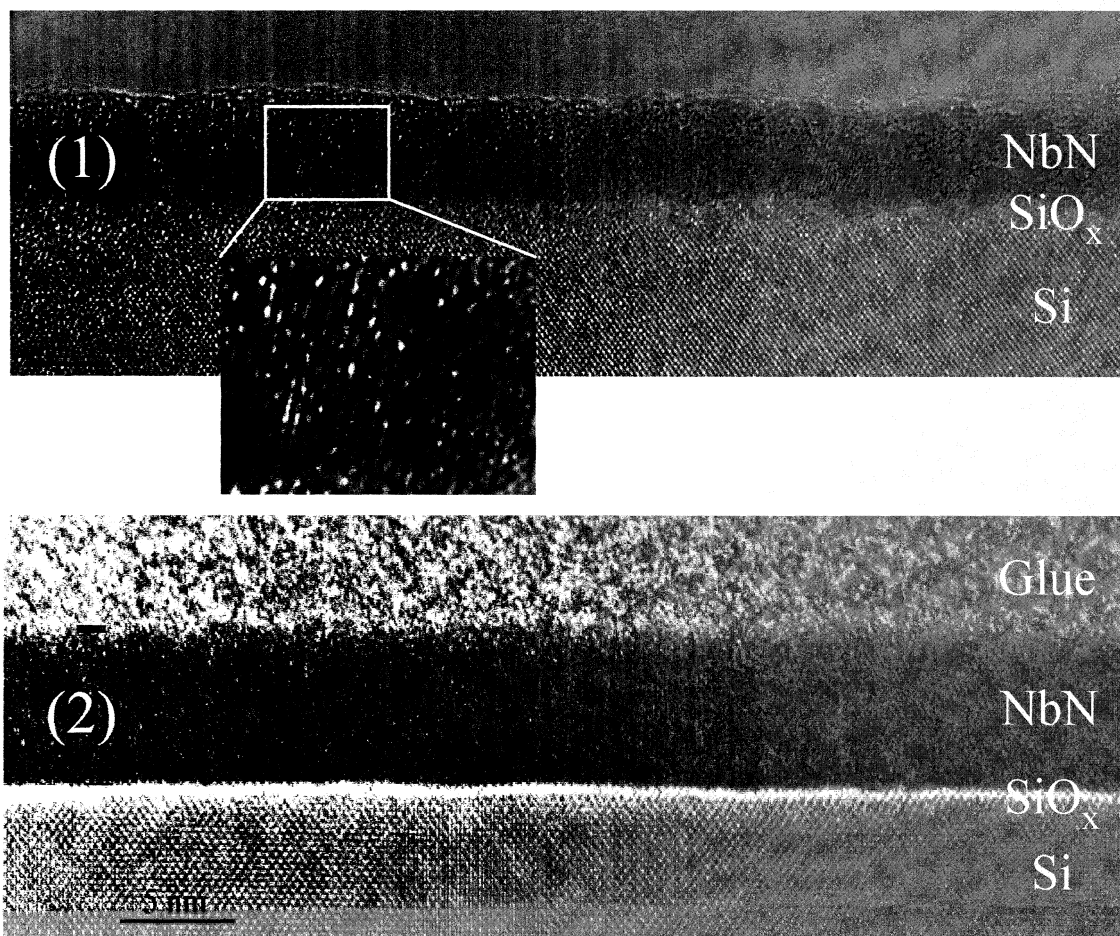


FIG.3. HRTEM micrographs of two thin NbN films grown on a Si substrate with a remaining native oxide layer. The top one (film 1) is for the film with a T_c of 9.4 K. The glue used to prepare the specimen for HRTEM inspection is removed. The zoom shows a polycrystalline structure of the NbN. The bottom one (film 2) is for the film with a T_c of 9.8 K. The glue in this case is remained.

the temperature dependence of the electron and phonon specific heat, and the thinner film favors a shorter phonon escape time to the substrate. In this simulation, we ignore the fact that the electron-phonon interaction time can also be film property dependent, in which a cleaner film can result in weaker electron-phonon interaction.

In addition, knowing the thickness correctly is crucial to simulate the measured IF impedance and bandwidth using the two-temperature model⁹ and is also valuable for correctly modeling¹⁰ and further improving HEBs.

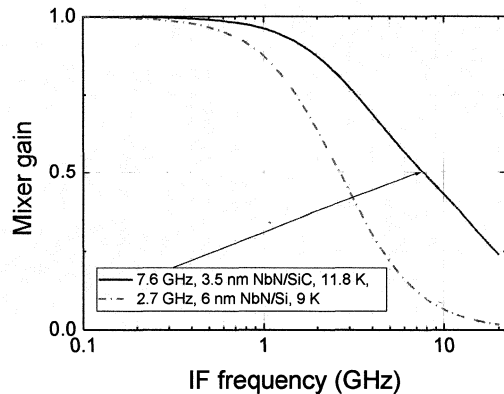


FIG.4. Calculated IF gain (normalized) versus intermediate frequency (IF) based on a two-temperature model for the NbN film on 3C-SiC and the film on Si substrate.

We acknowledge S.V. Svetchnikov who prepared the samples for HRTEM inspections, which were performed at National Centre for HREM at Delft. We thank also P. A. J. de Korte, J. J. A. Baselmans, K. Schuster, and J. W. Kooi for useful discussions on the topic of IF bandwidth.

REFERENCES

- [1] J.R. Gao, J.N. Hovenier, Z.Q. Yang, J.J.A. Baselmans, A. Baryshev, M. Hajenius, T.M. Klapwijk, A.J.L. Adam, T.O. Klaassen, B.S. Williams, S. Kumar, Q. Hu, and J.L. Reno, *Appl. Phys. Lett.*, **86**, 244104 (2005).
- [2] S. Cherednichenko, P. Khosropanah, E. Kollberg, M. Kroug, and H. Merkel, *Physica C*, **372-376**, 407 (2002).
- [3] J. J. A. Baselmans, M. Hajenius, J. R. Gao, T. M. Klapwijk, P. A. J. de Korte, B. Voronov and G. Gol'tsman, *Appl. Phys. Lett.*, **84**, 1958(2004).
- [4] Y. B. Vachtomin, M. I. Finkel, S. V. Antipov, B. M. Voronov, K. V. Sminov, N. S. Kaurova, V. N. Drakinski, and G. N. Gol'tsman, 13th International Symposium on Space Terahertz Technology, Harvard University, Cambridge, MA, 26-28 May 2002, p. 259.
- [5] M. Mehregany, C.A. Zorman, N. Rajan, and Chien Hung Wu, *Proceedings of IEEE*, **86**, 1594 (1998).
- [6] A. Shoji, S. Kiryu, and S. Kohjiro, *IEEE Transactions on Applied Superconductivity*, **5**, 2396 (1995).
- [7] N. Perrin and C. Vanneste, *Phys. Rev. B* **28**, 5150 (1983) and also *J. de Physique*, **48**, 1311 (1987).
- [8] R. S. Nebosis, A.D. Semenov, Yu. P. Gousev, and K. F. Renk, 7th International Symposium on Space THz Technology, March, 1996, Virginia, USA. Pages 601-713.
- [9] J. W. Kooi, J. J. A. Baselmans, J. R. Gao, P. Dieleman, Z. Q. Yang, A. Baryshev, M. Hajenius, G. de Lange, and T. M. Klapwijk, *The 16th Int. Symp. on Space terahertz Technology*, 2-4 May 2005, Gothenburg, Sweden. P465.
- [10] R. Barends, M. Hajenius, J. R. Gao, and T. M. Klapwijk, *Appl. Phys. Lett.*, **87**, 263506 (2005).

MgB₂ thin film terahertz mixers

S.Cherednichenko*, V.Drakinskiy

Abstract— Thin film (20 nm) MgB₂ bolometric devices were made on silicon substrates. The performance of the devices as THz mixers was investigated with respect to the gain bandwidth and the noise temperature. For the given film thickness the 3 dB gain roll-off frequency is 2.5 GHz, which is much higher than for the NbN HEB mixers of the same thickness. Corrected DSB mixer noise temperature is ~2000 K at 2 GHz IF. The noise bandwidth was measured in the IF range of 2-5 GHz.

Index Terms— MgB₂, mixer, THz, electron-phonon interaction.

I. INTRODUCTION

Superconducting hot-electron bolometer mixers have been under intensive investigation after early publications in 1990th [1, 2]. Due to fast electron temperature relaxation rate the resistance modulation in some superconducting films can be done up to GHz range without responsivity degradation. In clean films ($ql > 1$, where q is the phonon wavelength, and l is the electron mean free path), where electron diffusion coefficient D_e is large the electron temperature relaxation occurs via electron diffusion from the bolometer to the contact pads. Here, if bolometer is shorter than the electron diffusion length $\sim (D_e \tau)^{0.5}$, where τ is the time of electron inelastic scattering, which at LHe temperatures occurs mostly on the phonons, τ_{e-ph} , the bolometer response time is proportional to the bolometer length. E.g. for Nb, $(D_e \tau_{e-ph})^{0.5} \sim 1 \mu\text{m}$. It provides the mixer gain bandwidth of the order of 6 GHz [3]. Besides the bolometer length limitation the quality of the superconductor-normal metal contact has to be very good in order to achieve good electron transmission. Electron-phonon interaction time in Nb films is of the order of 1 ns [4]. On contrary, in superconducting films with much shorter electron-phonon interaction time (e.g. in NbN $\tau_{e-ph} \approx 10\text{ps}$ at 10 K [5]) the electrons scatter on phonons prior they get a chance to diffuse to the contact pads. In this case the phonons serve as the heat sink. If the phonon heat capacitance is not much higher than the electron heat capacitance, the phonon escape time τ_{esc} from the film to the substrate becomes important. A number of radioastronomical instruments have been equipped with such thin film NbN HEB mixers: HIFI 1.4-1.9 THz band (Herschel Space observatory); TELIS, SOFIA, Receiver Lab Telescope in Chile (SAO), APEX. A DSB noise temperature of about 450 K has been achieved for 500-700 GHz, 700 K at

1.6THz and 1100 K at 2.5 THz [6, 7, 8], 6400 K at 5.2 THz [9]. NbN films technology is able to provide films as thin as 3 nm with T_c about 9K. Currently, the bottle-neck of the hot electrons' relaxation process is the phonon escape from the NbN film into the substrate. The mixer gain bandwidth of about 2 GHz for the NbN HEB mixers on crystalline quartz [10], 4.5 GHz on MgO [11], 3.5 GHz on Si [12]. During the past years there was a continuous search for new materials. For example, Al, Ta, NbTiN, YBaCuO films have been tried. In this paper we report on successful implementation of THz bolometric mixers made of thin superconducting MgB₂ films.

A. DC characterization of MgB₂ microbridges.

The MgB₂ bolometers were lithographically made as $2 \times 1 \mu\text{m}^2$ bridges in a feed point of a planar spiral antenna [8]. The nominal film thickness is 20 nm with a T_c of about 25 K. The normal state resistivity of thicker MgB₂ films has been quoted to be in the range from 4-8 $\mu\text{Ohm}\cdot\text{cm}$ [13,14] (which is factor of 5 higher than normal state resistivity of bulk samples [15]) to 20-80 $\mu\text{Ohm}\cdot\text{cm}$ [16]. The RF resistivity in MgB₂ films is defined by the π -band ($2\Delta = kT_c = 1.7 \text{ meV}$). At 1.6THz the photon energy is 6meV.

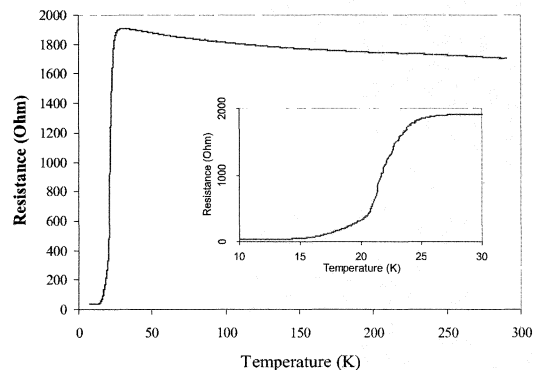


Fig. 1. Resistance versus temperature dependence for the MgB₂ mixer. The inset shows a close-up of the superconducting transition.

Therefore bolometer RF impedance at 1.6THz equals the normal resistance. The resistance of the MgB₂ microbridge versus temperature is shown in Fig. 1 (the inset zooms into the superconducting transition region). The transition is rather broad, ~4K with the middle of the transition at about 22 K. The broad superconducting transition and the long low temperature tail are probably due to the film non-

Manuscript received May 15, 2006. The authors are with the Department of Microtechnology and Nanoscience, MC2, Chalmers University of Technology, SE-412 96, Gothenburg, Sweden.
(Corresponding author: S.Cherednichenko, e-mail: serguei.cherednichenko@mc2.chalmers.se).

homogeneity.

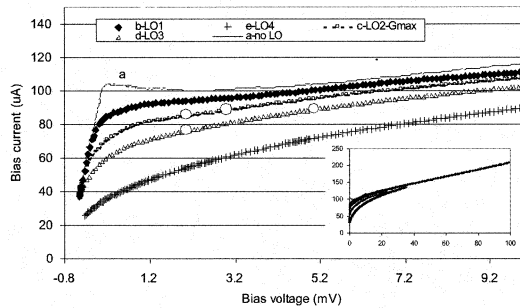


Fig. 2. Current- voltage (IV) curves of the MgB_2 mixer at 4.2 K bath temperature: without LO power (a) and with LO power applied (b-e). The maximum mixer gain was obtained for IV -c. The zero current corresponds to -0.8mV which is due to the thermal voltage on the bias lines. The curves are obtained with a bias voltage source. The inset shows the IV 's on a larger scale.

The current -voltage (IV) characteristic at 4.2 K is shown in Fig. 2 (curve a) as obtained with a bias voltage source. The residual resistance is about 8 Ohm which corresponds to the value from the $R(T)$ curve (Fig. 1). The critical current I_c is 105 μ A, what for the given film dimensions results in the critical current density $j_c=2.6 \cdot 10^5$ A/cm². Application of the THz Local Oscillator (LO) source (either at 0.6 THz or 1.6 THz) easily suppresses the critical current (Fig. 2, curves b-e). The dc resistance (U_0/I_0) on all bias points from Fig. 2 does not exceed 120 Ohm, which corresponds to the low temperature tail of the $R(T)$ -curve. The maximum RF responsivity (recorded during the gain bandwidth measurements at 0.6 THz) corresponds to the IV -c and therefore does not coincide with the maximum dR/dT .

B. MgB_2 mixer gain bandwidth.

The time constant τ of the MgB_2 bolometer as a mixer was measured by mixing two 0.6 THz backward wave oscillators (BWO). One BWO was used as an LO while the other served as a signal source. The mixer chip was mounted on an elliptical silicon lens. The mixer unit was mounted on the cold plate of a LHe optical cryostat (4.2 K bath temperature). The IF output from the mixer unit was sent out of the cryostat to two broadband (0.1-12 GHz) room temperature amplifiers. Both IF frequency and IF power were measured with a broadband spectrum analyzer. In order to improve mixer matching to (rather long) IF line a 3dB attenuator was connected to the mixer unit output (in the cryostat) and another attenuator was connected to the IF output from the cryostat. The signal BWO power was much lower than the LO BWO power, and its frequency was constant during the measurements. First, the IF response was measured at the IF of about 0.5 GHz and the IV -curve (LO power) corresponding to the maximum IF response was found. During the mixer response measurements versus IF the LO BWO was frequency tuned while its power (as well as the mixer bias voltage) was kept constant. The bias points where the mixer response vs IF was measured are shown in Fig. 2 with circles. The

experimental curves can be approximated with a single-pole Lorentzian $G(f)/[1+(2\pi f_i \tau)^2]$, where $G(f)$ is the IF response at zero frequency. For mixers it is more convenient to operate with a 3dB gain rol-off frequency $f_{3dB}=1/(2\pi\tau)$ which determines the mixer gain bandwidth. The maximum IF responses was observed at the LO power corresponding to the IV -c at the bias voltage 2-3 mV. At these points (2 mV, 84 μ A; and 3 mV, 87 μ A) the mixer gain bandwidth is 2.3-2.5 GHz (Fig. 3). For higher LO power (2 mV, 77 μ A) and for higher bias voltage (5mV, 90 μ A) the gain bandwidth increases to correspondingly 3 GHz and 6 GHz.

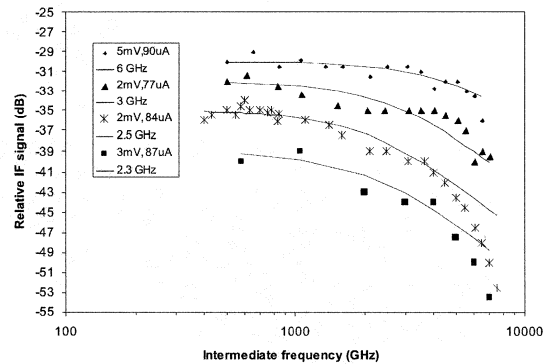


Fig. 3. Intermediate frequency response of the MgB_2 mixer at two different LO power levels and different bias voltages. The LO frequency is 600 GHz.

C. Mixer noise temperature.

The MgB_2 mixer noise temperature was measured at 1.63 THz LO frequency. An optically pumped FIR laser was used as the LO source. A 2-4.5 GHz low noise amplifier (LNA) with the noise temperature of 2 K and the gain of 32 dB was mounted on the LHe cryostat cold plate, next to the mixer unit. At room temperature the IF chain consisted of 58 dB extra amplification, 1-9 GHz tunable Yig-filter (50 MHz instantaneous bandwidth), and a low noise power meter. In the optical path, two Zitex (250 μ m thick) IR filters were installed on the 4.2K and 77K cryostat shields. The cryostat window was sealed with a 1 mm Teflon slab. The system noise temperature was obtained by measuring the Y-factor at each IF frequency by chopping the 300K/77K RF input load. The calibration signal was combined with the LO beam with a Milar beam splitter. The mixer noise temperature T_m was then calculated by taking into account the known RF losses in the air, cryostat window and the IR filters. Finally, the T_m was corrected for the reflection between the mixer and the antenna which is caused by the impedance mismatch: $R=(Z_{ant}-Z_m)^2/(Z_{ant}+Z_m)^2$, where $Z_{ant}=100$ Ohm is the calculated antenna impedance, and Z_m is the MgB_2 mixer normal state resistance (≈ 2000 K). It results in $R=0.18$, i.e. about 7.5 dB. The resulting mixer double sideband noise temperature is shown in Fig. 4. The ripples are caused by a standing wave in the IF line between the mixer and the LNA since no isolator was used.

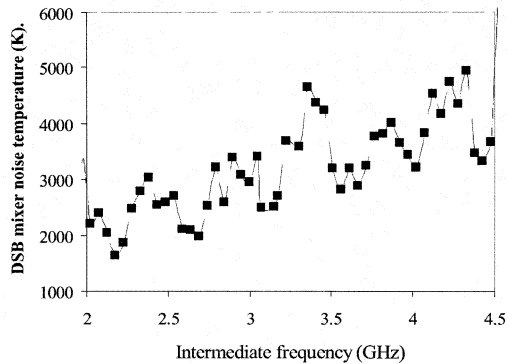


Fig. 4. Double sideband mixer noise temperature corrected for the bolometer-antenna mismatch (7.5 dB) as a function of the intermediate frequency (50 MHz instantaneous bandwidth).

II. CONCLUSION.

The gain bandwidth of 2.5 GHz obtained with the MgB_2 bolometers is an order of magnitude larger than for any type of superconducting bolometric mixers at the given film thickness (20 nm). An electron-phonon time constant in MgB_2 films \sim ps has been already reported [17]. However, in order to interpret our results a complete two temperature model [18] has to be applied which we will do in another paper. Dynamic resistance (dV/dI) at the maximum gain bias points is of the order of 300 Ohm, which is much higher than the IF line impedance (50 Ohm). This results in 3dB IF loss. Furthermore, it causes the observed IF ripples seen in Fig. 4.

Acknowledgements.

The authors are grateful to Prof. M.Naito and Dr. K.Ueda (NTT Basic Research Laboratories) for providing the MgB_2 films.

REFERENCES:

- 1 E.M. Gershenson, G.N. Gol'tsman, I.G. Gogidze, Y.P.Gousev, A.I. Elant'ev, B.S. Karasik, and A.D. Semenov, *Sov. Phys. Superconductivity*, **3**(10), 1582, 1990
- 2 D.E. Prober, *Appl. Phys. Lett.* **62**, 2119 (1993)
- 3 P.J.Burke, et al, *Appl.Phys.Lett.*, **68**, 3344 (1996).
- 4 E.M.Gershenson, M.E.Gershenson, G.N.Gol'tsman, A.M.Lyul'kin, A.D.Semenov, and A.V.Sergeev, *Sov.Phys.JETP* **70**(3), 505, (1990)
- 5 Y. Gousev, G. Goltzman, A. Semenov, and E. Gershenson, *J. Appl. Phys.*, **75**, 3695 (1994).
- 6 S. Cherednichenko, M. Kroug, P. Khosropanah, A. Adam, H. Merkel, E. Kollberg, D.Loudkov, B. Voronov, G. Gol'tsman, H.-W. Huebers, H. Richter, *Physica C*, vol.372.pp.427-431, Aug. 2002.
- 7 J.Kawamura, R.Blundell, C.E.Tong, G.Gol'tsman, E.Gershenson, B.Voronov and S.Cherednichenko *Applied Physics Letters*, **70**(12), pp.1619-1621, 24 March,1997.
- 8 M.Kroug, S.Cherednichenko, H.Merkel, E.Kollberg, B.Voronov, G.Gol'tsman H.-W.Huebers, H.Richter, *IEEE Trans. on Appl. Supercond.* Vol.11, n.11, pp. 962-965, 2001
- 9 H.-W. Hübers, A. Semenov, H. Richter, M. Schwarz, B. Günther, K. Smirnov, G. Gol'tsman, and B. Voronov, in: *Millimeter and Submillimeter Detectors for Astronomy II*, J. Zmuidzinas, W. S. Holland, and S. Withington, eds., *Proc. SPIE* **5498**, pp. 579-586, 2004.
- 10 J.Kawamura, R.Blundell, C.-Y.E.Tong, G.Gol'tsman, E.Gershenson, B.Voronov, and S.Cherednichenko, *Appl.Phys.Lett.* **70**, 1619 (1997).
- 11 S.Cherednichenko, M. Kroug, P.Yagoubov, H. Merkel, E. Kollberg, K.S. Yngvesson, B. Voronov and G. Gol'tsman, *Proc. 11th Intl. Symp. Space Terahertz Technol.*, 219, (2000), Ann Arbor, MI, USA.
- 12 H.Ekström, E.Kollberg, P.Yagoubov, G. Gol'tsman, E. Gershenson, and K.S. Yngvesson, *Appl. Phys. Lett.* **70**, 3296 (1997).
- 13 R.A.Kaindl, M.A.Carnahan, J.Orenstein, D.S.Chemla, H.M.Christen, H.-Y.Zhai, M.Paranthaman, and D.H.Lowndes, *Phys.Rev.Lett.*, **88**, 027003-1 (2002).
- 14 B.B.Jin, P.Kuzel, F.Kadlec, T.Dahm, J.M.Redwing, A.V.Pogrebnyakov, X.X.Xi, and M.Klein, *Appl. Phys.Lett.*, **87**, 092593 (2005).
- 15 T.Masui, and S.Tajima, *Physica C*, **385**, 91 (2003).
- 16 K.Ueda, and M.Naito, *Appl.Phys.Lett.*, **79**, 2046 (2001).
- 17 Y.Xu, et al, *Phys.Rev.Lett.*, **91**, 197004 (2003).
- 18 N.Perrin and C.Vanneste, *Phys. Rev.B.*, **28**, 5150 (1983).

Twodimensionally distributed Model for HEB based on Random Phase Transitions

Harald F. Merkel, Biddut K. Banik, Vladimir Drakinskiy^a

^aChalmers University of Technology

ABSTRACT

According to AFM measurements, ultrathin NbN films are not smooth but exhibit a more or less random distribution of microcrystallites. This gives rise to a superconducting to normal conducting phase transition that follows a first order percolation phase transition. Such a phase transition is easily described by a single critical exponent justifying the assumption of a simple, local $R(T)$ curve used in all distributed HEB models.

Keywords: percolation phase transition, hot electron bolometer, mixing theory, mixing

1. INTRODUCTION

HEB age as a function of film thickness. Due to the random nature of the sputtering process, NbN is deposited in a random manner (c.f. Fig. 1).

Exposing this film to aggressive reactants will remove atom for atom of the film. Keeping in mind, that only close stoichiometric $NbN_{0.92...1.08}$ will exhibit superconductivity at elevated temperatures, it becomes clear that any replacement of NbN by NbO locally will change the properties of the NbN film. Any attack will be associated with a reduction of the conduction properties of the film and lead to an increase of the resistivity of the film. For very thin films (as in the case for heterodyne receiver devices with a thickness of merely $3.5\mu m..5.5\mu m$) any individual attack will cause substantial deviations of the conduction pattern. In this paper we will first refer to a model for the random attack of a random thick conducting structure. One arrives at a resistance versus attack curve essentially describing the aging process of a HEB device. This curve is not sufficient to describe the superconducting properties of the film. So therefore the superconducting and super-to-normal conducting properties of the attacked NbN structure are taken into account to calculate the $R(T)$ curve for a specific attack state.

It becomes obvious that the critical current of the film scales differently on the conductivity reduction due to oxidization than the room temperature conductivity. Therefore a local critical current and critical temperature

Chalmers University of Technology, MC2, Kemigården 9, SE 412 96 Göteborg, Sweden

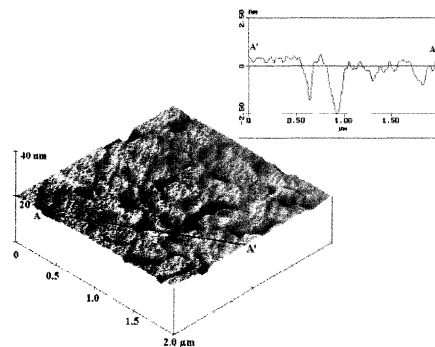


Figure 1. Atomic Force Microscopic cross section of a NbN film used for HEB production The inset shows the height curve along the line A A' in the 2D plot.

distribution is calculated and the two-dimensional current distribution is obtained in a way similar to a Bean model for the superconductor. Superconductivity breaks down as soon as the local distribution of the given bias current exceeds the maximum available critical current density along the most current bearing link in between the antennas. The so-obtained $R(T)$ curve still does not account for local heating phenomena. In a third step the two-dimensional resistance structure is used to calculate a two dimensional temperature distribution by taking the local LO and bias heating powers into account. From this a nonequilibrium resistive transition is obtained that is inherently different from the equilibrium (non-heated) transition used in the $R(T)$ curve. Based on the nonequilibrium heating properties, IV curves are calculated. In a fourth step, these nonequilibrium heating curves are used in a small signal model: The small signal model describes the current and power distribution in the HEB as a function of a (dominant) heating and a (small) beating term at the intermediate frequency. There local hot spots are generated wherever the local heating power density is sufficient to exceed the critical temperature at the (self consistently) obtained local critical current density. Classical expressions as conversion gain, quantum noise, thermal fluctuation noise and thermal noise can be derived from the small signal model. Nevertheless, the journey is not finished here: Creating hot spots in this random structure occurs almost instantaneously (at the time required to expel the magnetic fields from a previously superconducting area). The hot spot model here is no longer limited to a single normal conducting area but normal conducting random islands are created in regions where the heating conditions for local superconducting breakdown are fulfilled. Having created a hot spot, the delivered heating power is used much more efficiently than in the superconducting case due to local Andreev reflection boundaries. Therefore the film will exhibit local hysteresis (clearly seen in underpumped IV curves on HEB). In addition this hysteretic behavior explains part of the $1/f$ noise seen in HEB receivers. Small spontaneous fluctuations create an isolated hot spot that then takes arbitrarily long time to decay.

2. LUMPED CIRCUIT EQUIVALENT OF A NBN FILM

The HEB and its adjacent antenna pads are discretized using resistors in a 2D cartesian mesh. The local conductivity averaged over a discretization area is directly translated in a resistance value for this discrete element. For the antenna pads, the resistance of the film plus the Au cover resistance is taken into account. For the HEB film, the resistivity depends on the number of intact NbN molecules per area element. Discretizing the number of available NbN molecular layers, one ends up with a two dimensional resistance mesh containing all local properties of the element. Therefore, for each node point $[i : j]$ on the mesh, one has to solve Kirchhoff's law requiring the continuity of currents:

$$I_{source,i,j} - I_{ground,i-1,j} = I_{X,i,j} + I_{Y,i,j} - I_{Y,i,j-1} - I_{X,i-1,j} \quad (1)$$

There $I_{source,i,j}$ is the current injected at the node $[i, j]$ (mostly zero expect at the outer terminals), $I_{ground,i,j}$ is a current flowing from the node directly to ground (set zero here) and I_X (I_Y) denotes the current in X(Y) coordinate direction through the resistor "to the right of" (respectively "above") the node. The resistors are grouped in R_X (R_Y) being "horizontally" ("vertically") oriented and the indices i (j) runs in X(Y) coordinate direction (c.f. 2). In this part of the analysis $Y_{G,i,j} = 0$.

Relating the potentials of the neighboring nodes, one has to set up Ohm's Law for all resistors in the net allowing to eliminate the unknown currents from the above Equation system. One arrives in a linear set of Equations with the nodal potentials $\phi_{i,j}$ as unknown variables.

$$I_{X,i,j} = Y_{X,i,j} \cdot (\phi_{i,j} - \phi_{i+1,j}) \quad (2)$$

$$I_{Y,i,j} = Y_{Y,i,j} \cdot (\phi_{i,j+1} - \phi_{i,j}) \quad (3)$$

$$I_{ground,i,j} = Y_{G,i,j} \cdot (\phi_{i,j}) \quad (4)$$

This complete lumped element equivalent has no unique solution. It is nevertheless uniquely specified up to an arbitrary additive constant to all potentials. Therefore setting one arbitrary potential to zero, there is always exactly an unique solution (supposed the resistors are nonzero and finite).

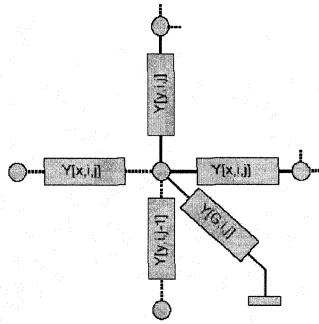


Figure 2. Lumped Element Mesh used to model the HEB circuit.

3. HEB AGING AS A RANDOM DESTRUCTION PROCESS

Aging is modeled starting with a film with a given thickness distribution: One sets all pad resistors to their (constant) values and the conductors on the NbN film are obtained using

$$Y_{X,i,j} = \frac{n[1, i, j]}{N_0} \cdot Y_{0X,i,j} \quad (5)$$

$$Y_{Y,i,j} = \frac{n[2, i, j]}{N_0} \cdot Y_{0Y,i,j} \quad (6)$$

where the "zero values" $Y_{0...}$ are taken from sheet resistance measurements. Assuming a certain number of atomic layers to be present in the film (e.g. $N = 5$ for a 35\AA thick film), the initial state matrix is set $n[... , i, j] = N$. Now random coordinates are calculated and to each random coordinate pair, the amount of intact layers is reduced by 1 until 0 is reached. During this Monte-Carlo like process ⁽¹⁾, the currents and voltages through the HEB structure can be calculated at any aging state. Instead of a time axis the number of successful oxidizing attacks is used. Obviously, providing water free environments and applying protection layers on the film will affect the scaling law relating the absolute number of attacks to the number of attacks per time unit and provides therefore a time axis in "storage time under given conditions" to the aging analysis. The scaling law to be used contains the temperature and moisture of the environment in the easiest possible way and models the applied protection layers simply as linear reduction factors of the oxidization attacks. One arrives at a relation where $\alpha \approx 0.1 \ln 2 \frac{1}{K}$ according to the thermodynamics of a binary process, a fit parameter $\beta \approx 1.2 \frac{1}{h}$ and the values for the protection layers are found in Table 1 :

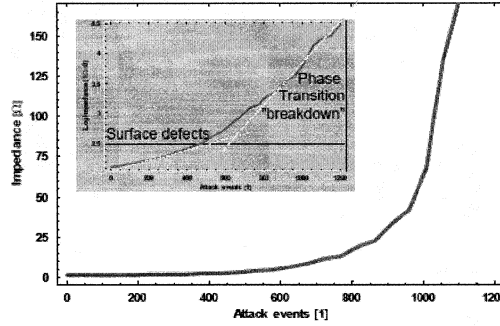
$$\eta = \frac{\#attacks}{time} = \beta \cdot r_{protection} \cdot c_{H_2O} \cdot e^{\alpha T} \quad (7)$$

From aging experiments comparing a set of protection layer technologies with each other, one finds delay factors summarized in the following Table 1.

Typical developments of the resistance versus number of attacks are shown in Figure 3. It is necessary to repeat the Monte Carlo process several times to arrive at a statistically relevant base for the development of the resistance with time. It is obvious, that this statistic nature of aging is also reflected in a spread in the measured resistance values in aging experiments. The following data refers therefore to mean values obtained by running a vast number of independent Monte Carlo simulations on the same geometry.

Table 1. Protection factors for a set of protection layer technologies

Protection Layer	r [1]	Comments
Photoresist	1.00	Reference case
SiO_2	1.90	
Si	3.1	
$Si + Si$	4	Worst Case
$Si + Si$	11	10 devices
$SiO_2 + SiN$	13	

**Figure 3.** Average room temperature resistance as a function of successful attacks for 100 individual random model runs.

4. A TWO DIMENSIONAL HEATING MODEL

Using a similar approach to model the RF performance of the HEB, we note that, the HEB chip is electrically small compared to a THz wavelength. Therefore the purely resistive electrical equivalent described in the above is still valid.

Knowing the evolution of the room temperature resistance, it is a straightforward extension to include superconducting effects in the model: One assigns a critical temperature and a critical current density to the film that is at first hand linear in the amount of still available molecular layers. Then the local resistance is either zero (when neither critical current and critical temperature are exceeded locally) or it is a normal resistor with the value given by the remaining thickness.

Obviously we have to calculate the temperature in each resistor of the equivalent lumped element circuit. For the first point, we know the current and voltages in each node and in each resistor allowing us directly to calculate the dc heating power locally. In addition, we know the absorbed THz signal power (being either uniformly in space or restricted to the normal conducting areas when not exceeding the quasiparticle bandgap). The only missing link is to relate the electron temperature in the resistor to the applied heating powers. Discretizing the heat balance equation ⁽²⁾ in two dimensions one arrives at a thermal equivalent mesh - the thermal resistors "to ground" contain the phonon cooling process and the resistors linking the neighboring sections of the film contain the diffusion cooling process. For the phonon cooling one obtains:

$$T(P) = Y_0 + Y_{phonon} \cdot P + \dots = \left(T_0^\mu + \frac{P_{lo}}{\sigma}\right)^{\frac{1}{\mu}} + \frac{\left(T_0^\mu + \frac{P_{LO}}{\sigma}\right)^{-1 + \frac{1}{\mu}} P}{\mu \sigma} + \left(\frac{\left(T_0^\mu + \frac{P_{LO}}{\sigma}\right)^{-2 + \frac{1}{\mu}}}{2 \mu^2 \sigma^2} - \frac{\left(T_0^\mu + \frac{P_{LO}}{\sigma}\right)^{-2 + \frac{1}{\mu}}}{2 \mu \sigma^2}\right) P^2 \quad (8)$$

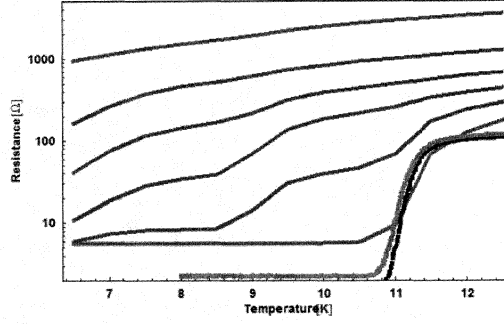


Figure 4. R(T) Curve for the TERASEC mixer chip (pixels 17 and 15 selected)

Please keep in mind that the node indices $[\tilde{i}, \tilde{j}]$ are indices referring to each resistor and are related to the voltage node indices by $[\tilde{i}, \tilde{j}] = [i + \frac{1}{2}, j]$ for a horizontal (X) thermal resistor and $[\tilde{i}, \tilde{j}] = [i, j + \frac{1}{2}]$ for a vertical (Y) thermal resistor. Now the heat flow from and to each node ψ_{\dots} are related to the electron temperature T by:

$$\psi_{X,\tilde{i},\tilde{j}} = Y_{thermal,X,\tilde{i},\tilde{j}}(T) \cdot (T_{\tilde{i},\tilde{j}} - T_{\tilde{i}+1,\tilde{j}}) \quad (9)$$

$$\psi_{Y,\tilde{i},\tilde{j}} = Y_{thermal,Y,\tilde{i},\tilde{j}}(T) \cdot (T_{\tilde{i},\tilde{j}+1} - T_{\tilde{i},\tilde{j}}) \quad (10)$$

$$\psi_{ground,\tilde{i},\tilde{j}} = Y_{phonon,\tilde{i},\tilde{j}}(T) \cdot (T_{\tilde{i},\tilde{j}}) \quad (11)$$

Using this equivalent, the temperature distribution in the HEB is obtained by solving the above linear equation system.

For each temperature calculation we have to run a set of steps: 1: calculate the random reduced amount of superconducting layers for the given HEB assuming a electron temperature to be equal to the bath temperature (e.g. 4.2K) to all resistors, 2: Find out, which resistors are superconducting and which resistors are normal conductors by comparing temperature and currents with the critical temperature and critical currents. 3: Calculate the voltages and currents on this structure. 4: Calculate the DC and LO powers present in each resistor in the structure. 5: Calculate the electron temperature distribution on the "dual grid". 6: Return to point 2 and repeat the loop until a fixed point is reached.

Performing this process, R(T)- curves (c.f. Fig 4)are readily obtained by setting a very low measurement current (e.g. $1\mu A$) and varying the bath temperature within the desired area.

Specifying a set of bath temperatures, IV curves are shown in Fig. 5.

5. A SMALL SIGNAL MODEL FOR HEB

For a small signal equivalent, the electric model is largely unchanged with the exception of a modified bias circuitry coupling the current sources to an inductor and coupling a 50Ω load (the IF amplifier) to the bias supply using a dc block capacitor. All this is easily accomplished within the 2D lumped element approach described below.

A more fundamental difference is found in the thermal equivalent. For the thermal equivalent, we have to take into account that the phonon cooling to the substrate is a reaction speed limiting bottleneck. Therefore the conductor to ground $Y_{phonon,\tilde{i},\tilde{j}}$ takes the form of a first order low pass RC circuit.

$$T_{\tilde{i},\tilde{j}} = Y_0 + Y_{phonon} \cdot P = \left(T_0^\mu + \frac{P_{lo}}{\sigma} \right)^{\frac{1}{\mu}} + \mu \sigma \cdot \frac{(T_0^\mu + \frac{P_{lo}}{\sigma})^{-1 + \frac{1}{\mu}}}{1 + i \cdot \tau_{phonon} \omega_{IF}} \cdot P \quad (12)$$

From the power dissipated in the load resistor, the conversion gain of the HEB is readily obtained.

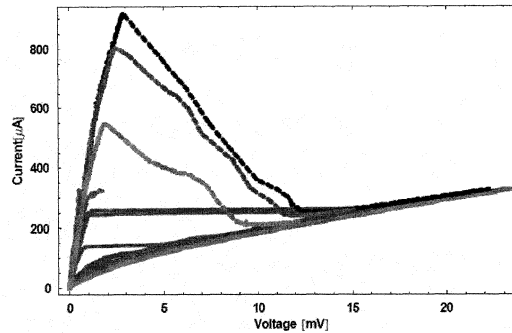


Figure 5. IV Curve for the TERASEC mixer chip (pixels 15 and 17 selected) at 4K, 6K and 8K measured and calculated using LO powers from $0nW$ to $1500nW$

6. 1/F NOISE AND SWITCHING BEHAVIOR IN HEB

For low heating powers, one observes that the conversion gain diverges. This is caused by instability of the HEB and to the failure of any small signal equivalent there. It is found by performing the iterative solution steps from Section 4, that for low LO powers, the obtained point on the IV curve does not converge to a single value but "jumps" between a set of values in a more or less periodic manner. This instability is caused by the fact that a newly formed hot spot (in one iteration) can be easily bypassed as long as there is still a more conductive superconducting link on the device eventually removing heating power from the normal conductor. In the next iteration step, the region is again superconducting and the process starts anew. The real time dependence of this process is determined by the inductive load on the bias supply and on cable lengths and cable position in the cryostat. Frequencies between $30kHz$ and $2MHz$ have been observed experimentally by moving one and the same device between two measurement setups. The switching regime begins as soon as the first resistor in the HEB sees superconductivity suppressed. This switching regime ends upon more pumping or more heating when the heating power loss in the normal conducting areas (due to bypassing) is equalled by the more efficient usage of heating power (due to the upcoming Andreev barrier around the hot spot). For hard pumping, the possibility and efficiency of bypassing shrinks (due to an overall warming of the HEB) therefore reducing the instable area and there is a pumping level where instability is suppressed completely.

REFERENCES

1. N. Metropolis and S. Ulam, "The monte carlo method," *J. Am. Stat. Ass.* **44** (247), pp. 335–341, 1949.
2. H. Merkel, "A hot spot model for hot electron bolometer mixers," *Proceedings of the 16.th International Symposium on Space Terahertz Technology, Goteborg*.

ORAL SESSION n°6

« Sources »

Thursday 11 May 16:30-18:00

Chaired by :

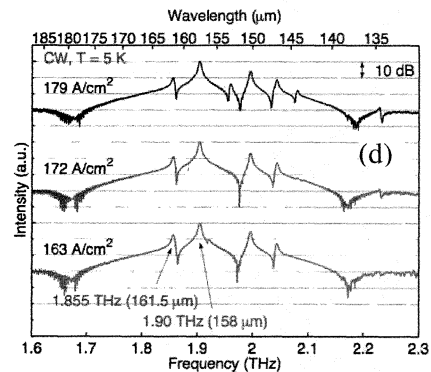
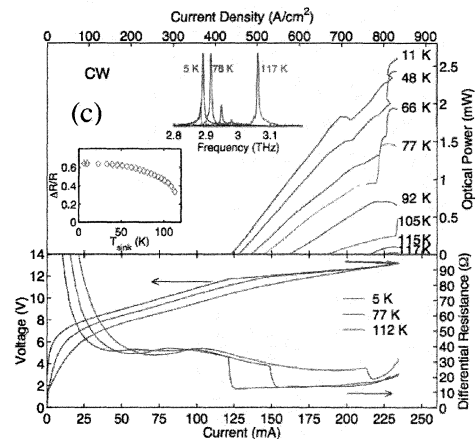
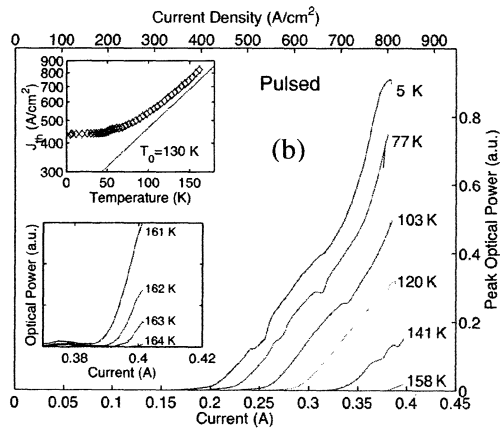
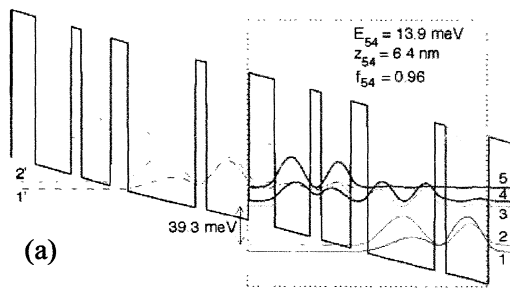
Dr. Thomas Crowe & Dr. Didier Lippens

Terahertz quantum-cascade lasers as local oscillators

Qing Hu

Massachusetts Institute of Technology, Cambridge MA 02139

The main challenge for the space THz program is solid-state local oscillators that can meet space qualifications in terms of output power levels and power efficiencies. Semiconductor electronic devices (such as frequency multipliers) are limited by the conversion efficiency and RC roll-off to below 2 THz. Conventional semiconductor photonic devices (such as bipolar laser diodes) are limited to above 10 THz even using small-gap lead-salt materials. Transitions between subbands in semiconductor quantum wells were suggested as a method to generate long wavelength radiation at customizable frequencies. The recently developed quantum-cascade lasers (QCL) at THz hold great promise to bridge the so-called "THz gap" between conventional electronic and photonic devices, especially for local-oscillator applications. Based on two novel features, namely resonant-phonon-assisted depopulation (Fig. 1(a)) and metal-metal waveguides for mode confinement, we have developed many THz QCLs with record performance. They include by not limited to: a maximum pulsed operating temperature of 164 K (Fig. 1(b)), a maximum cw operating temperature of 117 K (Fig. 1(c)), and the longest wavelength ($\sim 160 \mu\text{m}$, 1.9 THz) QCL to date without the assistance of magnetic fields (Fig. 1(d)), and more than 100 mW of cw power. Our collaborators have demonstrated the use of QCL as a local oscillator at 2.8 THz, and have achieved frequency/phase locking at ~ 3 THz. We will present more details and perspective at the symposium.



Phase-locking and Linewidths of a Two-color THz Quantum Cascade Laser

J.N. Hovenier*, A. Baryshev^{†‡}, A.J.L. Adam*, I. Kašalynas*, J.R. Gao[†], T.O. Klaassen*, B.S. Williams[§],
S. Kumar[§], Q. Hu[§], J. L. Reno[¶]

*Kavli Institute of NanoScience, Delft University of Technology, Delft, The Netherlands

[†]SRON Netherlands Institute for Space Research, Groningen/Utrecht, The Netherlands

[‡]Kapteyn Astronomical Institute, Groningen, The Netherlands

[§]Department of Electrical Engineering and Computer Science and Research Laboratory of Electronics,
Massachusetts Institute of Technology, Cambridge, U.S.A.

[¶]Sandia National Laboratories, Albuquerque, U.S.A.

Abstract— We report the phase stabilization and spectral linewidth of a 2.7 THz quantum cascade laser by heterodyning its two nearby lateral mode lasing lines using a superconducting NbN bolometer mixer. The beat signal at about 8 GHz is compared with a microwave reference by applying a conventional phase lock loop circuitry with a feedback to the laser bias current. Phase locking has been for the first time demonstrated, resulting in an extremely narrow beat linewidth of less than 10 Hz (limited by the resolution bandwidth of the spectrum analyzer). Moreover, our result demonstrates the feasibility of phase-lock of the THz signal itself. Under frequency-stabilization conditions we are able to study the emission spectrum of a THz QCL in a systematic way, which previously was impossible. We find that the line profile is virtually Lorentzian with a long-term minimum linewidth of the THz modes of about 6.3 kHz. Temperature dependent measurements suggest that this linewidth does not approach the Schawlow-Townes limit.

I. INTRODUCTION

Significant progress has made quantum cascade lasers (QCLs) promising coherent solid-state THz sources for various applications in spectroscopy, sensing, and imaging. As demonstrated at several frequencies, a THz QCL can be used as a local oscillator (LO) for a heterodyne receiver [2], [3] which is a crucial instrument for astronomical and atmospheric high-resolution spectroscopy. For those applications a narrow emission linewidth of a QCL under frequency stabilization is essential. In the case of a heterodyne space interferometer [4], phase locking to an external reference is also required. Ideally, phase locking of the THz QCL would take place with respect to a harmonic of a microwave reference signal; however it has not yet been demonstrated.

Recent work has demonstrated frequency locking of a QCL to a far-infrared (FIR) gas laser line at 3.105 THz [6]. This same work demonstrated a lasing linewidth of 65 kHz, which could be maintained indefinitely as a result of the frequency stabilization. The linewidths of QCLs that were reported earlier than ref. [6] could be measured only for a short sweep time of ~ 3 ms. They were measured using a room-temperature Schottky-diode to mix signals from a THz QCL and a FIR gas laser [7], two THz QCLs [8] or two longitudinal emission modes of a single QCL [3]. Linewidths as small as 20 kHz were observed [8]. When averaged for a longer time period

however, the linewidths in those experiments could exceed 10 MHz due to fluctuations of temperature and bias current, which affect the refractive index of the laser gain medium.

Here we report the first demonstration of phase locking of the beat signal of a two lateral-mode THz QCL to a microwave reference. Under frequency stabilization conditions, we are able to study the emission spectrum of the THz QCL as a function of the laser power, in order to investigate the nature of the limit to its linewidth.

II. QCL DESIGN

We use a THz QCL based on the resonant phonon design [9] also shown in figure 1. The active region contains 176 GaAs/Al_{0.15}Ga_{0.85}As quantum-well modules, with a total thickness of 10 μm . The cavity of the QCL is a double-sided metal waveguide, which is 40 μm -wide and 1 mm-long. In order to facilitate the experiment described in this article, we selected a laser with two closely spaced lasing modes. When operated in a CW mode at a heat-sink temperature of below 15 K, the emission spectrum measured by a Fourier-transform spectrometer (FTS) shows two lines at 2.742 THz and 2.749 THz, respectively. They correspond to two different order lateral modes of the cavity that are lasing with unequal intensities, but with a total maximum lasing output power of roughly 1 mW/facet. Their intensities and frequencies depend on the bias current of the QCL and the heat-sink temperature. Frequency tuning via the current bias is expected to be almost completely due to thermal effects as a result of ohmic heating. Because both modes have large confinement factors with the active region (close to unity), they should largely experience the same thermal environment. However, each lateral mode has a slightly different modal overlap since higher-order modes will extend further into free space and will have lower effective refractive indices η_{eff} . As a result, η_{eff} of each mode will have a different dependence on the refractive index of the active region. Hence each mode will have a different temperature or current dependence, which is the basis why the beat of the QCL should behave as a current controlled oscillator.

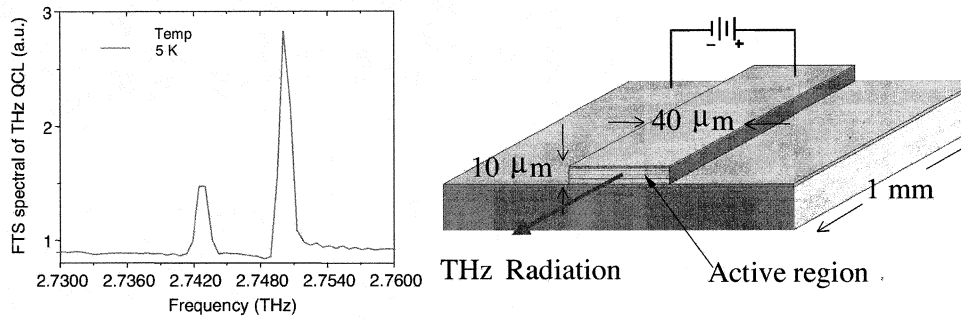


Fig. 1. FTS spectrum of two moded QCL (to the left) and layout of QCL chip (to the right).

III. EXPERIMENTAL SET-UP

To obtain the beat signal of the QCL, we use a spiral antenna coupled NbN hot electron bolometer (HEB) mixer, which is similar to those described in Ref. [5]. It works at liquid helium (L-He) temperature and requires less than 300 nW LO power. Although the 3-dB intermediate frequency (IF) noise-bandwidth of the mixer is only about 6 GHz, its sensitivity at the beat frequency (~8 GHz) of the present experiment is still much better than that of Schottky mixers. Figure 2 shows a schematic diagram of our measurement setup. The QCL is mounted in a L-He flow cryostat, while the HEB mixer is mounted in a separate vacuum-cryostat. The output beam

of the QCL is focused onto the quasi-optically coupled HEB mixer. The IF (beat) output is first amplified by a cryogenic MMIC IF amplifier of 0.1-12 GHz, then by a room temperature amplifier. Finally it is fed into an EIP 575 source-locking microwave counter. The phase error correction voltage of this counter is fed back into the DC bias-current circuit of the QCL through a variable feedback resistor. To monitor the IF spectrum, a fraction of the beat signal is coupled into a spectrum analyzer. Both spectrum analyzer and EIP 575 are phase locked to the same microwave frequency reference signal. The maximum loop bandwidth allowed by the EIP 575 counter is 10 kHz. This bandwidth can be reduced by

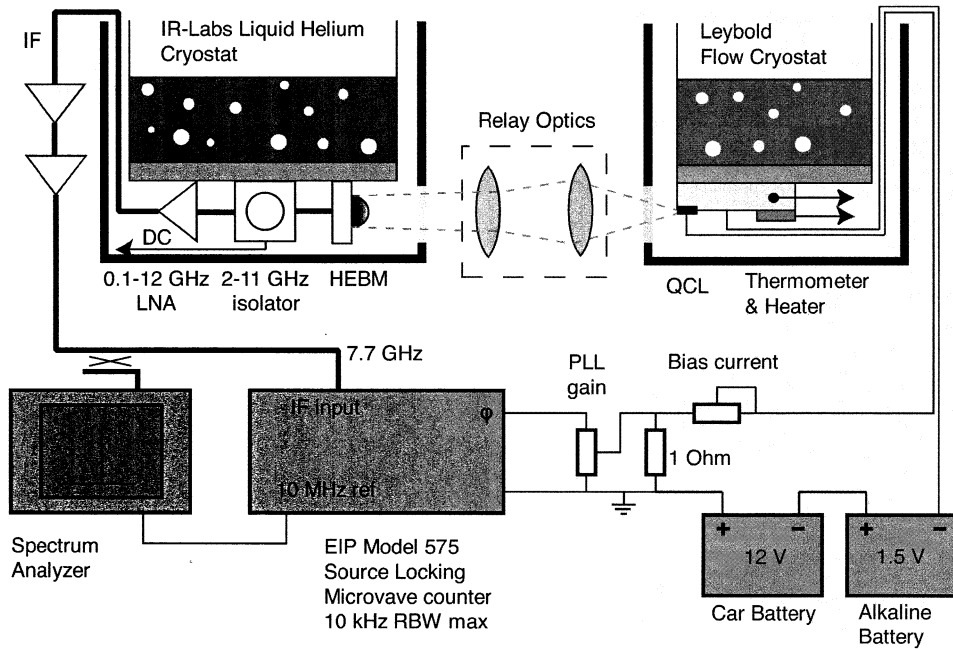


Fig. 2. Schematic diagram of the experimental setup to phase lock the beat signal of a two-mode THz QCL. Additional attenuators in the warm IF amplifier chain are not shown.

decreasing the phase locking loop (PLL) gain by adjusting the variable feedback resistor.

The DC bias-current circuit of the QCL consists of a car battery (to reduce fluctuations) and a variable resistor to change the bias current. Typical operating conditions are: DC bias voltage of 12.9 V, a current of 0.28 A and a heat-sink temperature of 7 K. The latter can be varied through a heater. We create a phase-lock condition by using the PLL with a high loop gain that gives the maximum regulation bandwidth of 10 kHz. The PLL, which is to reproduce the reference signal, rejects all amplitude modulation noise and all other noise that is separated sufficiently in frequency from the signal. It acts like a filter to track the reference signal frequency. Ideally, the spectrum of the beat signal will be the clean-up version of the reference spectrum.

IV. MEASUREMENT RESULTS AND DISCUSSION

Figure 3 shows a typical set of power spectra of the beat signal recorded by the spectrum analyzer using different resolution bandwidths (RBW) and spans. Both the temperature and the DC bias current are fixed. As indicated in the figure, the linewidth appears to decrease as the RBW of the spectrum analyzer is reduced. Apparently the linewidth is smaller than the instrumental RBW of 10 Hz, which is the minimum RBW of the spectrum analyzer. The data demonstrate that for an offset from the center frequency less than the PLL regulation bandwidth most of the signal power is located in a central peak of narrow bandwidth. This is a clear indication of phase locking. The recorded spectra resemble very much those found typically in a phase-locked Josephson flux flow oscillator [10]. The spectra are reproducible and stable for an arbitrarily long time. Experimentally, we can show that the QCL behaves as a current controlled oscillator, which is the key to enable phase locking. As shown in the inset of figure 3, the beat frequency decreases monotonically with increasing bias current for a given heat-sink temperature, e.g., from 7.9 to 7.5 GHz with the rate of roughly 10 MHz/mA. This means that phase locking conditions can be realized for the entire bias range above the lasing threshold, and moreover that stabilization of the beat frequency implies stabilization of the THz frequencies of both lasing modes. The second part of our study involves the measurement of the laser line profile and linewidth under frequency stabilization only. Starting from phase locking conditions we now reduce the loop gain such that the central frequency of the beat remains stable but the line shape is no longer influenced by the phase locking [10]. This is essentially a frequency-locking scheme of the two lasing modes. Under this frequency-stabilization, we are able to measure the power spectrum of the beat signal of the QCL in a controlled way (reproducible and stable for an arbitrarily long time), e.g. as a function of the heat-sink temperature. Figure 4 shows a measured beat signal with the minimum linewidth observed in this experiment [11], fitted with a Lorentzian curve. The fit shows the spectrum to be predominantly Lorentzian, as expected if the noise is due to spontaneous emission [12]. In some other cases, we find that a

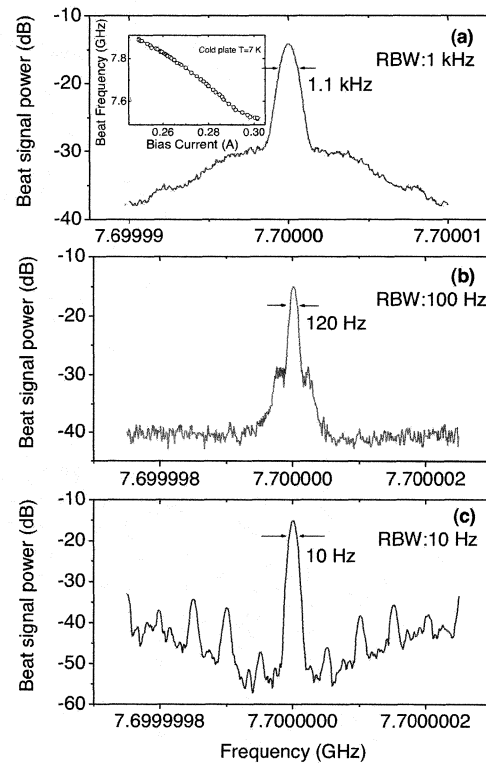


Fig. 3. The power spectra of the beat signal of two lateral-mode THz QCL that is phase locked to a microwave reference recorded by the spectrum analyzer with different resolution bandwidths (RBW) and spans, but a fixed video bandwidth (VBW) of 30 Hz. Other lines appeared in (c) are due to the pick-up of 50 Hz power-line signals. The 3-dB linewidth of each spectrum is also indicated. The inset in (a) shows the beat frequency as a function of the bias-current of the QCL at a heat-sink temperature of 7 K.

Voigt function gives a better fit than the Lorentzian, suggesting the coexistence of other noise sources, e.g. $1/f$ noise [13] and interference from pick-up noise. The minimum (FWHM) linewidth is found to be 12.6 kHz. Since this beat signal results from a convolution of two similar lines and assuming that their profiles are both Lorentzian, the lower limit of the linewidth of an individual emission line should be 6.3 kHz. This is the narrowest linewidth ever reported in THz QCLs and is much smaller than what required for astronomical (≤ 0.1 MHz) and atmospheric (≤ 1 MHz) observations.

The linewidth of any lasers is limited by quantum noise through spontaneous emission. Since intersubband lasers are not expected to have significant linewidth enhancement factors [14], the linewidth in our case is expected to follow the Schawlow-Townes limit [12]

$$\Delta\nu_{ST} = \frac{N_2}{N_1 + N_2} \frac{\pi h\nu(\Delta\nu_c)^2}{P} \quad (1)$$

Here $N_{1,2}$ are the populations in the upper and lower

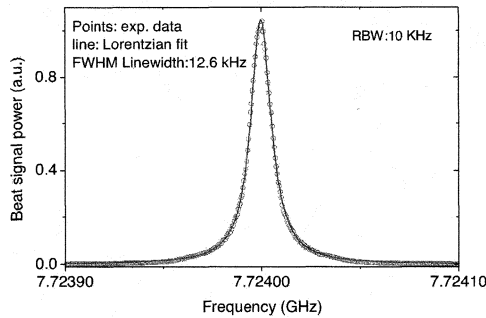


Fig. 4. Measured power spectrum of the beat signal under frequency stabilization (data points) [11]. A similar spectrum was obtained with a reduced resolution bandwidth (RBW). The curve is a fit with a Lorentzian profile.

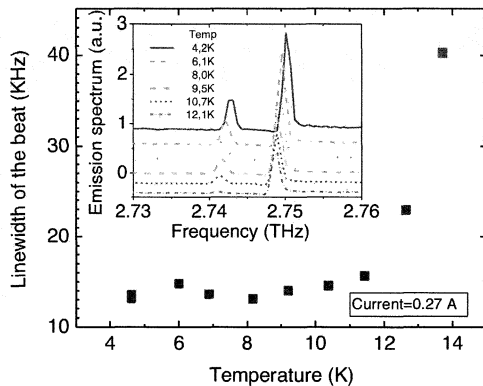


Fig. 5. Linewidth of the beat signal as a function of the heat-sink temperature of the QCL. The inset shows emission spectra of the two-mode QCL taken at several temperatures. For clarity an offset in the intensity for each spectrum is introduced.

laser states; $\Delta\nu_c$ is the cold cavity linewidth that equals $\alpha v_g / 2\pi$ with the group velocity v_g and the total loss α of the waveguide and mirror losses $\alpha = \alpha_w + \alpha_m$; P is the internal power in the mode relating to P_{out} by $P_{out} = \alpha_m P / \alpha$. We assume Eq. 1 to be valid for each of the two emission lines. Using the following parameters: $N_2 / (N_2 - N_1) \sim 1.3$, $\alpha_w \sim 20 \text{ cm}^{-1}$ at 2.7 THz, $\alpha_m = 2.2 \text{ cm}^{-1}$, and $P_{out} \sim 1 \text{ mW}$, we derive a Schawlow-Townes linewidth $\Delta\nu_{ST} = 0.7 \text{ kHz}$, which is ~ 9 times smaller than the measured linewidth. In view of large uncertainties in the input parameters, this result alone is not conclusive.

Eq. 1 suggests that the linewidth should be inversely proportional to the laser power. To test this, we have studied the linewidth of the beat signal as a function of heat-sink temperature, which influences the laser power for a fixed bias current. The results are shown in figure 5. We notice that, despite that the intensity (considered to be equivalent to the power) of both emission lines decreases monotonically (see the inset of figure 5), the linewidth remains essentially

independent of heat-sink temperature up to 12 K (the internal lattice temperature is likely higher), beyond which a sharp increase is seen. Clearly the linewidth does not follow Eq. 1 in the operating range of high-power (low device temperature), and consequently it does not approach the quantum-noise limit.

V. CONCLUSION

In summary, we have succeeded in phase locking of two lateral modes of a 2.7 THz QCL, demonstrating the feasibility of phase-locking of the THz laser to an external reference. Under frequency-stabilization conditions we have been able to study the intrinsic lineshape and linewidth of the QCL in a controllable manner and found the narrowest linewidth of 6.3 kHz.

ACKNOWLEDGEMENT

Authors acknowledge M. Hajenius and J.J.A. Baselmans for the use of their HEB mixer, and T.M. Klapwijk and W. Wild for their support and stimulating discussions. This work is supported partly by Radionet. The work at MIT is supported by AFOSR, NASA and the NSF. Sandia is a multi-program laboratory operated by Sandia Corporation, a Lockheed Martin Company, for the US Dept. of Energy under Contract DE-AC04-94AL85000.

REFERENCES

- [1] R. Köhler, A. Tredicucci, F. Beltram, H.E. Beere, E.H. Linfield, A.G. Davies, D.A. Ritchie, R.C. Iotti, and F. Rossi, *Nature (London)* 417, 156 (2002).
- [2] J.R. Gao, J.N. Hovenier, Z.Q. Yang, J.J.A. Baselmans, A. Baryshev, M. Hajenius, T.M. Klapwijk, A.J.L. Adam, T.O. Klaassen, B.S. Williams, S. Kumar, Q. Hu, and J.L. Reno, *Appl. Phys. Lett.* 86, 244104 (2005).
- [3] H.-W. Hübers, S.G. Pavlov, A.D. Semenov, R. Köhler, L. Mahler, A. Tredicucci, H.E. Beere, D.A. Ritchie and E.H. Linfield, *Optics Express*, 13, 5890(2005).
- [4] Th. de Graauw, et al, *Proc. SPIE* 5487, 1522 (2004).
- [5] J.J.A. Baselmans, M. Hajenius, J.R. Gao, T.M. Klapwijk, P.A.J. de Korte, B. Voronov, and G. Gol'tsman, *Appl. Phys. Lett.* 84, 1958 (2004).
- [6] A.L. Betz, R.T. Boreiko, B.S. Williams, S. Kumar, and Q. Hu, *Opt. Lett.* 30, 1837(2005).
- [7] A. Barkan, F.K. Tittel, D.M. Mittleman, R. Dengler, P.H. Siegel, G. Scalari, L. Ajili, J. Faist, H.E. Beere, E.H. Linfield, A.G. Davies and D.A. Ritchie, *Opt. Lett.* 29, 575 (2004).
- [8] S. Barbieri, J. Alton, H.E. Beere, E.H. Linfield, D.A. Ritchie, S. Withington, G. Scalari, L. Ajili, and J. Faist, *Opt. Lett.* 29, 1632 (2004).
- [9] Q. Hu, B.S. Williams, S. Kumar, H. Callebaut, S. Kohen and J.L. Reno, *Semicond. Sci. Technol.* 20, S228 (2005).
- [10] V.P. Koshelets, S.V. Shitov, L.V. Filippenko, V.L. Vaks, J. Mygind, A.M. Baryshev, W. Luinge, and N. Whyborn, *Rev. Sci. Ins.* 71, 289(2000).
- [11] We notice that the beat frequency of this QCL has shown a downshift of about 0.6 GHz after the measurements in figure 2.
- [12] A. Yariv, *Quantum Electronics*, 3rd ed., New York : Wiley, 1989. For equation 1, see page 199.
- [13] G.M. Stéphan, T.T. Tam, S. Blin, P. Besnard, and M. Tétu, *Phys. Rev.* A71, 043809(2005).
- [14] J. Kim, M. Lerttamrab, S.L. Chuang; C. Gmachl, D.L. Sivco, F. Capasso, and A.Y. Cho, *IEEE Journal of Quantum Electronics*, 40, 1663(2004).

A Photonic mm-Wave Local Oscillator

Robert Kimberk, Todd Hunter, C.-Y. Edward Tong, and Raymond Blundell

Abstract—A photonic millimeter wave local oscillator capable of producing two microwatts of radiated power at 224 GHz has been developed. The device was tested in one antenna of Smithsonian Institution's Submillimeter Array and was found to produce stable phase on multiple baselines. Graphical data is presented of correlator output phase and amplitude stability. A description of the system is given in both open and closed loop modes. A model is given which is used to predict the operational behavior. A novel method is presented to determine the safe operating point of the automated system.

Index Terms—Interferometer, photomixer, phase modulation, phase locked loop, frequency multiplication, millimeter waves.

I. INTRODUCTION

A photonic local oscillator has been developed and used to pump a SIS mixer at 224 GHz. The local oscillator was installed in one antenna of the Submillimeter Array [1]. A single dish scan of Saturn was performed on February 24 2006. Observations of an ultra compact HII region and three quasars successfully produced stable fringes and amplitudes on a five element array. The test was performed on the evening of April 26 2006 UTC and the following day.

The configuration of the photonic local oscillator phase locked to an external reference signal (open loop) is shown in figure 1. The optical path consists of a single 1550 nm diode laser,

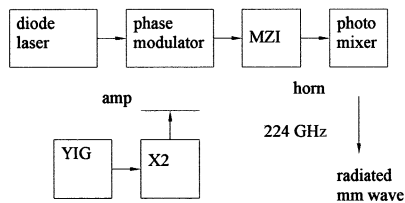


fig. 1 open loop system

a lithium niobate optical phase modulator, a Mach Zehnder interferometer and a photomixer whose output is connected to a horn antenna. The photomixer was obtained from P.G. Huggard and B.N. Ellison of Rutherford Appleton Labs [2] in November of 2003. All optical devices and connections are polarization maintaining. The electrical path consists of a YIG synthesizer, a frequency doubler, and a power amplifier connected to the RF port of the phase modulator. The light from the laser is phase modulated at twice the YIG frequency, then converted to an amplitude modulated signal by the Mach Zehnder interferometer (MZI). The photomixer responds to the amplitude modulated signal and radiates that

part of the am signal above the WR3 horn lower cutoff frequency. Figure 1 is a schematic of the open loop system.

II. THE OUTPUT SPECTRUM

The voltage output of the photomixer, V , can be described by the following expression:

$$V = 1 + \sum J_n(2aK_p) \cos((\pi\omega_c / \omega_m) + n\omega_m t) \quad (1)$$

where n ranges from plus to minus infinity, V is the amplitude of the output signal, ω_c is the optical angular frequency before modulation, and ω_m is the modulation angular frequency. $J_n(2aK_p)$ is the Bessel function of the first kind with $2aK_p$ as the argument. The quantity, aK_p , the peak phase deviation of ω_c , is the product of the amplitude of the modulation signal, a , in volts and the optical phase modulator response, K_p , in radians / volt.

An examination of expression (1) shows that:

- The photomixer output contains harmonics of the modulation frequency ω_m .
- Given $J_n = -1^n J_n$ and $\cos(\theta) = \cos(-\theta)$, when $\pi\omega_c / \omega_m$ is an even multiple of $\pi/2$, odd harmonics cancel and only even harmonics appear at one output of the MZI. The other output of the MZI has the odd harmonics due to the extra π phase shift at ω_c .
- Given $\cos(\theta + \pi/2) = -\cos(-\theta + \pi/2)$, when $\pi\omega_c / \omega_m$ is an odd multiple of $\pi/2$ then the even harmonics cancel and only odd harmonics appear at the output.
- When $\pi\omega_c / \omega_m$ meet the conditions of b) or c) the amplitudes of the harmonics are determined by $2aK_p$. Increasing the power into the optical phase modulator RF port will increase the number of harmonics.
- For values of $\pi\omega_c / \omega_m$ that do not meet the conditions of b) or c) both odd and even harmonics exist at both MZI outputs.

The frequency of the laser, ω_c , is controlled by the laser temperature. The laser used, JDS CQF935/808, has a wavelength temperature tunability of about $0.1 \text{ nm} / ^\circ\text{C}$, equivalent to about $7.85 \times 10^{10} \text{ rad} / \text{sec} / ^\circ\text{C}$ at 1550 nm. Figure 4 shows the measured power of a selected harmonic as the laser temperature is varied. Note that the power output completes a cycle in about 3°C . This corresponds to about $23.55 \times 10^{11} \text{ rad} / \text{sec}$, about ω_m . Note also that the maximum output power of the harmonic occurs at the middle value of photomixer bias current.

Expression 1 assumes a photomixer with a flat response over the output frequency. To estimate the true output power

Manuscript received May 10, 2006.

R. Kimberk, T. Hunter, C.-Y. E. Tong and R. Blundell are with the Harvard-Smithsonian Center for Astrophysics, 60 Garden St., Cambridge, MA 02138 USA. (e-mail: etong@cfa.harvard.edu, and rblundell@cfa.harvard.edu).

the results of expression 1 need to be multiplied by the photomixer's frequency response.

We normally tune the laser temperature so that the two outputs of the MZI are purely even and odd harmonics of the modulation frequency. The two advantages of this mode are that the frequency separation of harmonics is greatest

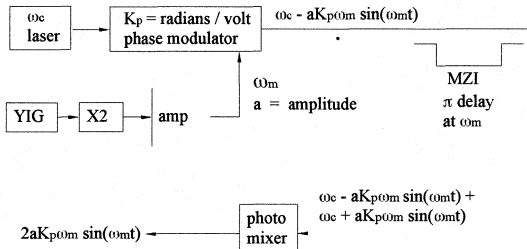


Fig. 2. output as difference of phase modulated laser and delayed phase modulated laser

(two times the modulation frequency), and the power is maximized for any harmonic.

Figure 2 shows the instantaneous angular frequency [3] ($d\theta/dt$, where θ = phase) at key points along the signal path. Instantaneous frequency is a useful concept when dealing with frequency or phase modulation. The MZI splits the incoming power, phase shifts one component, then sums the two components. The greatest frequency multiplication occurs when the modulation frequency is equal to one half of the free spectral range (FSR) of the MZI. This condition adds a π radian phase delay at the modulation frequency. The instantaneous difference frequency then becomes:

$$2aK_p \omega_m \sin(\omega_m t)$$

$$= \omega_c + aK_p \omega_m \sin(\omega_m t) - (\omega_c + aK_p \omega_m \sin(\omega_m t + \pi))$$

$$= \omega_c + aK_p \omega_m \sin(\omega_m t) - (\omega_c - aK_p \omega_m \sin(\omega_m t)).$$

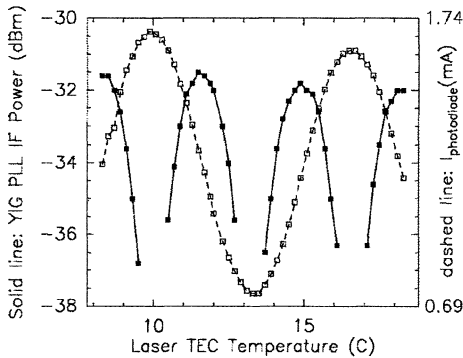


Fig.4 laser temperature vs single tone power and photomixer bias current

The resulting instantaneous frequency, $2aK_p \omega_m \sin(\omega_m t)$, describes a sinusoidal chirp. The maximum frequency of the chirp is equal to twice the product of the peak phase deviation, $2aK_p$, and the modulation frequency, ω_m . As the modulation frequency is moved away from FSR/2 the maximum instantaneous frequency of the output is reduced.

III. CLOSED LOOP SYSTEM

In order to operate a radio interferometer, the local oscillators of all the receivers must be phase locked to a common reference tone. The closed loop configuration of the photonic local oscillator, where the phase of the mm wave output is locked to a reference frequency, is shown in figure 3. A second photomixer is connected to the unused MZI output. The output of the added photomixer is connected to a harmonic mixer, which in turn is connected to the IF port of the phase locked loop (PLL) through a frequency diplexer and IF amplifier. The PLL control output is connected to the YIG fine tune input, and controls the YIG output phase. In this way the YIG is locked to a down converted 112GHz, the third multiple of ω_m . The multiples of the modulation frequency, ω_m , are all related with respect to phase. Locking to any multiple stabilizes the phase of all the other multiples. Not shown in figure 3, is the 6 to 8 GHz lo pumping the harmonic mixer, the 109 MHz reference connected to the PLL, and the coarse tuning signal to the YIG.

IV. OPEN LOOP PHASE NOISE AND STABILITY

The open loop phase drift of the system was tested by power splitting the output of a microwave synthesizer, modulating our system with one of the two identical outputs and using the other output to pump a conventional multiplier chain. The synthesizer's output frequency was 12.5 GHz and the final frequency in both legs was 75 GHz. The outputs of both the photonic and conventional multipliers were down converted using mixers with a common local oscillator and the phase was compared with a vector voltmeter. Differential phase drifts of 5 degrees / hr were observed. The phase drift tracked the room temperature

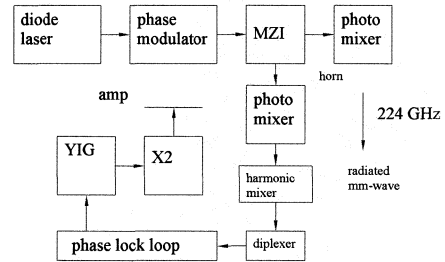


fig. 3 closed loop system

change. The differing lengths and temperature coefficients of coaxial cable and optical fiber involved in this test might explain the observed phase drifts. One degree at 75GHz is equal to about $7.4\mu\text{m}$ in quartz fiber.

The phase noise of the output of the photonic local oscillator is dominated by the multiplied phase noise of the modulation source. We expect the system to act like a classical multiplier, the output phase noise will be the phase noise of modulation source plus $20 \log M$. M is equal to the ratio output frequency / input frequency.

The open loop phase noise of a heterodyne two laser local oscillator is similar to the phase noise of two lasers. In contrast the contribution of the single laser phase noise to the open loop phase noise of our system is determined by phase noise of the laser times $(\tau / \tau_c)^2$, where τ_c is the coherence time of the laser and τ is the path delay of the MZI. The value of $(\tau / \tau_c)^2$ is very small for a MZI with a

free spectral range of 75 GHz (a delay of 1.3×10^{-11} s) and a laser coherence time of 10^{-6} s.

V. ASTRONOMICAL OBSERVATIONS

The photonic local oscillator was installed in antenna 6 of the Submillimeter Array on Mauna Kea, Hawaii, and tuned to 224 GHz. An observation of the quasar 3C273 was obtained on the evening of April 26 2006 UTC. The output of the correlator yielded stable phase and amplitudes for each of the baselines

with the seven operating antennas. The next day observations of the ultra compact HII region G138.295+1.555 [4], the quasar 3C84, and the quasar 3C454.3 were obtained with a five element array. Figure 5 shows the phase (dots) and amplitude (gray trace) of each baseline at the correlator output. Baselines that include antenna 6 do not show a greater scatter of values than baselines that do not include antenna 6.

Baseline lengths range from 16 m at the top to 69 m at the bottom of figure 5. Line spectra of 13CO₂-1 and 12CO₂-1 were observed in the source G138.295+1.555. The 232.4 GHz beacon attached to the Subaru building was observed as shown in figure 6. Figure 7 is a graph of the 12CO₂-1 line from G138.295+1.555 at the correlator output.

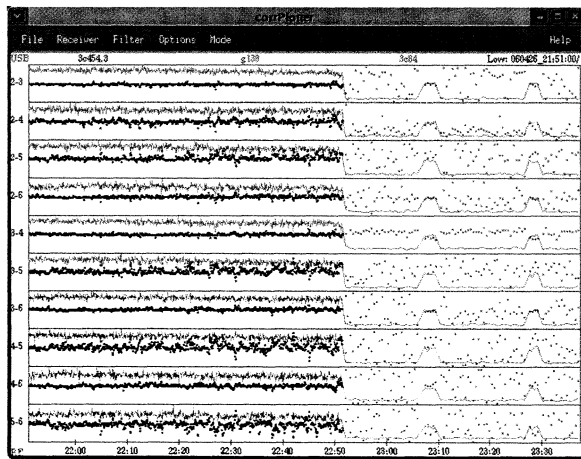


Fig.5 phase and amplitude at correlator output. The sources are 3C454.3, G138.295+1.555, and 3C84

VI. AUTOMATION

The photomixer bias current limit is 5mA, above which the photomixer will be damaged. The bias current is a function of laser power and temperature as well as modulation frequency. This fact makes it necessary to find a path through the various combinations of the variables that does not destroy the photomixer. To explore the effect of temperature on the modulated output power, we biased the laser with 60 milliamps of current (about 1/8 the normal operational current) and measured the photodiode current as a function of laser temperature at several modulation frequencies. As seen in Figure 4, we find a sinusoidal behavior of photodiode current with respect to laser

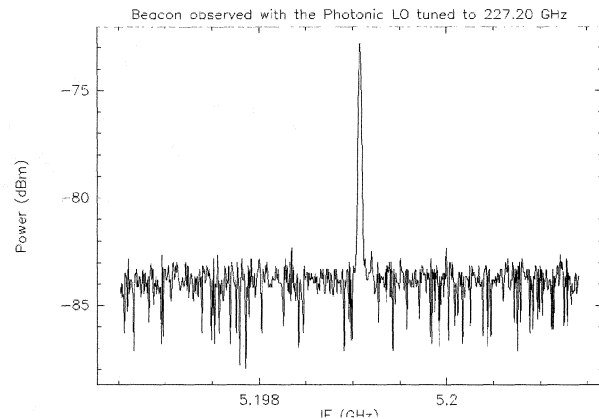


Fig.6 Beacon on Subaru Building observed from SMA antenna 6

temperature. Although the amplitude of the sinusoid depends on modulation frequency, we discovered that there exist "fixed point" temperatures where the photodiode current is independent of modulation frequency.

We next locked the photonic LO using a W-band harmonic mixer and a digital PLL. We measured the power of the locked signal at the PLL IF monitor port as a function of laser temperature. Figure 4 shows that the IF power is at maximum when the laser is operated at the fixed point temperatures.

To optimize the IF power, we can use the following algorithm. Change the modulation frequency by some significant amount (1 GHz) and observe the change in the photomixer current. Adjust the laser temperature slightly upward and change the modulation frequency back to the initial value. If the photomixer current decreases, then continue adjusting the laser temperature upward until the photomixer remains constant with respect to the modulation frequency.

Conversely, if the photomixer current increases, then adjust the laser temperature downward instead.

VII. CONCLUSION

We have demonstrated that a photonic local oscillator can be sufficiently phase and amplitude stable to be used as part of a radio interferometer at mm wave lengths. We believe that an increase in the frequency of modulation will allow for greater output frequencies as well as greater separation between the harmonics of the modulation frequency.

VIII. Acknowledgment

The authors want to thank Smithsonian Institution for its support. We want to thank Bob Wilson for early insight and for his belief that the system would work when most were skeptical. We want to thank Hugh Gibson for a numerical analysis of the system with both the Mach Zehnder and Fabry Perot interferometers, and Robert Christensen for instrumental instruction and observational guidance at Mauna Kea. As well we want to acknowledge those people that developed the concept before us, O.I. Kotov et al [5], E.J. Bochove et al [6] to name a few. A development of the ideas in this paper in greater detail was published in an

earlier ISST proceedings [7] and may be a useful background.

REFERENCES

- [1] R. Blundell, "The Submillimeter Array Antennas and Receivers" Proceedings of the 15th International Symposium on Space Terahertz Technology, April 27-29, 2004, p. 3
- [2] P.G. Huggard, B.N. Ellison, "Efficient Generation of guided Millimeter-Wave Power by Photomixing" IEEE Photonics Technology Letters, Vol.14,NO.2, February 2002.F.G. Stremler "Introduction to Communication Systems" Addison-Wesley, third edition page 320
- [3] F.G. Stremler, "Introduction to Communication Systems" Addison-Wesley, third edition, 1990, p. 320
- [4] T. Hunter "A Submillimeter Imaging Survey of Ultracompact HII Regions" Thesis, California Institute of Technology, Source DAI-B 58/01 July 1997.
- [5] O.I. Kotov, L.B. Liokumovich, V.M. Nikolaev, V.Yu. Petrun'kin, and Zekhraui Buabid, "Conversion of phase modulation of light into intensity by means of an external fiber-optic interferometer" St. Petersburg State Technical University, Pis'ma Zh. Tekh. Fiz. 23, 9-16, May 26, 1997.
- [6] E.J. Bochove, and E.M. de Carvalho, "Conversion of a wideband frequency-modulated signal to amplitude modulation through dispersion in an optical fiber" Optics Letters, Vol. 7, No. 3, March 1982.
- [7] R. Kimberk, C.E. Tong, H. Gibson, R.W. Wilson, R. Blundell, S. Paine, and T.R. Hunter, "An Interferometric Microwave Comb Generator" Proceedings of the 13th International Symposium on Space Terahertz Technology, March 26-28, 2002.

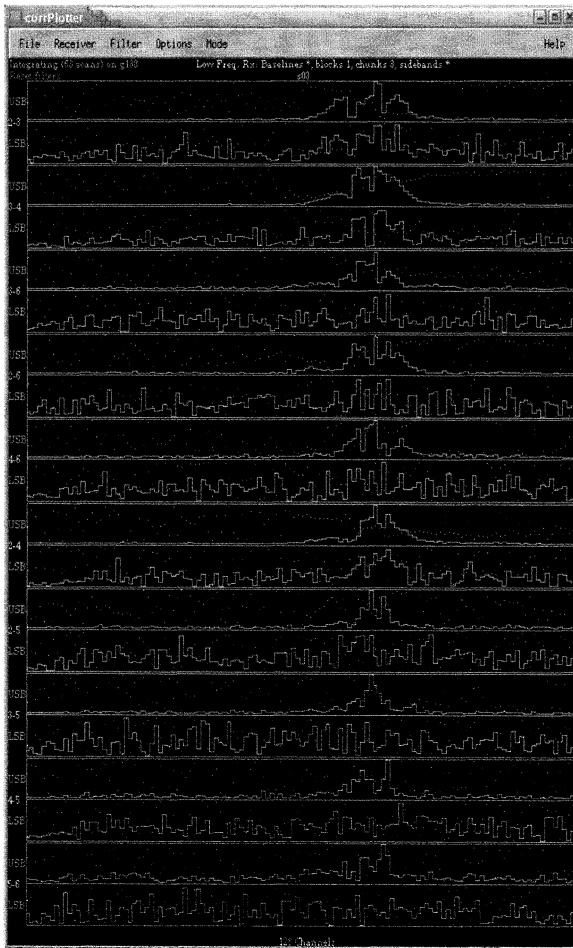


Fig.7 12CO₂-1 spectral line observed in source G138.295+1.555

Performance Improvements in Low-Noise Oscillators and Power Combiners with Harmonic-Mode InP Gunn Devices

Heribert Eisele, *Senior Member, IEEE*, and Ridha Kamoua, *Member, IEEE*

Abstract—InP Gunn devices with graded doping profiles were evaluated for second-harmonic power extraction above 260 GHz and third-harmonic power extraction above 400 GHz. The best devices generated radio frequency (RF) output power levels of more than 3.5 mW at 275–300 GHz, 1.6 mW at 329 GHz, and 0.7 mW at 333 GHz. The highest observed second-harmonic frequency was 345 GHz. Two devices each in an in-line power combining circuit generated 6.1 mW at 285 GHz and 2.7 mW at 316 GHz with combining efficiencies of more than 65%. In a third-harmonic mode, the best devices generated 45 μ W at 409 GHz, 40 μ W at 412 GHz, and 40 μ W at 422 GHz.

I. INTRODUCTION

ADVANCES in the performance of compact low-noise fundamental sources at terahertz frequencies are expected to have a far-reaching impact on many applications, such as wideband wireless communications, imaging, and chemical or biological sensing [1]. Transferred-electron devices, long known as Gunn devices and widely utilized as low-noise sources up to millimeter-wave frequencies, were originally thought to be limited to frequencies below 200 GHz [2]. Accurate device design tools [3], advanced fabrication technologies, and appropriate thermal management [4] vastly improved the performance of millimeter-wave InP Gunn devices and extended their operation in a second-harmonic mode to *J*-band (220–325 GHz) frequencies [5]–[7]. Power combining of oscillators is the method of choice to provide systems applications with higher radio frequency (RF) power levels and different techniques are widely known for oscillators at millimeter-wave frequencies [8]. The technique of a resonant-cavity combiner was demonstrated with Si impact avalanche transit-time (IMPATT) diodes up to 217 GHz [9] and this had so far been the highest frequency where a combined continuous-wave (CW) RF output power of more than 1 mW had been reported. This paper describes the performance improvements in second- and third-harmonic InP Gunn devices and the first successful demonstration of power combining above 260 GHz.

II. DEVICE PERFORMANCE IN A SECOND-HARMONIC MODE

Devices with two similar graded doping profiles as shown in

H. Eisele is with the Institute of Microwaves and Photonics, School of Electronic and Electrical Engineering, The University of Leeds, Leeds LS2 9JT, United Kingdom (e-mail: h.eisele@leeds.ac.uk).

R. Kamoua is with the Department of Electrical and Computer Engineering, Stony Brook University, Stony Brook, NY 11794-2350, USA (e-mail: ridha@ece.sunysb.edu).

Fig. 1 were evaluated. These profiles were designed for efficient operation in a second-harmonic mode at 240 GHz and above [7]. Devices with diameters of 25–40 μ m were selected and mounted on diamond heat sinks. Except for some different equipment and minor configuration changes [10], [11], the same test setup and the same type of a full-height WR-6 waveguide cavity [5], [6] was used.

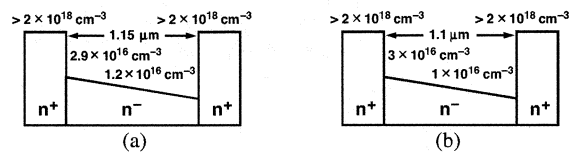


Fig. 1. (a) and (b) Nominal doping profiles of InP Gunn devices evaluated for second-harmonic power extraction.

Fig. 2 summarizes only the highest RF output power levels of the tested devices. Examples are the RF output power (and corresponding dc-to-RF conversion efficiency) of 4.8 mW (0.31%) at 281.9 GHz, 3.7 mW (0.32%) at 297.1 GHz, 1.6 mW (0.19%) at 329.1 GHz, and 0.7 mW (0.07%) at 332.8 GHz from devices with the doping profile of Fig. 1(b). Devices with the doping profile of Fig. 1(a) tended to work better at frequencies lower than those of devices with the profile of Fig. 1(b) and the best performance was an RF output power of 3.9 mW at 274.75 GHz with a corresponding dc-to-RF conversion efficiency of 0.24%. Conversely, the highest second-harmonic frequency of 344.85 GHz was observed with a device of the profile of Fig. 1(b). An RF output power of more than 0.1 mW was measured and the lack of a signal at 344.85/1.5 GHz confirmed operation in a second-harmonic mode. Operating active-region temperatures of these second-harmonic mode devices on diamond heat sinks were estimated to be typically much below 150 °C, and, therefore, reliable long-term operation is expected from these devices.

Although the differences in the doping profiles of Fig. 2 are small, they are the main cause of the observed performance differences. As described in Section IV, devices from both doping profiles generate state-of-the-art RF output power levels in a third-harmonic mode, which precludes major differences in contact and other series resistances. In addition, differences in performance are also present in the results of device simulations [3] as shown in Fig. 3. Devices with the doping profile of Fig. 1(a) exhibit better performance at lower frequencies and a steeper decline in RF output power levels

above 260 GHz when compared with devices of the other doping profile.

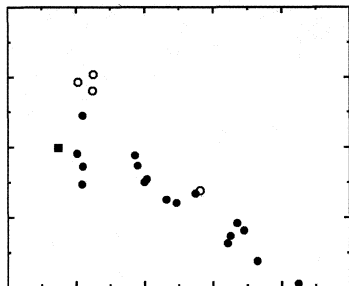


Fig. 2. RF performance of InP Gunn devices on diamond heat sinks, operating in a second-harmonic mode in the frequency range 270–350 GHz. ■: doping profile of Fig. 1(a); ●: doping profile of Fig. 1(b); ○: power-combined devices with doping profile of Fig. 1(b). Numbers next to the symbols denote dc-to-RF conversion efficiencies in %.

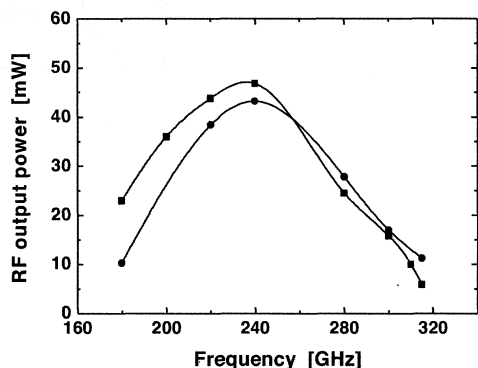


Fig. 3. Comparison of the predicted RF performance of InP Gunn devices operating in a second-harmonic mode in the frequency range 180–320 GHz. ■: doping profile of Fig. 1(a); ●: doping profile of Fig. 1(b).

III. POWER COMBINING

Phase lock between devices generally occurs in a power-combining circuit only if the devices are coupled at the fundamental and second-harmonic frequencies [12]. This is achieved with the in-line power-combining circuit as shown in Fig. 4. Two full-height WR-6 waveguide cavities, as used before for second-harmonic power extraction from individual devices, are mounted back-to-back and four dowel pins in their inner flanges help with the performance-critical alignment. A standard tunable WR-6 waveguide short is connected to the outer flange of one of the cavities. The section of a WR-3 waveguide, connected to the outer flange of the other cavity, keeps the signals at the fundamental frequencies from reaching the power meter.

Two pairs of devices with similar oscillation frequencies as shown in TABLE I were used in these experiments. Power

combining and phase-lock conditions were achieved with devices of pair #1 for three bias conditions and three positions of the tunable back short. At the same bias voltages, *i.e.*, those for maximum RF output power from the individual devices, a combined RF output power of 6.1 mW was measured at 285 GHz. This power level corresponds to a combining efficiency of 75% and an overall dc-to-RF conversion efficiency of 0.2%.

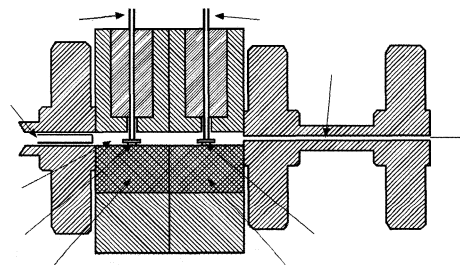


Fig. 4. Schematic of the WR-6 in-line waveguide power-combining circuit with the WR-3 output waveguide.

As can be seen from TABLE I, device B generated more than 3.2 mW at two different positions of the back short and corresponding second-harmonic frequencies. As a result, phase lock in the power combiner also occurred at 280.5 GHz with a combined RF output power of 5.8 mW. Furthermore, phase-lock conditions were achieved at a reduced dc input power (approximately 88%) for device A and close to maximum dc input power for device B (> 95%) and a combined RF output power of 5.6 mW at 284.8 GHz, which corresponds to a combining efficiency of 85%.

TABLE I
RESULTS OF DUAL-CAVITY POWER COMBINING WITH INP GUNN DEVICES IN A SECOND-HARMONIC MODE

Device Pair #	Frequency [GHz]	Power A & B [mW]	Overall Efficiency [%]	Power A [mW]	Power B [mW]	Combining Efficiency [%]	Frequency A [GHz]	Frequency B [GHz]
1	280.5	5.8	0.19	4.8	3.8	67	281.9	280.3
1	284.8	5.6	0.19	3.4	3.1	85	282.0	285.0
1	285.0	6.1	0.2	4.8	3.2	75	281.9	284.9
2	316.3	2.7	0.12	1.5	1.4	65 (est.) [†]	325.0	325.0

[†] estimated value, see text.

The devices of pair #2 exhibited very similar performance at 325 GHz. However, the spacing between the devices in the power combiner as determined by the individual cavities was fixed in all experiments and not as favorable as around 282 GHz. Therefore, phase-lock conditions occurred at a lower frequency of 316.3 GHz with an RF output power of 2.7 mW. As the individual devices are expected to have generated RF power levels approximately 30% higher at 316 GHz than at 325 GHz, the combining efficiency was estimated not to be 93%, but closer to 65%.

To verify that each pair of devices was phase-locked and without bias oscillations, the frequency range of 260–360 GHz

was scanned for spurious signals with the spectrum analyzer and harmonic mixer and none were found. Phase lock occurred instantly at always the same frequency as soon as both devices were biased. This was also independent of whether one device was turned on first or both devices were turned on at the same time.

The spectra of the oscillators with power-combined devices were as clean as those with single devices and this corresponds well to the clean spectra of power-combined devices in the fundamental mode at *D*-band [13]. Fig. 5 shows one example for pair #1 at 280.5 GHz.

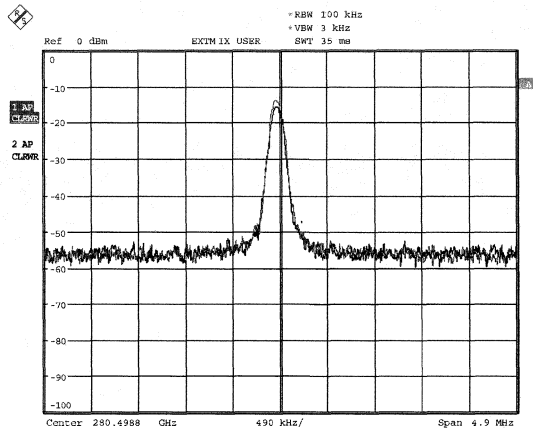


Fig. 5. Spectrum of the oscillator with device pair #1. Power level: 5.8 mW, center frequency: 280.499 GHz, vertical scale: 10 dB/div, horizontal scale: 490 kHz/div, resolution bandwidth: 100 kHz, video bandwidth: 3 kHz, reference level not calibrated.

IV. THIRD-HARMONIC POWER EXTRACTION

Devices on diamond heat sinks with the graded doping profiles of Fig. 1 and mesa diameters between 25 μm and 40 μm were also evaluated for third-harmonic power extraction. They were tested in the same type of a full-height WR-6 waveguide cavity as before [4]–[7], [11], [13] and, as shown in Fig. 6, the same tunable short as in Fig. 4 was mounted on one flange of the cavity to allow for frequency and power fine-tuning. A dielectric-filled conical horn was used to emit the third-harmonic power and connected to the other flange through a short waveguide section [14]. The rectangular waveguide section (approximate size WR-2) of the conical horn with a cut-off frequency of more than 285 GHz blocks the signals at the fundamental and second-harmonic frequencies. Further details of the test setup can be found in [14].

The InP Gunn devices with the smallest areas generally showed the best performance and such observations had been reported previously for other two-terminal devices [10], [15]. Careful assembly including the alignment of the waveguide transition proved critical in these experiments and improved the performance considerably from previous results in the frequency range 400–425 GHz [16]. RF power levels of more

than 45 μW at $3f_1 = 409$ GHz and 40 μW at $3f_2 = 412$ GHz from device A with the doping profile of Fig. 1 (a), and 40 μW at $3f_3 = 422$ GHz from device B with the doping profile of Fig. 1 (b) are the best results and were measured with a Thomas Keating quasi-optical power meter. The exact oscillation frequencies were determined using the IDENTIFY function of a spectrum analyzer with an external *J*-band harmonic mixer [14]. Fig. 7 shows the clean spectrum of the free-running oscillator with the RF output power of 40 μW . The narrow line width of the signal corresponds well to the clean spectra and excellent noise performance of InP Gunn devices with the same or similar graded doping profiles in the fundamental and second-harmonic modes [6].

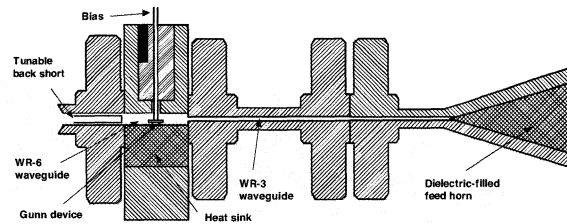


Fig. 6. Schematic of the WR-6 waveguide cavity, WR-3 waveguide section, and conical horn for third-harmonic power extraction.

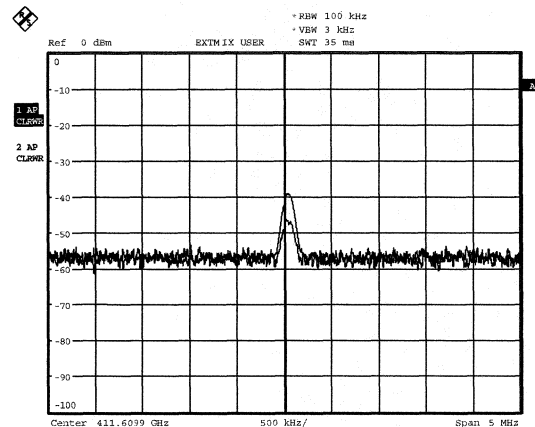


Fig. 7. Spectrum of a free-running InP Gunn device oscillator in a third-harmonic mode. RF power level: 0.04 mW, center frequency: 411.610 GHz, vertical scale: 10 dB/div, horizontal scale: 500 kHz/div, resolution bandwidth: 100 kHz, video bandwidth: 3 kHz, reference level not calibrated.

The corresponding second-harmonic frequencies were close to the cut-off frequency of the waveguide section of the horn. Therefore, the same setup with the spectrum analyzer and harmonic mixer was used not only to confirm single-frequency operation, but also to verify that the signals at the second-harmonic frequencies were sufficiently blocked. No other signals were detected, in particular, not around $2f_1 = 409/1.5$ GHz and $2f_2 = 412/1.5$ GHz from device A. Only a weak signal with less than 2 μW was found from device B at $2f_3 = 422/1.5$ GHz.

The RF output power from device A as a function of the dc input power was measured with the power meter PM3 [17], which had a *J*-band corrugated feed horn and the appropriate waveguide transition attached to it [10], [14]. The power readings from the PM3 as shown in Fig. 8 were not corrected for any losses (correction setting of PM3: 0%) nor was a coupling of clearly less than 100% between the two horns of different apertures taken into account [14]. Therefore, the actual output power levels are much higher and the maximum power of 24 μ W in Fig. 8 agrees reasonably well with the aforementioned value from the quasi-optical power meter at 412 GHz.

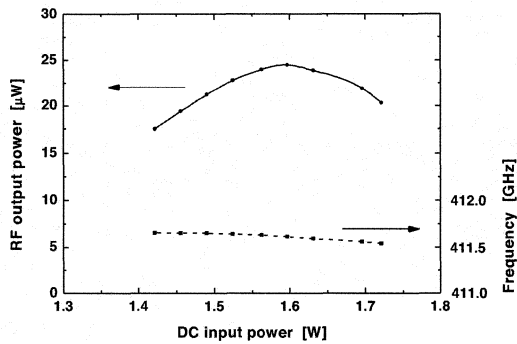


Fig. 8. Uncorrected RF power level readings of an InP Gunn device in a third-harmonic mode at 411.6 GHz as a function of the applied bias. \bullet : RF output power in a third-harmonic mode; \blacksquare : third-harmonic oscillation frequency.

The oscillation frequency in Fig. 8 decreases monotonically with dc input power and the change in RF output power remains well below 2 dB. A tuning range of more than 100 MHz for the Gunn device in a third-harmonic mode is sufficient to stabilize its oscillation frequency in a phase-locked loop.

V. CONCLUSION

All RF output power levels are the highest reported to date from any Gunn device, and more importantly, they are the highest from any fundamental RF source operated at room temperature in the frequency range 290–425 GHz. 344.85 GHz is the highest second-harmonic frequency reported to date for any Gunn device. Typical dc input power levels of less than 1.5 W and bias voltages of less than 6 V allow operation from a battery. Successful power-combining of active two-terminal devices with RF power levels of 2.7 mW and higher was demonstrated for the first time above 220 GHz. Values of DC power consumption and overall dc-to-RF conversion efficiency for individual and power-combined devices in a second-harmonic mode compare favorably with those of RF sources that employ frequency multipliers with GaAs Schottky-barrier or III-V heterojunction-barrier varactor diodes and millimeter-wave driver sources [1], [18]. The measured results confirm the predicted potential of InP Gunn devices as RF sources with substantial amounts of output power up to at least 500 GHz [7]. Improvements in performance of

the combiner circuit are expected from more optimized device spacing and an additional tuning element at the second-harmonic frequency. Likewise, improvements in third-harmonic power extraction are expected from more optimized doping profiles and oscillator circuits [14], [16].

ACKNOWLEDGMENT

The authors thank George I. Haddad, University of Michigan, for making it possible for devices to be fabricated in the Michigan Nanofabrication Facility.

REFERENCES

- [1] P. Siegel, "Terahertz technology," *IEEE Trans. Microwave Theory Tech.*, vol. 50, no. 3, pp. 910–928, March 2002.
- [2] I. G. Eddison, "Indium phosphide and gallium arsenide transferred-electron devices." *Infrared and Millimeter Waves*, vol. 11, *Millimeter Components and Techniques, Part III*, Academic Press, Orlando, pp. 1–59, 1984.
- [3] R. Kamoua, "Monte Carlo-based harmonic balance technique for the simulation of high-frequency TED oscillators," *IEEE Trans. Microwave Theory Tech.*, vol. 46, no. 10, pp. 1376–1381, Oct. 1998.
- [4] H. Eisele and G. I. Haddad, "High-performance InP Gunn devices for fundamental-mode operation in D-band (110–170 GHz)," *IEEE Microwave Guided Wave Lett.*, vol. 5, no. 11, pp. 385–387, Nov. 1995.
- [5] H. Eisele, "Second-harmonic power extraction from InP Gunn devices with more than 1 mW in the 260–320 GHz frequency range," *Electron. Lett.*, vol. 34, no. 25, pp. 2412–2413, 1998.
- [6] H. Eisele, A. Rydberg, and G. I. Haddad, "Recent advances in the performance of InP Gunn devices and GaAs TUNNETT diodes for the 100–300-GHz frequency range and above," *IEEE Trans. Microwave Theory Tech.*, vol. 48, no. 4, pp. 626–631, April 2000.
- [7] H. Eisele and R. Kamoua, "Submillimeter-wave InP Gunn devices," *IEEE Trans. Microwave Theory Tech.*, vol. 52, no. 10, pp. 2371–2378, Oct. 2004.
- [8] K. Chang, "Millimeter-wave power combining techniques," *IEEE Trans. Microwave Theory Tech.*, vol. 31, no. 2, pp. 91–107, Feb. 1983.
- [9] K. Chang, W. F. Thrower, and G. M. Hayashibara, "Millimeter-wave silicon IMPATT sources and combiners for the 110–260-GHz range," *IEEE Trans. Microwave Theory Tech.*, vol. 29, no. 12, pp. 1278–1284, Dec. 1981.
- [10] H. Eisele, "355-GHz oscillator with GaAs TUNNETT diode," *Electron. Lett.*, vol. 41, no. 6, pp. 329–331, March 2005.
- [11] H. Eisele and R. Kamoua, "High-performance oscillators and power combiners with InP Gunn devices at 260–330 GHz," *IEEE Microwave Wireless Comp. Lett.*, vol. 16, no. 5, pp. 284–286, May 2006.
- [12] H. Barth, "Oberwellen-Oszillatoren zur Leistungserzeugung im Millimeterwellen-Gebiet," Ph.D. dissertation, Technical Univ. Hamburg-Harburg, 1988.
- [13] H. Eisele and G. I. Haddad, "Efficient power combining with D-band (110–170 GHz) InP Gunn devices in fundamental-mode operation," *IEEE Microwave Guided Wave Lett.*, vol. 8, no. 1, pp. 24–26, Jan. 1998.
- [14] H. Eisele, "InP Gunn devices for 400–425 GHz," *Electron. Lett.*, vol. 42, no. 6, pp. 358–359, March 2006.
- [15] Plotka, P., Nishizawa, J.-i., Kurabayashi, T., and Makabe, H.: "240–325-GHz GaAs CW fundamental-mode TUNNETT diodes fabricated with molecular layer epitaxy," *IEEE Trans. Electron Devices*, vol. 50, no. 4, pp. 867–873, April 2003.
- [16] H. Eisele, M. Naftaly, and R. Kamoua, "Generation of submillimeter-wave radiation with GaAs TUNNETT diodes and InP Gunn devices in a second or higher harmonic mode," *Int. J. Infrared Millimeter Waves*, vol. 26, no. 1, pp. 1–14, Jan. 2005.
- [17] Erickson, N.: "A fast and sensitive submillimeter waveguide power meter," *Proc. 10th Int. Symp. Space Terahertz Technology*, Charlottesville, VA, March 16–19, 1999, pp. 501–507.
- [18] A. V. Räisänen, "Frequency multipliers for millimeter and submillimeter wavelengths," *Proc. IEEE*, vol. 80, no. 11, pp. 1842–1852, Nov. 1992.

Injection locked self-oscillating mixers for terahertz focal plane arrays

W.S. Truscott, A.I. Milne and H. Cantu

School of Electrical and Electronic Engineering
University of Manchester
P.O. Box 88
Manchester, M60 1QD

w.truscott@manchester.ac.uk

Terahertz imaging based on space-borne focal plane arrays has many potential applications. The challenge in implementing such arrays is the requirement for sufficient local oscillator power to achieve good conversion efficiency and noise figures from a large number of mixers. An attractive solution to this problem is the use of self-oscillating mixers which are injection locked to single local oscillator that provides a weak drive to each mixer.

We have already reported injection locking of room-temperature oscillations in structures in which a number of resonant tunneling diodes are connected at regular intervals to a transmission line. The use of resonant tunnelling diodes in these structures offers the possibility of extending their operation towards 1 THz, particularly because many of the parasitics become part of the transmission line structure. This paper reports the further work in which the conditions for these circuits to be used as mixers has been explored. Our results show many interesting features: in particular injection locking and mixing have been observed experimentally with very low levels (<-20 dBm) of local oscillator signal.

The use of such mixers poses some interesting problems which we have investigated using a number of theoretical models. The results of these will be discussed in this paper. The natural oscillation frequency of a transmission line with several (4 - 10) active devices is close to its cut-off frequency. As a result the structure shows strong dispersion and a very low effective impedance. The use of these structures as mixers requires that the self-generated local-oscillator signal and the received signal have similar relative phases on all active devices. In the presence of strong dispersion the range of frequencies for which this is true is severely limited. In a similar way the very low impedance of the structure makes effective matching of the received signal to it difficult. A solution to both these problems is to operate the structure at a frequency significantly ($\sim 5\%$) below that of the natural oscillations. This results in a considerable reduction of the problems associated with bandwidth and impedance matching, but requires greater injection-locking power.

A second issue with the application of these structures as mixers is the current-voltage characteristic of the resonant tunnelling diodes. It is possible for a diode to have a negative resistance characteristic, and hence generate the required oscillations, without having the quadratic features that are necessary to achieve good mixing behaviour. This is particularly a problem with diodes operated at room temperature and with those where series resistance is significant.

The paper will present estimates for the potential performance, both in terms of conversion efficiency and the required injection locking power, over a range of frequencies up to 1 THz.

Multiplier Development for the Upper ALMA Local Oscillator Bands

Jeffrey L. Hesler, W.L. Bishop & Thomas W. Crowe

Abstract— A series of broadband tunerless frequency multipliers applicable for use as local oscillators on the Atacama Large Millimeter Array (ALMA) have been successfully developed. These multipliers are based on GaAs Schottky barrier planar diodes, which are mechanically rugged and repeatable, and thus well suited for use on an array like ALMA. For ALMA Band 9, a cascaded pair of broadband triplers to 600-720 GHz has been successfully demonstrated, and with a drive power of 100 mW over the input range 66.7-80 GHz an output power of 30-40 uW has been achieved at ambient temperature. Preliminary cooled measurements of the cascaded triplers indicate an improvement of more than a factor of 2 upon cooling to 80K, and so these results are a very successful demonstration. The ultimate goal of this research is to create a technology base that expands the use of the terahertz spectrum to more routine but equally important scientific and military measurements, and in the longer term to enable a wide range of commercial applications.

Index Terms—Submillimeter-wave sources. Frequency Multiplier. Frequency Tripler. Spectral Measurements.

I. INTRODUCTION

THE Atacama Large Millimeter Wave Array (ALMA) requires electronically tunable sources covering the range from 100 GHz to 1000 GHz with individual bandwidths of up to 25%. These sources must be compact, rugged and reproducible in large (> 100) quantities in order to successfully meet the scientific needs of the ALMA project. This paper discusses the successful development of local oscillator sources applicable to the ALMA project.

The ALMA local oscillator sources rely on a combination of MMIC amplifiers (up to roughly 110 GHz) combined with frequency multipliers used to extend the frequency range up to 1000 GHz. The development of the MMIC amplifiers has been carried out by the National Radio Astronomy Observatory Central Development Laboratory (NRAO-CDL), located in Charlottesville, VA, USA. The development of the millimeter- and submillimeter-wave multipliers is being carried out at Virginia Diodes Inc. (VDI), also located in Charlottesville, VA, USA.

Previous research at VDI has resulted in the successful development of triplers for both ALMA Band 6 (211-275 GHz) and Band 7 (275-370 GHz). These multipliers are based on GaAs Schottky barrier planar diodes, which are mechanically rugged and repeatable, and thus well suited for a large array like ALMA. These triplers exhibited an efficiency of approximately 3% at drive powers ranging

from 10-20 mW, thus providing more than sufficient LO power for the SIS receivers. A quantity of over 120 Band 6 and 120 Band 7 multipliers were produced and fully characterized in a period of roughly 4 months. These multipliers are now being successfully integrated with the amplifiers at the NRAO-CDL for use in the ALMA receiver cartridges.

This paper will discuss the development of broadband local oscillators for use on the higher frequency ALMA bands, in particular ALMA Band 9, covering the frequency range from 600 GHz to 720 GHz. The development and characterization of both a cascaded doubler-tripler and tripler-tripler will be presented. Such issues as harmonic content and cryogenic performance will be discussed.

II. CASCADED DOUBLER-TRIPLER

A. Review Stage

One multiplier combination that has been considered for use with ALMA Band 9 is a cascaded doubler-tripler combination. Both the WR-4.3X2 doubler and the WR-1.5X3 tripler are standard VDI components, with typical efficiencies of 10% and 2%, respectively. With an input drive power of 30-40 mW over the band 100-120 GHz the expected output powers are 3-4 mW out of the doubler and 60-80 uW out of the tripler. Figure 1 shows the actual measured performance for several sextupler designs. The power level over most of the band matches the expected power level, but there are ripples in the power, and drop-

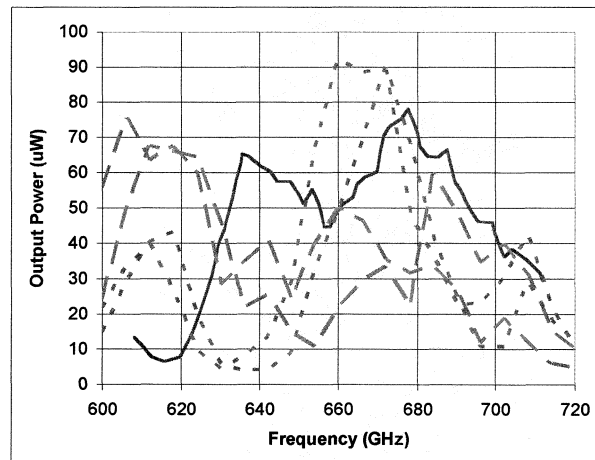


Fig. 1. Performance of cascaded WR-4.3X2 + WR-1.5X3 multipliers for three separate lengths of intervening waveguide. The spacings between the doubler and tripler are approximately 4.6 wavelengths for the solid curve, 3.5 wavelengths for the dashed curves, and 2.8 wavelengths for the dotted curves.

outs over part of the band. The standing wave is caused by interactions between the doubler and tripler, and so measurements were made using different spacings between these multipliers. The different curves in Figure 1 correspond to different physical lengths of waveguide between the doubler and tripler. In all of the cases there are significant nulls in the output power caused by standing waves between the multipliers. Also, the performance in the nulls was not found to improve significantly upon cooling, and thus it was necessary to determine a means to overcome this difficulty.

In order to better understand the source of the problem, measurements were performed on the return loss of the broadband triplers. Figure 2 shows the measured return loss for a standard WR-3.4X3 broadband tripler. The performance of the WR-1.5X3 used to produce the results in Figure 1 is expected to be very similar. As can be seen in the graph, as the input drive power becomes low (below approximately 5 mW) the return loss worsens dramatically for this tripler design. For the sextupler to 600-720 GHz described above the return loss of the tripler is expected to be as poor as 3-4 dB, and so the measured ripples in Figure 1 are consistent with this behavior.

In order to overcome this problem of poor return loss for low drive powers a new series of multipliers was developed for operation at ultra-low input drive. Fig. 2 shows the

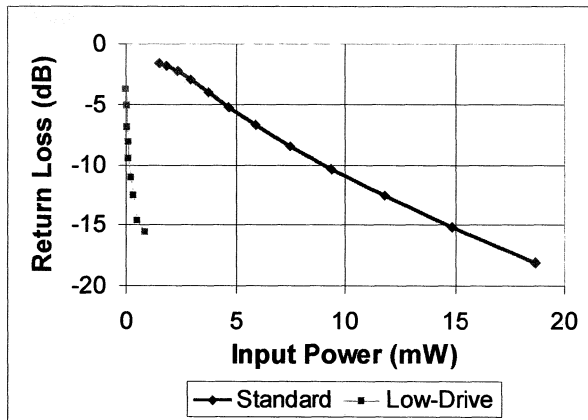


Fig. 2. Measured return loss for typical standard tripler and also for a low-drive tripler.

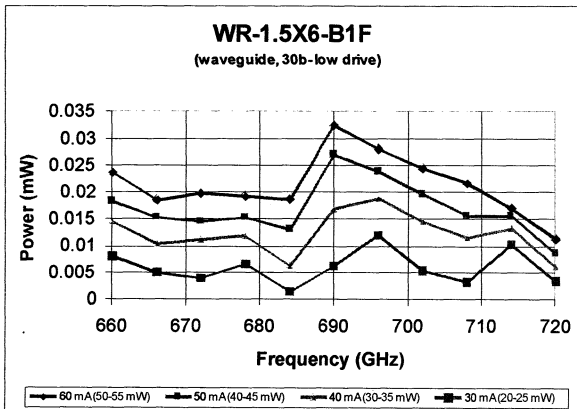


Fig. 3. Measurements of a broadband sextupler using a low-drive tripler.

measured return loss for a prototype WR-9.3X3 low-drive

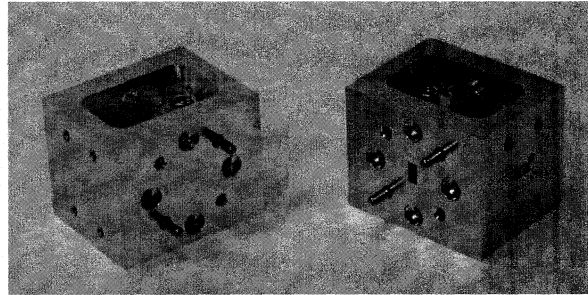


Fig. 4. Photograph of two WR-1.5X9 blocks (showing output side and input side). The WR-1.5X9 consists of a WR-4.3X3 tripler (170-265 GHz) integrated with a WR-1.5X3 tripler (500-750 GHz) into the same block housing.

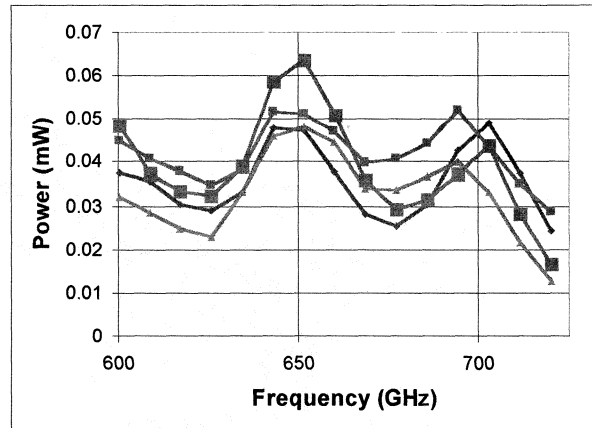


Fig. 5. Measured data for four identical-builds of WR-1.5X9 blocks.

broadband tripler. As shown in the graph, the return loss is still very good even for a drive power below ¼ mW. A batch of low-drive triplers was fabricated to cover the WR-1.5 band, and the test results for these devices are shown in Figure 3. Even for very low drive powers the sextupler is still performing well, and gives flat performance over the band, demonstrating the dramatically reduced standing-waves between the components. Subsequent cooled measurements performed at NRAO-CDL indicated an improvement of nearly a factor of 2 upon cooling to 80 K, and the output power was well above the required 20 uW over the entire band. However, because of concerns about the lifetime of the InP MMIC amplifiers required to produce the drive power (30-40 mW from 100-120 GHz), it was decided best to look into an alternate path, a cascaded tripler-tripler.

III. CASCADED TRIPLER-TRIPLER

Figure 4 shows a picture of a WR-1.5X9 multiplier, which consists of a WR-4.3X3 tripler integrated into the same housing with a WR-1.5X3 tripler. The input drive band to the multiplier is from 67-80 GHz, and it is assumed that an input drive power of 100 mW will be available at the multiplier input. The WR-4.3X3 has an efficiency of 3-4%, and so the power delivered to the WR-1.5X3 will be 3-4 mW. A low-drive tripler was used in the WR-1.5X3 tripler to avoid standing waves. The efficiency of the low-drive WR-1.5X3 tripler is in the range 1%, yielding an expected output power at room temperature of 30-40 uW. The

measured output power for several identical WR-1.5X9 blocks are shown in Figure 5, and indicate that the multipliers are working as expected.

One important consideration for the overall multiplier design is the analysis and minimization of unwanted harmonics. A graph of the frequency bands for the various harmonics for a tripler-tripler to ALMA Band 9 is shown in Figure 6, where the base harmonic N=1 covers 67-80 GHz, and the desired harmonic is N=9 covering 600-720 GHz. There are three waveguides to consider: 1) the input to the first tripler, 2) the waveguide between the triplers, and 3) the output waveguide. In the graph two different output waveguide sizes, WR-1.5 (500-750 GHz) and WR-1.2 (600-900 GHz) are shown to allow comparison between them, as discussed below.

In looking at the graph, it can be seen that any fifth harmonic output from the first tripler (N=5) will be blocked by the output waveguide over nearly the entire band, even with the larger WR-1.5 waveguide (TE10 cutoff 393 GHz), so this harmonic is not an issue. Another harmonic to

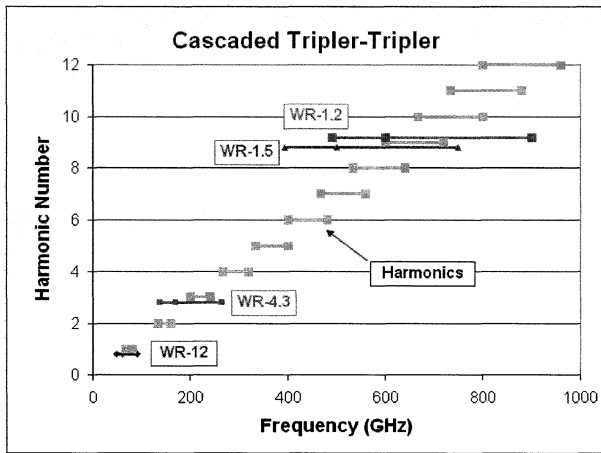


Fig. 6. Harmonic Design for a cascaded Tripler-Tripler to ALMA Band 9 (600-720 GHz). The light blue lines show the frequency ranges for the various harmonics of the input drive (100-120 GHz). The other lines show the range for the various waveguides in the cascade (the TE10 cutoff frequency, then recommended lower and upper band edges).

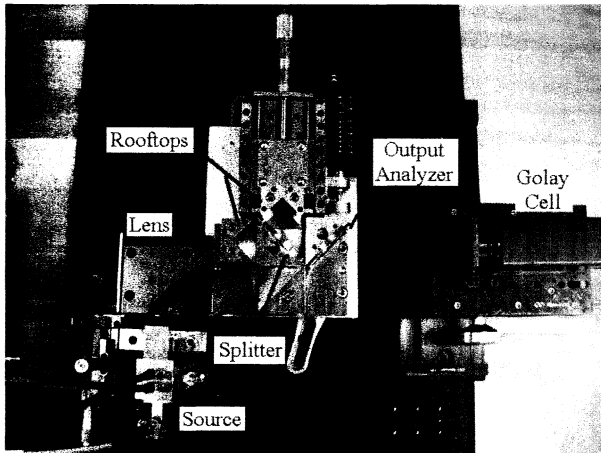
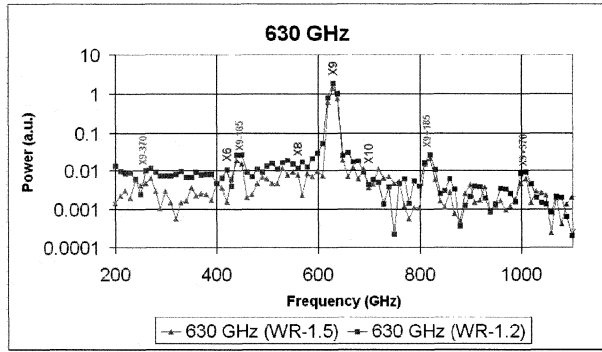
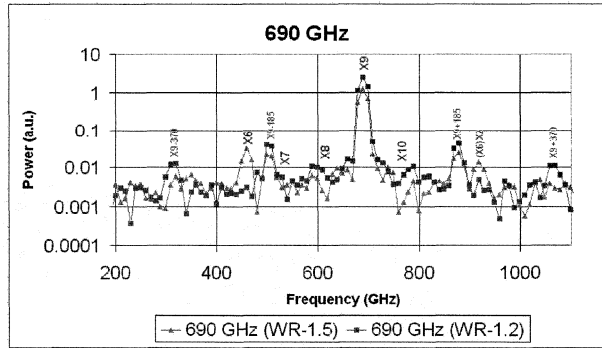


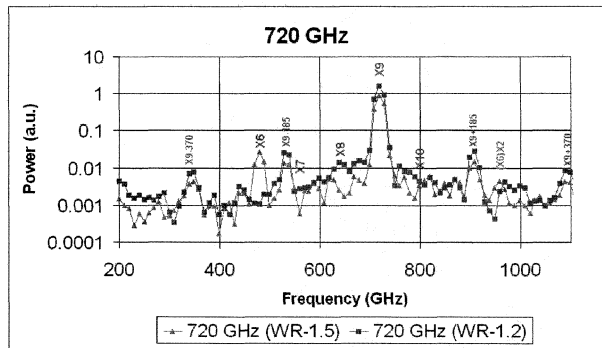
Fig. 7. Martin-Puplett interferometer used for spectral measurements of the WR-1.5X9. The micrometer has a stage wobble at 0.4 mm periodicity, which adds artifacts to the spectra at integer offsets of +/- 185 GHz from any strong tone.



(a)



(b)



(c)

Fig. 8 (a-c). Measured output spectra of the WR-1.5X9. The peaks marked in magenta are artifacts caused by stage wobble and quasi-optical system standing waves. The red curves are for blocks with WR-1.5 output, while the blue curves are for modified blocks with output waveguide equivalent to WR-1.2 (i.e. TE10 cutoff frequency of 492 GHz).

consider is the second harmonic content from the second tripler (i.e. the multiplication path X3-X2, N=6). For the WR-1.5 waveguide it is possible for this N=6 harmonic to propagate out the output waveguide. By switching to WR-1.2 waveguide (TE10 cutoff 492 GHz) it is possible to block this N=6 harmonic output. Other harmonics, for example the 7th, 8th and 10th, would be impossible to filter out if they are found to be present in the output, and so the suppression of these harmonics must rely on circuit balance.

The next issue to consider then is which harmonics are expected to be present in the output, and in what magnitude. Both of the triplers are balanced designs, and so even harmonics are suppressed by the inherent balance. The question then is what level of suppression is achieved for the present multiplier. A theoretical analysis of the harmonic content is possible, but because the presence of these

harmonics depend upon asymmetries, either electrical or in the embedding circuit, it is difficult to accurately predict their level. Previous measurements of the individual triplers have found that the even harmonics ($N=2, 4, \dots$) and higher odd harmonics (i.e. $N=5, 7, \dots$) are suppressed to a level 15-20 dB below the tripled output ($N=3$).

In order to gain a better understanding of the harmonic content of cascaded triplers, a polarizing Martin-Puplett diplexer was used to characterize the output spectrum. A picture of the spectrometer is shown in Figure 7. An input lens is used to collimate the power from the source, which then propagates through the interferometer. An output analyzer is then followed by a Golay cell that is used to detect the output signal. The source was electrically modulated using a coaxial SPST switch. There are two main sources of artifacts in this spectrometer. First, the stage translating the rooftop mirror has a wobble with a periodicity of 0.4 mm, effectively AM modulating the interferogram and producing "sidebands" on the output spectrum at integer multiples of 185 GHz above and below any tones present. A second artifact is caused by the presence of standing waves between the source and the detector, which produce artifacts at integer multiples of any tones present. These artifacts can be seen in the spectra shown in Figure 8. That these are artifacts and not true signals has been verified by a series of measurements on a variety of multipliers, as well as correlation of these results with measurements by other groups.

In looking at the measured spectra, the spectrum for an output frequency of 630 GHz (Figure 8(a)) shows that the only measurable signal is the desired 9th harmonic. The noise threshold for the measurement is approximately 25 dB below the desired output. If we look at the spectrum for an output frequency of 690 GHz (Figure 8(b)) with WR-1.5 waveguide (TE₁₀ cutoff 393 GHz) then it is possible to see the appearance of a 6th harmonic at a level approximately 15 dB below the main carrier. However, reducing the output waveguide size to WR-1.2 (TE₁₀ cutoff frequency of 492 GHz) chokes off the 6th harmonic. The measured output power for WR-1.5X9 with and without the WR-1.2 filter was measured to be the same. Figure 8(c) shows that the 6th harmonic has been successfully suppressed all the way to the upper edge of the band, 720 GHz. One final question is whether the 6th harmonic signal is generated by a doubling of the $N=3$ harmonic, or by a tripling of the $N=2$ harmonic. To determine this a similar measurement was performed with WR-1.5 output waveguide and WR-3.4 intermediate waveguide. In this case the 6th harmonic was still present in the output indicating that the path is indeed X3-X2, and not X2-X3.

IV. CONCLUSION

This paper has described the successful development a cascaded pair of broadband triplers, the WR-3.4X3 + WR-1.5X3, for use on ALMA Band 9, covering the frequency range from 600-720 GHz. With a drive power of 100 mW over the input range 66.7-80 GHz an output power of 30-40 uW has been achieved at ambient temperature. Preliminary cooled measurements of the cascaded triplers indicate an improvement of more than a factor of 2 upon cooling to 80K, and so these results are a very successful

demonstration for use with ALMA Band 9. In addition, research is now underway on the development of multipliers for ALMA band 10, covering 787-950 GHz. A tripler-tripler has been successfully testing with an output power of 15-20 uW when driven by an input power of 60-75 mW.

These sources are not only applicable to the ALMA project, but to a wide range of scientific and commercial applications. The ultimate goal of this research is to create a technology base that expands the use of the terahertz spectrum to more routine but equally important scientific and military measurements, and in the longer term to enable a wide range of commercial applications.

ACKNOWLEDGMENT

The authors thank K. Saini and D. Thacker of the NRAO Central Development Laboratory for performing the cryogenic measurements of the multipliers.

POSTER SESSION n°2

Presentation on
Friday 12 May 09:00-09:30

by Dr. Heribert Eisele & Dr. Imran Mehdi

Poster session n°2 from 11:00 to 12:30

Design & test of a 380 GHz sub-harmonic mixer using American and European Schottky diodes

Bertrand Thomas, Byron Alderman, David Matheson and Peter de Maagt

Abstract— We present here the development of a broadband fixed-tuned 360–400 GHz sub-harmonically pumped mixer, featuring an anti-parallel pair of planar Schottky diodes from VDI (Virginia Diodes Inc.). Simulations show that replacing the VDI discrete device by an optimized anti-parallel pair of planar Schottky diodes based on the BES fabrication process of UMS (United Monolithic Semiconductors) onto the same circuit would lead to similar performances. A comparison between the expected performances of both devices used with the same mixer circuit is presented. Measurements on a prototype featuring VDI diodes exhibit best DSB mixer noise temperature of 950 K and conversion losses of 8.5 dB at 380 GHz.

Index Terms— Submillimetre wave receiver, sub-harmonic mixer, planar Schottky diodes.

I. INTRODUCTION

In the framework of future ESA missions dedicated to the remote sensing of the Earth atmosphere in the millimetre and submillimetre wave domain [1], several frequency bands up to at least 380 GHz are highlighted as key priority for the development of highly integrated heterodyne receivers exhibiting high sensitivity at room temperature over a broad instantaneous bandwidth.

In that context, we report here on the development of a broadband fixed-tuned 360–400 GHz sub-harmonic mixer, featuring an anti-parallel pair of planar Schottky diodes. The simulated performances of the designed mixer circuit using two different models of an anti-parallel pair of planar Schottky diodes are presented, and compared with measurements on a prototype fabricated and tested.

II. DESIGN OF THE 380 GHz SUB-HARMONIC MIXER

The design of the 360–400 GHz fixed-tuned sub-harmonic mixer is presented in Fig.1. It features an anti-parallel pair of planar Schottky diodes flip-chip mounted and silver-epoxy glued onto a quartz-based microstrip circuit. The 50 μm thick quartz circuit is then directly reported and glued inside

the microstrip channel. A gold beam-lead is formed at the RF end during the circuit fabrication, providing a precise grounding of the diode pair at IF/DC frequencies. The LO/RF waveguides, the microstrip channel and the IF connector socket are milled into two split-waveguide metal blocks. A diagonal horn antenna, similar to [2], is also integrated to the mixer block.

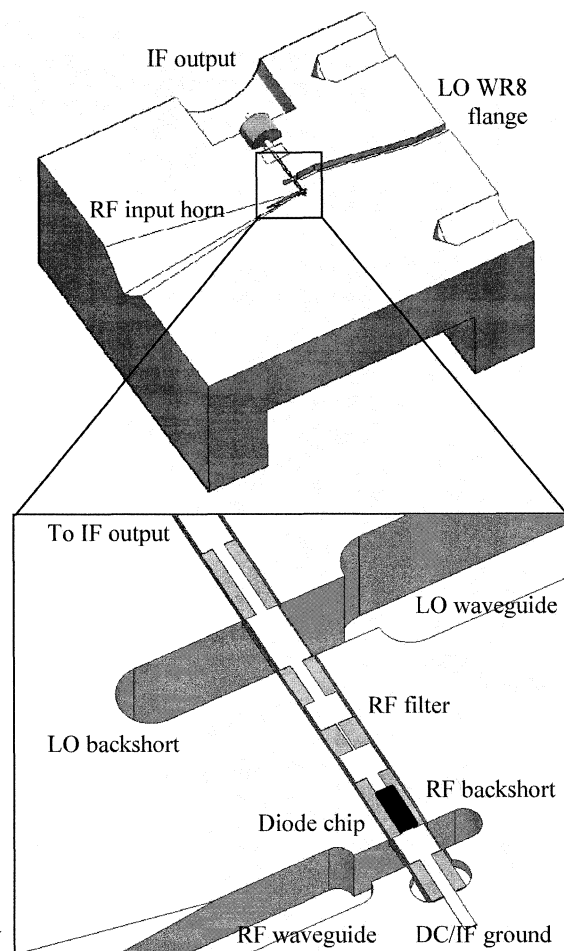


Fig.1. Schematic view of the 380 GHz SHP mixer circuit mounted into the lower half of the mechanical waveguide split block. The circuit has been optimized for best performances with an anti-parallel pair of planar Schottky diodes from VDI.

The mixer circuit has been initially designed to incorporate an anti-parallel pair of planar Schottky diodes from VDI (Ref. SC1T9-D20). However, a study in collaboration with the LERMA department at the Observatory of Paris has been done to test the mixer design using a novel anti-parallel pair of planar Schottky diodes compatible with the BES process

Manuscript received May 11, 2006. This work has been carried out at the Space Science & Technology Department of the Rutherford Appleton Laboratory and was funded in part by the European Space Agency under contract number 16142/02/NL/EC.

B.Thomas, B.Alderman and D. Matheson are with the Rutherford Appleton Laboratory, Chilton Didcot, OX11 0QX Oxfordshire, UK (contact phone: 1235-446343; fax: 1235-445848; e-mail: b.thomas@rl.ac.uk).

P. de Maagt is with the ESA/ESTEC, Keplerlaan 1, Postbus 299, 2200 AG Noordwijk, the Netherlands.

of the company UMS. The structure has been optimized by the LERMA for operation at 380 GHz and tested in simulation inside the mixer model developed at RAL. The novel designed pair of diodes does not include air-bridges, on the contrary of VDI diodes. Fig. 2a&b show both components' 3D model with their physical and electrical characteristics.

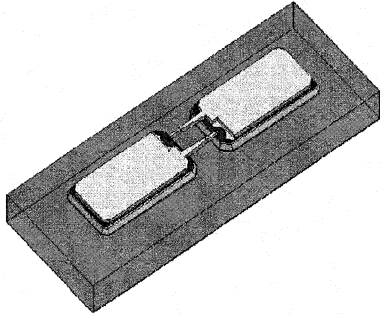


Fig.2a. Schematic view of the planar Schottky diodes from VDI (Ref. SC1T9-D20). The chip includes two air-bridges. Electrical parameters are: $R_s=10 \Omega$, $\eta=1.25$, $C_{j0}=2.5 \text{ fF}$, $I_{\text{sat}}=30 \text{ fA}$, $V_{\text{bi}}=0.8 \text{ V}$, $A=1.76 \mu\text{m}^2$.

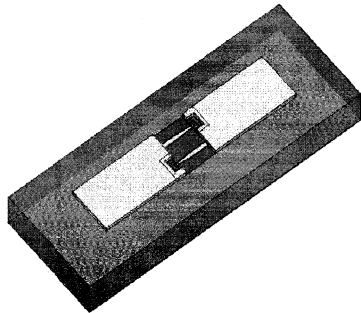


Fig.2b. Schematic view of the planar Schottky diodes based on the BES process from UMS. The chip has no air-bridge. Electrical parameters are: $R_s=10 \Omega$, $\eta=1.2$, $C_{j0}=2 \text{ fF}$, $I_{\text{sat}}=4 \text{ fA}$, $V_{\text{bi}}=0.85 \text{ V}$, $A=1.5 \mu\text{m}^2$.

III. DESIGN METHODOLOGY AND COMPUTED PERFORMANCES

The methodology used to design and optimize the mixer circuit uses a combination of linear/non-linear circuit simulations (Ansoft Designer [3]) and 3D EM simulations (Ansoft HFSS [3]) and is described in detail elsewhere [4]. From a first set of non-linear simulations of the diodes pair, considering an optimum LO power level of 1.5 mW, ideal embedding impedances of approx. $Z_{RF}=47+j.46$ at RF frequencies and $Z_{LO}=63+j.121$ at LO frequencies are found for the VDI diodes. The IF load impedance is set to 100Ω . Then, the microstrip circuit, as well as the fixed backshort positions and the waveguide-to-microstrip transition, are optimized to synthesize an embedding impedance as close as possible to these values. Additional losses from the horn antenna ($\approx 1\text{dB}$) and the IF mismatch with the first LNA ($\approx 1\text{dB}$) have been taken into account during the simulations.

The simulated performances of a SHP mixer using VDI and UMS-like diodes are presented in Fig.3. Despite the fact that they appear to be fairly similar, the centre frequency of the mixer using UMS-like diodes is slightly shifted towards 370 GHz, compared to the optimal centre frequency of 380 GHz

obtained using VDI diodes. This difference is attributed to slightly superior parasitic capacitance exhibited by the UMS-like diodes. A slight re-optimisation of the mixer circuit using UMS-like diodes would be necessary to achieve the optimal 360-400 GHz bandwidth.

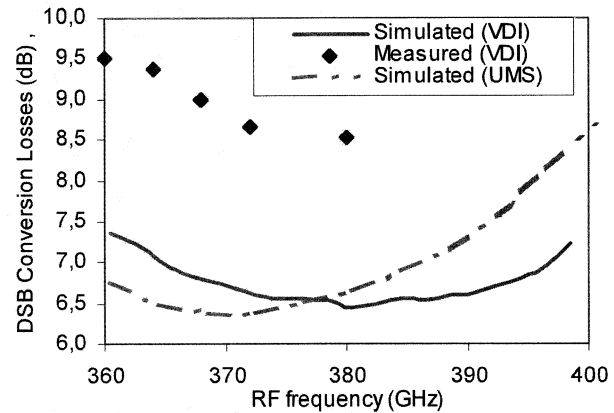


Fig.3. Predicted DSB conversion losses of the 380 GHz SHP mixer designed to incorporate an anti-parallel pair of Schottky diodes from VDI (full curve), along with the predicted performances of a similar mixer circuit incorporating UMS-type anti-parallel pair of planar Schottky diodes (dashed curve). Measured mixer conversion losses using a VDI diodes pair are shown (dots) for comparison.

IV. TEST OF THE 380 GHz FIXED-TUNED RECEIVER INCLUDING THE SUB-HARMONIC MIXER

In order to pump the subharmonic mixer using a fundamental Gunn oscillator source, a 190 GHz fixed-tuned doubler using an anti-series pair of 6 planar Schottky Varactor diodes from VDI has been developed in the framework of this project, and is described elsewhere [5]. The 190 GHz doubler is pumped by a Gunn oscillator from Carlstrom, which outputs 100 mW of LO power between 84 GHz and 92 GHz, and drops below 60 mW for frequencies above 96 GHz. The output power of the doubler reaches a maximum of 7 mW at 176 GHz and outputs an LO signal with a power greater than 2.8 mW between 172 GHz and 190 GHz. The power levels are measured with a PM3 Erickson power meter [6].

The complete 380 GHz fixed-tuned receiver including the 190 GHz fixed-tuned doubler and the 380 GHz fixed-tuned sub-harmonic mixer has been assembled and tested, as shown in Fig. 4a&b. The doubler is fed by a Gunn diode source followed by a variable attenuator. No isolator is inserted between the doubler and the mixer in order to maximize the available LO power. The IF signal is amplified by a low noise amplifier (1st LNA from Miteq) chain including a band-pass filter in between 2.5 GHz and 3.5 GHz. The output signal of the amplifier chain is measured using a HP 8481A power sensor.



Fig.4a. Detail of the 380 GHz mixer microstrip circuit mounted into the lower half of the mixer block. The mixer circuit includes an anti-parallel pair of planar Schottky diodes from VDI, flipped-chipped and silver-epoxy glued onto the quartz based circuit.

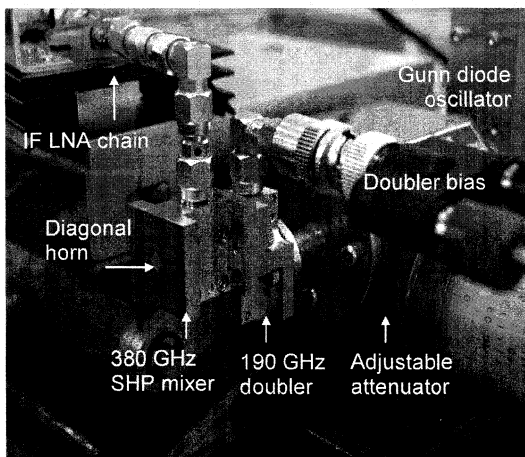


Fig.4b. View of the test setup showing the 190 GHz fixed-tuned doubler connected to the 380 GHz fixed-tuned SHP mixer. A waveguide attenuator is inserted between the doubler and the Gunn oscillator. The IF signal from the SHP mixer is output to a LNA IF chain.

The measured performances of the receiver including the mixer noise temperature are presented in Fig. 5. The best mixer performance is obtained at 380 GHz, with DSB receiver noise temperature of 1693 K. Varying the IF LNA noise temperature from 100 K to 450 K allows to calculate a corresponding DSB mixer noise temperature of 950 K and DSB mixer conversion losses of 8.5 dB. The measured mixer conversion losses are given in Fig.3, and can be compared with the predictions. The DSB mixer noise temperature remains below 1200 K between 360 GHz and 380 GHz. The amount of power required to pump the mixer between 360 GHz and 380 GHz is estimated between 2 mW and 3.5 mW.

Further tests using a more powerful fundamental source above 95 GHz will be necessary to characterise the mixer up to 400 GHz. The performances are indeed expected to be flat up to 400 GHz, as suggested by the results in simulations (Fig.3).

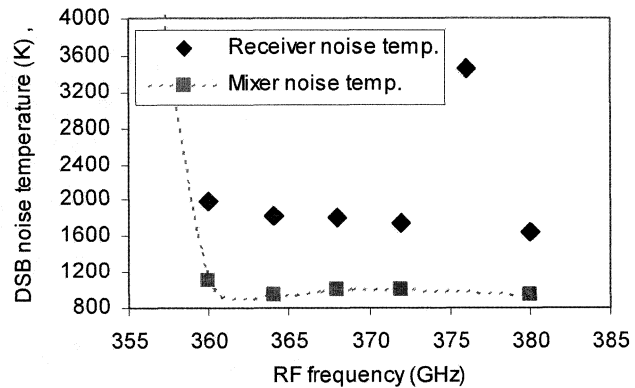


Fig.5. Measured DSB receiver and mixer noise temperature VS frequency. Degradation in the receiver noise temperature noticeable at 376 GHz is due to a sharp resonance in the LO signal coupling between the doubler and the mixer. Inserting an isolator between the mixer and the doubler would cancel the resonance.

V. CONCLUSION

The design, fabrication and test of a 380 GHz fixed-tuned mixer is presented. The mixer circuit has been designed for VDI diodes, but simulations show that using an optimized pair of planar Schottky diodes compatible with the BES process of UMS would give similar performances, providing a useful bench-mark for discrete American and European planar Schottky diodes. Measurements performed on a mixer using planar diodes chip from VDI give excellent performances, in accordance with the simulations.

ACKNOWLEDGEMENTS

The authors wish to thank Dr. Alain Maestrini and the LERMA department at the Observatory of Paris for their assistance and support. Professor T.W. Crowe is also acknowledged for supplying high quality diodes.

REFERENCES

- [1] U. Klein, C.C. Lin, J. Langen and R. Meynart, "Future Satellite Earth Observation Requirements in Millimetre and Sub-Millimetre Wavelength Region", *Proceedings of the 4th ESA workshop on Millimetre-Wave Technology and Applications*, Espoo, Finland, 15-17 February 2006.
- [2] J. Johansson and N.D. Whyborn, "The Diagonal Horn as a Submillimeter Wave Antenna", *IEEE Transactions on Microwave Theory and Techniques*, Vol. 40, No. 5, pp.795-800, May 1992.
- [3] Ansoft Designer V2.1 & Ansoft HFSS V10, Ansoft Corporation, 225 West Station Square Drive, Suite 200, Pittsburg, PA 15219, USA.
- [4] J. Hesler, K. Hui, S. He and T. Crowe, "A fixed-tuned 400 GHz subharmonic mixer using planar Schottky diodes," *Proceedings of the 10th International Symposium on Space Terahertz Technology*, Charlottesville, pp. 95-99, March 1999.
- [5] B. Thomas, B. Alderman, D. Matheson and P. de Maagt, "A fixed-tuned 380 GHz Schottky-based mixer and frequency doubler combination using aluminium nitride & quartz substrates", *Proceedings of the 4th ESA workshop on Millimetre-Wave Technology and Applications*, pp.547-552, Espoo, Finland, February 2006.
- [6] N.R. Erickson, "A fast and sensitive submillimeter waveguide power meter", *Proceedings of the 10th Int. Symp. on Space THz Technology*, Charlottesville, pp. 501-507, 1999.

A Low Noise Integrated Sub-Harmonic Mixer at 183GHz

Jean-Marc Rollin¹, Hui Wang², Bertrand Thomas³, Alain Maestrini^{4&2} and Steven Davies¹

¹ Department of Physics, University of Bath, Bath, BA2 7AY, UK.

² LERMA, Observatoire de Paris, 61 avenue de l'Observatoire, 75014 Paris, France.

³ Rutherford Appleton Laboratory, Chilton Didcot, Oxfordshire, OX11 0QX, UK.

⁴ LISIF - Université Paris 6, 4 place Jussieu, case 252, 75252 Paris cedex 5, France.

Abstract

Low-loss, heterodyne detection systems operating at terahertz frequencies are essential for applications in atmospheric remote sensing. Such applications need good quality air-bridged Schottky diodes for use in heterodyne mixers and multipliers. Sub-harmonic Schottky diode mixers are key components of these receivers since they provide high spectral resolution and good sensitivity at room temperature.

Conventional technology relies on the ability to flip-chip solder a diced diode chip onto a quartz wafer carrying filter metallisation. Successful flip-chip bonding requires highly specialised skills, is difficult to do well and inevitably introduces additional parasitic losses into the circuit.

This paper describes the development of integrated devices, whereby an anti-parallel pair of planar Schottky diodes is integrated with the associated filter metallisation, monolithically fabricated on a 50 μ m-thick GaAs substrate. The Schottky diodes are air-bridged to reduce the parasitic capacitance of the diode structure. Diodes with anode diameters of approximately 1 μ m have been fabricated, resulting in idealities, $\eta \sim 1.15$ and series resistances, $R_s \sim 15\Omega$.

The diode structure has been designed to operate in a fixed-tuned, reduced-height, crossed-waveguide mixer block. The mixer layout has been optimised using a combination of three dimensional electromagnetic and circuit simulations. The MMIC circuit is about 4 mm long, 0.28 mm wide and will be mounted in a waveguide block that includes matching elements inside the Local Oscillator (LO) and RF waveguides. The mixer is expected to operate in the band 160-190 GHz with a double side band (DSB) conversion gain greater than -6 dB when pumped with 2 mW of Local Oscillator (LO) power. A minimum DSB gain of -5.2 dB and a DSB noise temperature of 500 K are expected at 183 GHz.

The precision mixer block has been machined in the machine shop of RAL. The testing of the 183 GHz mixer is currently taking place.

Design of a 400 GHz Schottky Mixer for High-Performance Operation

José V. Siles, Jesús Grajal, and Viktor Krozer

Abstract— In this work we present the design of a 400 GHz Schottky diode mixer for high performance operation. In order to achieve a proper design a full and joint optimization of both the external circuit and the internal structure of the Schottky diode is performed. Two possible mixer topologies are analyzed: A fundamental mixer and a subharmonically-pumped (SHP) antiparallel diode pair mixer. The advantages and disadvantages of both topologies are discussed. The final results exhibit a single-side band (SSB) conversion loss of 8.6 dB @ 0.4 mW of LO power for the 400 GHz fundamental mixer and 10.3 dB @ 0.8 mW LO power for the 400 GHz SHP mixer, when parasitics are tuned-out. However, if parasitics are not tuned out, an increase in the required LO power is necessary for minimum conversion loss.

Index Terms— CAD, harmonic balance, submillimeter-wave technology, Schottky diode mixers, subharmonically-pumped mixers.

I. INTRODUCTION

This work deals with the design and full optimization of a 400 GHz Schottky diode-based mixer employing a numerical in-house CAD tool that combines an accurate physics-based numerical model of the Schottky diode with an external circuit simulator by means of accurate multi-tone harmonic balance techniques [1]. The diode model incorporates accurate boundary and interface conditions for self-consistent treatment of tunnelling transport, image-force effects and impact ionization. The simulator accounts for limiting mechanisms such as avalanche breakdown, velocity saturation, and increase in the series resistance with the input power. A further description of this CAD tool can be found in [1]-[2].

In order to achieve a high-performance 400 GHz mixer, the optimization of the Schottky mixer performed in this work includes all possible aspects that can be accounted for within the context of mixer design: Input and output matching networks, influence of bias, required LO power, image enhancement, effect of parasitics, mixer sensitivity to input and output mismatches and influence of the Schottky diode characteristics (anode area, length of each layer, doping profile, series resistance, etc.). But all these parameters cannot be individually treated. In this sense, the main advantage of our in-house CAD tool lies on the possibility to perform a joint optimization of both the external circuit and the internal structure of the semiconductor device.

Regarding the topology of the 400 GHz Schottky mixer, two options have been considered and analyzed: A single-diode fundamental mixer and a SHP antiparallel-diode pair mixer. The block diagrams of the analyzed circuits for these

two topologies are presented in Fig. 1. Antiparallel-diode pair SHP mixers have the advantage of the current cancellation at even order harmonics and intermodulation products of the LO and RF frequencies. This leads to two important results. On the one hand, the DC current cancellation makes SHP mixers to experiment an important noise reduction in comparison to fundamental mixers [3]. On the other hand, matching networks are much easier to implement as there is no need to take into account the impedances at those frequencies at which current cancellation occurs. However, SHP mixers demand 3 dB more LO power than fundamental mixers and have around 1-2 dB higher conversion losses [4].

A brief comparison between simulations performed with our in-house physics-based numerical CAD tool and measurements from the SHP mixer described in [5] will be also held for validation purposes.

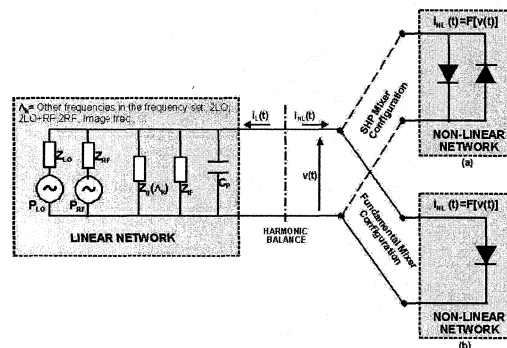


Fig. 1. Block diagram of the analyzed circuit for a SHP antiparallel diode pair (a) and a fundamental Schottky mixer (b).

II. DESIGN OF THE 400 GHz FUNDAMENTAL MIXER

It is well-known that the optimization of any of the parameters of a submillimeter-wave Schottky mixers has an influence on the optimum values of the rest of design parameters. Therefore, the joint optimization of them all is required to obtain the highest performance in the final mixer circuit. As the maximum input LO power available is limited to the state-of-the-art solid-state power sources at submillimeter-wave bands, a good methodology of design and optimization might consist of the following: The selection of the optimum bias voltage and epilayer length for each different doping level in order to find the most appropriate set of parameters to get the minimum

This work was supported by the Spanish National Research and Development Program under project number TEC2005-07010-C02-01/TCM.

José V. Siles and Jesús Grajal are with the Department of Señales, Sistemas y Radio-comunicaciones of the Universidad Politécnica de Madrid, E.T.S.I. Telecomunicación, Ciudad Universitaria s/n, Madrid, E-28040 SPAIN (phone: +34 91-336-73-58; fax: +34 91-336-73-62; e-mail: jovi@gmr.ssr.upm.es).

Viktor Krozer is with Orsted-DTU Technical University of Denmark, Orsted Plads, bdg. 348, DK-2800 Kgs. Lyngby (DENMARK)

conversion loss. This is because the higher the doping is, the shorter the space charge region of the Schottky diode is and, as a consequence, the optimum bias and epilayer length may vary. Of course, input and output impedances must be optimized as well for all the cases. This task is automatically performed by the design tool at every analyzed LO power.

Fig. 2 shows the influence of the bias voltage in the performance of the 400 GHz Schottky mixer for $2 \cdot 10^{17} \text{ cm}^{-3}$ doping in the epitaxial layer. It can be depicted that lower LO power levels are required when the bias is increased. The LO and RF impedances are conjugate-matched at each LO power in all the cases unless otherwise specified. The best results are obtained at 0.6 Volts. The effect of the doping level on the conversion loss is presented in Fig. 3. The increase in the doping makes longer the undepleted region of the epilayer so an increase in the LO power is required for minimum loss. There is no velocity saturation effects at 400 GHz, which can be noticed by the fact that the same conversion loss can be obtained with the appropriate LO power in all the cases. Therefore, low dopings ($1 - 2 \cdot 10^{17} \text{ cm}^{-3}$) are preferred as lower LO levels are necessary to get the best performance.

Furthermore, if the available LO power is fixed in advance, the curve of conversion loss can be shifted towards lower or higher LO powers to place the minimum at the available pump power. This can be done just by modifying the anode area of the Schottky diodes. Hence, a lower LO power will be needed for minimum loss if the area is reduced (Fig. 4). Besides, the change of the anode area modifies the optimum input and output impedance levels that in most of the cases leads to easier-to-built matching networks for lower areas. To exemplify this point, the optimum impedance values predicted by our CAD tool for a $2 \cdot 10^{17} \text{ cm}^{-3}$ doping at both LO and RF frequencies were $29 + j \cdot 31 @ A=5 \mu\text{m}^2$.

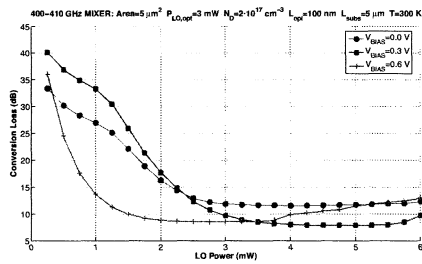


Fig. 2. Influence of bias in the single-side band (SSB) conversion loss of the 400 GHz fundamental mixer at room temperature. No parasitics have been considered ($C_p=0$ fF). IF optimized at 3 mW LO power.

It is obvious from Figs. 2 to 4 that there is a trade-off among the bias voltage, the doping and the anode area in order to get minimum conversion loss at a certain LO power level.

Another important aspect to be considered in the design process is the influence of parasitics in the mixer circuit. Although these parasitics can be tuned out with proper matching networks, the resultant impedances values required for these networks are usually difficult to synthesize in the practice. As an example, for the 400 GHz fundamental mixer with a $1 \mu\text{m}^2$

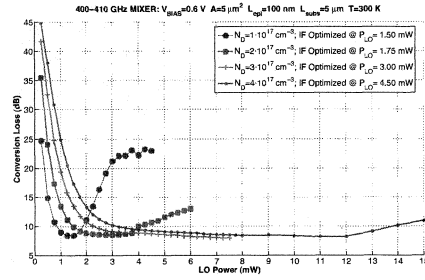


Fig. 3. Influence of epilayer doping in the SSB conversion loss of the 400 GHz fundamental mixer at room temperature. No parasitics have been considered ($C_p=0$ fF).

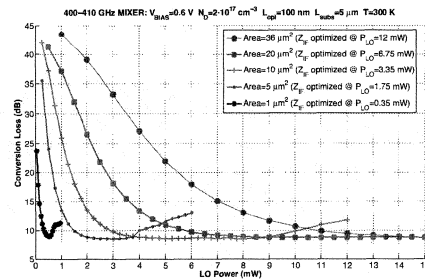


Fig. 4. Influence of anode area in the SSB conversion loss of the 400 GHz fundamental mixer at room temperature. No parasitics have been considered ($C_p=0$ fF).

anode area, the matched LO and RF impedances at 0.5 mW in absence of parasitics are $\sim 140 + j \cdot 150 \Omega$. For instance, if a 10 fF parasitic capacitance is present in the circuit, the matched LO and RF impedances that tune out this parasitic are $\sim 3 + j \cdot 30 \Omega$. Fig. 5 shows the effect of the parasitic capacitance in the mixer circuit when it has not been tuned out. The increase in the minimum conversion loss is due to RF input mismatches while the need for higher LO power levels is caused by LO input mismatches.

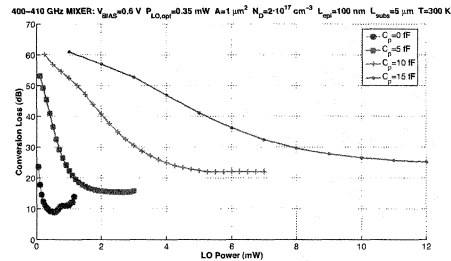


Fig. 5. Influence of the parasitic capacitance in the SSB conversion loss of the 400 GHz fundamental mixer at room temperature. IF optimized at $C_p=0$ fF and $P_{LO}=0.35$ mW.

The image enhancement that results of selecting a reactive impedance at the image frequency can be also evaluated by means of our mixer CAD tool. For the 400 GHz fundamental mixer, an improvement of 1.3 dB in the conversion loss has

been estimated.

The final results for the 400 GHz fundamental mixer exhibit a SSB conversion loss of 8.6 dB (7.3 dB including the image enhancement). These results corresponds to a $1 \mu m^2$ area, a $2 \cdot 10^{17} cm^{-3}$ epilayer doping and a series resistance $R_s = 84 \Omega$. The series resistance is numerically obtained by performing a DC analysis of the Schottky diode with our CAD tool. If the R_s of the Schottky diodes was reduced, for example by shortening the lengths of the its layers, an improvement in the SSB conversion loss will be obtained: 6.0 dB SSB conversion loss when $R_s = 25 \Omega$.

III. DESIGN OF THE 400 GHz SHP MIXER.

The design methodology of the 400 GHz SHP Schottky mixer is analogous to the one employed for the 400 GHz fundamental mixer. Thus, in this section we only present the most relevant results. Fig. 6 shows the influence of the epilayer doping in the performance of the SHP mixer. Again, lower doping levels are preferred at this frequency of operation. The influence of the anode area is also identical to the fundamental mixer case. If the area is divided by a factor 2, the curve of conversion loss shifts 3 dB towards lower LO powers.

It can be noticed in Figs. 6 and 7 that a 3 dB higher LO power is necessary to obtain minimum conversion loss for the SHP mixers as a consequence of using 2 diodes in antiparallel configuration instead a single diode. This also affects to the values of the impedances in the matching networks, which are different from those obtained for the fundamental mixer. This circumstance may sometimes represent an advantage in terms of impedance synthesization. The matched impedances levels when the SHP mixer is driven by the LO power level at which minimum conversion loss occurs are (for a $2 \cdot 10^{17} cm^{-3}$ doping and $A=5 \mu m^2$): $Z_{LO} = 20 + j \cdot 45 \Omega$ and $Z_{RF} = 16 + j \cdot 19 \Omega$.

The study of the influence of the parasitic capacitance has been omitted here, but the results are similar to those obtained for the 400 GHz fundamental mixer.

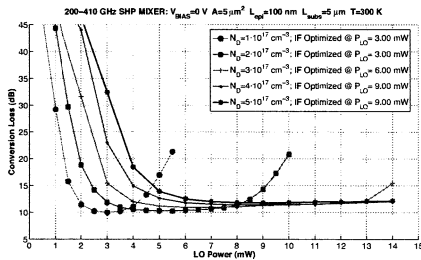


Fig. 6. Influence of epilayer doping in the SSB conversion loss of the 400 GHz SHP mixer at room temperature. No parasitics have been considered ($C_p=0$ fF)

IV. SHP MIXERS VS. FUNDAMENTAL MIXERS

A comparison between the performances of the 400 GHz fundamental Schottky mixer and the 400 GHz SHP antiparallel-diode pair mixer is provided in Fig. 8.

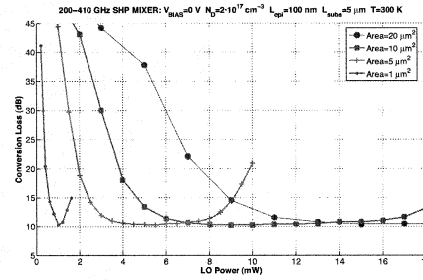


Fig. 7. Influence of anode area in the SSB conversion loss of the 400 GHz SHP mixer at room temperature. No parasitics have been considered ($C_p=0$ fF)

Although the optimum LO power is two times higher in the antiparallel-diode pair SHP mixer, pumping at half the LO frequency of the fundamental mixer may represent an important advantage at these frequency bands because the LO power provided by state-of-the-art solid-state sources decreases with the frequency [6].

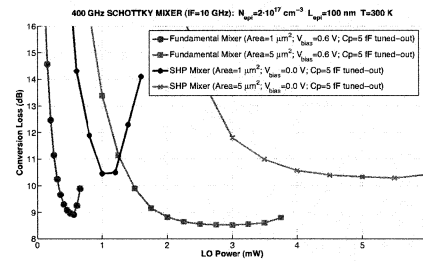


Fig. 8. Comparison between the performances of the 400 GHz fundamental Schottky mixer and the 400 GHz SHP antiparallel-pair Schottky diode mixer.

The minimum SSB conversion loss of the 400 GHz SHP mixer is ~ 1.5 dB worse than in the 400 GHz fundamental mixer, which is in agreement with the literature [4]. However, it is important to realize that a 0.6 V bias has been considered for the fundamental mixer while the SHP mixer has been left unbiased. The absence of bias circuitry makes circuits easier to fabricate, so this advantage must be positive considered in the designs.

Other advantages of the SHP mixer, which are predicted by our CAD tool, are the DC current reduction and the even-order harmonics and intermodulation products current cancellation within the diode pair for antiparallel-diode pair SHP mixers. Furthermore, no implementation efforts need to be made in the circuitry at the even-order frequency components as they do not have influence in the mixer performance. This is corroborated by results in Fig. 9. When all the idler frequencies impedances of the circuit are set to 50Ω , the conversion loss for the antiparallel-diode pair SHP mixer is not affected with respect to the case in which those impedances are short-circuited. When a single diode SHP mixer is considered a degradation of the performance can be noticed.

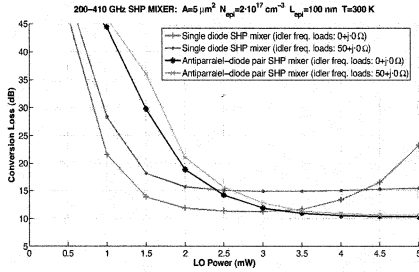


Fig. 9. Comparison between the performances of the 400 GHz fundamental Schottky mixer and the 400 GHz SHP antiparallel-pair Schottky diode mixer. Influence of the impedances at idler frequencies.

V. VALIDATION OF THE CAD TOOL

As an initial effort to validate the in-house mixer CAD tool presented in this work, a 330 GHz SHP mixer designed, fabricated and measured in the *Observatoire de Paris* [5], [7], has been simulated using this tool. The Schottky diode employed in the design and fabrication of the mixer is the *SD1T7-D20* from the *University of Virginia*. The characteristics of this diode (provided by the *University of Virginia*) can be found in [7]: An epitaxial layer of 100 nm, an anode area of $0.8 \mu\text{m}^2$, an epilayer doping of $2 \cdot 10^{17} \text{cm}^{-3}$, a built-in potential of 0.72 Volts, a zero junction capacitance of 1.3 fF and a series resistance of 11-15 Ω .

The DC analysis of the diode showed a series resistance of $\sim 14 \Omega$ and a 1.3 fF zero junction capacitance C_{j0} that are in good agreement with the nominal values specified by the *University of Virginia*.

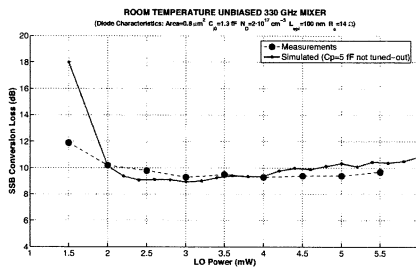


Fig. 10. Comparison between measurements and simulations for a 330 GHz SHP antiparallel-diode pair Schottky mixer [7].

The optimum impedances employed in the simulation were optimized at a 1.5 mW LO power in absence of parasitics: $Z_{RF} = 77 + j \cdot 138 \Omega$ and $Z_{LO} = 142 + j \cdot 238 \Omega$. These values are very close to those considered in [7]: $Z_{RF} = 83 + j \cdot 53 \Omega$ and $Z_{LO} = 147 + j \cdot 207 \Omega$.

A 100 Ω IF output impedance has been considered in both the fabrication and the simulation of the 330 GHz mixer. This value is optimum for the antiparallel-diode pair according to [7], and agrees with the result provided by the IF impedance optimization performed with our CAD tool. The parasitic

capacitance of the fabricated mixer is $\sim 5 \text{fF}$ according to [7]. The optimum impedances if C_p is considered predicted by our CAD tool ($Z_{RF} = 5 + j \cdot 56 \Omega$ and $Z_{LO} = 4 + j \cdot 120 \Omega$) are very different to those employed in the fabrication of the 330 GHz mixer so we have considered that the parasitic capacitance was not tuned out in the results presented in [7]. Taking into account all these considerations, simulations and measurements are in very good agreement as can be depicted from Fig. 10. In order to make possible the comparison, the quasi-optical losses (0.7 dB) and the losses in the IF circuit and SMA connectors (2.5 dB) predicted in [7] have been added to the simulation results. Hence, the final SSB conversion loss is 9.1 dB at 2.4 mW LO power.

If simulations are repeated considering the input impedances that tune out the 5 fF parasitic capacitance, the minimum SSB conversion loss (9.1 dB) occurs at 0.4-0.6 mW instead at 2.4 mW. Anyway, the low values required for the real part of the LO and RF impedances, 4 Ω and 5 Ω respectively, makes extremely difficult the synthesization in practice.

VI. CONCLUSION

We have presented an in-house CAD tool for the analysis and design of fundamental Schottky mixers and SHP Schottky mixers up to Terahertz frequencies. By means of this tool, a 400 GHz Schottky mixer have been designed and optimized considering the two possible topologies: a fundamental single-diode mixer and a SHP antiparallel-diode pair Schottky mixer. A deep comparison between the advantages and disadvantages of both topologies have been done. The predicted SSB conversion loss are 8.6 dB for the fundamental mixer and 10.3 dB for the SHP mixer. However, these results could be still improved, for example by reducing the series resistance of the diodes.

An initial validation of our CAD tool have been also presented with very good agreement between measurement and simulations of a 330 GHz SHP antiparallel-diode pair Schottky mixer.

REFERENCES

- [1] J. V. Siles, J. Grajal, V. Krozer, and B. Leone, "A CAD tool for the design and optimization of Schottky diode mixers up to Terahertz frequencies", *In Proc. 16th Int. Symp. on Space Thz Technology*, May 2005.
- [2] J. Grajal, V. Krozer, E. González, F. Maldonado, and J. Gismero, "Modelling and design aspects of millimeter-wave and submillimeter-wave Schottky diode varactor frequency multipliers", *IEEE Trans. on Microwave Theory and Techniques*, vol. 48, no. 4, pp. 910-928, April 2000.
- [3] P. S. Henry, B. S. Glance, and M. V. Schneider, "Local oscillator noise cancellation in the subharmonically pumped down-converter", *IEEE Trans. on Microwave Theory and Techniques*, vol. MTT-24, pp. 254-257, May 1976.
- [4] P. H. Siegel, R. J. Dengler, I. Mehdi, J. E. Oswald, W. L. Bishop, T. W. Crowe, and R. J. Mattauch, "Measurements on a 215-GHz subharmonically pumped waveguide mixer using planar back-to-back air-bridge Schottky diodes", *IEEE Trans. on Microwave Theory and Techniques*, vol. 41, no. 11, pp. 1913-1921, November 1993.
- [5] B. Thomas, A. Maestrini, and G. Beaudin, "A low-noise fixed-tuned 300-360-GHz sub-harmonic mixer using planar Schottky diodes", *IEEE Microwave and Wireless Components Letters*, vol. 15, no. 12, pp. 865-867, December 2005.
- [6] T. W. Crowe, W. L. Bishop, D. W. Porterfield, J. L. Hesler, and R. M. Weikle II, "Opening the Terahertz window with integrated diode circuits", *IEEE Journal of Solid-State Circuits*, vol. 40, no. 10, pp. 2104-2110, October 2005.
- [7] B. Thomas, "Etude et réalisation d'une tête de réception hétérodyne en ondes submillimétriques pour l'étude des atmosphères et surfaces de planètes", *These de doctorat, Observatoire de Paris*, December 2004.

Design of Heterostructure Barrier Varactor Frequency Multipliers at Millimeter-wave Bands

Virginia Bernaldo, Jesús Grajal, and José V. Siles

Abstract—A physics-based CAD tool for the design of heterostructure barrier varactor (HBV) frequency multipliers is presented in this work. This design tool is based on the Harmonic Balance method together with a physics-based drift-diffusion numerical device simulator. A joint optimization of the circuit parameters and the structure of the HBV diodes maximises the conversion efficiency at millimeter-wave bands. Different material systems have been considered for the designs: $AlGaAs/GaAs$, and $InGaAs/InAlAs$. An initial effort for validation has been carried out with measurements published in the literature for a 300 GHz $GaAs/AlGaAs$ -based tripler, and a 250 GHz $InGaAs/InAlAs$ -based tripler with very promising results.

Index Terms—CAD, Heterostructure Barrier Varactor (HBV), harmonic balance, submillimeter-wave technology, frequency multiplier.

I. INTRODUCTION

Varactor frequency multipliers play a key role in developing solid-state power sources at terahertz frequencies. Heterostructure barrier varactors represent a very interesting technological alternative to traditional Schottky diodes providing an alternative for the fabrication of frequency multipliers at millimeter-wave and submillimeter-wave bands [1], [2].

An HBV is a symmetric device composed of a high band-gap undoped or slightly doped semiconductor (*barrier*), placed between two low band-gap highly doped modulation layers. When an external bias is applied across the device, electrons are accumulated on one side of the barrier and depleted on the opposite side providing a voltage-dependent depletion region in one of the modulation layers. When the structure presents symmetry, an even C-V characteristic is obtained

HBV diodes show several advantages for the implementation of frequency multipliers:

- An easier power handling due to the possibility of stacking several barriers in a single device.
- The achievement of odd multiplication factors with no need of filtering the even harmonics of the RF signal.
- No bias is required for HBV multipliers with odd multiplication factors, contrarily to Schottky ones.

The integration of numerical simulators for active devices into circuit simulators avoids the need an equivalent-circuit model extraction providing another degree of freedom to improve the performance of circuits because they can be designed from both the device and the circuit point-of-view. The scope of this paper is to present a design tool for HBV-based multipliers at millimeter-wave and submillimeter-wave bands employing a physics-based HBV numerical model

This work was supported by the Spanish National Research and Development Program under project number TEC2005-07010-C02-01/TCM.

The authors are with the Department of Señales, Sistemas y Radiocomunicaciones of the Universidad Politécnica de Madrid, E.T.S.I. Telecomunicación, Ciudad Universitaria s/n, Madrid, E-28040 SPAIN (phone: +34 91-336-73-58; fax: +34 91-336-73-62; e-mail: jesus@ gmr.ssr.upm.es).

coupled with an external circuit simulator analogous to that one described for Schottky multipliers [3].

Our HBV simulator incorporates accurate interface conditions to account for the most important current transport mechanisms in an HBV: Thermionic emission of electrons over the barrier and electron tunnelling through it. The dominating one is determined by the temperature, bias voltage, effective barrier height, doping and thickness of the barrier and modulation layers. The physics-based model also incorporates different materials systems: $AlGaAs/GaAs$ or $AlAs/AlGaAs/GaAs$ on $GaAs$ substrate, $InAlAs/InGaAs$ or $AlAs/InAlAs/InGaAs$ on InP substrate.

The validation of the numerical simulator has been performed with experimental results for devices and multipliers fabricated at the University of Virginia (UVa), Charlottesville (USA), and at Chalmers University of Technology, Göteborg (Sweden) [1], [2], [4], [5].

The physics-based model for HBVs is presented in Section II. The validation of this analysis and design tool is carried out in Section III. An analysis of different critical aspects of HBV-based tripler design is accomplished in Section IV. Some conclusions are drawn in section V.

II. HBV PHYSICAL DEVICE MODEL

The electrical performance of the HBV diodes is investigated with a one-dimensional (1-D) drift-diffusion formulation. The recombination rate is modelled by the Shockley-Read-Hall recombination, and the generation rate is restricted to impact ionization [6].

Our physics-based model incorporates accurate boundary and interface conditions. We impose Dirichlet's boundary conditions at metal contacts for Poisson's and carrier continuity equations [6]. On the other hand, thermionic and thermionic-field carrier transport at the barriers is imposed at the different interfaces caused by the material composition discontinuities [7].

Tunnelling transport through the barrier is significant especially for HBV diodes with high doping in the modulation layer. In this model, the time-independent Schrödinger's equation is solved using the transfer matrix approach [8] particularized for HBV barriers. The same grid defined for Poisson's and carrier continuity equations is used for Schrödinger's equation.

The coupling of the physical device model and the circuit simulator is omitted in this paper but a detailed description can be found in [3].

III. VALIDATION OF THE PHYSICAL MODEL

Our physical model has been validated with measurements for several HBV diodes with different material composition,

modulation layer thickness, doping level, and area. The parameters for diodes analyzed in this paper are provided in Table I, [1], [9].

TABLE I
HBV DIODE PARAMETERS FOR DEVICES ANALYZED

Diode and Composition Materials	Modulation layer		Barrier
	Doping (cm^{-3})	Length (nm)	Length (nm)
UVa SHBV [1]: $Al_{0.7}Ga_{0.3}As/GaAs$	10^{17}	335	21.5
UVa-NRL-1174 (4-barrier)[1]: $Al_{0.7}Ga_{0.3}As/GaAs$	$8 \cdot 10^{16}$	250	20
SHBV [9]: $AlAs/In_{0.52}Al_{0.48}As/In_{0.53}Ga_{0.47}As$	10^{17}	300	5/3/5

A good agreement for I-V and C-V characteristics is demonstrated for $AlGaAs/GaAs$ HBV-based diodes: Fig. 1(a) represents the DC characteristics for a single-barrier HBV, and Fig. 1(b) shows the DC performance for a four-barrier HBV. For these simulations, the barrier height has been fitted as was suggested in [1]: $\Delta E_c = 300 meV$ for $Al_{0.7}Ga_{0.3}As/GaAs$ barriers. There is also a good agreement for $InGaAs/InAlAs$ HBV diodes. However, no fitting parameters have been used for this device.

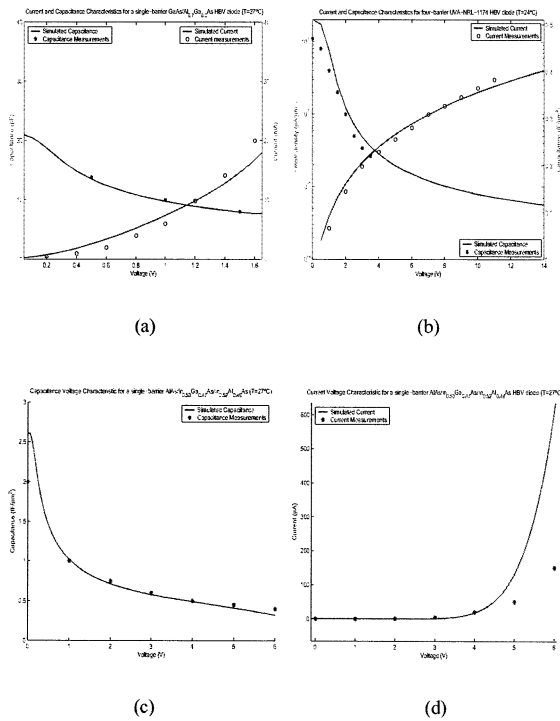


Fig. 1. Simulated and measured I-V and C-V characteristics for HBV diodes [1], [2], [9]. The diode parameters are indicated in Table I.

We have also performed RF simulations for two frequency triplers reported in the literature [1], [5] based on devices of table I. Efficiency versus input power for the $AlGaAs/GaAs$ SHBV tripler at 300 GHz is analysed in Fig. 2. Efficiency levels obtained are in good agreement with experimental data: A $\sim 10\%$ efficiency is obtained, while the maximum experimental efficiency [10] for the same device and in a similar range of input frequency, 70-100 GHz, is about 13% at 5 mW of input power. The load impedance at the output $Z_g(3f_o)$ was optimized for maximum efficiency, $Z_g(3f_o) \approx (6 + j8)\Omega$, while at the fundamental frequency the load is matched for each input power. Regarding the $InGaAs/InAlAs$ HBV-based tripler, we obtained a $\sim 13\%$ in good agreement with scaled measures for the same structure with four barriers [5] as showed in Fig 3.

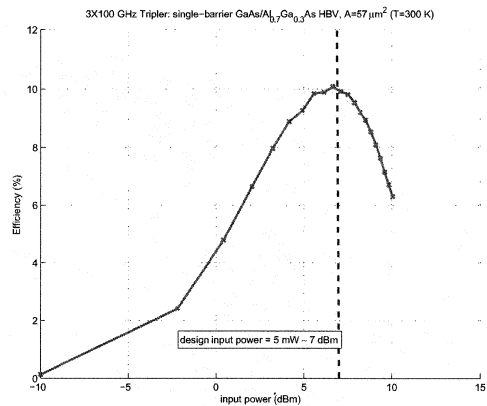


Fig. 2. Simulated efficiency versus input power for a single barrier $AlGaAs/GaAs$ HBV-based frequency tripler. The diodes parameters are indicated in Table I.

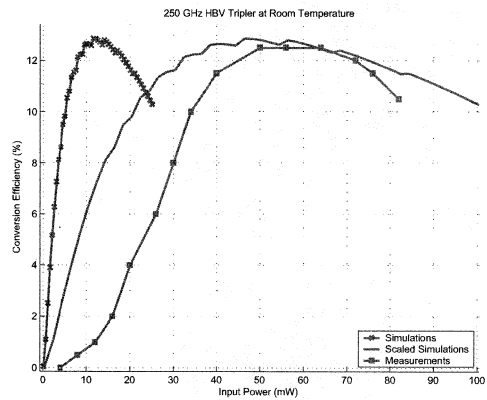


Fig. 3. Simulated and measured efficiency versus input power for $InGaAs/InAlAs$ single-barrier HBV-based frequency multiplier [5]. The diode parameters are indicated in Table I.

The selection of the impedance for the third harmonic is crucial for frequency triplers. The optimum values for the selected input frequency and power level are summarized in Table II, together with the matched impedance values for the fundamental frequency.

TABLE II
MAXIMUM CONVERSION EFFICIENCY AND IMPEDANCE LEVELS OF
HBV-BASED FREQUENCY TRIPLERS.

Multiplier	$\eta(\%)$	$Z(3f_o) \Omega$	$Z(f_o) \Omega$
UVa SHBV: ($Al_{0.7}Ga_{0.3}As/GaAs$) 3X100GHz, 5 mW	$\sim 10\%$	$6 + j8$	$3 + j22$
SHBV [9]: $AlAs/In_{0.52}Al_{0.48}As/$ $In_{0.53}Ga_{0.47}As$ 3X82.5 GHz, 12.5 mW	$\sim 13\%$	$9 + j13$	$3 + j21$

IV. HBV-BASED MULTIPLIERS: DEVICE, CIRCUITAL AND THERMAL ASPECTS.

The capabilities of our simulation tool for the analysis and design of frequency multipliers have been demonstrated for single or multiple barrier HBVs, with different material compositions, and in a wide range of input powers and frequencies. In this section, an in-depth analysis on the influence of the device structure and some limiting mechanisms is illustrated for the UVa SHBV-based frequency 3X100 GHz tripler presented previously.

A. Impact of the device structure

First of all we must select the number of barriers taking into account the required power handling. When the number of barriers in an HBV is increased, the maximum efficiency is achieved for higher input power levels, Fig. 4, and this increment is approximately proportional to the number of barriers. The matched impedance at the fundamental frequency is also scaled by the number of barriers. The multiplier circuit is more sensitive to changes in the embedding impedances at low-input power levels as compared to high-input power levels.

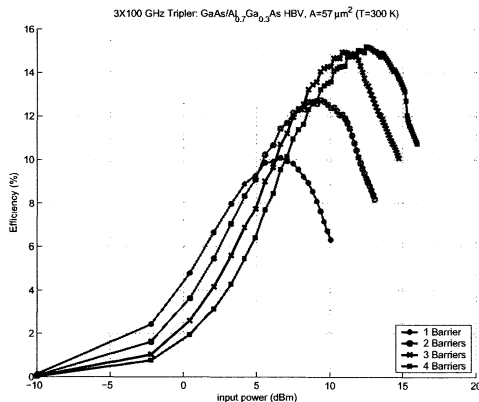


Fig. 4. Simulated efficiency versus input power for a 3x100 GHz frequency multiplier and different number of barriers. The basic diode parameters has been presented in Table I.

Once the number of barriers is selected, the device structure must be optimised. For thin and highly doped modulation

layers, the maximum of efficiency increases and is achieved for higher input powers, Fig. 5.

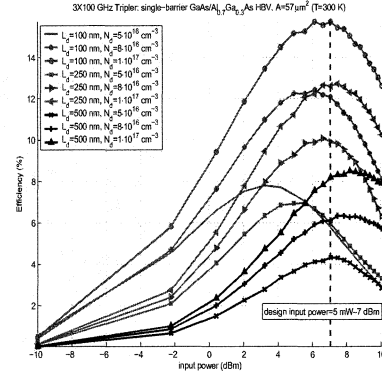


Fig. 5. Simulated efficiency versus input power for a single-barrier HBV-based 3x100 GHz frequency multiplier for different modulation layers' lengths (L_d) and dopings (N_d).

Finally, the area can be selected in order to get the maximum efficiency for the selected input power level.

B. Impact of avalanche breakdown

Figure 6 presents the influence of the carrier generation by impact ionisation on the tripler performance. When the voltage swing is high enough for reaching the breakdown voltage, a significant decrease in the efficiency is caused. Therefore, when the modulation layers are designed, the breakdown volatege of the HBV must be taken into account for power handling design.

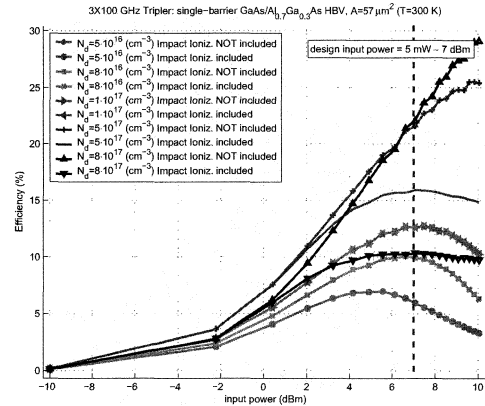


Fig. 6. Impact of avalanche breakdown on efficiency versus input power characteristic for a single-barrier HBV-based 3x100 GHz frequency multiplier as a function of modulation layer doping.

C. Impact of Device Temperature

It has also been demonstrated in [11], [12] that the increase in the temperature has a crucial responsibility on the decrease in the efficiency for HBV-based frequency multipliers, 7. In fact, self-heating could be the limiting mechanism for frequency multiplication if a proper thermal design is not carried out [11].

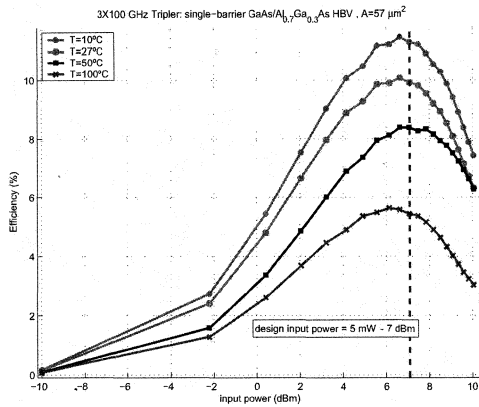


Fig. 7. Simulated efficiency versus input power for a single-barrier HBV-based 3x100 GHz frequency multiplier as a function of room temperature.

D. Loads at the fifth harmonic

One of the most important advantages of HBV-based multipliers is the generation of odd harmonics without filtering the even ones. This capability is based on the symmetry of the electrical characteristics for unbiased devices. Thus, the load impedances for even harmonics have no effect on the efficiency characteristic. However, the fifth harmonic load impedance has a significant influence on the tripler conversion efficiency as illustrated in Fig. 8. In this figure, the evolution of efficiency versus imaginary part of the embedding impedance for different real parts is presented.

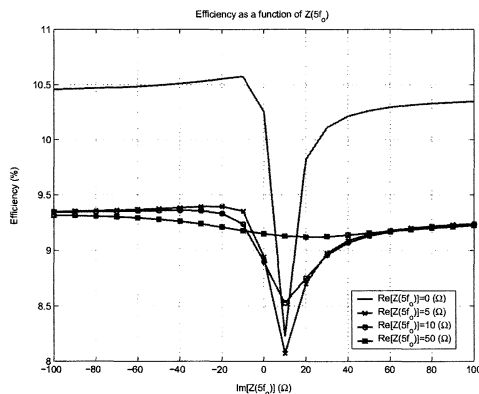


Fig. 8. Simulated efficiency versus input power for a single-barrier HBV-based 3x100 GHz frequency multiplier as a function of the fifth harmonic impedance.

V. CONCLUSIONS

The flexibility of our CAD tool allows the joint design of the internal HBV structure and the external circuit. The advantages of this integrated strategy has resulted in two designed triplers with good agreement between simulated results and experimental data at frequencies up to 300 GHz. This tool offers the opportunity to understand some limiting mechanisms in HBVs, such as self-heating effects and avalanche breakdown, and to mitigate them through a proper design.

REFERENCES

- [1] J.R. Jones, "CAD of millimeter wave frequency multipliers: An experimental and theoretical investigation of the heterostructure barrier varactor", *School of engineering and applied science, Ph. D. Thesis*, University of Virginia, January 1996.
- [2] M. Ingvarson, "Modelling and design of high power HBV multipliers", *Ph. D. Thesis*, Göteborg, Suecia, 2004.
- [3] J.Grajal, V. Krozer, E. González, F. Maldonado and J. Gismero, "Modeling and design aspects of millimeter-wave and submillimeter-wave Schottky diode varactor frequency multipliers", *IEEE Transaction on Microwave Theory and Techniques*, vol. 48, no. 4, pp. 910-928, April 2000.
- [4] L. Dillner, M. Ingvarson and E. L. Kollberg, "Modeling of the Heterostructure Barrier Varactor diode", *Proceedings of the 1997 International Semiconductor Device Research Symposium*, 1997, pp.179-182.
- [5] X. Melique, A. Maestrini, E. Lheurette, *et al.*, "12 per cent and 9.5 dBm output power InP based Heterostructure Barrier Varactor Tripler at 250 GHz", *IEEE MTT-S International*, vol. 1, pp. 123-126, December 2005.
- [6] S. Selberherr, "Analysis and simulation of semiconductor Devices", *Springer-Verlag*, Wien-New York, 1984.
- [7] K. Horio and H. Yanai, "Numerical Modelling of Heterojunction including the Thermionic Emission Mechanism at the Heterojunction Interface", *IEEE Transaction on Electron Devices*, Vol. 37 No. 4, April 1990.
- [8] W. W. Lui and M. Fukuma, "Exact Solution of the Schrodinger equation across an arbitrary one-dimensional piecewise-linear potential barrier", *Journal of Applied Physics*, Vol. 60, pp. 1555-1559, September 1986.
- [9] E. Lheurette, P. Mounaix, P. Salzenstein, F. Mollot and D. Lippens, "High performance InP-Based Heterostructure Barrier Varactors in single and stack configuration", *IEEE Electronic Letters*, Vol. 32, No. 15, pp. 1417-1418, 1996.
- [10] R. Meola, J. Freyer and M. Claasen, "Improved frequency tripler with integrated single-barrier varactor", *Electronics letters*, Vol.36, No. 99, pp. 803-804, 2000.
- [11] J. Stake, L. Dillner, S. H. Jones, C. Mann, J. Thornton, J. R. Jones, W. L. Bishop and E. L. Kollberg, "Effects of Self-Heating on Planar Heterostructure Barrier Varactor Diodes", *IEEE Transactions on Electron Devices Letters*, Vol. 45, No. 11, pp. 2298-2303, Nov. 1998.
- [12] M. Ingvarson, B. Alderman, A. O. Olsen, J. Vukusic and J. Stake, "Thermal Constraints for Heterostructure Barrier Varactors", *IEEE Electron Device Letters*, Vol. 25, No. 11, November 2004.

A High Efficiency Multiple-Anode 260-340 GHz Frequency Tripler

Alain Maestrini, Charlotte Tripon-Canseliet, John S. Ward, John J. Gill and Imran Mehdi

Abstract— We report on the fabrication at the Jet Propulsion Laboratory of a fixed-tuned split-block waveguide balanced frequency tripler working in the 260-340 GHz band. This tripler will be the first stage of a $\times 3 \times 3 \times 3$ multiplier chain to 2.7 THz (the last stages of which are being fabricated at JPL) and is therefore optimized for high power operation. The multiplier features six GaAs Schottky planar diodes in a balanced configuration integrated on a few μm -thick membrane. Special attention was put on splitting the input power as evenly as possible among the diodes in order to ensure that no diode is over-driven. Preliminary RF tests indicate that the multiplier covers the expected bandwidth and that the efficiency is in the range 1.5-7.5 % with 100 mW of input power.

Index Terms— Local oscillator, varactor, planar diode, Schottky diode, frequency multiplier, frequency tripler, balanced tripler, submillimeter wavelengths.

I. INTRODUCTION

Frequency multiplication offers the possibility to create tunerless compact frequency-agile terahertz sources working at room temperature that are well-suited to pump Hot Electron Bolometer (HEB) mixers [1],[2]. Nevertheless, there has been no demonstration of a fully solid-state local oscillator at frequencies above 1.95 THz. This limitation is due in part to the lack of drive power in the 600-1200 GHz range, which can in turn be traced to the power available in the 200-400 GHz range. The purpose of the current work is to create a wideband 300 GHz source with sufficient output power to be used as a first stage of a $\times 3 \times 3 \times 3$ chain to 2.7 THz.

II. DESIGN & FABRICATION

A preliminary design of the balanced 260-340 GHz tripler along with the predicted performance have been presented in [3]. The tripler is a split-block waveguide design that features six Schottky planar varactor diodes, monolithically fabricated on a $\sim 5 \mu\text{m}$ -thick GaAs membrane. The chip is mounted in a channel that runs between the input and the

The research described in this paper was carried out at the Jet Propulsion Laboratory, California Institute of Technology, under a contract with the National Aeronautics and Space Administration and at the Université Pierre et Marie Curie – Paris 6 and the Observatory of Paris.

A. Maestrini is with Laboratoire des Instruments et Systèmes d'Ile de France - Université Pierre et Marie Curie, 4 place Jussieu, case 252, 75252 Paris cedex 5, France, and is associated with Laboratoire d'Etude du Rayonnement et de la Matière en Astrophysique, Observatoire de Paris, France. Email : alain.maestrini@lisif.jussieu.fr

J. Ward, J. Gill and I. Mehdi are with the Jet Propulsion Laboratory, California Institute of Technology, MS 168-314, 4800 Oak Grove Drive, Pasadena, CA 91109, USA.

C. Tripon-Canseliet is with LISIF - Université Pierre et Marie Curie, Paris, France.

output waveguides (see Fig. 1).

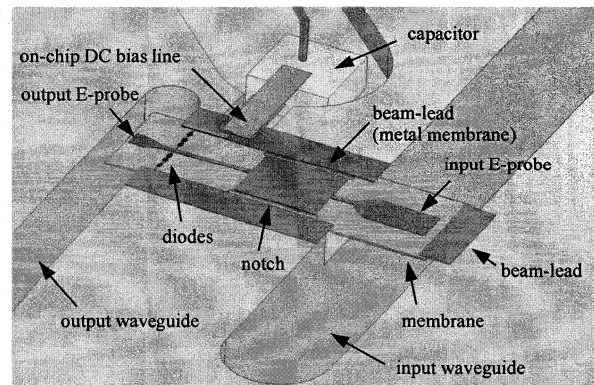


Fig. 1. 3D view of the bottom part of the waveguide block (partial view) with the 300 GHz tripler chip. The device is fabricated on a $5 \mu\text{m}$ thick GaAs membrane substrate. It features six Schottky diodes in a balanced configuration. The total length of the device is about 1 mm.

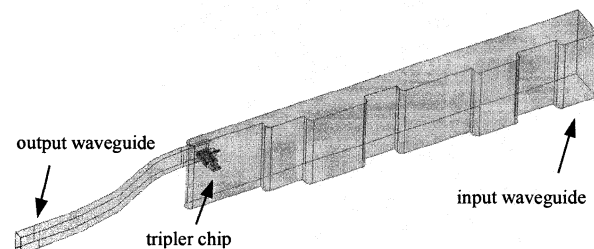


Fig. 2. 3D view of the entire 260-340 GHz frequency tripler. The total length of the matching circuit in the input waveguide is about 14 mm. The total length of the circuit is 20 mm.

An E-plane probe located in the input waveguide couples the signal at the fundamental frequency to a suspended microstrip line. This line has several sections of low and high impedance used to match the diodes at the input and output frequencies and to prevent the third harmonic from leaking into the input waveguide. The third harmonic produced by the diodes is coupled to the output waveguide by a second E-plane probe. The bandwidth of the multiplier was extended by adding to the input waveguide a succession of sections of high and low impedances [3]. With respect to the design presented earlier, the current design uses exactly the same device, but the waveguide input matching network has been slightly modified and the step in the output waveguide has been removed. The predicted performance of the final circuit are very similar to those published in [3].

Fig.1 shows a schematic of the 260-340 GHz tripler chip while Fig. 2 shows a schematic of the entire multiplier. Fig. 3 shows two pictures of a tested multiplier. Note that

the output probe on this particular chip is defective: it is only 50 μm long instead of 90 μm . At the time this paper was written, this was the only device available for testing.

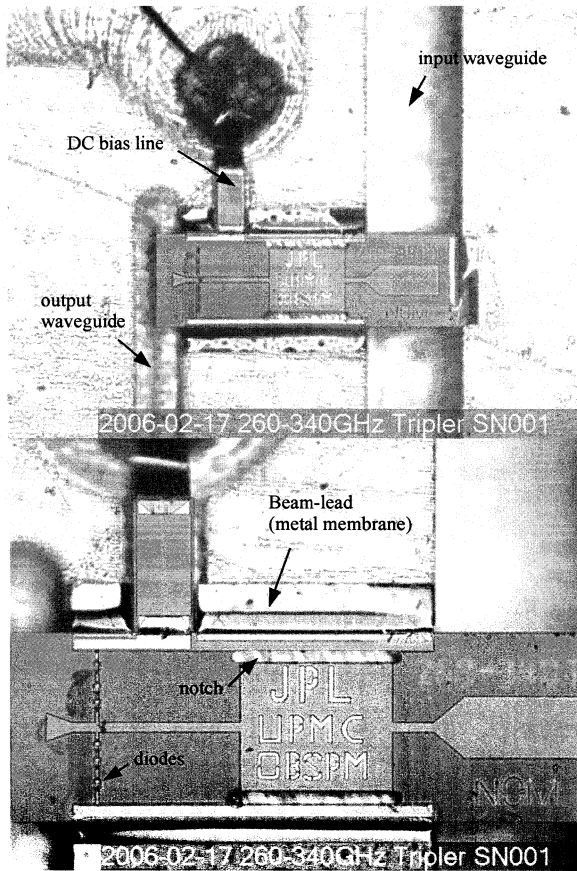


Fig. 3. Photograph of the bottom part of the waveguide block with a 300 GHz tripler chip and the DC capacitor installed (top). Detail of the 260-340 GHz tripler chip (bottom). NOTE that the output probe on this particular chip is defective: it is only 50 μm long instead of 90 μm (compare with the 3D schematic of Fig. 1).

III. PRELIMINARY MEASUREMENTS

The output power of the 260-340 GHz tripler was measured at room temperature using an Erickson Instruments PM3 power meter [4] and a one-inch long WR10 to WR3 waveguide transition. No corrections were made for the losses in the waveguide transition. Fig. 4 shows the output power and the conversion efficiency across the band while keeping the input power at 100 mW (except near the edges of the band). The bias was optimized for each frequency point. Despite the defective output probe, this multiplier shows excellent performance and covers the entire band 260-330 GHz band. Due to limitations of the W-band drive source, no measurements were made above 330 GHz, so it is not clear if the multiplier does actually reach 340 GHz as predicted.

The efficiency of the multiplier as a function of the input power was measured at room temperature by varying the input power from 3 mW (+4.8 dBm) to 192 mW (+22.8 dB) while optimizing the bias at each input power level (see Fig. 5). The output frequency was fixed at 318 GHz where the efficiency was close to the maximum and where almost 200 mW of drive power was available. Fig. 5 shows that the efficiency saturates at relatively low input power (+9 dBm = 8 mW) and decreases with the increasing input power above +9 dBm. This decrease of the efficiency becomes more noticeable for input power levels above +17 dBm (50 mW). This may indicate that the diodes are overheating due to the thin substrate under the diodes. No thermal study has been performed yet to verify this hypothesis.

Simulations were performed to estimate the impact of the flawed output probe (see Fig. 6). The 3D structure of the actual multiplier was re-simulated with a finite-element EM-solver (Ansoft HFSS V10.1). Fig. 6 shows the predicted performance of the defective chip biased with the same DC voltage and pumped with the same input power as the measurements. The results of this simulation are compared to the measurements in Fig. 6. The difference between measurements and predictions is in the range -3.2 dB to -1.2 dB (excluding a relatively narrow resonance around 300 GHz). It is important to note that these simulations were performed with the same set of parameters (series resistance, intrinsic junction capacitance, metallic losses, etc.) as the one used for the optimization of the circuit [3]. No retro-fit has been made. Since only one chip has been tested, it is impossible to say at this point if the initial predicted efficiency will be matched with a better chip, but it does appear likely that the predicted bandwidth will be achieved.

Fig. 6 also shows the predicted performance of the multiplier with a normal chip when pumped with a flat input power of 100 mW and when biased with a voltage of -13V. The same simulation is performed by replacing the normal chip by the defective chip. These simulations indicate that the performance of the multiplier should improve noticeably when a non-defective chip is mounted into the waveguide block. An increase of at least +3dB with respect to the measurements is expected for the lowest frequencies while an increase of at least +1dB is expected at the high end of the band.

IV. CONCLUSION

The preliminary results presented in this paper show that Schottky frequency triplers operating at 300 GHz can have both wide electronically-tunable bandwidth and high conversion efficiency. On-going research at the Jet Propulsion Laboratory in collaboration with the Université Pierre et Marie Curie-Paris 6 and the Observatoire de Paris focuses now on power-handling and power combining to increase the power produced at 300 GHz.

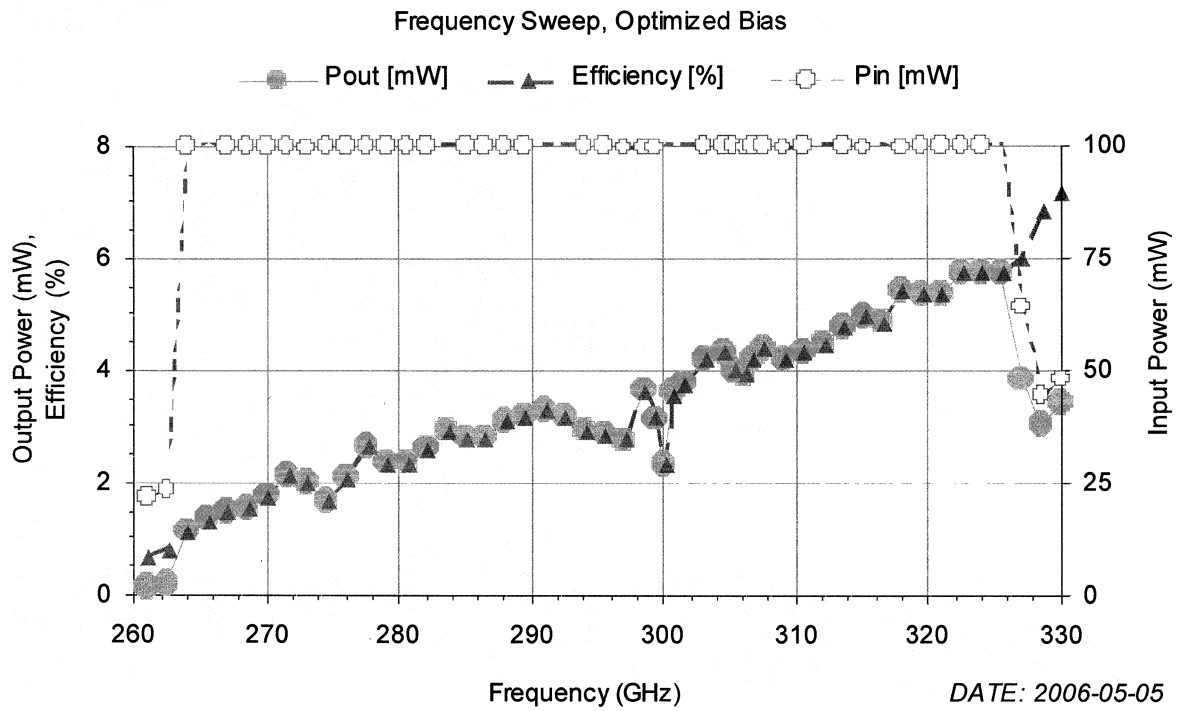


Fig. 4. Frequency sweep across the 260-330 GHz band. Input power is kept constant except at the edge of the band due to the roll-off of the W-band power amplifiers used for the measurements.

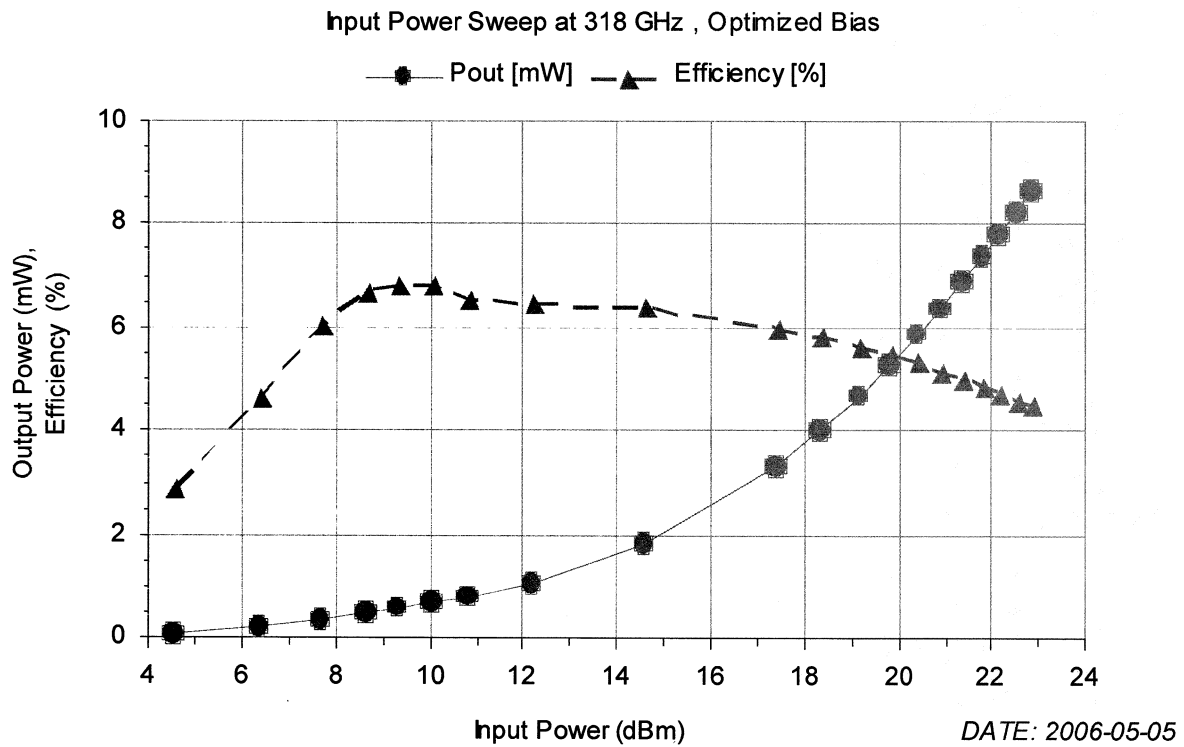


Fig. 5. Power sweep at the output frequency of 318 GHz. The bias is optimized for each input power level.

Measurements vs. Simulations at Room Temperature

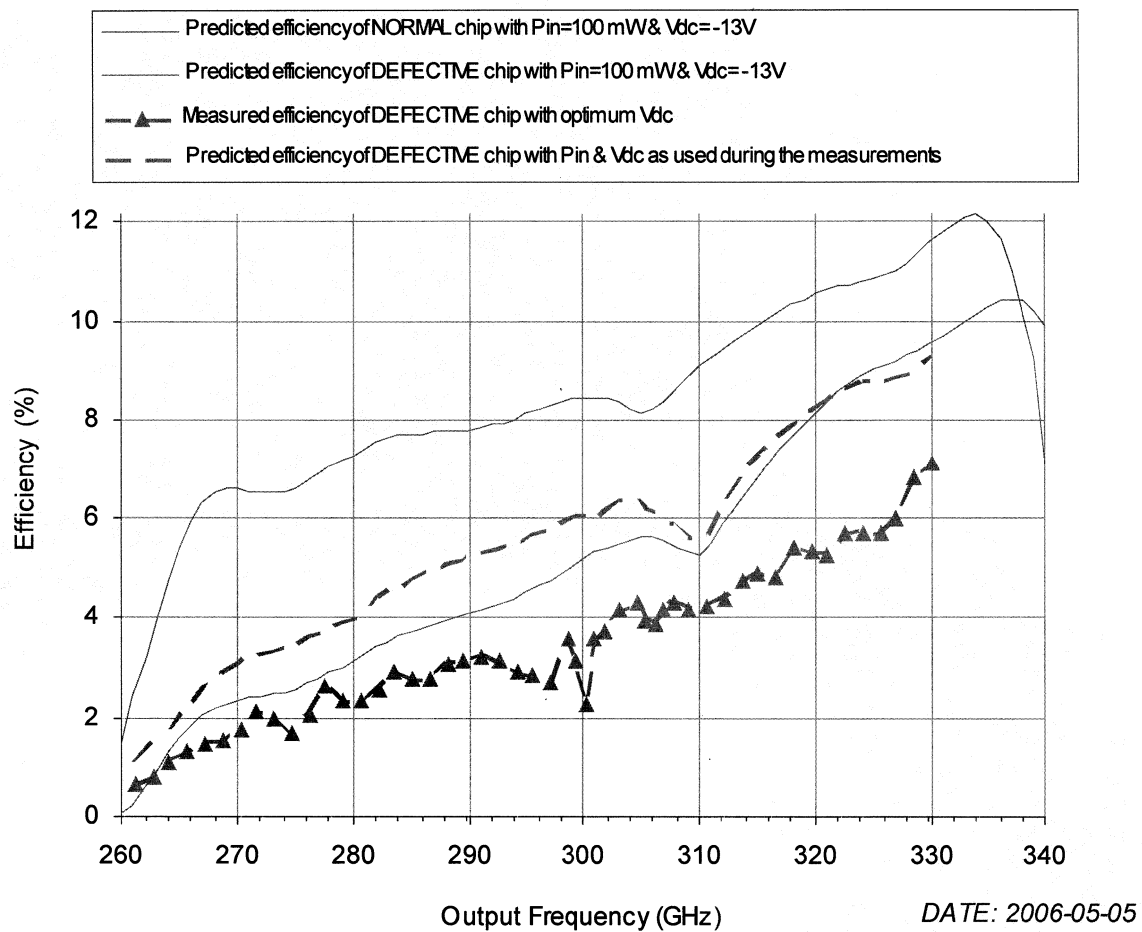


Fig. 6. Simulated efficiency versus frequency compared to the measured efficiency of the 260-340 GHz tripler.

ACKNOWLEDGMENT

The authors are grateful for the helpful technical discussions with Dr. Goutam Chattopadhyay and for the superb fabrication of the 260-340 GHz waveguide blocks by the JPL Space Instruments Shop.

REFERENCES

- [1] A. Maestrini, J. Ward, J. Gill, H. Javadi, E. Schlecht, G. Chattopadhyay, F. Maiwald, N.R. Erickson, and I. Mehdi, "A 1.7 to 1.9 THz Local Oscillator Source," *IEEE Microwave and Wireless Components Letters*, Vol. 14, no. 6, pp. 253-255, June 2004.
- [2] A. Maestrini, J. S. Ward, H. Javadi, C. Tripon-Canseliet, J. Gill, G. Chattopadhyay, E. Schlecht, and I. Mehdi, "Local Oscillator Chain for 1.55 to 1.75 THz with 100 μW Peak Power," *IEEE Microwave and Wireless Components Letters*, Vol. 15, no. 12, pp. 871-873, December 2005.
- [3] A. Maestrini, C. Tripon-Canseliet, J. Ward, H. Javadi, J. Gill, G. Chattopadhyay, E. Schlecht, and I. Mehdi, "Multi-Anode Frequency Triplers at Sub-Millimeter Wavelengths", in *Proceedings of the 16th International Symposium on Space Terahertz Technology*, Göteborg, Sweden, 2-4 May 2005.
- [4] N.R. Erickson, "A Fast and Sensitive Submillimeter Waveguide Power Sensor," in *Proceedings of the 10th International Symposium on Space Terahertz Technology*, pp. 501-507, Charlottesville, VA, 1999. Available from Erickson Instruments LLC, Amherst, MA.

A Design Methodology for Planar Triplers in Coplanar Waveguide on Thick Membranes

W.S. Truscott, P. Klasmann and R. Sloan

School of Electrical and Electronic Engineering
University of Manchester
PO Box 88
Manchester, M60 1QD, UK

The local oscillator is a key element of any Terahertz receiver. A typical Schottky mixer requires a drive of ~ 1 mW to achieve good conversion gains and noise figures. In many currently operating systems this power is provided by a chain of frequency doublers and/or triplers driven by a Gunn diode oscillator. This chain is implemented by a sequence of waveguide blocks in which both non-linear elements and filter structures are mounted on thin quartz membranes. These structures have a number of advantages for space applications including ruggedness (with the possible exception of the membranes) and good handling of the inevitable heat dissipation. On the other hand the weight of the waveguide elements would become an issue if a large number of local oscillators were required, as would be the case in a focal plane array.

We report research into methods of designing planar frequency triplers on GaAs substrates using coplanar lines to provide the impedance matching and frequency filtering elements for GaAs Schottky diodes. A methodology has been evolved that enables optimised tripler designs to be achieved without the exceptional computing times that would be needed for the unguided optimisation of a particular design topology. This methodology will be presented in this paper.

This research has identified a number of issues that are significant in determining the efficiency of coplanar waveguide structures in tripler circuits. The most significant of these is the excitation of substrate modes which can be minimised by using thick ($20 \mu\text{m}$) GaAs membranes for the substrate. These provide greater ruggedness and lateral thermal transport than the more commonly used thin membranes ($\sim 1 \mu\text{m}$). Mode conversion is an inevitable problem with coplanar waveguide junctions, but can be controlled by the use of bridges between grounds at appropriate places. A further problem, which is unique to frequency triplers is the very short distance between the fundamental feedpoint and the 50Ω third harmonic output point on the circuit. The methodology is based on recognising this as a major issue and deals directly with this problem. A final issue is the incorporation of a good representation of the Schottky diode with its parasitic elements within the electromagnetic software model. This issue will be specifically addressed within this paper.

The conclusions of the design study, supported by experimental work, is that coplanar waveguide triplers are feasible and can have useful efficiencies, but cannot achieve the efficiencies of the best waveguide structures. They are therefore good candidates for implementing local oscillators up to 500 GHz, but are unsuitable for applications where a chain of multipliers is required.

Experimental study of the harmonic generators and detectors, based on superlattices in wide frequency range 600-2200GHz.

*D.G.Paveliev, Yu.I.Koschurinov, A.M.Baryshev¹, W.Jellema²,
V.M.Ustinov³, A.E.Zhukov³.*

Radiophysics Department, Nizhny Novgorod State University, Russia,

¹Kapteyn Institute, Groningen University, Netherland,

²SRON-Groningen, Netherland

³Ioffe Physico-Technical Institute, St.Petersburg, Russia.

We present an experimental study of the harmonic generators based on superlattices at room temperature in wide frequency range 600-2200GHz. The non-biased superlattice diodes were driven by an electric field with of 120-140GHz and 190-220 GHz. The frequency synthesizers (20GHz) with frequency multiplier chains and MIMIC [1] power amplifiers were used for pump. We measured the power spectrum of output signal using Fourier Transform Spectrometer with cooled Si-bolometer. We observed intensive enough 3th (apr. 50-100mW), 5th (apr.10-20mW), 7th (apr.1-2mW), 9th (apr. less 0.1mW) and 11th (apr.1-20 pW) harmonics.

We present also an experimental study of the detector, based on superlattices at room temperature in wide frequency range 600-2200GHz. For this we used the second generator of harmonics with bias such as harmonic-mixer with the same frequency synthesizers (20GHz) with frequency multiplier chains and MIMIC [1] power amplifiers for heterodyne pump. For investigation we used the first harmonic generator such as the source of the THz signal.

In a result in a report we demonstrate that a transmission line for frequency range 600-2200GHz can be achieved at room temperature by making use of superlattice devices for both generation and detection of the radiation.

Experimental study of the harmonic generators

The central element of the harmonic generator was a superlattice electron device (SLED). The SLED (Fig. 1a), prepared by a microstructuring technique, had a quasi planar design with an active small-area superlattice mesa in series with a large-area mesa serving as ohmic contact [2].

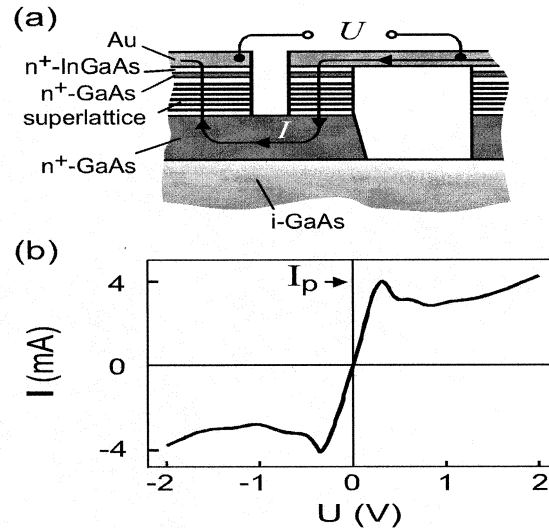


Fig. 1: (a) Sketch of the SLED based on the GaAs/AlAs superlattice; (b) SLED current-voltage characteristic at 300 K

High-frequency currents flow through a gold pad, the active element, an n^+ GaAs layer and the large-area mesa to the second contact pad or in the reverse direction.

The superlattice (length 112 nm) had 18 periods, each period (length 6.22 nm) with 18 monolayers GaAs and 4 monolayers AlAs and was homogeneously doped with silicon ($2 \times 10^{18} \text{ cm}^{-3}$). The miniband width (25 meV) was sufficient to lead to miniband rather than hopping transport. By molecular beam epitaxy, we had grown, on an intrinsic-GaAs substrate, an n^+ GaAs layer (thickness 1.5 μm ; doping $6 \times 10^{18} \text{ cm}^{-3}$), GaAs/AlAs gradual layer (thickness 32 nm), then the superlattice, again a gradual layer and n^+ GaAs and an n^+ InGaAs gradual layer (25 nm) and finally an n^+ InGaAs layer (20 nm, doping 10^{19} cm^{-3}) serving as ohmic contact. The gradual layers delivered smooth transitions with respect to layer thicknesses and doping, respectively. The same type of superlattice has been used for frequency multiplication [3].

Current-voltage characteristic of the SLED subject to a static voltage is presented in Fig. 1b. The current increases almost linearly for a voltage smaller than the critical voltage (U_c), reaches its maximum value (I_p) at the critical voltage and then decreases. Kinks in the current-voltage characteristic can be attributed to the formation of the electric field domain within the superlattice region.

Output spectrum of the harmonic generator was measured using Fourier Transform Spectrometer (FTS). The non-biased superlattice diodes was driven by an electric field with of 120-140GHz and 190-220 GHz. The frequency synthesizers (20GHz) with frequency multiplier chains and MIMIC [1] power amplifiers was used for pump. Absolute amplitude of the response was not calibrated. Results of the tests at 300 K are presented in Fig. 2a,b,c.

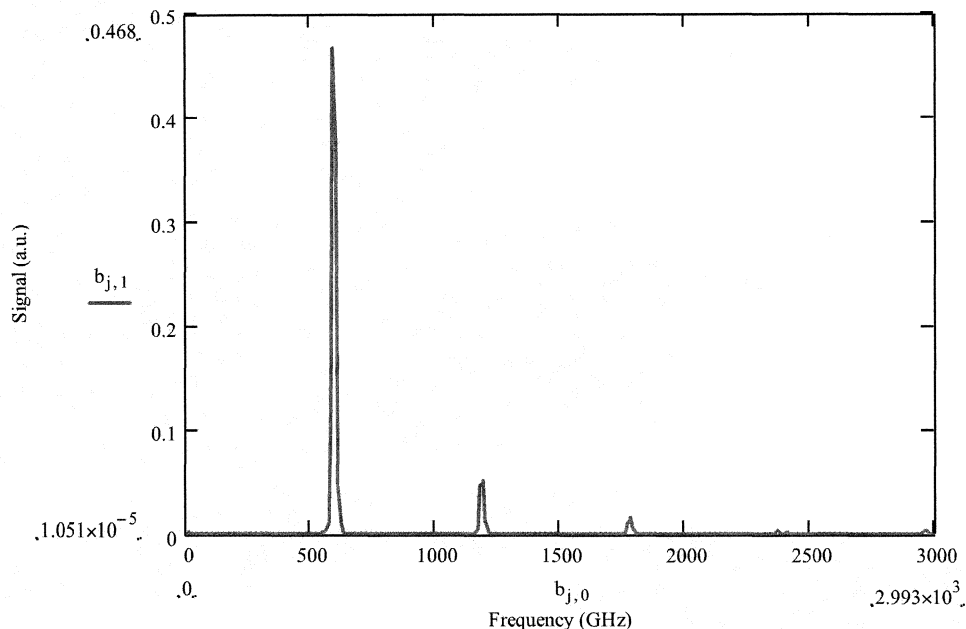


Fig2a. The output signal with input frequency 197.4GHz. Observed intensive enough 3th (apr.50-100mkW) harmonic. Befor bolometer was used 12dB attenuation.

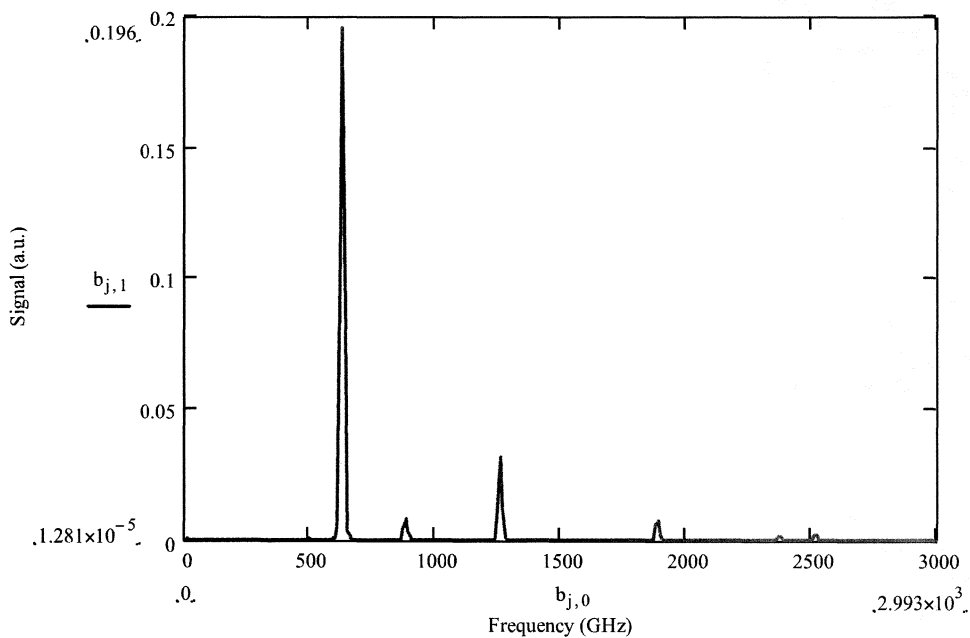


Fig2b. The output signal with input frequency 124 GHz. Observed the intensive enough 5th (apr.10-20mkW) and 7th (apr.1-2mkW) harmonics. Befor bolometer was used 12dB attenuation.

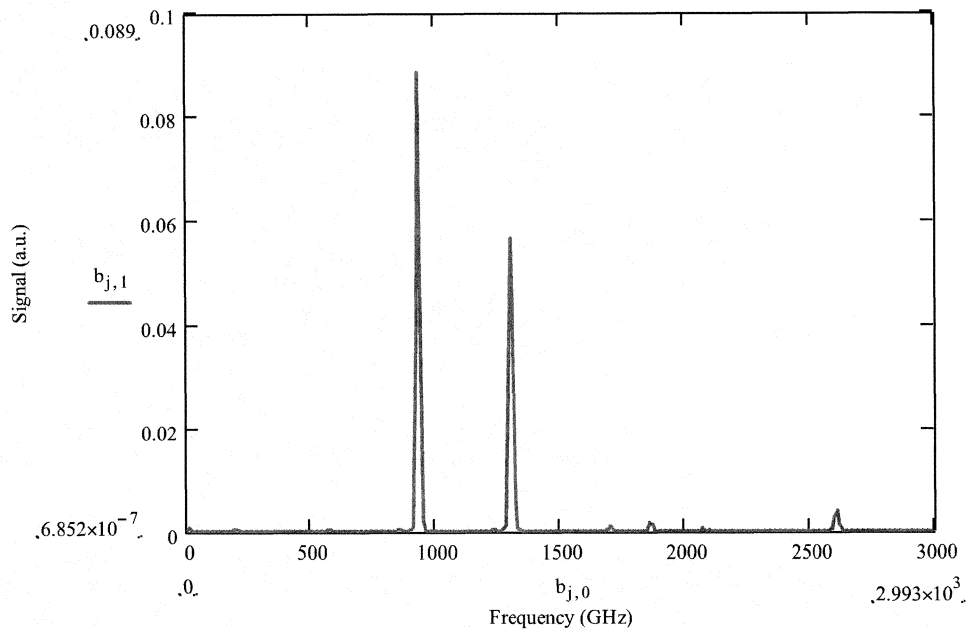


Fig.2c. The output signal with input frequency 187.2 GHz. Observed the intensive enough 5th,7th (apr.1-2mkW) harmonics. The 9th,11th harmonics was visible (apr.1-20pW).

Experimental study of the harmonic mixers

The principle of the semiconductor-superlattice frequency harmonic generators and mixers is based on the nonlinearity of the motion of miniband electrons. The nonlinearity manifests itself in the current-voltage (I-V) characteristic of a superlattice (Fig. 3a). Above a critical voltage V_c (and also below $-V_c$) a current jump appears, which is due to the formation of dipole domains. Under the action of the LO voltage, the superlattice is periodically brought into states of domain formation and annihilation (Fig. 3b), joint with current components at frequencies which are multiples of the LO frequency.

An RF field with a frequency near one of the harmonics of the LO frequency influences the domain dynamics and gives rise to a current, joint with an field at an intermediate frequency (IF); we performed our experiment with an LO frequency near 200 GHz and detected radiation of a frequency more 300 GHz, produced by harmonic generator, based on superlattice, by measuring the IF signal 0.5-5 GHz, i.e., we operated the superlattice mixer in (2 -11)th mixing order.

Fig. 4. Principle of the superlattice harmonic mixers. (a) Slope of an I-V characteristic of a superlattice with current jumps at the critical voltages V_c and $-V_c$; I_p , peak current. (b) LO voltage (frequency ~ 200 GHz) with an amplitude exceeding the critical voltage V_c and RF voltage due to the RF radiation (frequency more 300 GHz).

The typical IF signal (Fig. 4) showed a sharp peak and a broad background (halfwidth ~ 100 kHz). The noise (level of 10^{-11} W at a resolution bandwidth of 1 kHz) was caused by the frequency mixer.

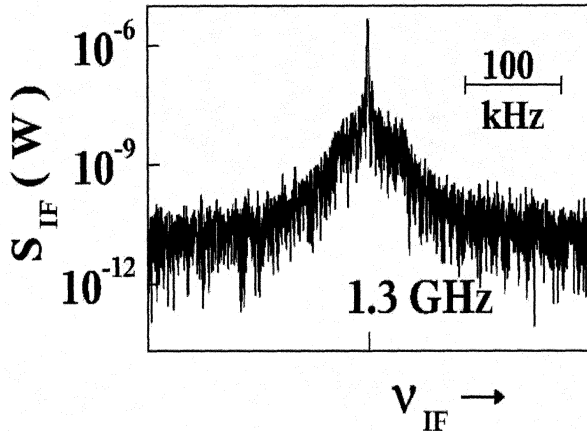


Fig. 4. IF signal at resolution bandwidth of 1 kHz (LO power 2-5 mW, LO frequency 193 GHz, RF Power 100 μ W, RF frequency 963.7 GHz).

Reduction of the power of the RF radiation resulted in a corresponding reduction of the signal peak.

Discussion

A superlattice mixer has already been used for stabilisation of a submillimeter flux flow oscillator (frequency range 270 GHz to 440 GHz) [4] and of a backward wave oscillator (700-900 GHz) [5].

The creation and annihilation of a domain can take place within a time which corresponds to a few times the electron relaxation time ($\sim 10^{-13}$ s). Accordingly, mixing on the basis of domains in a superlattice should be possible up to a frequency of few THz.

Our experiment also demonstrates that a transmission line for submillimeter radiation can be achieved by making use of the superlattice devices for both generation and detection of the radiation.

Support by the Russian Foundation of Basic Research (grant N 06-02-16598a) is acknowledged.

[1] Robert R. Ferber, John C. Pearson, Todd C. Gaier, Lorene A. Samoska, Frank W. Maiwald, Mary Wells, April Campbell, Gerald Swift, Paul Yocom, K.T.Liao, "W-Band MMIC Power Amplifiers for the Herschel HIFI Instrument," 14th Int. Symp. On Space THz Technology, Tucson, 22 April 2003.

- [2] D. Paveliev *et al*, "The millimeter wave length band Gunn diodes". Electronic Industry V. 4, 8-10 (1982) [in Russian].
- [3] F. Klappenberger, K. F. Renk, P. Renk, B. Rieder, Yu. I. Koschurinov, D. G. Pavel'ev, V. Ustinov, A. Zhukov, N. Maleev, and A. Vasilyev, "Semiconductor–superlattice frequency multiplier for generation of submillimeter waves", Appl. Phys. Lett. 84, 3924 (2004).
- [4] V. P. Koshelets, A. B. Ermakov, S. V. Shitov, P. N. Dmitriv, L. V. Filippenko, A. M. Barshev, W. Luinge, J. Mygind, V. L. Vaks, and D. G. Pavel'ev, "Externally phase locked submm-wave flux flow oscillator for integrated receiver", Conference Digest of the 11th Int. Symp. On Space Terahertz Technology, University of Michigan, Ann Arbor (2000), p. 532.
- [5] D. G. Pavel'ev, Yu. I. Koshurinov, V. P. Koshelets, A. N. Panin and V. L. Vaks, "Superlattice harmonic mixer for submillimeter frequency synthesis", Conference Digest of the 12th Int. Conf. on THz Electronics, Universität Karlsruhe (2004), p. 327.

Resonant terahertz detection in InGaAs/AlInAs and AlGaIn/GaN – based nanometric transistors.

A. El Fatimy¹, F. Teppe¹, W. Knap¹, D. Seliuta², G. Valušis², M. Orlov^{1,3}, S. Bollaert⁴, C. Gaquiere⁴, and A. Shchepetov⁴

¹GES CNRS UMR 5650, Montpellier, France,

²PFI, Vilnius, Lithuania, 3IEMN-DHS UMR CNRS 8520, Villeneuve d'Ascq, France

³Institute for Physics of Microstructures, Post Box GSP-105, 603950, Nizhny Novgorod, Russia

⁴IEMN-DHS URM CNRS 8250 Avenue Poincaré, 59652 Villeneuve d'Ascq, France

We report on resonant terahertz detection by two-dimensional electron plasma located in nanometric InGaAs/AlInAs and AlGaIn/GaN transistors. Up to now, the biggest part of the research was devoted to GaAs-based devices as the most promising from the point of view of the electron mobility. The resonant detection was observed/reported, however, only in the sub-THz range. According to predictions of the Diakonov-Shur plasma wave detection theory the increase of the detection frequency can be achieved by reducing the length or increase the carrier density in the gated region. We demonstrate that the limit of the 1THz can be overcome by using ultimately short gate InGaAs/AlInAs and/or AlGaIn/GaN nanotransistors. In the first one, InGaAs/AlInAs, – 50 nm length – gate was processed. The inherent feature of AlGaIn/GaN structures is high electron densities, reaching the values of 10^{13} cm⁻² which allowed to obtain the detection over 1THz frequencies even for 150nm gate length devices. For the first time the tunability of the resonant signal by the applied gate voltage is demonstrated. The photoresponse is interpreted in the frame of the Diakonov-Shur plasma wave detection theory. We discuss the possible application of detection by nanotransistors in different types of THz spectroscopy research.

Introduction

The terahertz (THz) range of frequencies is often referred to as the “terahertz gap”, since it lies in between the frequency ranges of electronic and photonic devices and it is hardly achieved from the both sides. Therefore, the development of the THz emitters and detectors is of the high importance. Dyakonov and Shur, proposed to use the nonlinear properties of plasma excitations in 2D gated electron gas for terahertz detectors, mixers, and THz radiation sources [1,2] The plasma waves in a field-effect transistor (FET) have a linear dispersion law [1], $\omega = sk$, where $s = \sqrt{e(U_{gs} - U_{th})/m}$ is the wave velocity, U_{gs} is the gate-to-source voltage, U_{th} is the threshold voltage, e is the electronic charge and m is the electron effective mass. This plasma wave velocity is typically much larger than the electron

drift velocity. A short FET channel of a given length, L , acts as a resonant “cavity” for these waves with the eigen frequencies given by $\omega_N = \omega_0(1 + 2N)$, where $N = 1, 2, 3, \dots$ and the fundamental plasma frequency $\omega_0 = \pi \sqrt{e(U_{gs} - U_{th})/m} / 2L$ can be easily tuned by changing the gate voltage, U_{gs} . When $\omega_0\tau \ll 1$, (τ is the momentum relaxation time), the detector response is a smooth function of ω and the gate voltage (broadband detector). When $\omega_0\tau \gg 1$, the FET can operate as a resonant detector. For the submicron gate lengths, the resonant detection frequency $f = \omega_0/2\pi$ can reach the THz range [1].

If the quality factor of the resonant cavity, $\omega_0\tau \gg 1$, the electron flow in the channel may become unstable (at certain boundary

conditions) with respect to formation the resonant plasma oscillations. In this paper, we review our recent experimental results for detection of terahertz and subterahertz radiation by submicron heterostructure field effect transistors.

The basic idea of detection can be formulated as follows: An electromagnetic radiation with the frequency ω excites plasma waves in the channel. The nonlinear properties of such waves and asymmetric boundary conditions at source and drain lead to the radiation-induced constant voltage drop along the channel ΔU [1,2], which is the detector response. The experimental exploration of the subject has begun long time ago, starting from the observation of the non-resonant detection in high mobility transistors [3,4]. A new boost to the research in this direction was given by a series of publications [5,6,7], observation of the infrared detection in short channel high electron mobility transistors (HEMTs) fabricated from different materials and in Si MOSFETs. The publications reporting non-resonant detection were followed by demonstration of resonant infrared detection in GaAs HEMTs [8,9] and gated double quantum well heterostructures [10,11]. In all devices, the 2D plasmon was tuned to the frequency of subterahertz radiation by varying the gate bias.

Recently, we observed the resonant detection using THz sources in the range from 0.7 to 3.1 THz [12]. The experiment was performed on InGaAs/AlInAs and AlGaIn/GaN HEMT with a 50 nm, 150 nm gate lengths respectively, employing the CO₂ pumped FIR gas laser as a source of THz radiation.

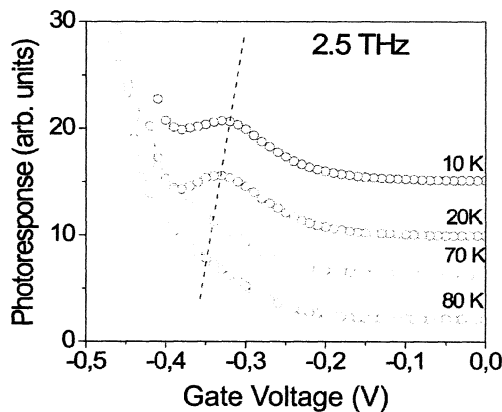


Fig. 1: Photoresponse of InGaAs device vs. the gate voltage at different device temperatures at 2.5 THz. For the sake of clarity; curves are shifted in the vertical scale. Dashed lines show the zero levels. (After Ref [12])

Figure 1 presents the results of the photoresponse measured in InGaAs/AlInAs-based devices. At the device temperature below 100 K, the shoulder becomes pronounced in the lower gate voltage side, in between $-0.4 \div -0.3$ V, in addition to the temperature-independent non-resonant detection peak near the transistor threshold voltage. It further evolves to the clearly resolved temperature-sensitive spike nicely visible below 40 K. We attribute these peaks to the resonance detection of THz frequencies by plasma waves. Since the electron mobility at 60 K is about $36\,000 \text{ cm}^2/\text{V}\cdot\text{s}$, which corresponds to the momentum relaxation time of 800 fs, we should expect the quality factor at 2.5 THz be of $\omega_0\tau \approx 13$. However, one can note, that even at 10 K, when the plasma resonance is visible around 0.33 V, it still remains very broad, about 60 mV, or about 1.5 THz in frequency domain. The corresponding relaxation time determined from the resonance half width at half as height, $\tau = 1/(\pi\Delta f)$, to be $\tau \approx 212$ fs, and the quality factor $\omega_0\tau \approx 3$. This additional resonance peak broadening shows that additional mechanisms of the plasma waves damping must be involved. These mechanisms might include the effect of ballistic transport [13], viscosity of the electron fluid due to the electron-electron collisions [1] and a possible effect of oblique plasma modes [14]. Figure 2 shows the photoresponse at difference excitation frequencies at 10 K. One can see, that with the increase of excitation frequency from 1.8 THz to 3.1 THz, the plasmon resonance moves to higher gate voltages in a decent agreement with the calculated fundamental plasma frequency as a function of the gate voltage.

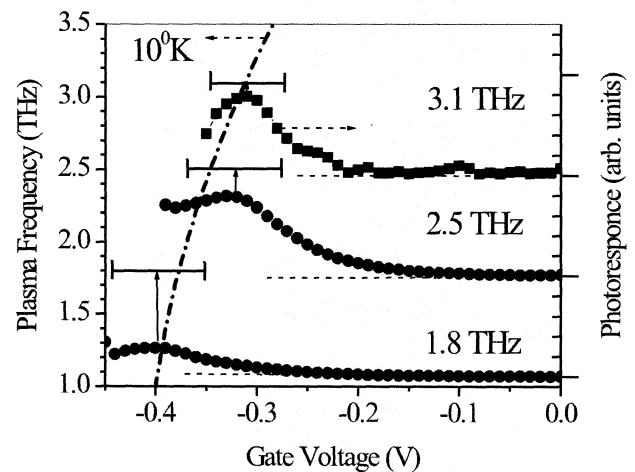


Fig. 2. Photoresponse in InGaAs/AlInAs-based device vs. the gate voltage at three different frequencies of excitation

(1.8 THz, 2.5 THz and 3.1 THz) at 10 K. (right axis). Curves are shifted in the vertical scale. Dashed lines indicate zero photoresponse at corresponding frequency. Arrows indicate resonance positions. Calculated plasmon frequency as a function of the gate voltage for $V_{th} = -0.41$ V (threshold voltage) is shown by the dash-dotted line (left axis). The error bars corresponds to the linewidth of the experimental resonance peaks. (After Ref [12].)

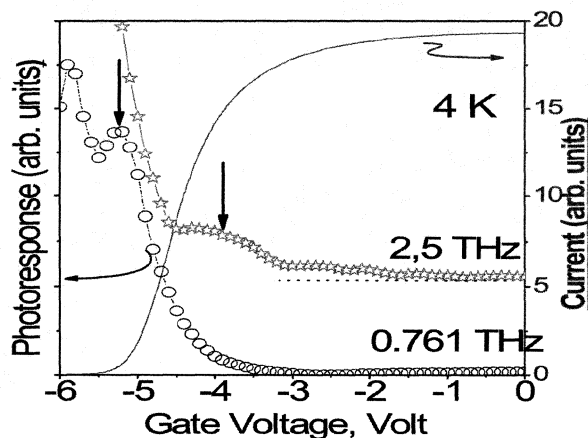


Fig. 3. Photoresponse in AlGaIn/GaN-based device vs. the gate voltage at two different frequencies of excitation (0.761 THz and 2.5 THz) at 4 K. (left axis). Curves are shifted in the vertical scale. Dashed lines indicate zero photoresponse at corresponding frequency. Arrows indicate resonance positions. Drain current vs. the gate voltage at 4 K (right axis). $V_{th} = -5.2$ V (threshold voltage).

Figure 3 shows the photoresponse at difference excitation frequencies at 4 K. One can see, that with the increase of excitation frequency from 0.761 THz to 2.5 THz, the plasmon resonance moves to higher gate voltages. In a agreement with the calculated fundamental plasma frequency as a function of the gate voltage.

The responsivity of the device was estimated to be of the order of 1V/W. Such a low value is due to a weak coupling of the THz radiation to the channel plasma, and to small area of the device, capturing only a tiny fraction of the incoming THz beam. According to the recent theoretical calculation [15] the coupling could be dramatically increased by using large area multi-finger design or employing THz antennas. Operating temperature, required for the resonant detection, could be increased then driving transistor into the saturation mode [16]

and ideally the temperature can reach 300 K.

To conclude, both resonant and non-resonant detection of sub-THz and THz radiation exploiting plasma waves have been observed in transistors of different materials including InGaAs/AlInAs and AlGaIn/GaN.

Acknowledgement

We are grateful also to Yahya Meziani, Edmundas Širmulis, and Zigmas Martūnas for the kind assistance during the experiments and enlightening discussions. The work of Montpellier group and collaboration with Vilnius group were supported by CNRS- GDR project "Semiconductor sources and detectors of THz frequencies", region of Languedoc Rousillon and French Ministry of Research and New Technologies through the ACI grant NR0091.

The collaboration between Montpellier and Vilnius is supported by the projects PRAMA via the programme "Centres of Excellence". The research conducted at Vilnius was performed under the topic "Study of semiconductor nanostructures for terahertz technologies" (No.144.1).

References

- [1] M. Dyakonov and M. S. Shur, Phys. Rev. Lett. **71**, 2465 (1993).
- [2] M. Dyakonov and M. S. Shur, IEEE Trans. Electron Devices **43**, 380 (1996).
- [3] Weikle et al, Electronics Letters **32**, 2148 (1996).
- [4] J. Lu et al, IEEE Electron Device Letters **19**, 373 (1998).
- [5] W. Knap et al, J. Appl. Phys. **91**, 9346 (2002).
- [6] W. Knap et al, Appl. Phys. Lett., **80**, 3433 (2002).
- [7] W. Knap et al, Appl. Phys. Lett. **85**, 675 (2004).
- [8] J.-Q. Lu et al, IEDM '98 Technical Digest, San Francisco, CA, december (1998).
- [9] W. Knap et al, Appl. Phys. Lett. **81**, 4637 (2002).
- [10] X. G. Peralta et al, Appl. Phys. Lett. **81**, 1627 (2002).
- [11] X. G. Peralta et al, in Proc. ICPS-26, Edinburgh, UC, (2002), Institute of Physics (2003).
- [12] A. El Fatimy et al, "Resonant and voltage tuneable terahertz detection in InGaAs/InP - nanometre transistors", Appl. Phys. Lett., submitted.
- [13] M. S. Shur, IEEE Electron Device Letters **23**, 511 (2002).
- [14] M. Dyakonov and M. S. Shur. Private communications.
- [15] V. V. Popov et al, Proc. SPIE **5772**, 63 (2005).
- [16] D. Veksler et al, Phys. Rev. B **73**, 125328(2006)

TeraHertz Emission and Detection From Ion-irradiated $\text{In}_{0.53}\text{Ga}_{0.47}\text{As}$ Gated at $1.55 \mu\text{m}$

N. Chimot, J. Mangeney, P. Crozat, K. Blary, J.F. Lampin

Abstract— We investigate terahertz (THz) emission and detection from heavy-ion-irradiated $\text{In}_{0.53}\text{Ga}_{0.47}\text{As}$ photoconductive antennas excited at 1550 nm . The spectrum of the electric field radiated from the Br^+ -irradiated $\text{In}_{0.53}\text{Ga}_{0.47}\text{As}$ antenna extends beyond 2 THz . The THz electric field magnitude is investigated and shown to saturate at high optical pump fluence.

Index Terms—photoconductive devices, electromagnetic radiation, telecommunication, antenna measurements

I. INTRODUCTION

The generation and detection of coherent terahertz radiation from photoconductive antenna has attracted considerable interest as it is a way to reach the intermediate THz frequency range. The best terahertz performance is achieved by a photoconductive antenna, excited by $\sim 800 \text{ nm}$ optical pulses, and made from low-temperature-grown (LTG) GaAs material [1]. Efforts are currently made to extend the spectral window of the excited signal to the $1.55 \mu\text{m}$ region. The major benefits of using optical telecommunication wavelengths are the access to optical-fiber technologies, the stability of optical sources and cost reduction. High radiation conversion efficiency for $1.55 \mu\text{m}$ wavelength requires narrow band gap material with short carrier lifetime and high resistivity. It has been shown that Fe-implanted $\text{In}_{0.53}\text{Ga}_{0.47}\text{As}$ lattice matched to InP is an efficient terahertz emitter [2] and detector [3] using 1560 nm optical command. We present Br^+ -irradiated $\text{In}_{0.53}\text{Ga}_{0.47}\text{As}$ photoconductive antenna excited at $1.55 \mu\text{m}$ as an emitter and detector of terahertz radiations. Ionic irradiation is an efficient method to introduce defects, which act as efficient trap and recombination centers for free carriers. Br^+ -irradiated $\text{In}_{0.53}\text{Ga}_{0.47}\text{As}$ is found to have both sub-picosecond carrier lifetime and relatively good electrical properties [4].

II. PHOTOCODUCTIVE ANTENNAS

Undoped $1\text{-}\mu\text{m}$ -thick n-type $\text{In}_{0.53}\text{Ga}_{0.47}\text{As}$ layers were epitaxially grown by gas-source MBE on semi-insulating InP:Fe substrates. A mesa etching process was used to define an $\text{In}_{0.53}\text{Ga}_{0.47}\text{As}$ absorbing area of $7 \times 14 \mu\text{m}^2$ on the InP substrate. The layers were then irradiated by 11 MeV heavy ions (Br^+) at irradiation doses up to $2.10^{12} \text{ cm}^{-2}$. With their high initial energy, the ions used for the bombardment are implanted in the InP substrate at a depth superior to $3 \mu\text{m}$, and, according to calculations using “Stopping Range of Ions in the Matter” [3] software uniform damage profiles through the $\text{In}_{0.53}\text{Ga}_{0.47}\text{As}$ layer are created. The $\text{In}_{0.53}\text{Ga}_{0.47}\text{As}$ layers are then free from ions used for bombardment and the damages are only host atom displacements distributed in defect condensates. Previous studies have shown that these defect clusters have deep energy levels that act as efficient capture and recombination

centers for free carriers. Degenerated pump-probe experiments and Hall effect measurements were performed. In figure 1 are shown the electron lifetime and the electron mobility deduced from these measurements.

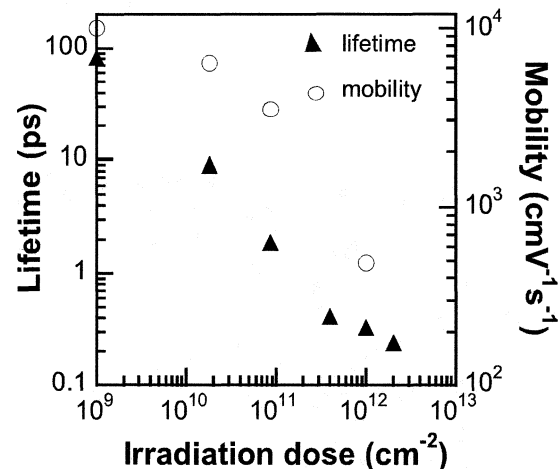


Fig. 1. electron lifetime and electron mobility as a function of irradiation dose.

Ionic irradiation is an efficient way to tune the carrier lifetime and to achieve subpicosecond values. When $\text{In}_{0.53}\text{Ga}_{0.47}\text{As}$ is irradiated at $1.10^{12} \text{ ions / cm}^2$, the carrier lifetime is as short as 330 fs . A relatively good Hall mobility of $490 \text{ cm}^2/\text{V}\cdot\text{s}$ and a resistivity of $3.1 \Omega\cdot\text{cm}$ are also measured. Antenna structures were fabricated by metal evaporation and a conventional lift-off photolithographic technique on this layer. In this work, Ti/Au coplanar electrodes of our emitter and detector are separated by gaps of 80 and $30 \mu\text{m}$, respectively. Each electrode is $5 \mu\text{m}$ wide and 20 mm long. The detector presents a $5 \mu\text{m}$ gap dipole antenna.

III. MEASUREMENTS

In the experiment, 200 fs optical pulses with a repetition rate of 14.3 MHz , delivered by a passively mode-locked fiber laser (Calmar Optcom) operating at 1550 nm were used to excite the both photoconductive switches via an optical fiber. The excitation beam was focused on our photoconductive antenna on a spot size of about $5 \mu\text{m}$ near the anode of our antennas. We used high-resistivity silicon hyper-hemispherical lens attached to the backs of the emitter and detector antennas. Emitter and detector antennas are separated by 5 cm . $\text{In}_{0.53}\text{Ga}_{0.47}\text{As}$ photoconductive antenna used for detection was irradiated by $1.10^{12} \text{ ions / cm}^2$ and is gated by 3 mW . Figure 2 shows the signal waveforms emitted by un-irradiated and $1.10^{12} \text{ ions / cm}^2$ irradiated photoconductive antenna. They are respectively biased at 5 and 25 volts . The average optical excitation power is 3 mW .

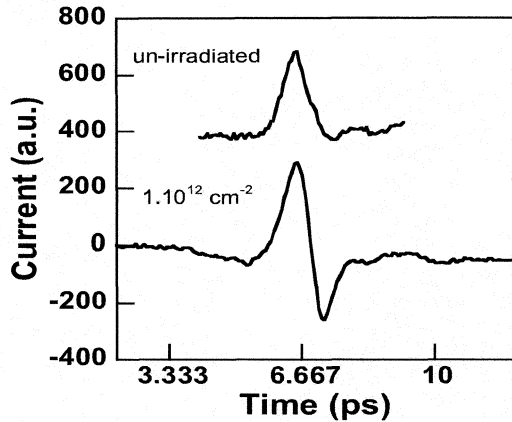


Fig. 2. normalized terahertz radiation waveforms emitted by un-irradiated and 1.10^{12} ions / cm^2 irradiated $\text{In}_{0.53}\text{Ga}_{0.47}\text{As}$ photoconductive antenna.

We observe a clear difference between the two waveforms presented in figure 2. The amplitude of negative peak of the signal emitted by the irradiated photoconductive antenna is higher than for the un-irradiated photoconductive antenna. Using the dipole radiation approximation in the far field, these typical waveforms result from the temporal derivative of the transient photocurrent. The main positive peak is attributed to the rises of the surge current by photocarrier injection and the carrier acceleration under the bias field. The second negative peak is attributed to the decay of the current governed by the carrier trapping time. This time is clearly shorter in the irradiated photoconductive antenna. This explains the difference between the two waveforms. The positive peaks of the waveforms show a full-width-at-half-maximum (FWHM) of 0.6 ps.

Figure 3 displays the radiation power spectra calculated from the fast Fourier transform of the waveforms in figure 2.

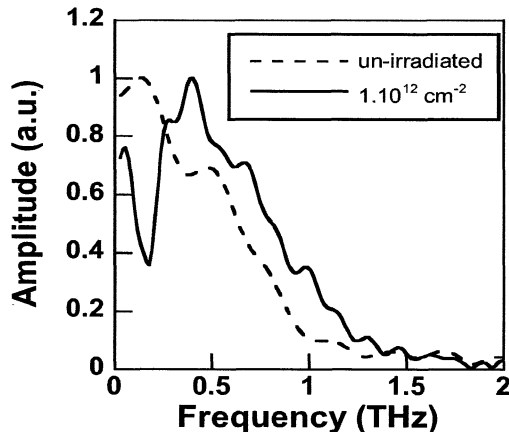


Fig. 3 Fast Fourier transforms of the temporal waveforms emitted by un-irradiated and 1.10^{12} ions / cm^2 irradiated $\text{In}_{0.53}\text{Ga}_{0.47}\text{As}$ photoconductive antenna.

These spectra extends up to 1.6 THz. The maximum of the spectrum is shifted from 0.15 THz for the un-irradiated emitter to 0.40 THz for the 1.10^{12} ions / cm^2 emitter. The fastest recovery of the photocurrent in the irradiated photoconductive antenna explains this spectrum shift to the higher frequency side [4]. The 30 dB dynamic range of the spectrum is limited by the signal to noise ratio of the experiment. The absolute amplitudes are not compared because of the critical positioning of the hyper-hemispherical lens.

IV. CONCLUSION

We have shown the generation and the detection of electromagnetic terahertz radiation from ion irradiated $\text{In}_{0.53}\text{Ga}_{0.47}\text{As}$ photoconductive antennas illuminated by 1,55 μm wavelength. This result opens new perspectives for the realization of terahertz spectroscopic bench using the telecommunication wavelength.

ACKNOWLEDGMENT

The authors would like to thank S. Henry from CSNSM in Orsay for ion irradiation. This work has been carried out in the frame of the French RTB network

REFERENCES

- [1] A.C. Warren, N. Katzenellenbogen, D. Grisckowsky, J. M. Woodall, M.R. Melloch, N. Otsuka, "Subpicosecond, freely propagating electromagnetic pulse generation and detection using GaAs:As epilayers", *Appl. Phys. Lett.*, **58**, pp. 1512-1514 (1991)
- [2] M. Suzuki, M. Tonouchi, "Fer-implanted InGaAs emitters for 1.56 μm wavelength excitation", *Appl. Phys. Lett.* **86**, pp. 51105-51107 (2005)
- [3] M. Suzuki, M. Tonouchi, "Fer-implanted InGaAs terahertz detectors triggered by 1.56 μm femtosecond pulses", *Appl. Phys. Lett.* **86**, pp. 163504-163506 (2005)
- [4] N. Chimot, J. Mangeney, L. Joulaud, P. Crozat, H. Bernas, K. Blary, J.F. Lampin, "terahertz radiation from heavy-ion-irradiated $\text{In}_{0.53}\text{Ga}_{0.47}\text{As}$ photoconductive antenna excited at 1.55 μm ", *Appl. Phys. Lett.*, **93**, pp. 193510-193512 (2005)
- [5] J. P. Biersack, L. G. Haggmark, "A Monte Carlo computed program for the transport of energetic ions on amorphous targets", *Nucl. Instrum. Methods*, **174**, pp. 257-280 (1980)
- [6] S. Salem, D. Morris, V. Aimez, J. Beauvais, D. Houde, "Improved characteristics of a terahertz set-up built with an emitter and a detector made on proton-bombarded GaAs photoconductive materials", *Semicond. Sci. Technol.*, **21**, pp. 283-286 (2006)

Spectral Characterization of a 2.5 THz Multi-Mode Quantum Cascade Laser

S. G. Pavlov, H.-W. Hübers, H. Richter, and A. D. Semenov
German Aerospace Center (DLR)
Rutherfordstr. 2, 12489 Berlin, Germany

A. Tredicucci, R. Köhler, and L. Mahler
NEST CNR-INFM and Scuola Normale Superiore
Piazza dei Cavalieri 7, 56126 Pisa, Italy

H. E. Beere and D. A. Ritchie
Cavendish Laboratory, University of Cambridge, Madingley Road, Cambridge CB3 0HE,
United Kingdom

Recently, terahertz-range semiconductor quantum cascade lasers (QCL) have attracted attention as potential local oscillators in heterodyne receivers. The basic characterization of the lasers, such as beam profiles, frequency and power stability as well as temperature and current-related frequency tunability has been carried out. Precise spectral analysis is required if the device is going to be used for applications requiring very accurate absolute frequency, spectral purity and fine frequency tunability, such as in heterodyne spectroscopy. By combination of Fourier transform spectroscopy with heterodyne and homodyne mixing measurements it is possible to create a complete picture of the QCL spectral output. We will report on the characterization of a 2.5 THz multi-mode QCL with respect to mechanisms determining the laser emission frequency and mode spectrum. The laser mechanism is based on a bound-to-continuum laser design. Laser emission spectra at different drive currents and heat sink temperatures have been measured by homodyne (QCL-QCL) and heterodyne (QCL-THz gas laser) mixing experiments. The analysis shows that variations of the laser frequency and modifications of the mode spectra are caused by fast processes which apparently control the gain of the device. The emission frequencies of the QCL based on a bound-to-continuum design can be described by a formalism similar to a Fabry-Perot-type cavity with additional corrections, depending on the QCL frequency and drive current. The detailed study of the spectral characteristics provides basic data about the direction, magnitude, and range of the frequency tunability of QCLs of this family/design. The data are necessary for implementation of the laser in a THz heterodyne receiver for example on board of SOFIA.

Micromachined Spatial Filters for Quantum Cascade Lasers

Abigail Hedden, Patrick Pütz, C. d'Aubigny, Dathon Golish, Christopher Groppi, Christopher Walker, Benjamin Williams, Qing Hu, and John Reno

Abstract—Quantum Cascade Lasers (QCL) are the most promising technology for producing compact, high power (> 1 mW), coherent signal sources above 2 THz. Due to their small size ($10 \mu\text{m} \times 25 \mu\text{m}$) and rectangular cross-section, the output beam from a QCL laser cavity is highly divergent and non-Gaussian. A single mode Gaussian beam is desirable for efficient coupling to optical systems. We have designed a waveguide spatial filter for this purpose. The 2.7 THz spatial filter consists of two diagonal feed horns connected by one wavelength of square waveguide ($92 \mu\text{m}$ on a side). The mode filtering efficiency and far field beam pattern of the structure have been modeled in CST Microwave Studio. We have fabricated the filter in tellurium copper using a Kern MMP micromilling machine. We present measurements of the QCL's throughput and emergent power pattern with and without the filter. Our preliminary findings suggest that spatial filtering significantly improves the QCL beam pattern, and further measurements are being made to more rigorously explore these results.

Index Terms—Quantum Cascade Lasers, waveguide spatial filters, terahertz, beam pattern.

I. INTRODUCTION

THERE is a growing need in the astronomical community for high frequency (>1 THz), high spatial and spectral resolution observations. Until recently, there has been a lack of high resolution astronomical data in the THz regime (1 THz – 10 THz) due to difficulties in constructing coherent receivers and the poor transmission of Earth's atmosphere at these frequencies. Space-based and airborne missions such as Herschel and SOFIA have spurred advances that have helped overcome some of these barriers, pushing the frontiers of heterodyne receiver technology to ~ 2 THz. Through diligent efforts of many researchers, astronomers are beginning to tap into the 1.3 and 1.5 THz atmospheric windows, obtaining spectroscopic observations of important tracers including high-J CO lines and the $205 \mu\text{m}$ [NII] line, e.g., [1]–[3]. Spectroscopy at THz frequencies is providing a wealth of information about the inner workings of our galaxy, encompassing

Manuscript received June 30, 2006. This work was partially supported by a NASA GSRP grant, no. NGT5-50463, to A. Hedden. P. Pütz is partially supported by DFG grano no. SFB494.

A. Hedden, P. Pütz, C. d'Aubigny, D. Golish, C. Groppi, & C. Walker are with Steward Observatory, University of Arizona, 933 N. Cherry Ave., Tucson, AZ 85721, USA (A. Hedden phone: 520-621-6535; fax: 520-621-1532; e-mail: ahedden@as.arizona.edu).

P. Pütz is also with KOSMA, I. Physikalisches Institut der Universität zu Köln, Zùlpicher Str. 77, 50937 Köln, Germany.

B. Williams & Q. Hu are with Department of Electrical Engineering and Computer Science & Research Laboratory of Electronics, Massachusetts Institute of Technology, Cambridge, MA 02139, USA.

J. Reno is with Sandia National Laboratories, Albuquerque, NM 87185, USA.

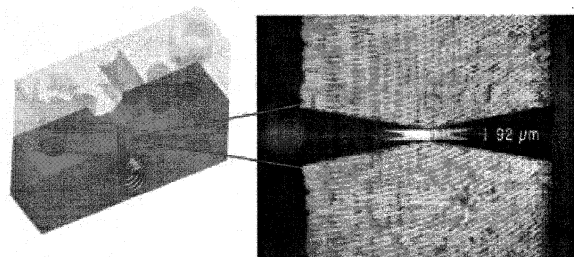


Fig. 1. Microscopic and CAD images of a split-block half of the 2.7 THz spatial filter structure. Two diagonal feed horns are connected by \sim one wavelength ($\lambda_g(\text{TE}_{10}) = 140 \mu\text{m}$) of $92 \mu\text{m}$ square waveguide.

protostellar cores, high-mass star formation, mechanisms of formation and destruction of molecular clouds, and life cycles of the galactic interstellar medium. These scientific goals continue to drive the developing technology toward higher frequencies and multi-pixel arrays.

Future missions will require spectroscopic capabilities at even higher frequencies (2 THz – 6 THz), e.g., [4]. The development of heterodyne instruments operating in this region depends upon the availability of coherent LO sources. At these frequencies, current solid state LO chains may not be capable of providing sufficient power much above 2 THz [5]. Although gas lasers operating in the far infrared and THz regime can supply sufficient mixer pumping power, their size, weight, and operation requirements limit their utility. QCL devices are the most promising technology for LO sources above 2 THz.

The small physical size ($10 \mu\text{m} \times 25 \mu\text{m}$) and rectangular cross-section of QCL devices lead to highly divergent, non-Gaussian emergent power patterns ([6], [7], and this work). Laboratory HEB-QCL receiver tests have been conducted at 2.8 THz [8] and 2.5 THz [9], but with relatively inefficient LO-receiver optical coupling. We have designed, fabricated, and tested a 2.7 THz waveguide spatial filter that transforms the output of a QCL into a well-behaved Gaussian beam, thereby permitting the implementation of efficient optical systems.

II. QCL WITH MICROMACHINED SPATIAL FILTER

A. Micromachined Spatial Filter

Hollow metallic waveguide devices have proven themselves as efficient spatial filters in the far infrared and THz regimes. Such a filter, machined at MIT Lincoln Laboratory, was assembled and measured at 2 THz in Steward Observatory

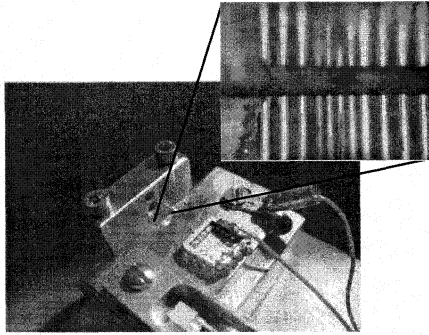


Fig. 2. Microscope image of QCL aligned with diagonal feed horn (illumination through feed horn). View of QCL chip and spatial filter mounted on cold finger of LN2 cryostat along with temp. sensor and device electrical connections.

[10]. These devices have been fabricated to frequencies as high as 5 THz using silicon laser micromachining techniques [11]. Recently, we have designed and metal machined a 2.7 THz spatial filter, consisting of two diagonal feed horns ($380\ \mu\text{m}$ aperture) arranged back-to-back and connected with one wavelength ($\lambda_g(\text{TE}_{10}) = 140\ \mu\text{m}$) of square waveguide ($92\ \mu\text{m} \times 92\ \mu\text{m}$, $170\ \mu\text{m}$ long).

Feedhorns provide very efficient coupling ($\sim 98\%$) for incident Gaussian beam modes, while coupling very poorly to any non-Gaussian components. The short section of waveguide between the feed horns is designed to provide excellent modal filtering; suppressing non-fundamental Gaussian modes by 6 orders of magnitude or more [12]. Spatially filtered signals then exit the device via the other feedhorn. In this manner, the designed filter not only passes Gaussian components from the divergent and non-Gaussian QCL emergent beam, but also, it ensures that the spatial filter output is single-moded. The far-field beam pattern of the filter's output was modeled in CST MWS and the device was micromilled in tellurium copper using a Kern MMP machine at Steward Observatory. Figure 1 shows CAD and microscopic images of the milled spatial filter cross-section.

B. QCL Chip

The QCL device used in these measurements was designed at MIT's Research Laboratory of Electronics and fabricated at Sandia National Laboratory. It uses a lower radiative level depopulation technique achieved through resonant tunnelling and LO-phonon scattering [13]. Mode confinement is accomplished with a low-loss, double-sided metal-metal waveguide fabricated via copper-to-copper thermocompression bonding [14]. Combined, these features permit a high CW operating temperature (110 K for device used in this work) and long lasing wavelengths (2.66 THz or 2.75 THz depending on bias). Figure 2 shows a microscopic image of the QCL chip and device used in this work. The active volume of the device is $19\ \mu\text{m} \times 800\ \mu\text{m} \times 10\ \mu\text{m}$ (width, length, and height, respectively) and $380\ \mu\text{W}$ output power was detected at 5 K operation with a Pyro detector and Winston cone mounted in front of the $19\ \mu\text{m}$ device facet.

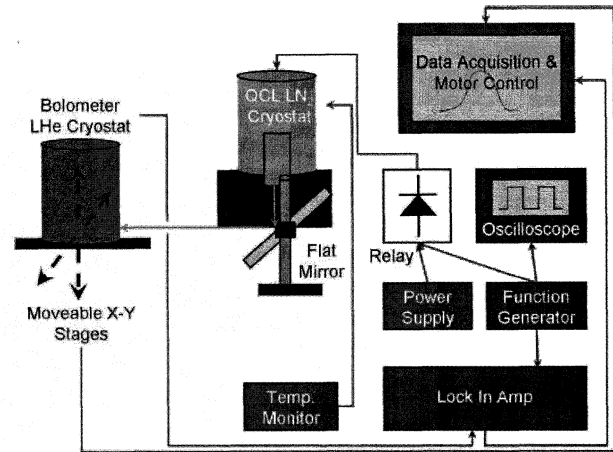


Fig. 3. Schematic of the measurement setup used to produce the presented beam patterns and cross-cuts. A 4.2 K Si bolometer mounted on moveable X-Y stages was used as a detector. The QCL device was electrically chopped with a 22 Hz square wave and was mounted on cold finger extension of a LN2 cryostat, operated under stable temperature conditions. Motions of the X-Y stages were controlled by a computer that also recorded the output of the lock-in amplifier used during measurements.

III. MEASUREMENT SETUP

Figure 2 shows the orientation of the QCL with respect to the spatial filter during beam pattern measurements. The QCL chip is indium soldered to a slotted copper mounting plate that was carefully aligned under a microscope so that the $19\ \mu\text{m}$ device facet faces the spatial filter's input diagonal horn. This assembly was mounted to a copper cold finger of a LN2 dewar and the temperature of the cold finger mount was monitored (81 K) to ensure stability during operations. The QCL chip and spatial filter were enclosed in a metal cavity for beam pattern measurements in order to reduce the risk that QCL radiation not coupling into the filter could leak through the cryostat window, resulting in spurious measurements.

Figure 3 is a schematic of the measurement setup used to produce the beam patterns presented in this work. The QCL device was electrically chopped with a 22 Hz, 50% duty cycle square wave at 11.50 V and 27 mA. A 4.2 K Si bolometer with a Winston cone was used as a detector. The bolometer cryostat was mounted to moveable X-Y stages capable of traveling a total of 60 cm in each axis. The LN2 dewar was mounted on an optical table with a 45° flat mirror to direct QCL power toward the X-Y stages. The total optical path length with the detector at the peak intensity location was 62.5 cm (with 1.4 cm in vacuum). Mylar windows 0.5 mil thick and 0.5 inches in diameter were used for both cryostats. Eccosorb was placed around the window and housing of the bolometer dewar, the X-Y stages, optical table, and LN2 cryostat in order to curb reflections during measurements. A Stanford Research Systems SR830 DSP lock-in amplifier was used during measurements. All motions of the moveable stages were computer controlled. In order to allow for settling of the bolometer cryostat, a dwell time of 2 s was used before each measurement was made. The integration time per position was 2 s.

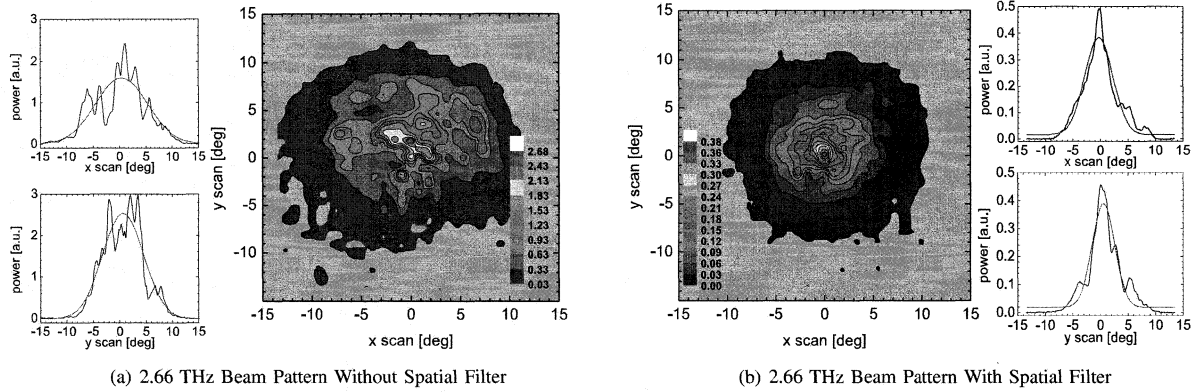


Fig. 4. Beam pattern measurements (2-D maps and high res. 1-D cross-cuts) at 2.66 THz of “bare” QCL (a) and QCL + spatial filter (b). Power is represented in arbitrary units. Resolution of 2-D maps is 0.9° and contours begin at 2σ and increase in 20σ steps to emission peak. Dynamic range achieved is 22 dB and 19 dB for measurements made with and without the spatial filter, respectively. High res. (0.2°) cross-cuts were made in two dimensions across the centers of each map. Gaussian fits to these cross-cuts yield 3 dB beam widths of 6.2° and 5.0° in “x” and “y” for measurements with the spatial filter and 11.6° and 9.2° for the “bare” QCL.

IV. RESULTS

With the described measurement setup, two dimensional (2-D) beam pattern measurements and high resolution 1-D cross-cuts were made with and without the spatial filter in front of the QCL device. The results are presented in Figure 4. Each of the 2-D beam pattern maps covers a total of 30 cm ($\sim 30^\circ$ with this experiment’s optical path) in each dimension and consists of raster-scanned measurements made at 1 cm spacing, resulting in 0.9° spatial resolution. The intensity scalings shown in the insets of Figure 4 represent power detected in arbitrary units, allowing for relative comparisons between data sets. The 2-D power patterns possess dynamic ranges of 22 dB and 19 dB for measurements made with and without the spatial filter, respectively. In addition, high resolution (0.2°) 1-D cross-cuts were made across the “x” and “y” centers of the maps.

Figure 4 indicates that spatial filtering improves the QCL beam pattern quality significantly. Measurements of the beam exiting the spatial filter show single-peaked, narrow features that are more Gaussian in shape than the unfiltered QCL output. For example, fitting Gaussian functions to the 1-D data yield 3 dB beam widths of 6.2° and 5.0° in “x” and “y” respectively for filtered measurements and 11.6° and 9.2° for the bare QCL. The throughput efficiency of the spatial filter is on the order of $\sim 10\%$; the ratio of peak power with and without the filter is 7% and the ratio of the integrated power within the 3 dB beam widths is 9%. This is a very encouraging preliminary result for telescope receiver and array applications, since $\sim 10\%$ of the QCL device’s output power is single-moded and Gaussian.

The strongest peak features appearing in the map and 1-D scans of the unfiltered data are repeatable and seem to be intrinsic to the QCL device’s output, supporting the interpretation that the observed output is divergent and non-Gaussian, potentially the result of internal interference [6]. Smaller peak features present in all data sets may partially arise from standing waves in the measurement setup. In

addition, there is a discrepancy in the 3 dB beam width of the spatial filter simulated in CST MWS (23.3°) and the measurements presented here (~ 5.0 – 6.2°). This mismatch is currently under investigation and has led us to redesign the QCL cold finger extension to permit a larger cryostat window and operation without the 45° flat mirror.

V. CONCLUSIONS AND OUTLOOK

We present a new method for improving the QCL beam pattern using waveguide spatial filters incorporating back-to-back feedhorns connected with square waveguide. We have designed, micromilled, and tested a 2.7 THz spatial filter with a resonant-phonon-assisted THz QCL device. We present 2-D maps and 1-D high resolution cross-cuts of power patterns with and without the spatial filter. Our results indicate that spatial filtering significantly improves the QCL beam pattern quality, with the emergent spatial filter signal being single peaked and more Gaussian. The measured throughput of the filter is $\sim 10\%$. Waveguide spatial filters provide a means of efficiently integrating QCLs into waveguide systems; e.g. power dividers, couplers, mixer blocks, etc. Silicon micromachining capabilities can extend the fabrication of waveguide spatial filters into the high THz range ([11]).

REFERENCES

- [1] M. C. Wiedner, G. Wieching, F. Biellau, K. Rettenbacher, N. H. Volgenau, M. Emprechtinger, U. U. Graf, C. E. Honingh, K. Jacobs, B. Vowinkel, K. M. Menten, L. Nyman, R. Güsten, S. Philipp, D. Rabanus, J. Stutzki, and F. Wyrowski, *Astronomy & Astrophysics manuscript no. 5341* (2006).
- [2] D. P. Marrone, R. Blundell, E. Tong, S. N. Paine, D. Loudkov, J. H. Kawamura, D. Lühr, and C. Barrientos, *16th Int’l Symp. on Space THz Tech.*, eds. J. Stake, H. Merkel, Göteborg, Sweden: Chalmers (2005).
- [3] D. P. Marrone, J. Battat, F. B. Besch, R. Blundell, M. Diaz, H. Gibson, T. Hunter, D. Meledin, S. Paine, D. C. Papa, S. Radford, M. Smith, and E. Tong, *Astrophysical Journal* **612**, 940 (2004).
- [4] Th. de Graauw, J. Cernicharo, W. Wild, A. Box, J-W. den Herder, A. Gunst, F. Helmich, B. Jackson, H-J. Langevelde, P. Maat, J. Martin-Pintado, J. Noordam, A. Quirrenbach, P. Roelfsema, L. Venema, P. Westelius, and P. Yagoubov, *Proc. SPIE* **5487**, 1522 (2004).
- [5] I. Mehdi, E. Schlecht, G. Chattopadhyay, and P. H. Siegel, *Proc. SPIE* **4855**, 435 (2003).

- [6] A. J. L. Adam, I. Kašalynas, J. N. Hovenier, T. O. Klaassen, J. R. Gao, E. E. Orlova, B. S. Williams, S. Kumar, Q. Hu, J. L. Reno, *Appl. Phys. Lett.* **88**, 1 (2006).
- [7] S. Kohen, B. S. Williams, and Q. Hu, *J. Appl. Phys.* **97**, 053106 (2005).
- [8] J. R. Gao, J. N. Hovenier, Z. Q. Yang, J. J. A. Baselmans, A. Baryshev, M. Hajenius, T. M. Klapwijk, A. J. L. Adam, T. O. Klaassen, B. S. Williams, S. Kumar, Q. Hu, J. L. Reno, *Appl. Phys. Lett.* **86**, 244104 (2005).
- [9] H.-W. Hübers, S. G. Pavlov, A. D. Semenov, A. Tredicucci, R. Köhler, L. Mahler, E. E. Beere, E. H. Linfield, and D. A. Ritchie, *16th Int'l Symp. on Space THz Tech.*, eds. J. Stake, H. Merkel, Göteborg, Sweden: Chalmers (2005).
- [10] C. K. Walker, G. Narayanan, H. Knoepfle, J. Kapara, J. Glenn, A. Hungerford, T. M. Bloomstein, S. T. Palmacci, M. B. Stern, J. E. Curtin, *8th Int'l Symp. on Space THz Tech.*, eds. R. Blundell, E. Tong, Boston: Harvard University (1997).
- [11] C. Y. Drouët d'Aubigny, C. K. Walker, D. Golish, M. R. Swain, P. J. Dumont, P. R. Lawson, *Proc. SPIE* **4852**, Interferometry in Space, ed. M. Shao (2002).
- [12] C. Y. Drouët d'Aubigny, *Laser Chemical Etching of Waveguides and Quasi-optical Devices*, Ph.D. Dissertation, Univ. of Arizona (2003).
- [13] Q. Hu, B. S. Williams, H. Callebaut, S. Kohen, and J. L. Reno, *Semicond. Sci. Technol.* **20**, S228 (2005).
- [14] B. S. Williams, S. Kumar, Q. Hu, and J. L. Reno, *Electron. Lett.* **40**, 431 (2004).

Phase matched frequency mixing between telecom wavelengths and THz radiation in a quantum cascade laser

S. Dhillon,^{1,3} C. Sirtori,^{1,3} J. Alton,^{2,4} S. Barbieri,^{2,4} A. De Rossi,³ M. Calligaro,³ H. E. Beere⁴ and D. A. Ritchie⁴

¹Matériaux et Phénomènes Quantiques, Université Denis Diderot - Paris 7, Paris, France

²TeraView Ltd., 304 Platinum Building, St John's Innovation Park, Cambridge, CB4 0WS, United Kingdom

³Thales Research and Technology, 91404 Orsay, France

⁴Cavendish Laboratory, University of Cambridge, Madingley Road, Cambridge CB3 0HE, United Kingdom

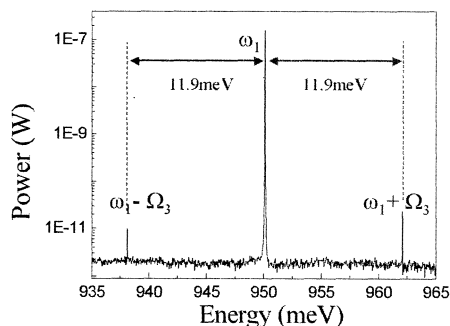
Abstract: Intra-cavity THz sideband generation at $\sim 1.3\mu\text{m}$ wavelength is demonstrated, achieved by injecting a near-infrared beam into a THz quantum cascade laser ($f=2.9\text{THz}$, $\lambda=104\mu\text{m}$). This process is shown to be phase matched due to the phonon-induced anomalous dispersion.

Owing to its large second-order susceptibility, GaAs is an interesting material for non-linear optical generation [1]. The lack of birefringence on the other hand makes phase matching difficult to realise, therefore limiting the non-linear conversion efficiency. However, owing to the anomalous dispersion produced by the *reststrahlenband*, the refractive index at long wavelengths (the far-infrared or terahertz (THz) range) is larger than that in the mid- and most of the near infrared (NIR). This opens up the possibility of a 'natural' phase matching between the THz range and the NIR [2].

In this investigation a GaAs-based quantum cascade laser (QCL) [3] operating at $104\mu\text{m}$ ($f=2.9\text{THz}$, $E=11.9\text{meV}$) is used both as a THz source and a non-linear medium. A NIR tunable diode laser, operating around 1300nm , is coupled into the THz QCL. Figure 1a shows the generated intra-cavity side-bands, which are clearly observed at the difference and sum frequency of the THz and NIR radiation [4]. The phase matching condition was verified by tuning the NIR wavelength between 1260nm and 1340nm and showed a phase matched point at 1305nm (Fig 1b). The conversion efficiency for the frequency mixing processes, $P(\omega_1 \pm \Omega_3)/P(\omega_1)$, is 1×10^{-5} at the peak of the phase matching curve, in reasonable agreement with the expected value. Recent investigations have demonstrated that this phase matched point can be tuned towards 1550nm using modal engineering of the THz guide, such that the THz refractive index is varied without effecting that of the NIR mode.

These results illustrate the possibility of detecting THz radiation using a up-conversion process of a low power NIR laser and to transport the THz radiation on an optical carrier.

(a)



(b)

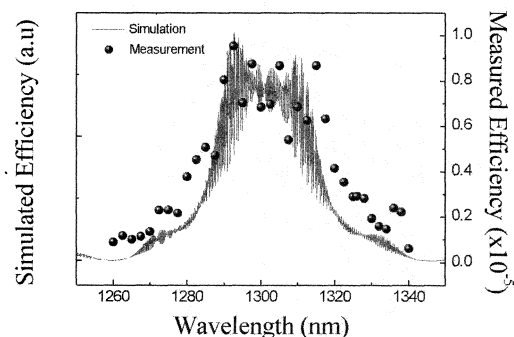


Figure 1. (a) Near infrared spectrum from the output of the THz QCL (fiber coupled). The QCL is cooled to 14K and is operated in CW. Side-bands are observed at $\omega_1 + \Omega_3$ and $\omega_1 - \Omega_3$. (b) Measured and expected efficiency as a function of pump wavelength for the sum frequency process showing a broad phase matching.

[1] J-Y. Bengloan, A. De Rossi, V. Ortiz, X. Marcadet, M. Calligaro, I. Maurin and C. Sirtori, *Appl. Phys. Lett.*, **84**, 2019 (2004).

[2] V. Berger and C. Sirtori, *Semicond. Sci. Technol.* **19**, 964 (2004).

[3] R. Köhler, A. Tredicucci, F. Beltram, H. Beere, E. H. Linfield, A. G. Davies, D. A. Ritchie, R. C. Iotti, and F. Rossi, *Nature* **417**, 156 (2002).

[4] S. S. Dhillon, C. Sirtori, A. de Rossi, M. Calligaro, H. E. Beere, S. Barbieri, E. H. Linfield, and D. A. Ritchie, *Appl. Phys. Lett.*, **87**, 071101 (2005).

Analysis of the stable two-mode operation of a 4-sections semiconductor laser for THz generation by photomixing

A. Akwoué Ondo*, J. Torres, P. Nouvel, C. Palermo, L. Chusseau
CEM2, UMR 5507 au CNRS, Université Montpellier II, 34095 Montpellier, FRANCE.

*email: akwoue@cem2.univ-montp2.fr

J. Jacquet, LMOPS Supélec, 2 Rue Édouard Belin, 57070 Metz, FRANCE.

M. Thual, FOTON, UMR 6082 au CNRS, ENSSAT, 6 rue de Kérampont, 22305 Lannion, FRANCE.

Abstract—The stable two-mode operation of a 4-sections semiconductor laser emitting at 1.55 μm is demonstrated and analysed. The two-mode operation only depends on the current feed in the Bragg section. We interpret this special behaviour by the presence of a saturable absorber within the structure. An original model based on Lamb's theory which take into account of a saturable absorber equation is developed in order to confirm our hypothesis. The characterization of the two-mode laser operation exhibits the possibility of terahertz (THz) wave generation by photomixing using this device.

Index Terms—Two-mode operation, 4-sections lasers, Lamb's theory, photomixing, terahertz .

I. INTRODUCTION

IN this paper, we report on a 4-sections laser structure able to operate continuously in a two-mode regime for photomixing THz applications. This solution was already explored at shorter wavelengths with LT-GaAs photodiode as rectifiers. We consider here the later case but apply at the 1.55 μm wavelength in order to take benefit of the future ultrahigh bandwidth uni-traveling carrier photodiodes [1] or of newly developed THz photoconductor from ion-implanted InGaAs [2], [3].

We have experimentally characterized the stable two-mode operation of the 4-sections semiconductor DBR laser and we propose here a physical explanation to this uncommon behavior. Indeed, theoretical studies of semiconductor laser dynamic have well illustrated only recently the possible multimode behavior of semiconductor lasers [4]–[6] just like it has long been observed experimentally. But a stable two-mode operation has never been predicted with laser parameters consistent with existing technologies. This is in accordance with a strong coupling between longitudinal modes of a semiconductor laser that is partly related to the ultrashort intraband-relaxation time (≈ 100 fs). We thus postulate the origin of this stable two-mode regime outside the usual laser model, namely by considering that a parasitic saturable absorber had been accidentally brought by the implanted areas used for insulation between the various laser sections. We discuss this hypothesis in depth by means of the classical Lamb theory of two-mode lasers [7].

II. THE 4-SECTIONS DBR LASER

The device is a classical 3-sections DBR laser (gain, phase and Bragg sections) with an additional integrated amplifier section. The Semiconductor Optical Amplifier (SOA) and the gain section are built with the same 6 InGaAs quantum wells (QW) epilayer while phase and distributed Bragg reflector (DBR) sections are obtained after etching and localized regrowth processes [8]. Optical gain is provided by the current I_{Gain} in the multiple QW. The laser beam is filtered by the DBR that imposes the emission wavelength (λ_{Bragg}) owing to the injection current I_{DBR} . The phase section inserted between gain and DBR sections allows a fine tuning of the emission wavelength by the electro-optical modification of the effective index through the current I_{ϕ} . Each section is electrically insulated from its neighbour using electron implantation on a few μm length area. The SOA section is bended and AR coated at its end to reduce simultaneously the beam divergence and drastically kill any optical feedback towards the DBR. A high reflectivity coating is deposited on the rear facet to increase the photon lifetime in the 3-section DBR laser. Complete performances (16 nm tunability and 55 mW output power) of this device are described in details elsewhere [8].

III. EXPERIMENTAL SET-UP

The experimental set up starts from a Suss PM5 Prober that allows to simultaneously supply the different currents to the laser and to couple the optical output of front and rear facets using specific microlens [9]. The main advantage of the selected configuration is to show that the two-mode operation doesn't require the SOA section. Indeed, we measured a two-mode laser operation on both sides (rear and front facet) of the device whatever the value of the SOA injected current I_{SOA} , especially for $I_{\text{SOA}} = 0$ mA. The major conclusion of this primary experiment was to reject the hypothesis of an imperfect antireflection coating at SOA end facet. Such a reflection would have cause the 4-sections DBR laser to behave as a coupled cavity device that is well known to operate frequently in two-mode regime. The occurrence of a stable two-mode regime should thus be ascribe to the 3-sections DBR only, the SOA section contribution being assumed subsequently to be a perfectly linear amplifier.

During all experiments, the working temperature was controlled owing to a thermoelectric cooler and stabilized within a few hundredth of Kelvin. The optical output was fed in an optical spectrum analyzer. The injection current was limited for each section of the device in order to avoid any destructive damage, namely $I_{SOA_{max}} = 150$ mA, $I_{Gain_{max}} = 100$ mA, $I_{DBR_{max}} = 50$ mA, $I_{\phi_{max}} = 30$ mA.

IV. MEASUREMENT RESULTS

When increasing I_{DBR} from 10 mA to 50 mA, we observed a succession of very different spectral behaviors of the 4-sections DBR laser (see Fig. 1). Transition from stable monomode generation to stable two-mode generation were registered together with their reverse transition. This was obtained while keeping all other parameters constant ($T = 300$ K, $I_{SOA} = 100$ mA, $I_{Gain} = 80$ mA and $I_{\phi} = 0$ mA). More precisely the laser is strictly monomode everywhere excepted for I_{DBR} close to 30 mA and to 40 mA. Usually the tuning process performed by I_{DBR} is to put in coincidence the Bragg maximum reflection and a Fabry-Pérot (FP) mode of the 3-sections laser. This behavior was observed with I_{DBR} increasing from 10 mA to 30 mA with a continuous singlemode tuning of the output from $1.550 \mu\text{m}$ to $1.554 \mu\text{m}$ over three FP mode hopping; the spacing between adjacent modes being $\delta\nu \approx 100$ GHz in this structure. Similar features were obtained for $30 \text{ mA} < I_{DBR} < 40 \text{ mA}$ and for $I_{DBR} > 40$ mA.

To the contrary, around $I_{DBR} \approx 30$ mA and $I_{DBR} \approx 40$ mA, a stable two-mode laser operation is measured, the two modes being separated by $\delta\nu \approx 100$ GHz, with balanced powers. This two-mode laser operation must be first attributed to the filtering of the DBR that roughly select two adjacent FP modes. We confirmed this assumption when observing that the two lasing modes at $I_{DBR} \approx 30$ mA were just shifted of $\delta\nu \approx 100$ GHz from the two lasing modes at $I_{DBR} \approx 40$ mA.

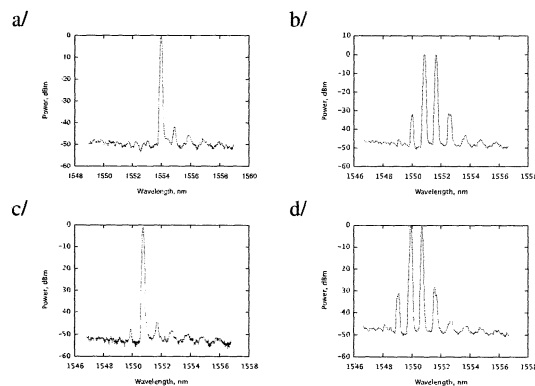


Fig. 1. Optical spectrum of 4-sections laser with $I_{SOA} = 100$ mA, $I_{Gain} = 80$ mA et $I_{\phi} = 0$ mA. a/ $I_{DBR} = 10$ mA; b/ $I_{DBR} = 30$ mA; c/ $I_{DBR} = 35$ mA; d/ $I_{DBR} = 40$ mA

Complementary investigations were directed in the vicinity of previously observed stable two-mode conditions. At $T = 300$ K and $I_{DBR} = 30$ mA we varied the gain current and

phase current in conjunction in order to maintain a strict two-mode operation with equal optical intensities on both modes. Results are given in Fig. 2a. It is observed that a stable two-mode operation is always possible as soon as I_{Gain} exceeds the laser threshold value. An increase of I_{Gain} is accompanied by a decrease of I_{ϕ} of exactly the same value since slopes of -1 are observed on the guidelines. This shows that the efficiency in index modulation of the phase section is exactly the same that the one of the gain section. Overall behavior depicted in Fig. 2 thus corresponds to a perfect locking on two given adjacent FP modes by simply keeping the sum $I_{Gain} + I_{\phi}$ constant. In more details the 4-sections DBR laser is locked on the two modes $\lambda_1 = 1549.96$ nm and $\lambda_2 = 1550.77$ nm when $I_{th} < I_{Gain} < 45$ mA and it is locked on $\lambda_1 = 1551.21$ nm and $\lambda_2 = 1551.98$ nm when $45 \text{ mA} < I_{Gain} < 80$ mA. The $I_{\phi} < 30$ mA current limit gives the corresponding limited range of locking and requires a mode hopping around $I_{Gain} \approx 45$ mA.

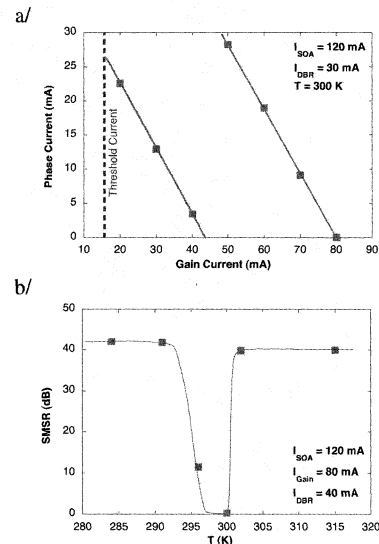


Fig. 2. a/ Observed stable two-mode operation with equal intensities for each mode as a function of gain and phase currents. Squares are some of the observed conditions while lines are guide to the eye between them. b/ Side mode suppression ratio (SMSR) measured as a function of device temperature.

Another characteristic was obtained by measuring the side mode suppression ratio (SMSR) of the 4-sections DBR laser as a function of temperature. Result is given in Fig. 2b with laser parameters of $I_{DBR} = 40$ mA, $I_{Gain} = 80$ mA and $I_{SOA} = 120$ mA. The higher the SMSR the most singlemode the 4-sections DBR. It was observed during experiments that uncertainties in the figure are pretty well represented by the size of square symbols. As seen, the 4-section DBR is highly singlemode almost everywhere except in a small temperature range around the room temperature. At this point, the SMSR is shown to change from 40 dB to 0 dB in less than 5 K when increasing the temperature and the reverse behavior is obtained in 2 K when increasing T from 300 to 302 K. In between, a stable two-mode behavior (SMSR < 3 dB) is

obtained within a range of ≈ 3 K in temperature. When referring to known values of the refractive index sensitivity with temperature in InP materials [10], this range corresponds to an overall modification of the guided mode refractive index of about $6 \cdot 10^{-4}$ within the 4-sections DBR laser. Although it is awfully stable when it occurs, the two-mode operation thus requires a quite precise set of values for laser operating parameters in order to be observed.

V. MODEL

The hypothesis to validate is that a saturable absorber may transform a 'usual' bistable semiconductor laser in a two-mode one. The most simple theory of two-mode laser comes from Lamb theory [7] and involves only simple differential equations of time to describe the dynamical intensity evolution and predict the occurrence of a two-mode regime. It differs from the usual rate equations commonly used for semiconductor lasers for which numerous typical parameters are known [11].

A. Lamb's model of the two-mode laser with saturable absorber

The existence of a stable two-mode operation implies particular coupling conditions between these modes [7]. Lamb's seminal analysis starts from two coupled ordinary differential equations describing the time evolution of mode optical intensities I_1 and I_2

$$\begin{aligned} \frac{dI_1}{dt} &= (\alpha_1 - \beta_1 I_1 - \theta_{12} I_2) I_1 \\ \frac{dI_2}{dt} &= (\alpha_2 - \beta_2 I_2 - \theta_{21} I_1) I_2 \end{aligned} \quad (1)$$

where the α_i are unsaturated net gain and where β_i and θ_{ij} are self- and cross-saturation coefficients. It is thus straightforward to show that steady state two-mode solutions in intensity are

$$I_{1SS} = \frac{\alpha_1 - (\theta_{12}/\beta_2) \alpha_2}{(1-C) \beta_1}, \quad I_{2SS} = \frac{\alpha_2 - (\theta_{21}/\beta_1) \alpha_1}{(1-C) \beta_2} \quad (2)$$

where

$$C = \frac{\theta_{12} \theta_{21}}{\beta_1 \beta_2} \quad (3)$$

is a dimensionless coupling factor that was shown by a perturbation analysis to dictate the existence of the stable two-mode operation. If $C > 1$, *i.e.* in the case of strong coupling, only singlemode operation is possible and the laser is bistable. This is the case expected for semiconductor lasers.

For stable two-mode operation, $C < 1$ is required. In practice an additional physical process must be invoked to reach this condition. This is easily obtained with a saturable absorber having a saturation characteristic similar to the gain medium [12]. In other words, if we suppose a non-dispersive saturable absorber a convenient modification of Eqs. (1) is to include characteristics terms of saturable absorber optical mode intensity $-(\gamma - \epsilon(I_1 + I_2))$:

$$\begin{aligned} \frac{dI_1}{dt} &= (\alpha_1 - \gamma - (\beta_1 - \epsilon) I_1 - (\theta_{12} - \epsilon) I_2) I_1 \\ \frac{dI_2}{dt} &= (\alpha_2 - \gamma - (\beta_2 - \epsilon) I_2 - (\theta_{21} - \epsilon) I_1) I_2 \end{aligned} \quad (4)$$

thus leading to a new coupling coefficient that must be less than 1 for possible stable two-mode operation with a saturable absorber

$$C' = \frac{(\theta_{12} - \epsilon)(\theta_{21} - \epsilon)}{(\beta_1 - \epsilon)(\beta_2 - \epsilon)} < 1 \quad (5)$$

When combined with the obvious constraint that coefficients in Eq. (4) must all be positive, it yields

$$\min(\beta_1, \beta_2, \theta_{12}, \theta_{21}) > \epsilon > \frac{\beta_1 \beta_2}{\theta_{12} + \theta_{21} - \beta_1 - \beta_2} (C - 1) \quad (6)$$

Provided that the condition Eq. (6) is validated, a bistable laser with a saturable absorber may switch to a stable two-mode laser.

B. Numerical estimation of bistable to two-mode operation

Numerical calculations were conducted using the typical parameters of a multi-quantum well semiconductor laser, *i.e.* a material gain $g = 4000 \text{ cm}^{-1}$, at a polarization current of 10 mA above threshold, and a photon cavity lifetime of $\tau_p = 1$ ps. The adjustment between single mode Lamb's theory and classical laser rate equations provided the numerical values of the linear gain and the self-saturation coefficients to be used in our model: $\alpha = 7.5 \cdot 10^{-2} \text{ ps}^{-1}$ and $\beta = 7.2 \cdot 10^{-6} \text{ } \mu\text{m}^3 \text{ ps}^{-1}$. Since our experimental device of interest operate on two spectrally close modes, we assumed $\alpha_1 = \alpha_2 = \alpha$ and $\beta_1 = \beta_2 = \beta$ in Eqs. (4). Starting from a naturally bistable laser with $C = 1.2$, we chose $\theta_{12} = 0.9\beta$ and $\theta_{21} = 1.33\beta$ as illustrating parameters. Then, Eq. (6) yields a corresponding range for the self-saturation of the saturable absorber that is $0.9 > \epsilon/\beta > 0.857$.

Experimental observations of Fig. 1 have shown that the two-mode operation depends on the DBR current value. It comes from the spectral dependence of the end mirror reflectivity provided by the DBR, the center wavelength of which being roughly driven linearly by I_{DBR} . In the framework of our model, this has been accounted for by variations in linear gains ($\alpha_i - \gamma$ terms in Eqs. (4)) so that their sum remains constant. This is a simple method to translate the effect of the DBR without trying to model exactly its transfer function that is out of the scope of the present work. This yields a 'relative detuning' parameter that can explore extensively the tuning practical possibilities of our true device.

Numerical calculations given in Fig. 3 illustrate the expected behaviors when ϵ lie without or within the range defined by Eq. (6). On the one side (Fig. 3a), we chose $\epsilon/\beta = 0.8$ that is outside the previous range. The result is that the laser is always bistable whatever the detuning parameter should be. A mode hopping is observed when the detuning parameter becomes larger than ≈ 0.42 and the two-mode regime is observed in the vicinity of this sudden change. On the other side (Fig. 3b), we chose $\epsilon/\beta = 0.9$ within the range defined by Eq. (6). The major result is a smoothing of the transition between the two modes that let open a detuning parameter range where the laser is effectively two-mode.

This behavior is in perfect accordance with experimental observations of Fig. 1 where an increase of I_{DBR} produce

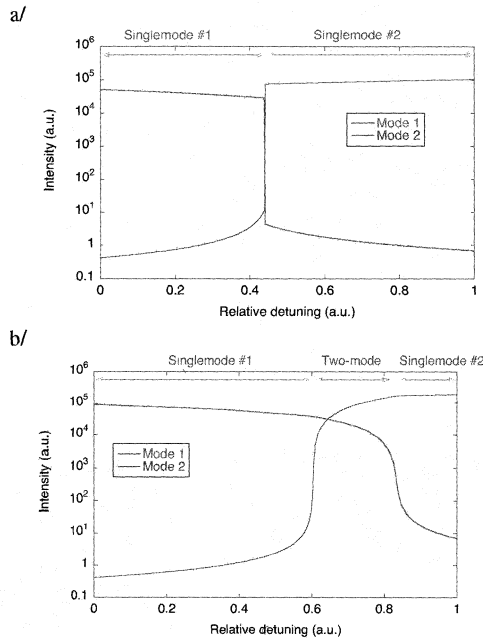


Fig. 3. Optical mode intensities obtained from Eqs. (4) as a function of the relative detuning parameter accounting for the DBR (see text), $\alpha_1 = \alpha_2 = 7.5 \cdot 10^{-2} \text{ ps}^{-1}$, $\beta_1 = \beta_2 = 7.2 \cdot 10^{-6} \text{ } \mu\text{m}^3 \text{ ps}^{-1}$, $\theta_{12} = 6.48 \cdot 10^{-6} \text{ } \mu\text{m}^3 \text{ ps}^{-1}$, $\theta_{21} = 9.61 \cdot 10^{-6} \text{ } \mu\text{m}^3 \text{ ps}^{-1}$. a/ $\epsilon = 5.76 \cdot 10^{-6} \text{ } \mu\text{m}^3 \text{ ps}^{-1}$. b/ $\epsilon = 6.41 \cdot 10^{-6} \text{ } \mu\text{m}^3 \text{ ps}^{-1}$.

successive occurrence and vanishing of stable two-mode operations. In order to accord in more details with experiments where the two-mode regime appears twice as I_{DBR} increases, it would have been necessary to account more than two modes in the model. Nonetheless, present calculations are demonstrative and can serve to estimate the saturable absorber parameters. It is however worth to note that the condition of Eq. (6) is quite restrictive so that it can explain that such a behavior may appear only with one technological run whereas it does not with all others. Reason should be that tiny variations in the laser gain material, in the process and/or in the absorption produced by the implanted area have occurred.

VI. CONCLUSION

The stable two-mode operation of a 4-sections DBR semiconductor laser has been characterized and modeled. The optical frequencies of the modes are separated by approximately 100 GHz. This behavior is obtained with two values of the current fed in the DBR zone. In the two mode regime, the laser oscillates on two adjacent modes belonging to the Fabry-Pérot mode set. The stability of this behavior has been studied as a function of phase current and temperature. In fact such a behavior seems unlikely due to the strong coupling that exists between two close Fabry-Pérot modes.

We postulate that the two-mode regime comes from a parasitic saturable absorber inside the structure that was brought by the implantation process devoted to electrical insulation between the four different sections of the device. An analytical criterion has been established using Lamb's theory to numerically simulate the complete device using rate equations. Results are in agreement with our initial assumption and typical parameters are obtained for the saturable absorber.

These devices are expected to be used for THz waves generation at $1.55 \text{ } \mu\text{m}$ by photomixing using either uni-travelling-carrier (UTC) photodiodes [1], ultrafast photoconductors [2] or by the excitation of the THz plasma waves in nanotransistors [14]. The present study may serve in the design rules to willingly build such two-mode lasers and improve them in order to produce very efficient and compact photomixing THz sources.

REFERENCES

- [1] T. Ishibashi, T. Furuta, H. Fushimi, S. Kodama, H. Ito, T. Nagatsuma, N. Shimizu, and Y. Miyamoto, "InP/InGaAs uni-traveling-carrier photodiodes," *IEICE Trans. Electron.*, vol. E83-C, pp. 938-949, 2000.
- [2] J. Mangeney, L. Joulaud, P. Crozat, J. M. Lourtioz, and J. Decobert, "Ultrafast response (2.2 ps) of ion-irradiated InGaAs photoconductive switch at $1.55 \mu\text{m}$," *App. Phys. Lett.*, vol. 83, pp. 5551-5553, 2003.
- [3] K. Bertulis, A. Krotkus, G. Aleksejenko, V. Pačebutas, R. Adomavičius, G. Molis, and S. Marcinkevičius, "GaBiAs: A material for optoelectronic terahertz devices," *Appl. Phys. Lett.*, vol. 88, p. 201112, 2006.
- [4] M. Ahmed and M. Yamada, "Influence of instantaneous mode competition on the dynamics of semiconductor lasers," *IEEE J. Quantum Electron.*, vol. 38, no. 6, pp. 682-693, 2002.
- [5] A. M. Yacomotti, L. Furfaro, X. Hachair, F. Pedaci, M. Giudici, J. Tredicce, J. Javaloyes, S. Balle, E. A. Viktorov, and P. Mandel, "Dynamics of multimode semiconductor lasers," *Phys. Rev. A*, vol. 69, p. 053816, 2004.
- [6] C. Serrat and C. Masoller, "Modeling spatial effects in multi-longitudinal-mode semiconductor lasers," *Phys. Rev. A*, vol. 73, p. 043812, 2006.
- [7] W. E. Lamb, "Theory of an optical maser," *Phys. Rev.*, vol. 134, no. 6A, pp. A1429-A1450, 1964.
- [8] A. Plais, H. Debregeas-Sillard, D. Locatelli, A. Vuong, T. Fillion, C. Duchemin, J. Jacquet, and P. Doussi re, "Optimisation of DBR-tunable laser performances by mean of an integrated amplifier," in *Photonics in Switching Conference*, 2003.
- [9] M. Thual, P. Chanclou, O. Gautreau, L. Caledec, C. Guignard, and P. Besnard, "An appropriate microlens to improve coupling between laser diodes and single mode fibers," *Elect. Lett.*, vol. 39, no. 21, pp. 1504-1506, October 2003.
- [10] P. Martin, E. M. Skouri, L. Chusseau, C. Alibert, and H. Bissessur, "Accurate refractive index measurements of doped and undoped InP by a grating coupling technique," *Appl. Phys. Lett.*, vol. 67, pp. 881-883, 1995.
- [11] L. A. Coldren and S. C. Corzine, *Diode lasers and photonic integrated circuits*. New York: John Wiley & Sons, 1995.
- [12] C.-F. Lin and P.-C. Ku, "Analysis of stability in two-mode laser systems," *IEEE J. Quantum Electron.*, vol. 32, pp. 1377-1382, 1996.
- [13] A. E. Siegman, *Lasers*. Mill Valley, CA: University Science Book, 1986.
- [14] W. Knap, J. Lusakowski, T. Parenty, S. Bollaert, A. Cappy, V. V. Popov, and M. S. Shur, "Terahertz emission by plasma waves in 60 nm gate high electron mobility transistors," *App. Phys. Lett.*, vol. 84, pp. 2331-2333, 2004.

THz generation by optical rectification and competition with other nonlinear processes

Z.Y. Zhao, S. Hameau, M. Voos, and J. Tignon

Abstract—We present a study of the terahertz (THz) generation by optical rectification in a 2 mm thick $\langle 110 \rangle$ ZnTe crystal. The conditions for the most efficient THz generation are described. We investigate the competition between optical rectification (OR), second harmonic generation (SHG), two-photon absorption (TPA) and free-carrier absorption in the diffraction limit, for excitation spot sizes smaller than the THz wavelength. We find that while free-carrier absorption contributes significantly to reduce the THz emission, this contribution does not depend on the excitation spot size. On the contrary, two-photon absorption induces a strong dependence of the THz emitted power for decreasing excitation sizes.

Index Terms—Terahertz, optical rectification, two-photon absorption, second harmonic generation, free-carrier absorption.

I. INTRODUCTION

ULTRA-FAST THz spectroscopy is a powerful technique for studying a wide variety of materials including gases, liquids and solids [1]. In this context, a now widely used technique consists in generating THz pulses by optical rectification of femtosecond laser pulses [2,3]. An ultra-fast optical pulse is focused on a nonlinear crystal, which then radiates a THz pulse with a duration of few cycles of the electromagnetic field. In the spectral domain, the radiation is broadband, from about 100 GHz to typically 3 THz for a 100 fs pulse. This process can also be seen as the result of the frequency difference between all the frequency components present within the optical pulse. For an excitation with a typical Ti:sapphire mode-locked laser, the generated THz power is in the range of only a few tens of nW, which stresses the importance of understanding and optimizing the THz generation in nonlinear crystals.

Efficient optical rectification requires using materials with large second-order nonlinear susceptibilities and well-suited phase-matching properties for THz generation. ZnTe crystals with a $\langle 110 \rangle$ orientation offer one of the best compromises in this context [4]. Unfortunately, when a ZnTe crystal is irradiated with a high-power laser pulse, other competing nonlinear processes such as second harmonic generation, two-photon absorption and subsequent free-carrier absorption may also occur, resulting in a decrease of the THz generation [5,6,7]. Additional

competing mechanisms have also been put forward, such as the fact that upon tight focusing, the size of the THz source (the laser spot size) becomes smaller than the typical THz wavelength, resulting in a decrease of the THz generation due to diffraction [8]. Nevertheless, to date, existing analysis of this competition are not comprehensive and the explanations are sometimes even contradictory.

In the present work, we investigate the THz generation by optical rectification in a $\langle 110 \rangle$ 10x10x2 mm ZnTe crystal as a function of power, focusing and crystal orientation. The conditions for the most efficient THz generation are described. Upon tight focusing, for excitation spot sizes smaller than the THz wavelength, SHG, TPA as well as free-carrier absorption are observed while the THz emission is strongly reduced. We find that free-carrier absorption cannot be neglected as often assumed in the past. Nevertheless, because of diffraction effects, this contribution is excitation-size independent upon tight focusing. On the contrary, TPA, which also contributes to the reduction of the THz emission, strongly depends on the excitation-spot size.

II. EXPERIMENTAL RESULTS

A. Optical rectification and THz emission

The excitation of the $\langle 110 \rangle$ 2 mm-thick ZnTe crystal is provided by a 800 nm Ti:sapphire laser (100 fs pulses) at 300 mW, using a 4 cm focusing lens. The ZnTe crystal is virtually transparent in the frequency domain of interest (0.1 – 3 THz). A liquid helium cooled bolometer connected to a lock-in amplifier was used to detect the spectrally integrated THz emission (after proper filtering of the transmitted 800 nm laser beam).

Figure 1 shows the THz emission as a function of the ZnTe azimuthal angle (closed symbols). The THz intensity is proportional to the square of the nonlinear polarization which angle dependence (angle between the polarization of the optical pump beam and the [001] axis) is determined by the nonlinear susceptibility tensor [9]. Figure 1 also displays the angle dependence of the measured SHG (open symbols) generated in the ZnTe crystal upon focusing ($z = 0$, where z is the distance between the beam waist and the crystal), which shows maxima and minima for the same azimuthal angles.

Manuscript received May 11, 2006.

Z.Y. Zhao, S. Hameau, M. Voos and J. Tignon are with the Laboratoire Pierre Aigrain de l'École Normale Supérieure, 24 rue Lhomond, F-75005 Paris, France (phone: +33 1 44 32 33 54; fax: +33 1 44 32 38 40; e-mail: Jerome.Tignon@pa.ens.fr).

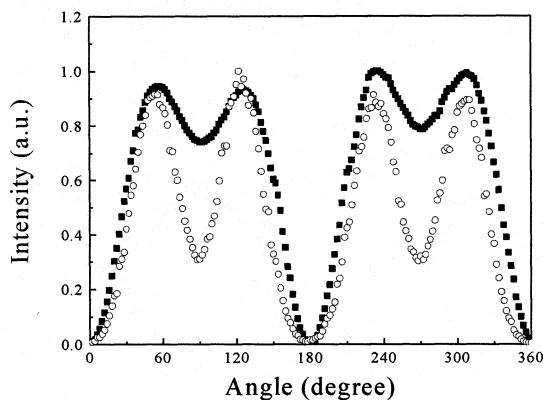


Fig. 1. Closed symbols : THz intensity (bolometric detection) as a function of the azimuthal angle. Open symbols : SHG intensity (measured with a PMT) upon focusing ($z = 0$), as a function of the azimuthal angle. Excitation power 300 mW.

Figure 2 shows the angle dependence of the THz emission (right axis) as well as the angle dependence of the direct transmission at 800 nm (measured with a simple photodiode) when the laser beam is focused ($z = 0$). Under proper crystal angle orientation, the transmission at 800 nm is reduced by about 10 % and a yellow-green luminescence induced by TPA can be observed on the ZnTe crystal surface. In principle, optical rectification, SHG as well as TPA can be responsible for the optical pump depletion for specific azimuthal angles. Nevertheless, the optical rectification efficiency is only on the order of 10^{-7} and, as already pointed out in previous studies [7], when rotating the ZnTe crystal, the SHG generation changes by several orders of magnitude whereas the transmission at 800 nm

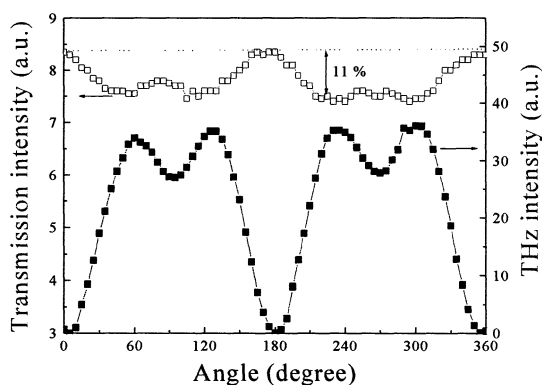


Fig. 2. Closed symbols : THz intensity (bolometric detection) as a function of the azimuthal angle. Open symbols : transmission at 800 nm (measured with a photodiode) upon focusing ($z = 0$), as a function of the azimuthal angle only varies by about 10 %. Thus, optical rectification and SHG are not responsible for the optical pump depletion.

Easy crystal axis determination is highly desirable when developing ultra-fast THz spectroscopy experiments based on optical rectification and Free-Space-Electro-Optical-

Sampling (which relies on a second ZnTe crystal). In this case, several parameters need to be properly adjusted simultaneously (ZnTe crystals orientation, optical pump focusing, time delay and spatial overlap between the THz pulse and the reference pulse, etc.), which renders the alignment tedious. In this context, Figure 2 also shows that the angle-dependence of the transmission is the simplest method for determining the crystal orientation (with the exception of very thin crystals).

B. Z-scan experiment

Competition between optical rectification and other nonlinearities was investigated using a modified z-scan method [7]. The THz emission, the SHG emission as well as direct transmission at 800 nm were measured as a function of the distance z between the beam waist and the crystal, along the optical axis for an optical pump power of 300 mW. The waist radius decreases down to about $10 \mu\text{m}$ upon focusing ($z = 0$), corresponding to a Rayleigh length of about 0.4 mm. As a consequence, in the following, the laser spot radius $w(z)$ lies mostly in the asymptotic region where it can be well approximated by $w(z) \propto z$. For small distances z (tight focusing), SHG generated by the ZnTe crystal is measured using a photomultiplier (after filtering

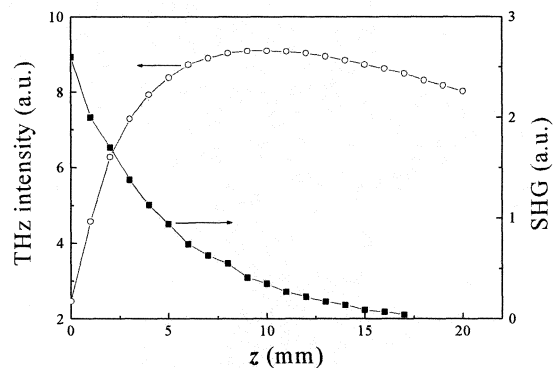


Fig. 3. Open symbols : THz intensity (bolometric detection) as a function of the distance to focus point. Open symbols : Second Harmonic Generation as a function of the distance to focus point. Focal 4 cm. Power 300 mW.

the direct transmission at 800 nm).

Figure 3 shows the THz emission measured as a function of the distance z to the focus (left axis) as well as the SHG (right axis). At first sight, the easiest method to increase the THz emission efficiency is to focus the optical pump beam on the nonlinear ZnTe crystal. Indeed, for large z , the THz emission first increases when decreasing the laser spot size. But the emission then tends to saturate for z on the order of 10 mm. For even smaller distances, the THz emission drops significantly, forming a 5 mm large 'z-hole'. Hence, as often reported, the best THz emission efficiency is obtained when slightly defocusing the optical pump from the ZnTe crystal. Several mechanisms have been put forward to explain the formation of this 'z-hole', among which optical pump depletion by TPA, THz absorption by free carrier absorption, or diffraction effects when the laser spot radius becomes comparable with the THz wavelength (which

occurs here when z is about 10 mm).

C. Two-color excitation

The free-carrier absorption was estimated using a two-color experiment. The free-carrier absorption is proportional to the carrier density in the ZnTe crystal generated at the second harmonic energy. The 800 nm laser beam is then transmitted through a BBO crystal prior to be focused on the ZnTe crystal. For this experiment, the distance z between the 800 nm beam waist and the ZnTe crystal is adjusted in order to maximize the THz emission while minimizing the SHG generated in the ZnTe crystal ($z = 15$ mm). In a first measurement, the BBO is not phase-matched (BBO angle adjusted to obtain zero SHG). We then measure the THz emission in the absence of any competing nonlinearities within the ZnTe crystal. In a second measurement, the BBO is phase-matched to generate SHG in order to provide a two-color excitation of the ZnTe crystal. Here, the azimuthal angle of the BBO crystal is adjusted in order to obtain a SHG on the order of the SHG emission observed when exciting the ZnTe crystal at $z = 0$. The measured THz emission is strongly reduced, corresponding to an absorption coefficient α_{THz} of about 4 cm^{-1} , showing that free-carrier absorption of the THz radiation cannot be neglected in this problem, contrary to what was previously assumed [6,7,8].

III. INTERPRETATION

A. Diffraction limit

As already pointed out above, the phenomena discussed here occur for z distances much larger the optical beam Rayleigh length and the laser spot radius $w(z)$ can well be approximated by its asymptotic limit ($w(z) = \lambda z / \pi w_0$, where w_0 is the beam waist. The spot size $S \propto z^2$). Since optical rectification is a second-order nonlinear process, the THz electric field E_{THz} is proportional to the laser intensity $I_0 = P_0 / S$, where P_0 is the input power. When diffraction effects can be neglected (spot size larger than the THz wavelength), the measured THz signal power is thus $P_{\text{signal}} \propto S (P_0 / S)^2 \propto S^{-1} \propto z^{-2}$. This z^{-2} dependence of the THz signal is indeed observed for large distances ($z > 13$ mm) as can be seen in Figure 4 (dashed line). On the contrary, as pointed out by Dakovski *et al.* [6], the situation is different when the THz emission is generated by a localized emitter of extension smaller than the THz wavelength (centered close to 300 μm). This typically occurs for z smaller than 10 mm. In this case, the THz emission from the whole emitter section interfere constructively and the THz emitted power now reads : $P_{\text{signal}} \propto (S E_{\text{THz}})^2 \propto (S (P_0 / S))^2 \propto S^0 \propto z^0$. As a consequence, the THz emitted power is expected to become independent of the spot size close to focus. This is sketched by the dotted line in Figure 4.

B. Free-carrier absorption

The equation describing the generation of THz has the form:

$$\frac{dE_{\text{THz}}}{dz} = aI_0 - \alpha_{\text{THz}} E_{\text{THz}}$$

where the first term corresponds to the generation of THz by optical rectification and the second term to the THz absorption by free carriers. In this situation, $E_{\text{THz}} \propto \eta a l I_0$, where l is the crystal length and $\eta = (1 - e^{-\alpha_{\text{THz}} l}) / \alpha_{\text{THz}}$ is a factor that reduces the THz field induced by optical rectification. As a consequence, in the diffraction limit (since z is small in this situation), the THz power signal is now $P_{\text{signal}} \propto (S E_{\text{THz}})^2 \propto (S (\eta P_0 / S))^2 \propto S^0 \propto z^0$. The THz emission is globally reduced by a factor η^2 , which can be very large, but still independent on the spot size. This is sketched in Figure 4 (dot-dashed line).

C. Two-photon absorption

As already discussed above, two-photon absorption is responsible for the depletion of the optical pump beam. The equation for the nonlinear absorption is:

$$\frac{dI}{dz} = -\beta I^2$$

in which the linear absorption at the optical frequency is neglected and where β is the nonlinear absorption coefficient. This results in the following optical intensity in the crystal:

$$I(z) = \frac{I_0}{1 + \beta I_0 z}$$

In this case, the emitted THz signal in the diffraction limit becomes:

$$P_{\text{signal}} \propto P_0^2 \left(1 + \beta P_0 l \frac{\pi w_0^2}{\lambda^2 z^2} \right)^2$$

which strongly depends on z and creates a z -hole as already mentioned in Ref. [6]. In the presence of free carrier

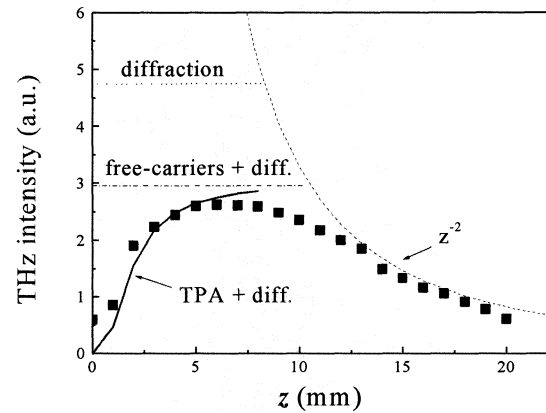


Fig. 4. Symbols : measured THz emission as a function of the distance to focus. Long dashed line : Theoretical THz emitted power beyond the diffraction limit. The THz emission decreases quadratically with the spot size and with the distance to focus. Dotted line: Theoretical THz emitted power in the diffraction limit (no competing nonlinearities included). The THz emission is then independent of the excitation spot size. Dot-dashed line: Theoretical THz emission in the diffraction limit when free-carrier absorption is included. The THz emission remains independent of the excitation spot size. Solid line: Theoretical THz emission in the diffraction

absorption, the input optical power in the above expression is multiplied by a factor η .

Fitting the z-hole in Figure 4 leads to a nonlinear absorption coefficient β on the order of 10 cm/GW, in good agreement with values reported in the literature [6,7,10].

Last, we remark that the above equation does not hold for $z \approx 0$ because the asymptotic approximation for the spot size radius does not hold any more. In this approximation, the spot size is zero for $z = 0$ and the fitted THz signal then drops exactly to zero at the focus. Taking into account the Gaussian profile of the beam leads to a finite THz emission at $z = 0$, as in the experiment.

IV. DISCUSSION

Diffraction effects are essential in the understanding of the THz emission when the pump beam is focused. As shown by Gaivoronskii *et al.* [7], if diffraction effects are not taken into account, TPA reduces the optical pump power, and thus the THz emission, but without forming a z-hole. In this case, TPA and SHG cannot explain this effect even qualitatively. On the contrary, when diffraction effects are properly taken into account, TPA can be shown to result in the formation of a strong reduction of the THz emission upon focusing in the form of a z-hole. Here, we also show that free-carrier absorption cannot be neglected in this analysis since it is responsible for a strong absorption of the THz radiation. Nevertheless, free-carrier absorption only tends to scale down the measured THz power and cannot, by itself, explain the formation of a z-hole.

REFERENCES

- [1] *Sensing with TeraHertz Radiation*, D. Mittleman editor, Springer, Berlin (2003).
- [2] D.H. Auston, *Phys. Rev. Lett.*, 53, p 1555, 1984.
- [3] L. Xu, X.-C. Zhang and D.H. Auston, *Appl. Phys. Lett.* 61, p 1784 (1992).
- [4] A. Nahata, A.S. Weiling and T.F. Heintz, *Appl. Phys. Lett.* 69, p 2321, 1996.
- [5] M. Schall and U. Jepsen, *Above-band gap two-photon absorption and its influence on ultrafast carrier dynamics in ZnTe and CdTe*, *Appl. Phys. Lett.* 80, pp 4771-4773, 2002.
- [6] G. Dakovski, B. Kubera and J. Shan *Localized terahertz generation via optical rectification in ZnTe*, *J. Opt. Soc. Am. B* 22, pp 1667-1670, 2005.
- [7] V.Y. Gaivoronskii, M.M. Nazarov, D.A. Spapozhnikov, E.V. Shepelyavyi, S.A. Shkel'nyuk, A.P. Shkurinov and A.V. Shuvaev, *Competition between linear and nonlinear processes during generation of pulsed terahertz radiation in a ZnTe crystal*, *Quant. Electron.*, 35, pp 407-414, 2005.
- [8] J.Z. Xu and X.-C. Zhang *Optical rectification in an area with diameter comparable to or smaller than the center wavelength of terahertz radiation*, *Opt. Lett.*, pp 1067-1069, 2002.
- [9] Q. Chen, M. Tani, Zhiping Jang and X.-C. Zhang, *Electro-optic transceivers for terahertz-wave applications*, *J. Opt. Soc. Am. B*, 18, pp 823-831, 2001.
- [10] J.H. Bechtel and W.L. Smith *Two-photon absorption in semiconductors with picosecond laser pulses*, *Phys. Rev. B* 13, pp 3515-3522 (1976).

Theory and Design of an Edge-Coupled Terahertz Photomixer Source

Daryoosh Saeedkia and Safieddin Safavi-Naeini

Abstract—A terahertz photomixer with guided-wave optical excitation scheme is analyzed, and as an example, an edge-coupled photomixer source is designed with low-temperature-grown (LTG) GaAs as its ultra-fast photoabsorbing layer and $\text{Al}_{0.2}\text{Ga}_{0.8}\text{As}$ and $\text{Al}_{0.35}\text{Ga}_{0.65}\text{As}$ as core and cladding layers of its optical waveguide structure, respectively.

Index Terms—Terahertz optoelectronics, Photomixers, CW terahertz sources, Optical waveguides.

I. INTRODUCTION

TERAHERTZ technology is a fast-growing field [1], [2] with applications in biology and medicine [3]-[5], medical imaging [6], material spectroscopy and sensing [7], security [8], monitoring and spectroscopy in pharmaceutical industry [9], and high-data-rate communications [10]. The direction of the terahertz technology is towards the implementation of compact and cost-efficient systems for different terahertz applications. Realization of a compact, high-power, and low-cost terahertz source is a crucial step towards this goal.

Photomixers are promising continuous-wave terahertz sources as potentially compact, low-power-consuming, coherent, low-cost, and tunable sources [11], [12]. In a terahertz photomixer, a beat-frequency signal is generated due to mixing of two frequency-detuned laser beams inside a dc-biased ultra-fast photoconductor [13], [14] or a superconductor [15], [16].

Terahertz photomixers can be realized as vertically illuminated or edge-coupled devices [17]-[22]. In the edge-coupled photomixer sources, the laser beams are guided inside an optical dielectric waveguide structure and being absorbed by an overlying ultra-fast photoabsorbing layer, wherein a terahertz signal is generated due to photomixing phenomena. The generated terahertz signal is guided by a transmission line, which can be a coplanar stripline (CPS), a coplanar waveguide (CPW), or a parallel-plate waveguide. The edge-coupled photomixer sources are attractive for system-on-chip configurations for terahertz spectroscopy and sensing and terahertz imaging applications.

Among the challenging issues for realization of the edge-coupled photomixer sources are: control over the optical power absorption rate inside the photoabsorbing layer in order to increase the thermal failure threshold of the device and maximize the generated terahertz power; realization of the velocity match between the optical beat signal and the terahertz signal; and

This work was supported by the NSERC/RIM Industrial Research Chair Program, and CITO.

The authors are with the Electrical and Computer Engineering Department, University of Waterloo, Waterloo, ON, Canada (email: daryoosh@maxwell.uwaterloo.ca; safavi@maxwell.uwaterloo.ca).

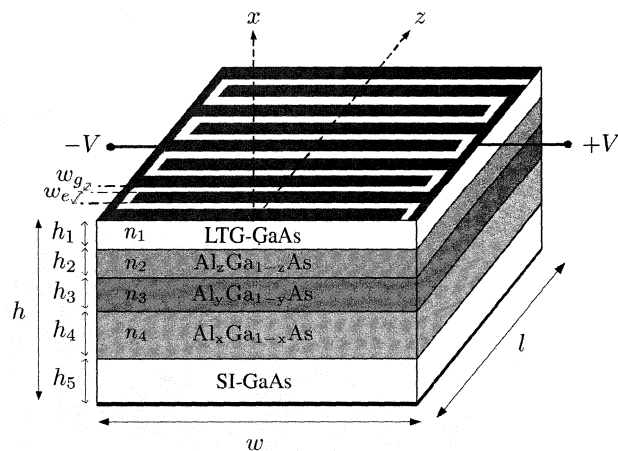


Fig. 1. Schematic of a terahertz photoconductive photomixer source with guided-wave optical excitation. For this structure $n_1 > n_3 > n_2 = n_4$.

implementation of a proper dc-bias configuration and terahertz waveguiding structure.

In this paper, we analyze an edge-coupled terahertz photomixer source, which contains an optical waveguide structure located above a grounded dielectric substrate and covered by interdigitated electrodes (Fig. 1). The top layer of the optical waveguide structure is made of an ultra-fast photoabsorbing material, wherein the photomixing phenomena takes place. One can control the optical power absorption rate by changing the thickness of the photoabsorbing layer. The dc bias is applied through the interdigitated electrodes. The electrode spacing is much smaller than the wavelength of the generated terahertz signal, hence, it is a good approximation to assume that the terahertz wave sees the electrode structure as a uniform metallic plate. The electrodes and the ground plane act as a parallel-plate waveguide for the generated terahertz signal. The velocity of the terahertz signal along the parallel-plate waveguide and the velocity of the optical signal are close together ($n_{\text{GaAs}} = 3.68$ and 3.61 at $\lambda = 800$ nm and $\lambda = 300$ μm , respectively [2]), which results in a good coupling between the two signals.

II. OPTICAL WAVEGUIDE

In the configuration shown in Fig. 1, two laser beams with their central frequency difference falling in the terahertz spectrum are coupled to a five-layer dielectric slab waveguide structure. The band gap for $\text{Al}_\xi\text{Ga}_{1-\xi}\text{As}$ is $E_g = 1.42$ eV, 1.66 eV, and 1.86 eV, for $\xi = 0$, $\xi = 0.2$, and $\xi = 0.35$, respectively

[23]. Hence, for the central wavelengths of the two lasers around 780 nm ($E = 1.59$ eV) the optical power absorption only takes place inside the LTG-GaAs layer. The thickness of the $\text{Al}_x\text{Ga}_{1-x}\text{As}$ buffer layer, h_4 , is large enough to prevent the evanescent tail of the propagating mode reaching to the SI-GaAs substrate.

Satisfying the following conditions together guarantees the single-mode operation of the five-layer dielectric waveguide

$$h_1 \leq \frac{\lambda \tan^{-1} \left(\sqrt{\frac{n_2^2 - n_0^2}{n_1^2 - n_2^2}} \right)}{2\pi \sqrt{n_1^2 - n_2^2}} \quad (1)$$

$$h_3 \leq \frac{\lambda}{2\sqrt{n_3^2 - n_2^2}} \quad (2)$$

$$h_2 > \lambda \quad (3)$$

For $h_2 < \lambda$, it is also possible to design the optical waveguide as a single mode waveguide, however, in this case the behavior of the dispersion equation becomes complicated and it is difficult to extract general conditions for the single mode operation of the waveguide. In a single mode structure, it is easier to achieve both weak coupling to the photoabsorbing layer and velocity phase match between the terahertz signal and the propagating optical mode.

For the structure shown in Fig. 1, we choose the Al contents of the $\text{Al}_\xi\text{Ga}_{1-\xi}\text{As}$ layers as $x = z = 0.35$ and $y = 0.2$. At the wavelength $\lambda = 780$ nm ($E = 1.59$ eV) the refractive index of the layers in Fig. 1 will be $n_1 = 3.66$, $n_2 = n_4 = 3.44$, and $n_3 = 3.554$.

The bias electrodes are made of gold with the refractive index $n_0 = 0.1383 - j4.7932$ at $\lambda = 780$ nm.

The total thickness of the dielectric region, h , must be small enough so that only TEM mode can be supported by the parallel-plate waveguide. This can be achieved by

$$h \leq \frac{c}{2f_c n_1} \quad (4)$$

where f_c is the cutoff frequency of the lowest order non-TEM modes. For example, for $h \leq 6.8$ μm and for the frequencies below 6 THz, the only supported mode by the parallel-plate waveguide is the TEM mode.

The optical intensity distribution across the dielectric layers and at the different positions along the waveguide is shown in Fig. 2. As it can be seen from Fig. 2, the optical intensity decreases as the optical field propagates along the waveguide, which is due to the optical power absorption inside the LTG-GaAs layer.

Fig. 3 shows the total optical power inside the waveguide along the z -axis and optical intensity distribution of TE_0 mode across the dielectric layers for different values of h_1 , h_2 , and h_3 . The total optical power decreases exponentially along the waveguide. The following equation fits the resulting graphs

$$P_{opt}(z) = P_{opt}(z=0)e^{-\alpha_e z} \quad (5)$$

where $\alpha_e < \alpha$ is the effective absorption coefficient. For the higher optical intensity inside the photoabsorbing layer, the effective absorption coefficient is higher. The optical power

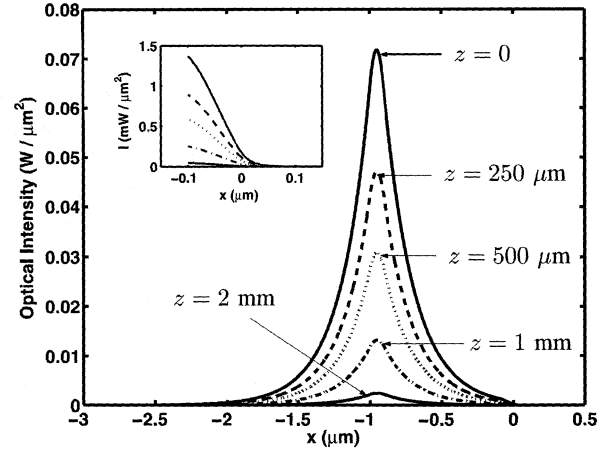


Fig. 2. Optical intensity distribution of TE_0 mode across the dielectric layers and at the different positions along the waveguide. The thicknesses of the dielectric layers in Fig. 1 are $h_1 = 100$ nm, $h_2 = 800$ nm, $h_3 = 100$ nm, and $h_4 = 2$ μm . The width of the waveguide is $w = 6$ μm . The optical power of each laser is 200 mW. The width of the electrode fingers and the gap between them are $w_e = w_g = 2$ μm . The propagation constants in the conductor-covered and air-covered regions are $\beta = 2.7813 \times 10^7$ rad/m and $\beta = 2.7814 \times 10^7$ rad/m, respectively. Inset shows the optical intensity inside the photoabsorbing layer and air.

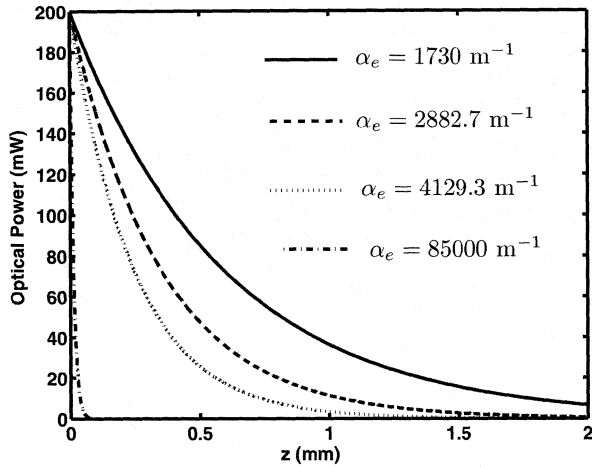
inside the LTG-GaAs layer decays at the same rate as the total optical power.

III. SIMULATION RESULTS

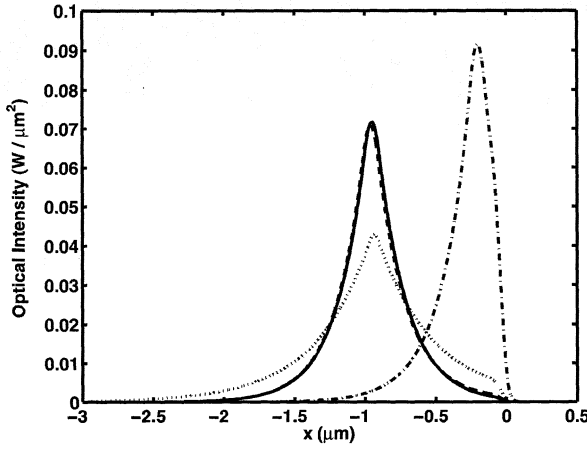
All the physical and dimensional parameters of the designed photomixers are given in Table I. For the designed devices, the ultra-fast photoabsorbing layer is LTG-GaAs and Al contents of the $\text{Al}_\xi\text{Ga}_{1-\xi}\text{As}$ layers are $x = z = 0.35$ and $y = 0.2$ (see Fig. 1). The propagation constants of the two laser modes in the air-covered region for the beat frequency of 1 THz are $\beta_1 = 2.7815 \times 10^7$ rad/m and $\beta_2 = 2.7742 \times 10^7$ rad/m.

Fig. 4 shows the terahertz photocurrent along the waveguide at 1 THz beat frequency and at different depths. The total static electric field is shown for comparison. The terahertz photocurrent is lower at the surface of the LTG-GaAs layer, where the optical intensity is smaller (see Fig. 2). The amplitude of the x -component of the terahertz photocurrent are smaller under the electrodes, where the amplitude of the electric field is low. As it can be seen from Fig. 4, the terahertz photocurrent follows the static electric field variation in low-field regime. For the static field above a certain value the carrier velocity saturates and the carrier lifetime become big enough to make $\Omega\tau \gg 1$, hence the terahertz photocurrent becomes independent of the electric field.

Fig. 4 also shows the x -component of the terahertz photocurrent along the waveguide at two different beat frequencies. For the beat frequency $f = 0.1$ THz, the terahertz photocurrent follows the static electric field variation even at the high-field regime. This is due to the fact that at the low frequencies the term $\Omega\tau$ is small and the terahertz photocurrent is proportional to the carrier lifetime and hence is a function of the electric field. For the beat frequency $f = 1$ THz, and except for



(a)



(b)

Fig. 3. Total optical power inside the waveguide along the z -axis and optical intensity distribution of TE_0 mode across the dielectric layers for different values of h_1 , h_2 , and h_3 and with $h_4 = 2 \mu\text{m}$: $(h_1, h_2, h_3) = (100, 800, 100)$ nm (solid line), $(h_1, h_2, h_3) = (110, 800, 100)$ nm (dashed line), $(h_1, h_2, h_3) = (100, 800, 50)$ nm (dotted line), and $(h_1, h_2, h_3) = (100, 50, 100)$ nm (dash-dot line). The width and the length of the waveguide are $w = 6 \mu\text{m}$ and $l = 2$ mm, respectively. The width of the electrode fingers and the gap between them are $w_e = w_g = 2 \mu\text{m}$. The input optical power is 200 mW.

very low electric field, the term $\Omega\tau$ becomes large and hence the terahertz photocurrent becomes independent of the electric field. One can see from Fig. 4 that the terahertz photocurrent is higher inside the air-covered regions, where the optical intensity is higher.

Fig. 5 shows the amplitude of the x -components of the terahertz photocurrent and the dc photocurrent for different values of the thicknesses of the dielectric layers. As it can be seen from Fig. 5, both the terahertz photocurrent and the dc photocurrent are higher when the coupled optical power inside the photoabsorbing layer is higher (see Fig. 3). Since the generated terahertz power is proportional to the square of the terahertz photocurrent, one can increase the generated terahertz power by increasing the coupled optical power inside

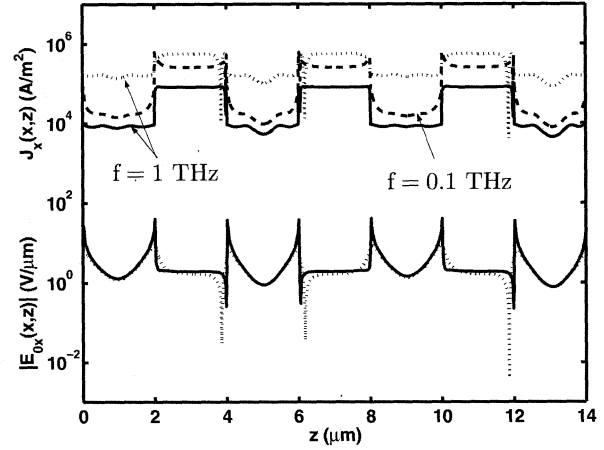


Fig. 4. Terahertz photocurrent along the waveguide at different beat frequency and at different depths: $x = -10$ nm, $f = 1$ THz (solid line), $x = -10$ nm, $f = 0.1$ THz (dashed line), and $x = -110$ nm, $f = 1$ THz (dotted line). The thicknesses of the dielectric layers are: $h_1 = 100$ nm, $h_2 = 800$ nm, $h_3 = 100$ nm, and $h_4 = 2 \mu\text{m}$. The static electric field is shown for comparison.

TABLE I
PHYSICAL AND DIMENSIONAL PARAMETERS OF A DESIGNED
PHOTOMIXER

Description	Notation	Value
Laser central wavelength	λ_1	780 nm
Applied dc voltage	V	10 V
Each laser power	P_{opt}	200 mW
Optical absorption coefficient[24]	α	10000 cm^{-1}
Electron (hole) saturation velocity[25]	v_{sn} (v_{sp})	40 (10) m/ms
Low-field electron (hole) lifetime[25]	τ_n (τ_p)	0.1 (0.4) ps
Low-field electron (hole) mobility[26]	μ_{n0} (μ_{p0})	400 (100) cm^2/Vs
Device width	w	6 μm
Total thickness	h	6 μm
Electrode width	w_e	2 μm
Gap between electrode fingers	w_g	2 μm
Buffer layer thickness	h_4	2 μm
LTG-GaAs refractive index	n_1	3.66
Cladding refractive index	n_2, n_4	3.44
Core refractive index	n_3	3.554
Electrode refractive index (at 780 nm)	n_0	0.1383 - $j4.7932$

the photoabsorbing layer. Hence, the optimum thicknesses for the dielectric layers are the thicknesses, which results in maximum possible optical intensity inside the LTG-GaAs layer. Nevertheless, one has to take into account the device thermal failure due to the resulting optical and electrical thermal power.

The generated terahertz power for an edge-coupled photomixer with parameters given in Table I and with $h_1 = h_3 = 100$ nm and $h_2 = 50$ nm is 0.9 μW at 1 THz beat frequency.

IV. CONCLUSION

An edge-coupled distributed terahertz photomixer source is analyzed and designed. The proposed device has potential applications in terahertz biosensing, imaging, and spectroscopy.

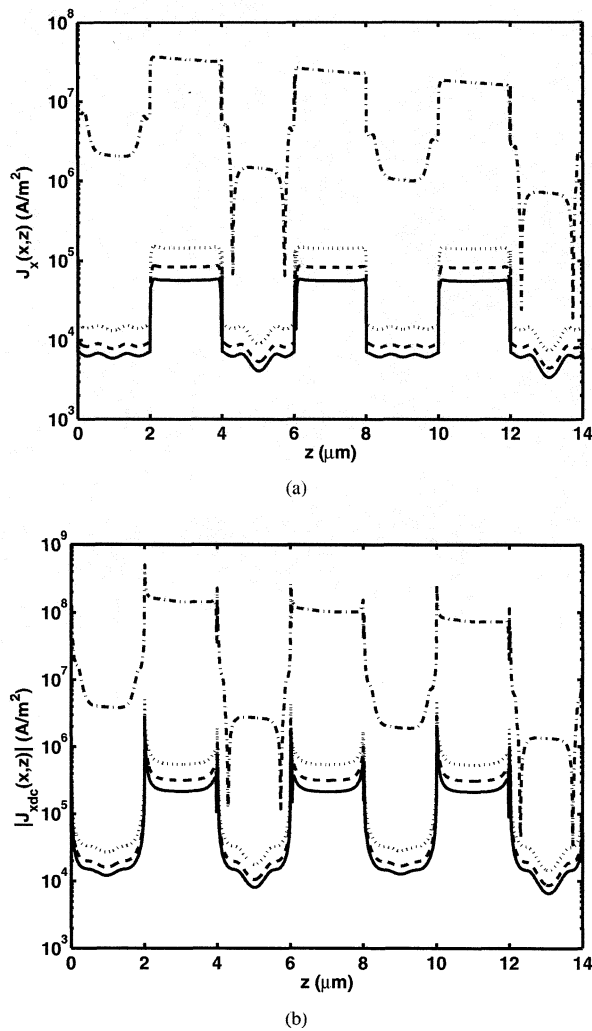


Fig. 5. Generated photocurrent along the waveguide at 1 THz beat frequency and at $x = -10$ nm for different values of h_1 , h_2 , and h_3 and with $h_4 = 2$ μm : $(h_1, h_2, h_3) = (100, 800, 100)$ nm (solid line), $(h_1, h_2, h_3) = (110, 800, 100)$ nm (dashed line), $(h_1, h_2, h_3) = (100, 800, 50)$ nm (dotted line), and $(h_1, h_2, h_3) = (100, 50, 100)$ nm (dash-dot line). (a) terahertz photocurrent (b) dc photocurrent.

REFERENCES

- [1] D. L. Woolard, E. R. Brown, M. Pepper, and M. Kemp, "Terahertz Frequency Sensing and Imaging: A Time of Reckoning Future Applications?" *Proceedings of the IEEE*, vol. 93, no. 10, pp. 1722–1743, 2005.
- [2] K. Sakai, Ed., *Terahertz Optoelectronics*. Springer-Verlag, 2005.
- [3] M. Nagel, P. Haring Bolivar, and H. Kurz, "Modular parallel-plate THz components for cost-efficient biosensing systems," *Semicond. Sci. Technol.*, vol. 20, no. 7, pp. S281–S285, 2005.
- [4] P. H. Siegel, "Terahertz Technology in Biology and Medicine," *IEEE Trans. Microwave Theory Tech.*, vol. 52, no. 10, pp. 2438–2447, 2004.
- [5] T. Globus, D. Woolard, M. Bykhovskaia, B. Gelmont, L. Werbos, and A. Samuels, "THz-frequency spectroscopic sensing of DNA and related biological materials," *International Journal of High Speed Electronics and Systems*, vol. 13, no. 4, pp. 903–936, 2003.
- [6] S. Wang, B. Ferguson, D. Abbott, and X.-C. Zhang, "T-ray imaging and tomography," *J. Biol. Phys.*, vol. 29, no. 2-3, pp. 247–256, 2003.
- [7] D. Mittleman, Ed., *Sensing with Terahertz Radiation*. Springer-Verlag, 2003.
- [8] M. C. Kemp, P. F. Taday, B. E. Cole, J. A. Cluff, A. J. Fitzgerald, and W. R. Tribe, "Security applications of terahertz technology," in *The Proceedings of SPIE Conference*, vol. 5070, August 2003, pp. 44–52.
- [9] P. F. Taday, "Applications of terahertz spectroscopy to pharmaceutical sciences," *Phil. Trans. R. Soc. Lond. A*, vol. 362, no. 1815, pp. 351–364, 2004.
- [10] A. Hirata, H. Ishii, and T. Nagatsuma, "Design and characterization of a 120-GHz millimeter-wave antenna for integrated photonic transmitters," *The Proceedings of International Topical Meeting on Microwave/Photonics*, pp. 229–232, 2000.
- [11] M. C. Teich, "Field-Theoretical Treatment of Photomixing," *Appl. Phys. Lett.*, vol. 14, no. 6, pp. 201–203, 1969.
- [12] E. R. Brown, F. W. Smith, and K. A. McIntosh, "Coherent millimeter-wave generation by heterodyne conversion in low-temperature-grown GaAs photoconductors," *J. Appl. Phys.*, vol. 73, no. 3, pp. 1480–1484, 1993.
- [13] E. R. Brown, "THz Generation by Photomixing in Ultrafast Photoconductors," *International Journal of High Speed Electronics and Systems*, vol. 13, no. 2, pp. 497–545, 2003.
- [14] D. Saeedkia, R. R. Mansour, and S. Safavi-Naeini, "The interaction of laser and photoconductor in a continuous-wave terahertz photomixer," *IEEE J. Quantum Elec.*, vol. 41, no. 9, pp. 1188–1196, 2005.
- [15] C. J. Stevens and D. J. Edwards, "Photomixing receiver using kinetic inductive effect in high T_c superconductors," *Electronics Letters*, vol. 37, no. 23, pp. 1420–1421, 2001.
- [16] D. Saeedkia, R. R. Mansour, and S. Safavi-Naeini, "Modeling and Analysis of High-Temperature Superconductor Terahertz Photomixers," *IEEE Trans. Appl. Superconduct.*, vol. 15, no. 3, pp. 3847–3855, 2005.
- [17] E. A. Michael, "Travelling-wave photonic mixers for increased continuous-wave power beyond 1 THz," *Semicond. Sci. Technol.*, vol. 20, no. 7, pp. S164–S177, 2005.
- [18] H. Ito, S. Kodama, Y. Muramoto, T. Furuta, T. Nagatsuma, and T. Ishibashi, "High-Speed and High-Output InP-InGaAs Unitraveling-Carrier Photodiodes," *IEEE J. Sel. Top. Quantum Electron.*, vol. 10, no. 4, pp. 709–727, 2004.
- [19] E. Peytavit, S. Arscott, D. Lippens, G. Mouret, S. Matton, P. Masselin, R. Bocquet, J. F. Lampin, L. Desplanque, and F. Mollot, "Terahertz frequency difference from vertically integrated low-temperature-grown GaAs photodetector," *Appl. Phys. Lett.*, vol. 81, no. 7, pp. 1174–1176, 2002.
- [20] J.-W. Shi, K.-G. Gan, Y.-J. Chiu, Y.-H. Chen, C.-K. Sun, Y.-J. Yang, and J. E. Bowers, "Metal-semiconductor-metal traveling-wave photodetectors," *IEEE Photon. Technol. Lett.*, vol. 16, no. 6, pp. 623–625, 2001.
- [21] L. Y. Lin, M. C. Wu, T. Itoh, T. A. Vang, R. E. Muller, D. L. Sivco, and A. Y. Cho, "High-Power High-Speed Photodetectors-Design, Analysis, and Experimental Demonstration," *IEEE Trans. Microwave Theory Tech.*, vol. 45, no. 8, pp. 1320–1331, 1997.
- [22] E. H. Botcher and D. Bimberg, "Millimeter wave distributed metal-semiconductor-metal photodetectors," *Appl. Phys. Lett.*, vol. 66, no. 26, pp. 3648–3650, 1995.
- [23] T. Tamir, Ed., *Guided-Wave Optoelectronics*. Springer-Verlag, 1988.
- [24] S. M. Sze, *Physics of Semiconductor Devices*. John Wiley and Sons, 1981.
- [25] E. R. Brown, "A photoconductive model for superior GaAs THz photomixer," *Appl. Phys. Lett.*, vol. 75, no. 6, pp. 769–771, 1999.
- [26] E. R. Brown, K. A. McIntosh, F. W. Smith, K. B. Nichols, M. J. Manfra, C. L. Dennis, and J. P. Mailia, "Milliwatt output levels and superquadratic bias dependence in a low-temperature-grown GaAs photomixer," *Appl. Phys. Lett.*, vol. 64, no. 24, pp. 3311–3313, 1994.

Catadioptric Microlenses for Submillimeter and Terahertz Applications

Biddut K. Banik, Harald F. Merkel, Stellan Jacobsson

Abstract— Existing dielectric lens geometries are optimized for remote sensing applications in order to produce a predetermined Gaussian beam in the far field that is matched to a radioastronomic setup. In this work, an optics suitable for object investigation in a point-to-point transmission setup is presented. Here it is required to create a focus point outside the lens with as low radiation leakage as possible. For this, a catadioptric dielectric lens is proposed. This paper presents the theoretical performance of the focusing property of catadioptric lens investigated at 50 GHz and 228 GHz having $\epsilon_r = 11.7$. 3D simulation results of the catadioptric lens also show a focus point. Imaging property of catadioptric and extended hemispherical lenses are presented and compared at 50GHz. A Transient analysis of the lens is also presented.

Index Terms— Catadioptric lenses, dielectric lenses, lens antennas.

I. INTRODUCTION

DIELECTRIC lenses have found an increasing range of applications during the last years. Planar radiating or receiving elements covered by dielectric lenses are being used in millimeter and submillimeter regime [1, 2]. They also provide the capability to be integrated [3, 4] with millimeter and submillimeter planar feeding structures and electronic components such as diode detectors, oscillators, mixers etc. Due to low feed loss, ease of construction and overall size reduction, microstrip antenna-lens configurations are an attractive solution for mm-wave high gain antennas. Hemispherical, elliptical, extended hemispherical and synthesized elliptical lenses [1, 3, 4] have already been investigated and used in various applications. Matching layers [5] are also used to reduce reflection losses. Different kinds of computational methods and algorithms [4, 6-10] have been used for determining near-field [11, 12] and far-field pattern [13, 14], internal reflections [15], input impedance [16], S parameters, focusing property [17] and imaging property [18] of such dielectric lenses.

Here a transmission setup is analyzed where a current dipole radiating structure is coupled to the lens. The first goal is to minimize the dielectric lens. As a benchmark, the hemispherical, elliptical and extended hemispherical (or synthesized elliptical lens) and catadioptric geometries have been taken into account. Next, a catadioptric dielectric lens is presented here and the simulation results are compared to that of an extended hemispherical lens. It has been shown,

that dielectric lens structures with an overall size of 3-5 vacuum wavelengths still work as focusing elements.

As a next step, focusing structures have been analyzed that can be made small and offer a distinct power maximum at a certain distance from the structure. Such a focusing behavior improves the condition of subsequent inverse scattering matrices considerably.

II. LENS GEOMETRIES AND MODELING STRATEGIES

A commercial FEM electromagnetic package [19] has been used during this investigation. Firstly, simulation concentrated on 2D modeling of hemispherical, elliptical, extended hemispherical and catadioptric lenses. For all the cases, the surrounding domain around the lens is vacuum and the outer boundary conditions of the vacuum represented by Absorbing Boundary Conditions fulfilling Sommerfeld radiation conditions in the far field. In order to facilitate comparison, the lenses are always placed and centered at the respective coordinate origin.

A. Dielectric Lenses

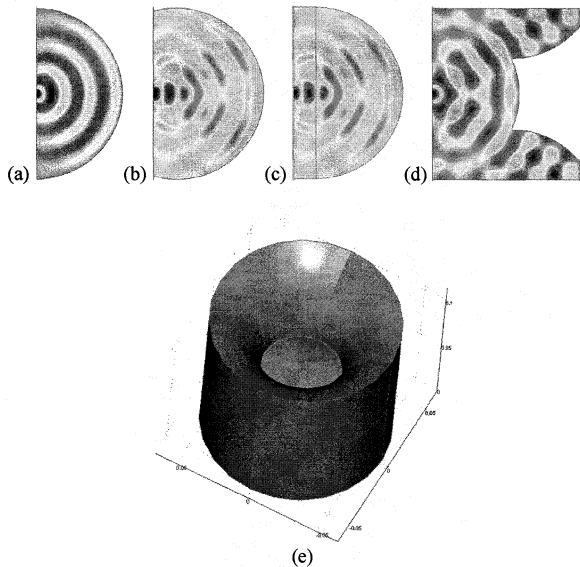


Fig. 1. Electric field distribution at 50 GHz in (a) hemispherical, (b) elliptical, (c) extended hemispherical and (d) catadioptric lens (e) 3D view of the catadioptric lens.

In Fig. 1, electric field distribution at 50GHz in hemispherical, elliptical, extended hemispherical and catadioptric lenses are shown. The dielectric constant of the lens is $\epsilon_r = 11.7$ and the lenses are of 16 mm diameter. The source is a current dipole. For the extended hemispherical lens, the extension $L = 1.6$ mm and $L/R = 0.2$ where R is the radius. The E field distributions in the elliptical and the

Manuscript received May 11, 2006.

B. K. Banik is with the Dept. of Microtechnology and Nanoscience, Microwave Electronics Laboratory, MC2, Chalmers University of Technology, Göteborg, Sweden (e-mail: biddut.banik@mc2.chalmers.se).

H. F. Merkel is with the Dept. of Microtechnology and Nanoscience, Microwave Electronics Laboratory, MC2, Chalmers University of Technology and Food Radar AB, Göteborg, Sweden (e-mail: harald.merkel@mc2.chalmers.se).

S. Jacobsson is with Food Radar AB, Göteborg, Sweden.

extended hemispherical lenses are similar. The E field distribution in the catadioptric lens indicates that the waves are guided towards the catadioptric portion. This phenomenon eventually produces a focus point.

B. Catadioptric Lens

Catadioptric lens systems have been invented by Fourier in 1826 for use in lighthouses combining a segmented Fresnel lens with lateral prisms to enhance efficiency and to reduce weight. Within the scope of the current investigation, a catadioptric lens has been realized having $\epsilon_r = 11.7$, 16 mm diameter. The extended catadioptric portion of the lens is of 8 mm radius and 11 mm length. For simplicity, two dimensional models were simulated and the lenses were assumed to be isotropic and homogenous. Fig. 2(a) shows the electric field (E_z) distribution at 50 GHz and Fig. 2(b) shows the absolute electric field (E_{norm}) distribution. A current dipole source is attached to the lens. The medium surrounding the lens is assumed to be vacuum. Fig. 2(c) shows E_{norm} along $y = 0$ axis for 48-52 GHz. The focus point

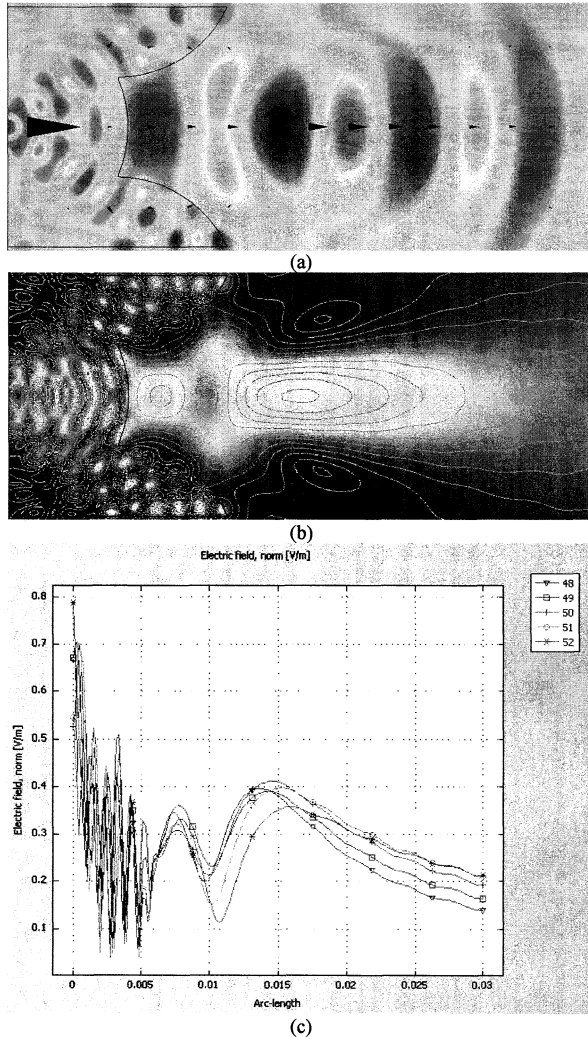


Fig.2. Field distribution at 50 GHz a) E_z b) E_{norm} c) E_{norm} along $y = 0$ axis for 48-52 GHz.

is observed at a distance $x = 0.015$ m for 50 GHz. The focusing property of the lens is frequency and lens-geometry

dependent.

Fig. 3(a) shows the normalized E_{norm} distribution at 228 GHz for the same catadioptric lens with a current dipole source. A focus point is observed at 0.0175 m. Fig. 3(b) demonstrates the normalized electric field distribution along $y = 0$ axis at 227-229 GHz.

Evidently, the quality of the calculated results depends on the density of generated mesh and the number of points where Maxwell's equations are to be solved. FEM requires very high computer resources for generating quality results at frequencies above 250 GHz, for the present case.

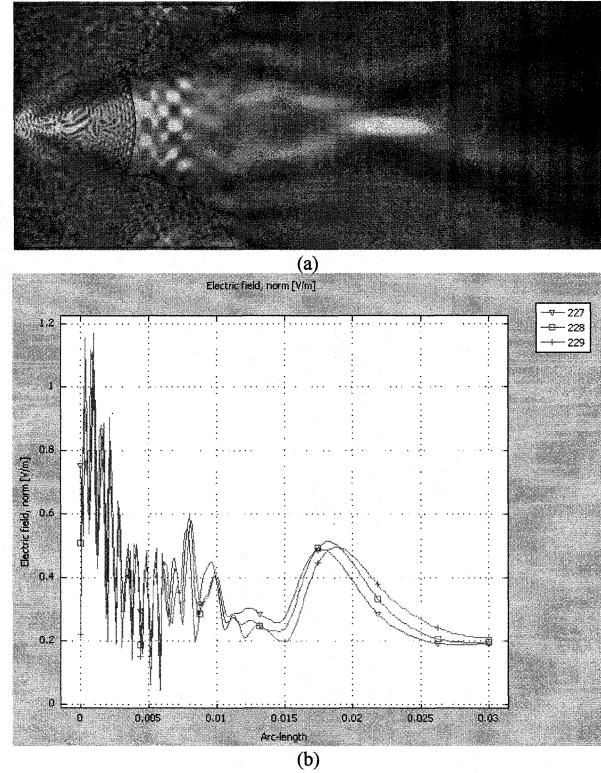


Fig.3. Field distribution at 228 GHz a) E_{norm} c) E_{norm} along $y = 0$ axis for 227-229 GHz.

C. 3D Modeling

For the 3D model of the catadioptric lens, dielectric constant $\epsilon_r = 5$, diameter $D = 16$ mm and the lens is attached to an open ended waveguide which acts as the source. The frequency is selected 28 GHz and the dimension of the waveguide is selected to be at TE_{10} mode. Higher frequency and higher dielectric constant of the lens require higher density of generated mesh, extensive amount of computer resource and eventually the simulator fails to generate any result. Fig.4 shows the isosurface plot of normalized time averaged power flow ($P_{oavnorm}$) and the color of the isosurface corresponds to the logarithm of $P_{oavnorm}$ (P_{oavdB}). Fig. 4(a) shows H plane and Fig. 4(b) shows E plane where a focus region is observed.

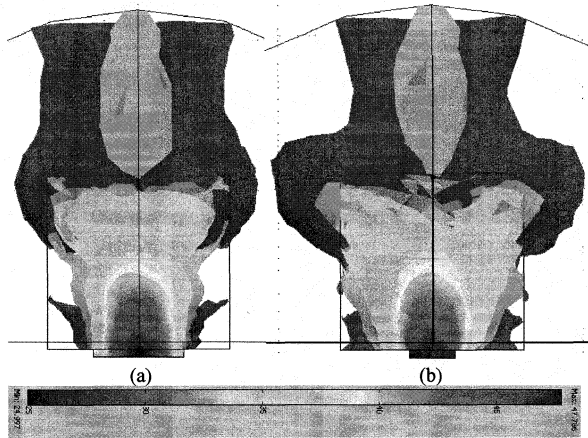


Fig. 4. Isosurface plot of normalized time averaged power flow ($P_{0avnorm}$). Waveguide source with TE_{10} excitation at 28GHz, $\epsilon_r = 5$

D. Imaging

Usually for modeling and characterizing near-field imaging setups, a planar wave is incident on the subject. For the case of catadioptric lens, a point current source is located at a distance $x = 0.016$ m, which was found to be the focus point of the lens. Fig. 5(a) shows the setup where a dielectric filled ($\epsilon_r = 11.7$) waveguide is attached to the lens and has the dimension to be excited at TE_{10} mode. The electric field distribution (E_z) is demonstrated in Fig. 5(a).

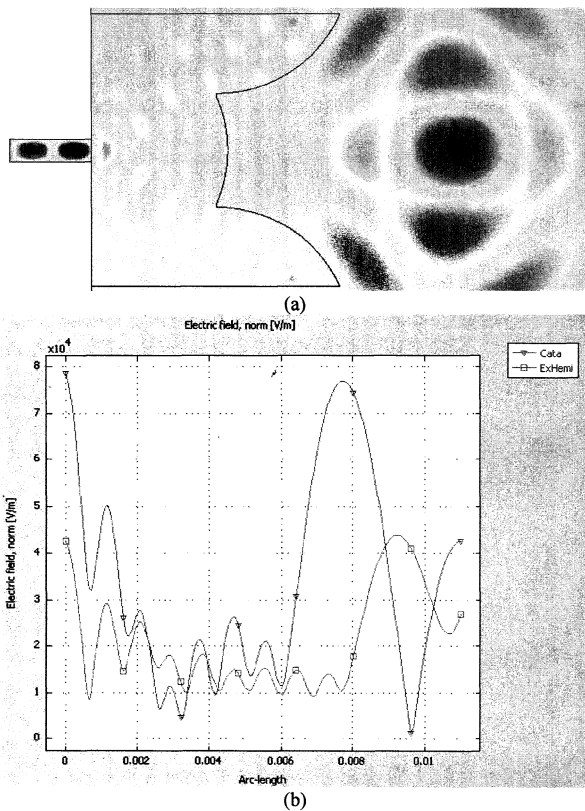


Fig. 5. (a) E_z field distribution at 50GHz with a current source located at $x = 0.016$ m. Dielectric filled waveguide is used at the receiving end. (b) E_{norm} distribution for catadioptric and extended hemispherical lenses along $y = 0$.

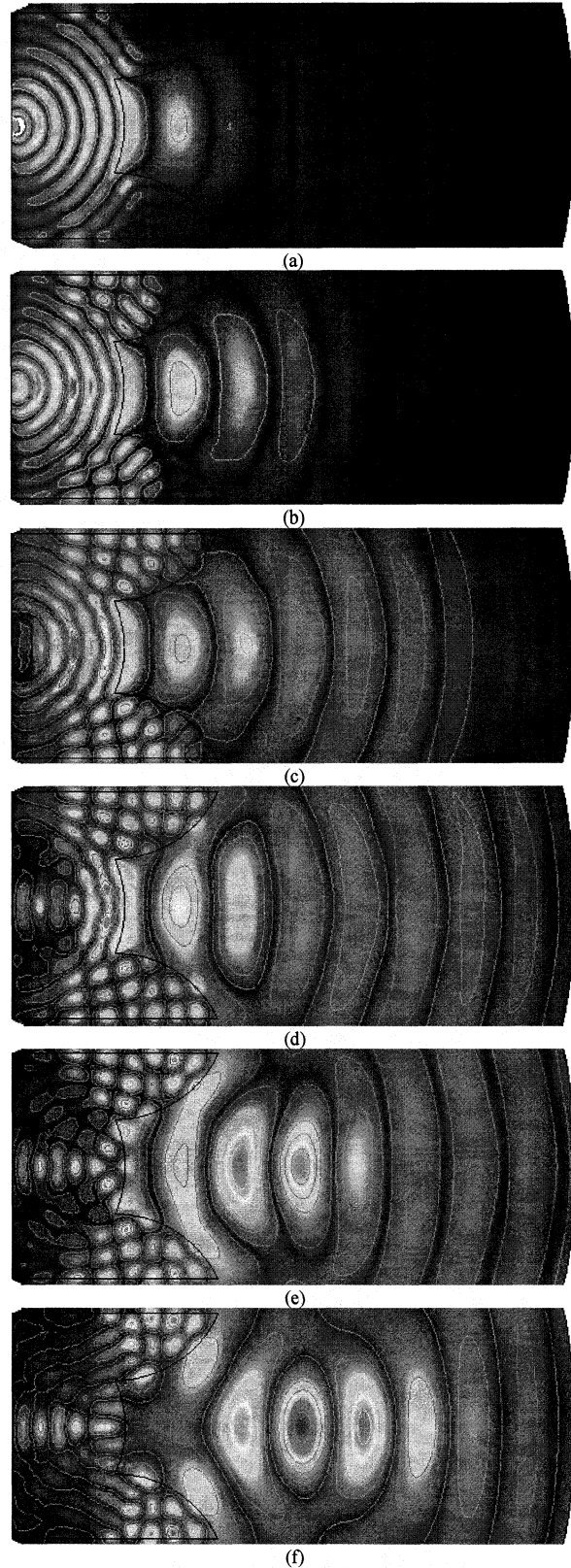


Fig. 6. Transient analysis of the catadioptric lens with a point current source located at the origin. Colors correspond to the magnitude of absolute E field distribution (E_{norm}), contour corresponds to E_z . (a) $T = 0.09$ ns (b) $T = 0.11$ ns (c) $T = 0.13$ ns (d) $T = 0.15$ ns (e) $T = 0.17$ ns (f) $T = 0.19$ ns

Afterwards, the catadioptric lens is replaced by an extended hemispherical lens having the same diameter ($D = 16$ mm) and the extension length (L) is 1.6 mm. Fig. 5(b) shows the absolute electric field (E_{norm}) distribution along $y = 0$ axis. The catadioptric lens shows approximately 3 dB better response compared to the extended hemispherical lens.

E. Transient Analysis

With a view to attain better understanding and pictorial view of the focusing property of the catadioptric lens, a transient analysis is done where a point current source is placed at the origin. It should be noted that the lens is also placed and centered at the origin. The current source generates cosine waves at 50 GHz up to the time instant $T = 0.1$ ns. Fig. 6(a-f) demonstrate the absolute electric field distribution (E_{norm}) at different time instants (0.09 ns, 0.11 ns, 0.13 ns, 0.15 ns, 0.17 ns and 0.19 ns). Fig. 6(f) shows a focus point is created at $T = 0.19$ ns.

III. CONCLUSION

The focusing property of catadioptric lens is simulated by FEM method. A 3D model also demonstrates a focus region. Nearfield imaging property is also investigated and compared to that of an extended hemispherical lens. The focusing process is presented pictorially. Our investigation results show that the catadioptric lens creates a focus point with low radiation leakage. Our future investigation encompasses introducing matching layer, reflection losses, PEC backed catadioptric lens, farfield radiation pattern, fabrication of catadioptric lenses and related measurements.

REFERENCES

- [1] L. Mall and R. B. Waterhouse, "Millimeter-wave proximity-coupled microstrip antenna on an extended hemispherical dielectric lens," *IEEE Transactions on Antennas and Propagation*, vol. 49, pp. 1769-1772, 2001.
- [2] J. Van Rudd and D. M. Mittleman, "Influence of substrate-lens design in terahertz time-domain spectroscopy," *Journal of the Optical Society of America B (Optical Physics)*, vol. 19, pp. 319-29, 2002.
- [3] D. F. Filipovic, S. S. Gearhart, and G. M. Rebeiz, "Double-slot antennas on extended hemispherical and elliptical silicon dielectric lenses," *IEEE Transactions on Microwave Theory and Techniques*, vol. 41, pp. 1738-49, 1993.
- [4] D. F. Filipovic, G. P. Gauthier, S. Raman, and G. M. Rebeiz, "Off-axis properties of silicon and quartz dielectric lens antennas," *IEEE Transactions on Antennas and Propagation*, vol. 45, pp. 760-6, 1997.
- [5] M. J. M. van der Vorst, P. J. I. de Maagt, and M. H. A. J. Herben, "Scan-optimized integrated lens antennas," Jerusalem, Israel, 1997.
- [6] J. R. Bray and L. Roy, "Physical optics simulation of electrically small substrate lens antennas," Waterloo, Ont., Canada, 1998.
- [7] A. Neto, S. Maci, and P. J. I. De Maagt, "Reflections inside an elliptical dielectric lens antenna," *IEE Proceedings-Microwaves, Antennas and Propagation*, vol. 145, pp. 243-7, 1998.
- [8] D. Pasqualini and S. Maci, "High-frequency analysis of integrated dielectric lens antennas," *IEEE Transactions on Antennas and Propagation*, vol. 52, pp. 840-847, 2004.
- [9] G. Godi, R. Sauleau, and D. Thouroude, "Performance of reduced size substrate lens antennas for Millimeter-wave communications," *IEEE Transactions on Antennas and Propagation*, vol. 53, pp. 1278-86, 2005.
- [10] B. Chantraine-Bares, R. Sauleau, L. Le Coq, and K. Mahdjoubi, "A new accurate design method for millimeter-wave homogeneous dielectric substrate lens antennas of arbitrary shape," *IEEE Transactions on Antennas and Propagation*, vol. 53, pp. 1069-82, 2005.
- [11] A. V. Boriskin, S. V. Boriskina, and A. I. Nosich, "Exact near-fields of the dielectric lenses for sub-mm wave receivers," Munich, Germany, 2003.
- [12] J. B. Pendry and S. A. Ramakrishna, "Near-field lenses in two dimensions," *Journal of Physics: Condensed Matter*, vol. 14, pp. 8463-79, 2002.
- [13] X. Wu, G. V. Eleftheriades, and T. E. Van Deventer-Perkins, "Design and characterization of single- and multiple-beam MM-wave circularly polarized substrate lens antennas for wireless communications," *IEEE Transactions on Microwave Theory and Techniques*, vol. 49, pp. 431-441, 2001.
- [14] P. Uhd Jepsen and S. R. Keiding, "Radiation patterns from lens-coupled terahertz antennas," *Optics Letters*, vol. 20, pp. 807-9, 1995.
- [15] M. J. M. Van der Vorst, P. J. I. De Maagt, A. Neto, A. L. Reynolds, R. M. Heeres, W. Luinge, and M. H. A. J. Herben, "Effect of internal reflections on the radiation properties and input impedance of integrated lens antennas - Comparison between theory and measurements," *IEEE Transactions on Microwave Theory and Techniques*, vol. 49, pp. 1118-1125, 2001.
- [16] A. Nato, L. Borselli, S. Maci, and P. J. I. de Maagt, "Input impedance of integrated elliptical lens antennas," *IEE Proceedings-Microwaves, Antennas and Propagation*, vol. 146, pp. 181-6, 1999.
- [17] W. B. Dou and E. K. N. Yung, "FDTD simulation for the focusing property of extended hemispherical lens as receiving antenna," *International Journal of Infrared and Millimeter Waves*, vol. 21, pp. 2077-86, 2000.
- [18] D. F. Filipovic, G. V. Eleftheriades, and G. M. Rebeiz, "Off-axis imaging properties of substrate lens antennas," Tucson, AZ, USA, 1995.
- [19] Comsol, www.comsol.com.

CFRP Mirror Technology for Submillimeter and Shorter Wavelengths

Robert C. Romeo and Robert N. Martin
Composite Mirror Applications
Tucson, AZ 85710
USA

Contact:

email: robertmartin@compositemirrors.com
Phone: 1-520-733-9302
Fax: 1-520-733-9306

Composite reflector, or mirror, panels using CFRP face sheets and honeycomb aluminum core have been used on several high frequency (100 GHz - 1 THz), precision, radio astronomical telescopes since the 1980's. CMA (Composite Mirror Applications, Inc.) has been extending this technology to higher precision mirrors using CFRP in the mirror structure as well as the mirror face sheets (surface). Optical wavelength, astronomical telescope mirrors are now being fabricated up to 1.4m in diameter. CFRP has a number of advantages compared to other materials for mirrors at submillimeter through optical wavelengths: (1) It has a low coefficient of thermal expansion, comparable to glass and an order of magnitude lower than aluminum. There is minimal dimensional change even over large changes in temperature. (2) It has a high stiffness to weight ratio, enabling a very lightweight mirror. (3) The thermal conduction is very good (similar to steel and other metals). (4) The low mass and high thermal conduction result in a structure which thermalizes on a short time scale. CFRP mirror technology is well suited to use in THz instrumentation as well as for telescope mirror surfaces.

We will briefly describe the principles of mirror fabrication with CFRP technology. We will present the status and results for several CFRP mirror projects CMA has been working on during the past two year: Optical telescopes of 0.4m, 1m and 1.4m diameter, a study of composite panels for the proposed 25m CCAT submillimeter telescope, subreflectors for ALMA, APEX and ALMA-J prototype telescopes, subreflectors for the CBI telescope, telescope systems for the AMiBA project, a RICH (Ring Imaging Cherenkov optical wavelength) conical mirror of 1.3m diameter for the AMS-02 satellite scheduled for launch with the Shuttle. The surface quality, areal density, and other parameters of the mirrors will be discussed. Results of finite element analysis (FEA) are presented for several mirrors and compared to results on tested mirrors. The advantages of this technology and various risks are discussed.

CFRP Structures for Astronomy Applications

Robert N. Martin and Robert C. Romeo
Composite Mirror Applications
Tucson, AZ 85710
USA

Contact:

email: robertmartin@compositemirrors.com
Phone: 1-520-733-9302
Fax: 1-520-733-9306

Carbon Fiber Reinforced Plastic (CFRP) technology has a number of advantages for critical structures associated with astronomical telescopes at submillimeter through optical wavelengths. This technology is used for both ground based and space borne applications. The material has a high stiffness to weight ratio, low thermal expansion coefficient, and high thermal conductivity. Thus, it is ideal for many support structure applications. We will present several examples of recent uses of CFRP structures fabricated at CMA (Composite Mirror Applications, Inc.): (1) The chopping secondary mirror system for the APEX telescope, (2) A 6m diameter platform for the AMiBA telescope, (3) 1m OTA (optical tube assembly) for the ULTRA optical telescope project, (4) 1.4m OTA for the NRL optical telescope NPOI project, (5) a complete 0.4m optical telescope mount, OTA and optics for the NRL. The use of CFRP results in a stiff, light weight structure. Several innovative features can be built into the structure which would not be possible with conventional technology using metal alone. We will discuss the structure, unique features, and present test results. Several features of CFRP structures would be of benefit to space THz instrumentation applications.

Micro-machined Planar THz Optics

K.-F. Schuster¹, N. Krebs¹, Y. Guillaud¹, F. Mattiocco¹, M. Kornberg² and A. Poglitsch²

¹ Institute Radio Astronomy in the Millimetre range IRAM, St Martin d'Herès, 38406, 300 Route de la Piscine, France

² Max-Planck-Institute for extraterrestrial Physics, Giessenbachstraße, 85748 Garching, Germany.

We present micro-machined artificial dielectrics and their application in THz technology. Different quasi-optical elements are presented and in particular the first design and realization of a planar focusing lens. We discuss the various modeling approaches and compare simulations with phase and amplitude measurements.

Characterization of Micromachined Waveguide Hybrids at 350 and 650 GHz

Axel Murk, Stephan Biber, Thomas Tils, Patrick Pütz, Lorenz-Peter Schmidt and Niklaus Kämpfer

Abstract—We present measurement results of two different hybrid couplers at submillimeter wavelengths. The devices under test were a 650 GHz coupler, which has been micromachined in Silicon by deep reactive ion etching, and two versions of a 345 GHz coupler machined out of brass. In order to determine the amplitude and phase balance of the coupling section the differences between the connecting waveguides have to be taken into account. We corrected the measurements under the assumption that the coupling section itself is fully symmetrical, which results in a good matching between the measured and the simulated performance.

I. INTRODUCTION

Waveguide hybrids are a prerequisite for balanced and sideband separating mixers. At lower frequencies they are available off-the-shelf from various suppliers, but above 100 GHz they are increasingly difficult to manufacture because of the tighter mechanical tolerances. Currently several research institutes are developing hybrids for submillimeter wavelengths, mostly for radio astronomical applications [1], [2]. Measurements have been reported so far for 70–110 GHz [3] and 257–370 GHz [4].

A 90° waveguide hybrid is a directional 4-port device that distributes a signal at its input port 1 equally and with a well defined phase shift of 90° between the two output ports 3 and 4. The second input port 2 is fully isolated from port 1 and has the same symmetrical coupling to ports 4 and 3. Figure 1 shows a typical layout of a branchline coupler and electrical field simulations with the software package CST Microwave Studio.

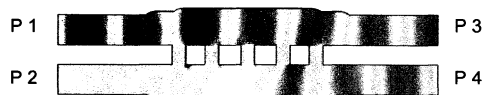


Fig. 1. Layout of a 90° branchline coupler. The colors represent the simulated electrical field when a signal is injected at port 1.

This work was supported by the Swiss National Science Foundation, grant 200020-100167, by the Deutsche Forschungsgemeinschaft, grant SFB 494, and by the European Union, grant FP6-Radionet. P. Pütz would like to thank C. Groppi, University of Arizona, for milling one of the 345 GHz couplers.

A. Murk and N. Kämpfer are with the Institute of Applied Physics, University of Bern, Switzerland (axel.murk@mw.iap.unibe.ch).

T. Tils is with the Kölner Observatorium für Submillimeter Astronomie, University of Köln, Germany.

P. Pütz is with the Steward Observatory Radioastronomy Laboratory, University of Arizona, USA, and also with the Kölner Observatorium für Submillimeter Astronomie, Germany.

S. Biber and L.P. Schmidt are with the Lehrstuhl für Hochfrequenztechnik, University of Erlangen-Nürnberg, Germany. S. Biber is now with Siemens Corporate Technology, Erlangen, Germany.

II. COUPLER DESIGN

The following two waveguide hybrids have been realized:

Coupler A from the Kölner Observatorium für Submillimeter Astronomie (KOSMA) has a center frequency of 345 GHz and was micromachined in brass on a high speed *Deckel FP-2* milling machine [5]. A second version of this coupler was manufactured at Steward Observatory Radioastronomy Laboratory (SORAL) using a more accurate *Kern MMP* milling machine.

Coupler B from the University of Erlangen-Nürnberg has a center frequency of 650 GHz and was micromachined in Silicon by photolithography, Deep Reactive Ion Etching (DRIE) and gold plating of the surfaces [6].

Both couplers are assembled from two symmetrical split-block halves that are cutting the waveguide in the E-plane. Figure 2 shows the 345 GHz brass coupler A, and Figure 3 the overall dimensions and electron microscope images of the etched Silicon coupler B. To have sufficient space for the input and output flanges both test devices include S-shaped waveguide sections that are much longer than the actual coupling regions. The phase errors in these waveguides and differences between their flanges have a significant effect on the measurement results.

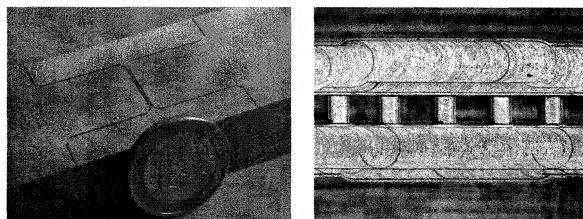


Fig. 2. Coupler A for 345 GHz: Split-block half milled out of brass (left) and its branchline section (right).

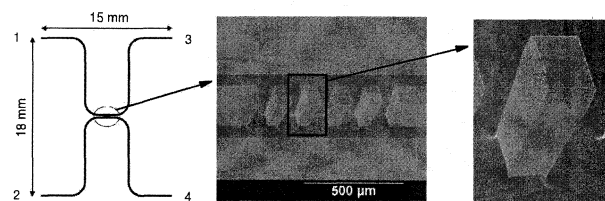


Fig. 3. Coupler B for 650 GHz etched out of a Silicon wafer.

III. MEASUREMENT SETUP

The transmission characteristics of the couplers were measured with an *AB-Millimetre* vector network analyzer. Its submillimeter wave source module, which consists of a phase-locked W-band Gunn oscillator and a multiplier, was connected to port 1 or 2 of the coupler through a 220 GHz or 550 GHz highpass filter and appropriate waveguide transitions. For the measurements of the 650 GHz device flexible dielectric waveguides with a high phase stability were used to simplify the change between different ports [7]. The detector was a simple harmonic mixer for the measurements around 345 GHz, and another harmonic mixer pumped by a second Gunn oscillator for those around 650 GHz. Again custom made waveguide transitions were used to connect the detector to the device under test.

The two unused ports of the coupler have to be terminated by a matched load during the measurements. Since waveguide loads were not available at these frequencies we used horn antennas that were pointing on a submillimeter wave absorber. For the 345 GHz coupler electroformed smooth-walled horn antennas with a spline profile were used [8], for the 650 GHz coupler octagonal horns etched in Silicon [9]. The mismatch and loss at the flanges was generally worse for the 650 GHz device because of the difficulties to machine them accurately in Silicon. For that reason these measurements are more affected by reflections and standing waves.

The maximum span of a frequency sweep was only about 1.5 GHz because of the limited electrical tuning range of the Gunn oscillator. For that reason each test sequence of all possible port combinations S_{ij} had to be repeated after tuning the vector analyzer to a new center frequency. A dedicated waveguide calibration kit was not available for these frequency bands, and only a simple through measurement (labeled *Ref*) without the coupler was made after each tuning step. Since the complete test procedure is very time consuming the couplers were tested with a limited number of frequency sweeps, and not continuously over their full bandwidth.

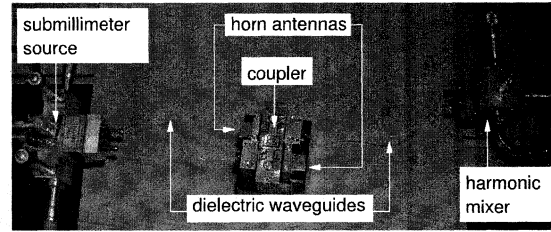


Fig. 5. Test setup for the 650 GHz coupler. The absorber terminations in front of the horn antennas are not shown in this picture.

IV. RESULTS

Figures 4 and 6 show the raw data of the measurement series. Amplitude and phase depend strongly on the sensitivity and the tuning of the detector and the source. In these and the following figures the span of the frequency sweeps has been expanded for clarity and the frequency axis is not to scale.

The measurements are also affected by standing waves in the test setup. The standing wave pattern is very similar for the various S_{ij} measurements because they involve the same number of waveguide interfaces and similar electrical lengths, but it is completely different for the *Ref* measurement. Since we are mostly interested in the amplitude and phase balance between the S_{31} and S_{41} , each series of frequency sweeps is calibrated using the complex S_{31} data as reference. In addition the data is scaled to obtain a mean amplitude of 0 dB for the through measurement *Ref*:

$$S_{ij\text{calibrated}} = \frac{S_{ij}}{S_{31}} \cdot \text{mean} \left(\left| \frac{S_{31}}{Ref} \right| \right)$$

Figures 7 and 9 show the calibrated data. The S_{31} measurements appear now with a constant amplitude and zero degree phase because they were used as reference plane. The phase slope of *Ref* is given by the electrical length of the coupler. The *Ref* measurements were repeated after each test series to check the repeatability of the measurements. A significant drift occurred only in the frequency sweeps around 675 and 700 GHz, and the results at these frequencies will be less

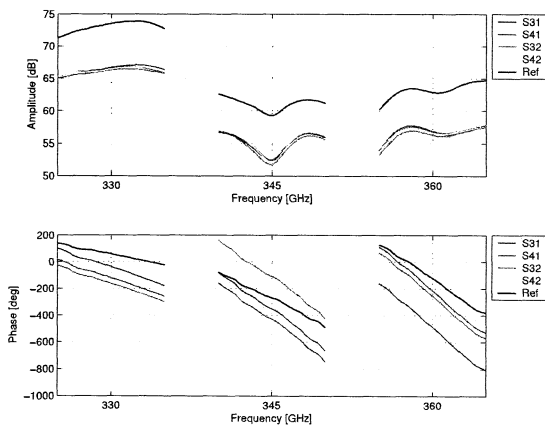


Fig. 4. Raw data of coupler A.

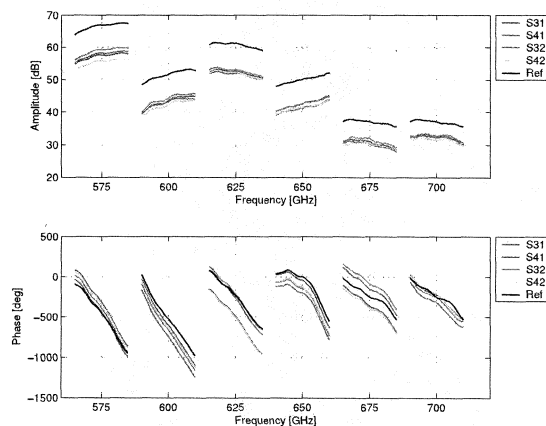


Fig. 6. Raw data of coupler B

reliable. The strong ripple on the *Ref* phase at 700 GHz also indicates that this measurement was more affected by standing waves than the others.

Another important parameter of a coupler is the isolation S_{12} and S_{34} . For both couplers values between -20 and -25 dB have been measured. Model simulations predict similar values, but some discrepancies exist because of the mismatch at the terminated ports.

V. ERROR CORRECTION

The calibrated data in Figures 7 and 9 differ significantly from the expected behavior. The design of both couplers has been optimized to be close to an ideal waveguide hybrid with $S_{41} = S_{31} \cdot \exp(i\frac{\pi}{2})$ and $S_{42} = S_{32} \cdot \exp(i\frac{\pi}{2})$. In addition the symmetrical layout should result in $S_{31} = S_{42}$ and $S_{41} = S_{32}$, which is not the case in the calibrated data.

A significant part of the observed unbalance is not a true characteristic of the branchline section of the coupler, but a difference in its electrically long waveguide connections and its flanges. These errors can be corrected under the assumption that the coupler itself is symmetric. Figure 8 shows a simple error model of the test setup. The coupling section C is connected with the four test ports through transmission lines that are not identical. Since S_{31} is used as reference plane ports 1 and 3 are free of errors, while port 2 and 4 have an additional complex gain e_2 and e_4 .

The measurements S_{ij} are related to the true values S_{ij}' as:

$$\begin{aligned} S_{31} &= S_{31}' && \text{reference plane} \\ S_{41} &= S_{41}' \cdot e_2 \\ S_{32} &= S_{32}' \cdot e_4 \\ S_{42} &= S_{42}' \cdot e_2 \cdot e_4. \end{aligned}$$

If we assume that the coupling section C is symmetric, then $S_{31}' = S_{42}'$ and $S_{32}' = S_{41}'$. In this case the error terms can be calculated with:

$$e_2 = \sqrt{\frac{S_{42} \cdot S_{41}}{S_{31} \cdot S_{32}}} \quad e_4 = \sqrt{\frac{S_{42} \cdot S_{32}}{S_{31} \cdot S_{41}}}$$

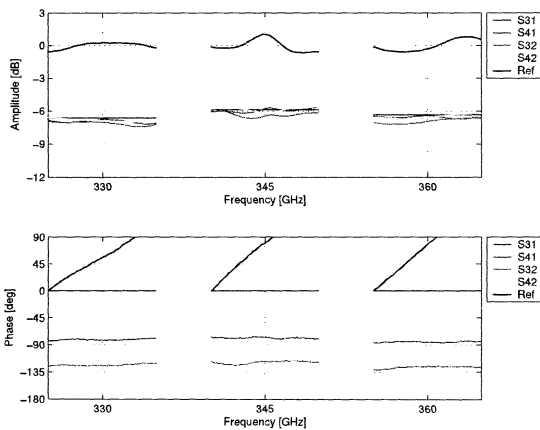


Fig. 7. Calibrated data of coupler A.

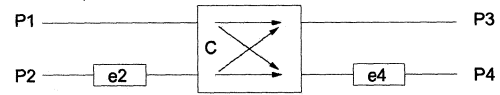


Fig. 8. Model for the error correction: if the coupler element C is assumed to be symmetric, then the errors e_2 and e_4 of ports 1 and 2 can be calculated from the four transmission measurements.

Figures 10 and 11 show the corrected results. The mean values of amplitude and phase are now equal for symmetrical signal paths according to the assumptions that were made, and for that reason only the S_{31} and S_{41} values are shown. The power is now distributed almost equally and with a phase shift close to 90° between the two output ports, at least for the designed band center of the coupler. This shows that the design goals of the couplers could be reproduced within the accuracy of our measurement setup. Two versions of the 345 GHz coupler have been tested. Device #2, which has been produced with the better milling machine, has a flatter amplitude and phase response over the frequency band. The measurements at 675 and 700 GHz remain questionable because of the observed drift and standing waves problems.

The absolute amplitude of the corrected data is significantly smaller than the -3 dB of an ideal coupler because of the losses in the waveguides and at the flanges. For the 345 GHz device the observed values below -6 dB correspond very well with CST simulations of the complete structure when the ohmic loss of brass is taken into account in the model. This losses could be significantly reduced by gold plating or machining in a low-loss material, e.g. Tellurium-Copper. For the 650 GHz device the losses differ by typically 1 to 2 dB from model estimates, most likely because of the imperfections of the waveguide flanges and of the etching process.

VI. DISCUSSION

There is some concern about the validity of the proposed correction scheme. It could be questioned whether the 90° phase difference of the corrected data is an implicit result of our assumptions because every matched ($S_{ii} = 0$), lossless

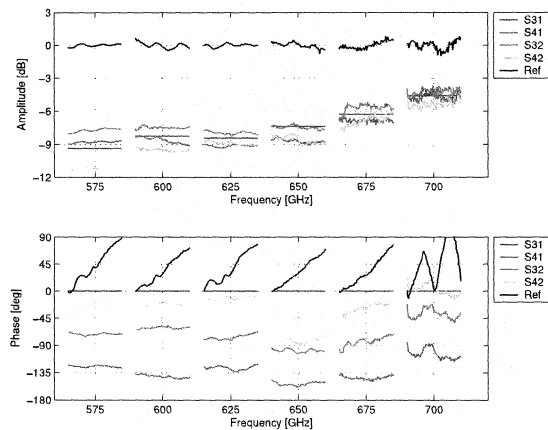


Fig. 9. Calibrated data of coupler B.

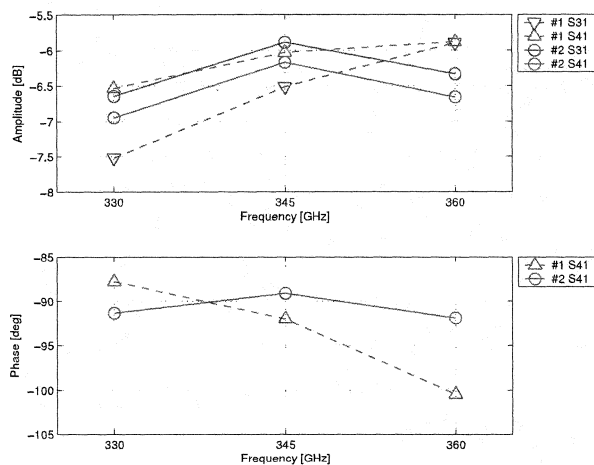


Fig. 10. Corrected data of coupler A (#1: KOSMA, #2: SORAL).

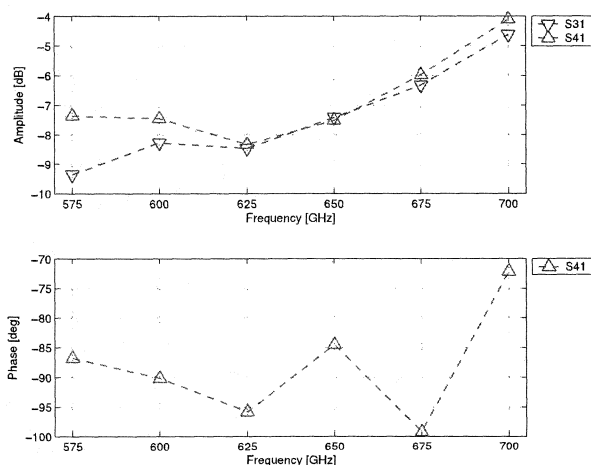


Fig. 11. Corrected data of coupler B.

and double-symmetric 4-port device produces exactly this phase shift between its output ports. Our correction scheme, however, includes only the assumption of a single symmetry plane in the coupling section. This is justified by the symmetric layout of the coupler, and it is still valid for the most likely manufacturing errors, e.g. when the two splitblocks are not perfectly aligned or when the width of the branchlines is incorrect. We tested with CST simulations that only large asymmetric machining errors will break this symmetry. In this case the correction will obviously lead to wrong results, but not automatically to a 90° phase shift.

Multiple reflections are not corrected with the described method, but this problem can not be resolved without further calibration standards, better flanges or much wider instantaneous frequency sweeps. Especially the measurements of the 650 GHz device are affected by standing waves. Another possible error source are phase shifts in the cables with the reference signals of the network analyzer when the source or detector are swapped between different ports. For that reason we used high quality cables and tried to move them as little as possible during a test series. The reproducibility of the *Ref2* measurement, the phase difference of the corrected data close to 90° and the consistency of the correction factors *e* at different frequencies indicate that these errors were only a couple of degrees in most cases. For the measurements of the 650 GHz coupler the source and detector remained fixed on the test bench, and only the dielectric waveguides had to be swapped between the ports. The phase stability of these waveguides had been tested before and proved to be sufficient for our measurements.

The reason for the necessary corrections has been investigated in more detail for two 345 GHz couplers. The amplitudes of *e*₁ and *e*₂ are within ± 0.2 dB with a variation of about ± 0.1 dB between different frequency sweeps. The phases are between $+10^\circ$ and -30° and change only little with frequency, which translates to a pathlength difference of up to 0.25 mm. Because it is unlikely that the mechanical length

of the waveguide sections differs that much we measured their width and height under a microscope at different locations in the split-block. It turned out that the milling tolerances cause a certain variability of the propagation constant, and because of the large total length of the waveguides this can add up to similar phase errors as the observed ones.

The length of the waveguide sections will be significantly shorter and flanges can be avoided by integrating the coupler into the mixer block of a sideband separating receiver. In this case it can be expected from our measurements that the power splitting and phase difference will be close to the design goal of -3 dB and 90° .

REFERENCES

- [1] J. W. Kooi, A. Kovács, B. Bumble, G. Chattopadhyay, M. L. Edgar, S. Kaye, R. LeDuc, J. Zmuidzinas, and T. G. Phillips, "Heterodyne instrumentation upgrade at the Caltech Submillimeter Observatory," in *Proceedings of SPIE: Astronomical Telescopes and Instrumentation*, vol. 5498-40, pp. 332-348, June 2004.
- [2] S. Claude, C. Cunningham, A. Kerr, and S. Pan, "Design of a sideband-separating balanced SIS mixer based on waveguide hybrids," in *ALMA Memo*, no. 316, Sept. 2000.
- [3] S. Srikanth and A. R. Kerr, "Waveguide quadrature hybrids for ALMA receivers," in *ALMA Memo*, no. 343, Jan. 2001.
- [4] S. Claude, "Sideband-separating SIS mixer for ALMA band 7, 275-370 GHz," in *ALMA Memo*, no. 357, Mar. 2001.
- [5] T. Tils, *Design and 3-D Electromagnetic Modeling of Terahertz Waveguide Mixers and Components*. Phd thesis, Universität zu Köln, 2006.
- [6] S. Biber, *Mikrostrukturierte Terahertz-Bauelemente auf Silizium-Basis*. Phd thesis, Technische Fakultät der Universität Erlangen-Nürnberg, 2005. Available online at <http://www.opus.uni-erlangen.de>.
- [7] A. Hofmann, E. Hörster, J. Weinzierl, L.-P. Schmidt, and H. Brand, "Flexible low-loss dielectric waveguides for THz frequencies with transitions to metal waveguides," in *33rd European Microwave Conference*, pp. 955-958, 2003.
- [8] T. Lüthi, D. Rabanus, U. Graf, C. Granet, and A. Murk, "A new multi-beam receiver for KOSMA with scalable fully reflective focal plane array optics," in *16th International Symposium on Space Terahertz Technology*, May 2005.
- [9] S. Biber, A. Murk, L. P. Schmidt, and N. Kämpfer, "Design and measurement of a 600 GHz micromachined horn antenna manufactured by combined DRIE and KOH-etching of silicon," in *16th International Symposium on Space Terahertz Technology*, May 2005.

New Standards for Submillimeter Waveguides

John S. Ward, Jet Propulsion Laboratory, California Institute of Technology,
M/S 168-314, 4800 Oak Grove Drive, Pasadena CA 91109, U.S.A.

Growth of the submillimeter-wave field has created the need for new standards for high frequency waveguides. The common "WR" standard for waveguide sizes gives no guidance for frequencies beyond 325 GHz, the upper band edge of WR-3 [1]. Similarly, standard waveguide flanges become increasingly problematic above about 100 GHz [2]. The result of this lack of standards is that hardware from different laboratories, universities, and commercial vendors is not in general intercompatible. Furthermore, adapters between incompatible waveguides typically introduce unacceptable performance degradation. It is clear that new standards are needed to maximize intercompatibility and minimize the costs associated with the proliferation of incompatible hardware.

The lack of waveguide standards beyond 325 GHz should not be solved by simply extending aging U.S. military standards. For example, the existing standards provide no guidance for selecting preferred sizes or for selecting in-between sizes, and the existing standards are in deprecated inch-pound units. A standard for waveguide sizes should, however, be based on existing widely-used international standards. It should provide guidance for selecting a minimum number of preferred sizes to provide continuous frequency coverage for generic laboratory equipment such as network analyzers, spectrum analyzers, sources, mixers, couplers, and horns. It should also provide guidance

Table 1. The preferred series of waveguide sizes suitable for generic laboratory equipment like network and spectrum analyzers, sources, mixers, horns, directional couplers, etc. The table can be extended indefinitely to larger and smaller sizes by multiplying by powers of 10. See the proceedings for tables of second, third, and fourth choices of waveguide sizes as well as recommendations for circular waveguide.

Length (μm)		Cutoff (GHz)	
a	b	TE ₁₀	TE ₂₀
1000	500	150	300
630	315	238	476
400	200	375	750
250	125	600	1200
160	80	937	1874
100	50	1500	3000

for choosing in-between sizes if the preferred sizes are not adequate for a particular application. Finally, it should include provisions for extending the standard indefinitely to higher and lower frequencies.

ISO 497 is a widely used global industry standard familiar to many people as the basis for the sizing of a wide variety of commercially-available hardware such as metric fasteners and stock metals. The preferred sizes are a logarithmic scale starting at 1 mm and spaced 2 dB apart. For applications where in-between sizes are needed, the second choice is the series of sizes spaced by 1 dB, the third choice sizes spaced by 0.5 dB, etc. All sizes are rounded appropriately. The series repeats every decade by multiplying by a power of ten, making it quick and easy to memorize. By providing guidance for first, second, third, and fourth choices, ISO 497 maximizes the likelihood of compatibility between independently-developed hardware. Finally, since ISO 497 is an infinite series, it never needs to be revised to extend to larger or smaller sizes.

ISO 497 can be applied directly to the "a" dimension of rectangular waveguide. The resulting 2 dB spacing in the preferred sizes is ideally suited to provide complete frequency coverage for generic test equipment with the minimum number of different sizes. Table 1 summarizes the first-choice preferred sizes.

A new standard waveguide flange should be compact, provide a high degree of repeatability without requiring undue skill and attention of the user, should be robust against damage to precision surfaces, and should include only metric threads. This paper will discuss in more detail requirements and choices for submillimeter waveguide flanges, and will present a concept for gendered waveguide flanges for directional components like sources, mixers, isolators, and (eventually) amplifiers that eliminates the need for insertable gender changers.

The research described herein was carried out at the Jet Propulsion Laboratory, California Institute of Technology, Pasadena, California, USA, under contract with the National Aeronautics and Space Administration.

[1] MIL-DTL-85/3B

[2] Kerr, A. R., Wollack, E., and Horner, N., "Waveguide Flanges for ALMA Instrumentation," ALMA Memo #278, 1999.

Quasi-Optical Faraday Rotator Design, Construction and Evaluation

R.I. Hunter, D.A. Robertson, G.M. Smith,
Millimetre Wave and High Field ESR Group, University of St Andrews,
North Haugh, St Andrews, Fife KY 16 9SS, Scotland, United Kingdom
tel: +44 1334 463156, 2669, fax: 463104, rih1, dar, gms@st-and.ac.uk
P. Goy, S. Caroopen, M. Gross,
AB MILLIMETRE, 52 rue Lhomond 75005 Paris, France
tel: +33 1 47 07 71 00, fax: +33 1 47 07 70 71, abmillimetre@wanadoo.fr

Abstract

Quasi-Optical Faraday Rotators (QOFRs) are a vital enabling technology for a wide range of millimeter and submillimeter wave applications. QOFRs are used in the construction of quasi-optical isolators and circulators for use in a wide variety of radar, imaging and precision measurement systems, where they provide a low loss and low VSWR alternative to conventional waveguide devices.

Using data from the characterization of magnetized ferrite samples, together with data for adhesives and dielectric matching materials, a model has been developed that accurately predicts the performance of finished QOFRs. This model can be used to optimise the design of QOFRs for any desired centre frequency and bandwidth. This model has been experimentally verified by the construction of several W-band (75-110 GHz) devices using these designs. The results show excellent agreement with those predicted by the model for devices constructed using both sintered and plastoferrites and a variety of matching materials. The model has also been extended to predict the likely performance which might be realized for devices designed for operation at up to 500 GHz.

Cross-polarization characterization of GORE-TEX[®] at ALMA band 9 frequencies

M. Candotti*, A. M. Baryshev[†], N. A. Trappe*, R. Hesper[†], J. A. Murphy*, J. Barkhoff[†].

*Experimental Physics Department
National University of Ireland
Maynooth, Co. Kildare, (Ireland)
email: Massimo.Candotti@nuim.ie

[†]Netherlands Institute for Space Research
and Kapteyn Astronomical Institute
9700-AV Groningen, (The Netherlands)
email: A.M.Baryshev@sron.rug.nl

Abstract—GORE-TEX[®] material, commonly used in radomes, is known to be transparent at microwave bands. In ALMA a thin GORE-TEX membrane will cover the aperture through which the RF beam enters the cabin at the primary vertex hole. Slabs of GORE-TEX[®] are also generally employed in windows for intermediate temperature shields inside the cryostat. The purpose of these windows ideally is to allow the beam to pass through them without introducing any alteration to the beam properties. The main concern is RF loss, but also cross-polarization efficiency degradation. This paper will concentrate on the results we have obtained for ALMA band 9 (602-720 GHz), in relation of loss of cross-polarization efficiency of a linearly polarized beam passing through a GORE-TEX[®] slab, depending on its orientation relative to the direction of polarization of the beam. In order to spot anisotropic behavior of the material under test, an ad hoc measurements set-up has been used. Systematic measurements of cross-polarization properties for different thicknesses of GORE-TEX[®] slabs were undertaken. Cross-polarization information is given in relation of the relative angle between the incident beam polarization and the material under test.

I. INTRODUCTION

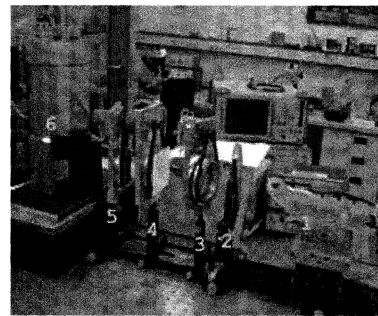
For the band 9 cryogenic receiver GORE-TEX¹ slabs are used at the windows of 12 and 90K intermediate shield temperature cryostat stages. During a cross-polarization measurement campaign of the two beam polarizations of the band 9 receiver, we noticed poor cross-polar efficiency performance of the system. After some trouble identifying the cause it remained to verify the transparency of the GORE-TEX windows. It became apparent that the slab of GORE-TEX was inducing extra cross-polarization levels according to its relative orientation with the signal polarization passing through it. Further systematic analysis confirmed this indicating an anisotropic behavior of the GORE-TEX material. The aim of this paper is to report the cross-polar measurements we have taken on various samples of GORE-TEX slabs. In section II we give a brief description of the measurement set-up and the kind of measurement techniques we adopted in order to show

¹GORE-TEX GR[®] sheet gasketing, according DIN 28091, TF-0-0.

the initial hypothesis. Section III shows the results obtained followed by conclusions.

II. MEASUREMENT SET-UP

In order to characterise various thicknesses of GORE-TEX samples we assembled an ad hoc measurement bench set-up. The system is depicted in figure 1 (a) including the numbering of the items that compose it. The system can allow total power measurement of a submillimeter signal using a computer controlled broadband source (600 – 700 GHz) (item #1) and a cryogenic high sensitivity bolometer (item #6). The sub-



(a) Measurement Set-up.



(b) GORE-TEX sample.

Fig. 1. Measurement set-up for the characterization of GORE-TEX slabs and GORE-TEX sample.

millimeter signal is obtained from a Gunn diode at 100 GHz and further multiplied times 6 by a $x2$ and $x3$ multiplier. The output of the source is propagated to the free space by

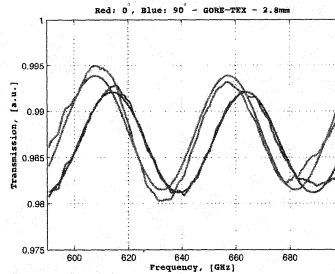


Fig. 2. Transmission for a 2.8 mm GORE-TEX slab rotated at 0° and 90° at band 9 frequencies.

mean of a diagonal horn. A plano-convex Teflon lens (item #2) is used to refocus the beam power along the other system components and finally at the bolometer aperture. In order to obtain a pure linearly polarised signal at the Sample Under Test (SUT) (item #4) a rotatable wire grid is located between the SUT and the lens. A second wired grid between the SUT and the bolometer is used to allow power detection of the co- or cross-polar polarization of the SUT transmitted signal. The standing wave phenomena occurring along the chain set-up was minimised by using Ecosorb sheets and rotating items 2, 3, 4, 5 in such a way the standing waves couldn't form. The SUT is mounted on a computer controlled rotational support. Grids #5 and #3 were manually rotated in order to ensure the measurement of only co- or cross- polar signal at the bolometer. The system as it is can be used for SUT power transmission measurements sweeping the source frequency and co- and cross-polarization power signal measurements of the transmitted signal at different rotation angles of the SUT. The aim of the first kind of measurement is to show at which frequencies the SUT is transparent. If this measurement procedure is taken for the two principal axis directions of the SUT than we can highlight the possible anisotropic properties. The second measurement procedure is performed at a fixed frequency but with the SUT rotating around the axis normal to the SUT surface. By measuring co- and cross-polar power versus the rotation angle of the SUT it is possible to show the level of cross-polarization introduced by the SUT at different relative orientation angles in relation with the source linear polarization direction.

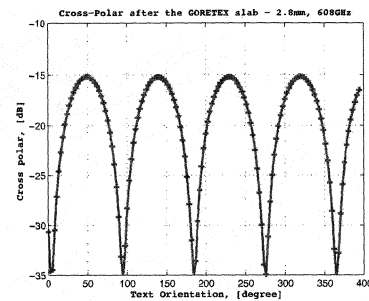
III. RESULTS

It has been noticed that by rotating the sample of GORE-TEX around the normal at the surface of the sample, different levels of power were recorded when the system of figure 1 (a) was tuned to a fixed polarization direction. This suggests that there is a material anisotropic behavior. It has also been noticed that there is a direction of preference of the sample rotation. When the text on the sample (figure 1 (b)) is aligned or at 90° with the polarization of the incident beam we have a peak in the transmitted signal. Thus in the following pictures the 0 in the abscissa axis will refer to co-alignment of the text

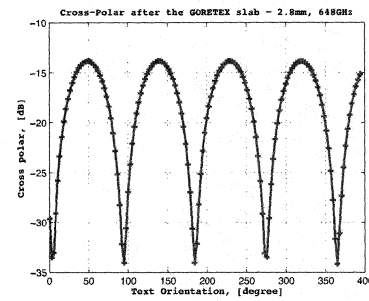
with the polarization of the incident signal.

A. Transmission

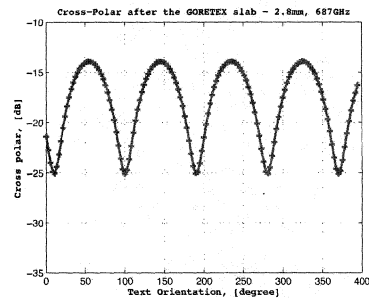
The aim of this measurement is to show possible differences in the refractive index along the two main axis directions of the sample (along and at 90° of the text direction). As an example a slab of 2.8 mm was tested sweeping the frequency source from 590 GHz to 700 GHz. Figure 2 shows the transmission varying with frequency and also with the sample text rotation, indicating a different refraction index along these directions. For the purpose of finding the peaks of transmission a sine curve was fitted to the data. At these peaks (607.7 and 657.4 GHz for 0° – 614.0 and 663.8 GHz for 90°)



(a) 608 GHz.



(b) 648 GHz.



(c) 687 GHz.

Fig. 3. Cross-polarization introduced by a 2.8 mm slab of GORE-TEX at various frequencies.

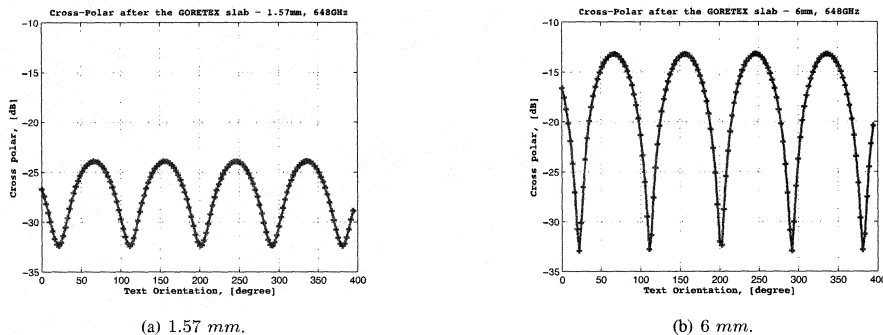


Fig. 4. Cross-polarization introduced by 1.57 mm and 6 mm slabs of GORE-TEX at 648 GHz.

the refractive index n , can be evaluated from the expression that gives the phase delay inside the slab of thickness d : $\phi = 2\pi dn/\lambda_0$ [3]. At peak locations the phase delay is an integer multiple of π . Solving this expression for two frequencies of maximum transmission we found a refractive index of 1.0587 at 0° and 1.048 at 90° . This preliminary result shows the anisotropy of GORE-TEX and brought us to investigate the cross-polarization properties of this material.

B. Cross-Polarization

We then acquired more data for different thicknesses and at different frequencies in order to find out how the transmitted cross-polar level was affected by the SUT at different rotation angles with respect to the incident polarization signal. We first considered the sample of 2.8 mm at three frequencies (608, 648 and 687 GHz). In figure 3 we observe that indeed the GORE-TEX slab introduces cross-polarization. The lowest peaks (no cross-polar introduced) coincide with the direction of the text on the slab surface and its orthogonal direction. At 45° and at 90° spaced multiples we notice a level of cross-polar introduced by the SUT of -14 dB at highest frequencies. Other two different sample thicknesses were tested, 1.57 mm and 6 mm. As expected for a thinner slab the cross-polarization introduced is lower compared with the 2.8 mm previous case. For a slab of 6 mm the extra cross-polarization does not appear to increase much more because of twice the thickness, in fact at 45° the level is at -13 dB for the frequency of 648 GHz.

Another interesting experiment was to measure the cross-polarization of a pair of same thickness sheet samples (2.8 mm) facing each other at 90° . Since the predominant orientation of the polymer chains in the GORE-TEX slab develops anisotropy (i.e. birefringence), it has two different dielectric constants for two different orthogonal axes inducing elliptical polarization. It is known that elliptical polarization can be converted back to linear by the same slab of material rotated 90° [4]. Figure 5 shows the results of this experiment. Indeed we observe a cancellation of the cross-polarization effect, leading to a low level flattered cross-polarization response.

IV. CONCLUSIONS

In this paper we have shown the cross-polarization effect introduced by a slab of GORE-TEX of different thicknesses at the frequencies of ALMA band 9. We have pointed out that there is a dependence on the rotation of the sample in relation to the incident signal linear polarization. In particular it looks that due to fabrication procedures, there are two preferred directions of minimum cross-polarization effect: along and normal to the text on the GORE-TEX sheets. At 45° it has been shown that there is indeed a high cross-polarization effect scattering co-polar power to the cross-polar component of the transmitted signal up to -13 dB of cross-polarization efficiency for a thickness of 6 mm. A further experiment having two identical slab samples of 2.8 mm thickness orthogonally faced has demonstrated that the cross-polarization effect induced by the first slab can be cancelled by the second one.

Despite the qualitative work carried out in this paper we suggest that further tests must be carried out on more samples, as well as on different kind of materials, even at different ALMA bands where cross-polarization is a concern.

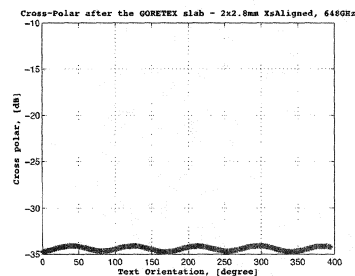


Fig. 5. Cross-polarization introduced by a pair of same thickness sheet samples (2.8 mm) facing each other at 90° . $f = 648$ GHz.

REFERENCES

- [1] http://www.gore.com/en_xx/products/fabrics/microwave/microwave.html

- [2] V. Gasho, S. Stanghellini, *Technical Specification for the Design, Manufacturing, Transport and Integration on Site of the 64 ALMA ANTENNAS*, ALMA-34.00.00.00-006-A-SPE Version: A, December 15th, 2003.
- [3] P. F. Goldsmith, *Quasioptical Systems: Gaussian beam quasioptical propagation and applications*, IEEE Press, New York, 1997.
- [4] R. C. Jones, *New calculus for the treatment of optical systems*, J. Opt. Soc. Am. 31, 488-493, (1941).

Rigorous Analysis and Design of Finline Tapers for High Performance Millimetre and Submillimetre Detectors

Chris North, Ghassan Yassin and Paul Grimes

Astrophysics, Oxford University, Denys Wilkinson Building, Keble Road, Oxford OX1 3RH

Email: cen@astro.ox.ac.uk

Abstract—Antipodal finline tapers have demonstrated excellent performance in conjunction with SIS mixers and have recently been used with TES detectors for the CMB polarisation instrument CLOVER. In this paper we present the computation of the finline parameters using the Transverse Resonance method and Spectral Domain Analysis and compare them with those obtained from Finite Element simulations. We also present a software package that can read an input file and then synthesise a minimum length taper for a requested return loss. The input file must contain the cutoff frequency as a function of the finline slot dimension which can be computed externally to the synthesis package.

I. INTRODUCTION

Previous publications [1] have demonstrated the advantages of finline mixers at submillimetre wavelengths. An antipodal finline taper allows the mixer to be fed by a high-performance corrugated horn, easy fabrication of the mixer chip and can be fully integrated with other planar circuit technology.

Experimental investigation of the mixers at frequencies between 230-700GHz has shown that finline mixers have high bandwidth, high optical performance (low sidelobes and cross polarisation) and low noise temperature. The larger substrate allows the integration of important planar circuits for sideband separation and balanced mixers [2]. Their ease of fabrication and high performance makes them ideal for use in large-format arrays.

Figure 1 shows some schematics of finlines in waveguides, along with dimensions and axis conventions. The metallisation layer lies across the middle of a split-block waveguide in the form of two fins separated by 400nm of oxide and deposited on a 220 μ m thick substrate. Figure 2 shows a mask of a finline chip and the Electric fields at various points along the transition from waveguide to microstrip.

At THz frequencies, rigorous analysis of finline tapers is complicated by the large variation in lateral dimensions and relatively large metallisation thickness. Previous analysis methods have divided the taper into three sections. When the fins are not overlapping, the taper was approximated to a unilateral taper and analysed with Transverse Resonance (TR) or Spectral Domain Analysis (SDA). For the second section, where the fins are overlapping, SDA was used, though this ignores the metallisation thickness and the substrate carrying the fins, which is only a valid assumption if the overlap is larger than the fin separation. The third section is microstrip,

which has been fully analysed using Conformal Mapping [3]. The taper itself can be synthesised using the Optimum Taper Method (OTM), which tapers cutoff frequencies to give a required return loss for a minimum taper length.

In this paper we present and compare new procedures for analysing the the performance of finline tapers which can be applied along the whole taper. The Optimum Taper Method is still used, but the cutoff frequencies can be supplied

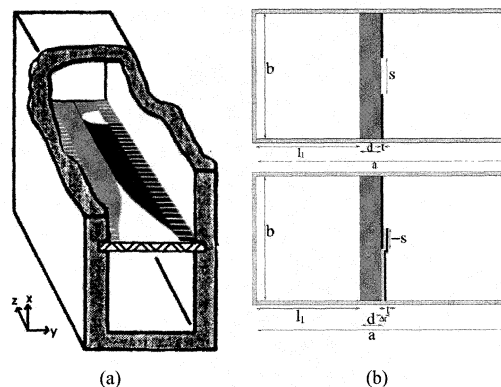


Fig. 1. (a) Schematic of a finline chip in a waveguide. (b) *Top*: Unilateral finline with dimensions; *Bottom*: Antipodal finline with dimensions.

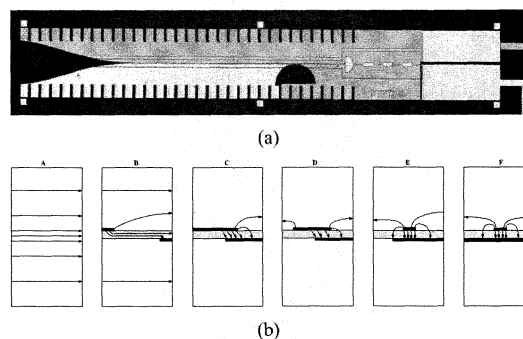


Fig. 2. (a) Mask of an SIS mixer chip utilising an antipodal taper at 230GHz. The metallisation layers are visible, as well as the semicircular structure which converts overlapping fins into a microstrip. (b) The Electric field lines at various points along the transition: empty waveguide (A), unilateral finline (B), antipodal finline (C), the start (D) and end (E) segments of the semicircular transition to microstrip (F).

from finite-element simulation software or any other rigorous simulation package. We have developed a software package, in Fortran90, which reads an array of electrical parameters and outputs a taper profile in numeric and graphical formats. We describe the current analysis methods in §II and the optimum taper method in §III. §IV outlines the proposed computational method, while §V discusses the results of the different methods.

II. CURRENT ANALYSIS METHODS

Previous analyses [1] have used Transverse Resonance (TR) and Spectral Domain Analysis (SDA) to calculate cutoff frequencies and propagation constants. While TR can be accurate for thick metallisation, but doesn't take dispersion into account, SDA gives full-wave computation including dispersion, but assumes infinitely thin metallisation (see §II-B). Consequently, the analysis is least rigorous when the fins overlap slightly, since both metallisation thickness and dispersion are important. Moreover, there is always a difficulty in matching the solutions produced by two separate methods.

A. Transverse Resonance

Transverse Resonance calculates the cutoff wave number k_c by finding the first zero of the transcendental equation [4]:

$$-\cot(k_c l_1) - \cot[k_c(l_1 + d)] + \frac{b}{s} \tan(k_c t) + \frac{B}{Y} = 0 \quad (1)$$

where the dimensions b, d, t, l_1 are those defined in Fig. 1. The term B/Y is the normalised susceptance of the gap, calculated using the equivalent circuit of the finline from:

$$\begin{aligned} \frac{B}{Y} &= \frac{b}{\pi} k_c [2P_1 + \epsilon(P_s + P_b)] \\ P_1 &= \ln[\operatorname{cosec}(\frac{\pi s}{2b})] \\ P_s &= \frac{d}{s} \cdot \arctan(\frac{s}{d} + \ln\sqrt{1 + (d/s)^2}) \\ P_b &= \frac{d}{b} \cdot \arctan(\frac{b}{d} + \ln\sqrt{1 + (d/b)^2}) \end{aligned} \quad (2)$$

The propagation constant (β) can be related to the cutoff frequency by the following relations:

$$\beta = k_0 \sqrt{\epsilon_{eq}} \sqrt{1 - (f_c/f_0)^2} \quad (3)$$

where ϵ_{eq} is an equivalent dielectric constant given by:

$$\epsilon_{eq} = (k_c/k_{c0})^2 \quad (4)$$

where k_{c0} is the cutoff for wave number $\epsilon_r = 1$, so it satisfies (1) and (2) with that condition.

B. Spectral Domain Analysis

Spectral Domain Analysis (SDA) is based on finding a matrix equation which relates the Fourier transforms of the current and fields by the dyadic Green's function. The advantage of this method is that it converts the differential equations given by Maxwell's equations into a homogeneous set of

algebraic equations. By setting the determinant of the coefficients to zero the propagation constant can be found, while finding the coefficients yields the characteristic impedance. The relationship between the Fourier transforms of the currents and fields may be written as:

$$\begin{pmatrix} \tilde{J}_y(\hat{k}_n) \\ \tilde{J}_z(\hat{k}_n) \end{pmatrix} = \begin{pmatrix} G_{yy}(\hat{k}_n, \beta) G_{yz}(\hat{k}_n, \beta) \\ G_{zy}(\hat{k}_n, \beta) G_{zz}(\hat{k}_n, \beta) \end{pmatrix} \begin{pmatrix} \tilde{E}_y(\hat{k}_n) \\ \tilde{E}_z(\hat{k}_n) \end{pmatrix} \quad (5)$$

where $\hat{k}_n = n\pi/b$ is the Fourier parameter of the y -coordinate.

The electric field is expanded in terms of basis functions such that

$$\tilde{E}_y(\hat{k}_n) = \sum_{i=1}^M a_i \tilde{\phi}_i(\hat{k}_n) \quad (6)$$

$$\tilde{E}_z(\hat{k}_n) = \sum_{j=1}^N b_j \tilde{\psi}_j(\hat{k}_n) \quad (7)$$

where $\tilde{\phi}_i(\hat{k}_n)$ and $\tilde{\psi}_j(\hat{k}_n)$ are Fourier transforms of the basis functions $\phi_i(y)$ and $\psi_j(z)$.

By substituting (6) and (7) into (5), and using Galerkin's method we obtain an $(M+N) \times (M+N)$ set of homogeneous linear equations with unknowns a_i and b_i . By solving the resulting equations we obtain the propagation constant β .

The choice of basis functions is important when using SDA, both in terms of the form and the number of terms M and N . In [5] rectangular and sinusoidal basis functions are discussed, while in [1] it is found that Legendre polynomials for $\phi(y)$ and sinusoidal functions for $\psi(z)$ give accurate results for both unilateral and antipodal finlines.

As mentioned previously, in our solution we did not take into account of the substrate, although it could easily be incorporated in the formulae.

III. THE OPTIMUM TAPER METHOD

A. Parameters

The parameters required to perform the analysis are:

- 1) The frequency to be analysed (f_0); in this case 90GHz.
- 2) The required cutoff frequency at the start and end of the taper ($f_c(0)$ and $f_c(l)$); in this case around 53GHz and 23GHz respectively.
- 3) The return loss required (R_{max}); in this case -30dB

B. The Method

Following [4], the reflection coefficient of a taper of length l is given by:

$$R(\beta) = - \int_0^l \kappa^{-+}(z') \cdot \exp\left\{ \int_0^{z'} -2\beta(f, z) dz \right\} dz' \quad (8)$$

If we only consider a given frequency f_0 (at which we want to analyse the taper) then by making the approximation that the exponent of (8) can be approximated to a product of a

frequency-dependent (which is normalised to 1 at $f = f_0$ and a z -dependent term, [4] show that (8) becomes

$$R(\eta) = \int_0^{2\theta} C \cdot K(\xi) e^{-i\eta\xi} d\xi \quad (9)$$

where ξ is a z -dependent phase-space variable given by [4]

$$\int_0^z 2\beta(f_0, z') dz' \simeq \xi(z) \quad (10)$$

and C is a normalising constant defined such that

$$\int_0^{2\theta} K(\xi) d\xi = 1 \quad (11)$$

The value of C is then given by:

$$C = \ln \left[\frac{f_c(0)}{f_c(l)} \cdot \left(\frac{1 - (f_c(l)/f_0)^2}{1 - (f_c(0)/f_0)^2} \right)^{\frac{1}{4}} \right] \quad (12)$$

where $f_c(z)$ is the z -dependent cutoff frequency.

The definition of θ is:

$$\theta = \operatorname{arccosh}(C/R_{max}) \quad (13)$$

where R_{max} is the maximum permissible return loss (one of the parameters mentioned above). The value of ξ is then in the range $0 \leq \xi \leq 2\theta$, with $\xi(0) = 0$ and $\xi(l) = 2\theta$.

C. Calculating the Cutoff Frequencies

The coupling distribution $K(\xi)$ is chosen to make sure the reflection coefficient is below R_{max} for all frequencies above f_0 . Due to the normalisation of $K(\xi)$ given by (11) and (12), the integral

$$I(\xi) = \int_0^\xi K(\xi') d\xi' \quad (14)$$

has boundary conditions $I(0) = 0$ and $I(2\theta) = 1$. The cutoff frequency for a given value of ξ is given by:

$$f_c(\xi) = f_c(0) \cdot \left(F + \sqrt{F^2 + (1 - 2F)\exp(4CI(\xi))} \right) \quad (15)$$

where $F = \frac{1}{2}(f_c(0)/f_0)^2$.

IV. PROPOSED METHOD

A. Finite-Element Simulation

Finite-element simulation software such as Ansoft HFSS¹ can be used to accurately simulate sections of transmission lines to calculate the electrical parameters. While the software returns the propagation constant accurately and straightforwardly, the cutoff frequencies must be obtained by scanning a range of frequencies around the expected value. In our calculation we made use of the fact that the cutoff frequency is usually accompanied by a sharp change in other parameters, such as the impedance or S-parameters.

¹<http://www.ansoft.com>

B. Computational Procedure

The computational procedure is as follows:

- 1) Select a return loss (R_{max}) and target frequency (f_0).
- 2) Determine initial and final cutoff frequencies ($f_c(0)$ and $f_c(l)$) from simulations.
- 3) Run simulations on a range of slot widths to obtain cutoff frequencies and propagation constants.
- 4) Input waveguide parameters:
 - a) Waveguide width and height
 - b) Substrate thickness and dielectric constant
 - c) Metallisation thickness
- 5) Run the code, which does the following:
 - a) Determine normalisation constant C from (12) and θ using (13).
 - b) Choose a step size for ξ based on θ and the number of steps along the taper (e.g. 500)
 - c) Set $z = \xi = 0$ and the initial slotwidth ($s(0)$).
 - d) Step through ξ by one step and calculate the cutoff frequency ($f_c(\xi)$) using (15).
 - e) Interpolate within the array of slot widths and cutoff frequencies from simulations to determine the new slot width ($s(\xi)$) and propagation constant ($\beta(\xi)$).
 - f) Using the relation in (10), calculate the step size in z , from $\Delta z = \Delta\xi/2\beta(\xi)$.
 - g) Repeat 5d) to 5f) until $\xi = 2\theta$.

V. RESULTS AND DISCUSSION

Figure 3 shows the results of the three different analysis methods combined with the OTM to synthesise the taper. The results are at 90GHz for a taper in a WR10 waveguide ($a = 2.54\text{mm}$, $b = 1.27\text{mm}$), with a final slot width of around 0.01mm and a maximum return loss of -30dB . The substrate was $220\mu\text{m}$ thick and had a dielectric constant of $\epsilon_r = 2.2$. The taper produced is 3.8mm long, or 1.14λ (see Fig. 3(d)). While all the results are for unilateral finlines, the process simply generates a sequence of slot widths based on the cutoff frequencies returned by the OTM, and so would work for antipodal finlines. Finite-element simulations return accurate results for any slot width and will therefore be used as a benchmark. We are in the process of using HFSS to generate the parameter of the antipodal section.

From Figure 3, it can be seen that the computations done using TR or SDA compare very well with the exact results computed using HFSS. This is because in the slotline geometry the effect of metallisation thickness and dispersion is not very large. It is interesting to notice that from 3(a) that there is a small deviation between HFSS and TR at large slot widths, which is to be expected since the TE approximation of a slotline fails when the slot is large. We also notice that there is a deviation between HFSS and SDA at large slot widths. This is, however, the result of the fact that the number of basis functions in (6) and (7) used in the computation was too small to give accurate results. In general, however, SDA and HFSS should agree very well at large slot widths.

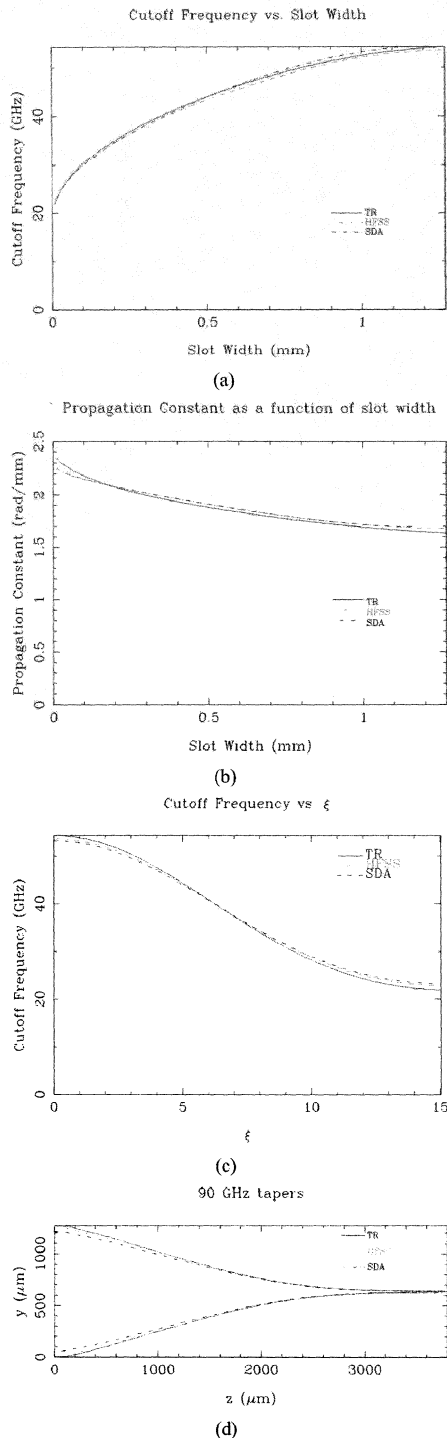


Fig. 3. Comparisons of the results of the three methods discussed in the text. Red solid: Transverse Resonance; Blue dot-dashed: Spectral Domain Analysis; Green dashed: HFSS Simulations. (a) Cutoff frequency vs. slot width, (b) Propagation constant vs. slot width, (c) Propagation constant vs. cutoff frequency, (d) The taper produced by the three methods.

The results shown in Figure 3(c) show the cutoff frequency as a function of the dimensionless phase variable, ξ (see §II-A). This is sensitive to the initial and final cutoff frequencies ($f_c(z=0; \xi=0)$ and $f_c(z=l; \xi=2\theta)$ respectively), which accounts for the small deviations.

The tapers produced by the OTM are shown in Figure 3(d). The deviation of SDA from HFSS is discussed above. The TR taper also shows deviation at large slot widths, as discussed above, though it is within current fabrication tolerances of 5–10%.

VI. CONCLUSION

We have investigated the synthesis of finline tapers using TR and SDA and compared them with HFSS simulations. Our results show that the two methods can be used accurately even when small slot widths must be reached. It should be noted that the SDA results can be further improved by taking the metallisation into account using the Wheeler correction [6].

So far we have designed antipodal finline tapers using the SDA, thereby neglecting metallisation thickness and the existence of the substrate carrying the fins. This approximation may not be accurate when the fins overlap is comparable to the thickness of the oxide that separate the fins. It can therefore be largely improved by including the substrate in the Dyadic Green function and the metallisation thickness using the Wheeler correction. Alternatively, accurate synthesis of the finline taper can be obtained by using the taper synthesis code presented in this paper, in conjunction with an array containing the cutoff frequency as a function of the slot dimension.

REFERENCES

- [1] G. Yassin, S. Withington, M. Buffey, K. Jacobs, and S. Wulff, "A 350 GHz single antipodal finline mixer," *IEEE Trans. Microwave Theory Tech.*, vol. 48, pp. 662–269, Apr. 2000.
- [2] P. Grimes, G. Yassin, K. Jacobs, and S. Withington, "A 700 GHz single chip balanced SIS mixer," in *16th International Symposium on Space Terahertz Technology*, Goeteborg, Sweden, May 2005, pp. 46–51.
- [3] G. Yassin and S. Withington, "Electromagnetic models for superconducting millimetre-wave and sub-millimetre-wave microstrip transmission lines," *J. Phys. D: Appl. Phys.*, vol. 28, pp. 1983–1991, Apr. 1995.
- [4] C. Schieblich, J. K. Piotrowski, and J. Hinken, "Synthesis of optimum finline tapers using dispersion formulas for arbitrary slot widths and locations," *IEEE Trans. Microwave Theory Tech.*, vol. 32, no. 12, pp. 1638–1644, Dec. 1984.
- [5] L.-P. Schmidt and T. Itoh, "Spectral domain analysis of dominant and higher order modes in fin-lines," *IEEE Trans. Microwave Theory Tech.*, pp. 981–985, Sept. 1980.
- [6] D. Mirchekar-Syahkal and J. B. Davies, "An accurate, unified solution to various finline structures of phase constant, characteristic impedance and attenuation," *IEEE Trans. Microwave Theory Tech.*, vol. 30, pp. 1854–1861, 1982.

Spectrometers for (sub)mm radiometer applications

A. Emrich, S. Andersson, Johan Dahlberg, Torgil Kjellberg, Mikael Krus

Abstract— The autocorrelation spectrometer is one of 5 types of spectrometers being considered for space based (sub)millimetre heterodyne systems. The advantages of the digital autocorrelation spectrometer compared to Chirp Transform, Acousto Optical and Filterbank spectrometers are; stability, compactness, high reliability and variability in bandwidth and resolution. FFT spectrometers based on the latest generation of FPGA devices now promise a cost effective alternative for low to medium bandwidth applications with high resolution requirements.

Omnisys has designed and implemented several generations of autocorrelation chip sets and spectrometers. This range from the ODIN satellite spectrometers now in LEO to our current 8 GHz single chip spectrometer under development.

The ODIN chip set was a breakthrough at the time (1998). The power consumption was lowered by a factor of 50 compared to state of the art. Since then we have further improved the power consumption with a factor of 40, and we are now reaching 8 GHz of bandwidth for a single spectrometer chip.

Index Terms—Spectrometer, Radiometer, Correlator, FFT.

I. INTRODUCTION

THE autocorrelation spectrometer is one of 5 types of spectrometers being considered for space based (sub)millimetre heterodyne systems. The advantages of the digital autocorrelation spectrometer compared to Chirp Transform, Acousto Optical and Filterbank spectrometers are; stability, compactness, high reliability and variability in bandwidth and resolution. FFT spectrometers based on the latest generation of FPGA devices now promise a cost effective alternative for low to medium bandwidth applications with high resolution requirements.

Omnisys has designed and implemented several generations of autocorrelation chip sets and spectrometers. This range from the ODIN satellite spectrometers now in LEO to our current 8 GHz single chip spectrometer under development.

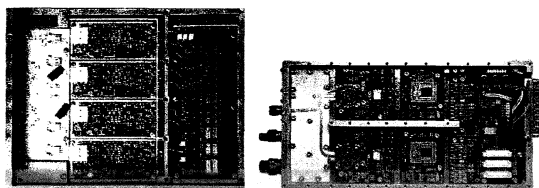


Fig. 1. Two generations of autocorrelation spectrometers, ODIN on the left and IntRad on the right.

The ODIN chip set was a breakthrough at the time (1998). The power consumption was lowered by a factor of 50 compared to state of the art. Since then we have further improved the power consumption with a factor of 40, and we are now reaching 8 GHz of bandwidth for a single spectrometer chip.

Omnisys has now a preliminary design of a single chip spectrometer with 8 GHz bandwidth and 1024 channel resolution, backed by simulation based on extracted parasitics. Tape-out for spectrometer chip is planned for June 2006 with devices available for commercial use 6-9 months later. This spectrometer can be configured for operation with 64, 128, 256, 512 and 1024 channels. The maximum power consumption with 1024 channels at 8 GHz is estimated to be 2.8 W and with 64 channels, we will have a power consumption of about 0.5 W.

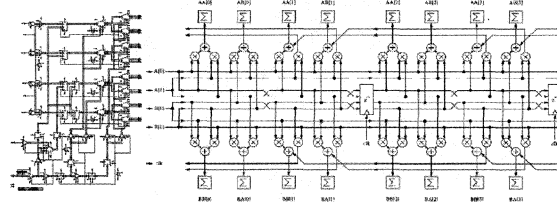


Fig. 1. Schematics of the single chip spectrometer. On the left is the bipolar digitiser and on the right, the CMOS correlator part.

Omnisys has also developed an FFT spectrometer for ground based applications. It follows the single Eurocard standard size and provides up to 2 GHz bandwidth and 1-4 inputs. With four inputs, the maximum processed bandwidth is 500 MHz. Two spectrometer boards will be delivered to customers during Q1 and Q2 of 2006, one for aeronomy and one for radio astronomy. The price starts at 20 000 Euro per board.

II. AUTOCORRELATION SPECTROMETERS

Omnisys development of autocorrelation spectrometers since 1992 has focused on minimising power consumption and mass to make them compatible with satellite operation. For ODIN, the power consumption was reduced with a factor of 49 compared to state of the art another factor of 100 is expected for the current generation. The processed bandwidth has increased from 20 MHz up to 8000 MHz in the same period.

A. ODIN

The ODIN spectrometers were developed and produced during 1996-1999 and being operated successfully on ODIN

since 2001. The main specifications are; 100-800 MHz bandwidth, 896 channels, 18 W, 1 kg.

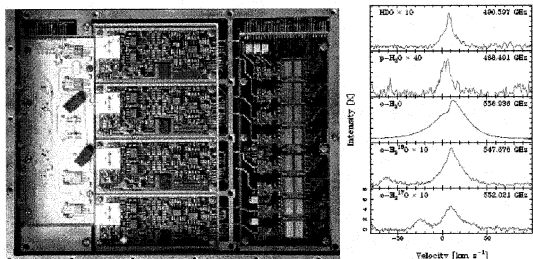


Fig. 3. The ODIN autocorrelator spectrometer and spectra obtained from space.

B. TELIS

The TELIS generation of spectrometers were developed and produced during 2000-2002 and will be operated on the TELIS balloon platform. The chip set was developed as demonstrators under an ESA contract, motivated by missions such as HIFI/HERSCHEL and MASTER.

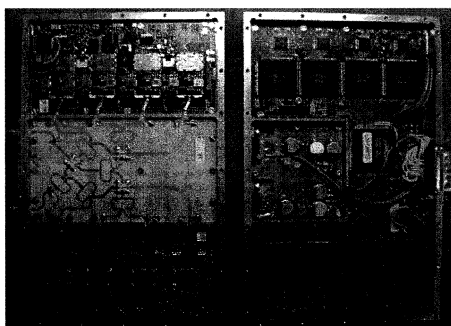


Fig. 4. The TELIS generation of spectrometers.

The main specifications are;

- 2x2 GHz bandwidth
- 2x1024 channels
- 2-4 GHz Input
- 22 W
- 1.1 kg
- 100 k Euro

C. INTRAD

The INTRAD generation of spectrometers were developed and produced during 2001-2003 and was demonstrated in a 300-380 GHz integrated 1 kg / 10 W radiometer in 2003. The chip set was developed as demonstrators under an ESA contract, motivated by missions such as Mambo. The main specifications are;

- 1x4 GHz bandwidth
- 1x4096 channels
- 4-8 GHz Input
- 10 W
- 493 grams

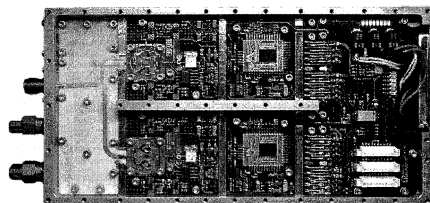


Fig. 5. IntrRad spectrometer.

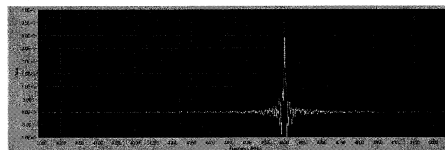


Fig. 6. Spectrum at 320 GHz input CW signal.

III. SINGLE CHIP AUTOCORRELATION SPECTROMETER

Based on the demonstration chip sets and production based single chip spectrometer is under realization. Tape out is planned for June-2006. The single chip spectrometer will be implemented in IBM 7WL 0.18 um BiCMOS process.

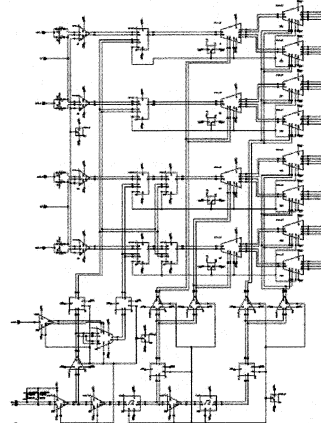


Fig. 7. Bipolar digitiser schematics.

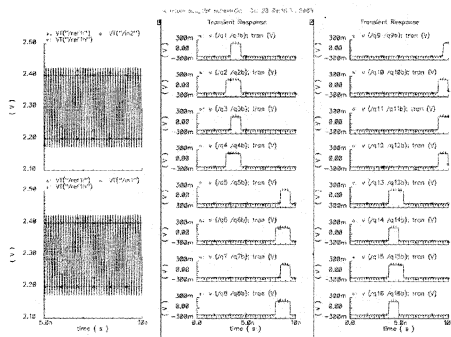


Fig. 8. Simulation at 7.9 GHz CW input signal.

The digitiser/ADC is a 100% bipolar design as this is required to make the analog part compatible with autocorrelation spectrometer requirements, in respect to sampling jitter, gain and bandwidth, analog comparator accuracy etc.

The correlation signal processing is implemented in CMOS, the technology of choice for fast, high density digital circuits today. The current design is scalable to 20 GHz bandwidth and beyond within a few years time.

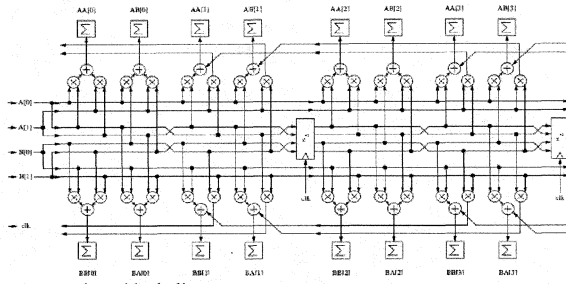


Fig. 9. Correlator block diagram.

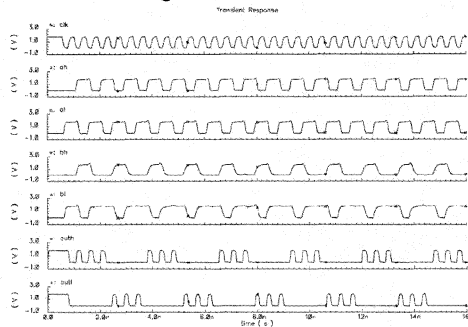


Fig.10. Simulation at 17.2 GHz effective sampling rate.

The chip will be directly compatible with the requirements for instruments and missions such as STEAM, CIWSIR and MASTER/MARSCHAL. In addition, it also suits interplanetary radiometers such as Mambo, making complete radiometers realistic with mass and power budgets compatible with such missions, i.e. < 1 kg, < 10 W.

- 0.1-8 GHz bandwidth
- 64-1024 channels
- 0.5-2.8 W
- 30 kRAD

IV. FFT SPECTROMETER

Not all radiometer spectrometers operate in the space environment with very hard restrictions in power consumption and mass in combination with radiation tolerance etc.

Omnisys has developed an FFT type of spectrometer compatible with ground based operation with emphasis on flexibility and cost effective design solutions. One spectrometer has been delivered in February 2006 and tested with the instrument and the second one will be shipped in May 2006. The board support up to 2x1000 & 4x500 MHz operation, Stokes parameter processing, and more that 32 k channels of resolution. Price will start at 20kEuro.

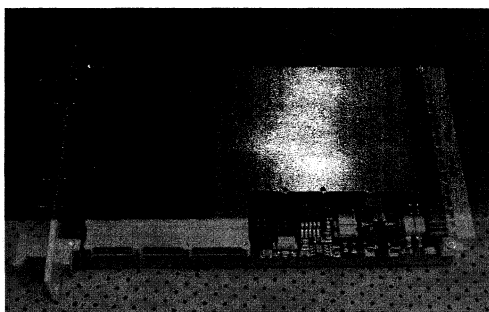


Fig. 11. FFT spectrometer board. 100x160 mm with 96-pin Euroconnector.

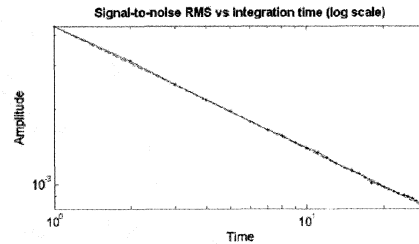


Fig. 12. SNR as a function of integration time.

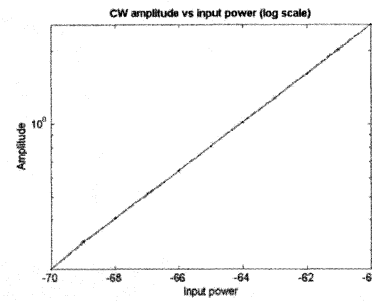


Fig. 13. Linearity over 10 dB.

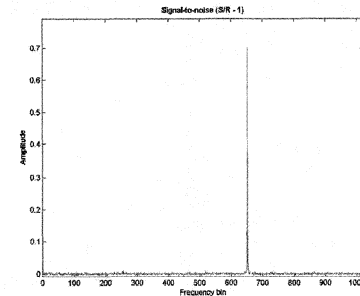


Fig. 14. Signal minus reference with noise + CW signal. (BW:500 MHz).

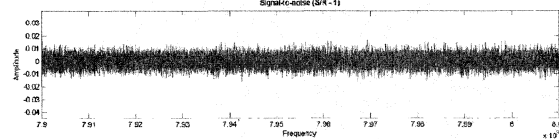


Fig. 15. Signal minus reference with noise.

V. CONCLUSION

Omnisys has developed several generations of autocorrelation spectrometers. The ODIN spectrometers have now started the 6th year of successful operation in orbit, while the generation that is scheduled for tape out in June 2006 promise to deliver up to 8 GHz of processed bandwidth with 1024 channels. The power budget is between 0.8-2.8 W depending on clock speed and configuration.

Omnisys has also developed an FFT spectrometer platform that can be used to realise highly flexible solutions providing up to 2 GHz bandwidth and more that 32k channels. Variable resolution, polarisation processing etc will be supported and it is available for shipping in Q3 2006.

ACKNOWLEDGMENT

The development has been supported by the Swedish National Space Board, ESA, CHACH (Chalmers competence centre) and direct flight model contracts from SSC.

Atmospheric Opacity Above 1 THz: Evaluation for the ALMA Site and for Laboratory Developments

Juan R. Pardo, Eugene Serabyn, José Cernicharo, and Martina C. Wiedner

Abstract—This contribution is aimed at reviewing the impact of the atmosphere for millimeter and submillimeter wave observations performed from platforms inside the Earth's atmosphere with special focus on the supra-THz regime. The current models have also been applied to typical laboratory conditions, because absorption and pathlength fluctuations there have to be taken into account when developing and measuring characteristics of Supra-THz components.

Index Terms—Atmospheric Measurements and Models, Terahertz Technology, Longwave Astronomy and Remote Sensing.

I. GROUND-BASED FOURIER TRANSFORM SPECTROSCOPY AND WATER VAPOR RADIOMETRY OF THE ATMOSPHERE

An extensive study of the atmospheric transmission at mm and submm wavelengths has been performed since the early 1990s with a Fourier Transform Spectrometer (FTS) mounted at the CSO telescope atop Mauna Kea (4100 m above sea level). The goal of this work, described in [1] has been to compile a data base of accurately calibrated spectra for use in refining atmospheric models.

non-resonant opacity terms is paramount. Due to the access to very dry conditions, we have been able to successfully separate the “wet” and “dry” non-resonant opacity terms up to 1.6 THz for the first time. The best spectra obtained in this series of experiments (see [1], [2] and [3]), and the resulting model, are shown in Figure 1.

A 3-channel water vapor radiometer, described in [4] operating near the 183.31 GHz water line has also been used for different site testing studies at Mauna Kea, included a cross-comparison with the FTS [5]. The instrument was a first prototype of a kind of device intended for monitoring of water vapor fluctuations on very short time scales to perform phase corrections for interferometry.

A. Latest Results on Non-Resonant Absorption at Frequencies above 1 THz

While our earlier work extending up to 1 THz [1] allowed the separation of the “wet” and “dry” non-resonant atmospheric opacity components with both shown to be following ν^2 laws in this regime, in [3] we report on the extension of these observations up to 1.6 THz. In the higher frequency regime, our results indicate that the ν^2 description may begin to fail due to the proximity of the FIR band centers. The far wings of lines above 2 THz account only for

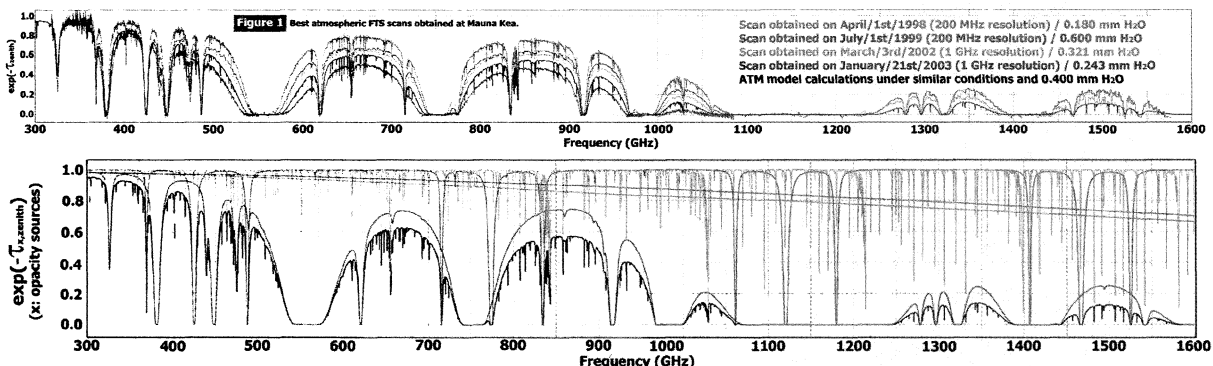


Fig. 1. Top panel: Best Atmospheric Fourier Transform Spectroscopy Scans obtained at Mauna Kea during the period 1995-2003. The estimated zenith water vapor column has been obtained from fitting the data with the model presented in [1]. Bottom panel: Resulting atmospheric transmission model for Mauna Kea for 0.4 zenith water vapor column (dark curve) and its splitting in different opacity sources (see [1]).

In this context, the separation of the resonant (lines) and

a very small fraction of the total opacity so that errors in them can explain the non-resonant continuum-like atmospheric opacity. This can be seen in the results plotted in Figure 2.

Juan R. Pardo and José Cernicharo are with the CSIC, Instituto del Estructura de la Materia, Departamento de Astrofísica Molecular en Infrarrojo, Serrano 121, E-28006, Madrid, Spain (phone: +34 915616800; fax: +34 915645557; e-mail: pardo,cermi@damir.iem.csic.es).

Eugene Serabyn, is with the Division of Physics, Mathematics and Astronomy, California Institute of Technology, MS 320-47, Pasadena, CA 91125, USA (e-mail: gene.serabyn@jpl.nasa.gov).

Martina C. Wiedner is with the Physikalisches Institut, Universität zu Köln, Zùlpicherstrasse 77, 50937 Köln, Germany (e-mail: wiedner@ph1.uni-koeln.de).

Reanalysis of the data presented in Fig 2, plus new data (of better quality) acquired in 2003 (all data can be found in Fig. 1) confirm the new findings about the non-resonant atmospheric absorption beyond 1 THz. The total continua extracted from the FTS measurements (dots in Fig. 3), are

compared to the result of combining the $N_2-N_2 + N_2-O_2 + O_2-O_2$ collision induced absorption (dashed line in Fig. 3) and the v^2 foreign- H_2O continuum (dotted line in Fig. 3). The overestimate above 1.2 THz of the combined result (solid line in Fig. 3) appears evident. The black crosses represent the total foreign- H_2O absorption according to the model presented in [6]. The dry non-resonant absorption, on the other hand, seems to be well described by the model presented in [7].

B. Water Vapor Retrievals and Phase Correction.

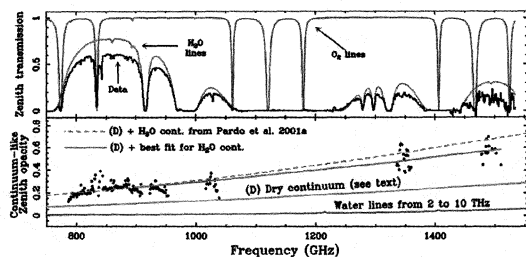


Fig. 2. Atmospheric FTS data acquired on 2002 March 3 above 750 GHz (upper panel) with the predicted contribution from O_2 and H_2O lines. The resulting excess of (non-resonant) absorption is represented by the dots in the lower panel. Considering the dry component of this non-resonant absorption to be as described in [7], it follows that the wet part of it departs from a v^2 behavior.

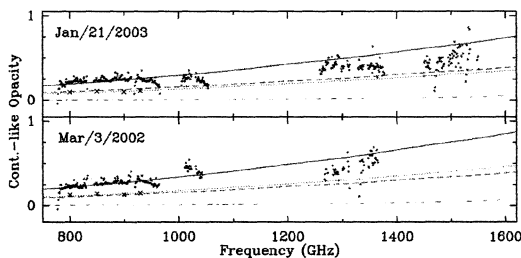


Fig. 3. Reanalysis of the data presented in Fig. 2 plus new data acquired in 2003 that confirm that the foreign- H_2O continuum in the Earth's atmosphere no longer follows a v^2 behavior (see text).

In an atmosphere without spectroscopic lines, the index of refraction would be non dispersive so that the extra phase difference due to different water vapor columns in two different geometric paths scales linearly with frequency. Water vapor fluctuations are fast and can act on all spatial scales. Since H_2O has strong lines in the submillimeter-wave domain, it is the main responsible for phase fluctuations affecting interferometric measurements that are, in addition, dispersive. In order to translate the phase difference measured at one frequency to other frequencies, it is necessary to take into account the dispersive terms calculated from the water line absorption coefficients by using the Kramers-Kronig relations, as described in [1]. In order to explore water vapor retrieval techniques for ALMA, we started a comparison campaign involving the FTS mounted at the Caltech Submillimeter Observatory and the Water Vapor Monitor (WVM) mounted on one of the antennas of the Smithsonian Millimeter Array. Both devices were therefore separated by only 250 m. Using the ATM model to derive the sky coupling of the WVM and to perform water vapor retrievals from the data provided by

both instruments has shown that it is possible to achieve an agreement of about 0.02 mm in the retrieved zenith water vapor column in time scales of several minutes (see Fig. 4). Therefore, a combination of WVMs for each antenna plus an accurate mm/submm model (based on extensive FTS work) provides a suitable tool for ALMA calibration in situations with less than 1.5 mm of zenith water vapor column. See [5] for details. WVM devices are currently being developed for ALMA by Cambridge and Chalmers. Another device has been developed for APEX and is currently being tested.

II. THE IMPACT OF THE ATMOSPHERE ON THZ LABORATORY DEVELOPMENTS.

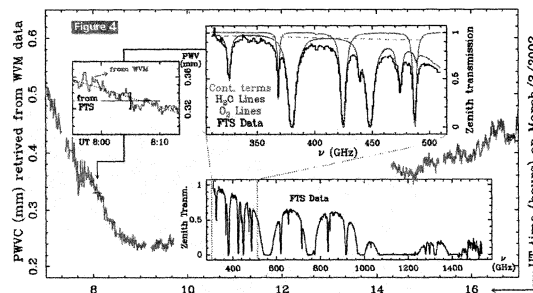


Fig. 4. Precipitable Water Vapor (PWV) zenith column obtained from fitting the WVM data recorded on 2002 March 3. At 8:00-8:10 UT we recorded an FTS spectrum (lower right inset). The 310-510 GHz data (upper right inset) was used to determine the PWV independent of the non-resonant absorption.

The detailed comparison of PWV retrieved from both instruments is shown in the left inset.

The detailed comparison of PWV retrieved from both instruments is shown in the left inset.

The detailed comparison of PWV retrieved from both instruments is shown in the left inset.

It is also important to consider the effect of the atmosphere when testing THz components in the laboratory. Even a column of air of about 1 meter can produce significant absorption beyond 1 THz and also can produce some "turbulence" due to pathlength or phase fluctuations due to water in that short column of air. These effects were considered and discussed in a recent paper [8]. We have included here some calculations of this effect (see Figure 5). A laboratory situation with ambient pressure of 990 mb, ambient temperature of 20 C and two different relative humidity values (55% and 20%) have been considered. The Figure provides the expected attenuation (represented in terms of transmission) through 1 meter of air in those conditions, as well as the total extra pathlength introduced by water vapor.

III. AVAILABILITY OF ATM

A Linux executable version of the code is available to the community upon request via e-mail at the following address: pardo@damir.iem.csic.es. Please describe briefly the type of calculations you need to perform so that a convenient macro can be prepared and delivered together with the executable. Within the ALMA project, a C++ interface is now under development for use in the official software. People involved in ALMA may ask also about this interface. For more information about this code and related works: <http://damir.iem.csic.es/PARDO/pardo.html>.

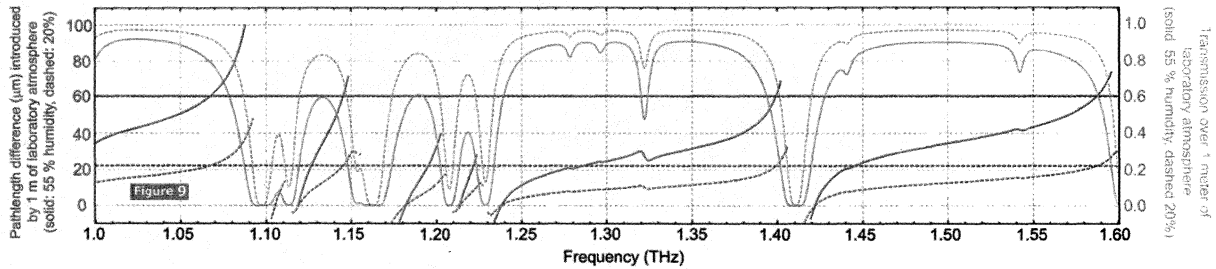


Fig. 5. The impact of the atmosphere (both absorption and extra pathlength) in the laboratory for 990 mb and 20° C of ambient pressure and temperature.

ACKNOWLEDGMENT

This work has been possible thanks to U.S. NSF grants ATM-9616766 and AST-9980846, and Spanish PNIE grant AYA2003-02785.

REFERENCES

- [1] J. R. Pardo, E. Serabyn, and J. Cernicharo, "Submillimeter atmospheric transmission measurements on Mauna Kea during extremely dry El Niño conditions: Implications for broadband opacity contributions," *J. Quant. Spectr. and Radiat. Transfer*, vol. 68, pp. 419-433, Jan. 2001.
- [2] J. R. Pardo, J. Cernicharo, and E. Serabyn, "Atmospheric Transmission at Microwaves (ATM): An Improved Model for mm/submm applications," *IEEE Trans. on Antennas and Propagation*, vol. 49, pp. 1683-1694, Dec. 2001.
- [3] J.R. Pardo, E. Serabyn, M.C. Wiedner, and J. Cernicharo, "Measured telluric continuum-like opacity beyond 1 THz," *J. Quant. Spectr. and Radiat. Transfer*, vol. 96, pp. 537-545, Dec. 2005.
- [4] M. C. Wiedner, R. E. Hills, J. E. Carlstrom, and O. P. Lay, "Interferometric Phase Correction Using 183 GHz Water Vapor Monitors," *Astrophysical Journal*, vol. 553, pp. 1036-1041, Jun. 2001.
- [5] J. R. Pardo, M. Wiedner, E. Serabyn, C. D. Wilson, C. Cunningham, R. E. Hills, and J. Cernicharo, "Side-by-side comparison of Fourier Transform Spectroscopy and Water Vapor Radiometry as tools for the calibration of millimeter and submillimeter ground-based observatories," *Astrophysical Journal Suppl. Ser.*, vol. 153, pp. 363-367, Jul. 2004.
- [6] Q. Ma, and R. H. Tipping, "The frequency detuning correction and the asymmetry of line shapes: The far wings of H₂O-H₂O". *J. Chem. Phys.*, vol. 116, pp. 4102-4115, Dec. 2002.
- [7] J. Boissoles, C. Boulet, R. H. Tipping, A. Brown, Q. Ma, "Theoretical calculation of the translation-rotation collision-induced absorption in N₂-N₂, O₂-O₂, and N₂-O₂ pairs," *J. Quant. Spectrosc. Radiat. Transfer*, vol. 82, pp. 505-516, Dec. 2003.
- [8] J. W. Kooi, J.J.A. Baselmans, A. Baryshev, R. Schieder, M. Hajenius, J.R. Gao, T.M. Klapwijk, B. Voronov, and G. Goltzman, "Stability of Heterodyne Terahertz Receivers", *J. Appl. Phys.*, in press, 2006.

Terahertz frequency metrology and sensitivity issues in photomixer spectrometer

L.F. Constantin, L. Aballea, J. Demaison

Abstract—We propose a compact photomixer spectrometer setup, using 2 laser diodes locked on the resonances of an ultrastable Fabry-Perot cavity, that generates difference-frequency Terahertz-waves with high spectral purity. We investigate a cavity-enhanced spectroscopic technique that would increase the spectrometer sensitivity proportionally with the cavity finesse. We demonstrate a broadband Terahertz Fabry-Perot cavity with microstructured metallic-grid mirrors that have a finesse of 50 at 1,2 THz. Its quality factor is greater than 10^4 in the 0,6-2 THz spectral range.

Index Terms—Photomixing, Terahertz, Cavity-enhanced spectroscopy, Submillimeter wave resonators, Frequency measurement, Q factor

I. INTRODUCTION

IN the last decades different coherent sources operating at terahertz frequencies were developed in order to bridge the electromagnetic gap between electronics and photonics. Among them, the optically-pumped gas lasers are covering the spectral range between 300 GHz to 3 THz with a dense grid of emission lines. The frequency tuning over a discrete spectral range can be ensured via the sideband generation technique, which made these sources suitable for high resolution molecular spectroscopy experiments.

The generation of terahertz-wave with a broad tuning bandwidth [1] was demonstrated from the difference-frequency of two detuned near-infrared diode lasers that are heterodyned in a non-linear element, the photomixer. We will focus in this paper on the design of a terahertz spectrometer relying on photomixers and frequency stabilised laser diodes and will approach sensitivity and Terahertz frequency metrology issues. An important theme in modern spectroscopy is the use of an extended interaction length between matter and the electromagnetic field confined inside a high finesse cavity for an increased detection sensitivity. For example, the noise-immune, cavity-enhanced, optical-heterodyne molecular spectroscopy technique allowed reaching in the infrared range an ultimate fractional detection sensitivity of 5.10^{-13} [2]. Another important theme is the application of frequency metrology for precision measurements. For example, infrared molecular lines with kilohertz-level linewidth have been measured using an intracavity Ramsey separated fields

Manuscript received May 31, 2006. This work was supported by the CNRS, French Education Ministry and the Conseil Régional du Nord-Pas de Calais under "Terahertz Spectroscopy and Photonics" contracts.

The authors are with the Centre National de la Recherche Scientifique, Laboratoire de Physique des Lasers, Atomes et Molécules, Université Lille 1, 59655 Villeneuve d'Ascq, France. Correspondence should be addressed to L.F. Constantin, phone: +33(0)3 20434790, fax: +33(0)3 20337020; e-mail: FL.Constantin@univ-lille1.fr.

spectroscopy technique [3]. This paper will thus explore some possible ways to extent these potentialities of optical cavities for precision measurements in the far-infrared domain.

II. DIFFERENCE-FREQUENCY GENERATION OF ULTRA-STABLE TERAHERTZ-WAVE

The non-linear element used for difference-frequency generation is a low-temperature-grown gallium arsenide layer (2 μm thickness). It was grown on semiinsulating GaAs substrate using molecular beam epitaxy and was subsequently annealed at IEMN. A pump-probe photoreflexivity experiment allowed us to estimate the photocarriers lifetime for different growth and anneal conditions. Electron-beam lithography and lift-off process were used to define a Ti:Au broadband spiral antenna with interdigitated electrodes (width 0.2 μm , periodicity 1,8 μm) over a 8 μm x 8 μm active area. Two monochromatic beams of near-infrared radiation, focused on the electrodes, modulate the conductance of the substrate. Upon biasing the photoconductor, THz currents generated in the photoconductor flows through the antenna that radiates THz radiation. A hyperhemispherical silicon lens collimates Terahertz radiation that can be further detected with an InSb bolometer. The possible ways for the optimisation of the output power of GaAs THz photomixer source [4] are essentially achieving low photo-carrier recombination times and low RC antenna constant and using a substrate with high thermal dissipation. The generated power is expected in the μW range up to 1 THz [5].

We propose a new setup for the photomixer spectrometer, shown in Figure 1, that allows synthesizing any difference frequency in the far-infrared domain from two diodes laser that are locked on different longitudinal modes of a high finesse Fabry-Perot cavity.

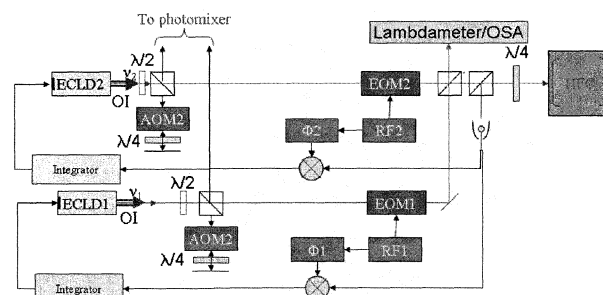


Figure 1: Frequency-locked Diode Laser setup for broadband difference-frequency Terahertz generation

Our setup uses two commercial extended-cavity diodes

laser in a Littrow configuration operating around 830 nm with an optical power of 100 mW. They can be tuned electrically over 30 GHz without mode-hops and mechanically over more than 15 nm. We recorded the beatnote between the free-running diode lasers (Figure 2) that have a Lorentzian lineshape. The FWHM linewidth of each laser is thus 1,5 MHz.

The emitted laser radiation is coupled to optical isolators and a pair of anamorphic prism pairs. A $\lambda/2$ waveplate associated with a polarising beamsplitter cube transmits a

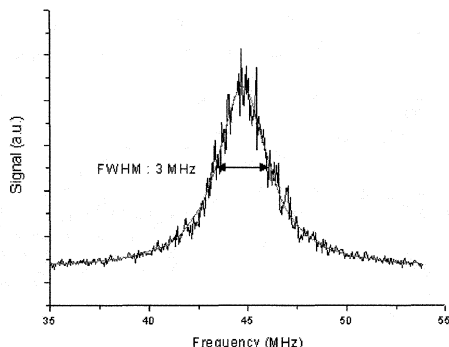


Figure 2: Beatnote of the free-running diodes laser small amount of diode laser radiation to the frequency locking system. We will use the Pound-Drever-Hall technique [6] that operates a heterodyne detection of the high-frequency phase modulated sidebands which are reflected by the Fabry-Perot cavity using an avalanche photodiode. It generates an error signal which is insensitive to the laser intensity noise and that has a bandwidth greater than the linewidth of the cavity. The error signal can be used to lock the diode laser on the top of the Fabry-Perot resonance by a slow lock-loop, with the PZT that tune the diode laser cavity length, and a fast-loop, with a high bandwidth direct current control of the diode laser.

We developed a ULE etalon with finesse greater than 10^4 and a 750 MHz free spectral range. This etalon is placed in a temperature-controlled evacuated chamber (pressure less than 10^{-5} Pa) and supported through a 3-level mechanical isolation stage that efficiently diminishes the acoustic noise of the cavity that limits the spectral purity and the ultimate frequency stability of the locked diode laser.

The main part of the diode laser power is reflected by the polarising beamsplitter to a set of double-passed acousto-optic modulators, that have a bandwidth larger than one half of the free spectral range of the cavity, that allows continuous tuning of the difference-frequency without causing the laser beams to deviate. The two frequency-shifted laser beams are superposed, injected in a polarisation-maintaining optical fiber - that guarantees spatial overlapping of heterodyned laser beams - and finally coupled to the photomixer. The synthesised terahertz frequency can be estimated by the sum of an integer multiple of the free spectral range of the Fabry-Perot cavity and the two acousto-optic frequency shifts. Absolute frequency calibration of the spectrometer can be further derived from the measurement of molecular lines [7].

III. PROJECTION FOR AN INTRACAVITY PHOTOMIXER SPECTROMETER

The main advantage of the photomixer spectrometer - its broadband tunability over the THz domain - is counterbalanced by a relatively small power level available that limits the ultimate sensitivity in direct absorption spectroscopy experiments. We propose the design of an intracavity photomixer spectrometer where THz radiation is coupled to a high-finesse Fabry-Perot cavity containing the molecular species of interest. This system represents the extension at THz frequencies of intracavity microwave spectroscopy experiments using the high-sensitivity Flygare FTMW technique [8] in the time domain. We will discuss a key issue of such a system that is obtaining a high quality factor of the resonator over a broad frequency range and we will overview some potential detection schemes.

A. Cavity-Enhanced Spectroscopy

We will discuss the cavity-enhanced spectroscopy by considering the absorbing molecules placed in a Fabry-Perot cavity obtained by aligning two mirrors at a separation d comparing to the cavity axis. The transmission T , the absorption A and the reflection R coefficients of the cavity mirrors ($R+T+A=1$) determine the finesse of the cavity

$$F = \frac{\pi}{T + A} = \frac{FSR}{FWHM} \quad (1)$$

that corresponds to the ratio of the free spectral range of the cavity to the linewidth of its modes.

If P_i is the incident Terahertz power coupled to the cavity, one can derive how the transmitted power P_t is modified by the absorbing medium:

$$\frac{P_t}{P_i} = \left(\frac{T}{T + A + \alpha d} \right)^2 \approx \left(\frac{T}{T + A} \right)^2 \left(1 - \frac{2\alpha d}{T + A} \right) \quad (2)$$

where the absorption coefficient α per unit length of the sample gas is supposed low comparing to the cavity loss ($\alpha d \ll T, A$). The contrast of the absorption signal

$$\frac{\delta P_t}{P_t} = - \frac{2\alpha d}{T + A} = - \frac{2F}{\pi} \alpha d \quad (3)$$

is enhanced by a factor of $2F/\pi$, compared to the contrast of the absorption signal in a direct absorption measurement in a sample cell of length d .

Although cavity finesse is a key element in improving the detection sensitivity, the role of T and A is not symmetric: one should optimize the transmission T over the mirror loss A in order to increase the absolute value of the transmitted signal. Finally, for a higher absorption coefficient ($\alpha d \sim T, A$) one should optimize the mirror parameters individually in order to maximise the molecular absorption signal.

Direct [1] and homodyne [9] detection schemes have been demonstrated with a photomixer-generated Terahertz-wave and can be further adapted to a cavity-enhanced photomixer spectrometer. The latter technique is closer to the original ideas of the Fourier-transform microwave spectrometer [8], where the radiation from free-induction decay of molecules is detected by an antenna and is processed through heterodyne mixing. A homodyne detection used for a cavity-enhanced photomixer spectrometer will allow phase-coherent detection of the molecular signal, although the photoresponse of LT-GaAs could be a limiting factor to the

overall detection sensitivity of the system. Commercial InAs bolometers with 1 MHz bandwidth, low detection noise ($NEP=2 \text{ pW}\cdot\text{Hz}^{1/2}$) providing a high responsivity ($4\cdot 10^4 \text{ V/W}$) could be promising for a sensitive direct detection scheme using high-frequency modulation techniques.

B. High finesse mirrors for the THz domain

Electroformed metal meshes have been used as reflecting elements for Fabry-Perot cavities in the far-infrared domain [10]. The flatness of such reflective material should be better than λ/F , in order to limit the cavity diffraction losses, that could be a critical factor for high-finesse resonators. Recently, multi-layer mirrors made of silicon wafers separated by empty gaps have been demonstrated [11] and used in the p-Ge laser cavity but accurate measurement of the Q-factor of the cavity is lacking.

We developed a prototype of high finesse mirror consisting in a metal-mesh deposited on a silicon substrate. High resistivity silicon provides low absorption in the far-infrared domain and have a relatively high index of refraction $n=3.42$. Electron-beam lithography followed by a metal lift-off process was used to define a Ni-Au (thicknesses: 100Å-100nm) one-dimensional metallic microstructure on a silicon wafer, shown in Figure 3. The reflection and the absorption coefficients of the

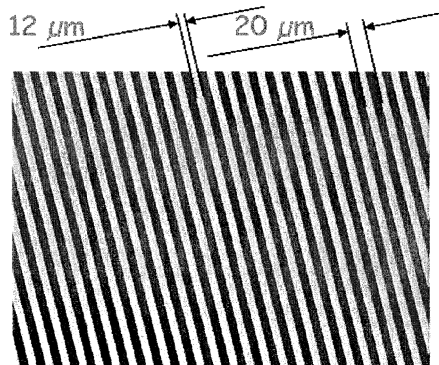


Figure 3: Metallic grid on a silicon substrate

dielectrically-backed mesh can be modelised from a transmission line formalism [12] that take into account the geometry of the structure and its resistive losses. At wavelengths longer than the periodicity of the stripes, the radiation with the electric field polarised along the metallic stripes (inductive grid) is strongly reflected, while the radiation with a crossed polarisation is transmitted (capacitive grid). The transmissivity of the inductive grid increases when the laser wavelength decreases to the periodicity of the grid. Because of interference effects in the high-index silicon substrate, a modulation is superposed on the transmission of the dielectric-backed grid. These features can be observed in Figure 4 that shows the numerical simulation of the transmissivity of a silicon wafer 1.2 mm thick with an inductive grid that have a width of 12 μm and a periodicity of 20 μm of its gold metallic stripes.

We characterised the far-infrared polarisation proprieties of this element at different emission lines of an optically pumped molecular laser [13]. The linearly polarised laser radiation is incident at normal angle on the silicon wafer fixed in a rotation mount. The transmitted beam is detected with a bolometer using an amplitude modulation technique.

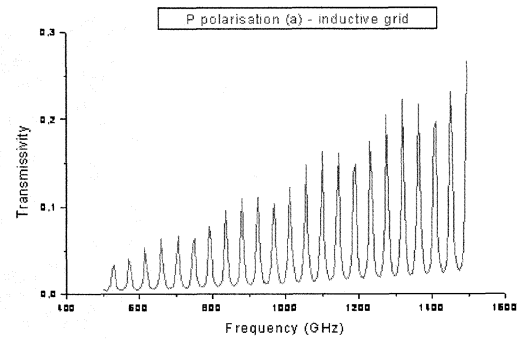


Figure 4: Simulation of the transmissivity of the metallic grid on a Silicon substrate

Figure 5 shows the fractional transmission on different laser lines when rotating the silicon wafer. At 635 GHz laser line, it varies from 70% for the capacitive grid and less than 1% for the inductive grid.

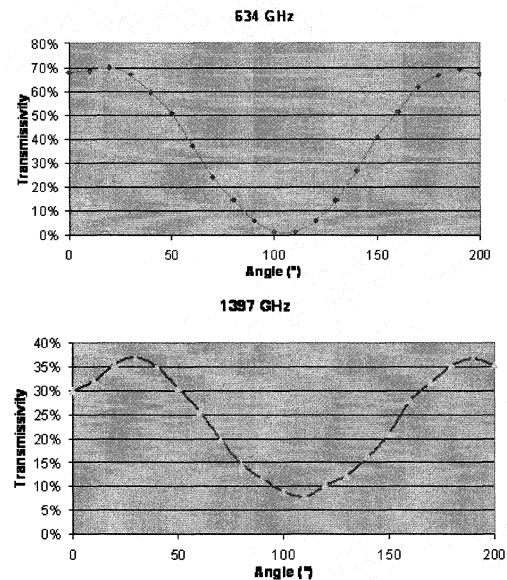


Figure 5: Extinction of linear polarised laser radiation for the inductive grid. At higher frequency on the 1397 GHz laser line, the fractional transmission of the inductive grid grows up at 7%, while the fractional transmission of the capacitive grid diminish at 36% due to the channel spectrum in the silicon substrate. An anti-reflection coating designed at the specified laser line should limit this parasitic interference effect. The high extinction factor achieved with the inductive grids seems very promising for using them as high-finesse mirrors.

C. A high-finesse Fabry-Perot interferometer with polarisation-dependent mirrors

We set up a prototype of a Fabry-Perot interferometer using two meshes as polarisation-dependent mirrors. The linearly polarised laser beam is collimated, crosses at normal incidence both mirrors that are distanced by 3 cm and the signal transmitted through the cavity is detected with a bolometer. One mirror is mounted on an encoder motor with submicron resolution for cavity tuning. The other is mounted on a PZT ceramic. A modulation is applied on the PZT and lock-in detection is performed on the signal

detected on the bolometer.

The cavity was operated in a "high-finesse" setup by aligning the mirror stripes parallel to the laser polarisation. Figure 6 shows the first derivative of the cavity modes interrogated with the 1267 GHz laser line. The finesse of the resonator is calculated by dividing the $\lambda/2$ periodicity of the fringes to the peak-to-peak width of the resonance, multiplied by a $\sqrt{3}$ factor due to the first derivative of its Lorentzian lineshape.

We measured a finesse of 50 that corresponds to a quality factor of $1.2 \cdot 10^4$ of our Terahertz tuneable resonator at 1.2 THz. An estimation of the finesse of the Fabry-Perot cavity can be derived from the reflection coefficient of the inductive grid that could be evaluated from previous transmissivity measurements by neglecting the absorption losses. We derive an approximate value of 70 which could point out that the measured finesse could be limited by the plan-plan cavity loss induced by the divergence of the laser beam. We noticed that a high-Q factor of the cavity is maintained over a broad spectral range: for example on the 634 GHz laser line the cavity has a finesse of 150

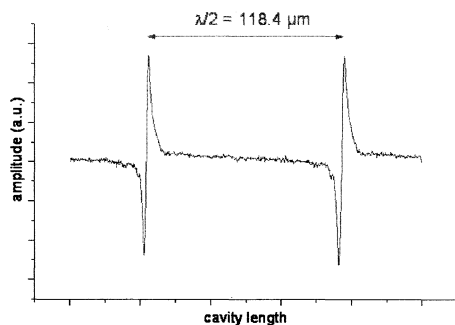


Figure 6: Fabry-Perot cavity modes at 1,2 THz with $Q=1.2 \cdot 10^4$

($Q=1.9 \cdot 10^4$) and on the 2522 GHz laser line the cavity have a finesse of 16 ($Q=0.8 \cdot 10^4$). These values are comparable with the typical quality factors of microwave cavities used in the high sensitive FTMW spectroscopy technique [8].

A careful design of plan-spherical silicon-backed mirrors, by depositing the grids on concave substrates, associated with the coupling of TEM_{00} mode in a spherical cavity, should improve its quality factor and allow the extension of the length of the interferometer. An efficient coupling of terahertz radiation to such cavity will open the way to intracavity spectroscopy over a broad spectral range.

ACKNOWLEDGMENT

The authors acknowledge Karine Blary and Isabelle Roch-Jeune from the Centrale de Technologie of Institut d'Electronique, Microelectronique et Nanotechnologies for providing the THz photomixers and the metallic grids.

REFERENCES

- [1] E. R. Brown, K. A. McIntosh, K. B. Nichols C. L. Dennis, "Photomixing up to 3.8 THz in low-temperature-grown GaAs," *Appl. Phys. Lett.*, vol. 66, pp. 285, 1995
- [2] J. Ye, L.S. Ma, J.L. Hall, "Ultrasensitive detections in atomic and molecular physics: demonstration in molecular overtone spectroscopy," *J. Opt. Soc. Am. B*, vol. 15, pp. 6, 1998

- [3] L.F. Constantin, R. J. Butcher, P. E. Durand, A. Amy-Klein, Ch. Chardonnet "2.3 kHz two-photon Ramsey fringes at 30 THz," *Phys. Rev. A*, vol. 60, pp. R753, 1999
- [4] I.S. Gregory, C. Baker, W.R. Tribe, I.V. Bradley, M.J. Evans, E.H. Linfield, A.G. Davies, M. Missous, "Optimization of Photomixers and Antennas for Continuous-Wave Terahertz Emission," *IEEE J. Quantum Electron.*, vol. , pp.1, 2005
- [5] S. Verghese, K.A. McIntosh, E.R. Brown, "Highly Tunable Fiber-Coupled Photomixers with Coherent Terahertz Output Power," *IEEE Trans. Microw. Theory Tech.*, vol. 45, pp. 1301, 1997
- [6] R.W.P. Drever, J.L. Hall, F.V. Kowalski, J. Hough, G.M. Ford, A.J. Munley, H. Ward, "Laser phase and frequency stabilization using an optical resonator," *Appl. Phys. B*, vol. 31, pp. 97, 1983
- [7] S. Matsuura, P.C., G.A. Blake, J.C. Pearson, H.M. Pickett, "A Tunable Cavity-Locked Diode Laser Source for Terahertz Photomixing," *IEEE Trans. MTT*, vol. 48, pp. 380, 2000
- [8] T.J. Balle, W.H. Flygare, "Fabry-Perot cavity pulsed Fourier transform Fourier microwave spectrometer with a pulsed nozzle particle source," *Rev. Scient. Instrum.* Vol 52, pp. 33, 1981
- [9] S. Verghese K. A. McIntosh, S. Calawa, W. F. Dinatale, E. K. Duerr, K. A. Molvar, "Generation and detection of coherent terahertz waves using two photomixers," *Appl. Phys. Lett.*, vol. 73, pp. 3824, 1998
- [10] D.B. Peterson, H.M. Pickett, "Cryogenic far-infrared Fabry-Perot etalon," *Appl. Opt.*, vol. 30, pp. 4493, 1991
- [11] T. W. Du Bosq, A. V. Muravjov, R. E. Peale, C. J. Fredricksen, "Multilayer silicon cavity mirrors for the far-infrared p-Ge laser," *Appl. Opt.*, vol. 44, pp. 7191, 2005
- [12] R. Ulrich, "Far-Infrared Properties of Metallic Mesh and Its Complementary Structure," *Infrared Phys.*, vol. 7, pp. 37, 1967
- [13] K. Demyk, L. Aballea, L. F. Constantin, "High resolution Terahertz spectroscopy of species of astrophysical interest," in *Proc. 17th ISSSTT*, Paris, 2006

Not only does this design facilitate the production of phase-coherent RF and LO signals but it also allows initial phase-noise cancellation. The phase-noise operation can be seen in the block diagram, Fig. 1, where Φ_v is the initial phase-noise. Most of the phase noise is cancelled in the down-conversion in the SIS-mixer and the remaining phase-noise, present at IF, is cancelled in the second down-conversion before the signal is fed into port two of the VNA for detection.

III. MEASUREMENTS

As we mentioned earlier, the measurements have been performed with the sideband separation mixer, which will be used for Band 1 (221-275 GHz) of the facility receiver for Atacama Pathfinder Experiment (APEX). The use of a harmonic mixer, with an open ended waveguide, as the transmitting source results in a signal to noise ratio (S/N) close to 40 dB for an IF-bandwidth of 10 Hz. This shows the advantage of using the VNA as the signal source and detector, since this allows use of a very narrow detection bandwidth. Further decrease of detection bandwidth down to 1 Hz is feasible with a trade of the increased scan time. Measurement results from a scan approximately 55 mm away from the horn aperture are shown in Fig. 2 and Fig. 3. It should be pointed out that only a rough alignment has been done between the scanner and the cryostat for this measurement. The beam absolute position with respect to the receiver optics will be defined by the use of position sensitive detectors (PSD) and lasers but has not yet been implemented. It can be seen from the measured data, Fig. 2, that the beam appears to be nearly circular down to 30 dB.

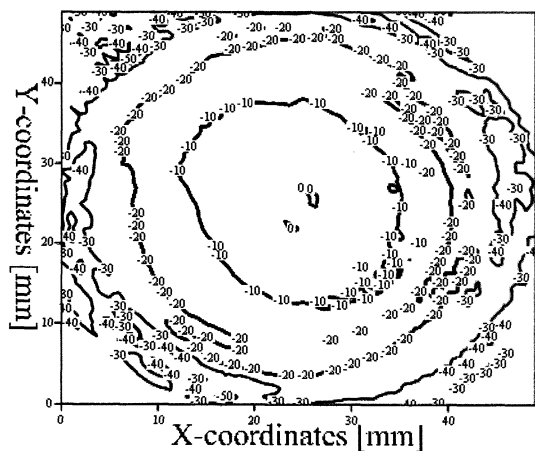


Fig. 2. Amplitude distribution of a scan performed at a cross-section at an approximate distance of 55 mm from the horn aperture.

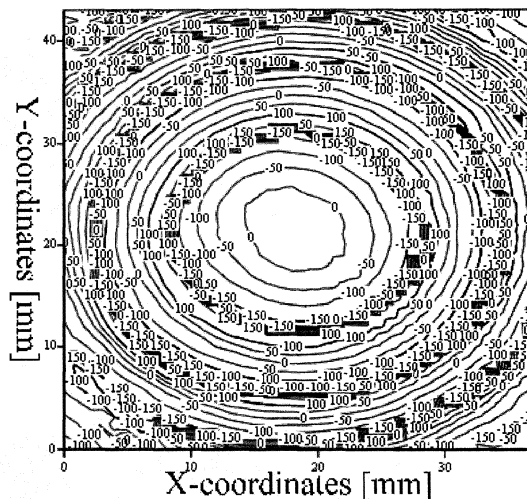


Fig. 3. Phase distribution of a scan performed at a cross-section at an approximate distance of 55 mm from the horn aperture.

To monitor the stability of the measurement, and add the possibility for calibration of the gain and the phase drifts in the system during the scan time, reference measurements were made. This was done by selecting a specific coordinate where the scanner returned to each time one row in the scan plane was completed. The reference plots can be seen in the Fig. 4 and the Fig. 5. The detected power varies less than 0.3 dB over the scan period, whereas the phase changes are less than 6 degrees, almost linear over the entire scan duration. To minimize the phase error due to cabling, all cables are fixed to preclude any movements except for a phase stable cable connecting the moving RF-source, placed on the scanner, to the fixed part of the system.

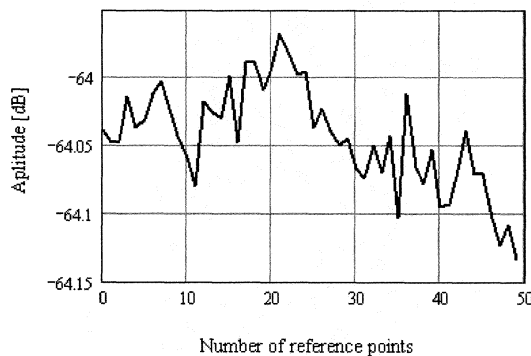


Fig. 4. Reference measurements of the amplitude taken at the same scan coordinate after the completion of each row. The amplitude varies less than 0.2 dB.

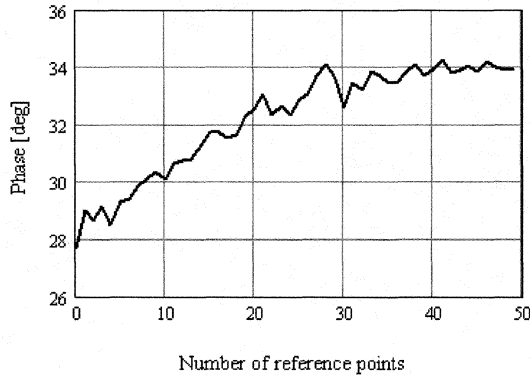


Fig. 5. Reference measurements of the phase taken at the same scan coordinate after the completion of each row. The phase increases, almost linearly, over the scan time.

To get an indication of possibilities to use a harmonic mixer as the RF-source even for higher frequency bands, the signal power was measured also at 341 GHz with the APEX Band 2 mixer [6] with a spectrum analyzer as detector. This measurement gave a S/N-ratio of 35 dB at a detection bandwidth of 1 kHz. The reason for using a spectrum analyzer instead of the VNA for detection was that the required filters for the set up with the VNA were not yet delivered. This, however, gives a promising indication that a harmonic mixer can be used as a signal source also for the higher bands, as the VNA set up is expected to offer even greater dynamic range with greatly reduced band.

IV. BEAM FITTING PROCEDURES

The measured amplitude and phase are combined into a complex beam, which is fitted to the fundamental Gaussian beam mode [7]

$$\psi_{00}(\Delta x, \Delta y) = \sqrt{\frac{2}{\pi\omega_x\omega_y}} \exp\left(-\frac{\Delta x^2}{\omega_x^2} - \frac{\Delta y^2}{\omega_y^2}\right) \times \exp(-j\beta_0(\frac{\Delta x^2}{2R_x} + \frac{\Delta y^2}{2R_y} + \delta_x\Delta x + \delta_y\Delta y)) \quad (1)$$

where $\Delta x = x - x_c$ and $\Delta y = y - y_c$, x and y are scan coordinates, whereas x_c and y_c are the scan coordinates for the amplitude center of the measured data [2]. R_x and R_y are the radii of curvature of the phase front in x - and y -direction, respectively, ω_x and ω_y are the beam radii, and δ_x and δ_y are the tilt of the beam, in x - and y -direction, with respect to the normal of the scan plane. To derive the parameters (x_c , y_c , ω_x , ω_y , R_x , R_y , δ_x , δ_y) that best fit to the fundamental Gaussian beam mode, the measured data is fitted for the optimum power coupling coefficient [7]

$$K = \left| \sum_x \sum_y (E_{ComplexMeasured} \times \overline{E_{ComplexFitted}}) \right|^2 \quad (2)$$

where both the measured data and the fitted data are normalized to unity power over the area to be fitted. For the measured data in Fig. 2 and Fig. 3, a coupling coefficient to

the fundamental Gaussian mode of 0.95 ± 0.02 was obtained when fitted down to -15 dB from the peak value. This coupling was slightly lower than expected, which we believe is the result of measurement errors due to standing waves and the beam truncation in the Dewar vacuum window. A higher coupling coefficient is expected once the standing waves are decreased. The fitting of the measured beam can be seen in Fig. 6 to Fig. 9, where the cross section, through the amplitude center, in x - and y -direction is presented.

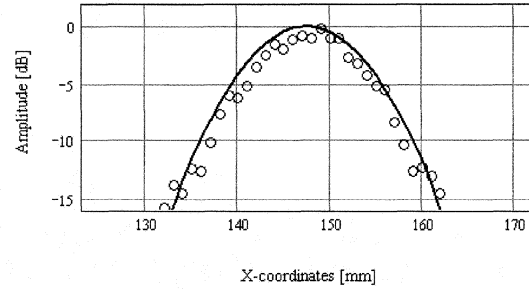


Fig. 6. Measured and fitted data for the amplitude (in dB) for the cross-section, in x -direction, at the amplitude center.

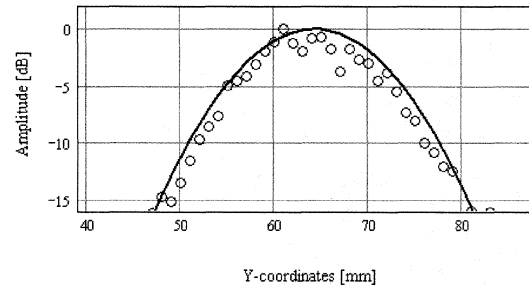


Fig. 7. Measured and fitted data for the amplitude (in dB) for the cross-section, in y -direction, at the amplitude center.

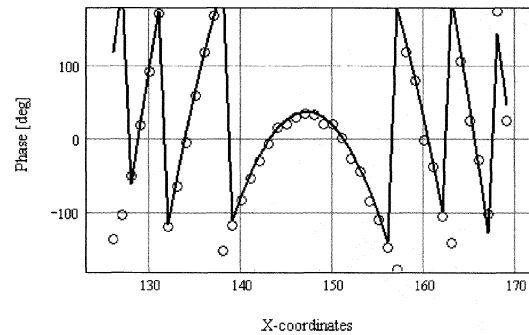


Fig. 8. Measured and fitted data for the phase (in degrees) for the cross-section, in x -direction, at the amplitude center.

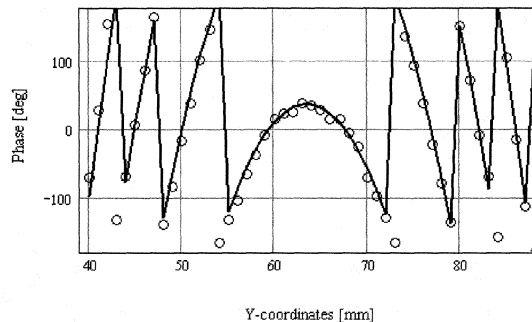


Fig. 9. Measured and fitted data for the phase (in degrees) for the cross-section, in y-direction, at the amplitude center.

Once the beam radius and the radius of curvature are fitted, the values can be used to calculate the size of the beam waist radius, ω_0 , and the distance from the amplitude center, located in the scan plane, to the waist location.

V. CONCLUSION

We have presented a vector measurement system for 221-275 GHz, which employs a combination of a single frequency source, a comb-generator, and a direct multiplication LO unit to achieve perfect phase-coherent RF- and LO signals as well as initial phase-noise cancellation. A dynamic range of about 40 dB has been demonstrated for measurements of the APEX Band 1 receiver. Since the presented set up is designed to cover also the higher bands (APEX-band 2 and 3) the RF-source has been tested at 341 GHz and the signal has been detected with a S/N-ratio of 35 dB with 1 kHz of the detection bandwidth. This is a very promising indication that we will be able to cover all three bands with our system by only switching two filters and the multiplication LO unit, since the use of a VNA as the phase detector allows us to decrease the detection bandwidth significantly and thereby attain even greater dynamic range.

ACKNOWLEDGMENT

The authors would like to thank Douglas Henke for all help during measurements, Magnus Svensson for his support with the Labview program, and Sven-Erik Ferm for his valuable help manufacturing hardware pieces. APEX Project is funded by the Swedish Research Council and the Wallenberg Foundation by their respective grants. Part of this work was supported by EU FP6 AMSTAR Program. We would like to thank Prof. H. Olofsson, Director, Onsala Space Observatory for his support.

References

- [1] M. T. Chen, C.E. Tong, R. Blundell, D.C. Papa, and S. Paine, "Receiver Beam Characterization for the SMA", in Proc. SPIE Conference on Advanced Tech. MMW, Radio, and THz Telescopes, Vol. 3357, pp. 106-113, Kona, Hawaii, Mars 1998.
- [2] C.-Y. E. Tong, D. V. Meledin, D. P. Marrone, S. N. Paine, H. Gibson, and R. Blundell, "Near Field Vector Beam Measurements at 1 THz",

IEEE Microwave and Wireless Components Letters, Vol. 13, No. 6, June 2003

- [3] C.-Y. E. Tong, D. n. Loudkov, S. N. Paine, D. P. Marrone, and R. Blundell, "Vector Measurements of the Beam Pattern of a 1.5 THz Superconducting HEB Receiver", 16th International Conference on Space Terahertz Technology-ISSTT 2005, Gothenburg, SWEDEN
- [4] W. Jellema, T. Finn, A. Baryshev, M. van der Vorst, S. Withington, J. A. Murphy, W. Wild, "Phase-Sensitive Near-Field Measurements and Electromagnetic Simulations of a Double-Slot HEB Integrated Lens-Antenna Mixer at 1.1, 1.2, and 1.6 THz", 16th International Conference on Space Terahertz Technology-ISSTT 2005, Gothenburg, SWEDEN
- [5] V. Vassilev, R. Monje, A. Pavolotsky, D. Dochev, D. Henke, and V. Belitsky, "A 211-275 GHz Sideband Separating SIS Mixer for APEX", 17th International Conference on Space Terahertz Technology-ISSTT 2006, Paris, France.
- [6] R. Monje, V. Belitsky, V. Vessen, A. Pavolotsky, I. Lapkin, "A 385-500 GHz SIS Mixer for APEX Telescope", presented at Astronomical Telescopes and Instrumentation, SPIE 2006, Orlando, Florida, USA
- [7] P. F. Goldsmith, "Quasi-optical Systems". New York: IEEE Press, 1998. ISBN 0-7803-3439-6.

Detection of the 205 μm [NII] Line from the Carina Nebula

ABSTRACT

Stacey¹, G.J., Oberst¹, T.E., Loehr², A., Nikola¹, T., Parshley¹, S.C., Tothill², N. F.H.,
Harnett², J.I., Lane², A. P., Stark², A. A., and Tucker³, C.R.

¹Department of Astronomy, Cornell University

²Harvard-Smithsonian Center for Astrophysics

³Cardiff University

We report the first detection of the 205 μm $^3\text{P}_1 \rightarrow ^3\text{P}_0$ [NII] line from a ground based observatory using a direct detection spectrometer. The line was detected and mapped in emission from the Carina starformation region in the Galaxy using the South Pole Imaging Fabry-Perot Interferometer (SPIFI) on the Antarctic Submillimeter Telescope and Remote Observatory AST/RO at the South Pole. The [NII] line is an important coolant for the diffuse ionized ISM, and (together with the 122 μm [NII] line) is an excellent probe of gas density. The [NII] 205 μm line emission peaks at the Carina II HII region, and its strength indicates a low density ($n < 30 \text{ cm}^{-3}$) ionized medium. When compared with the ISO [CII] observations of this region, we find about half the [CII] line emission arises from this low density ionized gas as well. The detection of this line demonstrates the utility of Antarctic sites for THz spectroscopy.

ORAL SESSION n°7

« Devices, Receivers & Instruments »

Friday 12 May 09:30-10:30

Chaired by :

Dr. Heribert Eisele & Dr. Imran Mehdi

A Novel 520 to 600 GHz Subharmonic Biasable Mixer

Erich Schlecht, John Gill, Robert Dengler, Alex Peralta, Peter Siegel, and Imran Mehdi

Jet Propulsion Laboratory, M/S 168-314, 4800 Oak Grove Drive, Pasadena CA 91109

E-mail: Erich.T.Schlecht@jpl.nasa.gov

Abstract

There is a demand for mixers operating in the submillimeter band between 300 and 1200 GHz for observation of various atomic and molecular lines. For Earth and planetary observations Schottky mixers have adequate sensitivity. Additionally, they have the substantial advantage of working with little or no cooling below room temperature, although their performance does improve at lower temperatures. Near term example missions is a proposal for water detection observations on Mars [1], and measurements of middle atmosphere trace gases and gas dynamics on Venus [2].

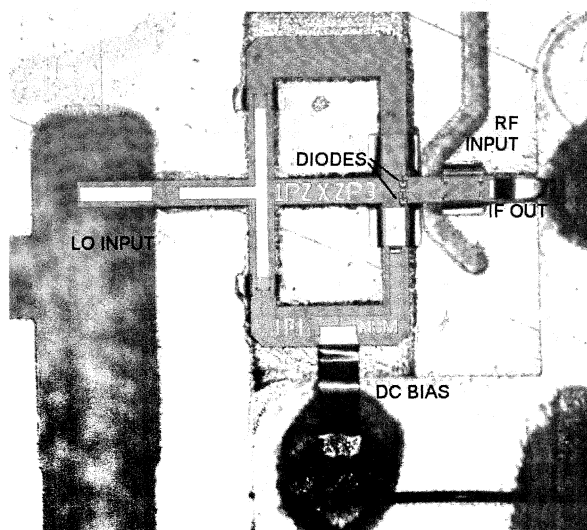


Figure 1. 560 GHz JPL biasable mixer.

To meet these requirements, we have developed a new biasable mixer that takes advantage of the frameless membrane technology developed at JPL [3]. Similarly to some previous designs [4], the diodes are fabricated in an antiparallel configuration with each diode having one electrode grounded using beam leads. See Figure 1. The ability to be biased makes these mixers operable from very low LO power, as required by many planetary missions. The mixers have been fabricated and will be measured soon. They are expected to give

single sideband noise temperatures at the diode of about 2000 K, with conversion loss around 10 dB.

- [1] Report of the NASA Science Definition Team for the Mars Reconnaissance Orbiter (MRO), available at http://mro.larc.nasa.gov/mro/MRO_SDTreport.pdf, Feb. 2001.
- [2] Solar System Exploration Survey, Space Studies Board of the National Research Council, "New Frontiers in the Solar System" available at <http://www.nas.edu/ssb/SSE-Survey-Report-Part-1.PDF>, July 2002.
- [3] S. Martin, B. Nakamura, A. Fung, P. Smith, J. Bruston, A. Maestrini, F. Maiwald, P. Siegel, E. Schlecht, and I. Mehdi, "Fabrication of 200 to 2700 GHz multiplier devices using GaAs and metal membranes," *2001 MTT-S International Microwave Symposium Digest*, pp. 1641-1644.
- [4] E.R. Carlson, M.V. Schneider, and T.F. McMaster, "Subharmonically pumped millimeter-wave mixers," *IEEE Trans. Microwave Theory Tech.*, vol MTT-26, no. 10, pp. 706-715, Oct. 1978.

TIP: A Terahertz Interferometer for Planets – A Concept StudyGoutam Chattopadhyay¹, John S. Ward¹, Imran Mehdi¹, Peter H. Siegel¹,
Paul F. Goldsmith¹, and Anthony C. S. Readhead²¹Jet Propulsion Laboratory, California Institute of Technology
4800 Oak Grove Drive, Pasadena, California 91109, USA.²Department of Astronomy, California Institute of Technology
1200 E. California Blvd, Pasadena, California 91125, USA.

The extraordinary discoveries of planets around nearby stars in recent years have opened up an exciting new field of research – the search for extrasolar planets. Studies of these planets are revealing new information about the star and planet forming processes, and have brightened the likelihood of the detection of Earth-like planets in our galaxy. Current extrasolar planet finding research is carried out mostly at optical wavelengths. Planet-finders use various techniques such as direct detection, where the faint light reflected by the orbiting planetary body is detected by nulling of the central bright star; or indirect detection, where the orbital variations or the wobbling of the central bright star is measured to identify the unseen companion. However, there are major limitations to both these techniques. In the first case, the brightness ratio between the star and the planet is in the range of 90 to 120 dB for our solar system not including Pluto, making nulling very difficult even for relatively bright planets at short orbital radii, not to mention planets at large separation distances where the reflected light is extremely weak. In the second case, due to sensitivity and time limits, only massive planets orbiting close to the star can be detected.

NASA is developing technologies for planet finding missions at near-infrared frequencies. The planned Terrestrial Planet Finder Interferometer (TPF-I) is a space-based 4-element interferometer centered at 10 μm wavelength where the 280 K black-body curve peaks. However,

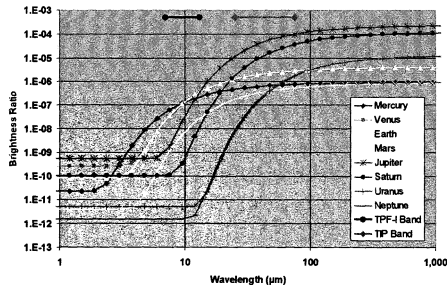


Fig.1 Brightness ratio of different planets in our solar system compared to the sun using a simple model of blackbody radiation and reflected starlight.

as can be seen from Fig. 1, at wavelengths around 10 μm the starlight is approximately 70 to 100 dB brighter than the planets for the solar system, making nulling still a very difficult task. At longer wavelengths, however, the brightness ratio is much more favorable for nulling (40-60 dB), and is more sensitive to planets at large separation distances where the reflected light from the planet is weaker and the black-body peaks at longer wavelengths, as shown in Fig. 1. Therefore, a space-based interferometer with modest baselines at terahertz frequencies will offer substantial advantage for finding planets around nearby stars.

In this study paper, we identify the scientific potential, technology drivers, and system requirements for undertaking a planet finding mission using interferometry from 4 to 12 THz (25-75 μm). We will show that a 4-element interferometer with 4 m antenna diameter, < 1 km baseline, and direct detector instruments with realistic NEP has the potential of detecting Earth-like planets out to ≈ 15 pc with only 24 hours of integration. Modest resolution ($R=20$) spectroscopy will also be possible with such an instrument.

The research described herein was carried out at the Jet Propulsion Laboratory, California Institute of Technology, Pasadena, California, USA, under contract with National Aeronautics and Space Administration.

A Very Wideband Analog Autocorrelation Spectrometer

Neal Erickson, Gopal Narayanan, Robert Goeller
University of Massachusetts, Amherst, MA, USA

Astronomical receivers for the THz range require very wideband spectrometers, several GHz or more for extragalactic spectroscopy, but the required frequency resolution is relatively low. The usual choice is a digital autocorrelator, but these spectrometers have bandwidths limited to ~1GHz for a single unit, and few bit samplers have a limited dynamic range without adding sampling noise. An alternative is to use analog techniques to autocorrelate the signals. While it may seem to be working against the trend of improved performance of digital circuits, in fact this technique is making equally rapid progress because of the ever increasing availability of low-cost high-performance microwave components.

Our technique of analog autocorrelation is to split a signal two ways and send it in opposite directions down a single transmission line. The line is tapped periodically, and the tap signals go to detector diodes as shown in Fig 1. A square law detector produces an output proportional to the sum of the power in each signal plus the product of the two voltages. Rapid phase switching of one signal produces an AC output for the product term while the other component remains constant. The outputs of all of the detectors form the autocorrelation function of the signal. In this work we have constructed an analog correlator with up to 8 GHz bandwidth having 256 lag measurements. Four delay lines with 64 taps each fit on a single circuit board along with the detectors, AC preamplifiers, A/D converters, and all of the digital logic needed to read out the A/D's and average the data. A second microwave circuit board produces the 10 mW signals needed to drive the lines as well as the phase switching. Components used in the driver are limited to 1.5-8.0 GHz, as increased bandwidth is possible but not cost effective. The full circuit is shown in Fig. 2.

The spectrometer is working with the expected 31 MHz resolution, and shows radiometric noise in 1 hr integrations on a wideband signal with a fast beam switch. Switching speed must be faster than 10 seconds on and off time in a completely unstabilized environment, but should be much better with temperature control. The cost is \$2500 for the complete correlator board, and \$1000 for the driver board making this a very inexpensive way to cover wide bandwidths. This spectrometer will be used as the backend for a 74-110 GHz receiver used to search for highly redshifted galactic lines.

Wider bandwidth is possible with this technique but the limit is set by the parts density on a PC board, and at present ~10 GHz is a practical limit. In the future, smaller parts will increase this limit. Higher resolution comes by simply adding delay lines.

Figure 1. Basic autocorrelator circuit. Signals A and B are the same input with a time delay.

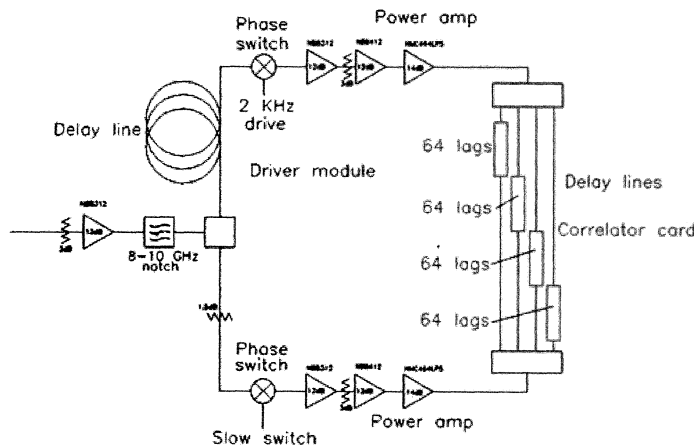
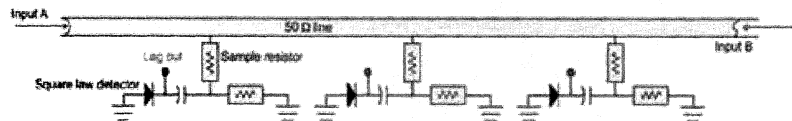


Figure 2. Complete autocorrelator with driver circuit. The delay lines are made using coaxial cable.

**A Modal and Quantum-Statistical Analysis of Imaging Phased Arrays
and Interferometric Phased Arrays.**

Stafford Withington, Cavendish Laboratory, University of Cambridge, UK.

A number of major projects are aimed at developing phased-arrays for radio astronomy; these include the Square Kilometer Array (SKA), the Low Frequency Array (LOFAR), the Electronic Multibeam Radio Astronomy Concept (EMBRACE), and the Karoo Array Telescope (KAT). All of these projects relate to microwave astronomy, but as technological understanding improves, phased arrays will also be constructed for submillimetre-wave and far-infrared astronomy. Two types of phased array are of interest: (i) Imaging phased arrays, where an array of coherent receivers is connected to a beam-forming network such that synthesised beams can be created and swept across the sky; the receivers may look at the sky directly or may be mounted on the back of a large reflecting antenna. (ii) Interferometric phased arrays, where the individual antennas of an aperture synthesis interferometer are equipped with phased arrays such that fringes are formed within the synthesised beams. In this way it is possible to extend the field of view, to observe completely different regions of the sky simultaneously, to steer the field of view electronically, and to observe spatial frequencies that are not available to the interferometer because the baselines cannot be made smaller than the diameters of the individual antennas. Of course, telescopes may operate in the 'imaging' and 'interferometric' modes simultaneously by configuring the arrays on the individual antennas to give low-resolution images, and cross correlating the outputs of the arrays on different antennas to give high-resolution data in the Fourier domain.

In this paper we describe the operation of imaging and interferometric phased arrays from a modal perspective, explaining how the behaviour of a phased array can be described completely in terms of the synthesised reception patterns, without any knowledge of the internal construction of the beam-forming networks. Beam patterns may be taken from electromagnetic simulations or experimental data. Crucially, we consider the general case where the synthesised beams do not have to be orthogonal or even linearly dependent; the close association with the mathematical theory of Frames is also mentioned. In the case of interferometric phased arrays, the arrays on the individual antennas do not even have to be the same. The ability to assess the behaviour of a system simply from the synthesised beam patterns separates the process of choosing the best beams for a given application from the process of understanding how to realise the beams in practice. It also suggests important techniques for analysing experimental data, particularly when cross talk between the primary feeds is present.

The paper explains how the powers, the fluctuations in the powers, and the correlations between the fluctuations in the powers at the outputs of different ports of a phased array can be determined from knowledge of the spatial state of coherence of the illuminating field, which for astronomical sources is usually fully incoherent: although not in the case of celestial masers. It is explained, by analogy with the behaviour of multimode detectors, how the quantum statistical behaviour of the source and noise fields can be included, taking into account the fact that the photon statistics may neither be fully bunched nor fully Poisson. This fundamental piece of work has implications for the way in which imaging and interferometric phased arrays are designed, how their performance is calculated, how they are characterised experimentally, and how astronomical data is analysed.

ORAL SESSION n°8

« Superconductors for Imagers & Detectors »

Friday 12 May 14:00-15:00

Chaired by :

Dr. Netty Honish & Dr. Jacob Kooi

Development of High-Q Superconducting Resonators for use as Kinetic Inductance Detectors

J.J.A. Baselmans, R. Barends, S.J.C. Yates, J.N. Hovenier, J.R. Gao, H. Hoevers and T.M. Klapwijk

Abstract— One of the greatest challenges in the development of future space based instruments for sub-mm astronomy is the fabrication of sensitive and large detector arrays. Within this context we have started the development of Microwave Kinetic Inductance Detectors (MKIDs). The heart of each detector consists of a high Q superconducting quarter wavelength microwave resonator. As a result it is easy to multiplex the readout by frequency division multiplexing. The flexibility of the MKID allows for radiation detection from sub-mm to X ray by choosing a suitable radiation absorber or antenna. The predicted sensitivity of the MKID is below NEP $\sim 1 \cdot 10^{-20}$ W/ $\sqrt{\text{Hz}}$, low enough for any envisionsable application in the sub-mm, optical and X ray wavelength ranges. We describe our initial experiments with these resonators, made of 100 nm Nb films on a high purity Si substrate. We measure the Q factors of several resonators using a vector network analyzer and find Q factors up to 50000, limited by the intrinsic quality of the resonators. We furthermore obtain the responsivity of these resonators, with values up to 0.08 radians per 10^6 quasiparticles.

I. INTRODUCTION

The science themes for future Far-InfraRed (FIR) and sub-mm astronomy are the emergence and evolution of stars and galaxies and the birth of stars and planetary systems [1]. The instrument of choice to address these science themes will be a space based telescopes with high spatial resolution, high observation speed and background limited sensitivity. High speed is accomplished by using large (100 x 100 pixels or more) detector arrays. High spatial resolution implies a larger mirror or interferometry by formation flying of several telescopes. Background limited sensitivity can be achieved by reducing the instrumental background noise significantly, which is only possible with actively cooled (< 10 K) telescopes. Only in that case can the sky background limited photon noise be reached, at a NEP $\approx 10^{-20}$ W/ $\sqrt{\text{Hz}}$ for spectroscopy with a resolving power $R \sim 1000$. No practical detector array exists to date with a NEP $< 10^{-17}$ W/ $\sqrt{\text{Hz}}$.

Manuscript received June 20, 2006. This work was partially supported by Radionet and the VENI program of NWO. The authors wish to thank P. de Korte for support and very fruitful discussions

J.J.A. Baselmans, S.J.C. Yates J.R. Gao and H. Hoevers are with *SRON National Institute for Space Research, Sorbonnelaan 2, 3584 CA Utrecht, The Netherlands. Mail: J.Baselmans@sron.nl*

R.Barends, J.R. Gao and T.M. Klapwijk are with *Kavli Institute of Nanoscience, Delft University of Technology, Lorentzweg 1, 2628 CJ Delft, The Netherlands*

Within this context we have started the development of Microwave Kinetic Inductance Detectors (MKIDs) [2]. For use in a sub-mm or FIR detector array each pixel of the MKID would consist of an antenna or absorber, coupled to a high Q $\frac{1}{4}\lambda$ Coplanar waveguide (CPW) microwave resonator. This resonator is coupled capacitively to a through line, which enables easy frequency division multiplexing of many resonators at slightly different frequencies. A picture of such a resonator with a through line but without any absorber or antenna, is shown in Fig. 1. At resonance the resonator acts as a short, with the result a strong reduction in the transmission measured from contact 1 to contact 2, S_{21} (indicated in Fig. 1). The principle of operation is as follows: Radiation that is coupled to the resonator at a frequency $h\nu > 2\Delta$ will break up Cooper pairs in the central superconducting strip of the resonator. The reduction in Cooper pair density gives rise to a reduction in the kinetic inductance L_K , causing a shift in resonance frequency. When used as a radiation detector one measures the phase of the signal transmitted from contact 1 to 2 exactly at the resonance frequency. Here the absorption of a photon causes a change in the transmitted phase proportional to $\alpha Q/V$, with Q is the resonator quality factor, V its volume α the kinetic inductance fraction [2,4,5]. Using a high Q resonator with a limited film thickness in combination with a low noise microwave amplifier, such as a InP based MMIC

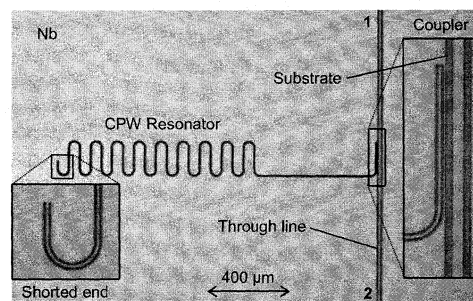


Fig.1: Scanning electron microscope picture of a Coplanar waveguide based Nb resonator on a Si substrate. The bright areas correspond to the 100 nm Nb film on top of the Si, the dark areas correspond to bare Si substrate. The coupling capacity of the $\frac{1}{4}\lambda$ long resonator is formed by the coupler, where the through line and resonator run parallel.

[3], enables, in principle, the detection of a single quasiparticle. The detector noise is, in theory, limited by the fundamental quasiparticle generation-recombination noise, enabling (in theory) sensitivities as low as $NEP < 10^{-20}$ W/√Hz at temperatures below 1/10 of the critical temperature of the superconductor [2,4,5]. Multiplexing of many pixels is done in the frequency domain, where every pixel (i.e. antenna or absorber) is coupled to a different resonator coupled to the same through line. By changing the length of every resonator slightly all resonators will have different resonant frequencies. A 2 μm length difference between the resonators would allow 2000 resonators in a 1 GHz bandwidth around 7 GHz (where the resonator length is about 4 mm on a Si substrate with $\epsilon=11.8$). The readout of the phase transmitted at each resonator can be done using only room temperature electronics (for details see Ref.[6]). The cryogenics will be limited to 2 coaxial cables to the sample holder and 1 microwave amplifier at about 4K. For a suitable MKID detector one should use, for the resonator, a superconductor with a low critical temperature T_c and a long quasiparticle lifetime, such as Al. However, as a first step, we have started with measurements of Nb based resonators. The Nb KID's are not suitable for real detectors because of its high T_c and short quasiparticle lifetimes (see [2]). But, they offer the advantage to quickly evaluate our resonator design and test setup.

II. EXPERIMENT

The resonators are fabricated using DC sputter deposition of a 100 nm Nb layer on top of a N doped Si <100> substrate with a resistivity in excess of 1 kΩcm. The KID patterns are subsequently defined using e-beam lithography and dry etching. We use a 3He sorption cooler mounted inside a liquid He vacuum cryostat as cryogenic system, achieving a base temperature of 300 mK, which is far below 1/10 of the critical temperature of the Nb films. At the cold stage of the 3He cooler we mount a specially designed copper sample holder. The holder has 2 microwave launchers that have a SMA connector on one side and a small pin at the other, which is soldered to the central strip of a copper CPW on top of a circuit board made of Duroid board. The board is used to form

the transition between the launcher and the KID chip and is designed using the commercial software package SONNET. It forms the transition from a grounded CPW at the launcher connection to an ungrounded CPW at the chip end. Connections to the CPW on the chip are made using several bond wires, additionally there are bond wires from the chip ground plane to the holder to prevent unwanted resonances. With careful mounting of the chip the setup has a resonance free bandwidth of 9 GHz [7]. Stainless steel coax cables are used from room temperature to the 4.2 K plate of the cryostat. From there we use a strapped Al coaxial cable, a strapped 20 dB attenuator, and 10 cm of stainless steel coaxial cable to reach the short copper coax cables connected to the holder at 300 mK. The hold time of the sorption cooler with the holder on top and all coax cables connected is in excess of 6 hours at 300 mK. A commercial room temperature Miteq amplifier, with a practical bandwidth from 1-10 GHz and a noise temperature of about 150 K, is used at room temperature to boost the signal, enabling faster measurements. We measure the fraction of the transmitted power, denoted by S_{21} , as a function of frequency and temperature using a Agilent PNA-L vector network analyzer. A Labview program is written to automatically measure many KID's in one single cool down as a function of temperature. Fig. 3A gives the measured resonance curves between 3.3 K and 300 mK for one of the Nb resonators. The dots indicate the resonance frequency. The high temperature data corresponds to the left most resonance dip, the lowest temperature to the rightmost resonance dip. It is obvious from the figure that the resonance frequency and Q factor increase with temperature. The Q factor is given by, $Q=f_{res}/2\delta f$, where the resonator bandwidth δf is defined by the difference between the two frequency points where $S_{21}=1/2$ ($S_{21,min}+1$). Since we can model every resonator as the series combination of a coupler with Q_c the coupling Q and the resonator itself, with Q_i the intrinsic Q, we can obtain from the measured Q factor and $S_{21,min}$ Q_i and Q_c using $Q=Q_c Q_i/(Q_i+Q_c)$ and the fact that $Q_i=Q/S_{21,min}$ [4]. The temperature dependencies of these three parameters are given in Fig.3 B. The line through the datapoints of the measured Q_i is a calculation of the Q factor using Mattis-Bardeen theory, using a Kinetic Inductance fraction as a fit parameter [3,8] and limiting the Q_i to the experimentally obtained maximum

ID	Design parameters			Measured parameters at low temperature						
	L [mm]	F ₀ [GHz]	Q _c	T [K]	F ₀ [GHz]	Q [$\cdot 10^5$]	Q _c [$\cdot 10^5$]	Q _i [$\cdot 10^5$]	S _{21,min} [dB]	$\delta\theta/dN_{qp}$ rad/ 10^6 qp
6a	4.101	7.2	$1 \cdot 10^5$	0.65157	6.8623	0.36246	0.49329	1.3666	-11.479	0.06
6b	3.990	7.4	$1 \cdot 10^5$	0.6476	7.0292	0.48569	0.66597	1.7942	-11.333	0.077
6c	3.885	7.6	$1 \cdot 10^5$	0.64359	7.2445	0.43671	0.82485	0.9280	-6.5331	0.056
6d	3.786	7.8	$4 \cdot 10^4$	0.63979	7.4148	0.21658	0.27531	1.0153	-13.372	0.031
9a	4.101	7.2	10^3	0.578	6.851	0.0248	0.0286	0.215	-18.8	0.0003
9b	3.990	7.4	$4 \cdot 10^4$	0.581	7.046	0.2468	0.315	1.14	-13.3	0.02
9c	3.885	7.6	$2 \cdot 10^5$	0.579	7.361	0.170	0.939	0.207	-1.7	0.04

Table 1: Measured parameters at low temperature (the temperature is given at column T) for several Nb KID resonators fabricated on a <100> Si substrate.

value. We find a kinetic inductance fraction of 0.2, in reasonable agreement with a direct calculation giving 0.26. Note that the coupling Q is constant with temperature as expected over this range. The resonance dips shown in Fig. 3A can be plotted as well in the complex plane, as in Fig. 3C, where the frequency increases clockwise around the circle. When operated as a radiation detector the KID measures the phase change at the resonance frequency due to the quasiparticles created by the radiation absorption. In this measurement we create the quasiparticles by increasing the temperature. In Fig. 3C the black dots indicate the resonance frequency at 300 mK on the resonance circles at other temperatures. The phase response of the resonator can be obtained by measuring the (phase) angle between the location of the 300 mK resonance frequency on the 300 mK circle and the location of the same frequency in the resonance circles at other temperatures. The centre of the resonance circle at 300 mK is taken as the origin. This procedure is indicated by the arrow in Fig. 3C and the result is plotted in Fig. 3 D. The resonator shows a very steep phase response between 1.5 and 2.5 K. At higher temperatures the phase change saturates, and at low temperatures the phase change shows a non-monotonic

behaviour, which we attribute to a substrate effect and not to a change in quasiparticle density. We take the positive phase change with temperature and convert the temperature scale to quasiparticle density using:

$$(1)$$

with N_0 the single spin density of states at the Fermi level ($1.3 \cdot 10^{11} \text{ eV}^{-1} \mu\text{m}^{-3}$ for Nb [8]). Numerically differentiating the phase change with respect to quasiparticle number gives now the responsivity in radians per quasiparticle for our resonators. Results from several resonators are given in Table 1. From the table several conclusions can be drawn. First, the resonance frequencies are lower than calculated, this can be attributed to the fact that in the design we did not take into account the kinetic inductance, which reduces the resonance frequency. A similar effect (or opposite in sign) can be observed if the CPW dimensions differ from the design values, which is not likely given the fact that the resolution of our e-beam lithographic process is of the order of 50 nm. Furthermore the intrinsic Q factor is limited to about 100.000 and not frequency dependent. This value is roughly 5 times lower than reported

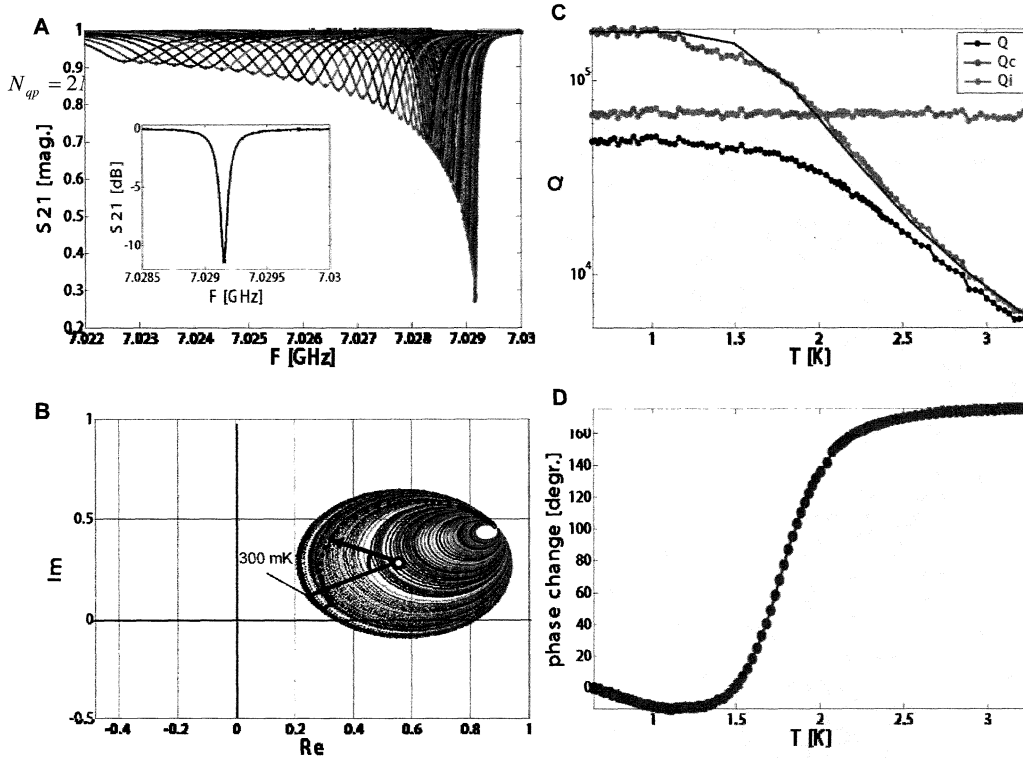


Fig.2: A: Measured transmission around the resonance frequency of one of the resonators for different temperatures between 3.3 K(left) and 0.3 K (right), the insert shows the 300 mK resonance feature over a smaller frequency range. B: Q factors obtained from the data shown in panel A. Q is the measured Q factor of the resonance dip, Q_c the coupling Q factor and Q_i the intrinsic Q factor of the resonator. The line is a theoretical calculation using the kinetic inductance fraction as a fit parameter. C: The data plotted in A in the complex plane, the dots represent the 300 mK resonance frequency at higher temperatures. The arrow indicates how the phase can be measured as a function of temperature. D: The phase change as a function of temperature as illustrated in C.

for Al resonators on Si [3] but comparable to results of Al on Sapphire [3]. Since we do not observe any dependence of Q_i with resonator length we can exclude radiative losses due to the substrate as the limiting factor. Possibly an excess surface resistance of the Nb films limits the Q factor. Furthermore, the coupling Q is roughly half the designed value which is not understood. The responsivities as shown in the last column are comparable to those of Al resonators [4] with similar Q factors and scale roughly linear with the measured Q factor as expected, since the device volumes quoted here are almost identical.

III. CONCLUSION

MKID's are a very promising detector concept for a great variety of wavelengths, ranging from the sub-mm to the X ray. The advantages are easy multiplexing of the readout using frequency division multiplexing at GHz frequencies and a high predicted sensitivity. We have presented initial results on 2 batches of Nb resonators made on Si substrates. We find that our microwave design allows measurements in a bandwidth from 1-10 GHz without any spurious resonances, indicating that the experimental setup is adequate. In the Nb resonators we find Q factors up to 50.000, good enough already for many applications. The measured Q values are found to be limited by the intrinsic quality of the resonators themselves. The latter can be caused by either the Nb film or the substrate. It is to be expected that material and substrate optimisation will result in even higher Q factors for similar systems.

REFERENCES

- [1] "Community Plan for Far-Infrared/Submillimeter Space Astronomy", http://www.sofia.usra.edu/det_workshop/papers/intro/i-02benford_cr_edjw021007.psd. (2002).
- [2] P. Day, H. leDuc, B. Mazin, A. Vayonakis, J. Zmuidzinas, Nature 425, 817 (2003).
- [3] Niklas Wadefalk, Sander Weinreb, "Very low noise amplifiers for very large arrays," to be presented at the IEEE IMS 2005 workshop WFF, "Very Large Microwave Arrays for Radio Astronomy and Space Communications" (2005).
- [4] B. Mazin, Ph.D. Thesis, California Institute of Technology (2004).
- [5] A. Porch, P. Mauskopf, S. Doyle, C. Dunscombe, IEEE Trans. on Appl. Superc. Volume 15, Issue 2, 552, (2005).
- [6] B. Mazin and J. Zmuidzinas Proc. of 11th int. workshop on low temp. det., 31 july - 5 august, Tokyo Japan (2005).
- [7] J.J.A. Baselmans, R. Barends, J.N. Hovenier, J.R. Gao, H. Hoevers, T.M. Klapwijk, Proc. of 11th int. workshop on low temp. det., 31 july - 5 august, Tokyo Japan (2005).
- [8] D.C. Mattis and J. Bardeen, Phys. Rev. 111, 412 (1958).

Development of a 585 GHz One-Dimensional Diffusion-Cooled Niobium HEB Mixer Imaging Array Based on the “Reverse-Microscope” Concept

L. Liu, Q. Xiao, H. Xu, A. W. Lichtenberger, and R. M. Weikle, II

Abstract—We have designed and fabricated prototype 585 GHz one-dimensional (1-D) slot-ring antenna (SRA) coupled d-HEB imaging mixer arrays (four pixels) based on the “reverse-microscope” concept. Due to the small element spacing, the mutual coupling between adjacent SRA’s in the mixer array can not be ignored. ADS momentum simulation has been performed to study the self- and mutual- impedances of the SRA array with various element spacings. The element SRA off-axis radiation patterns (with silicon lens) have been calculated using ray-tracing techniques and the imaging angular resolution has been predicted. Fabrication and measurement systems are discussed.

Index Terms—Diffusion-cooled, hot-electron bolometer, imaging array, reverse-microscope.

I. INTRODUCTION

HIGHLY-sensitive receivers employing superconducting diffusion-cooled hot-electron bolometers (d-HEB) have been intensively studied and applied for millimeter-wave and far-infrared (FIR) imaging and remote sensing in recent years [1-2]. However, for many applications, only one pixel of object information from the receiver is not sufficient. To map the distribution of radiation intensity, for instance, many pixels of imaging information are required. Although mechanical scanning can be applied to a single element mixer to fulfill this requirement, this approach can present problems due to the longer observing time. Imaging mixer arrays are needed for these applications since they can greatly reduce the observing and processing time by recording imaging information in parallel.

In 1982, Rutledge *et al* proposed a high-resolution imaging antenna array diagram with a “reverse-microscope” optical configuration [3]. On the bases of this concept, a UC-Davis group is currently working on a 90 GHz Schottky diode mixer array using bow-tie antennas [4]. Bow-tie antennas are difficult to use, however, for high resolution imaging applications in the THz region as they are not sufficiently

compact for single imaging element design. JPL proposed a 1.6 THz one dimensional array using diagonal horns feeding waveguide receivers [5]. However, two-dimensional arrays based on this scheme are difficult to realize. More recently, another approach called the “fly’s-eye concept” has been proposed [6]. A 3-element HEB focal plane array based on this concept has been reported demonstrating promising performance [7]. In this approach, each mixer element uses a separate imaging lens, which may cause some difficulties for design, fabrication and assembling.

This paper describes a prototype 585 GHz one-dimensional slot-ring antenna (SRA) coupled d-HEB mixer arrays (four pixels) that has been designed and fabricated based on the “reverse-microscope” concept. Due to the small element spacing, the mutual coupling between adjacent SRA’s in the mixer array can not be ignored. ADS momentum simulations have been performed to study the self- and mutual-impedances of the SRA array for various element spacings. The off-axis radiation patterns have been calculated using ray-tracing techniques, and the imaging angular resolution has been predicted. Fabrication results and the measurement setup are presented and discussed.

II. ARRAY DESIGN AND SIMULATION

A. “Reverse Microscope” Configuration

Fig. 1 shows a diagram of the proposed d-HEB imaging mixer array mounted on an extended hemispherical silicon lens. Each of the imaging elements employs a receiving

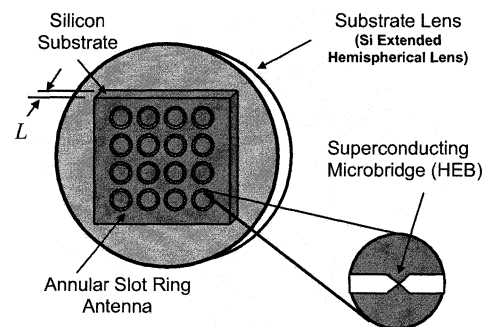


Fig. 1: Schematic of a d-HEB imaging mixer array mounted on an expanded silicon hemispherical lens (expansion length L).

antenna structure as the coupling component in which a

Manuscript received May 9, 2006. This work was supported by the National Science Foundation under grant AST-0242525 and the U.S. Army National Ground Intelligence Center under grant DASC01-01-C-0009.

L. Liu, A. W. Lichtenberger, and R. M. Weikle, II are with the Charles L. Brown Department of Electrical and Computer Engineering, University of Virginia, Charlottesville, VA 22904-4743, U.S.A. Q. Xiao and H. Xu are with the Department of Physics, University of Virginia, Charlottesville, VA 22904-4714, U.S.A.

superconducting d-HEB micro-bridge is integrated. An input image signal is focused through an objective lens (not shown in fig.1), the substrate lens and the substrate onto the mixer array. Images are obtained by measuring the IF output signal from each element in the array. By utilizing the same material (silicon) for both the array substrate and the imaging lens in this configuration, the trapped surface-wave can be eliminated and hence a high imaging resolution can be achieved [3].

B. Mixer Array Element Design and Mutual Coupling

Single element receivers and mixers employing HEB's have been proposed and studied by a variety of research groups including the Jet Propulsion Laboratory (JPL) in Pasadena, CA [2], and the Delft University of Technology in the Netherlands [1]. The RF circuit design and antenna structures utilized in these receivers, however, have not always been suitable for imaging mixer array applications. The slot-ring antenna provides a compact structure, making it an attractive candidate for the proposed mixer imaging arrays. 585 GHz d-HEB mixer element coupled with SRA's have been studied previously [8] and shown in Fig. 2 is the schematic of a one-dimensional array containing four SRA's. For operation at 585 GHz, each SRA has a radius a , of $36 \mu\text{m}$ and a slot width, w , of $2.6 \mu\text{m}$. High-resistivity silicon is chosen as the substrate

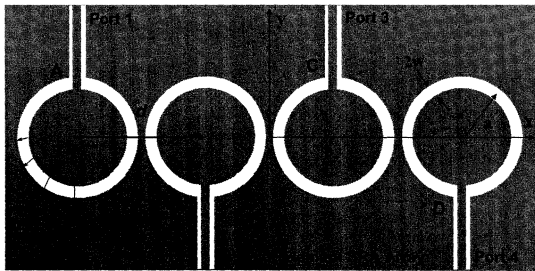


Fig. 2: Schematic of a one-dimensional SRA array with element spacing of d . Each SRA has a radius a , of $36 \mu\text{m}$ and a slot width, w , of $2.6 \mu\text{m}$.

due to its high dielectric constant ($\epsilon_r = 11.7$), which results in a high directivity and efficiency for the receiving antenna. The hemispherical silicon lens (see fig. 1) has a radius $R = 4.5 \text{ mm}$. The radiation patterns of a single element SRA mounted on the silicon lens have been calculated in [8] using ray-tracing technique [9] and an extension length $L = 1.6 \text{ mm}$ (see Fig. 1) is selected for the highest antenna directivity while maintaining an acceptable Gaussian coupling efficiency.

Due to the small element spacing required ($\sim \lambda_d$, where λ_d is the wave-length in the silicon substrate) for diffraction-limited imaging, the mutual coupling between adjacent SRA's in the mixer array can not be ignored. ADS momentum simulations have been performed to study the self- and mutual- impedance of the four-element SRA array with various element spacings. As shown in Fig. 2 ($d=0.8 \lambda_d$), the element-A's (or D) the self-impedance is $Z_{0A} \sim 75 + j0 \Omega$, and the mutual-impedance Z_{mA} ($Z_{mA} = Z_{21} + Z_{31} + Z_{41}$) is estimated to be approximately $1.6 + j0.8$

Ω at 585 GHz. For element B (or C), the self- and mutual-impedance are $Z_{0B} \sim 75 + j0 \Omega$, and $Z_{mB} \sim 4.2 + j0.8 \Omega$ ($Z_{mB} = Z_{12} + Z_{32} + Z_{42}$), respectively. Compared to self-impedances, the mutual-impedances are much smaller. This has a relatively minor effect at such an element spacing of $0.8 \lambda_d$. An EMF-based analysis has also been developed to study the SRA self- and mutual- coupling analytically. Results will be presented elsewhere [10].

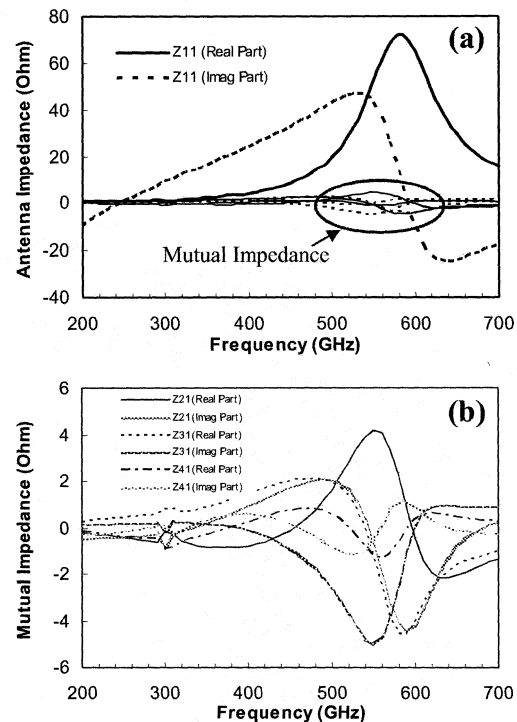


Fig. 3: ADS momentum simulated (a) self- and (b) mutual-impedances of element A in the 1-D SRA array.

C. Off-axis Radiation Patterns and Angular Resolution

The element SRA off-axis radiation patterns for various spacings in the array have been calculated again using ray-tracing technique. As shown in Fig. 4, the element SRA pattern has a 3-dB beam width of $\theta_{3\text{-dB}} \sim 3^\circ$ with side-lobe levels less than -10 dB. The beam spacings between adjacent SRA's are $\Delta\theta \sim 4.0^\circ, 5.0^\circ$, and 5.7° with crossover power level around -7.2 dB, -11.0 dB, and -12.5 dB for $d = 0.8 \lambda_d, 1.0 \lambda_d$, and $1.1 \lambda_d$, respectively. According to the imaging theories, the angular imaging resolution is determined by the beam pattern spacing and limited by 3-dB beam width. The relationship between the angular imaging resolution and SRA element spacing is calculated and shown in fig. 5. With decreasing element spacing, the imaging resolution increases nearly linearly. However, the imaging contrast may become worse. Thus, a trade-off between imaging resolution and contrast must be made by selecting appropriate element spacing in the one-dimensional mixer array.

III. ARRAY FABRICATION

The d-HEB mixer imaging array fabrication used in our research work is based on a process developed by the University of Virginia's Superconducting Devices and Materials Research Group [11]. The process begins with sputtering of a Nb/Au (10 nm/10 nm) bi-layer onto a Si wafer, followed by a standard lift-off process to define the base layer consisting of the SRA array, low-pass filters (LPF's) and tuning circuits.

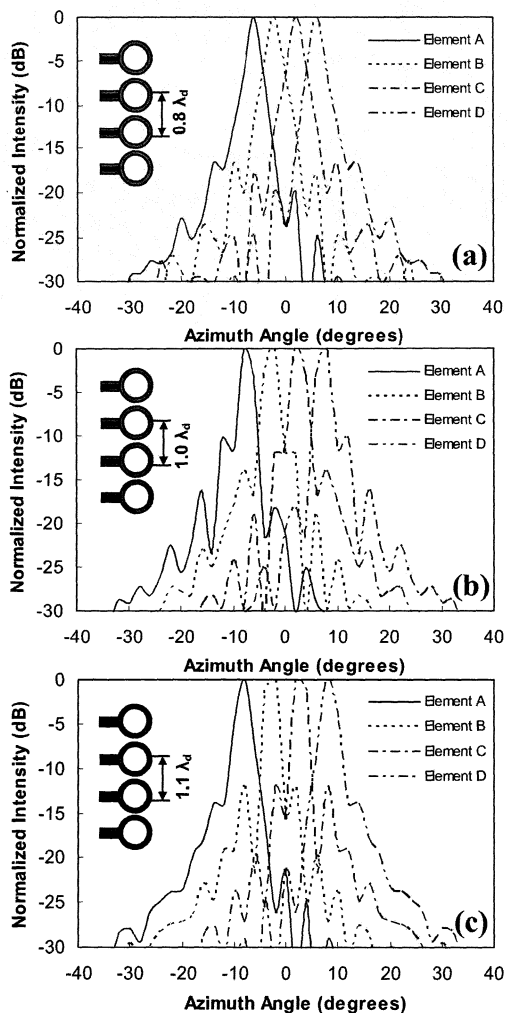


Fig. 4: Off-axis element radiation patterns for 1-D SRA array calculated using ray-tracing technique.

After the base layer is defined, the mixing elements – the HEB bridges – are then fabricated using a two-step electron-beam lithography (EBL) process. In the first EBL step, a bilayer PMMA (950/495) is spun on the base layer as the resist structure. The d-HEB cooling pad patterns are then directly written by an electron-beam controlled by the Nano-

Pattern Generation System (NPGS). The trilayer Nb/Au/Nb (10 nm/50 nm/10 nm) cooling pads are hence generated and the Nb microbridge lengths are defined after a lift-off process. During the second EBL step, the HEB bridges are first patterned by the NPGS with single layer PMMA (950). A Au/Nb (20 nm/20 nm) bilayer is deposited, and after lift-off, bridges are left spanning the cooling pads.

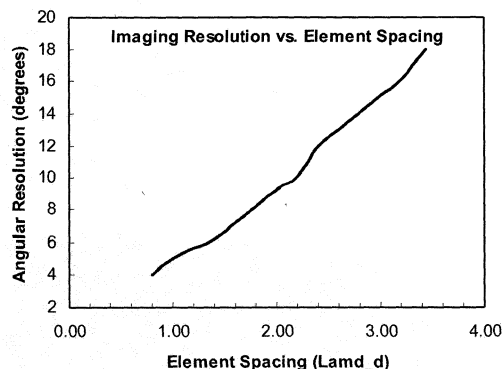


Fig. 5: Relationship between the angular imaging resolution and element spacing predicted using ray-tracing technique.

Reactive-ion etches (RIE) are then performed to remove the unwanted metal layers. First, an argon RIE is used to remove the Au capping layer. An SF_6 -based RIE is then used to etch the exposed Nb layer on top of the HEB bridges, followed by another Ar RIE to remove the other layer of Au on top of the bridge, which leaves Nb bridges between the gold cooling pads. The length of the HEB-bridge is chosen to be approximately 200 nm, a value significantly less than the inelastic electron-phonon length, resulting in a diffusion-cooled HEB device. The bridge width can be modified to produce the desired device resistance for circuit matching since the sheet resistance for 10 nm thick Nb film is known to be 30-35 Ω /square in the normal state [11].

From the ADS momentum simulation described in section II (B), the elementary SRA in the array has a self-impedance around 75 Ω . A d-HEB with such a resistance requires more than two squares of Nb thin film, hence the resulting device length may risk exceeding the diffusion cooling length. In addition, the resolution of the NPGS employed at the University of Virginia is approximately 100 nm. Decreasing the Nb bridge width will result in fabrication difficulties. Moreover, an HEB with substantial bridge width is required to reduce the susceptibility of electrostatic discharge during the measurement process. A short HEB is preferred for a receiver system to exhibit broad IF bandwidth and fast response. Thus, two impedance-matching schemes are proposed and studied to optimize power coupling from the SRA's to the mixer element. One scheme employs simple quarter-wavelength impedance transformers while the alternative approach utilizes two d-HEB's fabricated in series at the feed point of the SRA's, as shown in Fig. 6 the SEM pictures for the fabricated 1-D d-HEB mixer imaging arrays.

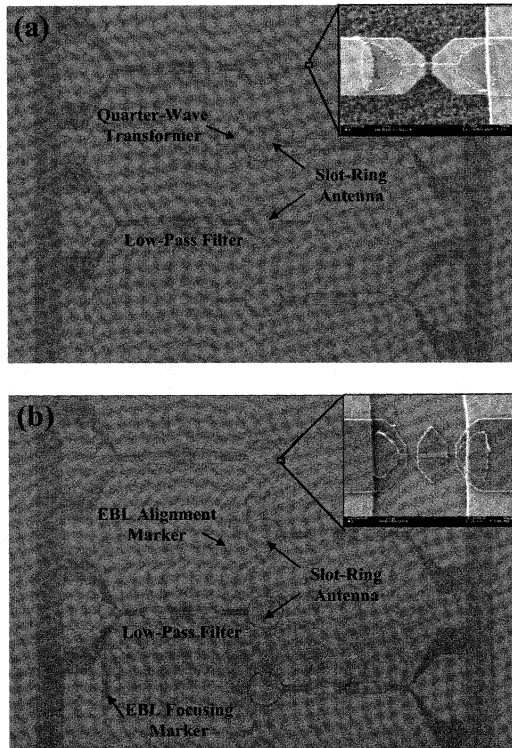


Fig. 6: SEM pictures of fabricated 1-D d-HEB mixer imaging arrays: (a) scheme-I mixer array with impedance transformers; (b) scheme-II mixer array with two HEB's in series.

IV. MEASUREMENT SETUP

A quasi-optical mixer array block has been designed as shown in Fig. 7. An IF output supporting circuit containing four CPW transmission-lines (50Ω) has been fabricated on a high-resistivity Si wafer with thickness of 1.1 mm . The HEB array chip will be mounted using cryogenic epoxy. This output supporting circuit also serves as the extension length for the SRA array and yields a total extension length of 1.6 mm . Another transmission-line circuit fabricated on a Duroid substrate with four SMA connectors is utilized to output the IF signal to bias-T's. The quasi-optical mixer block was fabricated and installed into an HD-3(8) dewar system for cryogenic tests and RF measurements. This dewar can be cooled to 4.2 K with a hold time of around 30 hours. For prototype demonstration, a commercial SP4T coaxial switch will be employed to select one IF signal from the four outputs. The selected IF signal is output to an isolator and low noise amplifier (LNA) before being fed to the external IF chain. An RF measurement system has been set up to characterize the performance of the mixer array, including the conversion gain, coupling efficiency and noise temperature. In this system, a VDI (Virginia Diodes, Inc.) 576 – 640 GHz FEM (Frequency Extension Module) is employed to provide LO power. A hot/cold load is utilized to provide blackbody radiation for a system Y-factor measurement. Both the LO and RF are

coupled into the cryogenic dewar through a set of lenses and mirrors. Imaging experiments will be performed with this system to evaluate its performance at 585 GHz

V. CONCLUSION

A 585 GHz one-dimensional slot-ring antenna (SRA) coupled d-HEB imaging mixer arrays (four pixels) based on the “reverse-microscope” concept has been designed and fabricated. ADS momentum simulations have been performed to study the self- and mutual- impedances of the SRA array with various element spacings. The element SRA off-axis radiation patterns (with silicon lens) have been calculated using ray-tracing techniques and the imaging angular resolution has been predicted. Fabrication and measurement systems are discussed.

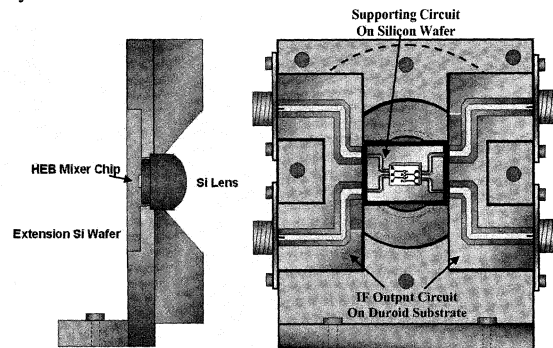


Fig. 7: Schematic drawing of the designed 1-D d-HEB mixer imaging array quasi-optical block.

REFERENCES

- [1] D. W. Floet, “Hotspot Mixing in THz Niobium Superconducting Hot Electron Bolometer Mixers,” *Ph.D. Dissertation*, Delft University of Technology, September, 2001.
- [2] D. Mittleman, M. Gupta, R. Neelamani, R. Baraniuk, J. Rudd, and M. Koch, “Recent advances in terahertz imaging,” *Appl. Physics B*, vol. 68, pp. 1085-1094, 1999.
- [3] D. B. Rutledge, and M. S. Muha, “Imaging Antenna Arrays,” *IEEE Trans. Antennas and Propagation*, vol. AP-30, no. 4, July 1982.
- [4] http://tempest.das.ucdavis.edu/mmwave/Antenna_array_New/
- [5] G. Chattopadhyay, I. Mehdi, J. S. Ward, E. Schlecht, A. Skalare, and P. H. Siegel, “Development of Multi-Pixel Heterodyne Array Instruments at Submillimeter Wavelengths,” *APMC*, 2004.
- [6] K. S. Yngvesson, et. al., “New results On THz HEB low-noise receivers and focal plane arrays,” *SPIE* 2000.
- [7] F. Rodriguez-Morales, K. S. Yngvesson, et. al., “A Terahertz Focal Plane Array Using HEB Superconducting Mixers and MMIC IF Amplifiers,” *IEEE Microwave and Wireless Components Letters*, vol. 15, no. 4, Apr. 2005.
- [8] L. Liu, R. M. Weikle, II, A. W. Lichtenberger, A. Isin, B. S. Deaver, Jr., “A 585 GHz of Diffusion-Cooled Nb HEB Mixers Element for Imaging Applications,” *16th ISSIT*, Geteborg, Sweden, May 2005.
- [9] Daniel F. Filipovic, Steven S. Gearhart, and Gabriel M. Rebeiz, “Double-slot antennas on extended hemispherical and elliptical silicon dielectric lenses,” *IEEE Trans. Microwave Theory Tech.*, vol. 41, no. 10, Oct. 1993.
- [10] L. Liu, R. M. Weikle, II, “EMF Analysis of Slot-Ring Antennas and Arrays,” to be published.
- [11] R. B. Bass, “Hot-electron bolometers on ultra-thin silicon chips with beam leads for a 585 GHz receiver,” *Ph.D. dissertation*, University of Virginia, May 2004.

Two-Dimensional Terahertz Imaging System Using Hot Electron Bolometer Technology*

Dazhen Gu, Eyal Gerecht, Fernando Rodriguez-Morales, and Sigfrid Yngvesson

Abstract—We present first results with a two-dimensional (2D) scanning terahertz passive heterodyne imaging system, currently under development. The imager is based on a phonon-cooled quasi-optically coupled hot electron bolometric (HEB) mixer integrated with an InP MMIC IF low-noise amplifier (LNA). A harmonic multiplier with an output power of about 250 μ W is employed as the local oscillator (LO) source, resulting in a very compact setup. Terahertz images are obtained by scanning the target with a flat mirror mounted on a computer-controlled elevation/azimuth translator. The receiver is designed to operate at 850 GHz, but can in principle operate at any terahertz frequency. We produced full 2D imagery of different objects. The demonstrated overall sensitivity of the imager in terms of a figure of merit NEAT is better than 0.5 K. We are working on extending the system into a multi-pixel array configuration for faster scanning rates and improved spatial resolution.

Index Terms— Hot electron bolometer, quasi-optical systems, terahertz imaging, terahertz receivers, twin-slot antennas.

I. INTRODUCTION

TERAHERTZ radiation (T-rays) can penetrate cloth, dust, and smoke better than infrared and visible light. The shorter wavelengths of T-rays allow for higher spatial resolution compared with that of microwaves or millimeter waves. This has opened the field to applications such as remote sensing and detection of concealed weapons and illicit drugs. Furthermore, the partial ability of terahertz radiation to penetrate biological materials offers excellent opportunities for imaging and spectroscopy appealed to healthcare.

In order to realize a passive terahertz imaging system with high sensitivity and a real video acquisition rate, we need to use multi-pixel arrays in which each detection element provides sensitivities near the quantum noise limit. Receivers based on hot electron bolometric (HEB) mixers have demonstrated near quantum-limited noise performance [1]. Moreover, the local oscillator (LO) power requirement of HEB mixers is about four orders of magnitude lower than that of Schottky barrier diode

(SBD) mixers. Maintaining a low LO power consumption is a major challenge in the development of multi-pixel focal plane arrays (FPAs) at terahertz frequencies. This is due to the difficulties encountered in producing high power at terahertz frequencies.

The feasibility of the passive detection technique presented here relies on the fact that all objects, whose temperatures are above absolute zero (0 K), emit terahertz radiation. Their actual emission is related to the black-body radiation by a wavelength dependent emissivity, which is specific to the material in question. In other words, all objects behave like grey-body emitters with respect to the ideal black-body. By using ultra sensitive HEB detectors, an imaging system can potentially distinguish between different materials in thermal equilibrium. We chose 850 GHz as the operating frequency for our system, as it is one of the atmospheric windows for terahertz radiation and it gives relatively high spatial resolution for this application.

In this paper, we present progress in the development of a two-dimensional passive imaging system operating at 850 GHz. The system is based on an integrated HEB/MMIC heterodyne receiver [2] with a solid state multiplier source used as the LO. We describe our design considerations, discuss recent experimental results, and present the challenges involved in future development of the next-generation terahertz imagers.

II. DESCRIPTION OF THE IMAGING SYSTEM

Fig. 1 shows a schematic of the terahertz passive imager we are developing. The scanning of the signal beam produced by the target is accomplished by use of a flat mirror mounted on a custom-designed translation unit. The receiver collects radiation from the scanned object in both the elevation and azimuth directions. This signal beam is chopped at 23 Hz against a room temperature black-body source. The LO and the signal beams are coupled to the HEB mixer through optical components, such as off-axis parabolic mirrors and a thin mylar beam-splitter. The intermediate frequency (IF) output signal is amplified using a cryogenic low-noise amplifier (LNA) cascaded with a back-end IF chain of tunable gain and bandwidth, operating at room temperature. The IF bandwidth of the receiver is limited by means of a band pass filter, which is, in turn, connected to a standard microwave detector to produce a rectified voltage signal. This signal is then fed to a

*Work partially supported by U.S. Government; not protected by U.S. copyright.

D. Gu and E. Gerecht are with the National Institute of Standards and Technology, Boulder, CO 80305 USA (phone: 303-497-3939; fax: 303-497-3970; e-mail: dazhen.gu@boulder.nist.gov).

F. Rodriguez-Morales and S. Yngvesson are with the Electrical and Computer Engineering Department, University of Massachusetts, Amherst, MA 01003 USA.

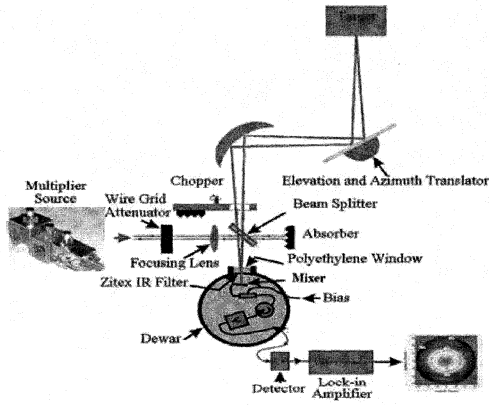


Fig. 1. A schematic of a two-dimensional terahertz passive imaging system.

lock-in amplifier referenced by the chopping frequency. A dedicated data acquisition (DAQ) system collects the lock-in amplifier's output signal as a function of position with respect to the target.

A. Quasi-optical coupling

In order to effectively couple the incoming radiations onto the HEB mixer, we have designed a quasi-optical system consisting of a silicon lens and a monolithic antenna centered at 850 GHz, shown in Fig. 2. The twin-slot antenna is patterned on a silicon substrate by using electron-beam metallization followed by a lift-off step. The HEB device, made of an ultra thin NbN film, with dimensions of 2 μm wide by 0.5 μm long, is fabricated between the terminals of the twin-slot antenna.

The twin-slot antenna has a highly symmetrical and linearly polarized radiation pattern and provides nearly perfect power coupling to the incident Gaussian beam [3]. The radiation pattern can be calculated by using the first excited modes and the electromagnetic field distribution inside the slots. The far-field pattern is then derived as:

$$E_{\theta}(\theta, \varphi) \sim M(\theta, \varphi) \cdot \sin \varphi \tag{1}$$

$$E_{\varphi}(\theta, \varphi) \sim M(\theta, \varphi) \cdot \cos \theta \cdot \cos \varphi, \tag{2}$$

where

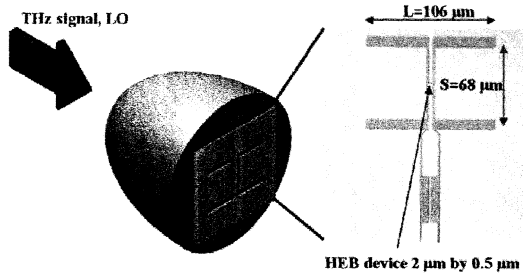


Fig. 2. Illustration of a quasi-optical system and a twin-slot antenna photograph.

$$M(\theta, \varphi) = \frac{\left[\cos\left(\frac{L}{2} k_d \sin \theta \cos \varphi\right) - \cos\left(\frac{L}{2} k_m\right) \right] \cos\left(\frac{k_d}{2} S \sin \theta \sin \varphi\right)}{k_m^2 - k_d^2 \sin^2 \theta \cos^2 \varphi}$$

and L and S are the length and separation of the twin slots, respectively, $k_d = 2\pi/\lambda_d$ is the wave-number at the dielectric side, and $k_m = 2\pi/\lambda_m$ is the effective wave-number at the vacuum/dielectric interface. The simulated radiation pattern is shown in Fig. 3. Evidently, most of the radiation propagates into the dielectric side.

The silicon lens is a rotational ellipsoid that functions as an aperture antenna, and hence reshapes the far-field radiation pattern. By using a ray-tracing technique, one can show that the radiation from the twin slot antenna, placed at the second focus of the lens, becomes a plane wave in the aperture plane outside the lens. By considering the combination of the silicon lens and the twin-slot antenna, one can show that the far-field beam has a full-width half-power (FWHP) width of about 3 degrees.

B. LO source

The available choices of LO sources at terahertz frequencies include far-infrared (FIR) lasers, quantum cascade lasers (QCLs) in the higher terahertz spectrum, and harmonic multiplier sources in the lower terahertz spectrum. We have chosen a harmonic multiplier source as the LO because of its compact size and ease of use.

A commercially available 850 GHz harmonic multiplier source [4] is employed as the LO signal. A phase-locked oscillator generates an output signal at 11.8 GHz. This signal is used to drive a multiplier chain, which is composed of one amplifier, two triplers, and three doublers. The entire chain produces a total of $2^3 \times 3^2 = 72$ times frequency multiplication, resulting in an output signal of $11.8 \times 72 \approx 850$ GHz. The terahertz signal injection is then achieved by using a WR 1.2 diagonal horn module assembled at the end of the multiplier chain. This particular harmonic multiplier source can produce an output power of up to about 250 μW.

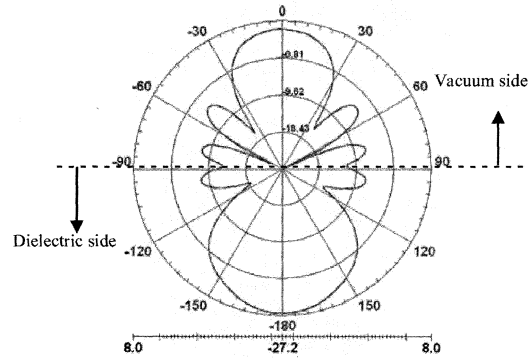


Fig. 3. Simulated radiation pattern of the 850 GHz twin-slot antenna on a silicon substrate.

C. Integrated receiver block

In a typical receiver system, the mixer and the LNA are assembled in separate blocks and connected by coaxial cables. An isolator is often included between the mixer and the LNA in order to minimize the standing wave between them. Although this configuration has been widely adopted in astrophysical receiver systems [5] [6], it does not meet the requirement for a compact multi-pixel FPA. Furthermore, the use of isolators limits the IF bandwidth to no more than an octave.

In order to eliminate the use of isolators, we have accomplished a design for integrating the HEB device and the MMIC LNA in the same block. A multi-section microstrip matching network is employed to achieve broadband coupling between the HEB and the MMIC LNA. The HEB device is located in close proximity to the MMIC chip, which is mounted in a narrow rectangular cavity for purpose of eliminating possible amplifier oscillations [2]. This particular MMIC LNA has been characterized against standards developed at the National Institute of Standards and Technology (NIST) and with a recently developed measurement technique [7], exhibits noise performance of below 5.5 K from 1 GHz to 11 GHz and a minimum of 2.3 K at 7 GHz. Fig. 4 is a photograph of the HEB/MMIC integrated mixer block.

D. Beam scan and data acquisition

A scanning scheme was designed to record the image of the target by means of a line-by-line sweep, often called a raster scan. Each line of the scan is divided into a number of pixels. The number of pixels and the distance between pixels can be adjusted according to the desired resolution and the size of the target.

The total wait period at each pixel is based on the lock-in integration time constant. In order to achieve fast scanning and stability of the signal, the wait period is made ten times longer than the lock-in time constant.

An automated motion controller, which also functions as a DAQ system, is used to drive the translator and collect the data in real-time. The motion controller provides a 0.001 degree angular resolution and can gather data with 14 bit accuracy ($\pm 600 \mu\text{V}$ on a $\pm 10 \text{ V}$ scale) at rates up to 10 kHz. The motion

controller has a built-in Pentium processor and is capable of communicating with a user PC via Ethernet protocol.

III. RESULTS AND DISCUSSION

Our terahertz system was used to take images of various objects. Fig. 5 shows an example of two room temperature objects forming a cross suspended over an absorber immersed in liquid nitrogen. The temperature difference (of about 200 K) can be clearly distinguished by the color contrast.

The HEB receiver in our imaging system has a noise temperature of 2200 K. This is not the most sensitive HEB mixer we have produced [1]. The integration time constant on the lock-in amplifier was 300 ms, which integrates 7 periods of the chopping frequency (23 Hz). The IF bandpass filter, with a center frequency of 2.35 GHz and a bandwidth of 2.3 GHz, ensures the best overall performance in terms of low noise and widest bandwidth. We can enhance the spatial resolution of the image by minimizing the beam waist on the target. In our case, we had a beam waist of about 3.6 mm. The DAQ system allows for ten periods of the lock-in amplifier time constant (3 s) at each pixel, resulting in about 90 minutes total to complete a scan of a 40 by 40 pixel image.

For our imager, the RMS fluctuation in the measured radiation temperature can be obtained according to the radiometer formula,

$$\Delta T_{RMS} = \frac{2T_{sys}}{\sqrt{B \cdot \tau}} = \frac{2 \times (2200 + 300)}{\sqrt{2.3 \times 10^9 \times 0.3}} \approx 0.2 \text{ K}, \quad (3)$$

where T_{sys} is the system noise temperature, B is the receiver bandwidth, and τ is the integration time. ΔT_{RMS} is the figure of merit to evaluate the thermal resolution of passive imaging systems. This figure of merit is also known as NE ΔT . In our case, the imaging system can theoretically resolve a temperature difference as small as 0.2 K. The system temperature can be decreased to 1000 K with optimum HEB detectors, while the bandwidth may be increased to at least 3 GHz, resulting in NE ΔT =37 mK, normalized to a 1 s integration time. The best published results for a direct detector passive imaging system translates to NE ΔT = 700 mK [8]. Presently, heterodyne systems are more sensitive by a factor of 20. Laboratory results for a direct detector [9] indicate

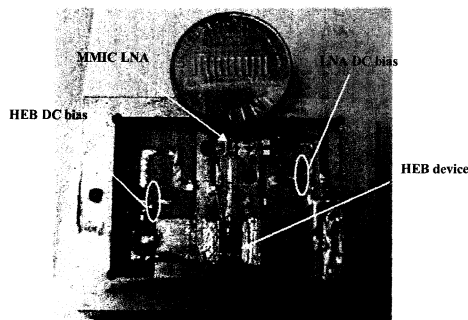


Fig. 4. An integrated mixer block housing an HEB device and an MMIC LNA.

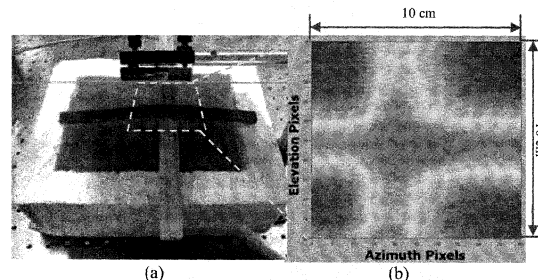


Fig. 5. (a) Photograph and (b) a 850 GHz image of two room temperature objects suspended over an absorber immersed in liquid nitrogen. Red corresponds to warm temperatures and blue corresponds to cold temperatures (about 200 K difference).

improved sensitivity but this direct detector is a long way from system realization.

A target made of a resistor coil in front of a room temperature absorber was used to measure the thermal resolution of our imaging system (Fig. 6). The temperature difference between the resistor coil and the absorber can be adjusted by changing the voltage across the resistor. Images at 850 GHz were taken for two different temperature differences: 35 K and 3 K. The hot spot corresponding to the warm coil for the 35 K temperature difference is clearly observed from Fig. 6b. For the 3 K case (Fig. 6c), the image became somewhat blurred. By using image post-processing based on a de-speckle algorithm, the image can be enhanced (see Fig. 6d). From the 3 K case we can estimate an actual $NE\Delta T = 0.5$ K for the present system.

IV. SUMMARY AND FUTURE PLANS

We have developed a two-dimensional passive terahertz imaging system operating at 850 GHz based on HEB technology. Preliminary results give evidence of a high thermal resolution (about 0.5 K). The detection speed can be increased by employing a faster chopper. The next step for increasing system speed will be to use an FPA. A prototype FPA containing three elements based on HEB mixers and MMIC LNAs has already been demonstrated [10].

Fig. 7 shows a conceptual architecture for future large FPAs using multiple HEB detectors. The lenses and the HEB devices will be arranged in a fly's eye configuration. Such a configuration can produce an angular resolution slightly larger than one diffraction-limited beamwidth. IF amplifiers and DC circuitry will be assembled on separate boards, connected to the

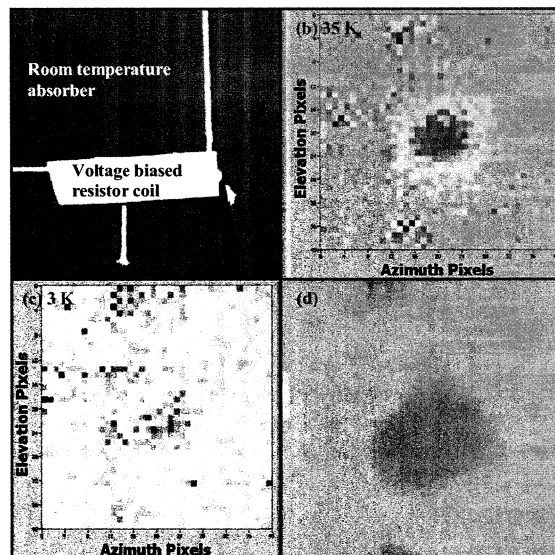


Fig. 6. (a) photograph of the resistor coil and the absorber; (b) image of 35 K difference; (c) image of 3 K difference; (d) the same 3 K difference image after post-processing.

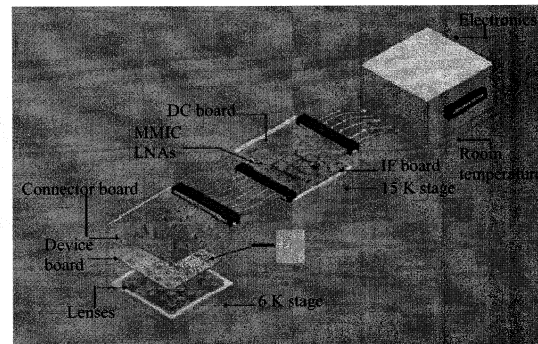


Fig. 7. A conceptual architecture for a terahertz FPA with multi pixels using HEB/MMIC technology.

HEB devices through kapton ribbon transmission lines. We expect that this new architecture, combined with MEMS micro-cryocooler technology, currently under development, will potentially be able to produce an extremely compact system for mobile terahertz imagers with video-rate speeds. Potential applications for these receivers range from medical diagnostics to security surveillance.

ACKNOWLEDGMENT

This work was supported by the National Institute of Standards and Technology in Boulder, CO.

REFERENCES

- [1] E. Gerecht, C. Musante, Y. Zhuang, K. Yngvesson, T. Goyette, J. Dickinson, et al, "NbN Hot Electron Bolometric Mixers, a New Technology for Low-Noise THz Receivers," IEEE Trans. Microw. Theory Tech., vol. 47, no. 12, pp. 2519–2527, Dec. 1999.
- [2] F. Rodriguez-Morales, S. Yngvesson, R. Zannoni, E. Gerecht, D. Gu, N. Wadefalk, and J. Nicholson, "Development of Integrated HEB/MMIC Receivers for Near-Range Terahertz Imaging," IEEE Trans. Microw. Theory Tech. vol. 54, no. 6, Jun. 2006.
- [3] D. F. Filipovic, S. S. Gearhart, and G. M. Rebeiz, "Double-Slot Antenna on Extended Hemispherical and Elliptical Silicon Dielectric Lenses," IEEE Trans. Microw. Theory Tech., vol. 41, no. 10, pp. 1738–1749, Oct. 1993.
- [4] Virginia Diodes, Inc, <http://www.virginiadiodes.com/multipliers.htm>
- [5] E. Gerecht, S. Yngvesson, J. Nicholson, Y. Zhuang, F. Rodriguez-Morales, X. Zhao, et al, "Deployment of TREND A Low Noise Receiver User Instrument at 1.25 THz to 1.5 THz for AST/RO at the South Pole," in Proc. 14th Int. Space Terahertz Technology Symp., Tucson, Az, Apr. 2003.
- [6] S. Cherednichenko, M. Kroug, H. Merkel, P. Khosropanah, A. Adam, E. Kollberg, et al, "1.6 THz heterodyne receiver for the far infrared spacetlescope." Physica C, vol. 372–376, pp. 427–431, 2002.
- [7] J. Randa, E. Gerecht, D. Gu, and R. Billinger, "Precision Measurement Method for Cryogenic Amplifier Noise Temperatures Below 5 K," IEEE Trans. Microw. Theory Tech., vol. 54, no. 3, pp. 1180–1189, Mar. 2006.
- [8] A. Luukanen, A. J. Miller, and E. N. Grossman, "Passive hyperspectral terahertz imagery for security screening using a cryogenic microbolometer," in Proc. SPIE Vol. 5879, 2004
- [9] A. Luukanen and J. P. Pekola, "A superconducting antenna-coupled hotspot microbolometer," Applied Physics Letters, vol. 82, pp. 3970–3972, Jun. 2003.
- [10] F. Rodriguez-Morales, K. S. Yngvesson, E. Gerecht, N. Wadefalk, J. Nicholson, D. Gu, et al, "A Terahertz Focal Plane Array Using HEB Superconducting Mixers and MMIC IF Amplifiers," IEEE Microw. Wireless Comp. Lett., vol. 15, no. 4, pp. 199–201, Apr. 2005.

SuperCam : A 64 pixel superheterodyne camera

Christopher Groppi¹, Christopher Walker¹, Craig Kulesa¹, Dathon Golish¹, Patrick Pütz^{1,6}, Paul Gensheimer¹, Abby Hedden¹, Shane Bussmann¹, Sander Weinreb^{2,3}, Niklas Wadefalk³, Glenn Jones³, Joseph Barden³, Hamdi Mani³, Tom Kuiper², Jacob Kooi³, Art Lichtenberger⁴, Gopal Narayanan⁵

1: University of Arizona, 2: NASA Jet Propulsion Laboratory, 3: California Institute of Technology, 4: University of Virginia, 5: University of Massachusetts, 6: Universität Zu Köln

Abstract—We report on the development of *SuperCam*, a 64 pixel, superheterodyne camera designed for operation in the astrophysically important 870 μm atmospheric window. *SuperCam* will be used to answer fundamental questions about the physics and chemistry of molecular clouds in the Galaxy and their direct relation to star and planet formation. The advent of such a system will provide an order of magnitude increase in mapping speed over what is now available and revolutionize how observational astronomy is performed in this important wavelength regime. Unlike bolometric detectors, heterodyne receiver systems are coherent, retaining information about both the amplitude and phase of the incident photon stream. From this information a high resolution spectrum of the incident light can be obtained without multiplexing. *SuperCam* will be constructed by stacking eight, 1x8 rows of tunerless, SIS mixers. The IF output of each mixer will be connected to a low-noise, broadband MMIC amplifier integrated into the mixer block. The instantaneous IF bandwidth of each pixel will be ~ 2 GHz, with a center frequency of 5 GHz. A spectrum of the central 500 MHz of each IF band will be provided by the array spectrometer. Local oscillator power is provided by a frequency multiplier whose output is divided between the pixels by using a matrix of waveguide power dividers. The mixer array will be cooled to 4K by a closed-cycle refrigeration system. *SuperCam* will reside at the Cassegrain focus of the 10m Heinrich Hertz telescope (HHT) with a dedicated re-imaging optics system. We report on single pixel integrated LNA testing, cryogenic system testing, performance of the prototype backend spectrometer module, and the fabrication of the first 1x8 array module. This module will be tested on the HHT in 2006, with the first engineering run of the full array in late 2007. The array is designed and constructed so that it may be readily scaled to higher frequencies.

Index Terms—Submillimeter heterodyne array

I. INTRODUCTION

SuperCam will operate in the astrophysically rich 870 μm atmospheric window, where the HHT has the highest aperture efficiency of any submillimeter telescope in the world and excellent atmospheric transmission more than 40% of the time. The proposed Superheterodyne Camera (*SuperCam*) will be an 8x8, integrated receiver array fabricated using leading-edge mixer, local oscillator, low-noise amplifier, cryogenic, and digital signal processing

technologies.

SuperCam will be several times larger than any existing spectroscopic imaging array at submillimeter wavelengths. The exceptional mapping speed that will result, combined with the efficiency and angular resolution achievable with the HHT, will make *SuperCam* the most uniquely-powerful instrument for probing the history of star formation in our Galaxy and the distant Universe. *SuperCam* will be used to answer fundamental questions about the physics and chemistry of molecular clouds in the Galaxy and their direct relation to star and planet formation. Through Galactic surveys, particularly in CO and its isotopomers, the impact of Galactic environment on these phenomena will be realized. These studies will serve as “finder charts” for future focused research (e.g. with ALMA) and markedly improve the interpretation, and enhance the value of numerous contemporary surveys.

II. SUPERCAM SCIENCE

From the Milky Way to the highest-redshift protogalaxies at the onset of galaxy formation, the internal evolution of galaxies is defined by three principal ingredients that closely relate to their interstellar contents:

- The transformation of neutral, molecular gas clouds into stars and star clusters (star formation).
- the interaction of the interstellar medium (ISM) with the young stars that are born from it, a regulator of further star formation.
- the return of enriched stellar material to the ISM by stellar death, eventually to form future generations of stars.

The evolution of (the stellar population of) galaxies is therefore determined to a large extent by the life cycles of interstellar clouds: their creation, starforming properties, and subsequent destruction by the nascent stars they spawn. The life cycle of interstellar clouds is summarized pictorially in Figure 1. Although these clouds are largely comprised of neutral hydrogen in both atomic and molecular form and atomic helium, these species are notoriously difficult to detect under typical interstellar conditions. Atomic hydrogen is detectable in cold clouds via the 21 cm spin-flip transition at 1420 MHz, but because the emission

line is insensitive to gas density, cold ($T \sim 70\text{K}$) atomic clouds are not distinguishable from the warm ($T \sim 8000\text{K}$) neutral medium that pervades the Galaxy. Furthermore, neither atomic helium nor molecular hydrogen (H_2) have accessible emission line spectra in the prevailing physical conditions in cold interstellar clouds. Thus, it is generally necessary to probe the nature of the ISM via rarer trace elements. Carbon, for example, is found in ionized form (C^+) in neutral HI clouds, eventually becoming atomic (C), then molecular as carbon monoxide (CO) in dark molecular clouds. The dominant ionization state(s) of carbon accompany each stage of a cloud's life in Figure 1. In general, however, only global properties can be gleaned from the coarse spatial resolution offered by studies of external galaxies. Therefore detailed interstellar studies of the widely varying conditions in our own Milky Way Galaxy serve as a crucial diagnostic template or "Rosetta Stone" that can be used to translate the global properties of distant galaxies into reliable estimators of star formation rate and state of the ISM.

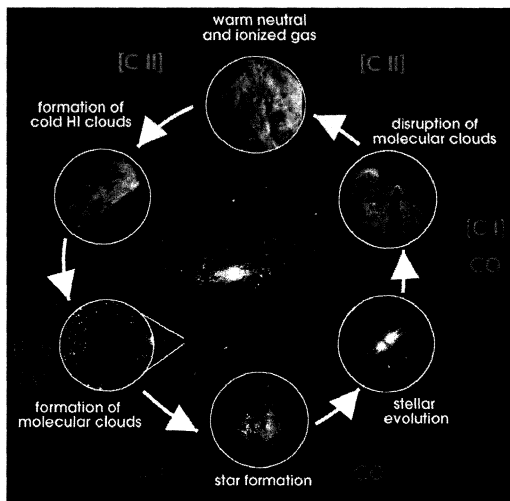


Figure 1: Life cycle of the ISM

III. SUPERCAM INSTRUMENT DESCRIPTION

A. Instrument Design

Unlike all other millimeter/submillimeter arrays composed of individual mixers and discrete components, SuperCam has a high degree of integration. Well conceived, efficient packaging is essential to the successful implementation of large format systems. The enormous complexity of even a small discrete system suggests a more integrated approach for larger systems. At the heart of the array is an 8×8 integrated array of low-noise mixers. The array mixer contains first stage, low-noise, MMIC IF amplifier modules with integrated bias tees. A single solid-state source provides local oscillator power to each array mixer via a waveguide corporate power divider and a simple Mylar diplexer. Below we discuss SuperCam's key components.

1) Cryogenics

The SuperCam cryostat is shown in Figure 2. Light from

the telescope enters the cryostat through a 127 mm diameter AR coated, crystalline quartz vacuum window and passes through an IR blocking filter on the 40 K radiation shield before illuminating the 4 K mixer array. SuperCam uses a Sumitomo SRDK-415D cryocooler. The cooler has 1.5 W of thermal capacity at 4.2 K and 45W at 40K with orientation-independent operation. The operating temperature of the cryocooler is stabilized by the addition of a helium gas pot on the 2nd stage. A CTI cryogenics CTI-350 coldhead supplements the cooling of the 40K shield, and provides 12K heatsinking for the 64 stainless steel semi-rigid IF cables. The addition of this second coldhead permits the use of moderate lengths of standard coaxial cable while maintaining low heat load at 4K. Calculations indicate the SRDK-415D load capacity is sufficient to cool the mixers, magnets, and amplifiers to the proper operating temperatures. The cryostat was constructed by Universal Cryogenics in Tucson, Arizona, USA. Cryogenic load testing using heaters at all temperature stages have verified that both the cryocoolers meet their rated load specifications. The cooling capacity is adequate given the expected heat loading from the DC wiring, semi-rigid cable,

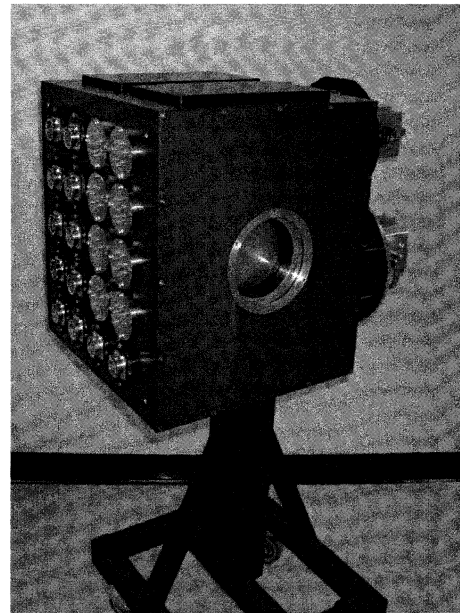


Figure 2: The SuperCam cryostat

amplifiers and magnets, with an expected load capacity margin of $\sim 50\%$.

2) Mixer Array

We are developing a compact, sensitive, 64 pixel array of SIS mixers optimized for operation in the 320-360 GHz atmospheric window. The two dimensional, 8×8 array will be composed of eight, 1×8 subarrays. The array mixers will utilize SIS devices fabricated on Silicon-On-Insulator (SOI) substrates, with beam lead supports and electrical contacts. The waveguide probe and SIS junction are based on an asymmetric probe design currently in use at the Caltech Submillimeter Observatory in their new facility 350 GHz receiver. The measured DSB noise temperature of this

receiver (40 K) is excellent and essentially frequency independent across the band. The 1x8 mixer subarrays will be constructed from tellurium copper using the splitblock technique. Stainless steel guide pins and screws are used to ensure proper alignment and good contact between parts. Figure 3 is a pictorial representation of one mixer in a 1x8 subarray. A low-loss, dielectric lens couples energy from the telescope into a diagonal feedhorn. The energy in the horn passes through a 90° waveguide bend before reaching the impedance transformer to full height rectangular waveguide. The SIS device is suspended above the suspended stripline channel via four small beamlead supports. Both the hot and ground beamleads are tack-bonded with a wirebonder to the MMIC module input pad and block, respectively. The mixer blocks will be fabricated at the University of Arizona using a Kern MMP micromilling machine purchased for this project. This numerically controlled mill can fabricate structures to micron accuracy with a high level of automation.

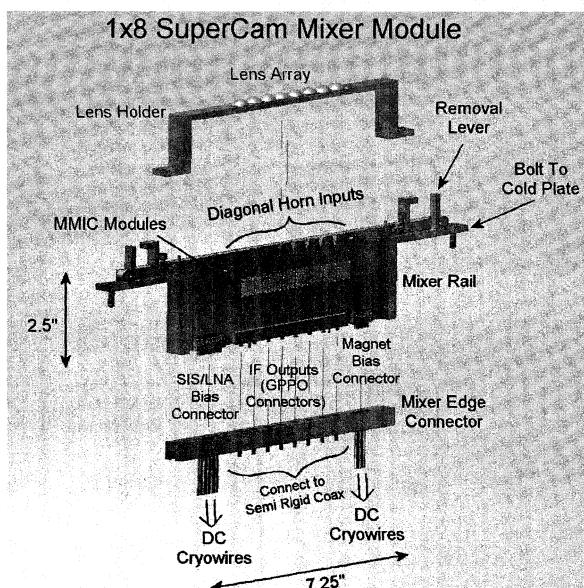


Figure 3: Assembly diagram of a single mixer module.

3) Local Oscillator

With an array receiver, LO power must be efficiently distributed among pixels. Depending on the mechanical and optical constraints of the array, a balanced distribution can be achieved using quasioptical techniques or waveguide injection. With the quasioptical approach, dielectric beam splitters or holographic phase gratings are used to divide the LO energy between array pixels. The quasioptical approach works well for modest sized arrays. However, for the large format system being proposed here, the size of the required quasi-optical power splitter and diplexer become prohibitive. Therefore we have chosen to use a hybrid waveguide/quasioptical LO power injection scheme. The LO power for the array will be provided by a single solid-state, synthesizer-driven source available from Virginia Diode Inc. The active multiplier chain consists of a high power solid-state amplifier followed by a series of tunerless broadband multipliers. The output of the multiplier is

coupled to an eight-way waveguide corporate power divider with splitblock machineable waveguide twists. Each of the eight outputs provides the drive power for a 1x8 subarray via an identical 8 way corporate divider with diagonal waveguide feedhorn outputs. A lens array similar to the mixer lens system then matches the LO beams to the mixers through a simple Mylar beamsplitter diplexer. This scheme ensures uniform LO power in each beam since the waveguide path lengths are identical for each beam. In addition, the waveguide feedhorns and lenses provide well controlled and predictable LO power distribution and coupling to each mixer. Accounting for conduction and surface roughness losses, we expect this 64-way network to add an additional 2dB of LO power loss compared to a lossless divider.

4) IF/Bias Distribution System

The IF outputs from the SIS devices are bonded directly to the input matching networks of low-noise, InP MMIC amplifier modules located in the array mixers. These amplifier modules have been designed and fabricated by Sander Weinreb's group at Caltech. The IF center frequency of the array is 5 GHz. The MMIC chip is contained in an 11mm x 11mm amplifier module that contains integrated bias tees for the SIS device and the amplifier chip. The module achieves noise temperature of ~5 K consuming 8 mW of power at 4K. The first 10 amplifier modules are complete. An example is shown in figure 4, with measured gain and noise data at 8 mW power dissipation. We have integrated an amplifier module into a single pixel SIS mixer and have verified that the amplifier module operates as expected. Allan variance times and mixer noise temperatures are unchanged within the measurement errors compared to a similar mixer used with an external commercial LNA and cryogenic isolator.

5) Array Spectrometer

The SuperCam spectrometer will deliver 64 channels at 512 MHz/channel with 125 kHz resolution, or 32 channels at 1 GHz with 250 kHz resolution. The system will be capable of resolving lines in the coldest clouds, while fully encompassing the Galactic rotation curve. Operated in 32 pixel mode with 1 GHz (880 km/s) of bandwidth, extragalactic studies are enabled. This leap in spectrometer ability is driven by the rapid expansion in the capabilities of high speed Analog to Digital Converters (ADCs) and Field Programmable Gate Arrays (FPGAs). The SuperCam spectrometer, to be provided by Omnisys AB of Sweden, is based on a real-time FFT architecture. High speed ADCs digitize the incoming RF signal at greater than 10 bits resolution, preventing any significant data loss as with autocorrelation based schemes. Then, large, high speed FPGAs perform a real time FFT on the digitized signal and integrate the incoming signal. Only recently has Xilinx released FPGAs fast enough and large enough to accommodate the firmware capable of this task. These systems are fully reconfigurable by loading new firmware into the FPGAs. In addition, the spectrometer can be easily expanded to increase bandwidth. We will receive 16 boards capable of processing 64x512 MHz or 32x1 GHz.

6) Optics

The existing secondary mirror of the Heinrich Hertz

Telescope provides a $f/13.8$ beam at the Nasmyth focus. The clear aperture available through the elevation bearing prevents the possibility of a large format array at this

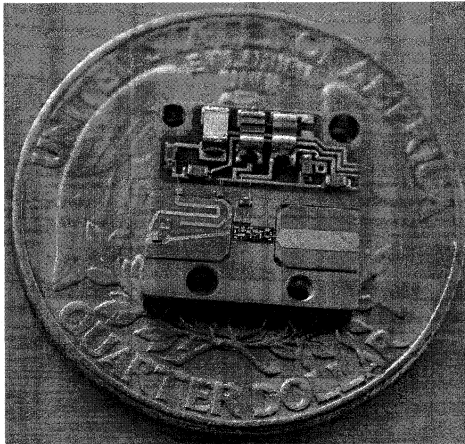
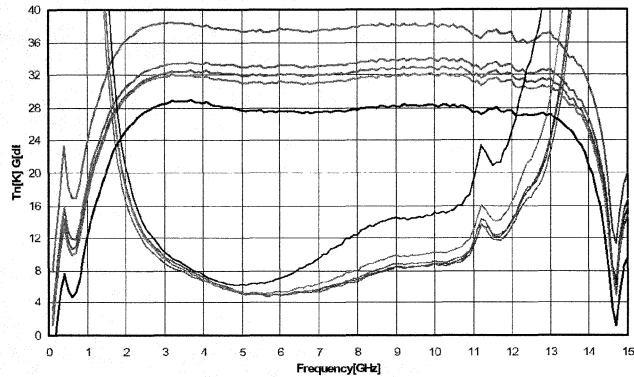


Figure 4: A SuperCam MMIC amplifier module, and typical measured results at 13K bath temperature for several bias points. Amplifier noise remains low for bias powers as low as 8 mW. Gain remains above 30 dB.

SuperCam LNA #SC09 at 13K

MMIC WBA13 RBC2MM CIT1 4254-065
MARCH13-2006

Bias Points:
Vb=1V Id=20mA Vg=2.2V
Vb=1V Id=10mA Vg=1.8V
Vb=0.8V Id=10mA Vg=1.9V
Vb=0.8V Id=10mA Vg=2.05V
Vb=0.6V Id=10mA Vg=2.2V



position. To efficiently illuminate a large format array like SuperCam, the telescope focus must fall within the apex room located just behind the primary. A system of re-imaging optics transforms the f number of the telescope to $f/5$. Since the physical separation between array elements in the instrument focal plane scales as $2f\lambda$, lower $f/\#$'s serve to reduce the overall size of the instrument. The reimaging optics are composed of a hyperbola and an ellipse with two flat mirrors. All the reimaging optics can be mounted on a single optical breadboard and left in the apex room. The cryostat and optics frame have been designed using finite element analysis to minimize gravitational deflection, and the calculated deflections have been fed into the tolerancing of the optical design. The optical system was initially designed and optimized with Zemax, and was then verified by BRO research using their ASAP physical optics package. The system's efficiency exceeds 80% for all pixels, and has been verified to be robust to alignment and fabrication tolerances.

IV. CONCLUSION

We are constructing SuperCam, a 64-pixel heterodyne imaging spectrometer for the 870 micron atmospheric window. A key project for this instrument is a fully sampled Galactic plane survey covering over 500 square degrees of the Galactic plane and molecular cloud complexes. This $^{12}\text{CO}(3-2)$ and $^{13}\text{CO}(3-2)$ survey has the spatial ($23''$) and spectral (0.25 km/s) resolution to disentangle the complex spatial and velocity structure of the Galaxy along each line of sight. SuperCam was designed to complete this survey in two observing seasons at the Heinrich Hertz Telescope, a project that would take a typical single pixel receiver system 6 years of continuous observing to complete. Prototypes of all major components have been completed or are being fabricated now. The first 1×8 mixer row will be integrated and tested in 2006, and the full array will be populated and tested in 2007. We expect first light observations in winter 2007.

REFERENCES

- [1] R.B. Bass, J.C. Schultz, A.W. Lichtenberger (University of Virginia); C. Walker (University of Arizona); J. Kooi (CalTech), "Beam Lead Fabrication Using Vacuum Planarization", submitted to Proceedings of the Fourteenth International Symposium on Space THz Technology, May 2003.
- [2] Carpenter, J. M., Snell, R. L., & Schloerb, F. P. 1995, "Star Formation in the Gemini OB1 Molecular Cloud Complex", *ApJ*, 450, 201
- [3] Dame, T. M. et al. 1987, "A composite CO survey of the entire Milky Way", *ApJ*, 322, 706
- [4] Dame, T. M., Hartmann, D., & Thaddeus, P. 2001, "The Milky Way in Molecular Clouds: A New Complete CO Survey", *ApJ*, 547, 792
- [5] Gillespie, A. R. & Phillips, T. G., 1979, "Array Detectors for Millimetre Line Astronomy", *A&A*, 73, 14.
- [6] Goldsmith, P., in "Quasioptical Systems", pub. IEEE Pressm 184.
- [7] Groppi, C. E. et al. 2003, "DesertSTAR: a 7 pixel 345 GHz heterodyne array receiver for the Heinrich Hertz Telescope", *SPIE*, 4855, 330
- [8] J.W. Kooi, C.K. Walker, and J. Hesler, "A Broad Bandwidth Suspended Membrane Waveguide to Thin Film Microstrip Transition", 9th Int. Conference on Terahertz Electronics, 15th - 16th October 2001.
- [9] Sakamoto, S., Hasegawa, T., Hayashi, M., Handa, T., & Oka, T. 1995, "The Five College Radio Astronomy Observatory CO Survey of the Outer Galaxy" *ApJS*, 100, 125
- [10] Simon, R., Jackson, J. M., Clemens, D. P., Bania, T. M., & Heyer, M. H. 2001, "The Structure of Four Molecular Cloud Complexes in the BU-FCRAO Milky Way Galactic Ring Survey", *ApJ*, 551, 747
- [11] E. Schlecht, G. Chattopadhyay, A. Maestrini, A. Fung, S. Martin, D. Pukala, J. Bruston, and I. Mehdi, "200, 400, and 800 GHz Schottky diode substrateless multipliers: Design and Results," 2001 IEEE, MTT-S International Microwave Symp. Digest, Phoenix, Az, pp. 1649-1652, May 2001.
- [12] Walker, C. K., Groppi, C., d'Aubigny, C., Kulesa, C., Hungerford, A., Jacobs, K., Graf, U., Schieder, R., & Martin, C., 2001, PoleSTAR: A 4-Pixel 810 GHz Array Receiver for AST/RO, "Proceedings of the 12th International Symposium on Space Tera- Hertz Technology", San Diego, CA, Eds. Mehdi & McGrath, JPL.

ORAL SESSION n°9

**« THz Spectroscopy &
Spectrometers »**

Friday 12 May 15:15-16:45

Chaired by :

Dr. Neal Erickson & Dr. Wolfgang Wild

High resolution Terahertz spectroscopy of species of astrophysical interest

K. Demyk, L. Aballea, L. F. Constantin

Abstract—We developed a high resolution Terahertz spectrometer relying on optically-pumped molecular lasers referenced to an absolute frequency standard and mixed with tunable microwave generators on Schottky diodes. The spectrometer is coupled to a cell for gas-phase production of light radicals, ions or floppy molecules that may be detectable with the future instruments Herschel, Sofia and ALMA. We observed the rotational spectrum of urea and of the isocyanic acid in the range of 875-901 GHz.

Index Terms—Submillimeter wave spectroscopy, Submillimeter wave lasers, Submillimeter wave technology, Schottky diode frequency converters, Frequency measurement

I. INTRODUCTION

MOLECULAR lasers are powerful tools for high resolution terahertz spectroscopy. The approach used from a number of years to generate tunable Terahertz radiation is to couple fixed frequency laser with tunable microwave to Schottky diodes and the resulting sidebands are reradiated and can be easily tuned by tuning the microwave source. For accurate spectral measurements, the laser frequency can be further referenced to an absolute frequency standard. We set up a sideband laser spectrometer in order to characterize the high amplitude motions of large flexible molecules (e.g. polycyclic aromatic hydrocarbons, prebiotic species) and the rotational spectrum of light radicals or molecular ions. These astrophysically relevant species may be detectable with the future instruments Herschel, Sofia and ALMA that will investigate the Terahertz Universe with high spectral resolution and sensitivity.

II. A TERAHERTZ MOLECULAR LASER SIDEBAND SPECTROMETER

A. THz optically-pumped molecular laser

The carbon dioxide pump laser is a commercial device (Edinburg Instruments, model PL6) using a DC-discharge, flowing gas technology that delivers up to 200 W on the strongest lines. The CO₂ laser could be precisely tuned over some 100 rovibrational lines of the 9 μm and 10 μm bands using a grating in zero-order autocollimation and a piezoelectric transducer. The CO₂ laser pumps coaxially a

lab-made Terahertz laser. The laser cavity consists of an input coupler for the CO₂ radiation and an output coupler for the Terahertz radiation, separated by a 2.7 m long, 38 mm diameter bore Pyrex tube which acts as a waveguide for both THz and CO₂ radiation. The input coupler is a flat gold-plated brass mirror with a 2 mm central pin-hole. The output coupler is a flat gold-plated brass mirror with 6 mm diameter central hole. It can be moved with a stepper motor in order to tune the cavity into resonance with the THz laser modes.

We operated the laser with HCOOH, CH₂F₂, CH₃OH, CH₃CH₂F as gain media, which provided more than 20 emission lines in the range 0.6-2.5 THz [1, 2] with power in the range 10-100 mW.

B. Mixing elements at terahertz frequencies

Non-linear mixing at terahertz frequencies has been demonstrated [3,4] with Schottky barrier diodes with ultra-high cut-off frequencies thanks to their femto-farad junction capacitance and low series resistance. We developed in our lab a triple-arm open mixing structure with whisker-contacted Schottky diodes using Virginia Diodes 1TXX diode chips. It allows mixing of THz radiation with microwaves coupled either through a coaxial Bias-Tee or a rectangular waveguide [5]. The lower part of a L-shaped whisker, defined by the bend of the whisker, contacts the sub-micron Schottky diode anode and acts as an antenna for THz radiation. A dihedral corner reflector positioned behind the antenna allows enhanced coupling of the laser beam at the diode. An off-axis parabolic mirror focuses THz radiation on the diode. Optimal coupling of a 4λ antenna mounted at 1,2λ from each face of the dihedral angle is reached when the waist size of the laser beam at the diode is $w_0=1,28\lambda$ [6].

C. Frequency stabilisation system

The frequency accuracy of the measurement of the molecular lines depends on the frequency accuracy of the terahertz laser. Thermal drift of the THz laser cavity and the CO₂ laser cavity can induce a slow variation of the THz laser frequency. Locking the CO₂ laser frequency against the far-infrared emission lines [7], or against the CO₂ saturated fluorescence lines [8] - although the last technique provide better frequency stability of the CO₂ laser [9] - allowed to control the THz emission frequency via a Doppler pulling effect. Direct locking of the THz laser frequency against an absolute frequency standard was performed by heterodyne mixing of THz radiation with stabilised CO₂ lasers on point-contact MIM diodes in the frequency measurement chains [10], or by mixing of THz radiation with a harmonic of a microwave standard [11] that can lead to millihertz-level

Manuscript received May 31, 2006. This work was supported in part by the CNRS through a PCMI grant.

The authors are with the Centre National de la Recherche Scientifique, Laboratoire de Physique des Lasers, Atomes et Molécules, Université Lille 1, 59655 Villeneuve d'Ascq, France. Correspondence should be addressed to L.F. Constantin, phone: +33(0)3 20434790, fax: +33(0)3 20337020; e-mail: FL.Constantin@univ-lille1.fr.

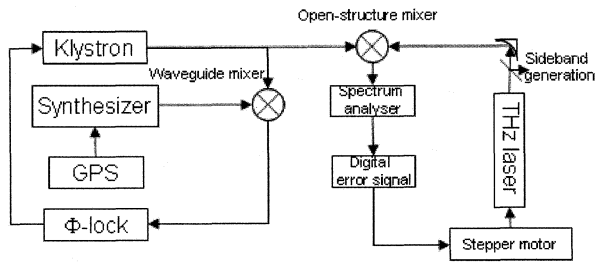


Figure 1: Frequency stabilisation system

spectral purity of the phase-locked THz laser when associated with pump laser frequency stabilisation [12].

For measuring Doppler-limited THz molecular lines with a Megahertz-level spectral linewidth, this phase-lock accuracy of THz molecular laser is not really necessary. We set up a THz laser stabilisation scheme, shown in Figure 1, for measuring THz laser against an absolute frequency standard (10 MHz signal from the Global Positioning System) and controlling its slow frequency drifts.

A 77-83 GHz klystron radiating 50 mW in a WR-12 waveguide is coupled, through a 3-port 20 dB directional coupler, to a harmonic mixer and heterodyned with the 8th harmonic of a microwave synthesizer referenced to the GPS. The intermediate frequency signal at 320 MHz is separated by the DC bias signal, filtered (bandwidth 10 MHz) and amplified with a broadband LNA and shows a typical signal at 30 dB above noise (RBW 1 kHz) that allows efficient phase-locking of the klystron to the synthesizer harmonic. The main line of the directional coupler goes through a power attenuator to the waveguide input of our THz mixer using a 1T12 Schottky diode. THz laser radiation is heterodyned with successive harmonics of the klystron and the intermediate frequency at 525 MHz is extracted through the Bias-Tee coaxial coupling of the mixer, filtered and amplified. Thanks to high LO power, the beatnote is detected with a small fraction of THz laser radiation (providing typical 20 mV video response of the Schottky diode biased at 0,7 V) which is extracted with our optical setup (Figure 2) by convenient adjusting of the waveplate, while the essential of the laser power is used for sideband generation.

The beatnote recorded on 1-s timescale (Figure 3) with 889 GHz laser line shows a 5 kHz FWHM linewidth that demonstrates high intrinsic spectral purity of our THz laser. The beatnote recorded with 1838 GHz laser line shows a broader linewidth (75 kHz FWHM) that could be associated

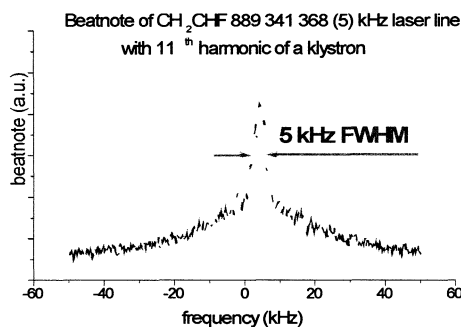
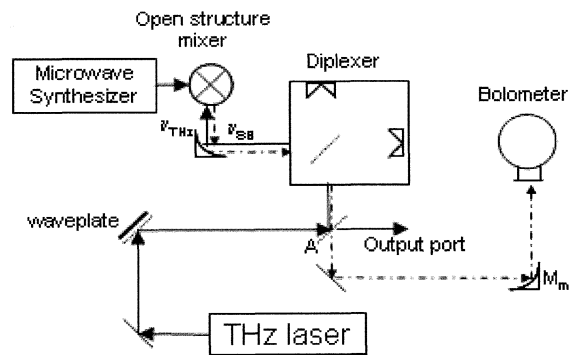


Figure 3: Spectral purity of the free-running THz molecular laser to increased phase noise due to high harmonic frequency

Figure 2: Optical setup of sideband generation. A: wiregrid analyser, M_m movable mirror. The Output port is used either for frequency stabilisation of the laser or for power calibration by conveniently aligning M_m

multiplication or specific phase noise of the pump laser induced by the optical feedback from THz laser cavity.

The free-running laser shows slow frequency drifts up to 400 kHz over 10 minutes with up to 40 kHz rms. The offset between the beatnote frequency and 525 MHz is recorded by a computer that generates a digital error signal with 1 s integration time and drives the stepper motor that control the laser cavity length. The frequency stability of the locked laser is better than 40 kHz rms over an hour that demonstrates efficient correction of slow frequency drifts.

D. Sideband generation and bolometric detection

The terahertz optical system allowing sideband generation is shown in Figure 2. It makes use of low dispersion polarising or reflecting optics that ensures broadband operation of the spectrometer.

The laser beam with linear polarisation impinges on a wire-grid polarizer which is rotated at 45° to the vertical direction and backed by a plane metallic mirror fixed on a micrometer translation mount. This device acts as a reflective waveplate and allows modifying continuously the laser polarisation from vertical to horizontal by adjusting the distance between polarizer and the mirror.

Vertically polarized THz radiation is reflected by a wire-grid polarisation analyser to a Martin-Puplet diplexer [13] which is essentially a Michelson interferometer with a polarisation-dependent beamsplitter (a wire-grid polarizer rotated at 45° to the vertical direction), two rooftop dihedral metallic reflectors and a Schottky diode mixer. The mixer preferentially couples vertically polarised radiation to the diode. The re-radiated power by the mixer at ν_{THz} is coupled through the same optical path in the diplexer as the incoming laser beam and is reflected back to the laser. The sidebands emitted at $\nu_{\text{THz}} + \nu_{\text{MW}}$ undertake a different phase change in the interferometer, thus a different polarisation status when reaching the analyser. If L is the pathlength difference and there are m, n integers such as: $2L = 2m\lambda_{\text{THz}} = (2n + 1)\lambda_{\text{SB}}$, sidebands emerge with a polarisation crossed to the polarisation of the incoming laser and are transmitted through the analyser. If $\nu_{\text{THz}} \gg \nu_{\text{MW}}$, the previous condition can be met accurately when $L = \lambda_{\text{MW}}/2$ and both sidebands are extracted from the diplexer with equal efficiency.

We operated the sideband generator with a 2-20 GHz synthesizer coaxially coupled to the diode through a Bias-

Tec and with guided-wave in the range of 50-110 GHz from Militech active multipliers.

This system allow in principle very efficient separation of the sidebands from the laser power. Non-ideal operation

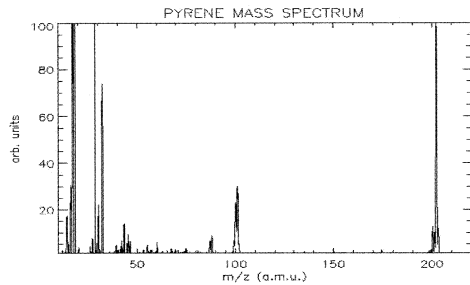


Figure 6: Mass-spectrum of laser-ablated pyrene

with low separation efficiency appear when polarisation state of the laser is changed, that obviously come out when incoming laser beam is reflected back by the corner cube of the antenna. However, one can precisely discern the part of sidebands in the radiation transmitted by the analyser by applying, for example, 100% full amplitude modulation of the RF power on the synthesizer that drives the mixer and using a lock-in detection scheme.

We performed a direct measurement of the efficiency of sideband generation. A QMC bolometer is used as detector providing a linear response for THz power up to a mW level with the calibration data granted by the manufacturer. The analyser, fixed in a kinematic mount, was removed and incoming laser radiation was focused with a movable mirror directly on the bolometer. That allowed us to estimate the THz laser power $P_{laser} = V_{laser} / S$ from the bolometer voltage response V_{laser} and its responsivity S . The pressure of the lasing gas and the current of the DC-discharge of the CO₂ laser were lowered providing a THz laser emission at a mW level that doesn't saturate the bolometer response. We set up the analyser afterwards and we aligned the movable mirror in order to focus on the bolometer the radiation exiting the diplexer. The AM detection technique allowed us to estimate the power in one sideband

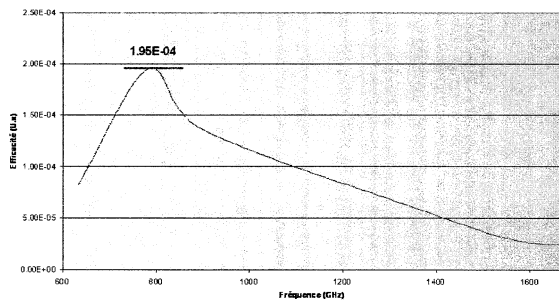


Figure 4: Sideband generation efficiency

$P_{SB} = V_{SB} / (S \cdot C_{AC-DC} \cdot C_{SSB})$ where V_{SB} is the lock-in output voltage and the last conversion factors, equals to 2, are determined by the AC to DC signal processing with the lock-in and by the detection of both sidebands.

Figure 4 shows the values of the sideband generation efficiency for different laser lines. We used an 1T21 Schottky diode biased at 0,7 V. The mixer was driven at 4

GHz with a synthesizer providing 8 dBm of microwave power. The diplexer pathlength was optimised for each laser line as well as the optical alignment of the corner cube mixer. The mixer has broadband operation, while the best sideband generation efficiency, that is around $2 \cdot 10^{-4}$, is reached on the 783 GHz laser line. Its wavelength corresponds to a quarter of the 1.6 mm whisker-antenna that allows optimal coupling of the laser power to the mixer. When the synthesizer that drives the mixer is swept from 2 to 20 GHz, the optimal values of sideband generation efficiency do not vary more that 15% of the listed values, that point out efficient broadband coaxial coupling of the microwaves to the diode. The sideband generation efficiency is typically one order of magnitude lower with a less efficient waveguide-coupling of 50-110 GHz microwaves to the mixer.

The detector is a two-channel QMC InSb cyclotron-resonance assisted hot electron bolometer with an improved spectral response up to 3 THz. The manufacturer specified a responsivity $S=4230$ V/W and a noise-equivalent power $NEP=2$ pW.Hz^{-1/2}. These values determinates the sensitivity of the spectrometer since the THz power level is not enough strong in order to overcome the detector noise. Absolute power calibration of the 783 GHz laser line [14] allow us to estimate the maximal sideband power at 10 μW, thus the minimum detectable fractional absorption of the spectrometer is $2 \cdot 10^{-7}$. This value neglect specific baseline problems of the THz spectrometer setup – the coupling of the sidebands to the THz laser cavity and the power

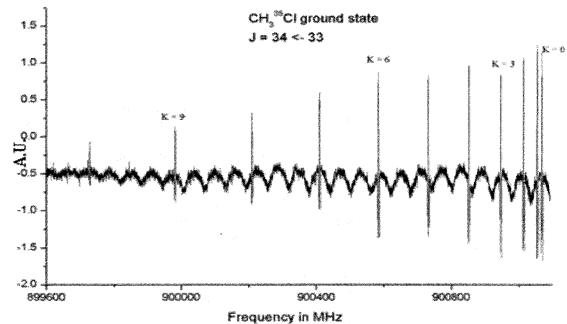


Figure 5: Fine structure of a rotational line of CH₃Cl

fluctuations of the CO₂ laser, induced by optical feedback – that could limit the ultimate sensitivity of the spectrometer.

The system allows broadband scans for molecular lines, improving the previous heterodyne detection scheme [2]. Figure 5 shows a rotational spectrum of the ground state of methyl chloride, a key-molecule for aeronomy that was studied extensively in our group [15 and references therein]. The spectrum shows the K rotational structure of J:34<-33 line over 1,2 GHz that was recorded with excellent SNR with 100 ms acquisition time per point in 10 minutes, using a frequency-modulation technique of the sidebands and 2-f lock-in detection. The spectrum baseline is determined by interference fringes in the 3 m long absorption cell.

III. GAS-PHASE PRODUCTION OF ASTROPHYSICALLY RELEVANT MOLECULES

We have coupled to the spectrometer a new cell for the gas-phase production of molecules that are astrophysically

relevant for the observation missions of the Terahertz Universe. A quadrupole mass spectrometer (Pfeiffer-QMG422, mass range 1-512 a.m.u.) in a differentially-pumped vacuum chamber is used to monitor the composition of gas-phase generated neutral or ionised species.

The laser desorption/ablation technique allows us to study a large range of species having low vapor pressure and/or which decompose or polymerize upon heating. The desorption of solid samples (pellets of thin films) is realized with a 10 ns Q-switched Nd:Yag laser which delivers 4-25 mJ at 1064 nm and its 532, 355, 266 nm harmonics. This set up has been tested on different species such as pyrene, glyceraldehyde, urea. The pyrene mass spectrum shown in Figure 6 has been obtained using the 2nd harmonic at 532 nm at maximum laser energy (25 mJ) with a repetition rate of 15 Hz.

The supersonic beam technique allows the production of intense cold molecular samples from the adiabatic expansion through a nozzle. Our setup uses a 1 mm diameter pulsed-nozzle with two stainless steel electrodes placed directly in the front of the nozzle that allow operating a high-voltage discharge of the molecular beam. Light hydrides, like OH [16], or molecular ions, which are the tracers of the ISM chemistry, will be investigated with this setup.

IV. THE TERAHERTZ SPECTRUM OF UREA

Urea is a prebiotic molecule of astrophysical interest. It is involved in the formation of pyrimidines which have been detected in the Murchinson meteorite [17]. Urea have been tentatively detected in icy grains [18] by comparison of the laboratory spectrum of VUV photolysed HNCO and $\text{NH}_3/\text{H}_2\text{O}$ ice mixture with spectroscopic observations from ISO at 6 μm of the protostellar object NGC7538IRS9. Urea could then be released to the gas phase via thermal desorption. Urea rotational transitions might thus be detected in the gas phase around protostars.

The rotational spectrum of urea and its isotopic species in their ground vibrational state have been studied in the 8-19 GHz frequency range [19,20]. Recent measurements was performed in the millimeter-wave range at the Institute of Radio Astronomy (Kharkow, Ukraine) around 200 GHz [21]. These results allowed us to predict the urea spectrum in the 870-910 GHz range with an accuracy better than 30 MHz.

The detection of the Terahertz absorption spectrum of urea ablation plume is challenging because of the ultra-low density of the molecular population in a specific rotational level and the direct detection scheme which is used.

To overcome this problem we have heated urea in a temperature-stabilised brass oven coupled to the cell. The pressure in the cell was typically 5.10^2 Pa when the oven was maintained at 373 K. The spectrum shown in Figure 7, recorded with 1 s acquisition time per point, displays two near-resonant transitions where one may be due to urea while the other is most probably a line of the isocyanic acid (HNCO), an urea thermal decomposition product. We measured many HNCO lines that are shifted up to 6 MHz from the predicted line frequencies provided by the JPL molecular spectroscopy database [22]. A new analysis of the spectroscopic constants taking into account our

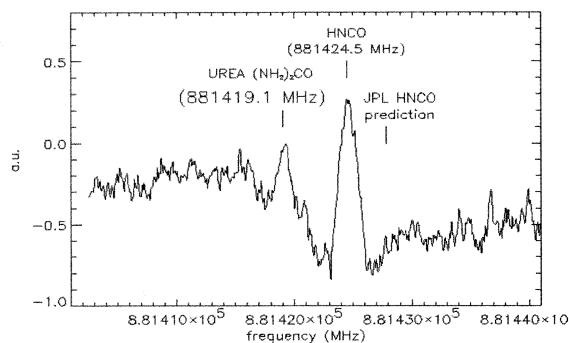


Figure 7: Absorption lines of urea and HNCO

measurements should improve the accuracy of the prediction of HNCO Terahertz spectrum. Further work for increasing the efficiency of urea gas-phase generation, by avoiding its condensation on the cold walls of the cell and its thermal decomposition, will allow the measurement of other terahertz urea lines.

ACKNOWLEDGMENT

The authors acknowledge skillful assistance from Laurent Margulès and fruitful discussions with Jean Demaison and Georges Wlodarczak.

REFERENCES

- [1] N. G. Douglas, *Millimeter and Submillimeter Wavelength Lasers*. New York: Springer-Verlag, 1989.
- [2] D. Boucher, R. Bocquet, J. Burie, W. Chen, "A far-infrared heterodyne sidebands spectrometer," *J Phys. III France*, vol. 4, pp. 1467, 1994
- [3] H. R. Fetterman, P. E. Tannenwald, B. J. Clifton, W. D. Fitzgerald, N. R. Erickson, "Far-ir heterodyne radiometric measurements with quasi-optical Schottky diode mixers," *Appl. Phys. Lett.*, vol. 33, pp. 151, 1978
- [4] D. D. Bicanic, B. F. J. Zuidberg, A. Dymanus, "Generation of continuously tunable laser sidebands in the submillimeter region," *Appl. Phys. Lett.*, vol. 32, pp. 367, 1978
- [5] L. Margulès, L. F. Constantin, "Spectroscopie Téraherz en phase gazeuse," *Revue de l'Electricité et de l'Electronique, Dossier Les ondes Téraherz*, vol. 1, pp. 50, 2003; H. Krautle, E. Sauter, G. V. Schultz, *Infrared Phys.*, v ol. 18, pp. 705, 1978
- [6] E. R. Mueller, J. Waldman, "Power and Spatial Mode Measurements of Sideband Generated, Spatially Filtered, Submillimeter Radiation," *IEEE Trans. MTT*, vol. 42, pp. 1891, 1994
- [7] C. R. Pidgeon, W. J. Firth, R. A. Wood, A. Vass, B. W. Davis, "Two-Photon Light Shift and Autler-Townes Splitting in Optically-Pumped FIR Lasers," *Int. J. IR MMW*, vol. 2, pp. 207, 1981
- [8] C. Freed, A. Javan, "Standing-wave saturation resonances in the CO_2 10.6 μm transitions observed in a low-pressure room-temperature absorber," *Appl. Phys. Lett.* 17, pp. 53, 1970
- [9] B. Frech, L.F. Constantin, A. Amy-Klein, O. Phavorin, C. Daussy, C. Chardonnet, M. Mürtz, "Frequency measurements of saturated-fluorescence-stabilized CO_2 laser lines: comparison with an OsO_4 -stabilized CO_2 laser standard," *Appl. Phys. B*, vol. 67, pp. 217, 1998
- [10] G.D. Rovera, O. Acef, "Absolute frequency measurement of mid-infrared secondary frequency standard at BNM-LPTF," *IEEE Trans. Instr. Meas.*, vol. 48, pp. 571, 1999
- [11] T. Sakurai, "Frequency Stabilization of CH_3OH Laser at 469 μm to Millimeter-Wave Standard," *Japanese Journal of Applied Physics*, vol. 25, pp. 124, 1986
- [12] G.D. Rovera, "Low frequency noise optically pumped FIR laser with frequency stabilized pump," *Opt. Comm.*, vol. 143, pp. 247, 1997
- [13] D. H. Martin, E. Pulett, "Polarised interferometric spectrometry for the millimeter and submillimeter spectrum," *Infrared Phys.*, vol. 10, pp. 105, 1969
- [14] W. Chen, "Techniques d'hétérodynage dans l'infrarouge lointain. Quelques applications en spectroscopie de rotation," Ph.D. dissertation, USTL, Villeneuve d'Ascq, 1990

- [15] L. F. Constantin, J. Demaison, L. Féjard, M. Litz, H. Bürger, P. Pracna, "Rovibrational and rotational spectroscopy of the $\nu_2=1$, $\nu_5=1$ and $\nu_3=2$ levels of $^{13}\text{CH}_3^{37}\text{Cl}$," *Mol. Phys.*, vol. 102, pp. 1717, 2004
- [16] H.J. Lewandowski, E. R. Hudson, J.R. Bochinski, Jun Ye, "A pulsed, low-temperature beam of supersonically cooled free radical OH molecules," *Chem. Phys. Lett.*, vol. 395, pp. 53, 2004
- [17] P. G. Stock, A. W. Schwartz., "Nitrogen-heterocyclic compounds in meteorites: significance and mechanisms of formation," *Geochim. Cosmochim. Acta*, 45, pp. 563, 1981
- [18] S. Raunier, T. Chiavassa, F. Duvernay, F. Borget, J.P. Aycard, E. Dartois, L. d'Hendecourt, "Tentative identification of urea and formamide in ISO-SWS infrared spectra of interstellar ices," *Astronomy&Astrophysics*, vol. 416, pp. 165, 2004
- [19] U. Kretschmer, D. Consalvo, A. Knaack, W. Schade, W. Stahl, H. Dreizler, "The ^{14}N quadrupole hyperfine structure in the rotational spectrum of laser vaporized urea observed by molecular beam Fourier transform microwave spectroscopy" *Mol. Phys.*, vol. 87, pp. 1159, 1996
- [20] S. Kassı, D. Petitprez, G. Włodarczak, "Microwave spectrum of isotopic species of urea $(\text{NH}_2)_2\text{CO}$," *J. Mol. Spec.*, vol. 228, pp. 293, 2004
- [21] E.A. Alekseev, private communication
- [22] <http://spec.jpl.nasa.gov/>

Quasi-Optical Characterization of Dielectric and Ferrite Materials

P. Goy, S. Caroopen, M. Gross,
AB MILLIMETRE, 52 rue Lhomond 75005 Paris, France
tel: +33 1 47 07 71 00, fax: +33 1 47 07 70 71, abmillimetre@wanadoo.fr
R.I. Hunter, G.M. Smith,
Millimetre Wave and High Field ESR Group, University of St Andrews,
North Haugh, St Andrews, Fife KY 16 9SS, Scotland, United Kingdom
tel: +44 1334 463156, 2669, fax: 463104, rih1, gms@st-and.ac.uk

I. Introduction.

In the millimeter-submillimeter range, Quasi-Optical QO benches can be relatively compact, typically of order 10cm wide and 1m long. The focussing elements used in these benches are dielectric lenses, or off-axis elliptical mirrors. Simultaneous Transmission, T, (corresponding to the complex S21 parameter) and Reflection, R, (corresponding to the complex S11 parameter) are vectorially detected versus frequency in the frequency range 40-700 GHz. A parallel-faced slab, thickness e , of dielectric material is placed at a Gaussian beam waist within the system. It is straightforward to determine the refractive index n (with $\epsilon' = n^2$) of this sample from the phase rotation $\Delta\Phi$:

$$(n-1)e/\lambda = \Delta\Phi/360$$

The loss factor $\tan\delta$ is known from the damping of the transmitted signal, Fig.1:

$$\tan\delta = 1.1 \alpha(\text{dB/cm})/nF(\text{GHz})$$

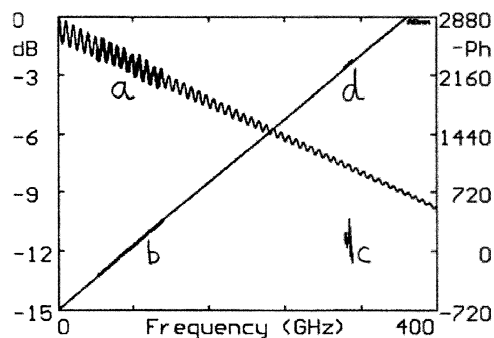


Fig.1. Transmission through 10.95mm nylon. a), thick line, is the observed amplitude in V-W bands, b) is the corresponding phase (represented in opposite sense for clarity). Around 305 GHz, the measured d) phase value, in good alignment with extrapolated b), shows that the permittivity $\epsilon' = 3.037$ is constant with frequency. On the contrary, the position of the amplitude c) shows that the loss, which was $\tan\delta = 0.013$ at low frequencies, has increased to $\tan\delta = 0.019$, since c) is far from the extrapolated a).

The samples in this measurement system act as Fabry-Perot resonators with maximum transmission corresponding to minimum reflection, and vice-versa, Fig.2, with a period $\Delta F = c/2ne$. For very low loss materials, there is however some difficulty in measuring the loss term by a single crossing, since the maximum transmission is very close to 0 dB. One uses the cavity perturbation technique, which makes visible the low losses after many crossings through the dielectric slab, Fig.3.

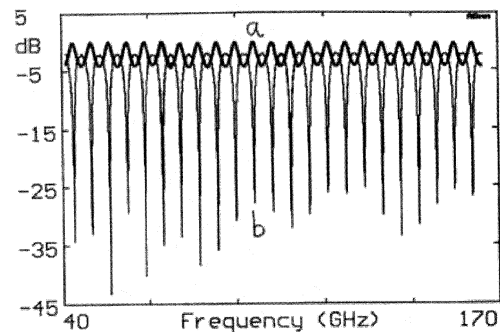


Fig.2. Transmission a) and reflection b) through 9.53 mm AlN. The dielectric parameters, observed in V-W-D bands, are constant with $\epsilon' = 8.475$, $\tan\delta = 0.0007$, also measured the same in cavity at 140.4 GHz.

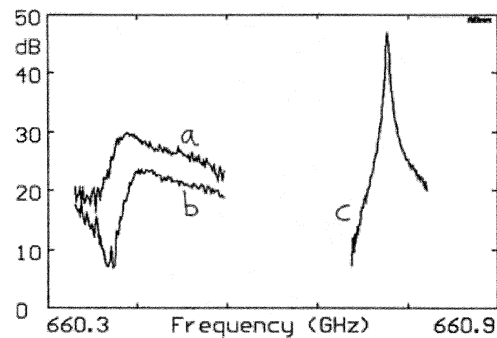


Fig.3. Resonances observed in an open Fabry-Perot cavity loaded by a 10.03mm thick slab of slightly birefringent Teflon. In a) the RF field is along the large index axis $\epsilon' = 2.0664$, in b) along the small

index axis $\epsilon'=2.0636$. In c) is the empty cavity resonance. The ϵ' anisotropy is exactly the same as observed at 135 GHz. The loss has increased from $\tan\delta=0.0003$ at 135 GHz to 0.0008 at 660 GHz.

II. Experimental setups for free-space propagation.

In V-W-D bands (extended down to ca 41 GHz, close to the V-band cutoff), we use the following waveguide components. On the source side, the Harmonic Generator HG sends its millimeter power through a full-band Faraday isolator FI1, cascaded with a fixed attenuator AT1, a directional coupler DC (from port 2 to port 1) and a Scalar Horn SH1. The reflection (Channel 1) is detected by a Harmonic Mixer HM1 attached to output 3 of the DC through the isolator FI2.

On the transmission detection side, the Scalar Horn SH2 sends the collected wave to the Harmonic Mixer HM2 (Channel 2) through cascaded AT2 and FI3.

III. Isolators FIs and Attenuators ATs, what for?

The first use of isolators is to assume a one-way propagation. The non-linear devices HG and HMs contain Schottky diodes. In case the wave can travel go-and-back from one device to the other, the combination of non-linear and standing waves effect can send microwave power from a given harmonic to another harmonic [1]. This is why multipliers cascaded without isolation (like x2x3) can create unexpected harmonics (like x5, or x7). We have also observed, for instance with cascaded triplers (x3x3), measurable amounts of unexpected x10, x11, or x12 [2]. The devices HG and HMs can be viewed as Schottky diodes across waveguides, meaning unmatched structures. The second use of the FIs is to reduced the VSWR. Their typical return is -20dB (VSWR ca 1.22). We improve this value down to -30dB (VSWR ca 1.07) when introducing the fixed attenuators ATs.

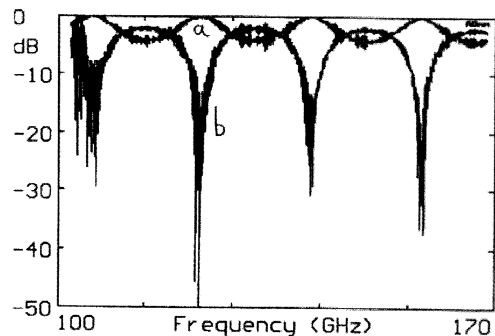


Fig.4. Transmission a) and reflection b) through a 3mm thick MgAl2O4 slab. These raw data show parasitic standing waves appearing as noise.

IV. Experimental difficulties.

Even with our best benches using the complete chains assuming a low VSWR (<1.1, see III.), the parasitic standing waves effects are clearly visible on raw data, Fig.4-5. They are due to multiple reflections between the sample, placed perpendicular to the beam, and the components of the bench. However, they can be completely filtered by FT calculations, Figs.6-7.

There is a lack of FIs waveguide isolators above 220 GHz and, as far as we know, of DCs above 400 GHz. As a consequence, characterization at submillimeter wavelengths is operated by transmission only, and is much more difficult, Fig.8, than in V-W-D-bands, due to large parasitic standing waves..

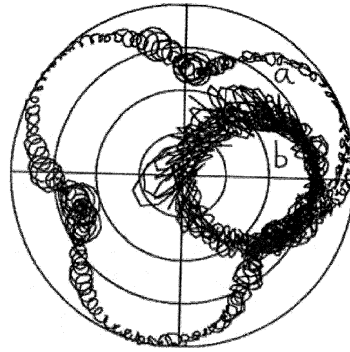


Fig.5. Polar plot of Fig.4.

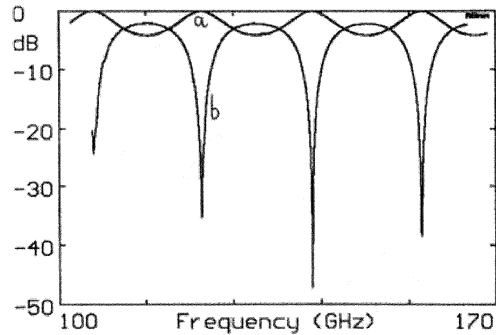


Fig.6. Same as Fig.4 after FT filtering.. The measured dielectric parameters are $\epsilon'=8.080$, and $\tan\delta=0.0005$.

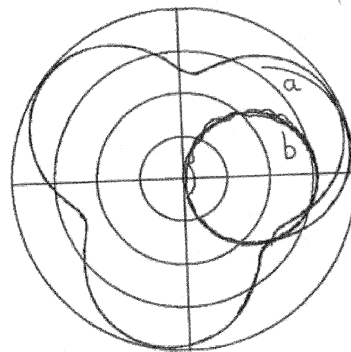


Fig.7. Polar plot of Fig.6.

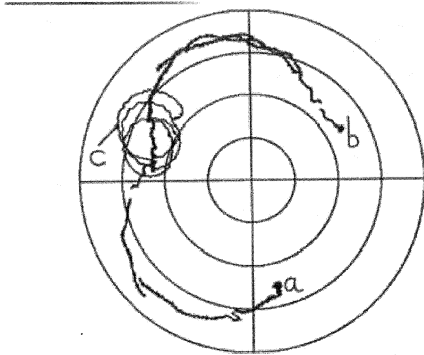


Fig.8. Transmission across 9.97mm sapphire, from 469 GHz, point a), to 479 GHz, point b), with absorbers, total 30 dB, between source and detection, in order to reduce the parasitic standing waves. Despite this strong attenuation, the measurement quality is far from being as good as at lower frequencies, like in Fig.7. In c) is the 473.3-474.5 GHz sweep without absorbers, showing big standing waves effects.

V. Non-magnetized ferrites characterization.

In the case of ferrite materials, the properties are very strongly frequency dependent. Non-magnetized ferrites show a strong resonance in the range 50-60 GHz, Fig.9, and the asymptotic behaviour, far from resonance, starts to be visible beyond 200 GHz. Measurements performed at 475 GHz on six samples give ϵ' in the range 18.8-21.4, and $\tan\delta$ in the range 0.012-0.018.

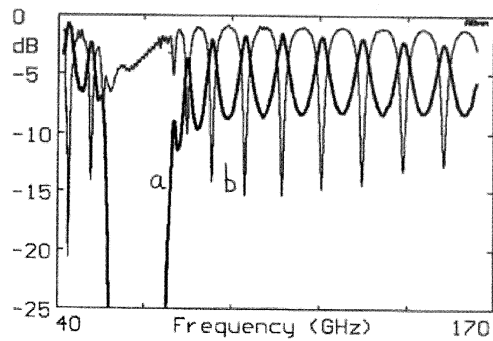


Fig.9. Transmission a), and reflection b), through a 2.55 mm thick non-magnetized TDK ferrite sample.

VI. Magnetized ferrites.

When a ferrite is submitted to an external, or internal, magnetic field, there is a strong anisotropy of propagation according to the circular polarization of the crossing electromagnetic wave [3]. The two refractive indices n_{\pm} are given by:

$$(n_{\pm})^2 = \epsilon' [1 \pm F_m / (F_0 \mp F)]$$
 where F is the frequency, F_0 the Larmor frequency, F_m is proportional to the remanent magnetization of the ferrite, and ϵ' is the dielectric constant. Any

linearly polarized wave, like ours at the SH outputs, can be viewed as the superposition of two opposite senses circularly polarized components. After crossing the ferrite, one of the components has experienced a larger retardation than the other, so that, when recombining the two, the plane of linear polarization has been rotated. In order to characterize magnetized ferrite samples, it is necessary to measure not only the transmitted signals with a polarization parallel to the source, but also those with polarization at +/-45 degrees, and 90 degrees, see Figs.10-11-12.

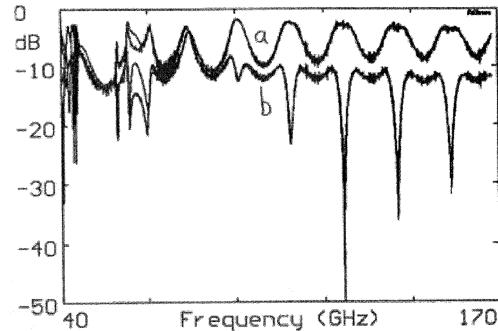


Fig.10. Transmission through 2mm magnetized sample FB6H1, a) is -45°, b) is +45°. Experimental traces and superimposed fittings.

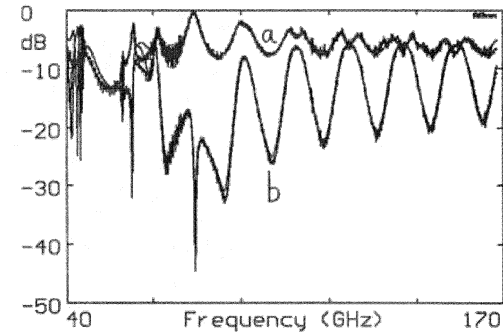


Fig.11. Same as Fig.10, where a) is 90° and b) is 0°.

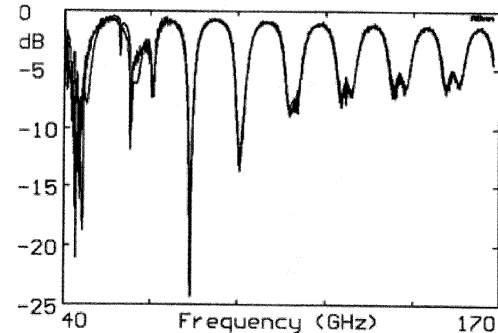


Fig.12. Reflection at 0° from the magnetized sample FB6H1, experiment and fit.

When adding an anti-reflection coating on each side of the magnetized ferrite, the thickness of the ferrite being chosen so that the rotation through it is 45° at

the required frequency, one can obtain a good QO Faraday Rotator, Fig.13. The performances observed around the central frequency, Figs.14-15, are at least similar (for isolation or matching) or better (for insertion loss) than the equivalent waveguide isolators.

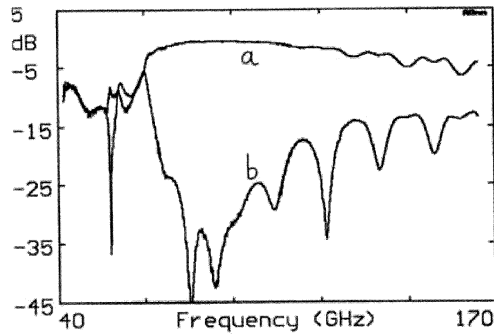


Fig.13. Magnetized ferrite c257, transmission with anti-reflection coatings on both faces. In the W-band, it works as an isolator. Top a) -45° , is low insertion loss, bottom b) $+45^\circ$, is good isolation.

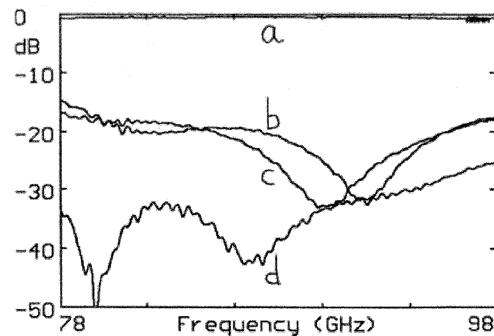


Fig.14. Magnetized ferrite c257 working as an isolator. The S_{21} parameter in a) is the particularly low insertion loss ca 0.5 dB. The S_{22} parameter in b) is the matching at the output, the S_{11} parameter in c) is the matching at the input, the S_{12} parameter in d) is the good isolation, around 30 dB.

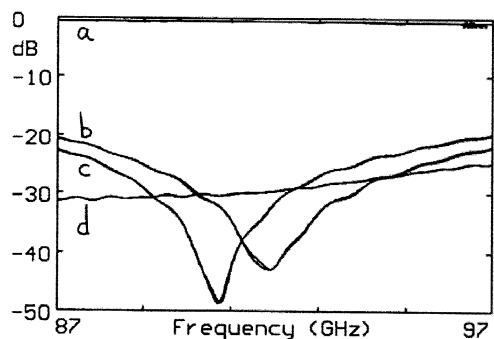


Fig.15. Same as Fig. 14, with another sample: c258.

VII. QOFRs expected to become submillimeter isolators and Directional Couplers.

Our QO benches studying samples perpendicular to the wave beam, are, up to now, less performing in submillimeter (Fig.8) than in the millimeter domain (Fig.7), due to parasitic standing waves. Introducing the appropriate QO Faraday Rotators will reduce this effect. On Fig.16 one can see how a QOFR can be simply configured for that purpose.

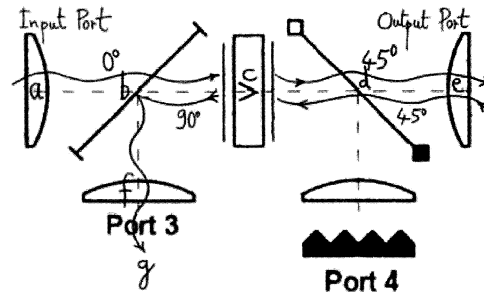


Fig.16. Schematic diagram of a QOFR used as an isolator (there is a matched load at g) Port 3, or as a Directional Coupler DC for detecting reflected waves at g). The vertical polarisation at a), fully transmitted through the horizontal grid b), rotates by $+45^\circ$ through the magnetized ferrite c), then is fully transmitted through the -45° grid d). Any reflected signal without polarisation change will cross back d) without loss, then will rotate by $+45^\circ$ again across c), becoming horizontal, then will be totally reflected by the horizontal grid b), towards Port 3.

VIII. Conclusion.

Precise and quick QO measurements in the 40-170 GHz interval, in particular for ferrites characterization, opens the possibility of similar precise and easy measurements at high frequencies, including the submillimeter domain, by using these ferrites in QOFRs in progress [4]. At the same time, widely sweepable solid-state submillimeter sources must be developed.

References.

- [1] P. Goy, M. Gross, S. Caroopen, *4th International Conference on Millimeter and Submillimeter Waves and Applications, San Diego, California USA, 1998 Jul 20-23* "Millimeter and Submillimeter Wave Vector Measurements with a network analyzer up to 1000 GHz. Basic Principles and Applications".
- [2] P. Goy, private communications 2005-2006.
- [3] R.I. Hunter, D.A. Robertson, G.M. Smith, *29th Int Conf on IR and mmWaves, Karlsruhe, 2004 Sep 27 – Oct 1*, "Ferrite Materials for Quasi-Optical Devices and Applications".
- [4] R.I. Hunter, D.A. Robertson, P. Goy and G.M. Smith, "Characterization of Ferrite Materials for use in Quasi-Optical Faraday Rotators", to be published.

550-650 GHz spectrometer development for TELIS

P. Yagoubov, R. Hoogeveen, M. Torgashin, A. Khudchenko, V. Koshelets,
N. Suttiwong, G. Wagner, M. Birk

Abstract—In this paper we present design and experimental results of the 550 - 650 GHz channel for the Terahertz Limb Sounder (TELIS), a three-channel balloon-borne heterodyne spectrometer for atmospheric research. This frequency channel is based on a phase-locked Superconducting Integrated Receiver (SIR). SIR is an on-chip combination of a low-noise SIS mixer with quasioptical antenna, a superconducting Flux Flow Oscillator (FFO) acting as Local Oscillator (LO) and SIS harmonic mixer (HM) for FFO phase locking. The microcircuit is designed as a quasioptical mixer. We report first results of the SIR mixer sub-assembly noise temperature and beam pattern measurements. We have also tested flight configuration of the 550-650 GHz receiver, which includes cold optics, flight electronics and digital backend spectrometer, to measure emission line of the OCS gas in the laboratory gas cell.

Index Terms — Josephson mixers, integrated receiver, superconducting devices

I. INTRODUCTION

TELIS (Terahertz Limb Sounder) is a cooperation between DLR (Institute for Remote Sensing Technology, Germany), RAL (Rutherford Appleton Laboratories, UK) and SRON (National Institute for Space Research, the Netherlands), to build a three-channel balloon-borne heterodyne spectrometer for atmospheric research. The three receivers utilize state-of-the-art superconducting heterodyne technology and will operate simultaneously at 500 GHz (channel developed by RAL), at 550-650 GHz (SRON in collaboration with IREE), and at 1.8 THz (DLR). TELIS is designed to be a compact, lightweight instrument capable of providing broad spectral coverage, high spectral resolution and long flight duration (~24 hours duration in a flight

campaign). The combination of high sensitivity and extensive flight duration will allow evaluation of the diurnal variation of key atmospheric constituents such as OH, HO₂, ClO, BrO together with longer lived ones such as O₃, HCL and N₂O. The balloon platform on which TELIS will fly also contains a Fourier transform spectrometer MIPAS-B developed by the IMK (Institute of Meteorology and Climate research of the University of Karlsruhe, Germany). MIPAS-B will simultaneously measure within the range 680 to 2400 cm⁻¹. The combination of the TELIS and MIPAS instruments will provide an unprecedented wealth of scientific data and will also be used to validate other instruments and atmospheric chemistry models. First flight is foreseen in April 2007.

II. TELIS CONFIGURATION

The optical front-end of TELIS consists of a pointing telescope, calibration blackbody and relay optics, common for the three channels: 500 GHz, 550-650 GHz and 1.8 THz [1]. The telescope is a dual offset Cassegrain antenna. Primary parabola has an elliptical cross-section of 260x140 mm. 2:1 anamorphicity is introduced by the cylindrical tertiary mirror. An anamorphic design was selected to improve telescope compactness, mass, and moment of inertia. A vertical (elevation) resolution at the tangent point is about 2 km at 500 GHz (FWHM), inversely proportional to the frequency. The limb scans range from upper troposphere (10 km) to stratosphere (30-40 km). Horizontal (azimuth) resolution is about a factor of 2 worse but not of prime importance for this mission as the atmospheric properties within the beam depend only on the altitude.

Calibration of the radiometric gain of the spectrometers will be done with two blackbody reference sources at submillimeter wavelengths: the hot-load, which is a conical black-body at the ambient temperature, and the cold sky.

Frequency separation between the channels is performed quasioptically, allowing simultaneous observations by all receivers. First, one linear polarization of the incoming signal is selected by a wire grid and is reflected into the 500 GHz channel. The other linear polarization, which is transmitted by the grid, is then split between two other frequency channels by a dichroic filter. After the splitting, the three beams enter a custom designed liquid helium cooled cryostat. A number of off-set reflectors are used to interface the optics from the telescope to the cryogenic channels. Fig. 1 shows schematics

Manuscript received June 1, 2006

The work was supported in parts by the RFBR projects 06-02-17206, the ISTC project # 3174, NATO SFP Grant 981415, and the Grant for Leading Scientific School 7812.2006.2

P. Yagoubov and R. Hoogeveen, are with the National Institute for Space Research SRON, P.O. Box 800, 9700 AV Groningen, the Netherlands, (telephone: 31-50-3634074, e-mail: p.a.yagoubov@sron.rug.nl)

M. Torgashin, A. Khudchenko and V. Koshelets are with the Institute of Radio Engineering and Electronics, Russian Academy of Science, Moscow, Russia; they are also partially with the National Institute for Space Research SRON, the Netherlands, (e-mail: valery@hitech.cplire.ru)

N. Suttiwong, G. Wagner and M. Birk are with the Institute for Remote Sensing Technology, DLR, Germany, (e-mail: manfred.birk@dlr.de)

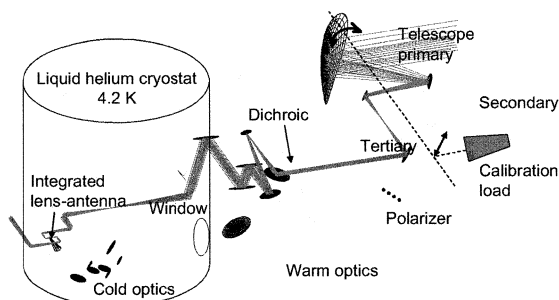


Fig. 1. Schematics of the 550-650 GHz channel optics. The telescope is rotated around the axis coinciding with the direction of the output beam. Wire grid polarizer and dichroic plate are used to separate this receiver from the two other frequency channels (not shown). The cold optics and mixer element are located inside the cryostat at the ambient temperature 4.2 K.

of the optics directly related to the 550-650 GHz channel. The optical beams of the two other frequency channels after the splitting as well as their dedicated optical elements are not shown here.

Inside the cryostat the receivers have dedicated cold optics, mixing element and IF amplifiers. Three amplified output IF signals are connected to an IF processor which converts the IF to the input range of the digital autocorrelator of 2×2 GHz bandwidth. An on-board microcontroller controls the instrument and interfaces with the ground station.

III. SIR DESIGN

A key element of the 550-650 GHz channel is Superconducting Integrated Receiver (SIR) [2], which comprises in one $4 \times 4 \times 0.5$ mm³ chip a low-noise SIS mixer with quasi-optical antenna, superconducting Flux Flow Oscillator (FFO) acting as Local Oscillator (LO) and SIS Harmonic Mixer (HM) for FFO phase locking. The SIR microcircuits are traditionally fabricated on a Si substrate using Nb-AlOx-Nb tri-layer [3].

Performance of all-Nb devices, however, is very critical to the ambient temperature, which should not exceed 4.5 K. This is difficult to achieve on a balloon platform since the TELIS liquid helium cryostat should be over-pressurized ($p > 1$ Bar) due to safety reasons. To overcome this problem, we have developed and studied Nb-AlN/NbN-Nb circuits with a gap voltage V_g up to 3.7 mV and extremely low leakage currents ($R_j/R_n > 30$). Based on these junctions integrated microcircuits comprising FFO, SIS and harmonic mixer have been designed, fabricated and tested; the radiation from such circuits has been measured at frequencies up to 700 GHz. Employment of NbN electrode does not result in the appearance of additional noise. For example, FFO linewidth as low as 1.5 MHz was measured at 595 GHz, that allows us to phase lock up to 85 % of the emitted by FFO power and realize very low phase noise of about -93 dBc. It is important to note that for Nb-AlN-NbN FFO there is a possibility to tune permanently the FFO frequency even in the Fiske regime, since Fiske steps are bended and overlapping. From the other

hand, for Nb-AlN-NbN junctions there is a considerable increase of the FFO linewidth just above of the $V_g/3$ (of about 600 GHz) due to self-adsorption of the FFO radiation [4] (effect of Josephson self-coupling).

The receiver chip is placed on the flat back surface of the 10 mm diameter elliptical Si lens, forming an integrated lens-antenna. SIR feed antenna is positioned at the more distant focus of the ellipse. To minimize the reflection loss at the lens-air interface, the curved surface of the lens is coated with a 74 micron thick Stycast antireflection coating, optimized for the center frequency 600 GHz. Further shaping of the beam is done by means of a number of curved and fold mirrors, all located at the cold plate of the liquid helium cryostat [5].

IV. MIXER NOISE TEMPERATURE AND BEAM PATTERN

Most of the experimental results discussed here have been obtained with the SIR device based on the Nb-AlN-NbN technology. SIR chip is mounted in a flight configuration mixer block surrounded by a magnetic shield. No other optical elements of the cold channel were installed for the noise temperature (NT) and beam pattern measurements reported in this section. All tests were done in a liquid helium cooled cryostat at 4.2 K ambient temperature. NT measurements are done using Y-factor technique by chopping between hot (295 K) and cold (80 K) loads in the signal path of the receiver. IF response of the mixer is amplified by a cryogenic InP based 4-8 GHz LNA amplifier followed by a 60 dB gain GaAs RT amplifier. The signal is detected by a fast power meter in 40 MHz bandwidth, selected by tunable YIG filter. We have also used flight configuration of the PLL system and could lock the FFO practically at any frequency in the 550-650 GHz range.

Fig. 2 shows results of the NT measurements, which are not corrected for any loss. The DSB NT below 400 K is measured in about 100 GHz wide frequency range. Rise of the NT around 560 GHz could be to a large extent explained by

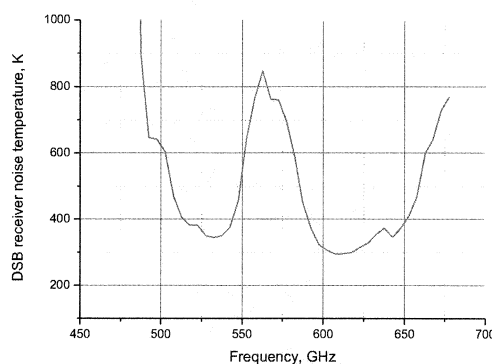


Fig. 2. Uncorrected DSB noise temperature of the SIR. Rise of the noise temperature around 560 GHz could be to a large extent explained by absorption in the atmosphere due to the strong and broad water line around that frequency.

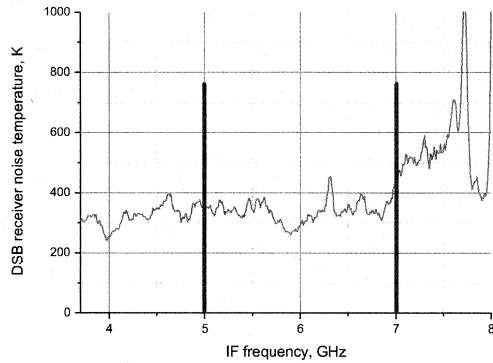


Fig. 3. DSB noise temperature of the SIR as a function of the IF frequency.

absorption in atmosphere due to the strong and broad water line around that frequency. Vacuum hot/cold measurements are planned for the future to exclude this effect from the measurement results.

Fig. 3 shows measured NT vs. IF of the receiver. One can see that the response is fairly flat in the 5-7 GHz frequency range, the input bandwidth of the SIR channel backend spectrometer. Further optimization of the coupling between the mixer and IF board should minimize ripples in the response which are probably due to the standing waves in the IF circuitry.

V. INTEGRATED ANTENNA BEAM PATTERN

Far-field amplitude beam pattern of the integrated antenna has been measured at 625 GHz in a heterodyne mode. The submillimeter source is a harmonic multiplier [6] driven by a microwave source. The dewar is placed on a rotation/tilt table to allow for the angular measurements [7]. The tilt movement is referred to as the vertical scan and the rotation as the horizontal scan. The angle resolution of the system is 0.1° .

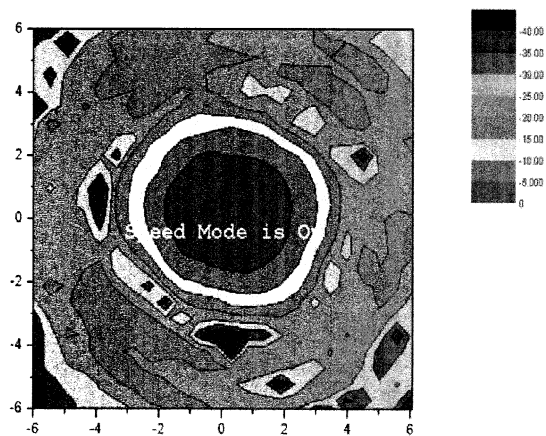


Fig. 4. Far-field 2D scan of the integrated lens-antenna beam pattern. The isolines are at -5 dB, -10 dB, -15 dB, -20 dB etc.

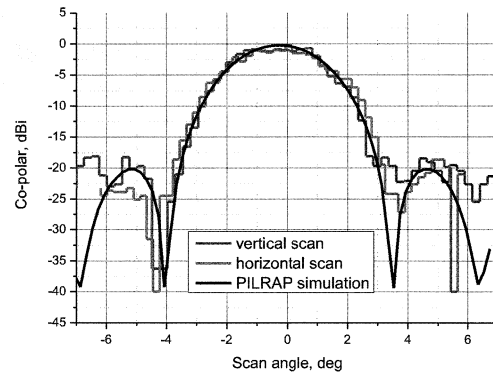


Fig. 5. Vertical (blue curve) and horizontal (red curve) far-field scans. The fit (black curve) is diffraction pattern calculated by PILRAP.

The integrated antenna is located at the center of rotation. The measured beam pattern of the antenna is therefore expected to be independent of the beam pattern of the signal source. Nevertheless, to exclude influence of a possible beam asymmetry in the measured results, we have rotated the source by 180 degrees and obtained similar pattern. There are no focusing elements between the signal source and the receiver and the distance between them is about 70 cm. Signal source is positioned with $\pm 0.2^\circ$ and ± 0.2 mm accuracy relative to the reference plane of the mixer block using He-Ne laser alignment system. The measured beam pattern includes thus information about boresight error of the beam.

Results of the measurements for the double dipole antenna coupled SIR are shown in the Fig. 4 and Fig. 5. The pattern is symmetric with the first sidelobe level of below -17 dB. It is close to the theoretically predicted diffraction pattern calculated by PILRAP [8] and similar to the patterns measured with the double slot or double dipole antennas at these frequencies. The full width half maximum (FWHM) is 3 deg.

VI. LABORATORY GAS CELL MEASUREMENTS

Gas cell measurements were done using a prototype cryostat which accommodates complete cold channel. Only SSB filter was not installed at this moment to allow DSB operation of the receiver. As a back-end spectrometer we used Digital AutoCorrelator (DAC). SIR was operated in a phase-locked mode. Spectra are integrated from about 20 individual calibrated spectra. DAC integration time of individual spectrum is 1 sec. Recorded by the DAC spectrum is a convolution product of the signal (gas emission lines) with the FFO line spectrum. To recover the signal, we apply a simple direct deconvolution process using the measured FFO line shape.

Photo of the measurement setup is shown in Fig. 6. Receiver beam is focused by an off-axis parabola. For radiometric calibration we used room temperature (300 K) and liquid nitrogen (77 K) cooled blackbodies (Eccosorb).

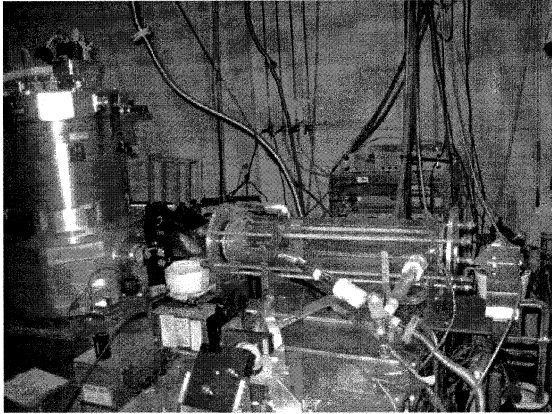


Fig. 6. Photo of the measurement setup. Switching mirror selects between "cold" load (receiver beam is directed downwards, as in the picture), "hot" (beam is directed upwards), or "signal" (beam is directed towards the gas cell).

Switching between two calibration loads and a signal (gas cell) is done by a computer controlled flat mirror. After the gas cell the beam is reflected by a flat mirror towards another cold (77 K) load. Gas cell windows are made from 2 mm thick HDPE. Measurements are done in a sequence Hot-Signal-Cold-Signal-Hot-Signal-...

For the measurements two OCS lines at 619.6213651 GHz and 631.7429035 GHz were selected. These lines could be observed at the same time, one in the upper and the other in the lower sideband of the receiver. The FFO was thus tuned at 625.240 GHz. The IF frequencies of these lines are 5618.6 MHz and 6502.9 MHz.

We have measured emission lines at different gas pressures, ranging from 0.2 mBar to 8 mBar. Example of the deconvolved spectrum at a gas pressure of 1.2 mBar is shown in Fig. 7. At this pressure both lines are expected to be saturated, pressure broadened and probably also saturation

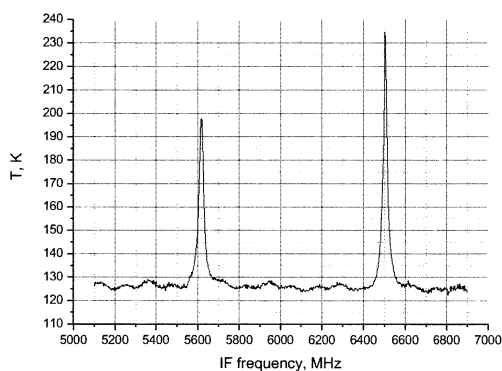


Fig. 7. Deconvolved spectrum of the OCS emission lines at a gas pressure 1.2 mBar. LO frequency 625.24 GHz. Lines are saturated, the difference in line strength reflects the sideband ratio of the receiver.

broadened. Modelling of these gas lines and comparison with the measured data is in progress. One can note that the two lines have different strength. We have measured the same levels also at higher gas pressures, proving that the lines are indeed in saturation. The difference in lines strengths should thus reflect the sideband ratio of the receiver.

There are ripples in the measured baseline which we believe have optical origin. In our lab test setup the calibration blackbodies are made from flat Eccosorb, the cryostat and gas cell windows have no antireflection coatings. Reflections of the optical beam from different surfaces cause appearance of the standing waves, which are then seen back in the measured spectrum. It is possible to exclude them from the line spectrums by measuring the baseline only (empty cell) and using these data to subtract the ripples (not done in Fig. 7). The baseline temperature is about 125 K, higher than the background temperature 77 K (cold load behind the cell) mainly due to the loss in the gas cell windows.

ACKNOWLEDGMENT

The authors thank L. Filippenko for fabrication Nb-AlN-NbN devices. M. van der Vorst is acknowledged for supplying PILRAP, A. Murk for useful and stimulating discussions, A. Selig and W. Wild for their support in this work.

REFERENCES

- [1] Hoogeveen, R.W.M., Yagoubov, P.A., Maurellis, A.N., Koshelets, V.P., Shitov, S.V., Mair, U., Krocka, M., Wagner, G., Birk, M., Hübers, H.-W., Richter, H., Semenov, A., Gol'tsman, G., Voronov, B., Ellison, B., Kerridge, B., Matheson, D., Alderman, B., Harman, M., Siddans, R., Reburn, J., eds. Strojnik, M., "New cryogenic heterodyne techniques applied in TELIS: the balloon borne THz and submm limb sounder for atmospheric research", Proc. of SPIE, Infrared Spaceborne Remote Sensing XI, 5152, p. 347-355, 2004.
- [2] V. P. Koshelets, S.V. Shitov, P.N. Dmitriev, A.B. Ermakov, L.V. Filippenko, V.V. Khodos, V.L. Vaks, A.M. Baryshev, P.R. Wesselius, J. Mygind, "Towards a Phase-Locked Superconducting Integrated Receiver: Prospects and Limitations," *Physica C*, vol. 367, pp. 249-255, 2002.
- [3] P.N. Dmitriev, I.L. Lapitskaya, L.V. Filippenko, A.B. Ermakov, S.V. Shitov, G.V. Prokopenko, S.A. Kovtonyuk, and V.P. Koshelets. "High Quality Nb-based Integrated Circuits for High Frequency and Digital Applications", *IEEE Trans. on Appl. Supercond.*, vol. 13, No 2, pp. 107-110, June 2003.
- [4] V.P. Koshelets, S.V. Shitov, A.V. Shchukin, L.V. Filippenko, J. Mygind, A.V. Ustinov. "Self-Pumping Effects and Radiation Linewidth of Josephson Flux Flow Oscillators" *Phys. Rev. B*, vol. 56, pp 5572-5577, (1997).
- [5] P.A. Yagoubov, W.-J. Vreeling, H. van de Stadt, R.W.M. Hoogeveen, O.V. Koryukin, V. P. Koshelets, O.M. Pylypenko, A. Murk, "550-650 GHz spectrometer development for TELIS", *Proc. 16th Intern. Symp. Space THz Technol.*, Gothenburg, Sweden, 2005, pp.438-443.
- [6] D. Pavel'ev, Yu. Koshurinov, N. Demarina, V. Ustinov, A. Zhukov, N. Maleev, A. Vasilyev, A. Baryshev, P. Yagoubov, N. Whyborn, "Temperature dependence of the radiation power emitted by a superlattice subject to a high-frequency electric field", *Conference Digest of IEEE Joint 29th IRMMW-2004/12th THz-2004, Karlsruhe, Germany*, 2004, pp.279-280.
- [7] P. Yagoubov, W.-J. Vreeling, P. de Korte, "Characterization of an integrated lens antenna at terahertz frequencies", *Proc. 12th Intern. Symp. Space THz Technol.*, San Diego, CA, 2001, pp.193-205.
- [8] M. J. M. van der Vorst. Integrated Lens Antennas for Submillimeter-wave Applications. PhD thesis, Elect. Eng. Dept., Eindhoven Univ. Technol., Eindhoven, The Netherlands, 1999.

CONDOR - AN ASTRONOMICAL HETERODYNE RECEIVER AT
1.25 - 1.5 THZ

M.C. Wiedner, G. Schmidt, S. Bedorf, F. Biela, U. Graf, C. E. Honingh, K. Jacobs, P. Muñoz, M. Olbrich, K. Rettenbacher, O. Siebertz, F. Schmülling, J. Stutzki, B. Vowinkel

¹Universität zu Köln, I. Physikalisches Institut, Zùlpicher Str. 77, 50937 Köln, Germany
wiedner, gschmidt, bedorf, biela, graf, honingh, jacobs, espacio, olbrich, rettenba, siebertz, schmuelling,
stutzki, vowinkel@ph1.uni-koeln.de

The CO N⁺ Deuterium Observations Receiver (CONDOR) is a heterodyne receiver that operates between 1250 - 1530 GHz. Its primary goal is to observe star-forming regions in CO, N⁺, and H₂D⁺ emission.

The instrument follows the standard heterodyne design. It uses a solid state local oscillator (LO) fabricated by Radiometer Physics GmbH. This LO consists of a high frequency Gunn followed by a tripler and quadrupler and produces 1370 - 1500 GHz. Alternatively, a multiplier chain from Virginia Diodes allows us to extend the frequency range to 1250 - 1530 GHz. Since the power of the LO is only a few

W, the LO and sky signal are overlaid with a Martin-Puplett interferometer. The heart of the receiver is a superconducting NbTiN hot electron bolometer (HEB) (see contribution by Muñoz et al.). The bolometer has an area of 0.25 x 2.8 m and is mounted on a SiN membrane in a waveguide mixer block. To facilitate operation at remote sites, CONDOR is the first receiver that cools the HEB with a closed-cycle system. Since HEBs are particularly sensitive to temperature fluctuations as well as modulations in LO power, we use a Pulse Tube Cooler, which has less vibration than, e.g., a Gifford McMahon cooler. In order to further minimize vibrations and temperature fluctuations, the mixer and first amplifier are mounted on a separate plate connected via flexible heat straps to the 4 K stage. To improve the matching at the intermediate frequency (IF) we inserted an isolator between the mixer and the cryogenic, high electron mobility transistor (HEMT) amplifier. This reduced the receiver temperature by about 25%, but unfortunately, also decreased the IF bandwidth from the intended 1.0 - 2.0 GHz to about 1.0 -1.8 GHz.

We consistently obtain receiver noise temperatures below 1800 K using hot (ambient temperature) and cold (liquid nitrogen) calibration loads. However, reliable noise temperatures as low as 1400 K were seen on dry days and with optimal tuning. Receiver temperatures are flat over the entire 800 MHz band. We measured spectral Allan variances by computing the variance of the calibrated differences of consecutive spectra. These variances are important for spectral line observations because they indicate baseline ripples caused by temporal deformations of the passband. We obtain minimum Allan variances at 25 - 35 s, which is approximately the optimum individual on-source integration time (see Schieder & Kramer 2001). As expected, the Allan variance is dominated by the mixer and the LO and not the IF. (The minimum time of the total power Allan variance is about 10s over a 1 MHz bandwidth. This variance is important for continuum observations.)

In November 2005, CONDOR was successfully commissioned on the 12-m Atacama Pathfinder Experiment (APEX) telescope, which is located at an elevation of 5100 m in the Atacama desert in Chile. Pointing observations were performed on the Moon and Mars. The first spectral line observations were obtained of CO J=13-12 emission at 1497 GHz from several sources in Orion. (For details on the first light observations see Wiedner et al. (2006).)

References:

- Schieder, R. & Kramer, C. 2001, 373, 746
Wiedner, M. C., et al. 2006, A&A submitted

High Resolution Spectroscopy with a Quantum Cascade Laser at 2.5 THz

Heinz-Wilhelm Hübers, Sergey G. Pavlov, Heiko Richter, Alexei D. Semenov, Lukas Mahler, Alessandro Tredicucci, Harvey E. Beere, David A. Ritchie

Abstract—The quantum cascade laser (QCL) is a powerful, narrow linewidth, and continuous wave source of terahertz radiation. We have characterized a 2.5 THz distributed feedback QCL with respect to linewidth and frequency tunability. Both were found to be sufficiently good for high resolution gas phase spectroscopy. The QCL was implemented in a spectrometer for high-resolution gas phase spectroscopy where the absolute frequency of the laser was determined by mixing its radiation with the radiation of a 2.5 THz optically pumped gas laser. The absolute frequency as well as the pressure broadening of a rotational transition of methanol at 2.519 THz was measured. The results demonstrate that THz QCLs are well suited for either direct absorption or heterodyne high resolution spectroscopy.

Index Terms—quantum cascade laser, spectroscopy, terahertz

I. INTRODUCTION

HIGH resolution gas phase spectroscopy at terahertz (THz) frequencies is a powerful tool for investigations of the structure and energy levels of molecules and atoms. Besides information on the species itself, important information on Doppler and pressure broadening can be obtained from THz spectra. These data are a prerequisite for the interpretation of spectra obtained from astronomical sources or planetary atmospheres including the Earth [1]. While in the low THz region many different methods have been developed, spectroscopy above 2 THz is hampered by the lack of frequency tunable, continuous wave, powerful, and narrow linewidth radiation sources. The recently developed THz quantum cascade laser (QCL) [2] has attractive features for gas phase spectroscopy, namely, its intrinsic linewidth of less than 20 kHz [3, 4] and high output power [5]. The goal of the work described in this paper is to characterize a distributed feedback (DFB) THz

QCL with respect to linewidth and frequency tunability and to implement it into a THz spectrometer for high resolution gas phase absorption spectroscopy. The experiment also allows assessing the performance of the QCL when used as local oscillator (LO) in a heterodyne spectrometer.

II. DESIGN OF THE QCL

A distributed feedback (DFB) QCL has been used for the experiments described in this article. It is designed for an operation frequency at about 2.5 THz. The active medium of the laser is based on a GaAs/AlGaAs superlattice. The design follows the so-called bound-to-continuum approach [6] with a rather uniformly chirped superlattice and no marked distinction between the injection and lasing regions. The active medium is formed by 110 repeat units of the superlattice (total thickness 15 μm) covered on top by a Cr/Au layer. Between the ~ 250 μm thick substrate and the active medium is a highly doped GaAs layer. This layer has two doping concentrations: $2.7 \times 10^{18} \text{ cm}^{-3}$ in the 530 nm next to the superlattice and $2.6 \times 10^{17} \text{ cm}^{-3}$ in the 500 nm close to the substrate. By these means the boundary conditions at the two sides of the buried doped layer can be controlled separately. The resonator is a mesa-etched, 240 μm wide ridge with a length of 2.5 mm defined by cleaving. The top layer of the QCL is patterned into a series of narrow slits with half-wavelength period to create the DFB structure [7]. The laser is soldered to a copper bar, wire bonded, and mounted on a copper holder thermally coupled to a 4 K stage of a mechanical cryo-cooler. In order to minimize vibrations the laser holder is mechanically isolated from the 4 K stage by copper wires. The cooler has a heat extraction capacity of 1 W at 4 K. Since the input power of the laser is 5–10 W the smallest achievable temperature at the position of the QCL is ~ 20 K during laser operation. The laser threshold is about 80 A/cm² at 20 K, the maximum output power is about 6 mW, and the laser works up to 58 K in continuous wave. Due to the limited capacity of the cryo-cooler the operation temperature changes with current.

III. FREQUENCY CHARACTERIZATION OF THE QCL

The linewidth and frequency tunability of the QCL were measured by mixing the radiation from the DFB laser with the radiation from an optically pumped gas laser operating on the methanol emission line at 2.5227816 THz (pump line of the CO₂ laser: 9P36 [8]). The radiation from both lasers was superimposed by a wire grid and focused onto a GaAs Schottky

Manuscript received May 19, 2006. This work was supported in part by the Investitionsbank Berlin and the European Commission through the PASR project "TeraSec", the IP project "Teranova", and the Marie Curie RTN "Poise".

H.-W. Hübers is with the Institute of Planetary Research, German Aerospace Center (DLR), Rutherfordstr. 2, 12489 Berlin, Germany (phone: +49-30-67055596; fax: +49-30-67055507; e-mail: heinz-wilhelm.huebers@dlr.de).

S. G. Pavlov, H. Richter, and A. D. Semenov are with the Institute of Planetary Research, German Aerospace Center (DLR), Rutherfordstr. 2, 12489 Berlin, Germany.

L. Mahler and A. Tredicucci are with NEST CNR-INFM and Scuola Normale Superiore, Piazza dei Cavalieri 7, 56126 Pisa, Italy.

H. E. Beere and D. A. Ritchie are with Cavendish Laboratory, University of Cambridge, Madingley Road, Cambridge CB3 0HE, United Kingdom.

diode with a quasi-optical 4λ corner cube antenna [9]. The difference signal was amplified and analyzed with a spectrum analyzer up to a maximum frequency of 18 GHz which was set by the available amplifiers. By these means the linewidth as well as the absolute frequency and the frequency tunability of the QCL as a function of current and temperature were measured. The experimental set-up is shown in Fig. 1.

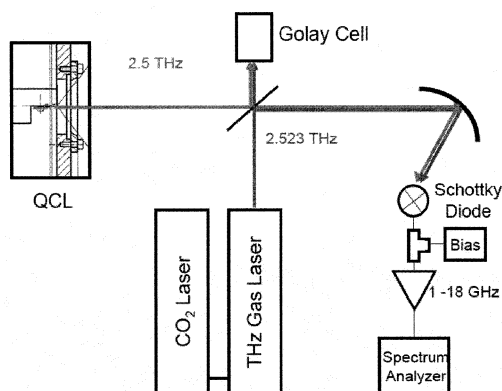


Fig. 1: Experimental set-up of the mixing experiments.

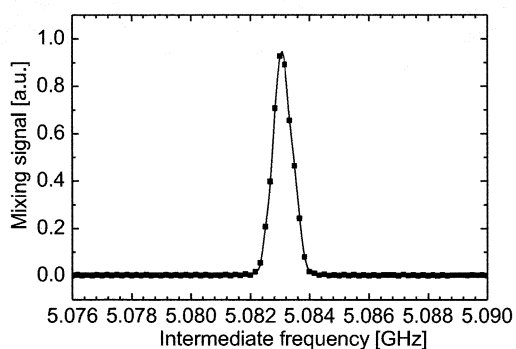


Fig. 2: Mixing signal of the QCL and the 2.5 THz gas laser.

The linewidth measured with an integration time of 5 s is shown in Fig. 2. The full width at half maximum (FWHM) is ~ 1 MHz. With an integration time of 0.3 s it reduces to 300 kHz. This is sufficient for many applications in high resolution gas phase spectroscopy. For example the Doppler limited linewidth of $^{12}\text{CH}_3^{16}\text{OH}$ is 5.5 MHz at 2.5 THz and 300 K. The tuning rate is almost linear with current (+8.0 MHz/mA, Fig. 3). The temperature related frequency tuning varies between -20 MHz/K and -100 MHz/K depending on current and temperature (Fig. 4). For both lasers the tunability is mainly caused by changes of the refractive index with temperature and current.

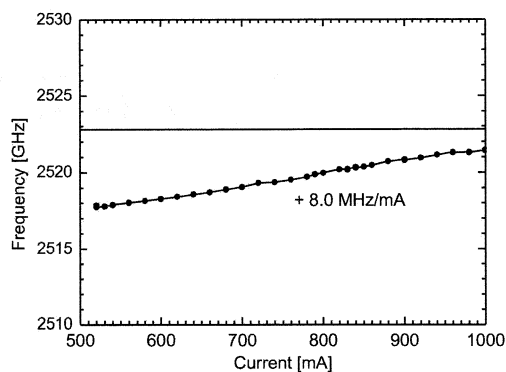


Fig. 3: Frequency of the QCL as a function of current (solid line: gas laser frequency).

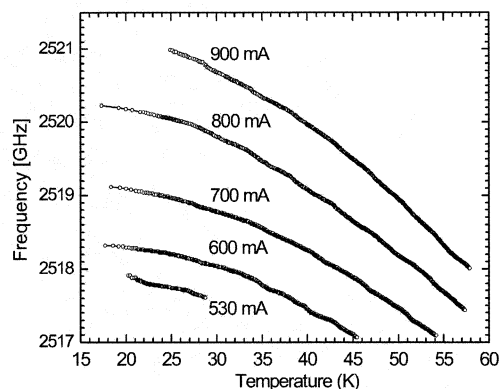


Fig. 4: Frequency of the QCL as a function of temperature for fixed current.

The set-up of the spectrometer is sketched in Fig. 5. For frequency tuning the temperature of the QCL is set and the current is swept in steps corresponding to frequency steps of 0.2 MHz to 2 MHz. The radiation from the QCL is reflected by a wire grid into a 0.5 m long absorption cell. The cell was equipped with two polyethylene windows and the pressure was measured with a capacitance manometer. For each measurement the cell was filled with methanol gas at a certain pressure and sealed off. The transmitted radiation is collimated by an off-axis parabolic mirror and detected with a Ge:Ga photoconductive detector. The transmitted radiation was mechanically chopped in front of the detector and detected with a lock-in amplifier. A small part of the radiation from the QCL is transmitted through the wire grid. This is superimposed with the radiation from the gas laser operating on the 2.5 THz line. At the output of the gas laser a grid with wires oriented perpendicularly to the wires of the first grid was used to define the polarization in a way that it is reflected by the first grid. The radiation from both lasers is focused onto a GaAs Schottky diode. The signal at the difference frequency is amplified and its frequency is measured with a spectrum analyzer. This is especially important because the frequency tun-

ing of the QCL is not linear with current. In total a frequency range from 2.517 THz to 2.521 THz is available.

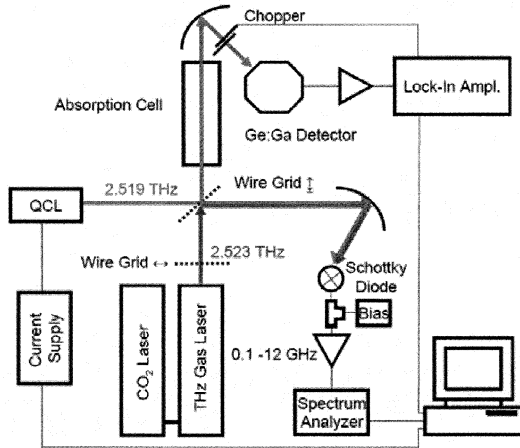


Fig. 5: THz spectrometer for high resolution gas phase spectroscopy.

V. RESULTS

Fig. 6 shows the absorption line measured with the QCL along with a Voigt profile fitted to the measured profile. As can be seen the agreement is very good. The center frequency of the absorption line is 2.519112(1) THz. This agrees well with published data measured with a Fourier transform spectrometer (2.519107(2) THz [10]). The pressure broadening of the methanol line was determined by measuring its profile at different pressures up to 1000 Pa and determining the full width at half maximum (FWHM). A least squares fit to the FWHM data yields a pressure broadening coefficient of 229(2) kHz/Pa (Fig. 7). This is similar to pressure broadening coefficients of other methanol lines (265.6(2) kHz/Pa at 76 GHz [11] and 290 kHz/Pa at 2.524 THz [12]).

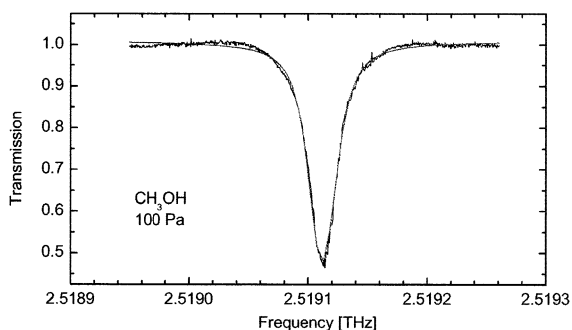


Fig. 6: CH₃OH absorption spectrum measured at 100 Pa. The solid line is a fit of a Voigt profile to the absorption line.

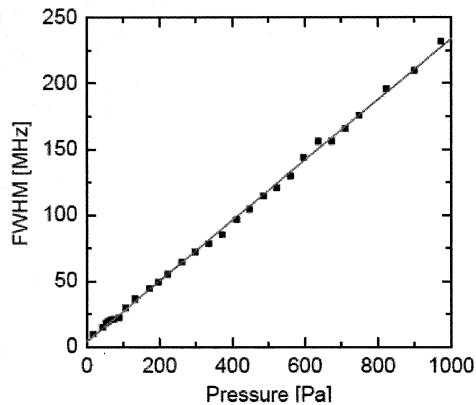


Fig. 7: FWHM of the CH₃OH rotational transition as a function of pressure.

VI. SUMMARY AND CONCLUSIONS

In summary, the linewidth of a DFB QCL operating at 2.5 THz as well as its tuning rates as a function of current and temperature have been determined. Based on these results, a THz spectrometer for high-resolution gas phase spectroscopy with a QCL as the radiation source has been realized. Frequency calibration of the spectra was achieved by instantaneously measuring the frequency difference between the QCL and a THz gas laser. We have measured the transition frequency and pressure broadening of a methanol rotational transition at 2.5 THz. The comparison of our data with other spectroscopic data shows good agreement. The results show that QCLs are very promising radiation sources for high resolution absorption spectroscopy. In a heterodyne receiver the frequency resolution is to a large extent determined by the linewidth and frequency stability of the LO. Our results show that the QCL performance is sufficient also for high resolution heterodyne spectroscopy.

REFERENCES

- [1] J. Demaison, K. Sarka, and E. H. Cohen (eds.), *Spectroscopy from Space*, Dordrecht: Kluwer, 2001.
- [2] R. Köhler, A. Tredicucci, F. Beltram, H. E. Beere, E. H. Linfield, A. G. Davies, D. A. Ritchie, R. C. Iotti, F. Rossi, "Terahertz semiconductor-heterostructure laser", *Nature*, vol. 417, pp. 156-159, 2002.
- [3] A. Barkan, F. K. Tittel, D. M. Mittleman, R. Dengler, P. H. Siegel, G. Scalari, L. Ajili, J. Faist, H. E. Beere, E. H. Linfield, A. G. Davies, and D. A. Ritchie, "Linewidth and tuning characteristics of terahertz quantum cascade lasers", *Opt. Lett.*, vol. 29, pp. 575-577, 2004.
- [4] H.-W. Hübers, S. G. Pavlov, A. D. Semenov, R. Köhler, L. Mahler, A. Tredicucci, H. E. Beere, D. A. Ritchie, E. H. Linfield, "Terahertz Quantum Cascade Laser as Local Oscillator in a Heterodyne Receiver", *Optics Express*, vol. 13, pp. 5890-5896, 2005.
- [5] B. S. Williams, S. Kumar, Q. Hu, and J. L. Reno, "High-power terahertz quantum-cascade lasers", *Elec. Lett.*, vol. 42, pp. 89-90, 2006.
- [6] J. Faist, M. Beck, T. Aellen, and E. Gini, "Quantum-cascade lasers based on a bound-to-continuum transition", *Appl. Phys. Lett.*, vol. 78, pp. 147-149, 2001.
- [7] L. Mahler, A. Tredicucci, R. Köhler, F. Beltram, H. E. Beere, E. H. Linfield, and D. A. Ritchie, "High performance operation of single-mode terahertz quantum cascade lasers with surface plasmon gratings", *Appl. Phys. Lett.*, vol. 87, 181101, 2005.

- [8] N. G. Douglas, *Millimetre and Submillimetre Wavelength Lasers*, Berlin: Springer, 1989.
- [9] H. P. Röser, H.-W. Hübers, T. W. Crowe, and W. C. B. Peatman, "Nanostructure GaAs Schottky diodes for far-infrared heterodyne receivers", *Infrared Phys. Technol.*, vol. 35, pp. 451-462, 1994.
- [10] G. Moruzzi, F. Strumia, P. Carnesecchi, B. Carli, and M. Carlotti, "High resolution spectrum of CH₃OH between 8 and 100 cm⁻¹", *Infrared Physics*, vol. 29, pp. 47-86, 1989.
- [11] P. Minguzzi, M. Tonelli, G. Carrara, and A. Di Lieto, "CH₃OH and CH₃⁸¹Br self-broadening measurements with a millimeter-wave stark interferometer", *J. Mol. Spectr.*, vol. 109, pp. 395-401, 1985.
- [12] A. D. Semenov, H.-W. Hübers, H. Richter, M. Birk, M. Krocka, U. Mair, K. Smirnov, G. Gol'tsman, and B. V. Voronov, "2.5 THz Heterodyne Receiver with NbN Hot-Electron Bolometer", *Physica C*, vol. 372-376, pp. 448-453, 2002.

2.8 THz heterodyne receiver based on a surface plasmon quantum cascade laser and a hot electron bolometer mixer

M. Hajenius^{a,b}, P. Khosropanah^b, J.N. Hovenier^a, J.R. Gao^{a,b}, T.M. Klapwijk^a
S. Dhillon^c, S. Barbieri^c, P. Filloux^c, C. Sirtori^c
D.A. Ritchie^d, and H.E. Beere^d

^a Kavli Institute of NanoScience, Faculty of Applied Science, Delft University of Technology
Lorentzweg 1, 2628 CJ, Delft, the Netherlands

^b SRON, Netherlands Institute for Space Research
Sorbonnelaan 2, 3584 CA Utrecht, the Netherlands

^c Matériaux et Phénomènes Quantiques, Université de Paris 7
75251 Paris Cedex 05, France
Thales Research and Technology, Domaine de Corbeville
91404 Orsay Cedex, France

^d University of Cambridge, Cavendish Laboratory
J.J. Thomas Avenue, Cambridge, CB3 0HE, UK

Email: M.Hajenius@tudelft.nl

Abstract—This work focuses on surface plasmon quantum cascade lasers (QCL) as a local oscillators (LO) for heterodyne receivers operating above 2 THz. The far-field beam pattern of a 214 μm wide and 1500 μm long 2.84 THz surface plasmon QCL is measured and found to be less divergent compared to metal-metal waveguide QCLs, which is preferable for coupling the radiation to a quasi-optical mixer. We successfully used this QCL to pump a NbN HEB mixer integrated with spiral antenna. At optimized LO power and bias voltage we measured double side band receiver noise temperatures of 1150 K and 1050 K at bath temperature of 4 K and 2 K respectively. To the best of our knowledge these represent the highest reported sensitivities at such a high frequency.

I. INTRODUCTION

Nowadays heterodyne receivers operating up to 2 THz use a combination of an electronically tunable solid state LO source [1], with either a superconductor-insulator-superconductor (SIS) [2] or a hot electron bolometer (HEB) mixer [3]. The latter type of mixer is the detector of choice for frequencies above 1.5 THz. Future space borne missions require an increase in frequency, e.g. 2-6 THz [4]. The development of new receivers operating at such high frequencies is limited by the availability of suitable LO sources. Existing solid state LOs [1] are unlikely to generate sufficient output power at such high frequencies since the power falls off rapidly with increasing frequency due to reduced multiplication efficiency. Optically pumped gas lasers can operate at higher frequencies, but are

in general not suitable for space borne applications. Recently, a new type of solid-state THz source has been developed based on quantum cascade laser (QCL) structures [5]. This new source holds great promise for LO applications because of its compactness and high power efficiency. The demonstration of a HEB-QCL receiver at 2.8 THz has recently been reported using a HEB mixer and a QCL as LO [6]. In this case a QCL based on a double-sided metal-metal waveguide, developed at MIT/Sandia [7], was used. The far field beam patterns of this type of devices have also been measured [8] and modeled [9], showing that the beam is not only strongly divergent but also presents ring-like interference features. These characteristics are the consequence of the small lateral dimensions of the QCL cavity (at the limit of subwavelength) and of the interference due to the coherent emission from all the facets. Obviously, such beam pattern prevents an efficient optical coupling of the radiation to a mixer.

In this work we exploit a different type of QCL, which is based on surface plasmon waveguide. Because of the different cavity design and the geometry difference in lateral dimensions, a better quality beam pattern is expected compared to metal-metal waveguide QCLs. Here we measure the beam pattern of a 2.8 THz surface plasmon QCL and also determine the heterodyne sensitivity obtained by using the QCL with a HEB mixer. A similar surface plasmon QCL has been used as LO source for a 2.5 THz, HEB-based heterodyne receiver [10].

However, here we demonstrate a substantially lower receiver noise temperature at a slightly higher frequency.

II. QCL CHARACTERIZATION

The QCL used in this work is reported in reference [11] and is based on a bound-to-continuum active region design and a surface plasmon waveguide. The active region consists of 90 GaAs/Al_{0.15}Ga_{0.85}As repeated modules grown by MBE, giving a total thickness of 11.64 μm . A 214 μm wide ridge waveguide was cleaved at both ends to form a 1500 μm -long Fabry-Perot cavity. The active layer grown on top of a semi-insulating GaAs substrate is sandwiched between a metallic top contact and a heavily n-doped GaAs bottom contact channel. As a consequence, unlike metal-metal QCLs, the optical mode is not confined within the active region, but penetrates inside the substrate down to a depth of approximately 100 μm at $\lambda_0=107 \mu\text{m}$ ($f=2.8 \text{ THz}$). Fig. 1 shows a schematic drawing of the QCL and the computed one-dimensional mode intensity profile.

The lasing spectrum of this QCL was measured at different bias currents using a Fourier-transform spectrometer (FTS). As shown in Fig. 2, we observe a single longitudinal mode at 2.835 THz (wavelength $\lambda_0=105.8 \mu\text{m}$). The measured linewidth of 1 GHz is limited by the resolution of the FTS [12]. The output power of this particular QCL was not measured directly. However, based on measurements done on similar devices, a few mW of output power is expected at around 5 K operating temperature. At maximum output power the laser is biased at 6 V and 900 mA, which means that the QCL dissipates a DC power of about 5.4 W in continuous wave (CW) operation mode.

Before undertaking heterodyne measurements, we measured the laser far-field beam pattern with the same setup used previously for the metal-metal waveguide QCLs [8]. A Schematic of the measurement setup is shown in Fig. 3. The QCL is Indium-bonded to a copper holder and is mounted on the cold plate of a He-flow cryostat. The output power was measured using a 5 mm diameter aperture pyrodetector, placed at a distance of about 90 mm from the QCL. The laser was operated in pulse mode and the emitted power was recorded at different positions of the detector using a lock-in amplifier. The measured beam pattern is shown in Fig. 4. We find that most of the power is concentrated in the center of the beam. Such good directionality allows for an efficient coupling to a HEB mixer.

III. HETERODYNE RECEIVER SETUP

Figure 5 shows a schematic view of the measurement setup. We use two cryostats, in which the QCL and the HEB are mounted separately.

As mixer, we used a NbN HEB mixer integrated with a spiral antenna. The NbN superconducting bridge is 2 μm wide, 0.2 μm long, and 5.5 nm thick. The normal state resistance of the device (at room temperature) is 80 Ω . The critical temperature is approximately 10 K and the critical current at 4.2 K is 180 μA . A similar HEB mixer from the same

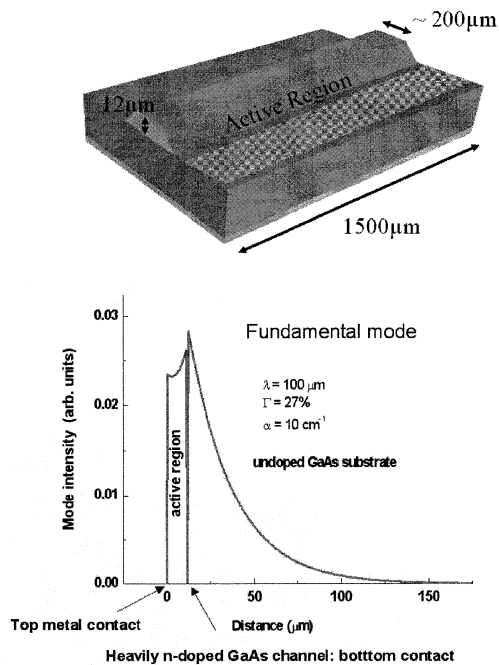


Fig. 1. Schematic view of the QCL ridge-cavity together with the computed mode intensity profile at $\lambda_0=107 \mu\text{m}$. The field penetration inside the substrate is about 100 μm . We compute waveguide losses (α) of 10 cm^{-1} and an overlap factor with the active region (Γ) of 27%.

batch has been measured using a gas laser as LO at 1.63 THz, yielding an excellent receiver noise temperature of 700 K.

A large vacuum liquid helium cryostat with a high cooling capacity was used to operate the QCL in CW mode. When operating in CW mode, as the QCL heats up, the output power drops until the temperature of the device is stabilized. Under stable CW operation the power of QCL is about half of the pulse mode operation. Nevertheless there is enough power to pump the HEB with a thin Mylar beam splitter (3.5 μm thick).

The output power of the QCL is coupled to the HEB antenna using a standard quasi-optical technique: the Si chip with the HEB is glued to the back of an elliptical, anti-reflection coated Si lens. The lens is placed in a metal mixer block, thermally anchored to the 4.2 K cold plate. The beam from the QCL passes through a high density polyethylene (HDPE) dewar-window and is collimated with a HDPE lens. The radiation is further guided to the HEB cryostat by a 3.5 μm thick Mylar beam splitter. The blackbody radiation from a slab of Eccosorb is used as a signal source defining a hot load at 295 K and a cold load at 77 K. The signal is combined with the QCL beam through the beam splitter. Both beams pass through the thin HDPE window at room temperature and a metal mesh heat filter (QMC Ltd.), mounted on the 4 K shield of the HEB cryostat.

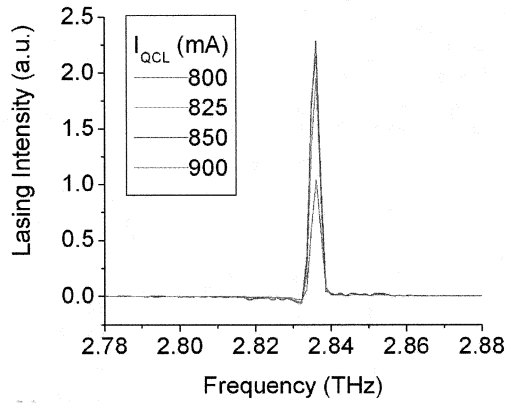


Fig. 2. Measured lasing spectrum of the QCL at different bias currents. The device radiates in a single mode at 2.835 THz. Changing the bias current does not affect the frequency.

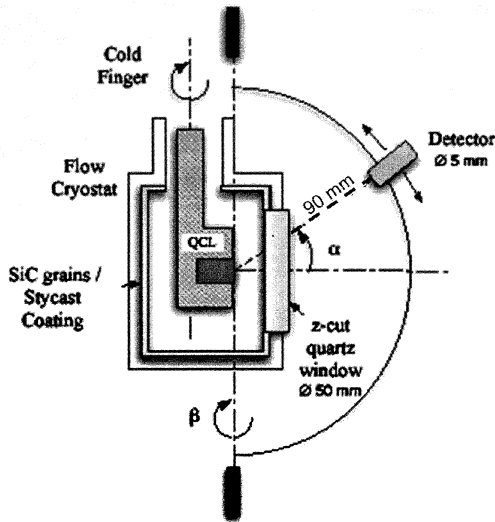


Fig. 3. Schematic picture of the beam pattern measurement setup. The power was measured using a 5 mm diameter aperture pyrodetector.

IV. HETERODYNE MEASUREMENT RESULTS

The key results of the heterodyne measurements are displayed in Figure 6. A set of current versus voltage (I-V) curves of the HEB is shown for various levels of absorbed LO power in the HEB, together with the receiver noise temperature as a function of the bias voltage of the HEB mixer. The power level, which is estimated at the HEB by the isothermal technique [13], is varied by changing the bias current of the QCL. The receiver noise temperature is determined from the ratio of the IF output noise power when a hot and a cold load are used as signal source [14]. The best sensitivity of 1150

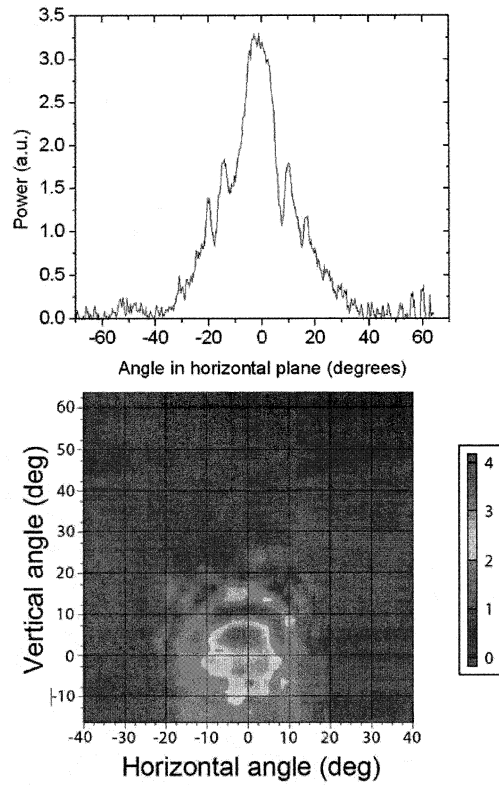


Fig. 4. Measured far-field beam pattern of the surface plasmon QCL. The upper panel: the profile along the plane of the QCL, but measured at an offset of +5 degree in the 2D plot shown in the lower panel. The lower panel: the 2D plot of the beam pattern. Due to the tilt in the QCL mounting, the 2D plot has a negative offset of 5 degrees in vertical direction.

K is obtained for 300 nW LO power and 0.6 mV DC bias at a (HEB) bath temperature of 4 K. A slightly lower noise temperature of 1050 K is obtained at the same bias voltage, but with a reduced bath temperature of 2 K. The latter represents the lowest receiver noise temperature ever reported in literature and corresponds to $7.7 \times hf/k_B$, where h is Planck's constant, f is the radiation frequency, and k_B is the Boltzman constant. This value is also approximately 25% lower compared to what we reported previously using a metal-metal waveguide QCL operating at nearly the same frequency [6].

V. CONCLUSIONS

The beam pattern of QCLs is a crucial parameter for their use as LO source. Compared to metal-metal waveguide QCLs, the surface plasmon QCL under test was characterized by a weaker mode confinement in the direction perpendicular to the surface and by relatively large lateral dimensions (larger or comparable with the wavelength), yielding a much improved beam pattern. This allows us to pump a HEB mixer to the optimum operating point, using a very thin beam splitter (3.5

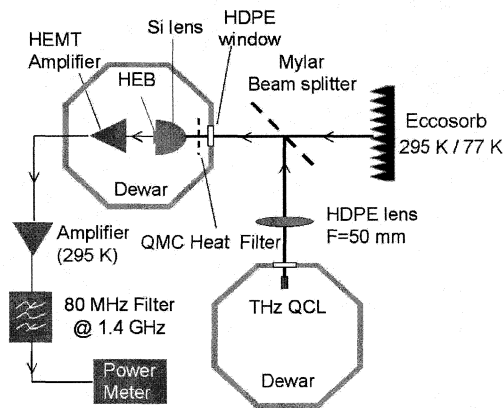


Fig. 5. Heterodyne measurement setup

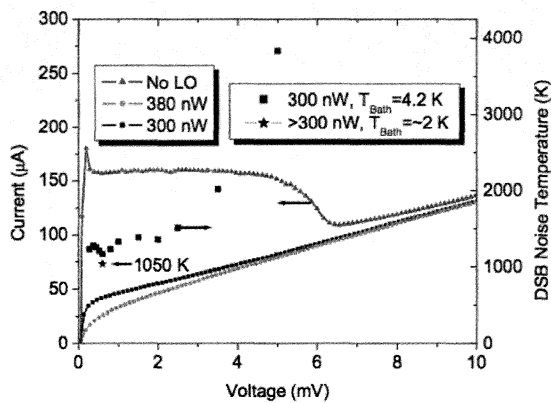


Fig. 6. Lines, left axis: Current-voltage characteristics of a spiral NbN HEB mixer with and without radiation from the QCL (LO) at 2.83 THz as LO. Symbols, right axis: The measured double side band (DSB) receiver noise temperature versus the bias voltage for the optimal LO power (300 nW).

μm Mylar). This way we obtained a measured DSB receiver noise temperature of 1050 K at a 2 K bath temperature, which represents the best sensitivity at $f \sim 2.8$ THz ever reported in literature, uncorrected for any optical loss. This sensitivity corresponds to $7.7 \times hf/k_B$, suggesting that the receiver noise temperature of a NbN HEB mixer may remain below $10 \times hf/k_B$ even when the frequency is increased beyond 2.8 THz.

ACKNOWLEDGEMENTS

We acknowledge A. Baryshev, J.J.A. Baselmans, and Z.Q. Yang for their help, and H. Hoevers for his support. The work is financially supported by the EU through RadioNet. We also acknowledge the partial financial support from European Community through the Framework IV Integrated Project Teranova and the PASR 2004 Project Terasec.

REFERENCES

- [1] I. Mehdi, E. Schlecht, G. Chattopadhyay, and P.H. Siegel. THz local oscillator sources: performance and capabilities. *Proc. of SPIE*, 4855:435–446, 2003.
- [2] B. D. Jackson, A. M. Baryshev, G. de Lange, J.-R. Gao, S.V. Shitov, N. N. Iosad, and T. M. Klapwijk. Low-noise 1 thz superconductor-insulator-superconductor mixer incorporating a NbTiN/SiO₂/Al tuning circuit. *Applied Physics Letters*, 79:436–438, 2002.
- [3] J. J. A. Baselmans, M. Hajenius, J.R. Gao, T. M. Klapwijk, P. A. J. de Korte, B. Voronov, and G. Gol'tsman. Doubling of sensitivity and bandwidth in phonon cooled hot electron bolometer mixers. *Applied Physics Letters*, 84:1958–1960, 2004.
- [4] Th. de Graauw, J. Cernicharo, W. Wild, A. Bos, J.-W. den Herder, A.W. Gunst, F. Helmich, B.D. Jackson, H.-J. Langevelde, P. Maat, J. Martin-Pintado, J. Noordam, A. Quirrenbach, P.R. Roelfsema, L.B. Venemac, P. Wesselius, and P.A. Yagoubov. Exploratory submm space radio-interferometric telescope (esprit). *Proc. of SPIE*, 5487:1522–1525, 2003.
- [5] R. Köhler, A. Tredicucci, F. Beltram, H.E. Beere, E. H. Linfield, A. G. Davies, D. A. Ritchie, R. C. Iotti, and F. Rossi. Terahertz semiconductor-heterostructure laser. *Nature*, 417:156–159, 2002.
- [6] J.R. Gao, J.N. Hovenier, Z.Q. Yang, J.J.A. Baselmans, A. Baryshev, M. Hajenius, T.M. Klapwijk, A.J.L. Adam, T.O. Klaassen, B.S. Williams, S. Kumar, Q. Hu, and J.L. Reno. A terahertz heterodyne receiver based on a quantum cascade laser and a superconducting bolometer. *Applied Physics Letters*, 86:244104, 2005.
- [7] Q. Hu, B.S. Williams, S. Kumar, H. Callebaut, S. Kohen, and J.L. Reno. Resonant-phonon-assisted thz quantum cascade lasers with metal-metal waveguides. *Semiconductor Science and Technology*, 20:228–236, 2005.
- [8] A.J.L. Adam, I. Kašalynas, J.N. Hovenier, T.O. Klaassen, J.R. Gao, E.E. Orlova, B.S. Williams, S. Kumar, Q. Hu, and J.L. Reno. Beam patterns of terahertz quantum cascade lasers with subwavelength cavity dimensions. *Applied Physics Letters*, 88:151105, 2006.
- [9] E.E. Orlova, J.N. Hovenier, T.O. Klaassen, I. Kašalynas, A.J.L. Adam, J.R. Gao, T.M. Klapwijk, B.S. Williams, S. Kumar, Q. Hu, and J.L. Reno. Antenna model for wire lasers. *Physical Review Letters*, 96:173904, 2006.
- [10] H.-W. Hübers, S.G. Pavlov, A.D. Semenov, R. Köhler, L. Mahler, A. Tredicucci, H.E. Beere, D.A. Ritchie, and E.H. Linfield. Terahertz quantum cascade laser as local oscillator in a heterodyne receiver. *Optics Express*, 13(15):5890, 2005.
- [11] S. Barbieri, J. Alton, H.E. Beere, J. Fowler, E.H. Linfield, and D.A. Ritchie. 2.9 THz quantum cascade lasers operating up to 70 k in continuous wave. *Applied Physics Letters*, 85(10):1674, 2004.
- [12] S. Barbieri, J. Alton, C. Baker, T. Lo, H. Beere, and D. Ritchie. Imaging with THz quantum cascade lasers using a Schottky diode mixer. *Optics Express*, 13(17):6497–6503, 2005.
- [13] H. Ekstrom, B.S. Karasik, E.L. Kollberg, and K.S. Yngvesson. Gain and noise of niobium superconducting hot-electron mixers. *IEEE Trans. Microwave Theory and Techniques*, 43(4):938, 1995.
- [14] A.R. Kerr. Suggestions for revised definitions of noise quantities, including quantum effects. *IEEE Transactions on Microwave Theory and Techniques*, 47(3):325–9, 1999.

AUTHOR INDEX

AUTHOR NAME	AFFILIATION	Paper ID
Aballea	Université de Lille 1, Laboratoire Ph. L. A. M., Lille, France	P2-27
Adam	Delft University of Technology, Kavli Institute of Nanoscience, Delft, Netherland	TH4-2
Adema	University of Groningen, Kapteyn Institute & SRON Netherland Institute for Space Research, Groningen, Netherland	P1-17
Alderman	Rutherford Appleton Laboratory, Space Science Technology department, Chilton Didcot, UK	P2-01
Alton	TeraView Ltd-St John Innovation Park, Cambridge, UK & University of Cambridge, Cavendish Laboratory, Cambridge, UK	P2-12
Andersson	Omnisys Instruments-Göteborg, Sweden	P2-25
Antipov	Moscow State Pedagogical University, Moscow, Russia	P1-04, TH3-1
Appenzeller	IBM T. J. Watson Research Center, New York, USA	TH1-1
Asayama	National Astronomical Observatory of Japan, National Institute of Natural Sciences, Japan	TH2-6
Audley	MRAO, Cambridge, U.K	WE2-5
Badi	LHAC - Campus scientifique - Université de Savoie, Le Bouget du Lac, France	P1-23
Banik	Chalmers University of Technology, MC2, Food Radar Systems & Microwave Electronic Laboratory, Göteborg, Sweden	P1-01, P1-13, TH3-8, P2-16
Barbieri	TeraView Ltd-St John Innovation Park, Cambridge, UK & University of Cambridge, Cavendish Laboratory, Cambridge, UK	P2-12
Barden	California Institute of Technology, Pasadena, CA, USA	FR2-4
Barends	SRON Netherland Institute for Space Research, Utrecht, Netherland	FR2-1
Barker	MRAO, Cambridge, U.K	WE2-5
Barkhof	University of Groningen, Kapteyn Institute & SRON Netherland Institute for Space Research, Groningen, Netherland	P1-17, P2-23
Baryshev	University of Groningen, Kapteyn Institute & SRON Netherland Institute for Space Research, Groningen, Netherland	P1-12, P1-17, WE1-4, TH3-4, TH4-2, P2-07, P2-23, FR3-6
Baselmans	SRON Netherland Institute for Space Research, Utrecht, Netherland	FR2-1, P1-12, TH3-4, FR3-6
Baubert	Observatoire de Paris, LERMA, Paris, France	P1-07, P1-08, P1-09
Bedorf	Universität zu Köln, I.Physikalisches Institut, KOSMA, Köln, Germany	TH3-3, FR3-4
Bedyk	Munich University of Technology, Institute for Physics of Electrotechnology, Munich, GERMANY	TH1-4
Beere	University of Cambridge, Cavendish Laboratory, Cambridge, UK	P2-10, P2-12, FR3-5
Belitsky	Chalmers University of Technology, Göteborg, Sweden	TH2-1, P2-28
Benoit	CNRS Grenoble, France	P1-02
Berg	Chalmers University of Technology, Microwave Electronic Laboratory & Microtechnology/ Nanoscience, Göteborg, Sweden	P1-07, P1-08, TH3-7, TH3-8

Bernaldo de Quiros	Universidad Politecnica de Madrid, Sistemas y Radiocommun., Madrid, Spain	P2-04
Biber	University of Erlangen, Institute for Microwave Technology, Nuremberg, Germany	P2-20
Bielau	Universität zu Köln, I.Physikalisches Institut, Köln, Germany	FR3-4
Birk	DLR, Institute for Remote Sensing Technology, Germany	FR3-3
Bishop	Virginia Diodes, Inc., Charlottesville, VA, USA	TH4-6
Blary	Institut d'Electronique de Microelectronique et de Nanotechnologie, UMR CNRS 8520, Villeneuve D'Ascq, France	P2-09
Blundell	Harvard Smithsonian Center for Astrophysics, Cambridge, MA, USA	WE1-2, TH4-3
Bolatto	University of California, Radio Astronomy Laboratory, Berkeley, CA, USA	P1-21
Bollaert	IEMN-DHS URM CNRS 8250 Villeneuve d'Ascq, France	P2-08
Boussaha	Observatoire de Paris, LERMA, Paris, France	P1-24
Bréelle	Université Paris 7, Laboratoire AstroParticule et Cosmology, Paris, France	WE2-6
Bumble	California Institute of Technology, Jet Propulsion Laboratory, Pasadena, CA, USA	WE1-5
Bussmann	University of Arizona, Steward Observatory, Tucson, USA	FR2-4
Calligaro	Thales Research and Technology, Orsay, France	P2-12
Camus	CNRS Grenoble, France	P1-02
Candotti	National University of Ireland, Maynooth, Co. Kildare, Ireland	P2-23
Cantu	University of Manchester, School of Electrical and Electronic Engineering, Manchester, UK	TH4-5
Caputa	Herzberg Institute of Astrophysics, National Research Council, Victoria, Canada	TH2-4
Caputo	INSA de Rouen, Laboratoire de Mathématique, Mont-Saint-Aignan, France	P1-24
Caroopen	AB Millimetre, Paris, France	P2-22, FR3-2
Cernicharo	Departamento de Astrofisicamolecular e infrarroja, Madrid, Spain	P2-26
Chattopadhyay	California Institute of Technology, Jet Propulsion Laboratory, Pasadena, CA, USA	FR1-2
Chaubet	Centre national d'études spatiales, Toulouse, France	P1-15
Cherednichenko	Chalmers University of Technology, Microwave Electronic Laboratory & Microtechnology/ Nanoscience, Göteborg, Sweden	P1-07, P1-08, P1-09, TH3-7
Chimot	Université Paris 11, UMR CNRS 8622, Orsay, France	P2-09
Chusseau	Université Montpellier II, CEM2, UMR 5507 CNRS, Montpellier, France	P2-13
Claude	Herzberg Institute of Astrophysics, National Research Council, Victoria, Canada	TH2-4
Cohn	Russian Academy of Sciences, Institute of Radio Engineering and Electronics, Moscow, Russia	P1-18, WE2-2
Constantin	Université de Lille I, Laboratoire Ph. L. A. M., Lille, France	P2-27, FR3-1

Crane	MRAO, Cambridge, U.K	WE2-5
Crawford	California Institute of Technology, Jet Propulsion Laboratory, Pasadena, CA, USA	P1-03
Crépin	Université de Lille 1, Lille, France	TH1-3
Crowe	Virginia Diodes, Inc., Charlottesville, VA, USA	TH4-6
Crozat	Université Paris 11, UMR CNRS 8622, Orsay, France	P2-09
Dace	MRAO, Cambridge, U.K	WE2-5
Daryoosh	University of Waterloo, Department of electrical and Computer Engineering, Waterloo, CA, USA	P2-15
Dauplay	Observatoire de Paris, LERMA, Paris, France	P1-09
Davies	University of Bath, Department of Physics, Bath, UK	P2-02
de Jong	SRON National Institute for Space Research, Groningen, Netherland	P1-16
De Korte	SRON Netherland Institute for Space Research, Utrecht, Netherland	FR2-1
de Lange	SRON National Institute for Space Research, Groningen, Netherland	P1-16, TH3-4
De Rossi	Thales Research and Technology, Orsay, France	P2-12
Degardin	Universités Paris 6 et 11, SUPELEC, Labo Génie Electrique Paris, Gyf/Yvette, France	P1-15
Delorme	Observatoire de Paris, LERMA, Paris, France	P1-09
Demaison	Université de Lille 1, Laboratoire Ph. L. A. M., Lille, France	P2-27
Demyk	Université de Lille 1, Laboratoire Ph. L. A. M., Lille, France	FR3-1
Dengler	California Institute of Technology, Jet Propulsion Laboratory, Pasadena, CA, USA	FR1-1
Dentinger	Sandia National Laboratories, Albuquerque, USA	TH1-2
Derdall	Herzberg Institute of Astrophysics, National Research Council, Victoria, Canada	TH2-4
Désert	CNRS Grenoble, France	P1-02
Dhillon	Université Denis Diderot, Paris VII, Matériaux et Phénomènes Quantiques, Paris, France & Thales Research and Technology, Orsay, France	P2-12
Dieleman	SRON Netherland Institute for Space Research, Groningen, Netherland	TH3-4
Dindo	Herzberg Institute of Astrophysics, National Research Council, Victoria, Canada	TH2-4
Dochev	Chalmers University of Technology, Onsala Space Observatory, Göteborg, Sweden	TH2-1
Drakinskiy	Chalmers University of Technology, Microwave Electronic Laboratory & Microtechnology/ Nanoscience, Göteborg, Sweden	P1-07, P1-08, P1-09, TH3-7
Drouin	California Institute of Technology, Jet Propulsion Laboratory, Pasadena, CA, USA	P1-03
Dufour	Université Paris 7, Laboratoire AstroParticule et Cosmology, Paris, France	WE2-6
Duncan	Herzberg Institute of Astrophysics, National Research Council, Victoria, Canada	TH2-4

Durant	CNRS Grenoble, France	P1-02
Eggen	SRON National Institute for Space Research, Groningen, Netherland	P1-16
Eisele	University of Leeds, Institute of Microwaves and Phototonics, Leeds, UK	TH4-4
El Fatimy	Université Montpellier II, UMR 5650 CNRS, Montpellier, France	P2-08
Ellison	Rutherford Appleton Laboratory, Chilton, UK	TH2-3
Emrich	Omnisys Instruments, Göteborg, Sweden	P2-25
Endo	National Astronomical Observatory of Japan, Tokyo, Japan	P1-18
Erickson D.	Herzberg Institute of Astrophysics, National Research Council, Victoria, Canada	TH2-4
Erickson N.	University of Massachussets, Astronomy Department, Amherst, USA	FR1-3
Ermakov	Institute of Radio Engineering and Electronics, Moscow, Russia	FR3-3
Febvre	Université de Savoie, LHAC, Campus scientifique, Le Bouget du Lac, France	P1-23
Ferrari	Institute for Microelectronics Electromagnetism and Photonics, Grenoble, FRANCE	TH1-4
Filipenko	Institute of Radio Engineering and Electronics, Russia	FR3-3
Finkel	Moscow State Pedagogical University, Moscow, Russia	TH3-1
Fischetti	University of Massachussets, Department of Electrical and Computer Engineering, Amherst, USA	TH1-1
Fontana	Institut de Radio Astronomie Millimétrique, St. Martin d'Herès, France	TH2-3
Foulon	Université de Lille 1, Lille, France	TH1-3
Frunzio	Yale University, Department of Applied Physics, New Haven, USA	P1-06
Gao	Delft University of Technology, Kavli Institute of NanoScience, Delft, & SRON Netherland Institute for Space Research, Utrecht, Netherland	P1-05, P1-12, TH3-4, TH3-6, TH4-2, FR2-1, FR3-6
Gaquièr	IEMN-DHS URM CNRS 8250 Villeneuve d'Ascq, France	P2-08
Garcia	Herzberg Institute of Astrophysics National Research Council, Victoria, Canada	TH2-4
Gensheimer	University of Arizona, Steward Observatory Radio Astronomy Laboratory, Tucson, USA	FR2-4
Gerecht	National Institute of Standards and Technology, Boulder, USA	P1-11, FR2-3
Gerolfsma	SRON - Groningen, Netherland	WE1-4
Gershenson	Rutgers University, Piscataway, New Jersey, USA	WE2-1
Gill	California Institute of Technology, Jet Propulsion Laboratory, Pasadena, CA, USA	FR1-1, P2-05
Giraud-Héraud	Université Paris 7 - Laboratoire AstroParticule et Cosmology, Paris, France	WE2-6
Glenn	Universität zu Köln, Physikalisches Institut, Köln, Germany	P1-20
Glowacka	MRAO, Cambridge, U.K	WE2-5

Goeller	University of Massachusetts, Astronomy Department, Amherst, USA	FR1-3
Gol'tsman	Moscow State Pedagogical University, Moscow, Russia	P1-04, P1-05, P1-12, WE2-3, TH3-1, TH3-6
Goldie	MRAO, Cambridge, U.K	WE2-5
Goldsmith	California Institute of Technology, Jet Propulsion Laboratory, Pasadena, CA, USA	FR1-2
Golish	University of Arizona, Steward Observatory, Tucson, USA	P2-11, FR2-4
Golstein	SRON National Institute for Space Research, Groningen, Netherland	P1-16
Goy	AB Millimetre, Paris, France	P2-22, FR3-2
Graf	Universität zu Köln, Physikalisches Institut, Köln, Germany	FR3-4
Grajal	Universidad Politecnica de Madrid, Sistemas y Radiocommunicación, Madrid, Spain	P2-03, P2-04
Grimes	University of Oxford, Department of Astrophysics, Oxford, UK	P1-19, WE2-5, P2-24
Grishina	Moscow State Pedagogical University, Moscow, Russia	TH3-6
Groppi	University of Arizona, Steward Observatory, Tucson, USA	P1-06, P2-11, FR2-4
Gross	AB Millimetre, Paris, France	P2-22, FR3-2
Gu	National Institute of Standards and Technology, Boulder, USA	P1-11, FR2-3
Guillaud	IRAM, Grenoble, France	P2-19
Guillet	Observatoire de Paris, LERMA, Paris, France	P1-09
Gulevich	Loughborough University, Department of Physics, Loughborough, UK	P1-22
Hajenius	Delft University of Technology, Kavli Institute of NanoScience, Delft, Netherland	P1-05, P1-12, TH3-4, TH3-6, FR3-6
Halpern	University of British Columbia, Vancouver, Canada	WE2-5
Hameau	Ecole Normale Supérieure, Laboratoire Pierre Aigrain, Paris, France	P2-14
Harnett	Harvard-Smithsonian Center for Astrophysics, Cambridge, MA, USA	P2-29
Hedden	University of Arizona, Steward Observatory, Tucson, USA	P1-06, P2-11, FR2-4
Henke	Chalmers University of Technology, Onsala Space Observatory, Göteborg, Sweden	TH2-1, TH2-4
Hesler	Virginia Diodes, Inc., Charlottesville, VA, USA	TH4-6
Hesper	SRON National Institute for Space Research, Groningen, Netherland	P1-17, P2-23
Heyminck	Max Planck Institut für Radioastronomie, Bonn, Germany	TH2-2
Highstrete	Sandia National Laboratories, Albuquerque, CA, USA	TH1-2
Hoovers	SRON Netherland Institute for Space Research, Utrecht, Netherland	FR2-1
Honingh	Universität zu Köln, Physikalisches Institut, KOSMA, Köln, Germany	P1-20, WE1-3, TH3-3, FR3-4

Hoogeveen	NISR, Earth Oriented Science Division, Groningen, Netherland	FR3-3
Hovenier	Delft University of Technology, Kavli Institute of Nanoscience, Delft, Netherland & SRON Netherland Institute for Space Research, Utrecht, Netherland	TH4-2, FR2-1, FR3-6
Hu	Massachusetts Institute of Technology, Cambridge, MA, USA	TH4-1, TH4-2, P2-11, FR3-6
Hübers	DLR, Institute of Planetary Research, Berlin, Germany	P1-08, P1-10, P2-10, FR3-5
Huggard	Rutherford Appleton Laboratory, Chilton, UK	TH2-3
Hunter R.I.	University of St Andrews, Millimetre Wave and High Field ESR Group, St Andrews, Scotland	P2-22, FR3-2
Hunter T.R.	Harvard Smithsonian Center for Astrophysics, Cambridge, MA, USA	TH4-3
Iizuka	National Astronomical Observatory of Japan, National Institutes of Natural Sciences, japan	TH2-6
IL'in	University of Karlsruhe, Institute of Micro- and Nanoelectronic Systems, Karlsruhe, Germany	P1-10
Irwin	National Institute of Standards and Technology, Boulder, USA	WE2-5
Ito	National Astronomical Observatory of Japan, National Institutes of Natural Sciences, japan	TH2-5, TH2-6
Jackson	SRON National Institute for Space Research, Groningen, Netherland	P1-16, P1-17
Jacobs	Universität zu Köln, I.Physikalisches institut, KOSMA, Köln, Germany	P1-20, WE1-3, TH3-3, FR3-4
Jacobsson	Food Radar Systems AB, Göteborg, Sweden	P2-16
Jacquet	LMOPS Supélec, Metz, France	P2-13
Jellema	SRON, Groningen, Netherland	P2-07
Jiang F.	Herzberg Institute of Astrophysics, National Research Council, Victoria, Canada	TH2-4
Jiang L.	Purple Mountain Observatory, NAOC, CAS, China	P1-04
Johnson	Oxford University, Department of Astrophysics, Oxford, UK	WE2-5
Jones F.E.	Sandia National Laboratories, Albuquerque, CA, USA	TH1-2
Jones G.	California Institute of Technology, Pasadena, CA, USA	FR2-4
Justen	Universität zu Köln, I.Physikalisches institut, KOSMA, Köln, Germany	P1-20, WE1-3
Kamba	National Astronomical Observatory of Japan, National Institutes of Natural Sciences, japan	TH2-5, TH2-6
Kamikura	University of Tokyo, Department of Astronomy School of Science & National Astronomical Observatory of Japan, National Institutes of Natural Sciences, Japan	TH2-5, TH2-6
Kamoua	Stony Brook University, Department of Electrical and Computer Engineering, Stony Brook, USA	TH4-4
Karasik	California Institute of Technology, Jet Propulsion Laboratory, Pasadena, CA, USA	P1-03, WE2-1
Karpov	California Institute of Technology, Pasadena, CA, USA	WE1-5
Kasalynas	Delft University of Technology, Kavli Institute of Nanoscience, Delft, Netherland	TH4-2
Kaurova	Moscow State Pedagogical University, Moscow, Russia	P1-04, WE2-3, TH3-1

Kawamura	California Institute of Technology, Jet Propulsion Laboratory, Pasadena, CA, USA	WE2-1
Kerr	National Radio Astronomy Observatory, Charlottesville, USA	WE1-1
Khosropanah	Chalmers University of Technology, Microwave Electronic Laboratory & Microtechnology/ Nanoscience, Göteborg, Sweden	P1-09, TH3-7
Kikken	SRON National Institute for Space Research, Groningen, Netherland	P1-16
Kimberk	Harvard Smithsonian Center for Astrophysics, Cambridge, MA, USA	TH4-3
Kittara	Mahidol University, Mathematical Physics Research Group, Thailand.	P1-19
Kjellberg	Omnisys Instruments, Göteborg, Sweden	P2-25
Klaassen	Delft University of Technology, Kavli Institute of Nanoscience, Delft, Netherland	TH4-2
Klapwijk	Delft University of Technology, Department of Applied Physics & Kavli Institute of NanoScience, Delft, Netherland - SRON Netherland Institute for Space Research, Utrecht, Netherland	P1-05, P1-12, P1-16, P1-17, TH3-4, TH3-6, FR2-1, FR3-6
Klasmann	University of Manchester, School of Electrical and Electronic Engineering, Manchester, UK	P2-06
Knapp	Université Montpellier II, UMR 5650 CNRS, Montpellier, France	P2-08
Köhler	NEST CNR-INFN and Scuola Normale Superiore, PISA, Italy	P2-10, FR3-5
Kooi	California Institute of Technology, Pasadena, CA, USA	WE1-4, TH3-4, FR2-4
Kornberg	Max-Planck-Institute for extraterrestrial Physics, Garching, Germany	P2-19
Korotetskaya	Moscow State Pedagogical University, Moscow, Russia	TH3-1
Koryukin	Russian Academy of Sciences, Institute of Radio Engineering and Electronics, Moscow, Russia	P1-18
Koschurinov	Nizhny Novgorod State University, Radiophysics department, Russia	P2-07
Koshelets	Russian Academy of Sciences, Institute of Radio Engineering and Electronics, Moscow, Russia	FR3-3
Kovalenko	Russian Academy of Sciences, Institute of Radio Engineering and Electronics, Moscow, Russia	WE2-2
Krebs	IRAM, Grenoble, France	P2-19
Kreisler	Universités Paris 6 et 11, SUPELEC, Laboratoire Génie Electrique Paris, Gyf/Yvette, France	P1-15
Krieg	Observatoire de Paris, LERMA, Paris, France	P1-07, P1-08
Kroug	Delft University of Technology, Department of Applied Physics, Delft, Netherland	P1-16
Krozer	Orsted-DTU Technical University of Denmark, Lyngby (Denmark)	P2-03
Krus	Omnisys Instruments, Göteborg, Sweden	P2-25
Kuiper	California Institute of Technology, Jet Propulsion Laboratory, Pasadena, CA, USA	FR2-4
Kulesa	University of Arizona, Tucson, USA	FR2-4
Kumar	Massachusetts Institute of Technology, Cambridge MA & Sandia National Laboratories, Albuquerque, USA	TH4-2, FR3-6
Kusmartsev	Loughborough University, Department of Physics, Loughborough, UK	P1-22

Kuzmin	Chalmers University of Technology, Göteborg, Sweden	TH3-5
Laauwen	SRON National Institute for Space Research, Groningen, NL	P1-16
Lambeth	National Radio Astronomy Observatory, Charlottesville, USA	WE1-1
Lampin	Institut d'Electronique de Microelectronique et de Nanotechnologie, UMR CNRS 8520, Villeneuve d'Ascq, France	P2-09
Lane	Harvard-Smithsonian Center for Astrophysics, Cambridge, MA, USA	P2-29
Lasenby	MRAO, Cambridge, U.K	WE2-5
Lauria	Arizona Radio Observatory, Tucson, USA	WE1-1
Lazareff	Institut de Radio Astronomie Millimétrique, St. Martin d'Herès, France	TH2-3
Leckie	Herzberg Institute of Astrophysics, National Research Council, Victoria, Canada	TH2-4
Leduc	California Institute of Technology, Jet Propulsion Laboratory, Pasadena, CA, USA	P1-03, WE1-5
Lee	Sandia National Laboratories, Albuquerque, USA	TH1-2
Li	Purple Mountain Observatory, NAOC, CAS, China	P1-04
Lichtenberger	University of Virginia, Charles L. Brown Department of Electrical and Computer Engineering & Microfabrication Laboratory, Charlottesville, USA	WE1-1, TH2-4, FR2-2, FR2-4
Lin	Purple Mountain Observatory, NAOC, CAS, China	P1-04
Lippens	Université de Lille 1, Lille, France	TH1-3
Liu	University of Virginia, Charles L. Brown Department of Electrical and Computer Engineering, Charlottesville, USA	FR2-2
Lodewijk	Delft University of Technology, Kavli Institute of Nanoscience, Delft, Netherland	P1-17, WE1-4
Loehr	Harvard-Smithsonian Center for Astrophysics, Cambridge, MA, USA	P2-29
Loudkov	Delft University of Technology, Kavli Institute for Nanoscience, Delft, Netherland60	P1-17
Loukitch	INSA de Rouen, Laboratoire de Mathématique, Mont-Saint-Aignan, France	P1-24
Lyons	University of Virginia, Microfabrication Laboratory, Charlottesville, USA	WE1-1
Maestrini	Observatoire de Paris, LERMA, Paris, France	P2-02, P2-05
Mahler	NEST CNR-INFEM and Scuola Normale Superiore, PISA, Italy	P2-10, FR3-5
Mangency	Université Paris 11, UMR CNRS 8622, Orsay, France	P2-09
Mani	California Institute of Technology, Pasadena, CA, USA	FR2-4
Martin	Composite Mirror Applications, Tucson, USA	P2-17, P2-18
Masi	University La Sapienza, Roma, Italy	WE2-6
Maslennikov	Moscow State Pedagogical University, Moscow, Russia	TH3-1
Matheson	Rutherford Appleton Laboratory, Space Science Technology dept., Chilton Didcot, UK	P2-01

Matsunaga	National Astronomical Observatory of Japan, ALMA-J Project Office, Japan	P1-18
Matsuo	Advanced Technology Center, National Astro Observatory of Japan, Tokyo, Japan	WE2-4
Mattiozzo	IRAM, Grenoble, France	P2-19
Mauskopf	Cardiff University, Cardiff, Wales, UK	WE2-3
McGrath	California Institute of Technology, Jet Propulsion Laboratory, Pasadena, CA, USA	WE2-1
Mehdi	California Institute of Technology, Jet Propulsion Laboratory, Pasadena, CA, USA	FR1-1, FR1-2, P2-05
Mena	SRON, Groningen, Netherland	WE1-4, P1-17
Merkel	Chalmers University of Technology, MC2, Microwave Electronic Laboratory, Göteborg, Sweden	P1-01, P1-13, TH3-8, P2-16
Miao	Purple Mountain Observatory, NAOC, CAS, China	P1-04
Miller	California Institute of Technology, Pasadena, CA, USA	WE1-5
Milne	University of Manchester, School of Electrical and Electronic Engineering, Manchester, UK	TH4-5
Minaeva	Moscow State Pedagogical University, Moscow, Russia	WE2-3
Monje	Chalmers University of Technology, Göteborg, Sweden	TH2-1
Morozov	Cardiff University, Cardiff, Wales, UK & Moscow State Pedagogical University, Moscow, Russia	WE2-3
Muñoz	Universität zu Köln, KOSMA, I.Physikalisches Institut, Köln, Germany	TH3-3, FR3-4
Murk	University of Bern, Institute of Applied Physics, Bern, Switzerland	WE1-3, P2-20, FR3-3
Murphy	National University of Ireland, Maynooth, Ireland	P2-23
Narayanan	University of Massachusetts, Astronomy Department, Amherst, USA	FR1-3, FR2-4
Navarrini	University of California, Radio Astronomy Laboratory, Berkeley, CA, USA	P1-21, TH1-4, TH2-3
Nicholson	University of Massachusetts, Department of Electrical and Computer Engineering, Amherst, MA, USA	P1-11, TH1-1
Nikola	Cornell University, Department of Astronomy, USA	P2-29
Niranjanan	Herzberg Institute of Astrophysics, National Research Council, Victoria, Canada	TH2-4
Noguchi	National Astronomical Observatory of Japan, National Institutes of Natural Sciences, Japan	P1-18, TH2-6
Noroozian	Delft University of Technology, Kavli Institute of Nanoscience, Delft, Netherland	P1-17
North	University of Oxford, Department of Astrophysics, Oxford, UK	P2-24
Nouvel	Université Montpellier II, CEM2, UMR 5507 CNRS, Montpellier, France	P2-13
Nyström	Chalmers University of Technology, Göteborg, Sweden	P2-28
Oberst	Cornell University, Department of Astronomy, USA	P2-29
Olaya	Rutgers University, New Jersey, USA	WE2-1

Olbrich	Universität zu Köln, I.Physikalisches Institut, Köln, Germany	FR3-4
Ondo	Université Montpellier II, CEM2, UMR 5507 CNRS, Montpellier, France	P2-13
Orlov	Institute for Physics of Microstructures, Nizhny Novgorod, Russia	P2-08
Palermo	Université Montpellier II, CEM2, UMR 5507 CNRS, Montpellier, France	P2-13
Pan	National Radio Astronomy Observatory, Charlottesville, USA	TH2-4
Pantaleev	Chalmers University of Technology, Göteborg, Sweden	P2-28
Pardo	Departamento de Astrofísica molecular e infrarroja, Madrid, Spain	P2-26
Parshley	Cornell University, Department of Astronomy, USA	P2-29
Paveliev	Nizhny Novgorod State University, Radiophysics department, Russia	P2-07
Pavlov	DLR, German Aerospace Center, Berlin, Germany	P1-10, P2-10, FR3-5
Pavolotsky	Chalmers University of Technology, Göteborg, Sweden	TH2-1
Pearson	California Institute of Technology, Jet Propulsion Laboratory, Pasadena, CA, USA	P1-03
Peralta	California Institute of Technology, Jet Propulsion Laboratory, Pasadena, CA, USA	FR1-1
Pereverzev	Rutgers University, New Jersey, USA	WE2-1
Peroz	Universités Paris 6 et 11, SUPELEC, Laboratoire Génie Electrique Paris, Gyf/Yvette, France	P1-15
Pfleger	Herzberg Institute of Astrophysics, National Research Council, Victoria, Canada	TH2-4
Piat	Université Paris 7, Laboratoire AstroParticule et Cosmology, Paris, France	WE2-6
Piccirillo	University of Cardiff, Cardiff, UK	WE2-5
Pieters	SRON National Institute for Space Research, Groningen, Netherland	P1-16
Pisano	University of Cardiff, Cardiff, UK	WE2-5
Plambeck	University of California, Radio Astronomy Laboratory, Berkeley, CA, USA	P1-21
Poglitsch	Max-Planck-Institute for extraterrestrial Physics, Garching, Germany	P2-19
Polenta	University La Sapienza, Roma, Italy	WE2-6
Polyakov	Moscow State Pedagogical University, Moscow, Russia	TH3-1
Pons	LAAS, Toulouse, France	P1-08
Porterfield	Virginia Diodes, Inc., Charlottesville, VA, USA	TH4-6
Prober	Yale University, Department of Applied Physics, New Haven, USA	P1-06
Pütz	University of Arizona, Steward Observatory, Tucson, USA & Universität zu Köln, KOSMA, I. Physikalisches Institut, Köln, Germany	WE1-3, P1-06, P1-20, P2-11, P2-20, FR2-4
Rauly	CNRS Grenoble, France	P1-02

Readhead	California Institute of Technology, Department of Astronomy, Pasadena, CA, USA	FR1-2
Reese	Yale University, Department of Applied Physics, New Haven, USA	P1-06
Reno	Sandia National Laboratories, Albuquerque, USA	TH4-2, P2-11, FR3-6
Rettenbacher	Universität zu Köln, I.Physikalisches Institut, Köln, Germany	FR3-4
Rice	California Institute of Technology, Pasadena, CA, USA	WE1-5
Richter	DLR, German Aerospace Center, Berlin, Germany	P1-10, P2-10, FR3-5
Ritchie	University of Cambridge, Cavendish Laboratory, Cambridge, UK	P2-10, P2-12, FR3-5
Robertson	University of St Andrews, Department of Physics & Astronomy, St Andrews, Scotland, UK	P2-22
Robinson	Sandia National Laboratories, Albuquerque, USA	TH1-2
Rodrigues G.	Herzberg Institute of Astrophysics National Research Council, Victoria, Canada	TH2-4
Rodriguez-Morales F.	University of Massachusetts, Department of Electrical and Computer Engineering, Amherst, MA, USA	P1-11, TH1-1, FR2-3
Rollin	University of Bath, Department of Physics, Bath, UK	P2-02
Romeo	Composite Mirror Applications, Tucson, USA	P2-17, P2-18
Saeedkia	University of Waterloo, Department of electrical and Computer Engineering, Waterloo, CA, USA	P2-15
Safavi-Naeini	University of Waterloo, Department of electrical and Computer Engineering, Waterloo, CA, USA	P2-15
Salez	Observatoire de Paris, LERMA, Paris, France	P1-24
Santaviceca	Yale University, Department of Applied Physics, New Haven, USA	P1-06
Satou	National Astronomical Observatory of Japan, National Institutes of Natural Sciences, Japan	TH2-5, TH2-6
Schaeffer	University of Groningen, SRON National Institute for Space Research, Groningen, Netherland	P1-17
Scherer	IRAM, Grenoble, France	P1-14
Schicke	IRAM, Grenoble, France	P1-14, TH1-4
Schlecht	California Institute of Technology, Jet Propulsion Laboratory, Pasadena, CA, USA	FR1-1
Schmidt	Universität zu Köln, I.Physikalisches Institut, Köln, Germany	FR3-4
Schmülling	Universität zu Köln, I.Physikalisches Institut, Köln, Germany	FR3-4
Schrag	Munich University of Technology, Institute for Physics of Electrotechnology, Munich, Germany	TH1-4
Schultz	Universität zu Köln, I.Physikalisches Institut, Köln, Germany	P1-20
Schuster	IRAM, Grenoble, France	P1-14, TH1-4, P2-19
Sekimoto	University of Tokyo, Department of Astronomy School of Science & National Astronomical Observatory of Japan, National Institutes of Natural Sciences, Japan	TH2-5, TH2-6
Seleznev	Moscow State Pedagogical University, Moscow, Russia	WE2-3

Seliuta	Semiconductor Physics Institute, Vilnius, Lithuania	P2-08
Semenov	DLR, German Aerospace Center & Institute of Planetary Research, Berlin, Germany	P1-08, P1-10, P2-10, FR3-5
Serabyn	Division of Physics, Mathematics and Astronomy, Pasadena, CA, USA	P2-26
Sergeev	Buffalo University, State University of New York, Buffalo, USA	WE2-1
Serizawa	University of Tokyo, Department of Astronomy, School of Science, Tokyo, Japan	TH2-5, TH2-6
Shan	Purple Mountain Observatory, Chinese Academy of Sciences, China & National Astronomical Observatory of Japan, National Institutes of Natural Sciences, Japan	TH2-5, TH2-6
Shaner	Sandia National Laboratories, Albuquerque, USA	TH1-2
Shechetov	IEMN DHS URM CNRS 8250 , Villeneuve d'Ascq, France	P2-08
Shechetov	IEMN-DHS URM CNRS 8250 Villeneuve d'Ascq, France	P2-08
Shi	Purple Mountain Observatory, NAOC, CAS, China	P1-04
Shitov	National Astronomical Observatory of Japan, Tokyo, Japan & Institute of Radio Engineering and Electronics, Russian Academy of Sciences, Moscow, Russia	P1-18
Siebertz	Universität zu Köln, I.Physikalisches Institut, Köln, Germany	FR3-4
Siegel M.	University of Karlsruhe, Institute of Micro- and Nanoelectronic Systems, Karlsruhe, Germany	P1-10
Siegel P.H.	California Institute of Technology, Jet Propulsion Laboratory, Pasadena, CA, USA	FR1-1, FR1-2
Siles	Universidad Politecnica de Madrid, Sistemas y Radiocommun., Madrid, Spain	P2-03, P2-04
Sirtori	Université Denis Diderot, Paris VII, Matériaux et Phénomènes Quantiques, Paris, France & Thales Research and Technology, Orsay, France	P2-12
Skalare	California Institute of Technology, Jet Propulsion Laboratory, Pasadena, CA, USA	TH3-2
Sloan	University of Manchester, School of Electrical and Electronic Engineering, Manchester, UK	P2-06
Smirnov	Moscow State Pedagogical University, Moscow, Russia	TH3-1
Smit	SRON National Institute for Space Research, Groningen, Netherland	P1-16
Smith	University of St Andrews, Millimetre Wave and High Field ESR Group & Department of Physics and Astronomy, St Andrews, Scotland	P2-22, FR3-2
Stacey	Cornell University, Department of Astronomy, Cornwell, USA	P2-29
Stark	Harvard-Smithsonian Center for Astrophysics, Cambridge, MA, USA	P2-29
Stern	California Institute of Technology, Jet Propulsion Laboratory, Pasadena, CA, USA	WE1-5, TH3-2
Stevenson	MRAO, Cambridge, U.K	WE2-5
Stutzki	Universität zu Köln, I.Physikalisches Institut, Köln, Germany	FR3-4
Suttiwong	DLR, Institute for Remote Sensing Technology, Germany	FR3-3
Svechnikov	Moscow State Pedagogical University, Moscow, Russia	P1-04, TH3-1
Szeto	Herzberg Institute of Astrophysics, National Research Council, Victoria, Canada	TH2-4

Talin	Sandia National Laboratories, Albuquerque, USA	TH1-2
Tamura	National Astronomical Observatory of Japan, Tokyo, Japan	P1-18
Teipen	Universität zu Köln, I.Physikalisches Institut, Köln, Germany	P1-20
Tepe	Université Montpellier II, UMR 5650 CNRS, Montpellier, France	P2-08
Tharkov	Moscow State Pedagogical University, Moscow, Russia	WE2-3
Thomas	Rutherford Appleton Laboratory, Space Science Technology department, Chilton Didcot, UK	P2-01, P2-02
Thual	FOTON, UMR 6082 CNRS - ENSSAT, Lannion, France	P2-13
Tichelaar	Delft University of Technology, Kavli Institute of NanoScience, Delft, Netherland	TH3-6
Tignon	Laboratoire Pierre Aigrain, Ecole Normale Supérieure, Paris, France	P2-14
Tils	Universität zu Köln, I.Physikalisches Institut, KOSMA, Köln, Germany	P1-20, WE1-3, P2-20
Tomimura	University of Tokyo, Department of Astronomy School of Science & National Astronomical Observatory of Japan, National Institutes of Natural Sciences, Japan	TH2-6
Tong	Harvard Smithsonian Center for Astrophysics, Cambridge, MA, USA	WE1-2, TH4-3
Torres	Université Montpellier II, CEM2, UMR 5507 CNRS, Montpellier, France	P2-13
Tothill	Harvard Smithsonian Center for Astrophysics, Cambridge, MA, USA	P2-29
Trappe	National University of Ireland, Maynooth, Ireland	P2-23
Tredicucci	NEST CNR-INFM and Scuola Normale Superiore, PISA, Italy	P2-10, FR3-5
Tripon-Canseliet	Université Pierre et Marie Curie-LISIF	P2-05
Truscott	University of Manchester, School of Electrical and Electronic Engineering, Manchester, UK	TH4-5, P2-06
Tsaneva	MRAO, Cambridge, U.K	WE2-5
Tucker	Cardiff University, Cardiff, UK	P2-29
Ueda	National Astronomical Observatory of Japan, National Institutes of Natural Sciences, Japan	TH2-5
Ustinov	Ioffe Physico-Technical Institute, St.Petersburg, Russia	P2-07
Uvarov	Institute of Radio Engineering and Electronics, Russian Academy of Sciences, Moscow, Russia	P1-18
Uzawa	National Astronomical Observatory of Japan, Tokyo, Japan	P1-18
Vachtomin	Moscow State Pedagogical University, Moscow, Russia	P1-04, TH3-1
Valusis	Semiconductor Physics Institute, Vilnius, Lithuania	P2-08
Van Nguyen	SRON National Institute for Space Research, Groningen, Netherland	P1-16
Vassilev	Chalmers University of Technology, Göteborg, Sweden	TH2-1, P2-28
Villégier	CEA, Laboratoire de Cryophysique, Grenoble, France	P1-15

Voos	Ecole Normale Supérieure, Laboratoire Pierre Aigrain, Paris, France	P2-14
Voronov	Moscow State Pedagogical University, Moscow, Russia	P1-04, P1-05, P1-12, WE2-3, TH3-1, TH3-6
Vowinkel	Universität zu Köln, I.Physikalisches Institut, Köln, Germany	FR3-4
Vystavkin	Institute of Radio Engineering and Electronics, Russian Academy of Sciences, Moscow, Russia	WE2-2
Wadefalk	California Institute of Technology, Pasadena, CA, USA & Chalmers University of Technology, Göteborg, Sweden	P1-11, FR2-4
Wagner	DLR, Institute for Remote Sensing Technology, Germany	FR3-3
Walker	University of Arizona, Steward Observatory, Tucson, USA	P1-06, P2-11, FR2-4
Wang	Observatoire de Paris, LERMA, Paris, France	P2-02
Ward	California Institute of Technology, Jet Propulsion Laboratory, Pasadena, CA, USA	P2-05, P2-21, FR1-2
Wei	Rutgers University, New Jersey, USA	WE2-1
Weikle	University of Virginia, Charles L. Brown Department of Electrical and Computer Engineering, Charlottesville, USA	FR2-2
Weinreb	California Institute of Technology, Jet Propulsion Laboratory, Pasadena, CA, USA	FR2-4
Welle	Herzberg Institute of Astrophysics National Research Council, Victoria, Canada	TH2-4
Wen	Moscow State Pedagogical University, Moscow, Russia	TH3-1
Wiedner	Universität zu Köln, I.Physikalisches Institut, Köln, Germany	P2-26, FR3-4
Wild	SRON - Groningen, Netherland	WE1-4
Williams	Massachusetts Institute of Technology, Cambridge, USA	TH4-2, P2-11, FR3-6
Withington	University of Cambridge, Cavendish Laboratory, Cambridge, UK	P1-19, WE2-5, FR1-4
Wittmann	Munich University of Technology, Institute for Physics of Electrotechnology, Munich, Germany	TH1-4
Wood	Herzberg Institute of Astrophysics, National Research Council, Victoria, Canada	TH2-4
Xiao	University of Virginia, Department of Physics, Charlottesville, USA	FR2-2
Xu	University of Virginia, Department of Physics, Charlottesville, USA	FR2-2
Yagoubov	SRON National Institute for Space Research, Groningen, Netherland	FR3-3
Yang	Delft University of Technology, Kavli Institute of NanoScience, Delft, Netherland	P1-05
Yao	Purple Mountain Observatory, NAOC, CAS, China	P1-04
Yarekha	Université de Lille 1, Lille, France	TH1-3
Yassin	University of Oxford, Department of Astrophysics, Oxford, UK	P1-19, WE2-5, P2-24
Yeung	Herzberg Institute of Astrophysics, National Research Council, Victoria, Canada	TH2-4
Yngvesson	University of Massachusetts, Department of Electrical and Computer Engineering, Amherst, MA, USA	P1-11, TH1-1, FR2-3

Zannoni	University of Massachusetts, Department of Electrical and Computer Engineering, Amherst, MA, USA	P1-11, TH1-1
Zao	Ecole Normale Supérieure, Laboratoire Pierre Aigrain, Paris, France	P2-14
Zhang	Purple Mountain Observatory, NAOC, CAS, China	P1-04
Zhukov	Ioffe Physico-Technical Institute, St.Petersburg, Russia	P2-07
Zijlstra	Delft University of Technology, Department of Applied Physics & Kavli Institute for Nanoscience, Delft, Netherland	P1-16, P1-17
Ziurys	Arizona Radio Observatory, Tucson, USA	WE1-1
Zmuidzinas	California Institute of Technology, Pasadena, CA, USA	WE1-5
Zöpfl	Munich University of Technology, Institute for Physics of Electrotechnology, Munich, Germany	TH1-4
Zorman	Case Western Reserve University, Ohio, USA	TH3-6

